University of Denver
Digital Commons @ DU

Electronic Theses and Dissertations | Graduate Studies

1-1-2012

The Effect of Atmospheric Aging on a Hybrid Polymer Matrix Composites' Material Properties

Brian Michael Burks
University of Denver

Follow this and additional works at: https://digitalcommons.du.edu/etd

Recommended Citation

Burks, Brian Michael, "The Effect of Atmospheric Aging on a Hybrid Polymer Matrix Composites' Material Properties" (2012). *Electronic Theses and Dissertations*. 771.
https://digitalcommons.du.edu/etd/771

This Dissertation is brought to you for free and open access by the Graduate Studies at Digital Commons @ DU. It has been accepted for inclusion in Electronic Theses and Dissertations by an authorized administrator of Digital Commons @ DU. For more information, please contact jennifer.cox@du.edu,dig-commons@du.edu.

THE EFFECT OF ATMOSPHERIC AGING ON A HYBRID POLYMER MATRIX COMPOSITES' MATERIAL PROPERTIES

A Dissertation

Presented to

the Faculty of Engineering and Computer Science

University of Denver

In Partial Fulfillment

of the Requirements for the Degree

Doctor of Philosophy

---

by

Brian Burks

June 2012

Advisor: Dr. Maciej Kumosa

© Copyright by Brian M. Burks 2012

All Rights Reserved

Author: Brian Burks
Title: THE EFFECT OF ATMOSPHERIC AGING ON A HYBRID POLYMER MATRIX COMPOSITES' MATERIAL PROPERTIES
Advisor: Dr. Maciej Kumosa
Degree Date: June 2012

ABSTRACT

Mechanical failure modes associated with elevated temperature exposure of the load bearing unidirectional hybrid composite (based upon glass and carbon fibers reinforcing a high temperature epoxy matrix) of a next generation transmission line design were investigated in this research. In particular, the flexural performance (in both static and fatigue loading) of the composite which had been exposed to elevated temperatures for prolonged periods of time was studied. To this end, a fatigue test was developed in an attempt to simulate the multi-axial loading conditions present on transmission lines. This test was used to evaluate the fatigue behavior of unaged specimens, as well as the evolution of fatigue performance of aged specimens. Furthermore, a four point loading configuration was used to assess the effect that aging had on the static flexure strength of the hybrid composite.

It was found that the magnitude in static and fatigue material property reduction increased with aging time, and was dictated by which aging mechanism was dominant. Microstructural changes revealed that the modest reduction in mechanical properties at intermediate aging times was predominantly attributed to thermal oxidation, while for longer aging times physical aging was the primary cause for the substantial reduction.

Finite element models were developed to quantify a newly discovered stiffening phenomenon observed in the composite subjected to fatigue. A mesh morphing scheme

was developed to account for the scatter in the stiffening phenomenon due to the inherent geometric variability of the carbon fiber composite. In addition, 3-dimensional viscoelastic representative volume element finite element models were developed to understand the damage mechanisms of the hybrid composite system.

Finally, the utility of waveform based broadband acoustic emission was explored to identify the types of damage which were occurring within the hybrid composite, as well as which material a particular mechanism originated from. To demonstrate the method as a potential in-service nondestructive evaluation technique, explicit dynamic finite element models simulating the 3 most common composite failure mechanisms (i.e. matrix cracking, fiber/matrix delamination, and fiber fracture) were developed. Based upon the spectral content of the simulated signals, a damage classification scheme based upon the method of Partial Powers was developed. The efficacy of the methodology was validated using waveforms captured during the quasi-static flexure testing of aged hybrid composite rods.

Acknowledgements

The author would first like to thank the Western Area Power Administration (WAPA), Tri-State Generation and Transmission, and the Bonneville Power Administration (BPA) for their financial support of this research, as well as the positive interactions had with them during the process of this research. In particular, the author is grateful to Mr. Ross Clark, Mr. Allen Turner, Mr. Art Mander, Mr. Steve Anderson, and Mr. Mike Staats.

The author is also incredibly grateful to Dr. Maciej Kumosa for his guidance throughout this process. Without his guidance, and support this research would not have been possible. In addition, the author would like to acknowledge Dr. Paul Predecki, Dr. Peter Laz, Dr. Paul Rullkoetter, and Dr. Marvin Hamstad for their guidance and discussion on various aspects of this research. Without those discussions this work would not have been as successful. Thanks also go to Dr. Suraj Rawal, Dr. Yun-Bo Yi, and Dr. Richard Ball for their participation as members of the Dissertation committee.

Finally, the author wishes to thank his family for all of their love and support during this process. Thanks also go to Ms. Amber Gerard for her patience, love, and encouragement throughout this process.

Table of Contents

List of Tables

List of Figures

1. INTRODUCTION

1.1 Growing energy demand

Over the past few decades energy consumption has increased in the United States of America (NERC 2008), as well as globally (EIA 2010). The North American Energy Reliability Corporation (NERC) predicts that by the year 2017, US energy demand will have increased 7.1% from 2007 levels (NERC 2008). From a global perspective, the US Energy Information Administration (EIA), forecasts that global energy consumption will rise from 495 quadrillion British Thermal Units (btus) in the year 2007 to 739 quadrillion btus in the year 2035 (EIA 2010). If accurate, this would represent a staggering 49% increase in energy consumption in less than 3 decades.

Two obvious issues arise from such growth in energy consumption. First, the ability to generate such amounts of energy becomes problematic. Much work has been, and continues to be, done towards reducing mankind's dependency on fossil fuels through the development of renewable energy sources such as wind energy, photovoltaics, and alternative fuels. The second issue, and motivating factor behind this dissertation, is the ability to safely and reliably transmit this increased amount of energy to consumers. Current high voltage electric transmission grids are not equipped to handle such an increase in demand (Lerner 2003).

The limitation to power transmission originates from the design of the existing transmission lines, and the fact that these lines must be thermally restricted as to not violate sag clearances (EPRI 2002). To aid in improving the dated electric grid the White House is prepared to offer $250 million in loans to rural utility companies, and work with utilities to invest in new power technologies as of June 2011 (Vastag 2011). The necessity for such commitment from the US government stems from the fact that the existing transmission line design has been in place for nearly a century. US Energy Secretary Steven Chu proclaimed in June 2011 that,

> *"(19th-century electricity pioneer Thomas Edison) would feel right at home with most of today's power… system. We do need a modernized electric grid."(Vastag 2011).*

1.2 A solution for the constrained grid

The most common transmission line found in operation today is known as the Aluminum Conducting Steel Reinforced (ACSR) design (Figure 1.1). The ACSR design is based upon a stranded steel core, wrapped in strands of work-hardened 1350-H19 Al. Because steel and aluminum have relatively large coefficients of thermal expansion, the operating temperature of the ACSR design must be restricted to ~100 °C to avoid violating established sag clearances (EPRI 2002). Limiting the operating temperature of the line restricts the amount of energy that can be transmitted by the ACSR design. An obvious solution would be to construct more transmission lines.

Figure 1.1 An example of the Aluminum Conducting Steel Reinforced (ACSR) design with the stranded steel inner core (small diameter wires), wrapped in the conductive 1350-H19 Al (larger diameter wires).

Unfortunately, building more transmission lines is often not a viable solution for two reasons. First, obtaining new right-of-ways is frequently met with resistance from the general public and almost always becomes cost prohibitive (EPRI 2002). Secondly,

building a new transmission line requires the construction of the associated structures to support the line, which are costly as well (EPRI 2002).

As a potential solution to the shortcomings of the ACSR design a few companies have turned to polymer matrix composite (PMC) materials, and designed a transmission line with a composite load bearing core. An example of this type of transmission line comes in the form of the Aluminum Conducting Composite Core Trapezoidal Wire (ACCC/TW^{TM}, henceforth referred to as the ACCC design for brevity) design, which is produced by the Composite Technology Corporation (CTC) (Figure 1.2). There are variations of this type of transmission line produced by other manufacturers (e.g. – Mercury Cable, and Nexxans), but as the ACCC design was the most commercially deployed design at the time this dissertation work was being undertaken, it was the composite that was investigated.

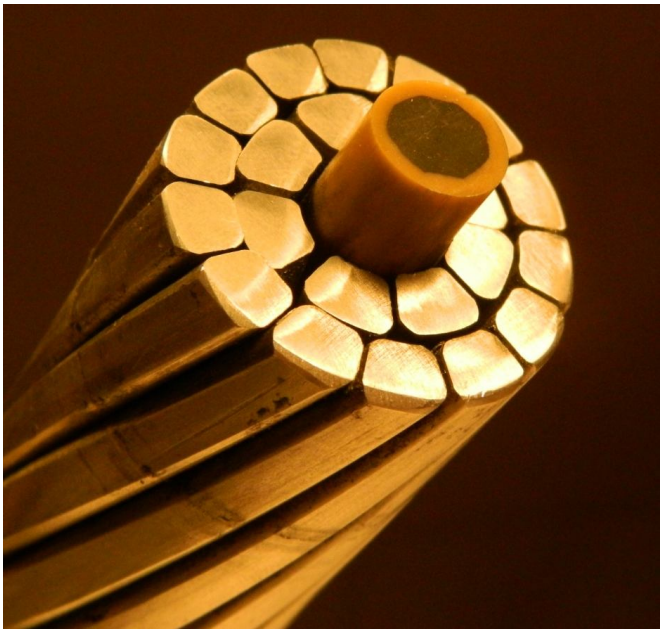

Figure 1.2 The Aluminum Conducting Composite Core Trapezoidal Wire (ACCC/TW^{TM}) design.

The load bearing core of the ACCC design is a hybrid polymer matrix composite material. The inner composite (black material in Figure 1.2) is comprised of unidirectional high strength carbon fibers embedded within a high temperature epoxy matrix (hereafter referred to as the CFC). Surrounding the CFC is a sheath of unidirectional Electrically Corrosion Resistant (ECR) glass fibers embedded in the same high temperature epoxy (tan material in Figure 1.2, henceforth referred to as the GFC). The conductive member of the ACCC design is strands of trapezoidal 1350-O' Al wire.

Advantages that the ACCC design offers are numerous. By incorporating carbon fibers into the ACCC design, the issue of line sag at elevated temperatures is mitigated. Carbon fibers have an axial coefficient of thermal expansion (CTE) that is negative (Hull and Clyne 1996), which results in significantly reduced sag at elevated temperatures in comparison to the ACSR conductor. Additionally, unidirectional carbon fiber composites are often a perfectly elastic material, thus, the transmission line will retain its' initial tensioning sag after thermal cycling and ice loading, to a far greater extent than the ACSR design. Because of the plasticity of steel and aluminum, the ACSR conductor will not fully recover its' initial sag if a substantial overloading event were to occur. From this perspective, the probability of sag clearances being violated by the ACCC design is substantially less than for the ACSR design as the transmission line ages.

Another benefit of utilizing carbon fibers is the superior tensile strength that is offered; the ACCC core has a tensile strength of 2400 MPa (Alawar, Bosze and Nutt 2005). The ability to tension the ACCC design to greater values (while still maintaining appropriate factors of safety) enables the number of structures for a given transmission

line to be reduced. By reducing the number of necessary structures, the potential for an economic incentive could be realized with the ACCC design.

Since the composite core in the ACCC design is less dense than the traditional steel core, ~28% more aluminum per line foot can be included while still matching the linear weight of ACSR conductors (Alawar, Bosze and Nutt 2005). This manifested itself in the form of the trapezoidal wire design, as opposed to the traditional circular wire design. Using trapezoidal wires for a conductor results in greater current carrying capacity when compared to round wire conductors, for equivalent outer diameter conductors. Also, because of the impressive tensile strength of the ACCC core, the aluminum does not need to provide much in the way of structural support. Hence, a high purity 1350 O'-tempered fully annealed aluminum is used in the ACCC design, which has a greater conductivity than the work hardened 1350 H-19 aluminum of the conventional ACSR design, allowing for better conduction with less line loss (Alawar, Bosze and Nutt 2005).

The final advantage that the ACCC conductor offers is the capability of being operated at higher temperatures than the ACSR design. Because of the polymer matrix, most designers limit the operating temperature of ACCC lines to that of the glass transition temperature (T_g) of the polymer (typically with some factor of safety). This appears a valid approach, as polymers will act rubbery and begin to lose mechanical properties at temperatures above the glass transition temperature. The value of T_g for the ACCC composite has been disputed in the literature, with values ranging from 187 °C (EPRI 2010) to 225 °C (Barjasteh, Kar and Nutt 2011). As will be discussed later, the

manner in which T_g is measured can have a substantial effect on the value, with certain techniques resulting in more conservative values than others.

While the benefits of the ACCC design are substantial, there are associated disadvantages that arise from the new technology. The first of which, is simply that the technology is new, with the implication being that the designs' limitations are presently not well understood. Moreover, this is not the high voltage electric power transmission industries first experience with polymer matrix composites. In the early 1990's ceramic insulators began to be replaced by E-glass reinforced composite insulators. In-service failures of composite insulators led to hesitancy within the power transmission industry to use composite materials. The failures led to significant research efforts, from which it was discovered that the in-service failures were a result of stress corrosion cracking from nitric acid attack (Chugtai, Smith and Kumosa 1998). Further research was done, from which it was learned that ECR glass fibers were far more resistant to stress corrosion cracking than E glass fibers, resulting in the subsequent successful implementation of composite insulators (Kumosa, Armentrout and Kumosa 2001). The manufacturers of the ACCC design were well-read in the issue of stress corrosion cracking of E glass composites, causing them to use ECR glass fibers in the new conductor design.

Finally, the most daunting drawback of the ACCC design is the fact that it is based upon a polymer. In general, polymers are known to age at significantly accelerated rates in comparison to metals at equivalent temperatures (Struik 1978). Also, the rate at which polymers' age is known to increase with increasing temperature (Struik 1978). Hence, the ability for the ACCC design to be operated at elevated temperatures without

sagging brings into question the longevity of the hybrid composite material. The hesitancy on the part of utility companies stems from wanting to know for how long, and at what temperature can the ACCC design be safely and reliably operated; by no means a trivial inquisition. Table 1.1 provides a brief summary of the advantages and disadvantages of the ACCC design.

Table 1.1 Summary of advantages and disadvantages of new hybrid polymer composite material core transmission lines.

Advantage		**Disadvantage**	
Property	**Manifestation**	**Property**	**Manifestation**
CF negative CTE	Reduced sag at elevated temperature operation.	New Technology	Misunderstood. Limits unknown.
High Tensile Strength	Greater line tensions, less structures. Fully annealed Al (more conductivity).	Previous poor experience with PMCs	Lack of trust in PMCs. Hesitancy to use PMCs in a non-redundant system.
Hybrid composite density	More aluminum, increased ampacity.	Accelerated Aging	Presently unknown. Feeds into hesitancy to use technology.

1.3 Scope of work

In light of the preceding discussion, the long-term failure modes associated with elevated temperature exposure of the load bearing hybrid composites of these next generation transmission lines were investigated. In section 1.2 the concept of elevated temperature operation causing polymer aging was introduced. As will be shown in Chapter 2, the literature is abundant on the topic of polymer aging, with a few studies evaluating its' effects on static material properties, but remains void on the subsequent effect that aging has on the fatigue performance of polymer matrix composites.

Thus, the evolution of flexural performance (in both static and fatigue loading) of the hybrid composite which had been exposed to elevated temperatures for prolonged periods of time was investigated in this work. To this end, a fatigue test was developed in an attempt to simulate the multi-axial loading conditions present on transmission lines. This test was used to study the fatigue behavior of unaged specimens, and then subsequently the evolution of fatigue performance of aged specimens. Additionally, a four point loading configuration was used to evaluate the effect that aging had on the static flexure strength of the hybrid composite.

Finite element models were developed to quantify an interesting stiffening phenomena observed in the unaged composite specimens, and a mesh morphing technique was developed to account for the inherent geometric variability in the hybrid composite. 3-dimensional viscoelastic representative volume element finite element models were also developed to understand the interesting failure mechanisms of the hybrid composite system.

Finally, it was believed that the use of waveform based broadband acoustic emission could identify the types of damage that were occurring within the hybrid composite, as well as which material the particular mechanisms were occurring in. To substantiate such a claim, explicit dynamic finite element models simulating the 3 most common composite failure mechanisms (i.e. - matrix cracking, fiber/matrix delamination, and fiber fracture) were developed. Based upon the spectral content of the signals, a damage classification scheme based upon the method of Partial Powers was developed. The efficacy of the aforementioned methodology was validated using waveforms captured during the quasi-static flexure testing of aged hybrid composite rods.

2. BACKGROUND

2.1 Literature review

2.1.1 Aeolian vibration

One of the most common detrimental long-term loading conditions to high voltage electric transmission lines is a type of wind induced conductor motion known as Aeolian vibration (EPRI 2009). Aeolian vibrations of transmission lines are most prone to occur in open, flat terrain that is free of obstructions, in the presence of a steady cross-wind with a velocity between 1 and 7 m/s (EPRI 2009). Vortex shedding of a bare or uniformly iced conductor generates a periodic forcing function that results in transverse motion of the conductor. Non-uniform or unbalanced icing most often results in a different type of conductor motion known as galloping (EPRI 2009), which generates a type of loading beyond the scope of this work. Transverse motions caused by Aeolian vibration generally occur at frequencies between 3 and 150 Hz, with an amplitude on the order of one conductor diameter (EPRI 2009).

Fatigue failure of traditional ACSR conductors generally occurs at suspension clamps (EPRI 2009). Ramey, Brunair, and Duncan attributed this to the fact that the state of stress at a suspension clamp is affected by six sources; they identified the six sources as : 1) axial tension from "sagging the line in," 2) static bending due to the weight of the line, 3) dynamic bending from the Aeolian vibrations, 4) bearing stress from the compression

fitting, 5) tension from line extension due to thermal expansion, and 6) inter-strand bearing from the conductors' tension (Ramey, Brunair and Duncan 1988). Typically only sources 1-3 are considered in the fatigue analysis; sources 5 and 6 are extremely small in comparison, and source 4 is compressive in nature and is often neglected for the conventional metallic structures.

Several researchers have experimentally studied Aeolian vibration motion of electric transmission lines, and the resulting dynamic bending stresses that are the result. Ramey and Townsend used the application of foil strain gages to characterize the effect of clamp geometry on static and dynamic bending stress near a suspension clamp (Ramey and Townsend 1981). Ramey, Brunair, and Duncan later implemented a Miner's Law relationship to develop a damage accumulation approach to fatigue design of ACSR transmission lines (Ramey, Brunair and Duncan 1988). Claren and Diana used displacement pick-up transducers to characterize the state of strain near a suspension clamp due to simulated Aeolian vibration motion (Claren and Diana 1969).

Others have used analytic methods in an attempt to predict the magnitude of the dynamic bending stress amplitudes due to Aeolian vibration events. A broadly accepted method for analytically predicting the magnitude of Aeolian vibrations comes from the "Power-Balance" method (Kraus and Hagedron 1991). The method is essentially a conservation of power approach, stating that the input power provided by the wind energy must be equivalent to the power dissipated by the conductor from both self-damping mechanisms, as well as installed damping devices (EPRI 2009). The initial analytic approach to the calculation of idealized dynamic bending stress amplitude

predictions came from Poffenberger and Swart, in which they considered the conductor to behave like an ideal cantilevered beam under tension with a forced transverse deflection (Poffenberger and Swart 1965). This approach has been widely accepted in the power transmission industry for over the past forty years (EPRI 2009). In addition to their experimental work, Claren and Diana also proposed modeling Aeolian vibration motion of conductors as a taught homogeneous string subjected to transverse motion (Claren and Diana 1969). Verma and Hagedorn developed an approach similar to the power balance method to consider the strain distribution along a line with objects located in the span (Verma and Hagerdon 2005). Recently, Sinha and Hagedorn extended this approach to predict the relative magnitude of dynamic bending stresses at splice locations along a transmission line (Sinha and Hagerdon 2007).

In keeping the aforementioned work in mind, an analytic model was developed in order to predict the magnitude of dynamic bending stress amplitudes within the hybrid composite material.

2.1.2 Aging of polymers, and polymer matrix composites

Aging of polymers and their associated composites encompasses several mechanisms (e.g. physical aging, chemical aging, UV exposure, hygrothermal aging, etc.). With the scope of the present work and the service environment of the hybrid composite core, we limit ourselves to the cases of thermal oxidation (chemical aging, or scission of polymer chains) and volumetric relaxation (physical aging, or loss of free volume). It is quite well known that polymers exposed to elevated temperatures (even in inert environments) experience mass loss (Akay and Spratt 2008), (Lowe, Fox and Otieno-Alego 2002),

(Schoeppner, Tandon and Ripberger 2007), and (Gentz, Benedikt, et al. 2004). The extent of mass loss has a proportional relationship with aging temperature, as well as aging environment. Accompanying mass loss is an associated loss in volume.

Leindert Struik provided, arguably, the most complete assessment of physical aging of neat resin polymers. Struik explained that generally polymers age at a significantly accelerated rate, in comparison to metals at equivalent temperatures (Struik 1978). This observation was explained from the fact that polymers at a temperature below their respective glass transition temperature (T_g) are not in a state of thermodynamic equilibrium. Consequently, polymers (below their T_g) have a finite amount of free volume, and as time progresses the associated free volume decreases (Struik 1978). Struik noted that as the aging temperature increased so too did the rate of volumetric relaxation (Struik 1978).

When considering the effect that physical aging of the polymer has on the composite material, volumetric relaxation is also important. Benedikt et al. and Gentz et al. showed for a unidirectional carbon fiber/PMR-15 composite, that as aging time and/or temperature increased (i.e. an increase in volumetric relaxation) so too did the state of stress within the matrix material (Benedikt, et al. 2004), (Gentz, Benedikt, et al. 2004). Additionally, through micro-mechanics modeling they showed that the fiber packing arrangement had an effect on the predicted stress state within the matrix material as a function of aging time (Gentz, Benedikt, et al. 2004).

When polymers are exposed to temperatures near their T_g in non-inert environments, thermo-oxidation has been shown to attack the surface and degrade several polymers

through chemical aging. Wolfrum, Eibl, and Lietch studied the thermo-oxidative behavior of two commonly available carbon fiber reinforced, epoxy matrix composites. They concluded that thermal oxidation of the cross-linked epoxy mers resulted in the formation of aliphatic oxygen containing species, resulting in substantial fiber/matrix debonding, which diminished static inter-laminar shear strength (ILSS), tensile strength, and compressive strength (Wolfrum, Eibl and Lietch 2009). Lowe, Fox and Otieno-Alego studied the effect that thermal exposure had on the Mode I fracture toughness of double cantilever woven carbon fiber/bismaleimide composites (Lowe, Fox and Otieno-Alego 2002). They observed a moderate post-cure effect of fracture toughness initiation values at short aging times, and a substantial decrease in fracture toughness propagation values at longer aging times (Lowe, Fox and Otieno-Alego 2002). Interestingly, they found greater degradation in Mode I fracture toughness at a lower aging temperature; such conclusions go against intuition, as well as a vast majority of the established literature. Thus, the results of their study must be treated cautiously. Akay and Spratt studied a quite similar composite weave comprised of carbon fibers reinforcing a bismaleimide matrix. They found that mass loss, and reduction in ILSS was proportional to aging time and temperature (Akay and Spratt 2008).

Schoeppner, Tandon, and Ripberger studied the anisotropic aging behavior of carbon fiber/PMR-15 composites, and concluded that thermal oxidation penetrated to a far greater extent in the 0° direction of a composite as compared to the 90° direction (Schoeppner, Tandon and Ripberger 2007). Additionally, they concluded that aging environment, played a role in the mass loss and dimensional stability of the composite

(Schoeppner, Tandon and Ripberger 2007). Barjasteh et al. studied the thermo-oxidative behavior of the hybrid composite of the present study. They concluded that transverse thermal oxidation was a self-limiting process in which an oxide layer (~100 μm thick) was developed on the surface of the composite, which subsequently inhibited further oxygen ingress into the bulk of the composite (Barjatesh, et al. 2009). In their study, oxide layer thickness was measured via nano-hardness measurements through the thickness of the composite (Barjatesh, et al. 2009).

From the perspective of the current work, elevated temperature exposure in an atmospheric environment is expected to affect the hybrid composite material in two ways. Certainly, thermal oxidation is expected to affect the surface of the GFC as was shown by Barjasteh et al. Surface oxidation may then have an impact on the fatigue performance of the hybrid composite. Additionally, in light of Gentz et al. and Benedikt et al. work, physical aging for extended periods of time may adversely affect both the static and fatigue performance of the hybrid composite due to microstructural changes.

2.1.3 Fatigue of composites

A substantial amount of work has been done to characterize the fatigue performance of polymer matrix composite materials. Beaumont and Harris, Owen and Morris, Sturgeon, and Jones et al. have reported on the excellent performance of unidirectional carbon fiber composites in fatigue loading (Beaumont and Harris 1972), (Owen and Morris 1972), (Sturgeon 1975), and (Jones, et al. 1984). In axial tensile loading below the failure strain of carbon fiber composites the slope of the S-N curve is nearly horizontal, indicating superior fatigue performance (Beaumont and Harris 1972), (Owen

and Morris 1972). When the loading condition was changed to flexure, or incorporated a compressive stress during block sequence loading, the performance of the material was slightly diminished, and a so-called "endurance limit" was not as readily observed (Beaumont and Harris 1972), (Owen and Morris 1972), (Harris, Gathercole, et al. 1997), (Adam, et al. 1994). Glass fiber composites generally show good fatigue performance, but are less prone to exhibiting an "endurance limit" than carbon fiber composites at significantly lower stress amplitudes (Jones, et al. 1984), (Boller 1964).

Gathercole and coworkers investigated the effect of stress ratio (or "R ratio," where R $\equiv \sigma_{MIN}/\sigma_{MAX}$) for T800/5245 $[(\pm 45,0_2)_2]_S$ carbon fiber composite lay-ups. They found that a negative correlation existed between the stress-life slopes and R values (Gathercole, et al. 1994). They were able to reconcile the discrepancy by normalizing the peak stress with respect to either the tensile strength (for Tension/Tension R ratios), or the compressive strength (for Compression/Compression R ratios) (Gathercole, et al. 1994). Such data certainly highlight the fundamental difference in fatigue behavior of composite materials in comparison to metallic materials.

The difference in fatigue behavior of composite materials has often brought into question what defines fatigue failure for composite materials. For metallic materials, failure is generally associated with the growth of a flaw to either a critical size, or completely through a specimen (Stephens, et al. 2001). Alternatively, for composite materials Harris originally proposed the use of a damage parameter as a measure of fatigue failure (Harris 1977).

Since Harris' work, the definition of a damage parameter has taken on several connotations. A common means of quantifying the amount of damage that a composite has sustained that has been used in the literature is the degradation of stiffness. Dependent upon the type of testing, this has manifested itself as the reduction in load carrying capacity for constant displacement amplitude testing (Newaz 1985), a reduction in secant modulus of the load-extension curve for axial loading (Reifsnider and Jamison 1982), or Hwang's concept of a "fatigue modulus" (Hwang and Han 1986).

Due to the viscoelastic nature of polymer matrix composite materials, the hysteresis loop of stress-strain data (or load-displacement data) has also been used to quantify the amount of damage present. Towo and Ansell used hysteresis loops to study the fatigue behavior of sisal fiber reinforced composites under axial loading conditions; they observed a positive correlation with the area of the hysteresis and damage sustained by the composite (Towo and Ansell 2008). Kim and Ebert used information from hysteresis loops to show how dissipated energy changed during the occurrence of different failure mechanisms in unidirectional glass fiber composites subjected to flexural loading (Kim and Ebert 1981). However, Van Paepegem et al. have recently shown both experimentally and numerically that the area of the hysteresis loop in flexure loading was drastically affected by the contact conditions at the loading pins (i.e. – coefficient of friction between the sample and load pins) (Van Paepegem, et al. 2006). Their findings bring into question the appropriateness of hysteresis loop analysis when considering flexural fatigue.

Dickson et al. studied $[(\pm 45/0_2)_2]_S$ hybrid XAS carbon fibers and E-glass fibers reinforcing a 913 epoxy matrix. They concluded that static properties could be predicted by conventional hybrid models, but found a synergistic improvement in fatigue performance for the hybrid laminates from a strain-life perspective (Dickson, et al. 1989). Hofer et al. have reported similar findings on the improved fatigue performance of glass fiber/carbon fiber hybrid composite lay-ups (Hofer, Stander and Bennet 1978). Unfortunately, before the present work, the literature had only considered the fatigue behavior of laminated hybrid composite materials, and was absent of work that considered the fatigue performance of a bulk hybrid composite material.

A considerable amount of work has been done in identifying initial fatigue failure mechanisms of polymer matrix composite materials, with several authors reporting that fatigue damage within a polymer matrix composite material initiates as matrix cracking (Kaynak and Mat 2001), (Manjunatha, et al. 2010), (Lambert, et al. 2012), (Tanimoto and Amijima 1975), (Lafarie-Frenot, Henaff-Gardin and Gamby 2001). Kaynak and Mat studied the fatigue behavior of filament wound glass fiber/epoxy tubes, and found that fatigue damage initiated as matrix crazing, later propagating into saturation, as well as fiber/matrix debonding (Kaynak and Mat 2001). Manjunatha et al. investigated the fatigue performance of glass fiber/epoxy and glass fiber/hybrid-toughened epoxy $[(+45/-45/0/90)_S]_2$ composites, from which they concluded that initial failure commenced from matrix cracking within the ±45 plies (Manjunatha, et al. 2010). Lambert et al. studied the evolution of fatigue damage and the effect that voids had on $[+45/-45/0]_{3S}$ glass fiber/epoxy laminates during fatigue loading using computed tomography, concluding

that damage initiated as transverse matrix cracking originating from free edges (Lambert, et al. 2012). Furthermore, Tanimoto and Amijima found that fatigue damage initiated from matrix cracking in their study of glass fiber/polyester weaves (Tanimoto and Amijima 1975). Lafarie-Frenot, Henaff-Gardin, and Gamby also investigated the initiation of fatigue damage of several carbon fiber/epoxy composite laminates. Their study of several lay-up configurations concluded that fatigue damage always initiated as matrix cracking, subsequently propagating into fiber/matrix debonding, the extent to which was found to be dependent on the interfacial properties of the fiber and matrix (Lafarie-Frenot, Henaff-Gardin and Gamby 2001).

2.1.4 Representative volume element modeling

During fatigue testing of the hybrid composite material, a unique failure process was observed, which was in need of explanation. To address this issue, a representative volume element (RVE) approach was adopted. A representative volume element model (alternatively referred to as a unit cell) exploits the periodic nature of a material. In the case of unidirectional composites, periodicity is rampantly observed, enabling such a modeling technique.

RVEs have commonly been used in the literature to study the distribution of stresses within composite materials subjected to various mechanical and thermal loads. Bonora and Ruggiero used unit cell models to study the macroscopic response of unidirectional SiC/Ti-15-3 metal matrix composites (Bonora and Ruggiero 2006). Xia, Zhang, and Ellyin developed their so-called "unified periodical boundary condition," which eliminated the over constraint of other periodic boundary conditions in the presence of a

shear stress (Xia, Zhang and Ellyin 2003). Through the development of their boundary conditions, the effect of off-axis loading on laminates can now be accurately evaluated (Xia, Zhang and Ellyin 2003). Zhang, Xia, and Ellyin demonstrated the utility of their technique in modeling the damage progression of a laminate subjected to off-axis loading (Zhang, Xia and Ellyin 2005). Gentz et al. used an RVE approach to quantify the effect that physical aging of a composite material at elevated temperatures had on the residual stress within the matrix material (Gentz, Benedikt, et al. 2004).

A common issue with RVE modeling has been the application of appropriate boundary conditions. Aboudi developed a micromechanical theory based upon "homogeneous" boundary conditions (Aboudi 1991). However, several researchers have shown that the "planes remain planes" boundary conditions are over constraining when loading conditions other than normal surface tractions are considered (Sun and Vaidya 1996), (Neddleman and Tvergaard 1993), (Suquet 1987). Xia, Zhang, and Ellyin developed their "unified periodical boundary condition" that eliminated the over-constraint (Xia, Zhang and Ellyin 2003). For this reason, the boundary conditions of Xia were adopted for this dissertation.

Essentially, the "unified periodical boundary conditions" impose that the difference in nodal deformations on opposite faces of an RVE must be equal to a constant, that is to say

$$u_i^{+j} - u_i^{-j} = c_i^j \qquad i, j = x, y, z. \qquad (2.1)$$

Where u_i^j indicates the nodal displacement in the i^{th} degree of freedom on the j^{th} face, and c_i^j is a constant proportional to the normal deformations (when i = j), or the shear

deformation (when $i \neq j$) of the composite (Xia, Zhang and Ellyin 2003). The difference in sign on the j^{th} term of equation (3) refers to the pair of nodes on opposite faces (with otherwise equivalent coordinates) of the RVE.

2.2 Viscoelasticity

When considering the dependence that deformations of materials have with respect to time (or frequency), a few simple phenomenological models provide some key insight, but are of course limited. Models with greater complexity can be built that enable us to more appropriately capture the behavior of the material. With respect to the micro-mechanics of composite materials, such models are invaluable. Thus, we derive two of the simple models, and then provide the extension into considering multiple relaxation spectra which will be critical for implementation into finite element codes.

2.2.1 The Maxwell Model

One of the first attempts at explaining viscoelastic deformation was proposed by James Clerk Maxwell; his model is schematically depicted in Figure 2.1. The spring deforms in an elastic manner, and as such stress (σ_S) will be linearly related to strain (ε_S) through Young's modulus (E). The dashpot behaves in a Newtonian manner, and the stress within the dashpot (σ_D) is related to rate of strain ($d\varepsilon_D/dt$) through the viscosity (η).

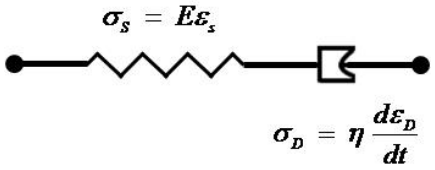

Figure 2.1 Representation of Maxwell's model to describe viscoelastic deformation.

From equilibrium considerations, the stress within each member must be equivalent

$$\sigma = \sigma_D = \sigma_S . \tag{2.2}$$

From compatibility of deformations, the strains in each member will be additive

$$\varepsilon = \varepsilon_D + \varepsilon_S . \tag{2.3}$$

Differentiating equation (2.3) with respect to time yields

$$\frac{d\varepsilon}{dt} = \frac{d\varepsilon_D}{dt} + \frac{d\varepsilon_S}{dt} = \frac{\sigma}{\eta} + \frac{1}{E}\frac{d\sigma}{dt}. \tag{2.4}$$

If we then consider stretching the material a fixed amount (ε) and holding it in that deformed position (noting that dε/dt = 0), equation (2.4) becomes

$$\frac{d\sigma}{dt} = \frac{E\sigma}{\eta}. \tag{2.5}$$

Separating variables, and integrating equation (2.5) from 0 to some arbitrary time t

$$\int_{\sigma_0}^{\sigma(t)} \frac{d\sigma}{\sigma} = -\frac{E}{\eta}\int_0^t dt. \tag{2.6}$$

The result becomes

$$\ln\left(\frac{\sigma(t)}{\sigma_0}\right) = -\frac{Et}{\eta}. \tag{2.7}$$

If we define the relaxation time (also referred to as the characteristic time) as $\tau = \eta/E$, equation (2.7) becomes

$$\sigma(t) = \sigma_0 \exp\left(-\frac{t}{\tau}\right). \tag{2.8}$$

Equation (2.8) is the so-called stress relaxation expression. The implication of the magnitude of τ on the ability of stresses to relax out of the material is shown in Figure 2.2. As the magnitude of τ increases (i.e. as viscosity increases, or stiffness decreases), it takes a longer amount of time for stress to relax out of the material.

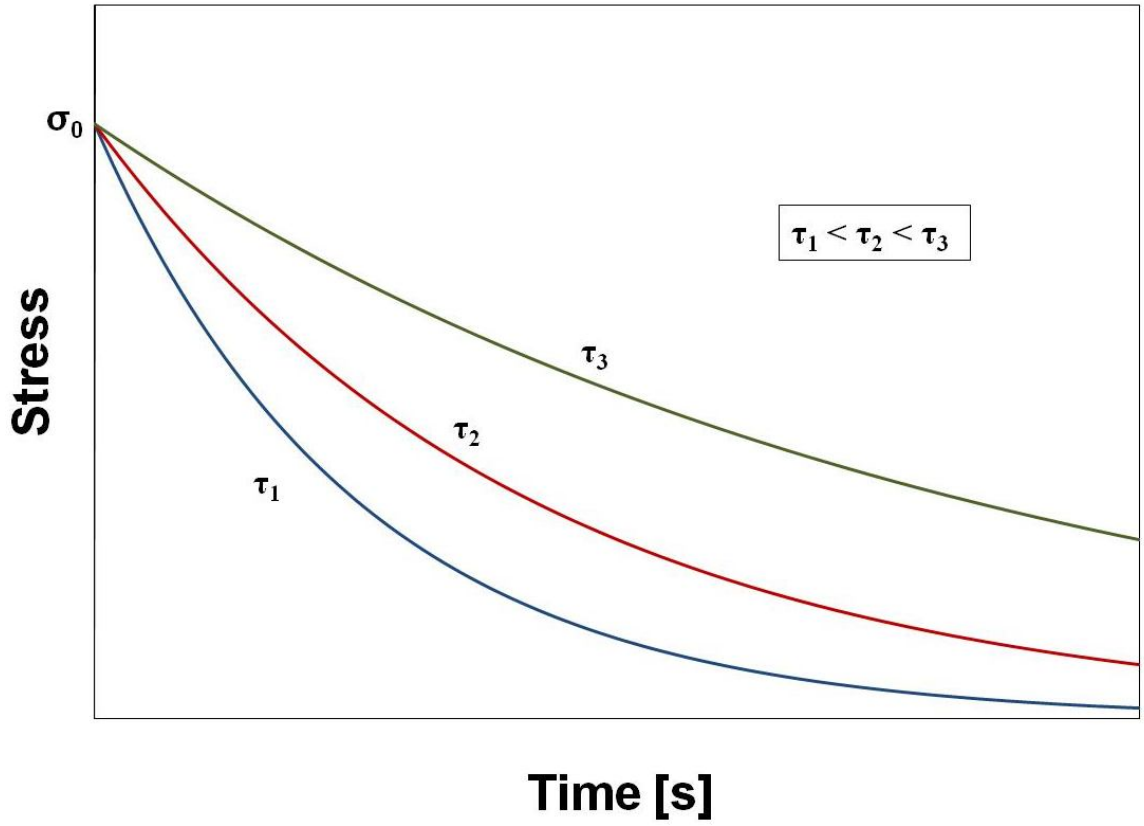

Figure 2.2 Stress response for the Maxwell model to an instantaneous strain, with various values of τ shown.

If instead of applying a known amount of strain to the material and holding it, as was the previous case, we applied an instantaneous stress (σ_0) to the Maxwell model and allowed the material to deform, integration of equation (2.4) would then become

$$\varepsilon(t) = t\frac{\sigma_0}{\eta} + \frac{\sigma_0}{E}. \qquad (2.9)$$

The implication becoming that strain is a linear function of time. If then at some time t_1 the stress were removed, the strain in the spring would be recovered immediately, but the strain in the dashpot would not be recovered

$$\varepsilon_{IRREVERSIBLE} = t_1 \frac{\sigma_0}{\eta}. \qquad (2.10)$$

The strain-time profile for the latter case is shown in Figure 2.3.

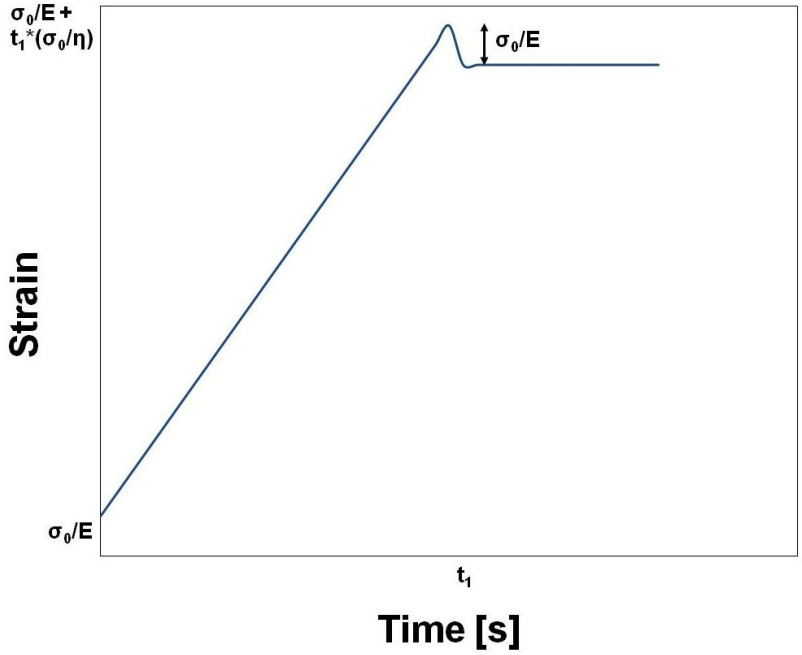

Figure 2.3 Strain response of the Maxwell model to an instantaneous stress, followed by a removal of the the stress at $t = t_1$.

It is seen that the material deforms in a linear fashion for $t < t_1$, at t_1 the elastic portion of strain is recovered, but the irreversible strain contribution of the dashpot is not recovered. The latter case highlights the deficiency of the Maxwell model in not being able to capture the experimentally observed phenomena of creep, nor recovery.

2.2.2 The Kelvin-Voigt Model

An alternative to the Maxwell model is the Kelvin-Voigt model which was proposed by Lord Kelvin and Woldemar Voigt, and is shown schematically in Figure 2.4.

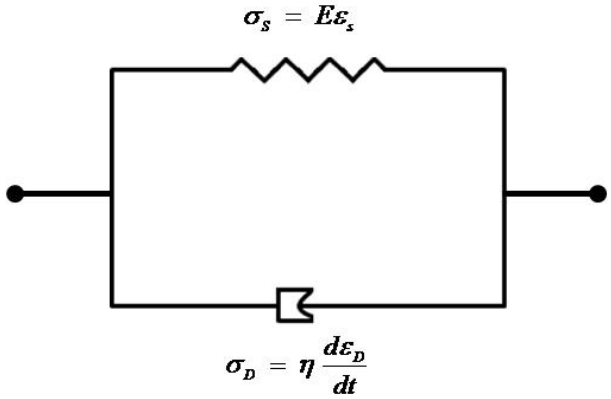

Figure 2.4 Representation of the Kelvin-Voigt model to describe viscoelastic deformation.

Since the spring and dashpot are connected in parallel in this configuration, the governing differential equation changes. From equilibrium considerations

$$\sigma = \sigma_S + \sigma_D . \tag{2.11}$$

And from compatibility of deformations it is known

$$\varepsilon = \varepsilon_S = \varepsilon_D . \tag{2.12}$$

If we then, define the compliance of the spring (D) as 1/E, and imagine applying an instantaneous stress (σ_0) to the material

$$\sigma(t) = \sigma_0 = E\varepsilon_S + \eta \frac{d\varepsilon_D}{dt} = E\varepsilon + \eta \frac{d\varepsilon}{dt} . \tag{2.13}$$

Rearranging equation (2.13)

$$\frac{d\varepsilon}{dt} = \frac{\sigma_0}{\eta} - \frac{E\varepsilon}{\eta} . \tag{2.14}$$

Once again using separation of variables, and integrating

$$\int_0^t dt = \int_0^{\varepsilon(t)} \frac{d\varepsilon}{\left(\frac{\sigma_0}{\eta} - \frac{E\varepsilon}{\eta}\right)} . \tag{2.15}$$

Using a standard look-up table, equation (2.15) evaluates to

$$t = -\frac{\eta}{E}\left[\ln\left(\frac{\sigma_0}{\eta} - \frac{E\varepsilon(t)}{\eta}\right) - \ln\left(\frac{\sigma_o}{\eta}\right)\right]. \tag{2.16}$$

After some algebra, and rearrangement of equation (2.16) the result yields

$$\varepsilon(t) = \frac{\sigma_0}{E} - \frac{\sigma_0}{E}\exp\left(-\frac{Et}{\eta}\right). \tag{2.17}$$

Simplification yields

$$\varepsilon(t) = \frac{\sigma_0}{E}\left[1 - \exp\left(-\frac{t}{\tau}\right)\right]. \tag{2.18}$$

In looking at a plot of strain vs. time, it is clear that the Kelvin-Voigt model adequately describes the phenomenon of creep (Figure 2.5). As time progresses towards t_1, there is not an instantaneous jump in strain as there was in the Maxwell model, but rather the material gradually approaches the total elastic strain in the limit as $t \rightarrow \infty$.

If instead of leaving the stress on, and letting $t \rightarrow \infty$, we were to remove the stress at some time t_1, equation (2.13) becomes

$$\eta\frac{d\varepsilon}{dt} + E\varepsilon = \sigma(t) = 0. \tag{2.19}$$

The first order homogeneous differential equation with constant coefficients has a solution of the form

$$\varepsilon(t) = \frac{\exp\left(-\frac{t}{\tau}\right)}{E}\int \exp\left(\frac{t}{\tau}\right)\sigma(t)dt + c\exp\left(-\frac{t}{\tau}\right) \tag{2.20}$$

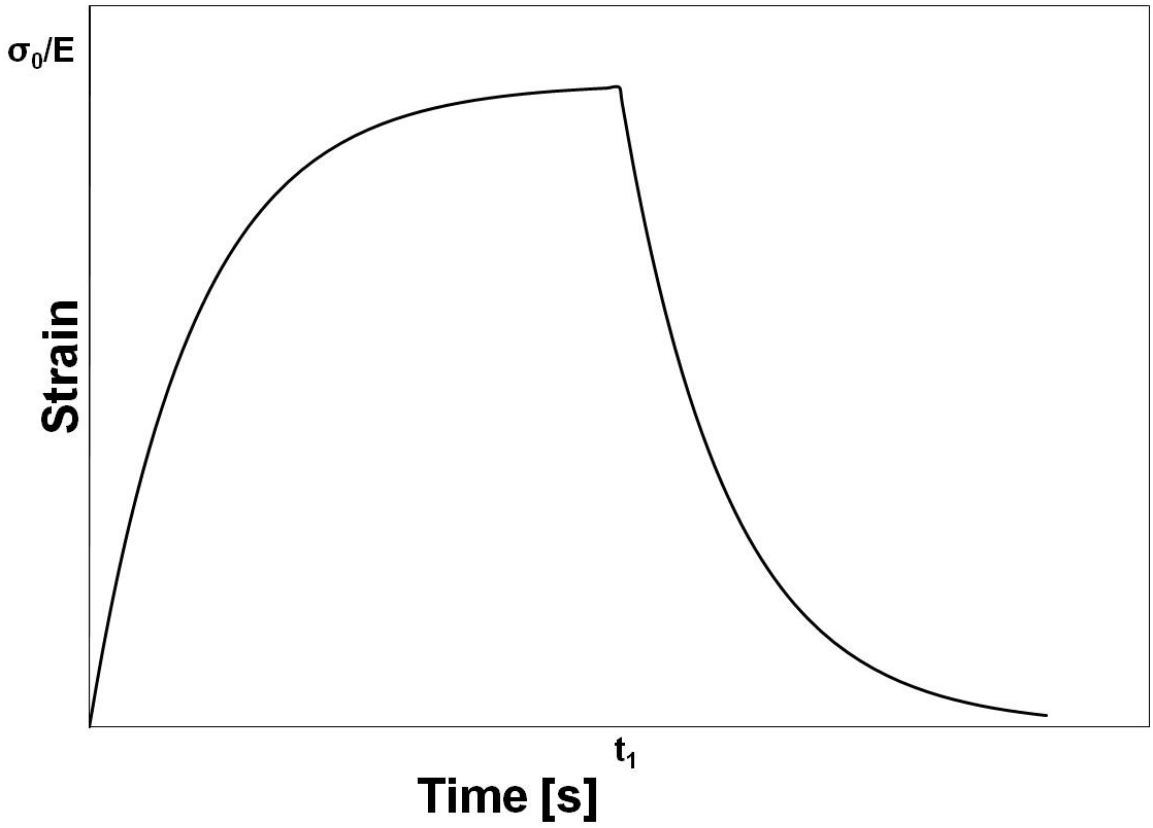

Figure 2.5 Response of the Kelvin-Voigt model to an instantaneous stress.

in which, c is a constant to be determined from the initial conditions. Noting $\sigma(t_1) = 0$, the result yields

$$\varepsilon(t) = c \exp\left(-\frac{t}{\tau}\right). \tag{2.21}$$

Using the calculated value of strain at t_1 from equation (2.18) allows the determination of c

$$c = \frac{\sigma_0}{E}\left[\exp\left(\frac{t}{\tau}\right) - 1\right]. \tag{2.22}$$

Thus, upon the removal of the stress σ_0 at time t_1, the strain response of the Kelvin-Voigt model is

$$\varepsilon(t) = \left[\frac{\sigma_0}{E}\left(\exp\left(\frac{t_1}{\tau}\right) - 1\right)\right]\exp\left(-\frac{t}{\tau}\right). \tag{2.23}$$

This response is shown in Figure 2.5, after time t_1. It can be seen that strain decreases in an exponential fashion with time, but does not exhibit initial elastic recovery of strain upon removal of the applied stress.

Finally, if we were to imagine applying a fixed strain (ε_0) to the material, and left the material in the deformed configuration (noting $d\varepsilon/dt = 0$), equation (2.13) becomes

$$\sigma(t) = \frac{\varepsilon_0}{D} = E\varepsilon_0. \tag{2.24}$$

The consequence of equation (2.24) is that the Kelvin-Voigt model predicts that stress will remain constant with time. Thus, the Kelvin-Voigt model is capable of exhibiting the creep phenomenon and to a first order is capable of exhibiting recovery, but remains inadequate in capturing the stress relaxation.

2.2.3 Generalizations of viscoelastic models

As has been shown in the previous sections, the Maxwell model quite nicely captures the effect of stress relaxation, but is inadequate in describing creep and recovery. Conversely, the Kelvin-Voigt model is able to express the creep phenomena and to a first approximation recovery, but is not able to exhibit stress relaxation. To reconcile the issue, several other models have been proposed, such as the standard linear solid (the Zener model), or the Burger model. These models are combinations of springs and dashpots in series and parallel, from which the governing differential equations are written from considerations of equilibrium and continuity. Such models are adequate in reconciling the issues shown by the Maxwell and Kelvin-Voigt model.

However, as experimental observations of polymers have necessitated, it is quite often that not a single relaxation mechanism occurs, but rather several relaxations occur. To account for multiple relaxations it has been customary to combine Maxwell models in parallel (shown in Figure 2.6). Such a model is referred to as a generalized Maxwell model. The advantage of this model is that is not limited to a single characteristic relaxation. For the generalized Maxwell model shown in Figure 2.6 the stresses in each element sum and the viscoelastic modulus may be defined as

$$E(t) = \sum_{i=1}^{N} E_i \exp\left(-\frac{t}{\tau_i}\right). \tag{2.25}$$

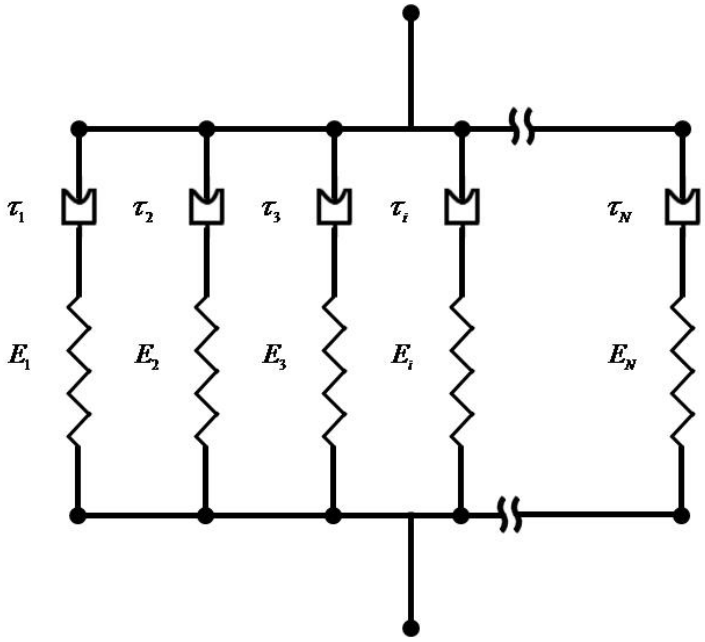

Figure 2.6 Representation of the generalized Maxwell model to describe viscoelastic deformation.

2.2.4 Concept of the storage and relaxation moduli

As an alternative to the long and tedious process of performing stress relaxation, or creep tests one may use Dynamic Mechanical Analysis, and obtain equivalent

information. As it turns out, the techniques are identical when recovered through a Fourier transform. For the purposes of this work, in which fatigue loading was of primary concern, the technique is arguably more applicable. To understand Dynamic Mechanical Analysis the concept of the storage and relaxation moduli must first be introduced. If a harmonically varying stress was applied to a viscoelastic material, the strain response of the system would lag the stress by an amount, δ (as shown in Figure 2.7).

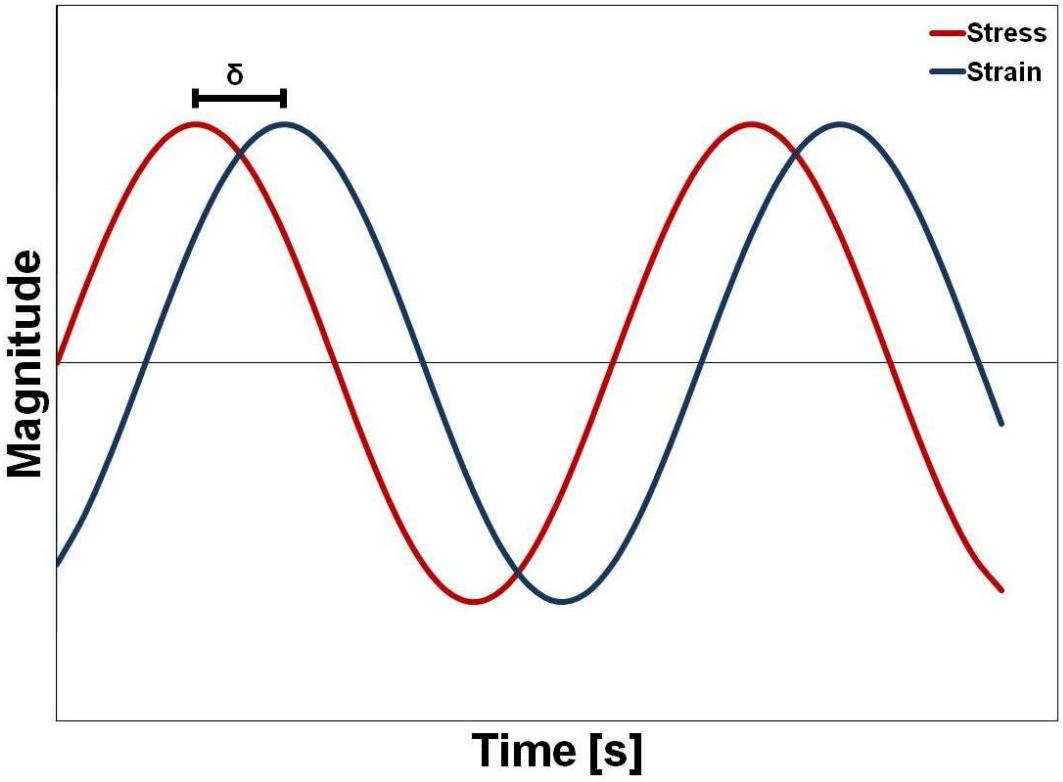

Figure 2.7 Viscoelastic material's response to a harmonically varying stress.

From such a response two quantities are defined, called the storage modulus and the relaxation modulus. The storage modulus (E_S) may be thought of as the in-phase response of strain to the applied stress, while the relaxation modulus (E_R) is the out-of-

phase response of strain to the applied stress. The storage modulus is associated with the amount of energy stored by the material, and is calculated by

$$E_S = E_0 \cos(\delta). \tag{2.26}$$

Similarly, the relaxation modulus is related to the amount of energy lost by the material, and is given by

$$E_R = E_0 \sin(\delta). \tag{2.27}$$

Finally, from the storage and relaxation moduli the complex modulus (E*) may be defined as

$$E^* = E_S + iE_R. \tag{2.28}$$

From equations (2.26 and 2.27) it then follows that

$$\tan(\delta) = \frac{E_R}{E_S}. \tag{2.29}$$

Hence, the term tan(δ) can often be thought of as the "lossiness" of the viscoelastic material. From the practical perspective of Dynamic Mechanical Analysis, we can quite easily apply a harmonically varying stress (or strain) to a material, and measure the corresponding response of strain (or stress). If this procedure were done over several decades of frequency (e.g. - 10^{-2} Hz to 10^{2} Hz), the corresponding relaxation times (i.e. - the τ_i of equation (2.25) in the time domain) of the material can be determined. In the frequency domain the storage modulus may be written as

$$E_S(\omega) = E_0\left[1 - \sum_{i=1}^{N} e_i\right] + E_0 \sum_{i=1}^{N} \frac{e_i \tau_i^2 \omega^2}{1 + \tau_i^2 \omega^2} \tag{2.30}$$

where E_0 is the instantaneous modulus, e_i is the i^{th} material constant, τ_i is the i^{th} relaxation time, ω is the angular frequency, and N is the number of terms to be used in the fit (Abaqus 2009). Likewise, the relaxation modulus in the frequency domain is given by

$$E_R(\omega) = E_0 \sum_{i=1}^{N} \frac{e_i \tau_i \omega}{1 + \tau_i^2 \omega^2} . \qquad (2.31)$$

Equations (2.30) and (2.31) are the so-called Prony series expansions for a viscoelastic material. These expansions are quite valuable in defining viscoelastic materials in commercial finite element software packages. In general, one takes data from a DMA test and then fits the experimental data with equation (2.30). To fit the experimental data, a few items are critical. First, equations (2.30) and (2.31) cannot be fit using linear least squares regression; a non-linear algorithm must be used, in this work an adaptation of the modified Levenberg-Marquardt algorithm was employed (Madsen, Nielsen and Tingleff 2004). Additionally, based upon the complexity of the polymer (i.e. – the number of characteristic relaxation times), an appropriate number of terms must be included in the Prony series to accurately represent the material response over the frequency range one wishes to characterize. Finally, for a unique solution to exist, if N terms are to be used in the Prony series expansion, there must be at least 2N+1 data points to fit.

2.3 Material property prediction for composite materials

For the development of valid predictive numeric models, accurate knowledge of the material properties is necessary. For composite materials, the issue is complicated by the inherent anisotropy of the material. Thus, one is left to the costly (and tedious) process of mechanically testing coupons to fully characterize all material properties. Unidirectional composite materials (the focus of this dissertation) have 5 independent material constants. To accurately characterize such materials, at least 3 specimen types would be necessary.

As an alternative to the costly procedure of mechanically testing the composite material, one may use models to predict the properties of the composite material based upon knowledge of the constituent material properties. Such methods range in complexity, the simplest of which being the so-called "Rule of Mixtures." Equations based upon the rule of mixtures for the axial, transverse, and shear moduli can be developed from the assumptions of the Voigt (iso-strain assumption) and Ruess (iso-stress assumption) models, respectively. The Voigt model has been shown to agree quite well with experimental measurements of the axial modulus of unidirectional composites (Hull and Clyne 1996), indicating that the iso-strain assumption is quite reasonable for axial loading. On the contrary, the Ruess model has been shown to consistently under-predict the transverse and shear moduli of unidirectional composite materials (Hull and Clyne 1996), suggesting that the iso-stress assumption is less appropriate. Empirical corrective factors, such as the Halpin-Tsai corrections, have been made to reconcile the low predictions of the transverse and shear moduli, with moderate success (Halpin and Tsai 1967). However, the empirical parameters are material system dependent, requiring

mechanical testing for validation of the corrective models, defeating the purpose of avoiding the cost of experimentally characterizing the material.

A more advanced method for 3-Dimensional material property predictions was developed by Eshelby, and subsequently modified by Mori/Tanaka to correct for large volume fraction of fibers. Before the method can be addressed, the 3-Dimensional compliance and stiffness matrices must first be introduced. For a transversely isotropic material, the compliance matrix is written as

$$S = \begin{bmatrix} \frac{1}{E_1} & \frac{-\upsilon_{21}}{E_1} & \frac{-\upsilon_{31}}{E_3} & 0 & 0 & 0 \\ & \frac{1}{E_2} & \frac{-\upsilon_{32}}{E_3} & 0 & 0 & 0 \\ & & \frac{1}{E_3} & & 0 & 0 \\ & & & \frac{1}{G_{21}} & 0 & 0 \\ & sym & & & \frac{1}{G_{31}} & 0 \\ & & & & & \frac{1}{G_{32}} \end{bmatrix} \tag{2.32}$$

In which E_i is the modulus in the i^{th} direction of the material, ν_{ij} is the Poisson ratio ij^{th} direction, and G_{ij} is the ij^{th} shear modulus. The stiffness matrix of the material can then be calculated from

$$C = S^{-1}. \tag{2.33}$$

For an isotropic material, $E_1 = E_2 = E_3$, $G_{21} = G_{31}=G_{32}$, and $\nu_{21} = \nu_{31}=\nu_{32}$, reducing the number of independent material constants necessary to fully define a 3-Dimensional isotropic material to 2.

With the stiffness matrices for common polymer matrix composite constituent materials defined, Eshelby's method for material property prediction can now be defined. In his pioneering work Eshelby considered the theoretical system of an elliptical mis-fitting inclusion embedded in an infinite homogeneous, isotropic matrix (Eshelby 1957). From his work, a closed form solution for the elastic response of the composite system was derived. Unfortunately, because of the assumptions inherent to his work, the agreement of the method was restricted to dilute volume fractions of fibers, diminishing its' utility for practical composite systems. Mori and Tanka remedied this issue by considering the volume averaged stress within the material (Mori and Tanaka 1973), from which they derived the expression

$$C_C = \left[C_M^{-1} - v_f\left\{(C_F - C_M)\left[S - v_f(S - I)\right] + C_M\right\}^{-1}(C_F - C_M)C_M^{-1}\right]^{-1} \qquad (2.34)$$

Where the subscripts C, M and F denote the composite, matrix and fiber material, respectively, S is the Eshelby matrix, I is the identity matrix, and v_f is the volume fraction of fibers. The Eshelby matrix is a function of the Poisson ratio of the matrix material and the geometric dimensions (and shape) of the inclusion (Mura 1987). The utility of this method for material property prediction is that it has shown to be in outstanding agreement with experimental measurements of all mechanical properties for several composite material systems, over a large range of volume fraction of fibers (Hull and Clyne 1996).

3. ANALYTIC MODEL FOR AEOLIAN VIBRATIONS OF A NEXT GENERATION TRANSMISSION LINE

As discussed in Section 2.1.1, Aeolian vibrations are the most common form of fatigue loading for transmission lines. Much work has been done analytically and experimentally in attempting to quantify the state of stress within ACSR conductors due to Aeolian vibrations (refer to the discussion of Section 2.1.1). However, as transmission lines with polymer matrix composite cores are a new technology, no work has been done to quantify the magnitude of Aeolian vibrations on them. Thus, an analytic model was developed to quantify the state of stress within the hybrid polymer matrix composite core, as it is the load bearing member of the design. Specifically, the maximum bending stress amplitude within the GFC was determined, as it will later turn out (see Chapters 4 and 5) that the GFC was the material that accumulated damage during fatigue loading.

With the model developed, two separate studies were then undertaken. First, the effect that key variables of the governing partial differential equation had on the predicted magnitude was parametrically evaluated. Then, uncertainty in all variables was assigned, and a probabilistic analysis performed to evaluate the uncertainty in the predicted stress amplitude. Moreover, from the probabilistic analysis, the relative importance of all variables was quantified. To perform the probabilistic analysis, the Matlab® software package was interfaced with the probabilistic software Nessus®. Monte Carlo (MC), First Order Reliability Methods (FORM), and Advanced Mean Value

(AMV) Methods were utilized for a comparison of accuracy and computational efficiency.

To highlight the value of the probabilistic approach, stress amplitude predictions due to Aeolian vibration events for identical transmission lines located in Denver, CO and Dodge City, KS were performed. Wind speed data was obtained from the National Oceanic and Atmospheric Association (NOAA) (NCDC 2008), and modeled with distributions as inputs into the probabilistic solution. The two locations were selected because Denver, CO has a relatively moderate wind climate, while Dodge City, KS experiences a considerably larger average wind speed.

As the governing partial differential equation and corresponding solution have several variables unique to this chapter, a definition of variables specific to this chapter (however, intended to be as consistent with the rest of the dissertation as possible) is provided in Table 3.1. The variables may be modified by a subscript to identify the particular material, or quantity of interest.

Table 3.1 Definition of symbols specific to Chapter 3.

Symbol	Definition of symbol	Symbol	Definition of symbol
E	Young's Modulus	v	wind speed
ρ	density	I	moment of inertia
d	diameter	μ	linear density
r	radius	f	frequency
G	standing wave amplitude	ω	angular frequency
v_f	volume fraction of fibers	A	cross-sectional area
T	line tension	CFC	carbon fiber composite
L	span length	GFC	glass fiber composite

3.1 Model development

To quantify the state of stress within the next generation conductor, we began by considering an infinitely long taught Drake sized conductor, rigidly clamped at one end, subjected to transverse deformations (shown schematically in Figure 3.1).

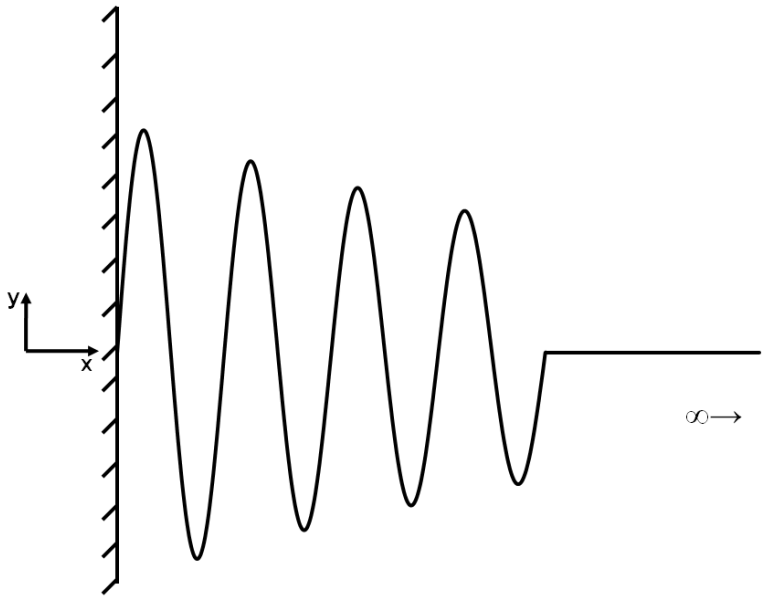

Figure 3.1 Schematic of the boundary conditions, assumptions, and deformations of the analytic model.

The partial differential equation that governs the motion of an infinitely long taught string is given by

$$EI\,\frac{\partial^4 y(x,t)}{\partial x^4} + \mu\,\frac{\partial^2 y(x,t)}{\partial t^2} - T\,\frac{\partial^2 y(x,t)}{\partial x^4} = q(x,t,y,y_t) \quad . \tag{3.1}$$

where $q(x, t, y, y_t)$ is an arbitrary loading function. If we consider the case of free vibrations of the transmission line, separation of variables can be utilized, and the partial differential equation becomes a fourth order ordinary differential equation in the spatial domain

$$EI\frac{d^4y(x)}{dx^4} + T\frac{d^2y(x)}{dx^2} - \rho A\omega^2 y(x) = 0. \tag{3.2}$$

A solution to equation (3.2) is of the form

$$y(x) = C\exp(\alpha x) + D\exp(-\alpha x) + G\sin(\beta x + \phi). \tag{3.3}$$

in which, C, D, ϕ, α, and β are constants of the system being analyzed. The parameters α and β are given by

$$\alpha = \sqrt{\frac{T + \sqrt{T^2 + 4 * E * I * \rho * A * \omega^2}}{2 * E * I}}$$

$$\beta = \sqrt{\frac{-T + \sqrt{T^2 + 4 * E * I * \rho * A * \omega^2}}{2 * E * I}}$$

The solution is subjected to the boundary conditions: y(0) = y'(0) = 0, additionally the solution must be bounded and finite. The latter boundary condition results in C being equal to 0, while applications of the former boundary conditions provides the solution of

$$\phi = \arctan\left(-\frac{\beta}{\alpha}\right). \tag{3.4}$$

The coefficient D can then be determined by back substitution, if an assumption on the amplitude of the standing wave (G) is made. Since the magnitude of Aeolian vibrations has been measured to be on the order of one conductor diameter, making assumptions about the magnitude of the standing wave is acceptable (EPRI 2009).

The applied moment (M_A) at the suspension clamp can then be determined by taking the second derivative of equation (3.3), and evaluating at x = 0. With the applied

moment known, the radius of curvature (ROC) of the neutral axis of the conductor can be determined

$$ROC_{CONDUCTOR} = \frac{\left(E_{CORE}I_{CORE} + E_{AL}I_{AL}\right)}{M_A}. \quad (3.5)$$

From the radius of curvature of the neutral axis of the conductor, the bending stress amplitude within the GFC is calculated by (Burks, Middleton and Armentrout, et al. 2010)

$$\sigma_{BA} = \frac{E_{GFC}r_{CORE}}{ROC_{CORE}}. \quad (3.6)$$

Aeolian vibrations occur when the Strouhal frequency from the wind input approaches the natural frequency of the transmission line (EPRI 2009). The Strouhal frequency is given by

$$f_{ST} = S\frac{V}{D} \quad (3.7)$$

where S is the Strouhal number. For the Reynold's numbers encountered in-service (and working in SI units), typical Strouhal numbers for transmission lines are 0.18 (EPRI 2009). The natural frequency of a transmission line can be calculated from

$$f_n = \frac{n}{2L}\sqrt{\frac{T}{m_L}}. \quad (3.8)$$

where n is the mode of vibration, and m_L is the linear denstiy (units of kg/m). By equating equations (3.7) and (3.8), the mode of vibration that would be excited based upon the line parameters and the wind speed can be determined.

This research differs from previous treatments of this problem in the form of the core material of the transmission line being considered. Polymer matrix composite materials

are often utilized in engineering designs due to the ability of the designer to tailor the material properties by controlling the volume fraction of fibers (v_f) (Hull and Clyne 1996). By modifying the volume fraction of fibers both the axial modulus and the density will be greatly affected. Prediction of composite material properties ranges from simple algebraic expressions to more complex tensor mathematics, with varying degrees of agreement with experimental measurements. It has been shown that the Voigt model is quite accurate in predicting the axial modulus of unidirectional composite materials (Hull and Clyne 1996), thus permitting the use of a simplistic algebraic expression to predict the axial modulus of the composite materials

$$E_{composite} = v_f E_{fiber} + (1 - v_f) E_{matrix}. \quad (3.9)$$

The accurate "iso-strain" assumption is valid for unidirectional composite materials, and leads to the observed agreement with experimental data. An extension of the Voigt model allows one to predict the axial modulus of the hybrid composite core

$$E_{CORE} = a_C E_{CFC} + (1 - a_C) E_{GFC}. \quad (3.10).$$

where a_c is the area fraction ratio of CFC:GFC. A similar set of expressions can be derived for the density of the composite materials, and hybrid composite core. The primary implication is that the solution to the bending stress amplitude for the composite core conductor has become a compound function of the volume fraction of fibers of the composite materials, i.e. – $\alpha(v_f)$, $\beta(v_f)$, as well as $E_{GFC}(v_f)$.

3.2 Results and Discussion

3.2.1 Parametric deterministic study

Necessary values to complete the parametric analysis are presented in Table 3.2. The rated tensile strength (RTS) of a Drake sized ACCC/TW conductor was taken from (Alawar, Bosze and Nutt 2005). The range of volume fraction of fibers evaluated was between 50 – 70%, which are typical values for a pultruded composite material (Hull and Clyne 1996). The amplitude of the standing wave was arbitrarily taken to be one-half the conductor diameter.

Table 3.2 Values of parameters used in the deterministic analysis.

Parameter	Value
E_{CARBON} [GPa]	230
E_{GLASS} [GPa]	69
E_{EPOXY} [GPa]	3
ρ_{CARBON} [kg m^{-3}]	1800
ρ_{GLASS} [kg m^{-3}]	2560
ρ_{EPOXY} [kg m^{-3}]	1200
ρ_{AL} [kg m^{-3}]	2700
d_{CORE} [mm]	9.53
d_{AL} [mm]	29.21
r_{CARBON} [mm]	3.55
RTS [N]	177,930
G [mm]	14.61
V [m/s]	6.21
L [m]	366

Results for the predicted bending stress amplitudes are presented in Figure 3.2. The largest bending stress amplitudes were predicted at a combination of the largest value of volume fraction of fibers and lowest value of tension considered. It was interesting to

note that for a given volume fraction of fibers, the bending stress amplitude decayed in what appeared to be an exponential fashion with respect to the RTS.

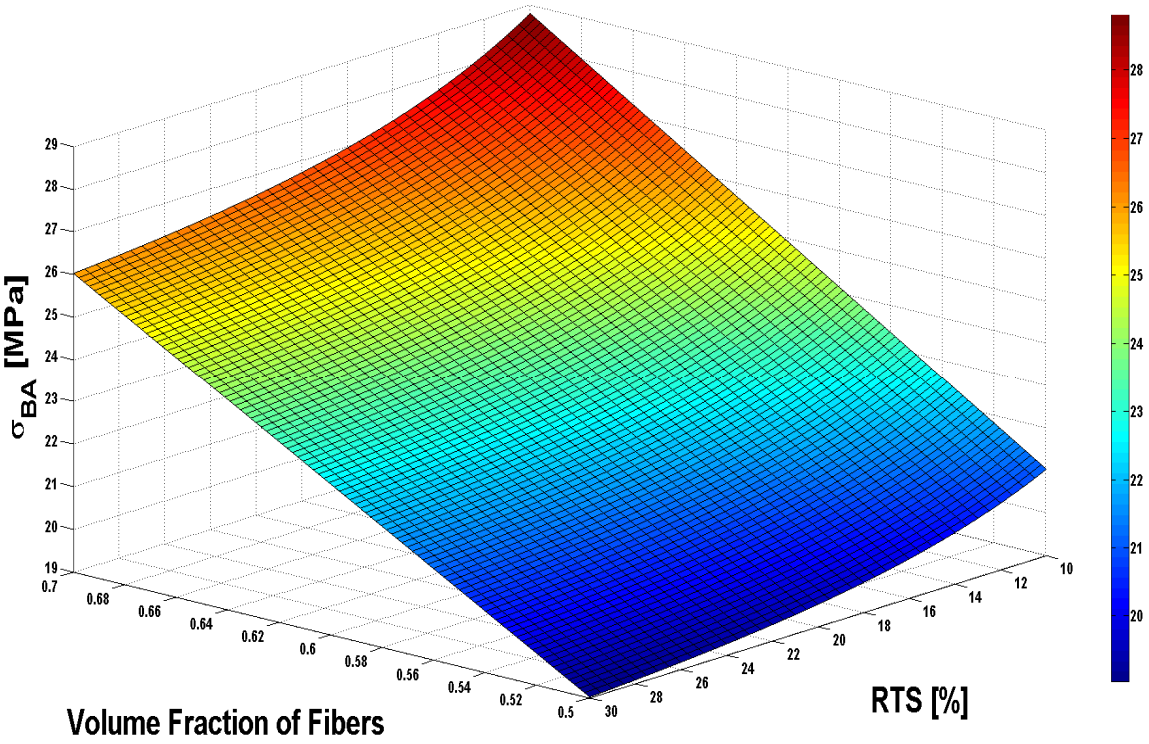

Figure 3.2 Solution space for the parametric study in which the value of the volume fraction of fibers and the line tension were evaluated.

Additionally, it was observed that the rate of decrease of the bending stress amplitude with respect to the RTS increased as the volume fraction of fibers being considered increased (Figure 3.3). Least Squares regression determined that a stretched exponential function was appropriate to describe the relationship between the bending stress amplitude, and the tension of the line (Figure 3.4). Moreover, for tension values above approximately one-half the rated tensile strength the bending stress amplitude was nearly independent of the tensile value.

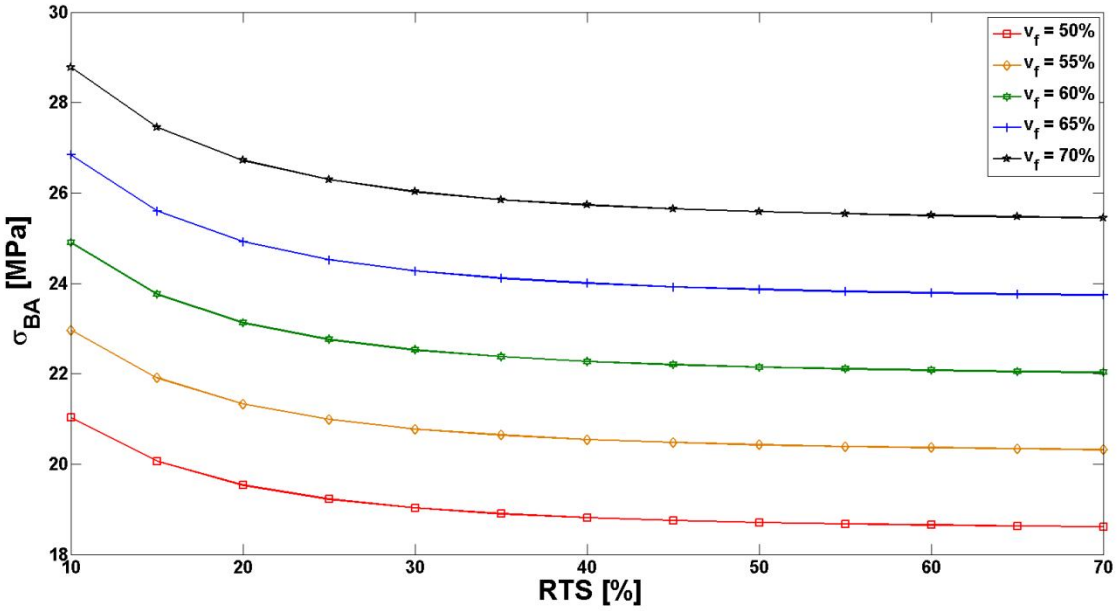

Figure 3.3 Effect that the volume fraction of fibers had on the predicted bending stress amplitude.

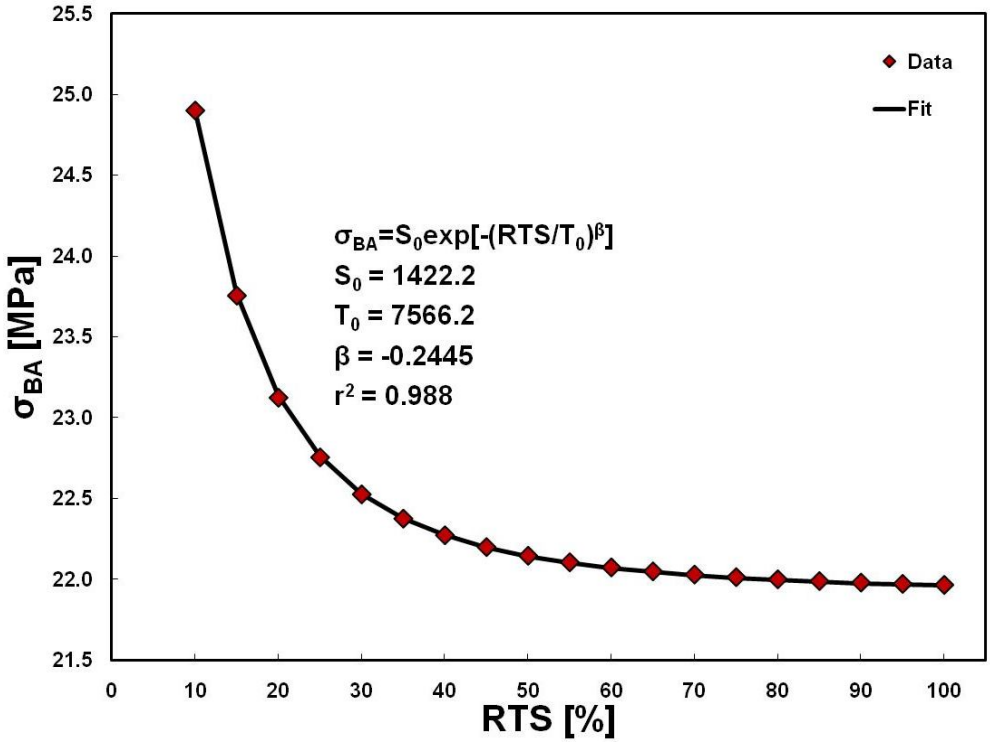

Figure 3.4 Predicted bending stress amplitude as a function of line tension for v_f = 60%. It was observed that a stretched exponential function well modeled the data (r^2 = .988).

The decrease in bending stress amplitude with increasing values of tension is in contrast with field experience, which shows that the vibration amplitude (i.e. - bending stress) increases with increasing tension (EPRI 2009). For circularly stranded conductors, as the line tension increases the self-damping of the conductor decreases resulting in increased conductor motion, and therefore increased bending stress amplitudes. Since the present treatment considered free vibrations of the conductor, no internal damping term was present that would allow reconciliation between the two. However, it is at present an open area of research to determine if the self-damping of a trapezoidal wire conductor decreases with increasing line tension. Ideally, the present treatment could be compared to an actual ACCC/TW^{TM} line under tension to evaluate the validity, and limitations of the present solution.

3.2.2 Probabilistic study

For the probabilistic study, a summary of the types of distributions that were found to best model the particular variable, and the corresponding statistical parameters can be found in Table 3.3. The span length and line tension were modeled as arbitrary normal distributions that were meant to be representative of an average transmission line. Variability in the standing wave amplitude was modeled as a normal distribution, with a mean value of one-half a conductor diameter and a coefficient of variation of 0.2. The variability of the span length, line tension, and standing wave amplitude could easily be tailored to fit a designers' particular transmission line. The variability in volume fraction of fibers and axial modulus of the composite materials was assumed to follow a normal distribution, with the mean value and standard deviation taken from values reported in the

literature (Burks, Armentrout, et al. 2009). The modulus of the epoxy material was modeled from available data (Middleton, et al. in preparation, 2012). Variability in the density of the materials was represented by a normal distribution with a COV of .001. The variability in the conductor diameter and hybrid composite core diameter were fit with distributions from 20 measurements that were made on a piece of as received ACCC/TW^{TM} conductor. Variability in the CFC radius had previously been reported (Burks, Middleton and Kumosa 2010). Average monthly wind-speed data was acquired from (NCDC 2008), and the distribution that best fit the data was determined.

Table 3.3 Summary of distribution types and parameters used in the probabilistic study. Associated Nomenclature: μ = mean, σ = standard deviation, λ = mean of the ln(x), ζ = standard deviation of the ln(x), α = shape parameter, β = scale parameter.

Variable	Distribution Type	Parameter 1	Parameter 2
E_C [GPa]	Normal	$\mu = 230.0$	$\sigma = 3.1$
E_G [GPa]	Normal	$\mu = 76$	$\sigma = .9$
E_M [GPa]	Weibull	$\alpha = 43.29$	$\beta = 2.216$
ρ_C [kg/m^3]	Normal	$\mu = 1800$	$\sigma = 1.8$
ρ_G [kg/m^3]	Normal	$\mu = 2560$	$\sigma = 2.56$
ρ_M [kg/m^3]	Normal	$\mu = 1200$	$\sigma = 1.2$
ρ_{AL} [kg/m^3]	Normal	$\mu = 2700$	$\sigma = 2.7$
d_{CORE} [mm]	Normal	$\mu = 9.5$	$\sigma = 3.4E\text{-}3$
d_{COND} [m]	Lognormal	$\lambda = -3.5485$	$\zeta = 0.0034$
r_{CARBON} [mm]	Normal	$\mu = 3.55$	$\sigma = 0.14$
G [m]	Normal	$\mu = 0.0146$	$\sigma = 0.00292$
v_f	Normal	$\mu = 0.64$	$\sigma = 0.03$
T [N]	Normal	$\mu = 35586$	$\sigma = 3559$
L [m]	Normal	$\mu = 366$	$\sigma = 10$
V_{Denver} [m/s]	Lognormal	$\lambda = 1.3473$	$\zeta = 0.0800$
V_{Dodge} [m/s]	Lognormal	$\lambda = 1.8241$	$\zeta = 0.0650$

The cumulative distributions of predicted bending stress amplitudes using the AMV method for Denver and Dodge City can be seen in Figure 3.5 and Figure 3.6, respectively. Table 3 provides a comparison between the three probabilistic methods considered in this study; their predicted 50^{th} percentile value (with their 1 and 99% bounds), as well as their respective computation times. All three methods agreed well with one another for both locations; however, it was clear that the Monte Carlo method was significantly less computationally efficient, when compared to the two most probable point probabilistic techniques.

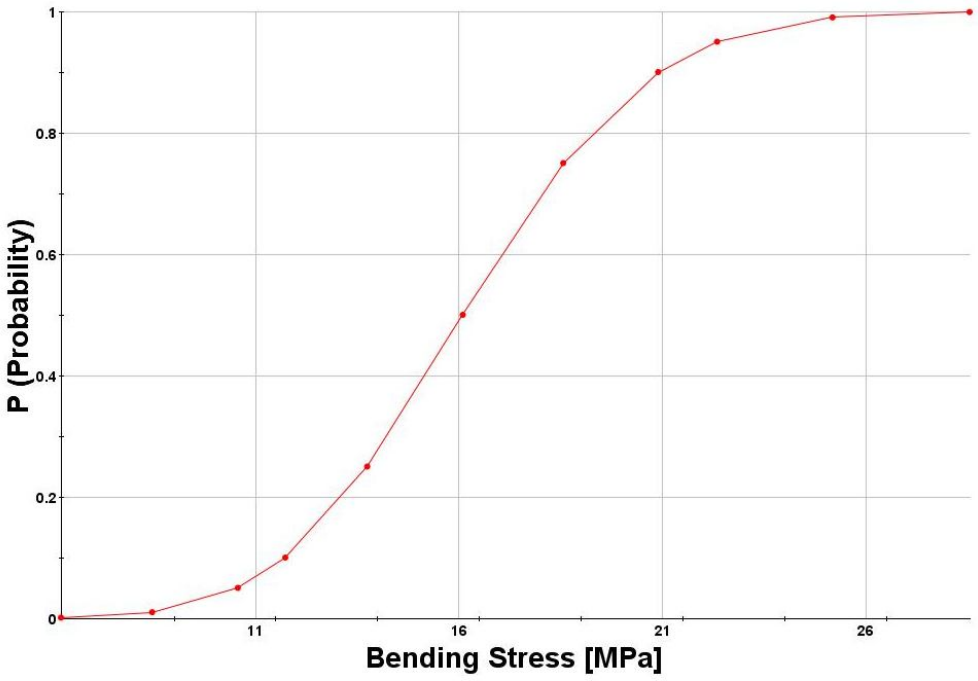

Figure 3.5 Cumulative Density Function (CDF) of the predicted bending stress amplitude for Denver, CO from using the AMV method.

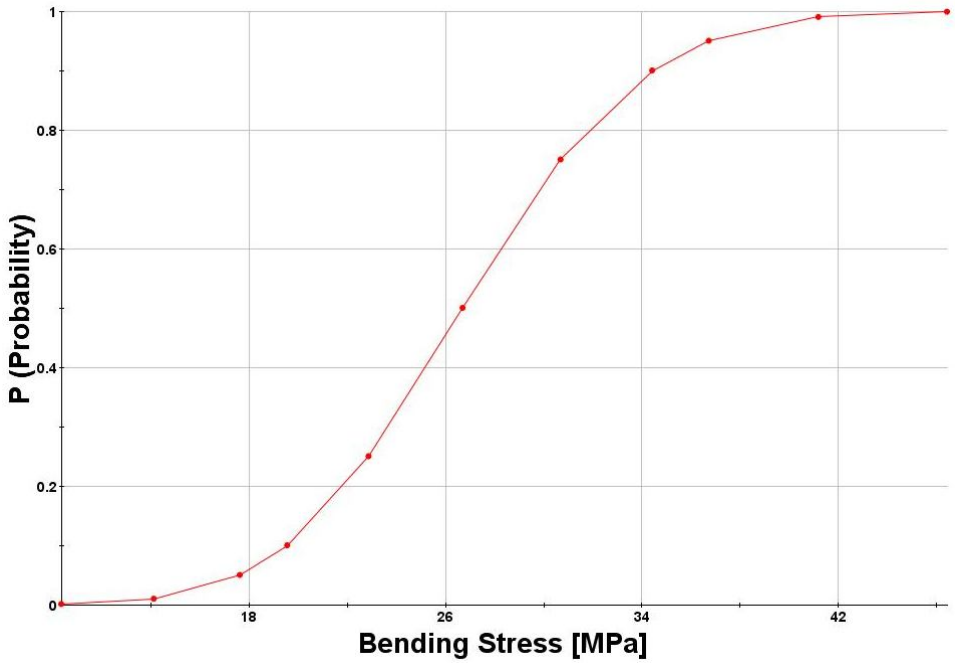

Figure 3.6 Cumulative Density Function (CDF) of the predicted bending stress amplitude for Dodge City, KS from using the AMV method.

Table 3.4 Comparison of probabilistic methods predicted bending stress amplitudes and computational efficiency for Denver, CO and Dodge City, KS.

Location	Probabilistic Method	50th Percentile Bending Stress (1-99 Bounds) [MPa]	Computation Time [s]
Denver, CO	MC (1E6 trials)	16.0 (8.3 – 25.2)	481.28
	FORM	16.1 (8.4 – 25.3)	1.05
	AMV	16.1 (8.5 – 25.2)	0.80
Dodge City, KS	MC (1E6 trials)	26.6 (13.9 – 41.2)	481.33
	FORM	26.7 (14.0 – 41.3)	1.19
	AMV	26.7 (14.1 – 41.2)	0.80

It was observed that the predicted 50th percentile value for the bending stress amplitude in Dodge City was 61% greater than the predicted value in Denver. This observation indicated that the wind speed was an important factor in bending stress amplitude, all

other parameters being equivalent. Additionally, the spread in the predicted bending stress amplitudes were significantly greater for Dodge City. This was largely attributed to the greater variability in wind speed in Dodge City. To further confirm the importance of the wind speed, the importance level of the variables for Denver and Dodge City are presented in Figure 3.7 and Figure 3.8, respectively. For both sites, wind speed was identified as the second most important random variable in the probabilistic solution, behind the standing wave amplitude.

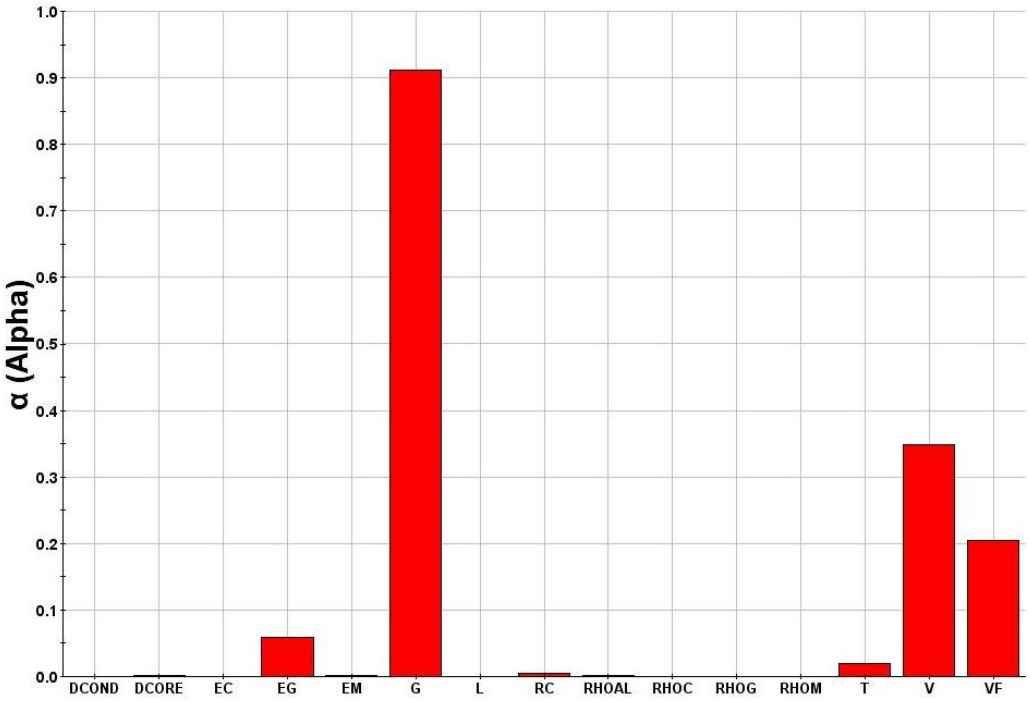

Figure 3.7 Relative Importance values for the random variables in the Denver, CO probabilistic model.

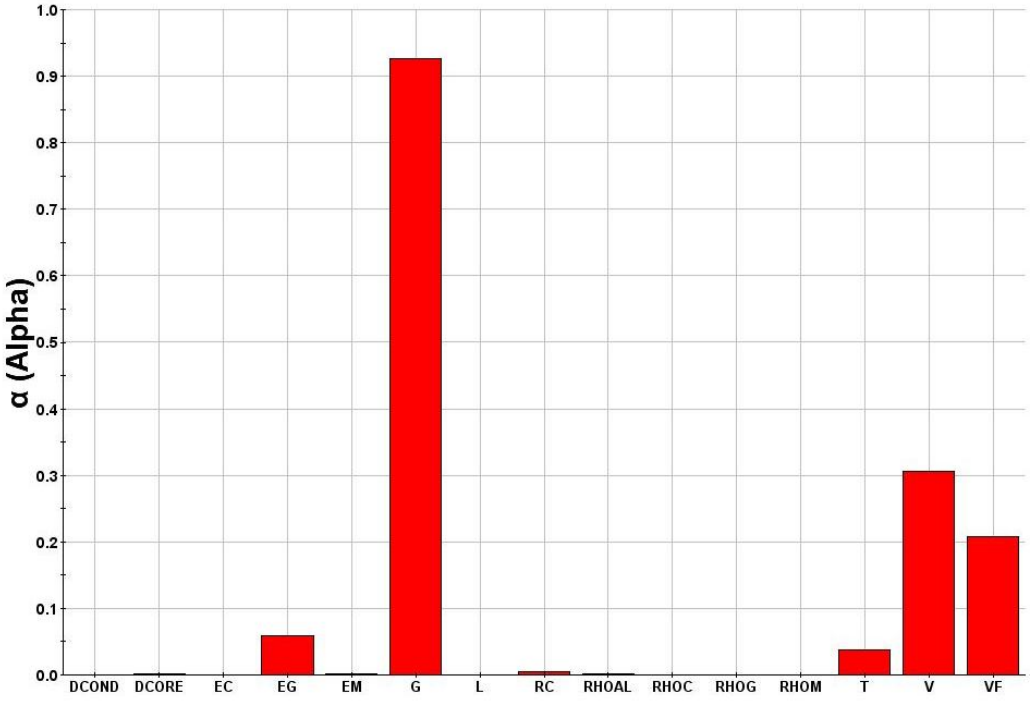

Figure 3.8 Relative Importance values for the random variables in the Dodge City, KS model.

It was not surprising that the standing wave amplitude, wind speed, and line tension were important variables to the predicted bending stress amplitude of the transmission line; this has been well documented (EPRI 2009). It was however interesting to note that for both locales, that the volume fraction of fibers, and glass fiber modulus were more important variables to the solution than the tension in the line (Figure 3.7 and Figure 3.8). Designers of transmission lines are left facing a decision in which they must weigh out the pros and cons of increasing the modulus of a transmission line. Increasing the modulus of the GFC (by including a larger volume fraction of fibers) would stiffen the transmission, which would be a positive effect. However, in this study, it was found that by increasing the volume fraction of fibers that the bending stress amplitude of the GFC increases. The probabilistic approach developed provides transmission line designers a

tool to evaluate how changes in material, or line characteristics affects the distribution of dynamic bending stress that will occur due to an Aeolian vibration event. If used in conjunction with proper fatigue data of the hybrid composite core, next generation high voltage electric transmission lines could be reliably designed against fatigue failure from Aeolian vibration motion.

4. FATIGUE CHARACTERISTICS OF THE UNAGED HYBRID COMPOSITE MATERIAL

To characterize the fatigue performance of the hybrid polymer matrix composite material, a fatigue test based upon the rotating beam concept was developed. A rotating beam test operates on the principle of applying a constant force at a known distance, causing an applied moment to be placed on the test specimen. The test specimen is held in a collet that interfaces to an electric motor; as the motor rotates the collet, the bending stress on the specimen is cycled from maximum tension to maximum compression, resulting in what is known as a fully reversed state of stress (i.e. $R = \sigma_{MIN}/\sigma_{MAX} = -1$). By employing an R ratio of -1, the fatigue data were expected to be conservative if compared to a test program in which an algebraically larger R ratio were utilized (Harris, Gathercole, et al. 1997), (Adam, et al. 1994). The rotating beam test was found preferable for the fatigue program, as it was able to incorporate a transverse compressive stress component to the hybrid composite. From Ramey's work, a compressive stress at mechanical connections will be present in-service (Ramey, Brunair and Duncan 1988). Hence, utilization of the rotating beam test enabled investigation of the sensitivity of the hybrid composite to a multi-axial loading condition, facilitating investigation of whether or not the bearing stress at mechanical connections for transmission lines can be neglected.

4.1 Methods

4.1.1 Experimental methods

Drake sized (9.50 mm outer diameter) ACCC hybrid composites were supplied by the Composite Technology Corporation (CTC) for testing. The composites came directly from the pultrusion process in 1.5 m sections; these composites were never stranded, nor were they mechanically stressed to any significant level pre-test. Fatigue specimens were cut to their final length of 71.1 mm using an abrasive diamond saw, and maintained at room temperature in a desiccant chamber until the specimen was to be tested.

To seat the specimens in the test machine's collet, sleeves were machined out of 2011 - T3 Aluminum. The sleeves were gripped in the test machine's collet (Figure 4.1), resulting in a compressive traction being applied to the sleeve's outer surface; this action was intended to simulate the crimping that occurs on the transmission line at a compression fitting or suspension clamp and imitate the transverse stress state present in-service.

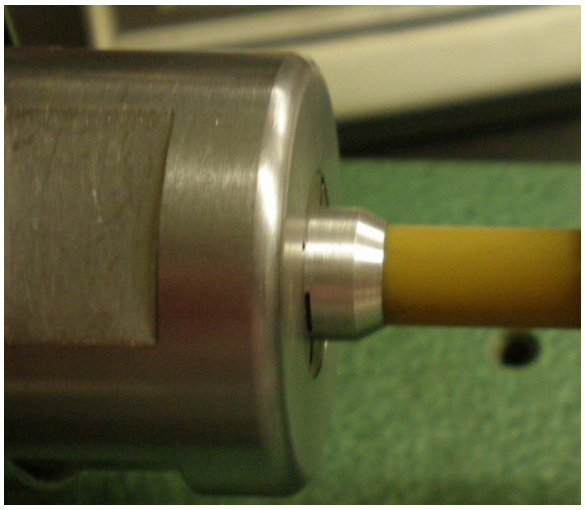

Figure 4.1 Hybrid composite interfacing with test frame through an aluminum sleeve.

Sensor Products Inc.'s Pressurex high polymer pressure film (sensitive to pressures between 49.0 and 127.5 MPa) was used to measure the distribution of contact pressure that was applied to the specimen from gripping the sleeve (Figure 4.2). For each measurement a 32.0 mm x 25.4 mm strip was placed in between the aluminum sleeve, and the ACCC specimen. Six measurements were made using the Pressurex film, one measurement for gripping the specimen (applying no load), and one measurement for gripping the specimen and statically loading the specimen to the stress amplitude at which tests were performed.

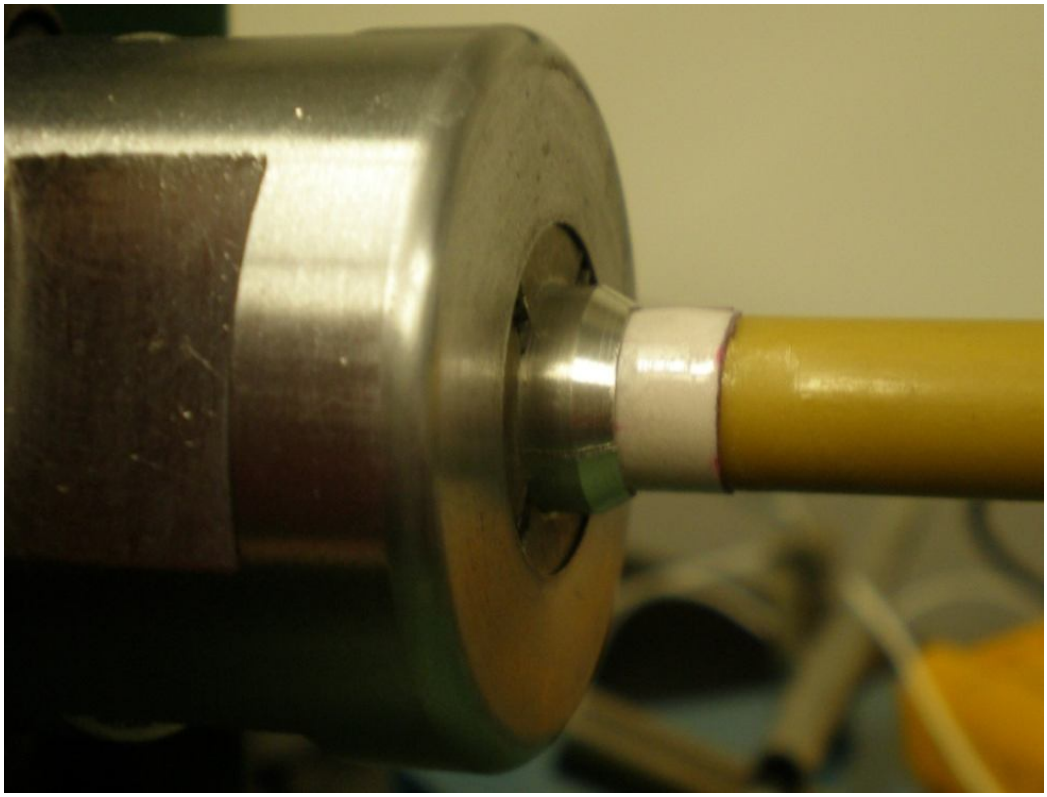

Figure 4.2 Measurement of the amount of transverse compression applied to the hybrid composite via Pressurex's high polymer pressure film.

Five different cyclic stress amplitudes (identified as σ_1 - σ_5) were considered to characterize how changes in the bending stress amplitude affected fatigue performance (Table 4.1).

Table 4.1 Applied force for the 5 stress amplitudes investigated.

Test Series	Applied Load (N)
σ_1	52.4
σ_2	62.8
σ_3	78.6
σ_4	94.2
σ_5	104.8

Ten replicates were run at each of the 4 higher stress amplitudes, and 5 replicates were tested for the lowest stress amplitude. The amount of bending stress was increased by increasing the applied load, while keeping the maximum distance of the moment arm a constant (L = 231 mm). All test specimens were cycled at a frequency of 31 Hz. The test frequency fell within the range expected from Aeolian vibrations (EPRI 2009), and was the greatest frequency that fell below the first resonant frequency of the test frame for all 5 stress amplitudes.

The test frame was modified by adding a Fastar FS1000HP LVDT which was input into a Newport signal conditioner. The signal from the conditioner was sent to an HP 34970A DASU, and then recorded with a PC using software written in LabView© 2009. The data was later post-processed by being passed through a low-pass first order Butterworth filter to attenuate the higher frequency noise that was present in the

measurement. Each data set was transformed into the frequency domain, to determine an appropriate cut-off frequency. By measuring the deflection of the test system throughout the test, the axial stiffness of the material as a function of the number of cycles was monitored. The entire test set-up can be seen in Figure 4.3.

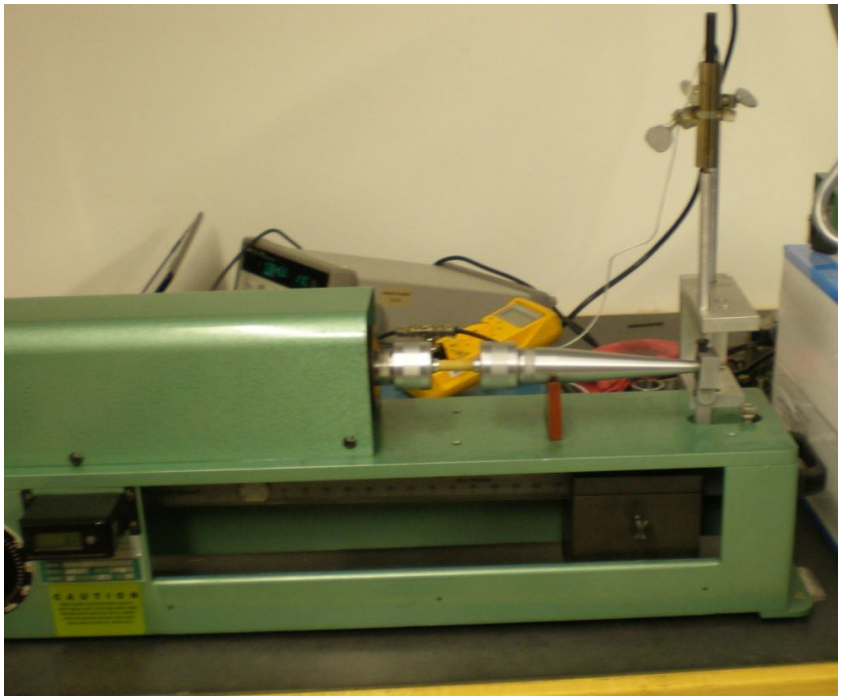

Figure 4.3 Modified rotating beam fatigue test frame, with an LVDT to monitor the state of damage within the hybrid composite.

To insure that the appropriate stress amplitudes were applied during testing, calibration of the test frame was performed between each change in stress amplitude, or whenever a component on the test frame had to be replaced. As there is no load sensing device on the test frame, an in-house load cell was built that acted as an instrumented specimen. The load cell was constructed out of 41L40 steel, and had a strain gage bonded to it in the axial direction. From beam mechanics, material properties, and the geometry of the load cell, a theoretical strain value could be calculated based upon the

applied moment. Calibration was performed on the full scale of the machine (0 N-mm to 22600 N-mm) in increments of 1130 N-mm. In accordance with ASTM E74, the machine was considered in conformance with calibration if the error was less than 1% over the full scale. A representative calibration curve is shown in Figure 4.4.

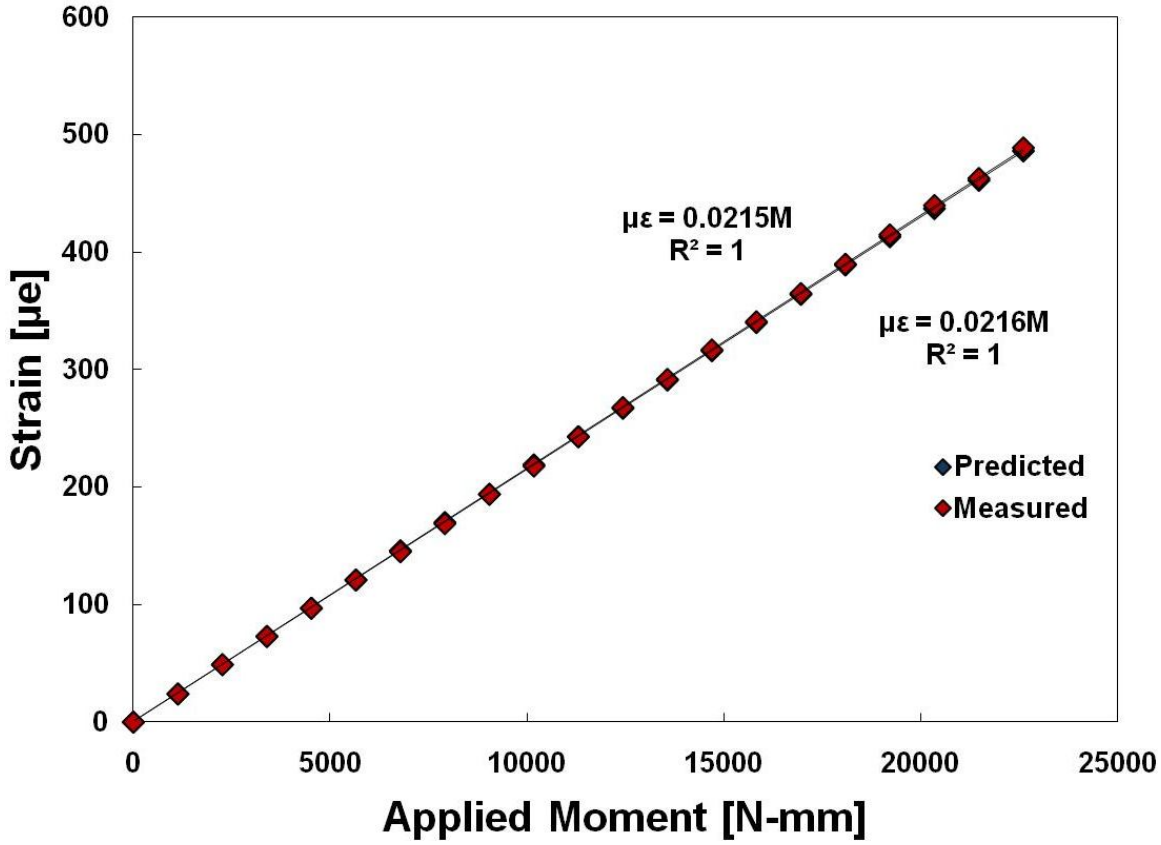

Figure 4.4 Representative calibration curve for the rotating beam fatigue test frame.

4.1.2 Macromechanics modeling of the fatigue experiment

A finite element model of the experiment was developed to aid in analysis and to compare with the experimental data (Figure 4.5). Reduced integration hexahedral elements were used for computational efficiency and accuracy (Liu, Hu and Belytschko 1994). The CFC was modeled as being perfectly circular and concentric with the GFC

and having a diameter of 7.10 mm, while the entire hybrid composite was modeled as having an outer diameter of 9.50 mm. The aluminum sleeve had an outer diameter of 12.70 mm, and an inner diameter of 9.50 mm. The taper on the aluminum sleeve was designed and modeled to have an angle of 30°. To model the moment arm connecting the specimen to the location of the concentrated force, quadratic Timoshenko beam elements were used.

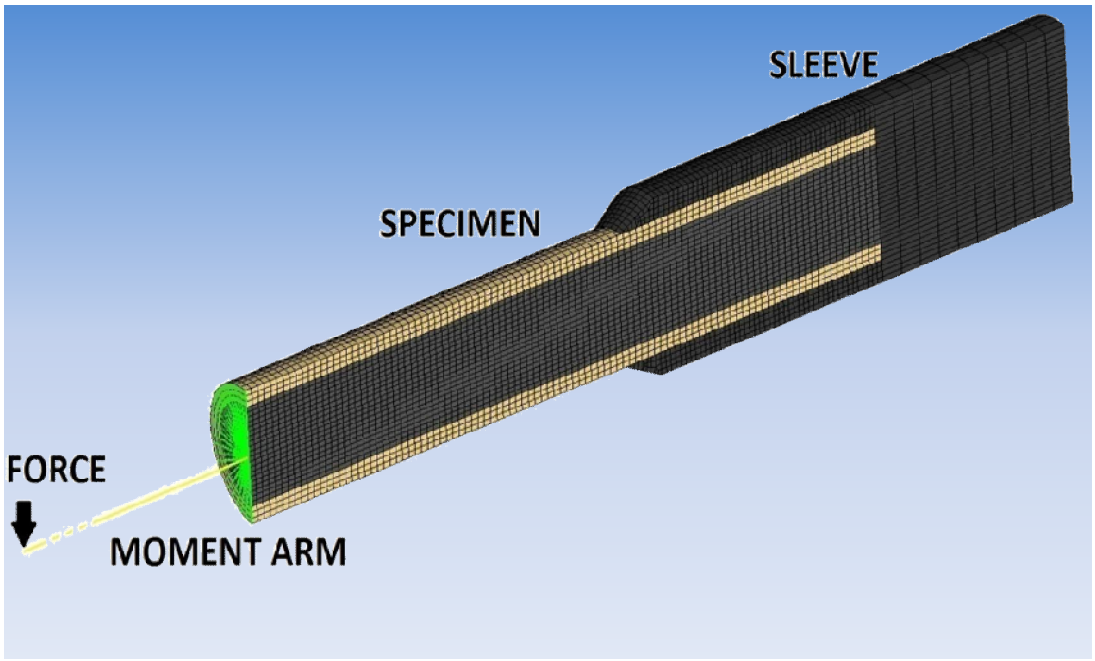

Figure 4.5 Schematic of the FE model developed to simulate the experiment.

The beam elements were modeled as having a circular cross-section. Actual dimensions of the moment arm on the rotating beam test frame could not be obtained from the manufacturer, thus a constant cross-sectional profile was used. To determine the effective diameter of the moment arm, experimental static deflection data was obtained, and a steepest descent minimization procedure was used to tune the numerical model to match the experimental deformation data.

A kinematic constraint was imposed on all of the nodes on the free end of the ACCC core by rigidly beaming them to the center node on that end of the core; this constraint allowed the moment arm to be attached to the entire face of the specimen, and transfer the applied load to all of the nodes on the free end of the specimen, as opposed to a single node, in order to avoid hour-glassing of the elements or a hot spot in the mesh. The center node on the free end and a node that was positioned at the location where the concentrated load was to be applied comprised the end points for the beam elements that modeled the moment arm.

The unidirectional carbon fiber and glass fiber composites were modeled as linear-elastic transversely isotropic materials. Material properties were calculated from the constituent material properties using the Mori-Tanaka adaptation of the Eshelby method (equation 2.34), assuming a volume fraction of fibers of 60% (Alawar, Bosze and Nutt 2005). The composite material properties are summarized in Table 4.2.

Table 4.2 Material properties calculated from the modified Eshelby method, and used as input for the FE model.

Material Property	Glass Fiber Composite	Carbon Fiber Composite
Axial Modulus [GPa]	46.8	145.2
Transverse Modulus [GPa]	10.7	8.2
Axial Poisson's Ratio	.0621	.0155
Transverse Poisson's Ratio	.5408	0.5540
Axial Shear Modulus [GPa]	5.3	5.1

To model the plasticity of the aluminum sleeve, a monotonic tension test was performed to obtain a true stress-strain curve, from which relevant data was extracted. The 2011-T3 Al was modeled as having a Young's modulus of 64 GPa, and a Poisson's

ratio of 0.29 (Figure 4.6). The plasticity of the Al was modeled using the Ramberg-Osgood relationship with K = 498 MPa, n = .091 (Ramberg and Osgood 1943) (Figure 4.7). The moment arm was assigned linear elastic steel material properties (E = 210 GPa, ν = 0.3), as stresses in the moment arm remained elastic.

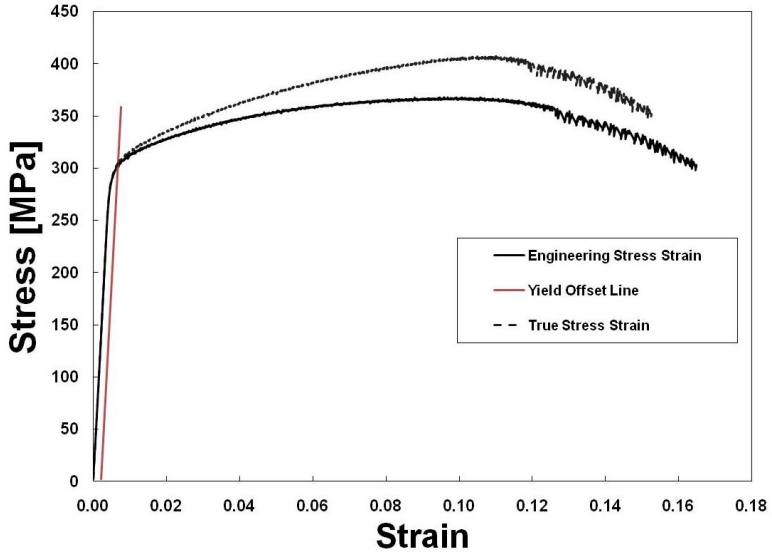

Figure 4.6 True and engineering stress-strain curve of 2011 Al - T3.

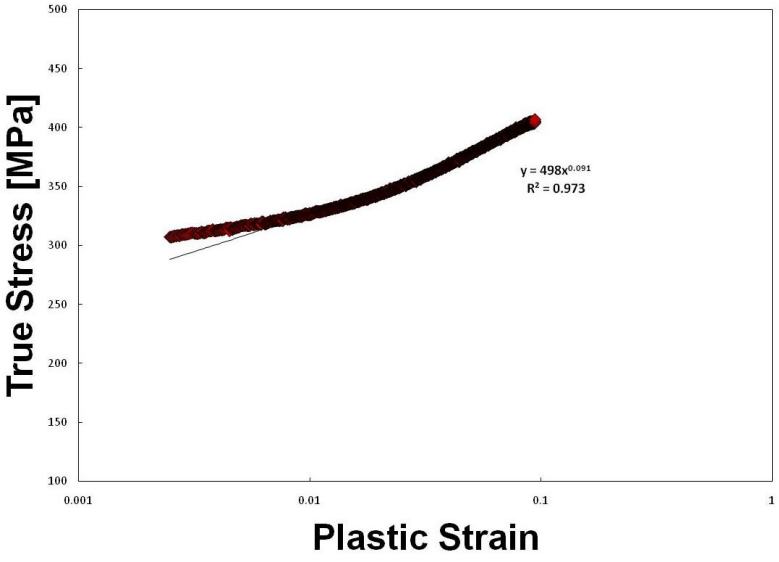

Figure 4.7 Plot of true stress vs. plastic strain for Ramberg-Osgood coefficient determination.

Analyses were performed in two steps. The first step was to apply a compressive stress to the free surface of the portion of the aluminum sleeve that would be seated in the collet. Applying the compressive stress to the aluminum sleeve represented gripping the test specimen in the collet. The magnitude of the compressive load applied was tuned for the analyses such that the maximum contact pressure between the aluminum sleeve and the GFC matched the measurement made from the Pressurex polymer film analysis in which the specimen was only gripped in the collet. Deformable-deformable contact between the ACCC core and the aluminum sleeve was modeled using a finite-sliding, surface-to-surface contact definition. The second step was to constrain all of the nodes that were within the collet in their axial degree of freedom, and apply a concentrated force to the node that was at the moment arm location.

4.1.3 Probabilistic adaptation of the macromechanics model

During fatigue loading the hybrid composite was found to "Wear-in," or stiffen, upon initial cycling; the process was reported as having pronounced variability, as will be elaborated upon in section 4.2.1. In section 4.1.2 a finite element model was developed with the simplifying assumption that the CFC was perfectly circular and concentric with the GFC. This model will henceforth be referred to as the nominal geometry model. With the nominal geometry model an optimization procedure was used to determine the effective v_f for each composite, subjected to each stress amplitude, which accounted for the mean stiffening effect. However, this model could not account for the prominent variability reported.

Two sources of variability were identified that were anticipated to affect the stiffening phenomena. First, when viewing multiple cross-sections of the hybrid composite, it is clear that the circular assumption is simplistic and that the cross-sectional geometry is variable when viewing different cross-sections of the hybrid composite core (Figure 4.8). This cross-sectional variability along the length of the material is a result of the unique dual fiber pultrusion process that is used to manufacture the hybrid composite material. The second source of variability identified was the misalignment of the reinforcing fibers. Thus, to account for both sources of variability, a numeric framework was developed that could capture the observed scatter in the stiffening effect.

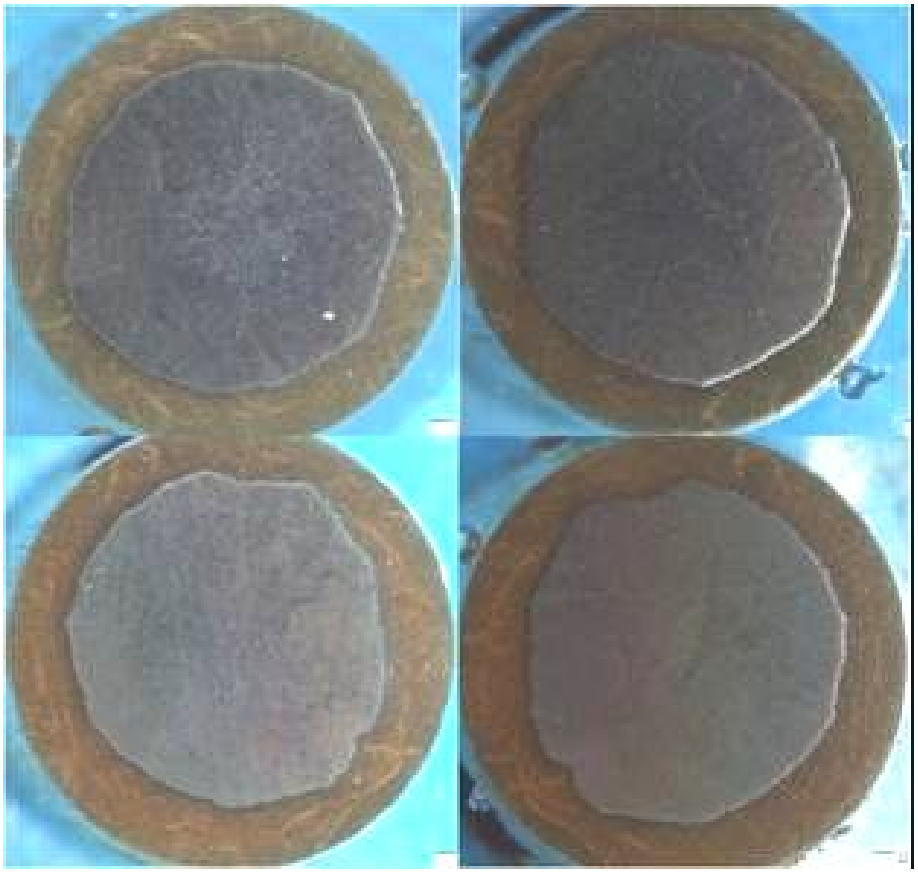

Figure 4.8 Multiple cross sections of the hybrid composite, highlighting the geometric variability.

It has been reported that the radii of the CFC was best modeled by a normal distribution (μ = 3.55 mm, σ = 0.14 mm) (Burks, Middleton and Kumosa 2010). To incorporate this geometric variability into the FE model, a platform was developed between Matlab® and the FE preprocessor HyperMesh®. Using the same axial dimensions as the nominal model, six 2D template meshes were spaced equidistantly along the axial direction of the hybrid composite material (Figure 4.9a). Using the HyperMorph tool within HyperMesh, sixteen handles were created along the CFC perimeter of each template mesh. Four elements in the radial direction of both the CFC and GFC closest to the interface of the two composites were associated with the handles that were to be morphed. This was done to prevent element distortion upon morphing, allowing seamless transition from the underlying template mesh to the morphed geometry.

A custom Matlab script was developed to randomly sample the CFC radius distribution for each of the handles, and morph the handle of the original template mesh the appropriate distance in the radial direction (Figure 4.9b). Once all of the template meshes had been morphed, a solid mapping technique was used to generate the 3D hexahedral elements that would be used in the analyses through a linear interpolation scheme that connected adjacent template meshes. Element checks were performed on all hexahedral elements in the models before analyses were run; elements had to have a minimum Jacobian of 0.7, and the maximum allowable element warpage was 2.0. The element checks insured that a high quality mesh had been generated, and that spurious

stress results would not be computed. A comparison of the nominal geometry model and a morphed geometry model can be seen in Figure 4.10.

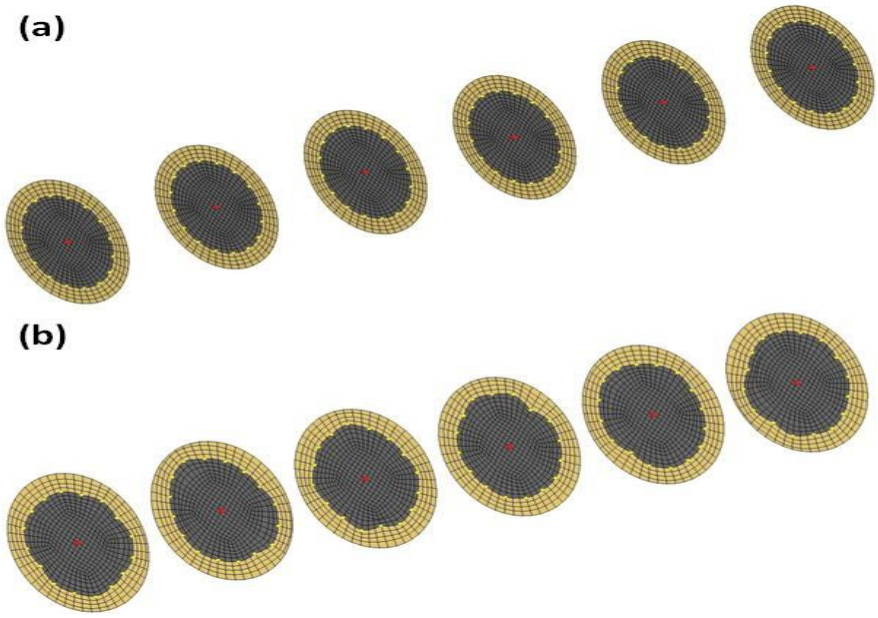

Figure 4.9 Unmorphed (a) and morphed (b) template meshes.

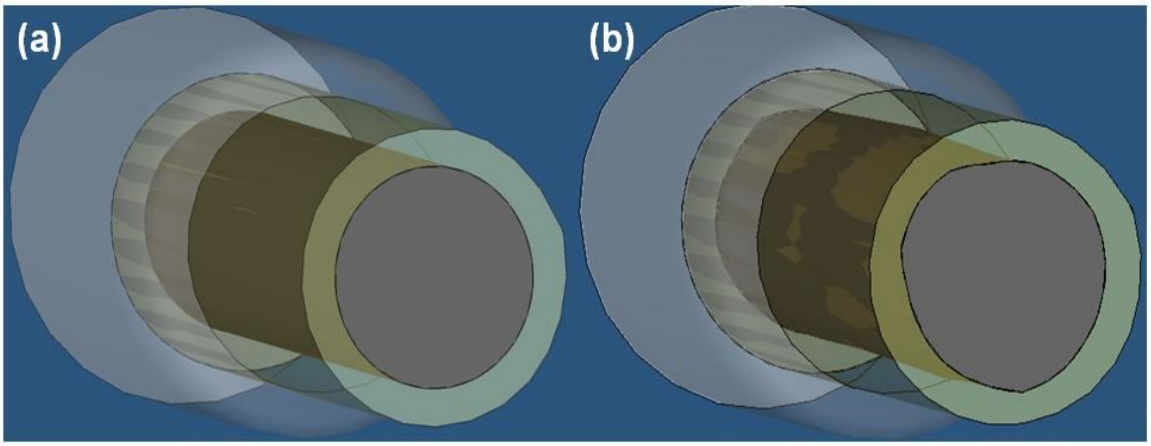

Figure 4.10 3-D representation of (a) the nominal geometry model, and (b) a morphed geometry model.

To incorporate the material property variability into the framework, distributions of volume fractions of fibers were determined based upon experimental data coupled with results from the nominal geometry FE model. Using the nominal geometry model and the previously described minimization process, the volume fraction of fibers of either the CFC or the GFC was varied (holding the other composites' v_f constant), until the error had been minimized. This process was done for the mean value of increase in deflection, as well as ± 1 standard deviation of increase in deflection for all stress amplitudes. The values for the minimized v_f were assumed to be the parameters of the normal distribution of v_f for the composite material. The normal distribution parameters for each stress amplitude are presented in Table 4.3.

Table 4.3 Summary of the respective v_f normal distribution parameters for each stress amplitude, reported mean [standard deviation].

Stress Amplitude	Modified CFC v_f	Modified GFC v_f
σ_1	63.24 [1.66]	64.51 [2.29]
σ_2	64.23 [2.63]	65.56 [3.65]
σ_3	66.81 [3.12]	69.35 [4.56]
σ_4	68.32 [2.80]	71.54 [4.02]
σ_5	65.09 [3.42]	66.96 [4.77]

Monte Carlo sampling of these distributions was then used for random material property assignment via equation (2.34). One hundred analyses for each stress amplitude were performed in parallel using Abaqus® v.6.9.2 on an 8 processor Linux workstation.

4.1.4 Micromechanics modeling of the "Wear-in" effect

As will be elaborated upon in section 4.2.1 the proposed mechanism that facilitated the initial increase in stiffness was misaligned fibers improving their alignment under the influence of an applied tensile stress. To investigate the effect of various parameters on the ability of fibers to align under a tensile load, representative volume element models (RVEs) of both the GFC and CFC were developed. In the RVEs, all fibers were assumed to be perfectly misaligned a known amount, θ. A square packing arrangement was assumed as a representative example of the periodicity of the microstructure. A schematic of the RVE is shown in Figure 4.11, from which it is clear that the entire mesh consisted of linear hexahedral elements which used a full integration formulation. Periodic boundary conditions were applied in accordance with Equation (2.1).

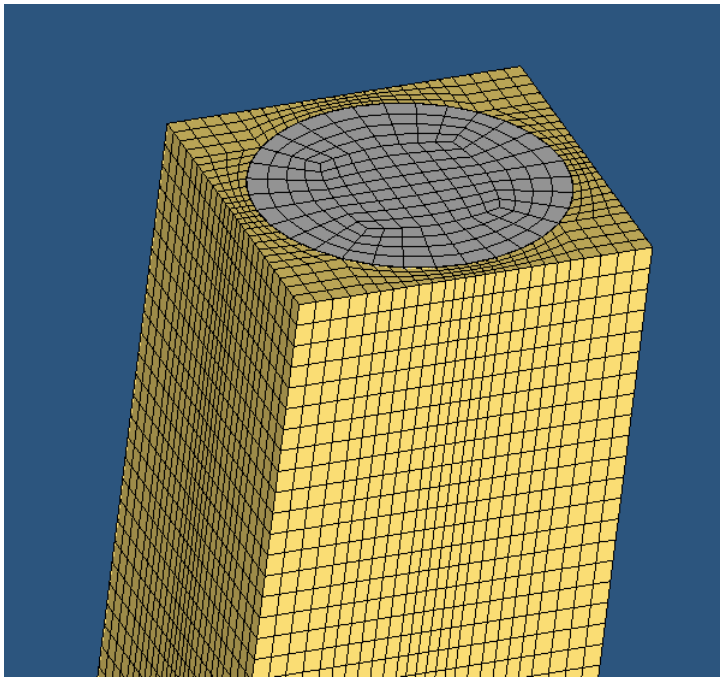

Figure 4.11 Schematic of a square packed RVE, with the reinforcing fiber misaligned an amount θ from the axial direction.

Carbon fibers were modeled as a transversely isotropic material, with properties taken from (Rupnowski and Kumosa 2003), the material properties are summarized in Table 4.4. For the glass fibers, isotropic material properties were taken from (Hull and Clyne 1996), in which E = 76 GPa, $\nu = 0.22$, and $\rho = 2500$ kg/m^3. For the epoxy matrix, $\rho =$ 1200 kg/m^3 and $\nu = 0.40$ for all analyses. The viscoelastic material properties of the epoxy resin were measured via a DMA dual cantilever configuration, specifics of which can be found in the literature (Middleton, Wells, et al. 2011), the results of which are presented in Section 4.2.4. For all CFC RVEs the diameter of the carbon fibers were modeled as 7 μm, while for the GFC RVEs the diameter of the glass fibers were modeled as 20 μm.

Table 4.4 Summary of transversely isotropic material properties for the carbon fibers.

Material Property	Value
E_{Axial}	241 GPa
$E_{Transverse}$	20 GPa
ν_{AT}	0.2
ν_{TT}	0.4
G_{AT}	27 GPa
ρ	1785 kg/m^3

Direct steady state dynamics analyses were performed, allowing the transient response of the RVEs subjected to a harmonically varying applied force to be determined. Such an analysis is directly applicable to the fully reversed fatigue loading presently considered, and allows for the viscoelastic nature of the epoxy resin to be considered. For all analyses in which frequency was not a variable, the excitation frequency was 31

Hz, to match the test frequency of the experimental work. An axial concentrated load was applied to a "dummy" node that had been coupled to the free surface of the RVE to which the axial stress was to be applied. Nodes on the opposite face of the RVE were constrained in the axial direction, while the node on the center of that face was additionally constrained in the transverse directions to eliminate the rigid body modes. The improvement in fiber alignment with the axial direction ($\Delta\theta$) was then extracted from all analyses.

4.2 Results and Discussion

4.2.1 Unaged fatigue performance

Figure 4.12 shows a surface plot of the distribution of pressure that was applied to the specimen. Post-measurement, the pressure film was removed from the collet (Figure 4.2), and shipped to Sensor Product's Inc. for digital image analysis. The pressure distribution for a specimen that was only gripped in the collet is shown in Figure 4.12a, whereas the pressure distribution for a specimen that was gripped in the collet and loaded to the σ_5 stress amplitude is shown in Figure 4.12b. It was noted that in both measurements that the pressure distribution was highly non-uniform and localized near the edge of the collet. Additionally, it was observed that the amount of area that exhibited high contact pressure, and the intensity of localization were significantly greater in the specimen that was loaded to the largest stress amplitude in comparison to the specimen that was merely gripped in the collet.

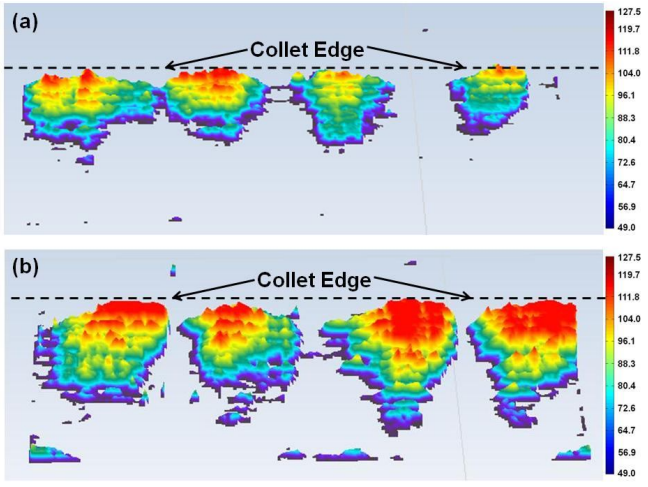

Figure 4.12 Three dimensional surface plots for (a) a specimen that was gripped in the collet and, (b) a specimen that was gripped and statically loaded to the σ_5 amplitude. Pressure values shown in MPa.

Due to the highly non-uniform pressure distributions, the amount of area that was subjected to a high contact pressure for each loading condition was of interest. By considering the amount of area that experienced a high transverse compressive stress state (greater than 90 MPa), an effect of the amount of contact area on the failure mechanism(s) in the hybrid composite could be established. Table 4.5 presents the total area (percentage) of the specimen that was seated in the sleeve that was subjected to 90 MPa or more of transverse contact pressure for each load case.

Table 4.5 Percentage of the experimentally measured gripped area that experienced greater than 90 MPa contact pressure for each loading condition.

Stress Amplitude	Percent of Area
σ_1	14.5
σ_2	18.5
σ_3	29.1
σ_4	32.7
σ_5	33.7

Representative curves for the change in deflection from the first cycle for each of the five different stress amplitudes can be seen in Figure 4.13. Two distinct regions of fatigue life were observed. The first region was termed a "Wear-in" region, in which the bending stress was found to cause the deflection of the system to decrease (i.e. – a positive change in deflection), indicating that the material was becoming stiffer. The average maximum change in deflection for all five stress amplitudes was plotted against the maximum bending stress amplitude in the GFC in Figure 4.14. In general, as the bending stress state increased, a greater stiffening effect was observed in both magnitude and rate.

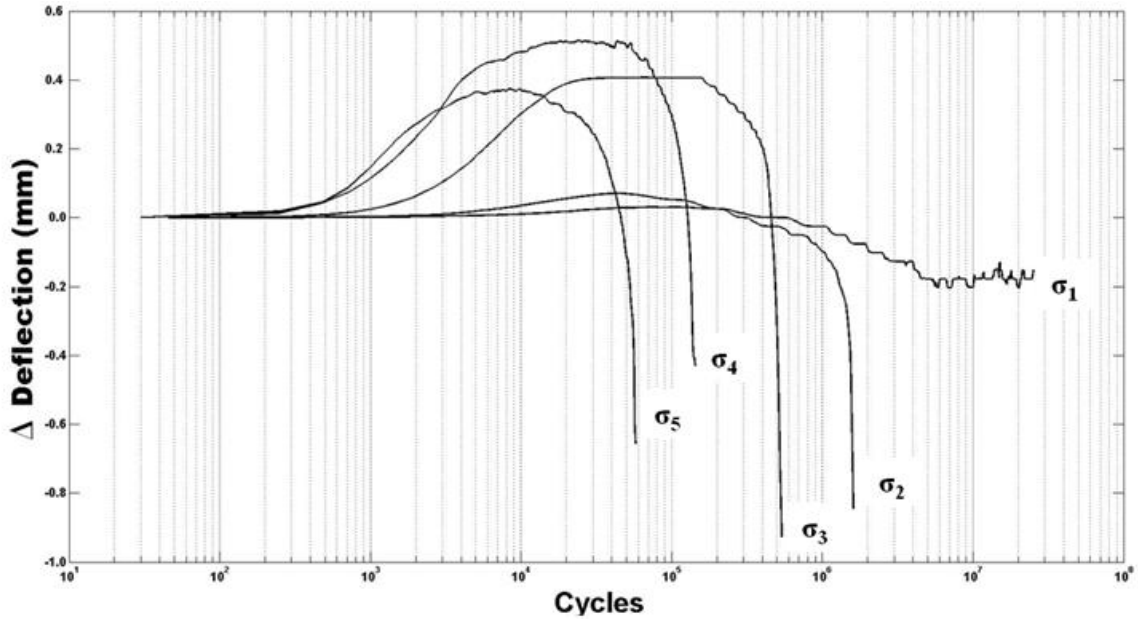

Figure 4.13 Representative Change in Deflection vs. N curves for the 5 stress amplitudes considered.

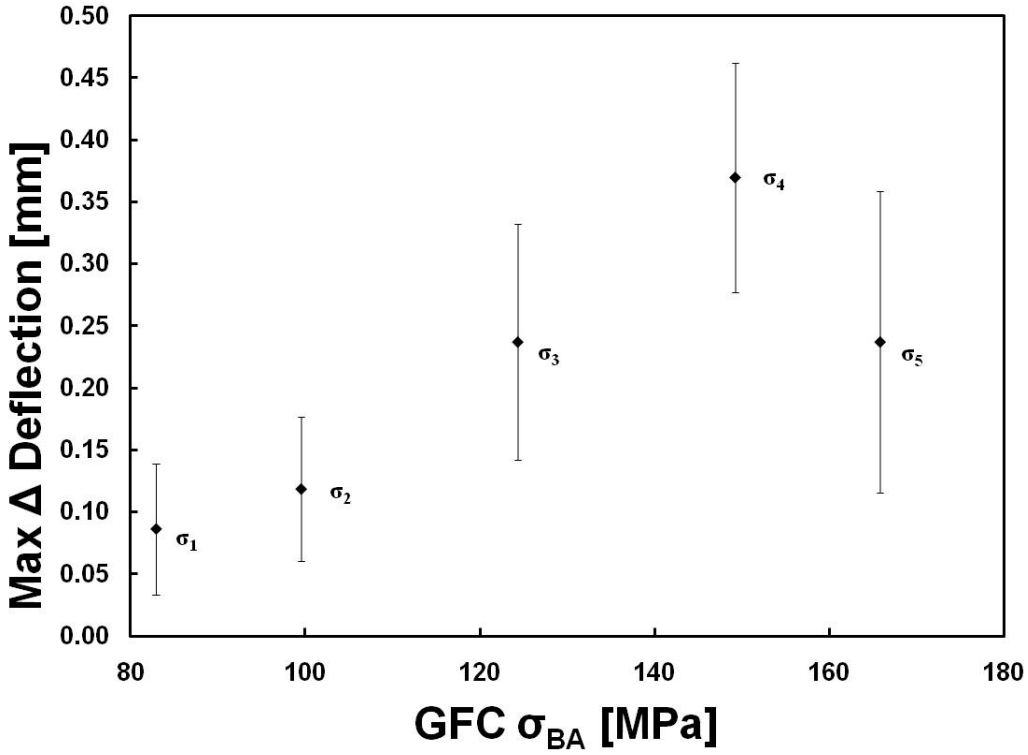

Figure 4.14 Average maximum change in deflection as a function of the bending stress amplitude, with the 95% confidence interval.

The rate of stiffening increased as the stress amplitude increased for all stress amplitudes (Figure 4.13). However, the trend in the increase in magnitude was not observed for the largest amplitude, the reason for which will be elaborated upon shortly.

The second region of fatigue life, which was only observed for the four highest amplitudes considered, was the portion of life in which the sample accumulated damage, and eventually failed. This region of life was identified by an increase in the deflection of the system (negative change in deflection from the first cycle) as the accumulated number of cycles increased, indicating that the stiffness of the material was decreasing. As a means of quantifying the amount of damage that the hybrid composite had accumulated, we define the damage parameter as

$$D = \frac{(EI)_N}{(EI)_0} - 1 = \frac{\delta_N}{\delta_0} - 1 \qquad (4.1)$$

where $(EI)_N$ is the section stiffness on the N^{TH} cycle, $(EI)_0$ is the section stiffness on the first cycle, δ_N is the deflection of the system on the N^{TH} cycle, and δ_0 is the deflection of the system on the first cycle.

For all stress amplitudes, it was found that damage was accumulated in a two stage fashion. In the initial portion of damage accumulation, damage was accumulated in a linear fashion with respect to the number of cycles (N)

$$D_I = \alpha N + \beta \qquad (4.2)$$

in which α and β are stress amplitude dependent material properties. During the second stage of damage accumulation, it was observed that damage was accumulated in an exponential manner with respect to the number of cycles

$$D_{II} = \kappa \exp(\lambda N) \tag{4.3}$$

where κ and λ are stress amplitude dependent material properties. Representative plots of damage vs. number of cycles for all stress amplitudes that failed are shown in Figure 4.15 through Figure 4.18. A comparison of the damage curves for all four stress amplitudes is shown in Figure 4.19. (Note: the y-axes of all damage plots have been scaled to a log base e to highlight the exponential fashion of damage accumulation during Stage II). Damage plots for all specimens can be found in Appendix A.

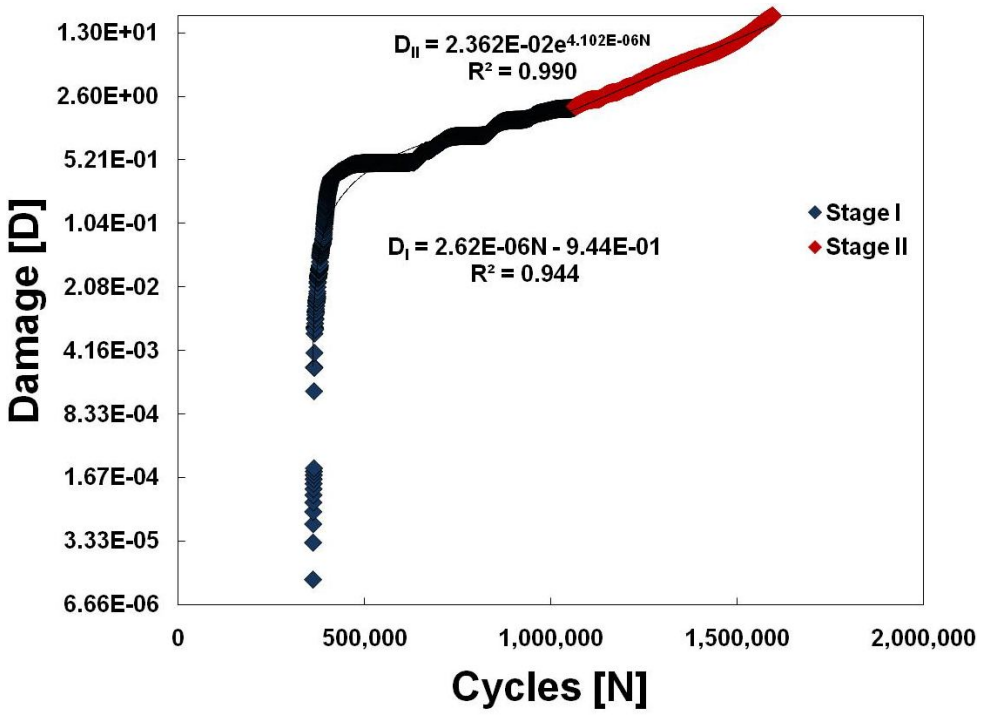

Figure 4.15 Damage accumulation as a function of the number of cycles subjected to σ_2.

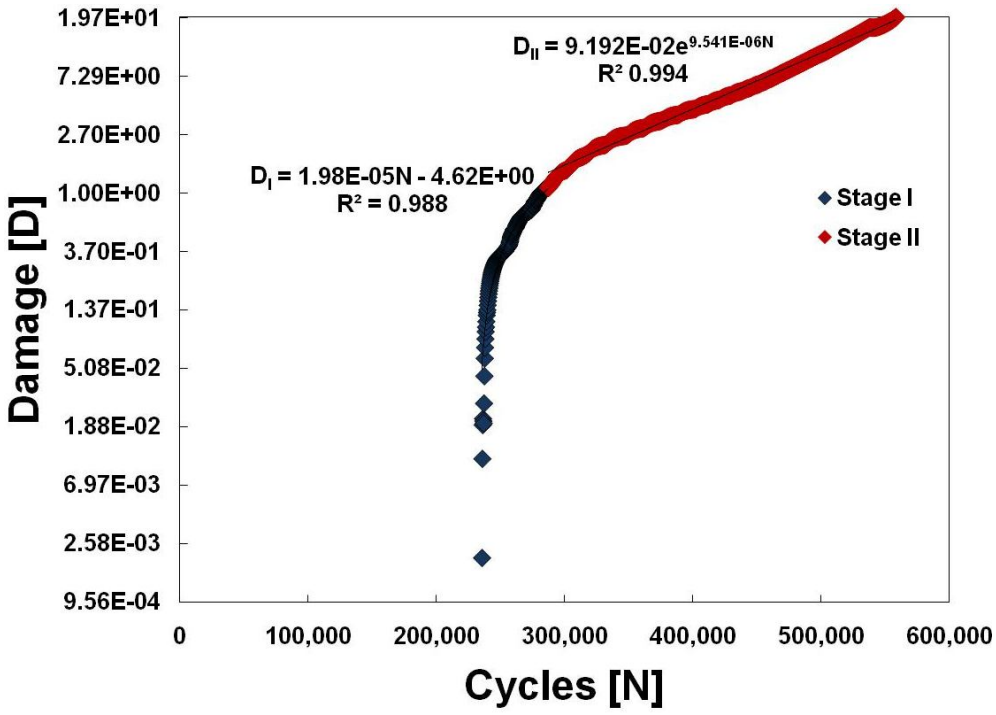

Figure 4.16 Damage accumulation as a function of the number of cycles subjected to σ_3.

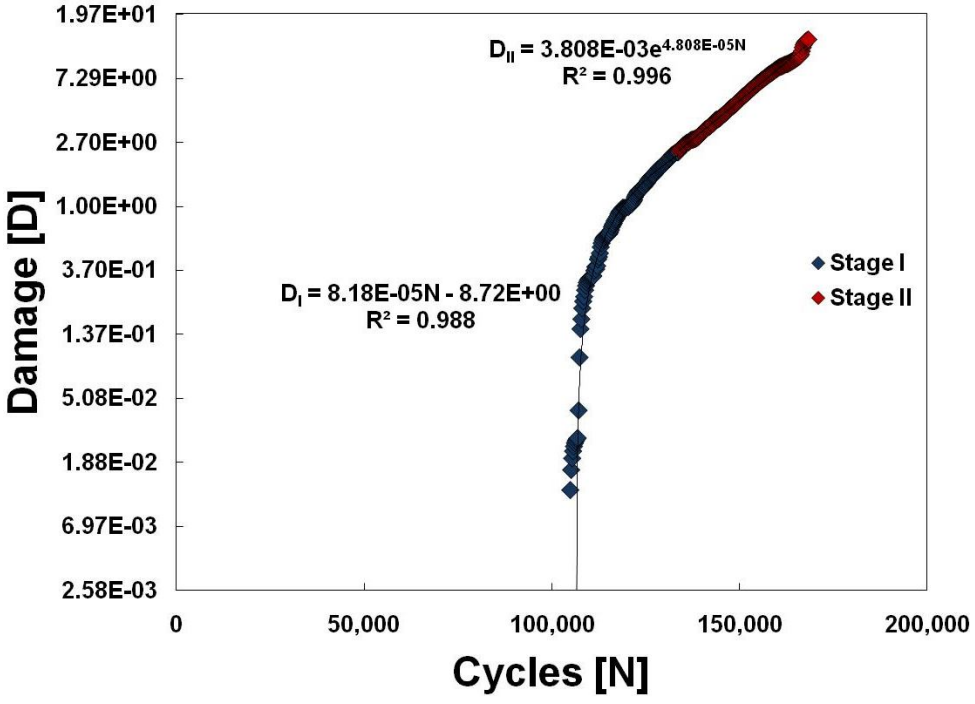

Figure 4.17 Damage accumulation as a function of the number of cycles subjected to σ_4.

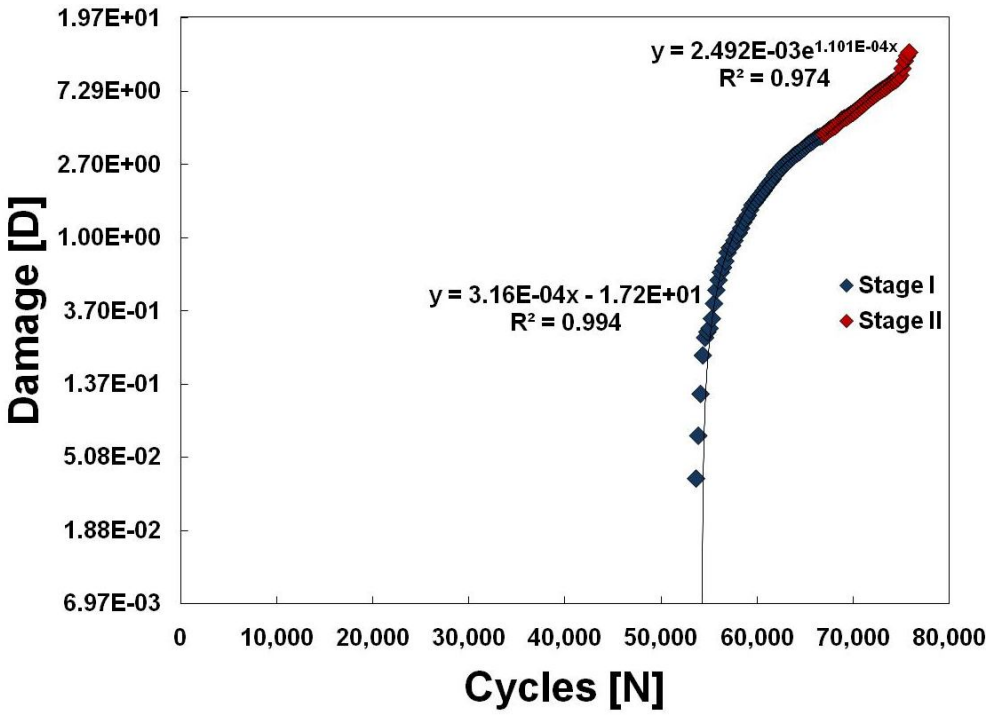

Figure 4.18 Damage accumulation as a function of the number of cycles subjected to σ_5.

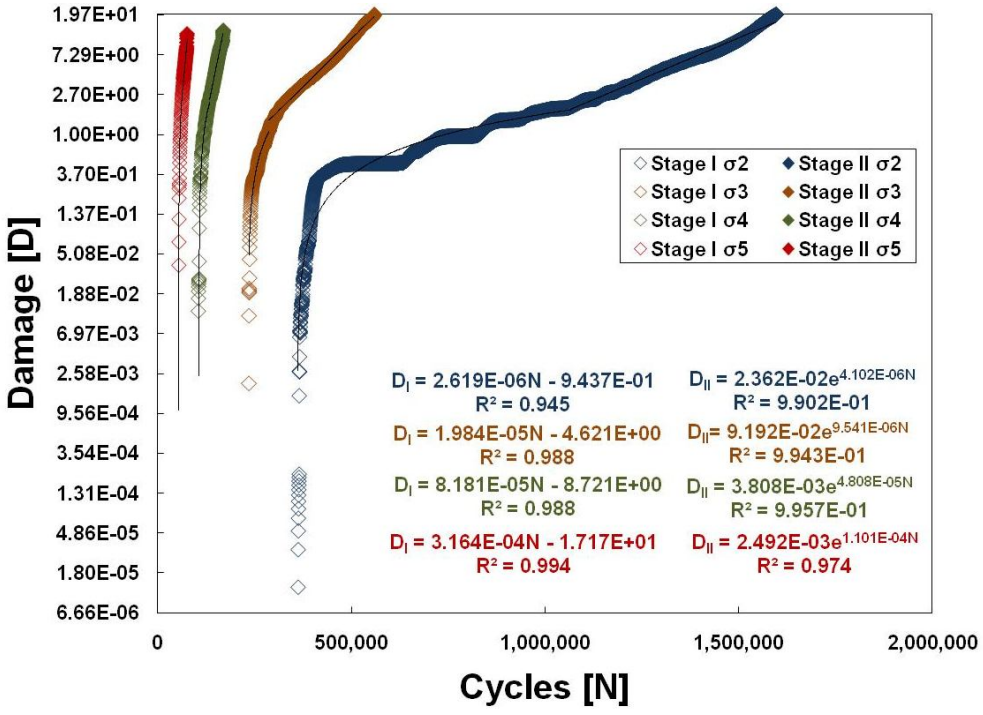

Figure 4.19 Comparison of damage accumulation curves for σ_2 through σ_5.

Table 4.6 Summary of the material parameters of equations (4.2) and (4.3), reported mean [± 1 standard deviation].

Stress Amplitude	α	β	κ	λ
σ_2	8.14E-6 [± 4.74E-6]	4.47 [± 7.07]	0.40 [± 0.72]	5.07E-6 [± 3.24E-6]
σ_3	3.72E-5 [± 2.49E-5]	12.07 [± 12.43]	0.04 [± 0.05]	2.31E-5 [± 1.82E-5]
σ_4	1.03E-4 [± 3.32E-5]	8.46 [± 3.05]	0.04 [± 0.05]	4.77E-5 [± 9.67E-6]
σ_5	1.56E-4 [± 8.20E-5]	1.46 [± 0.47]	0.57 [± 0.31]	5.32E-5 [± 2.84E-5]

Table 4.6 summarizes the mean and spread of the material parameters from equations (4.2) and (4.3). It was observed that the rate terms of the damage relationships for both Stage I and II (i.e. – α and λ) increased with increasing stress amplitude.

In order to further characterize the rate at which damage was accumulated, the data for Stage II was numerically differentiated to determine the rate of damage accumulation (dD_{II}/dN). To this end, the Incremental Polynomial Method (using the 5 data point technique) was utilized (ASTM 2000). With this technique 5 successive data points are fit with a quadratic polynomial of the form

$$D_{II}(N) = c + b\left(\frac{N_i - C_1}{C_2}\right) + a\left(\frac{N_i - C_1}{C_2}\right)^2 \qquad (4.4)$$

where a, b, and c are the regression parameters to be determined from least squares regression, D is the fitted value, and C_1 and C_2 are given by

$$C_1 = \frac{\left(N_{i-n} + N_{i+N}\right)}{2}; C_2 = \frac{\left(N_{i+n} - N_{i-n}\right)}{2} \qquad (4.5)$$

in which i is the iteration under evaluation, and n = 2 when using 5 data points. The fact that damage accumulation rates were quite small, and the number of cycles were comparatively large necessitated C_1 and C_2 being introduced as "centering" parameters to avoid poorly scaled regression coefficients. Noting the conversion back from the centering parameters, the derivative of equation (4.4) is

$$\frac{dD_{II}}{dN} = \frac{b}{C_2} + 2a\left[\frac{(N_i - C_1)}{C_2}\right]^2 . \tag{4.6}$$

This procedure was used for all Stage II damage data, and it was found that the relationship between the rate of damage accumulation and the number of cycles was exponential in nature

$$\frac{dD_{II}}{dN} = \gamma \exp(\eta N) \tag{4.7}$$

where γ and η are stress amplitude dependent parameters. Figure 4.20 through Figure 4.23 provide representative rate of damage accumulation curves for all stress amplitudes in which failures were observed, while Figure 4.24 compares the rate of damage accumulation for the different stress amplitudes. Plots of rate of damage accumulation for all specimens can be found in Appendix B.

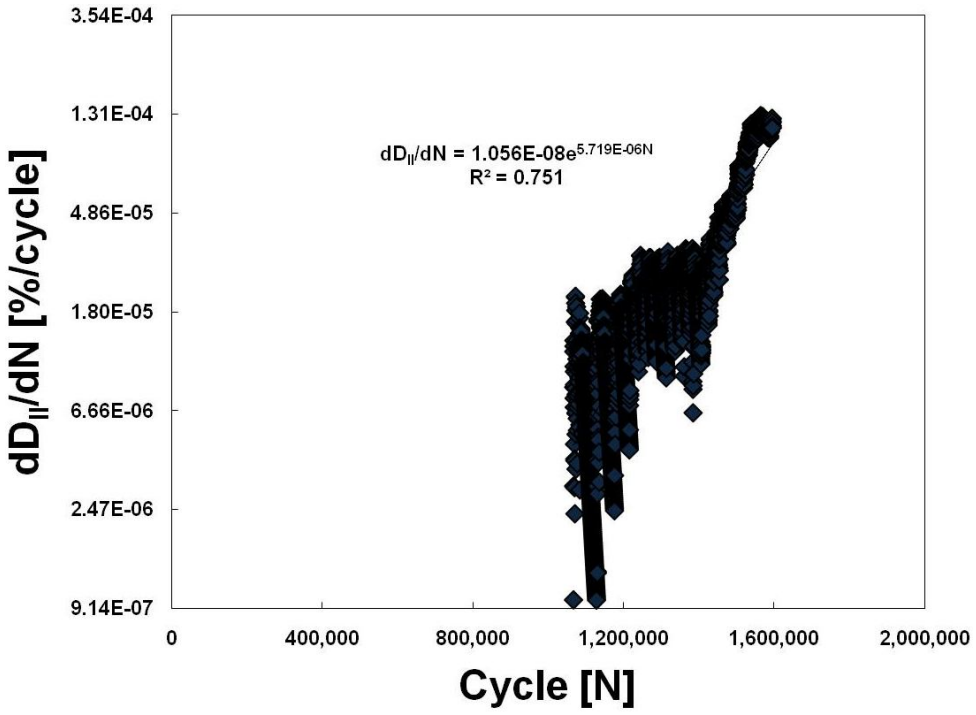

Figure 4.20 Rate of damage accumulation for a specimen subjected to σ_2.

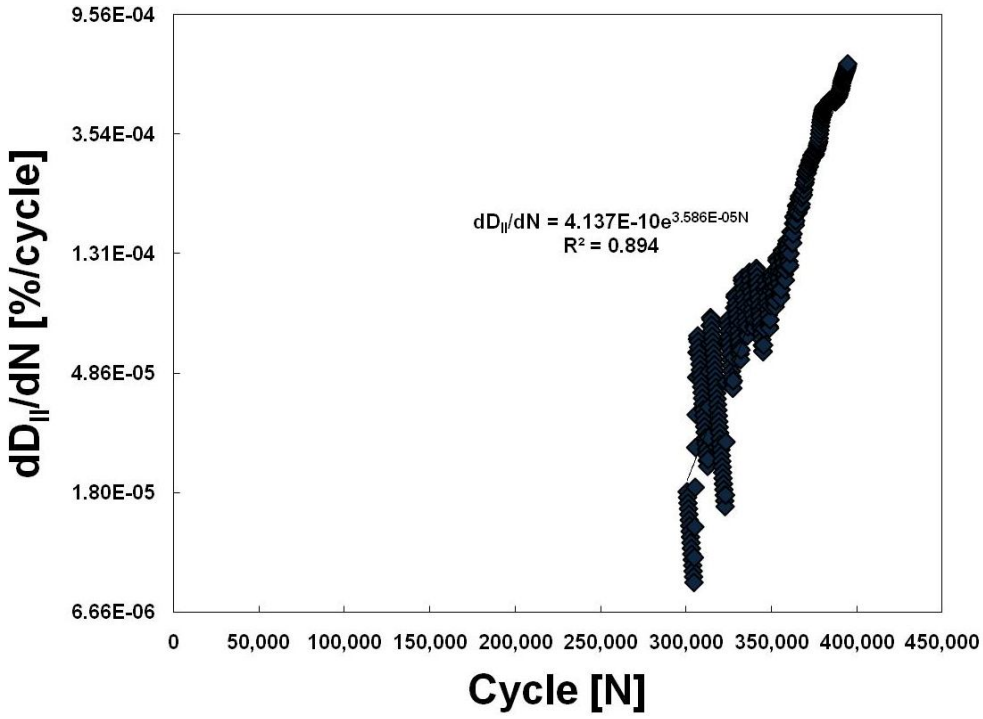

Figure 4.21 Rate of damage accumulation for a specimen subjected to σ_3.

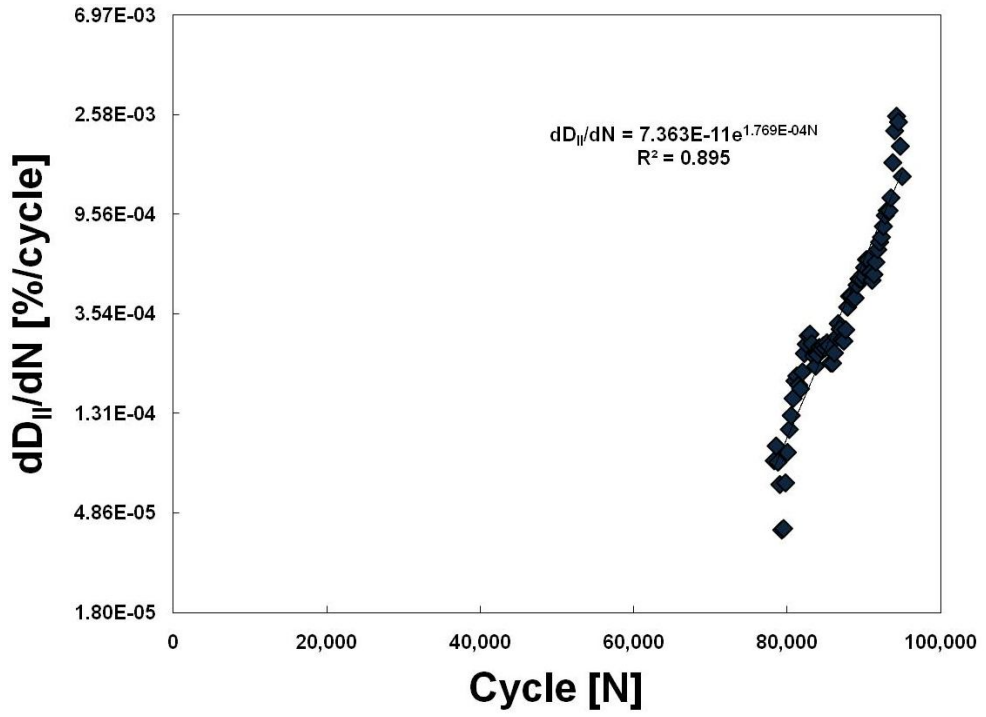

Figure 4.22 Rate of damage accumulation for a specimen subjected to σ_4.

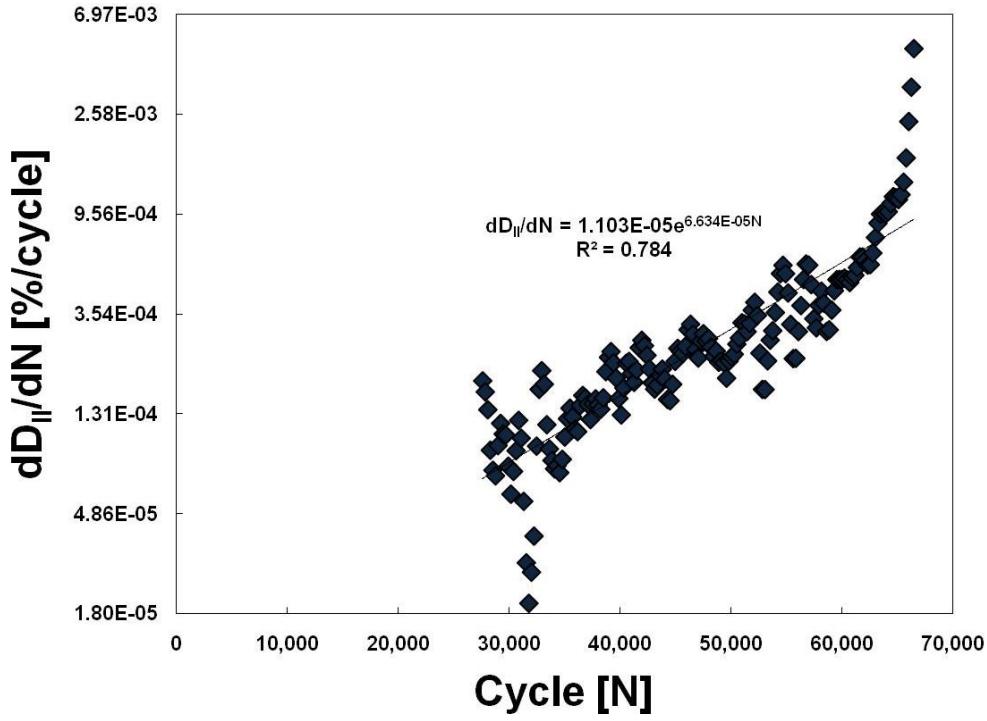

Figure 4.23 Rate of damage accumulation for a specimen subjected to σ_5.

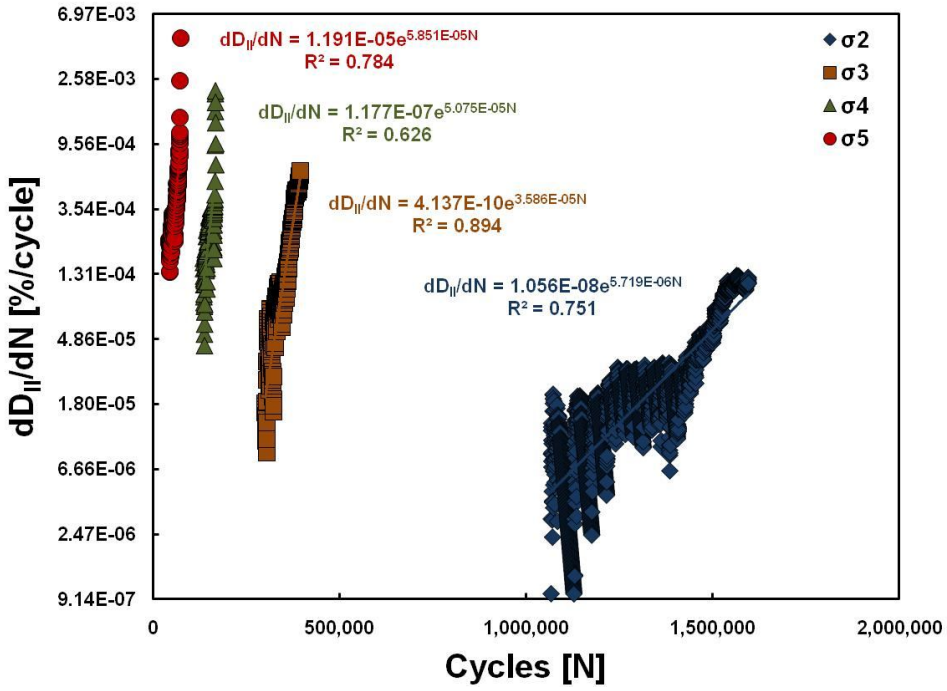

Figure 4.24 Comparison of rates of damage accumulation for σ_2 through σ_5.

From Figure 4.24, it appeared that the rate of damage accumulation increased with increasing stress amplitude. All material parameters are summarized in Table 4.7. With increasing stress amplitude, damage was accumulated at a greater rate, with the exception being between the two highest stress amplitudes, in which no statistical difference existed between the rate term (η) of the two sets of data.

Table 4.7 Summary of rate of damage accumulation material parameters, reported mean [± 1 standard deviation].

Stress Amplitude	γ	η
σ_2	3.83E-6 [± 5.77E-6]	4.89E-6 [± 4.76E-6]
σ_3	5.06E-7 [± 1.01E-6]	2.11E-5 [± 1.09E-5]
σ_4	3.12E-6 [± 7.32E-6]	7.07E-5 [± 5.60E-5]
σ_5	2.81E-5 [± 2.45E-5]	6.75E-5 [± 5.93E-5]

To consider an end of life criteria, failure was defined as a 20% reduction in initial stiffness. This selection appears well justified in light of Figure 4.24, where the rate of damage accumulation had an exponential relationship with respect to cycles. Nearing 20% damage accumulation, the composites' ability to sustain load was rapidly diminishing, indicating fatigue failure (Figure 4.15 through Figure 4.18). The stress amplitude versus the number of cycles to failure (N_f) for each test series is shown in Figure 4.25. When the S-N curve was plotted on a semi-log scale, it was observed that a power law relationship was obeyed for the four highest stress amplitudes considered. The lowest stress amplitude was not included in the power law relationship fit because all five of the specimens tested at that loading condition exhibited run-out behavior (i.e. – did not fail).

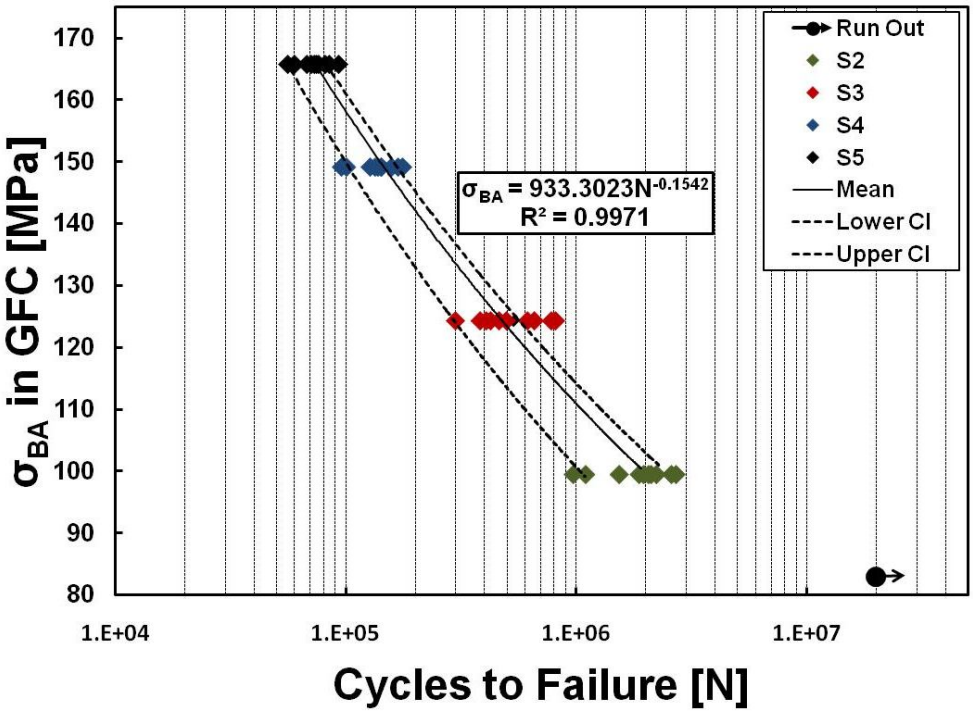

Figure 4.25 S-N curve for the ACCC composite with the 95% confidence interval shown.

It should be noted in Figure 4.25 that the use of the word stress amplitude needs to be put in context since during flexure loading the axial stress gradient within the test specimen is discontinuous (Burks, Middleton and Armentrout, et al. 2010). It was decided in this study to plot the maximum stress amplitude that was present in the GFC versus the number of cycles to failure. This decision was made because of the observation that macroscopic damage in failed specimens was present only in the GFC (Figure 4.26). It was interesting that fatigue damage was confined to the GFC for this hybrid composite in light of the fact that the GFC was at a significantly lower state of axial stress than the CFC; maximum axial stress values for each composite and stress amplitude are summarized in Table 4.8. This peculiarity was the motivating factor behind the micromechanics study of Chapter 5.

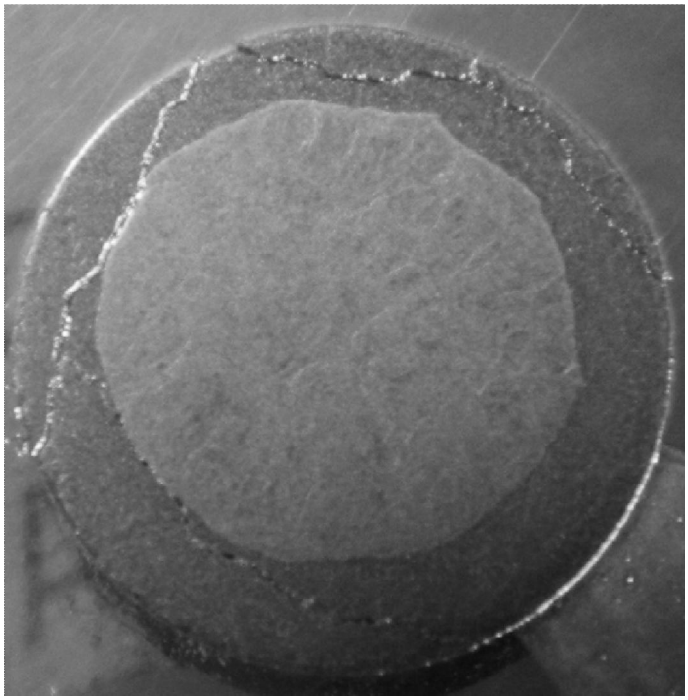

Figure 4.26 Cross section of an ACCC specimen failed in fatigue. Both transverse cracking and axial splitting were observed, and were confined to the GFC.

Table 4.8 Maximum axial stress within each composite subjected to $\sigma_1 - \sigma_5$.

Stress Amplitude	GFC Max Stress [MPa]	CFC Max Stress [MPa]
σ_1	82.9	183.2
σ_2	99.5	219.9
σ_3	124.3	274.8
σ_4	149.2	329.8
σ_5	165.8	366.4

Further investigation of Figure 4.25 lent insight into the statistical scatter of the data. The 5-95 confidence intervals were plotted along with the mean fatigue life line. It was found that in general, an increase in fatigue life corresponded to an increase in the confidence interval as well. All stress amplitude failure distributions were fit with a two parameter Weibull distribution; the appropriateness of fit was verified with a Kolmogorov-Smirnoff goodness of fit test at the 5% significance level (Haldar and Mahadevan 2000). Weibull scale (w) and shape (k) parameters are summarized in Table 4.9, while the cumulative distribution functions (CDFs) are shown in Figure 4.27 through Figure 4.30 for σ_2 through σ_5, respectively.

Table 4.9 Weibull parameters for fatigue failure cycle distributions.

Stress Amplitude	w	k
σ_2	2,106,198	4.18
σ_3	593,862	3.53
σ_4	148,557	6.57
σ_5	78,229	7.67

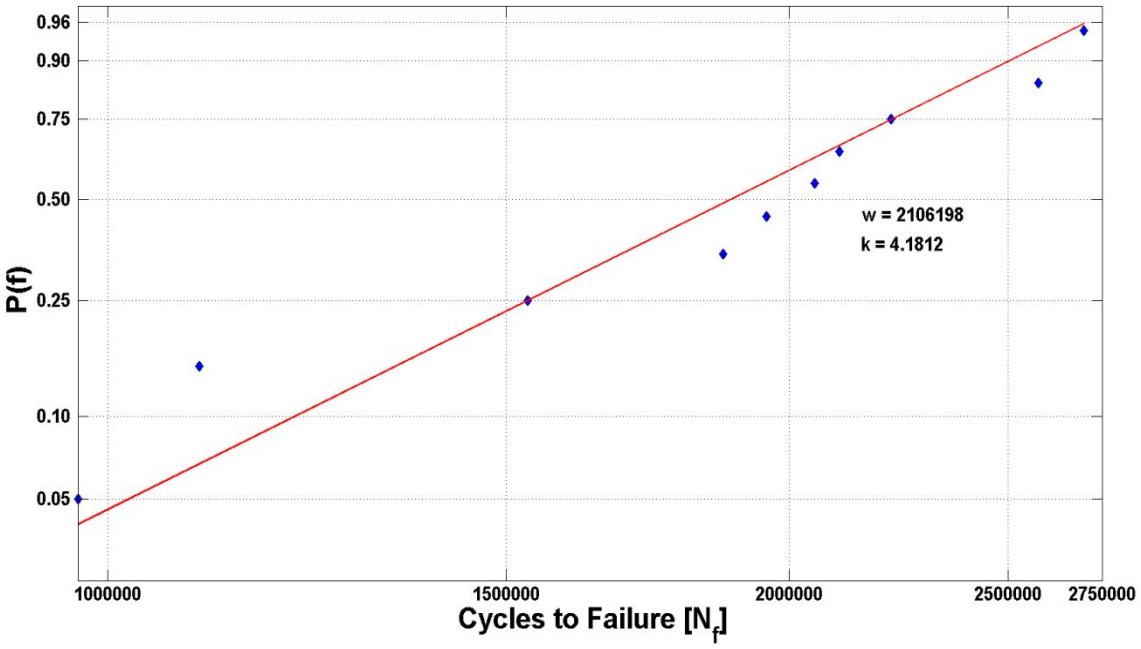

Figure 4.27 Weibull CDF for σ_2; w = 2,106,198, k = 4.18.

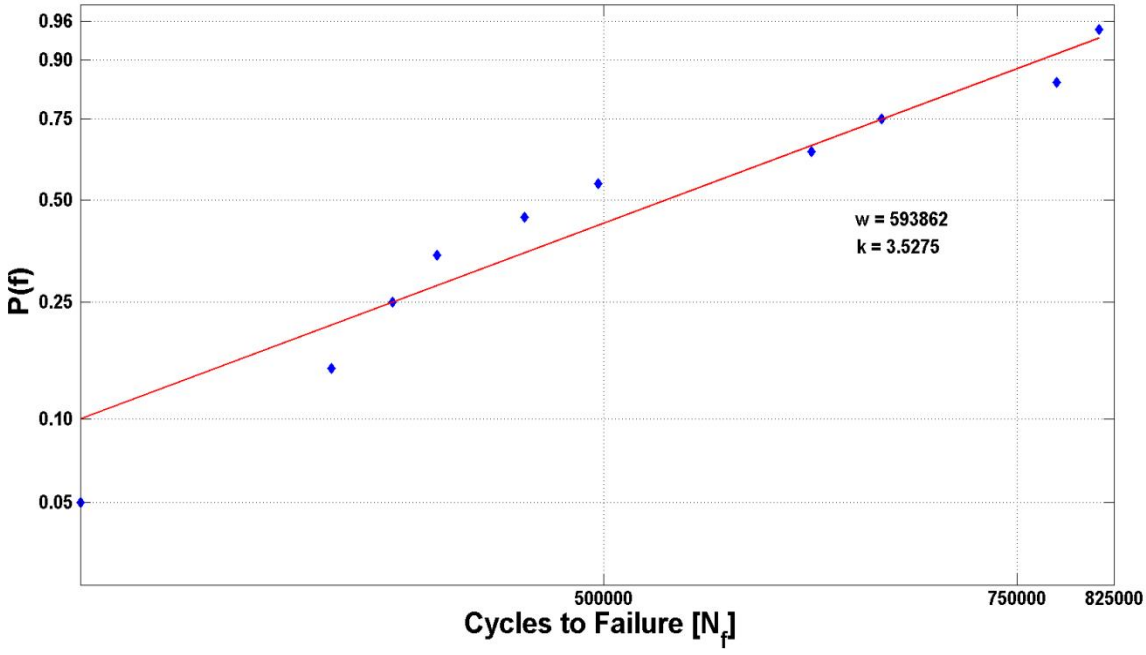

Figure 4.28 Weibull CDF for σ_3; w = 593,862, k = 3.53.

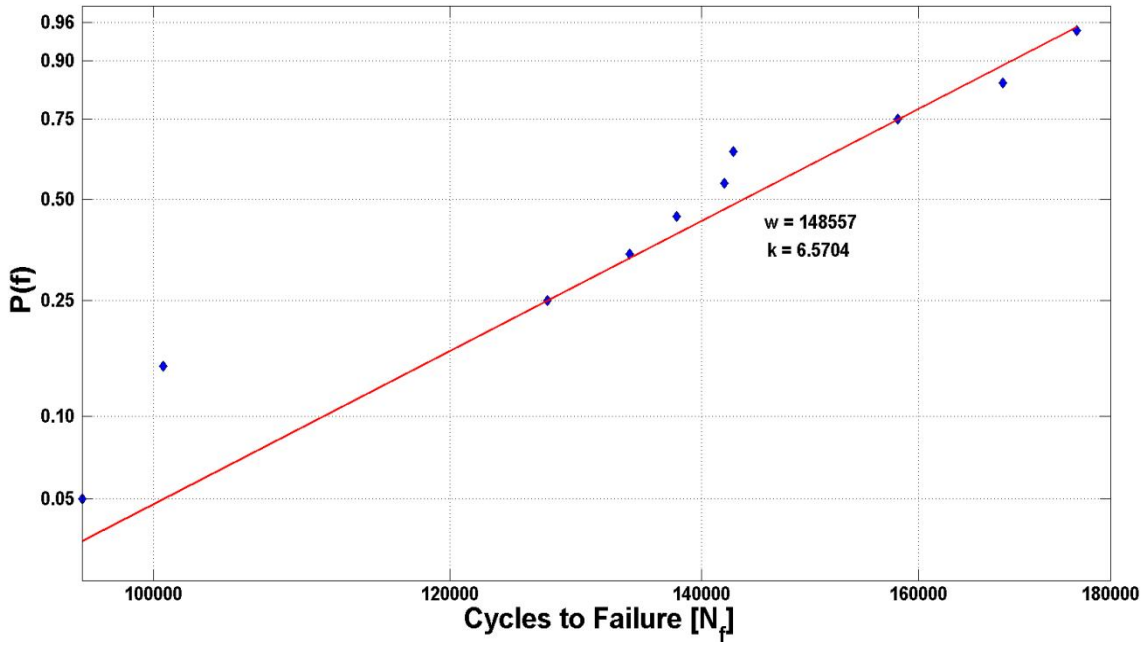

Figure 4.29 Weibull CDF for σ_4; w = 148,557, k = 6.57.

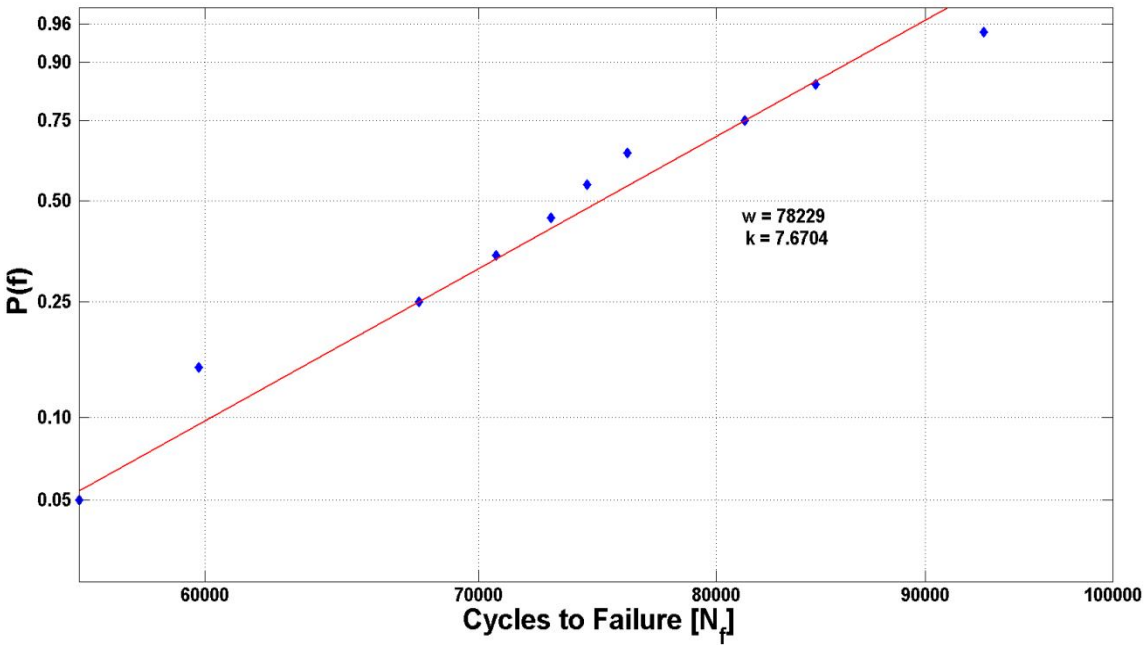

Figure 4.30 Weibull CDF for σ_5; w = 78,229, k = 7.67.

The fact that the higher stress amplitudes followed a power law relationship was found interesting because not only was the axial stress state increasing with increasing stress amplitude (the primary purpose of the experiment), but the amount of significant transverse compression experienced by the specimen was increasing as well (Table 4.5). At the lower stress amplitudes, the amount of the composite that was highly stressed transversely was small, which was not greatly influencing the axial failure of the material, and was manifested in the large scatter of the fatigue life data (i.e. – comparatively small shape parameters). Conversely, as the axial stress amplitude was increased, so to was the amount of the composite that was subjected to a large transverse state of stress. As more of the composite was subjected to a large transverse state of stress the scatter in the data shrank significantly, implying that the failure was no longer predominantly axial, but a mixed mode failure. In the case of a unidirectional composite the scatter inherent to the material will primarily be evidenced in its' axial properties (i.e. – fiber dominated properties). Thus, for axial failures, larger confidence intervals would be expected. However, for a mixed mechanism failure in a unidirectional composite, the transverse state of stress drives the failure, resulting in a significant reduction in the scatter in the data.

Failed specimens for all five loading conditions can be seen in Figure 4.31. For the smaller stress amplitudes, transverse damage was present, but axial splitting in the GFC was more prevalent (Figure 4.32a). It was observed that for the larger stress states (both axial and transverse) that the failure was highly localized where the transverse stress was highest, and damage was present primarily in the form of transversely cracked glass

fibers with axial splitting also being present (Figure 4.32b). At the lower stress amplitudes, the total area of the composite that was subjected to a significant transverse compressive stress was less, allowing enough time for significant axial splits to propagate within the specimen before failure. In all specimens the transverse cracking was arrested at the interface of the glass fiber/ carbon fiber composite (Figure 4.26). Crack arrest at the interface of the two composites occurred because it was energetically favorable for cracks to propagate in the resin rich region.

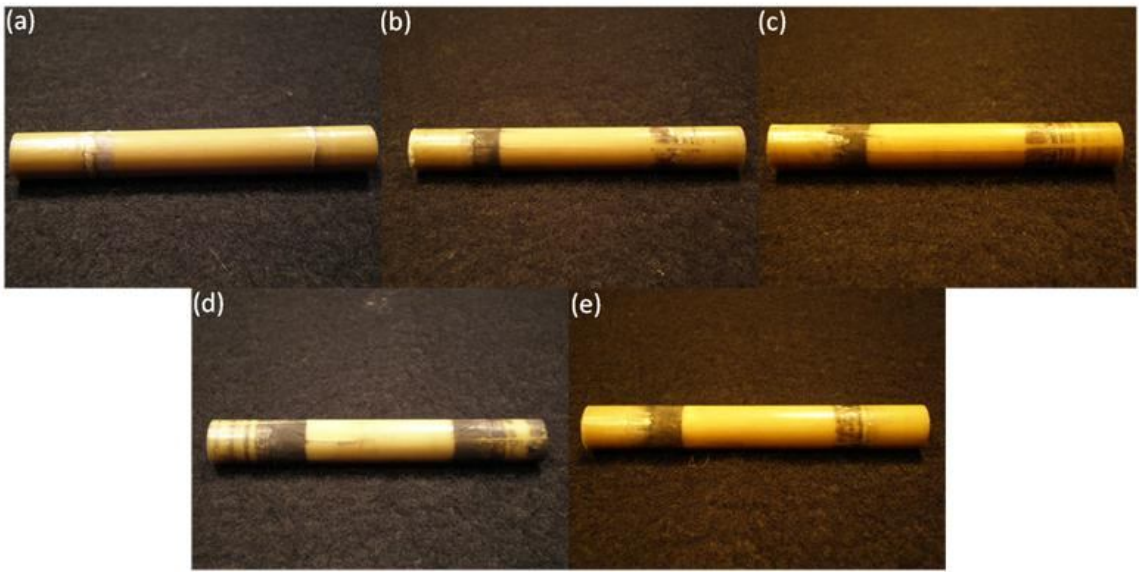

Figure 4.31 Representative failed specimens for the 5 stress amplitudes considered in ascending alpha-numeric order (i.e. – (a) corresponds to σ_1, etc.).

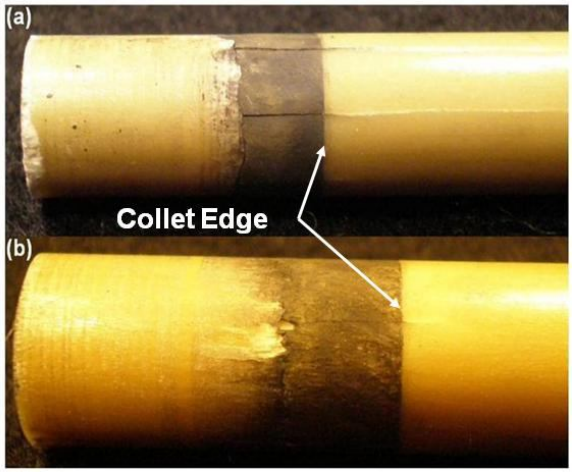

Figure 4.32 Failure morphology of ACCC specimens that were subjected to (a) σ_2, the lowest stress amplitude in which failures where observed and, (b) σ_5, the highest stress amplitude.

Also, it was evident from Figure 4.13 and Figure 4.14 that for specimens subjected to the largest stress amplitude, the rate in stiffening was greater than that of the rest of the stress amplitudes, yet the average maximum increase in deflection did not follow the same increasing trend as the four previous stress amplitudes. For the σ_5 loading condition, the transverse stress state had become too large and damage began to accumulate before the fibers were able to fully align. Thus, a push-pull relationship existed in which fiber alignment (stiffening) was working against damage accumulation. This interaction reduced the magnitude of "Wear-in," and slightly retarded the rate of damage accumulation for the highest stress amplitude, causing it to be statistically indifferent than the damage accumulation rate of σ_4 (Table 4.7).

4.2.2 Numeric macromechanics study

It was proposed that the stiffening effect in Figure 4.13 and Figure 4.14 was caused by an alignment of the reinforcing fibers with the axial direction under the influence of an applied load. Harris proposed that under an applied load, fibers are able to improve their

axial alignment due to small, stress induced, viscoelastic deformations of the matrix resulting in improved ultimate strength values (Harris 2003). We propose that these stress induced deformations enabled the reinforcing fibers of the hybrid composite to improve their alignment, resulting in the increase in stiffness that was observed (Figure 4.13).

To quantify how significant the observed stiffening effect was, the numerical model was initially tuned to match the experimental static deflection data of a specimen that had not been cyclically loaded. Figure 4.33 compares the deflection of the tuned model, to the static experimentally determined deflection for all 5 stress amplitudes.

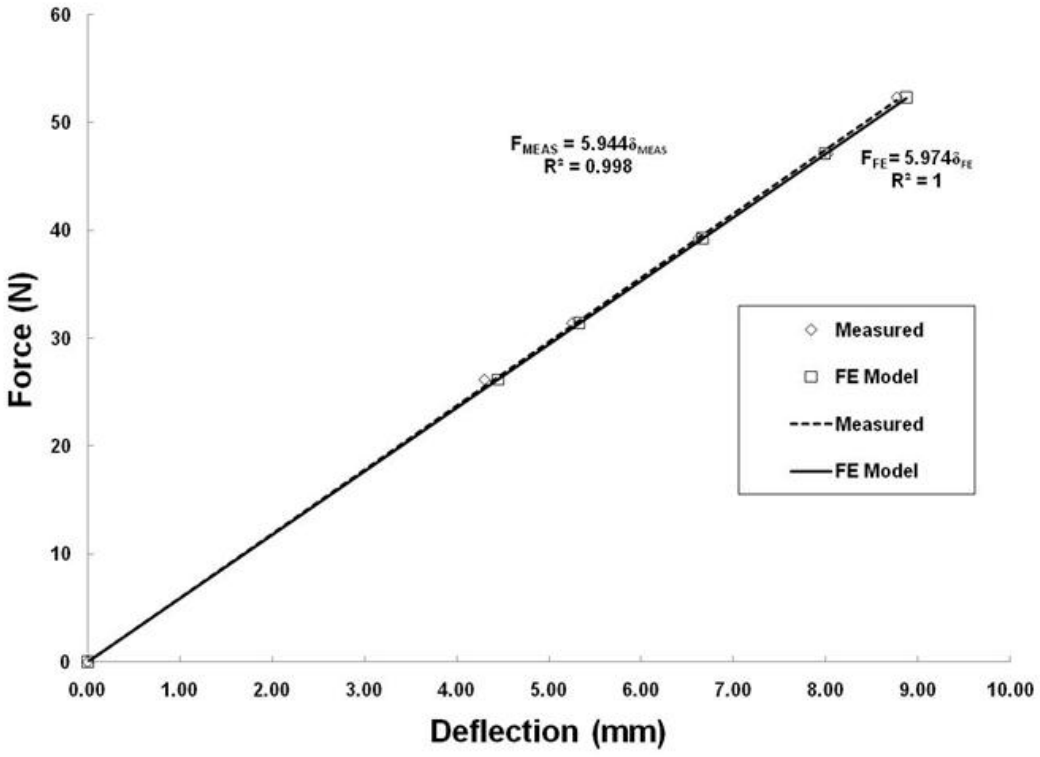

Figure 4.33 Deflection comparison between the tuned finite element model, and experimentally measured values.

Good agreement with experimental data was found from the tuned model; from the minimization procedure, an effective diameter of the moment arm of 8.20 mm was determined.

With the numerical model tuned, the stiffening effect was investigated by modifying the volume fraction of fibers for the individual composite materials (assuming that the other material's v_f remained constant) until the deflection of the system calculated by the model was equivalent to the mean change in deflection experimentally measured for each of the stress amplitudes (Figure 4.14). An equivalent volume fraction of fibers were determined via a steepest descent minimization procedure for each stress amplitude.

It is shown in Table 4.10 that the effect was found to be significant, and was comparable to obtaining an increase between 4 percent at the lowest stress amplitude and 11 percent in the volume fraction of fiber of the composite at the higher stress amplitudes. It was expected that at higher stress amplitudes, fibers would be able to align to a greater extent. Unit cell modeling was performed to investigate the effect of several of the parameters associated with the "Wear-in" effect; results are forthcoming in section 4.2.4.

Nevertheless, recently published data strongly support the results of the present optimization study. Recall that the initial finite element model was developed assuming that the CFC and the GFC had a volume fraction of fibers of 60%, a value reported in (Alawar, Bosze and Nutt 2005). In a more recent study (funded by the manufacturer of the hybrid composite) the volume fraction of fibers for the GFC was reported as 64%, while for the CFC v_f was reported as 69%. These values are in reasonable agreement

with the equivalent volume fraction of fibers reported presently (in particular the CFC results), supporting the notion that fibers improved their alignment during cyclic loading.

Table 4.10 Equivalent volume fraction of fibers for all stress amplitudes from the "Wear-in" process determined via the minimization procedure.

Test Series	Equivalent CFC v_f	Equivalent GFC v_f
σ_1	63.2	64.5
σ_2	64.2	65.6
σ_3	66.8	69.4
σ_4	68.3	71.5
σ_5	65.1	67.0

4.2.3 Probabilistic macromechanics study

For all 100 Monte Carlo analyses the deflection of the system was extracted, and the mean and standard deviation calculated. It was found that the experimental variability in maximum "Wear-in" was well captured through the use of the numeric platform. Results for the variability in the modification of both composite materials are presented in Figure 4.34. The excellent agreement confirmed that it was possible to numerically capture the experimental scatter.

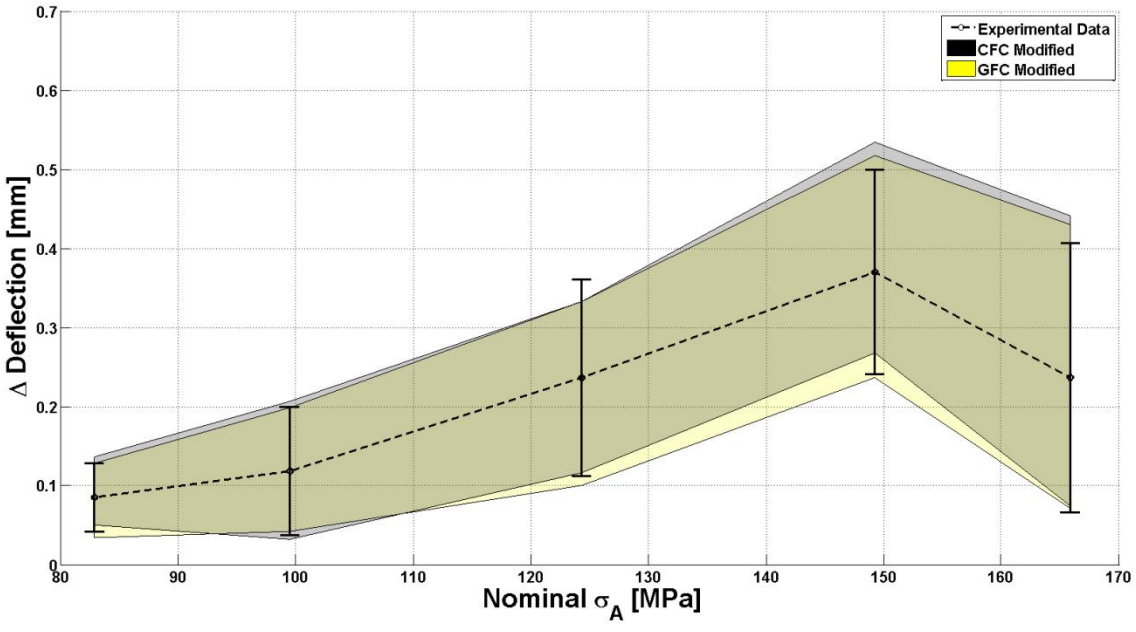

Figure 4.34 Comparison of the probabilistic FE results with experimental data (1 standard deviation scatter bands shown).

In section 4.2.1, it was shown that all observable fatigue damage was accumulated in the GFC, and that the CFC remained undamaged. For this reason, the maximum axial stress within the GFC was extracted for each analysis. For the case in which the CFC was considered to stiffen, the maximum axial stress in the GFC was found to negatively correlate with the change in deflection of the system (Figure 4.35).

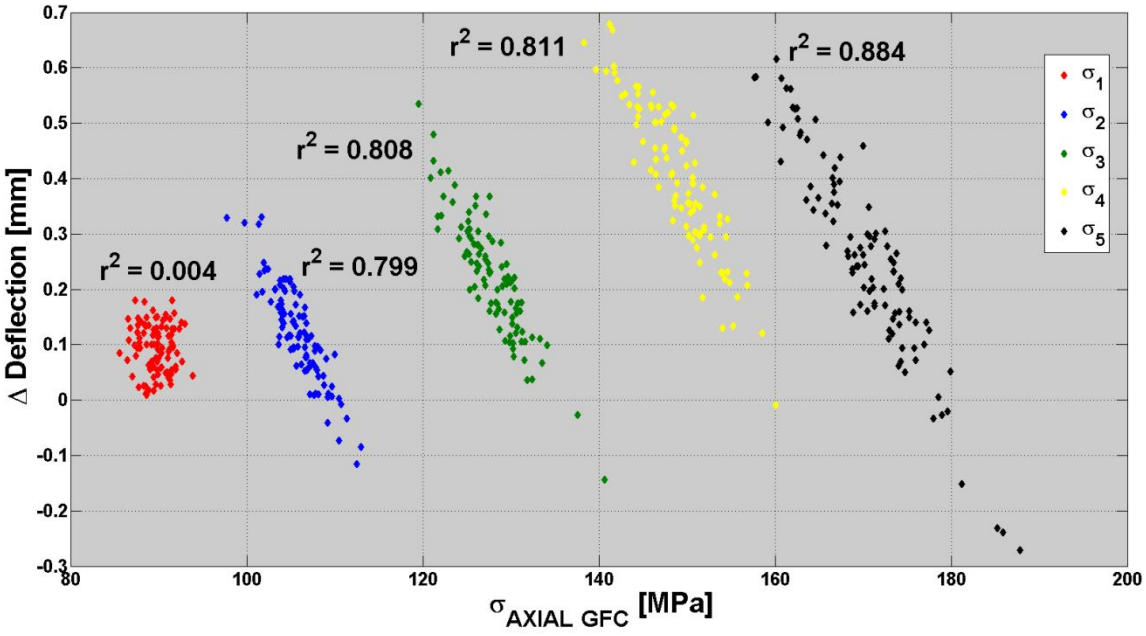

Figure 4.35 Correlation between the change in system deflection and the max $\sigma_{AXIAL\ GFC}$ for the case in which the CFC v_f was modified.

Conversely, for the case in which the GFC was considered to stiffen, the maximum axial stress within the GFC was found to positively correlate with the change in system deflection (Figure 4.36). In both cases, the amount of correlation was found to increase with increasing stress amplitude; the coefficients of determination are summarized in Table 4.11.

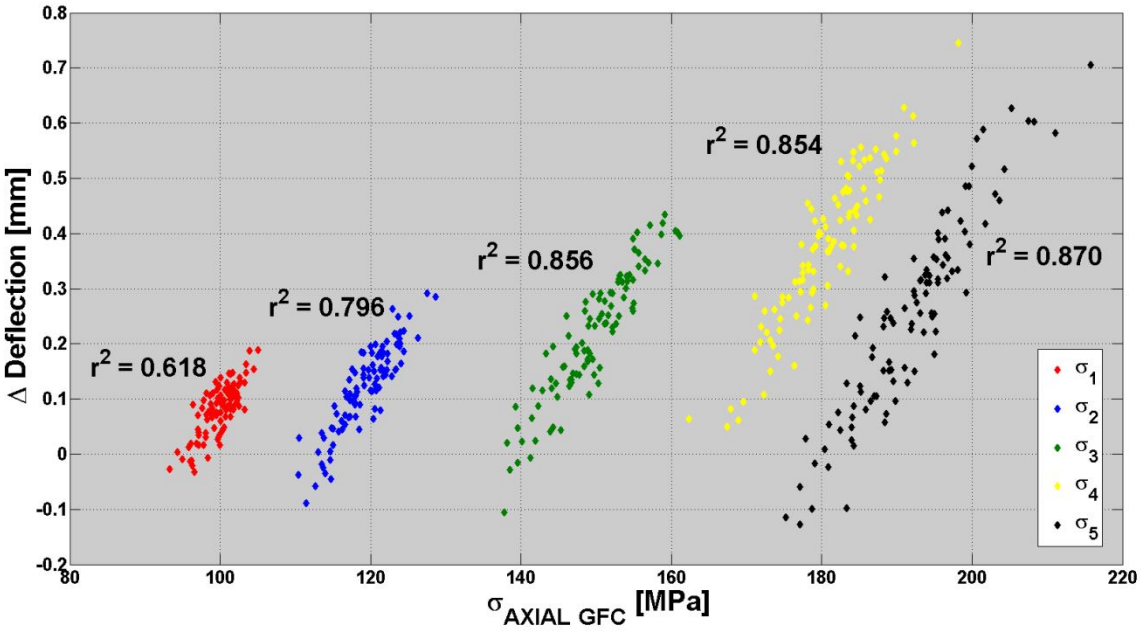

Figure 4.36 Correlation between the change in system deflection and the max $\sigma_{AXIAL\ GFC}$ for the case in which the GFC vf was modified.

Table 4.11 Coefficient of determination between the maximum stress in the GFC and the change in deflection for each stress amplitude.

Stress Amplitude	Modified CFC v_f	Modified GFC v_f
σ_1	0.004	0.616
σ_2	0.799	0.796
σ_3	0.808	0.856
σ_4	0.811	0.854
σ_5	0.884	0.870

An analytic solution for the axial stress state within the hybrid composite material during flexure loading was previously developed (Burks, Middleton and Armentrout, et al. 2010). In this derivation, it was shown that the axial state of stress within the hybrid composite is a function of the ratio of the axial stiffnesses of the respective composites.

In view of this, one may understand the results presented in Figure 4.35 and Figure 4.36. For the study where the CFC v_f was modified (i.e. – increased from its' nominal value), the ratio of the axial stiffness' was shifted towards the CFC. The implication becomes that the CFC bears more of the bending moment, reducing the state of axial stress within the GFC, and resulting in the negative correlation that was observed with the increase in system deflection. On the contrary, for the study in which the GFC v_f was modified, the ratio was slighted towards the GFC, increasing the amount of the bending moment that the GFC was bearing. This in turn increased the axial state of stress within the GFC, and resulted in the observed positive correlation between the increase in deflection and the maximum axial stress within the GFC. The fact that the correlation between the change in deflection and the maximum axial stress in the GFC was not perfect (i.e. – $r^2 \neq 1$) for any of the stress amplitudes indicated that the cross-sectional geometric variability had an impact on both response variables.

For all ten cases considered in this research the maximum axial stress within the GFC was fit with a distribution that best described the data. Normal, log-normal, and Weibull distributions were considered. The appropriateness of fit was checked at the 5% significance level via the Kolmogorov-Smirnoff goodness of fit procedure (Haldar and Mahadevan 2000). An example of the cumulative distribution function (CDF) for the σ_3 CFC modified v_f can be seen in Figure 4.37. Table 4.12 presents all distributions, and their respective parameters, that best described the maximum axial stress within the GFC. Additionally, for all stress amplitudes the maximum axial state of stress analytically calculated (Table 4.8) was compared to the appropriate distribution; recall that the

aforementioned deterministic stress values were calculated assuming the nominal geometry and material parameters.

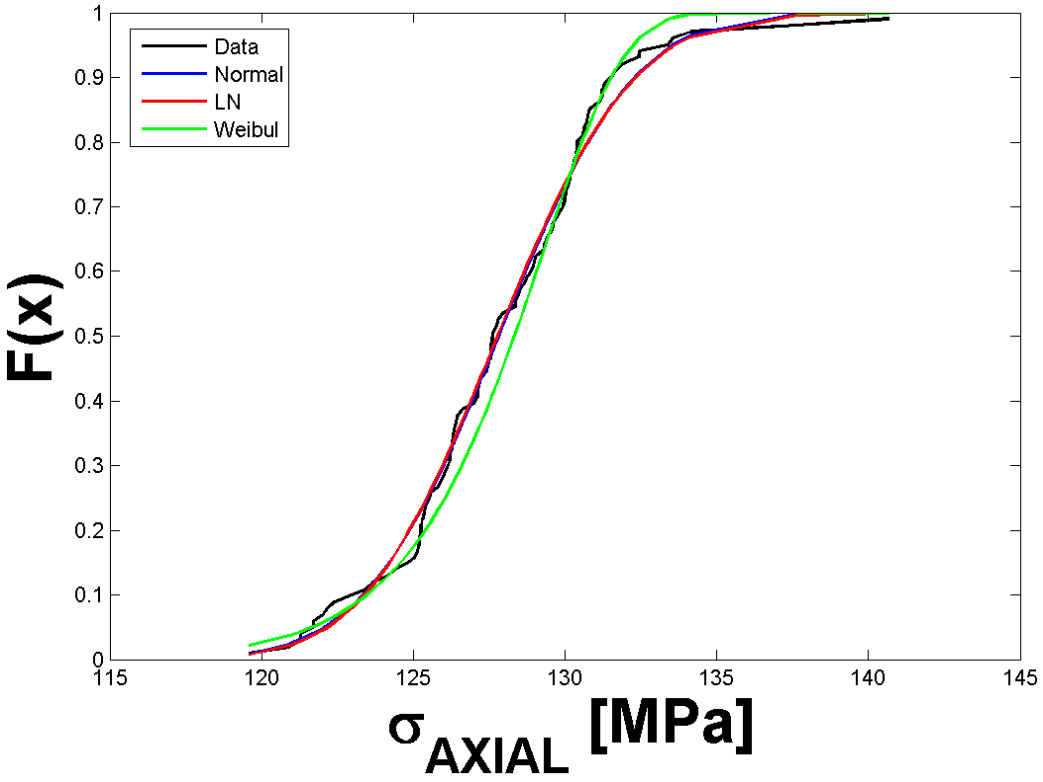

Figure 4.37 Representative empirical CDF with all distribution fits. Results are presented for σ_3 in the CFC modified vf study.

Table 4.12 Best fit distribution parameters for each stress amplitude, and the corresponding percentile of the deterministic stress value.

	CFC Modified v_f				GFC Modified v_f			
σ_A	**Type**	**Param 1**	**Param 2**	**Percentile**	**Type**	**Param 1**	**Param 2**	**Percentile**
σ_1	**Normal**	89.76	1.670	0.0%	**Weibull**	59.57	100.886	0.000831%
σ_2	**Normal**	105.92	2.687	0.8%	**Normal**	119.39	3.712	0.000004%
σ_3	**Normal**	127.83	3.488	15.6%	**Normal**	149.63	5.477	0.000187%
σ_4	**Weibull**	46.62	150.861	44.9%	**Normal**	180.42	6.090	0.000015%
σ_5	**LN**	5.14	0.035	22.9%	**LN**	5.26	0.040	0.012880%

It was found for each σ_A considered, that the experimental deterministic maximum axial stress in the GFC fell below the 45th percentile for all of the Monte Carlo FE simulation distributions. This finding implies that an understanding of the local variability in both geometry and material properties is essential for understanding the axial state of stress within the GFC, which will greatly impact the fatigue performance of the hybrid composite material as has been shown experimentally (Figure 4.25), and will be further pontificated via the micromechanics analyses in section 5.2.2.

4.2.4 Micromechanics modeling of the "Wear-in" effect

The viscoelastic material properties of the epoxy resin were measured via a DMA dual cantilever configuration, specifics of which can be found in the literature (Middleton, Wells, et al. 2011). It was found that a 5 term Prony series expansion was adequate in capturing the material behavior over the frequency range investigated (0.01 Hz to 50.0 Hz) (Figure 4.38). The coefficients of the fit are summarized in Table 4.13.

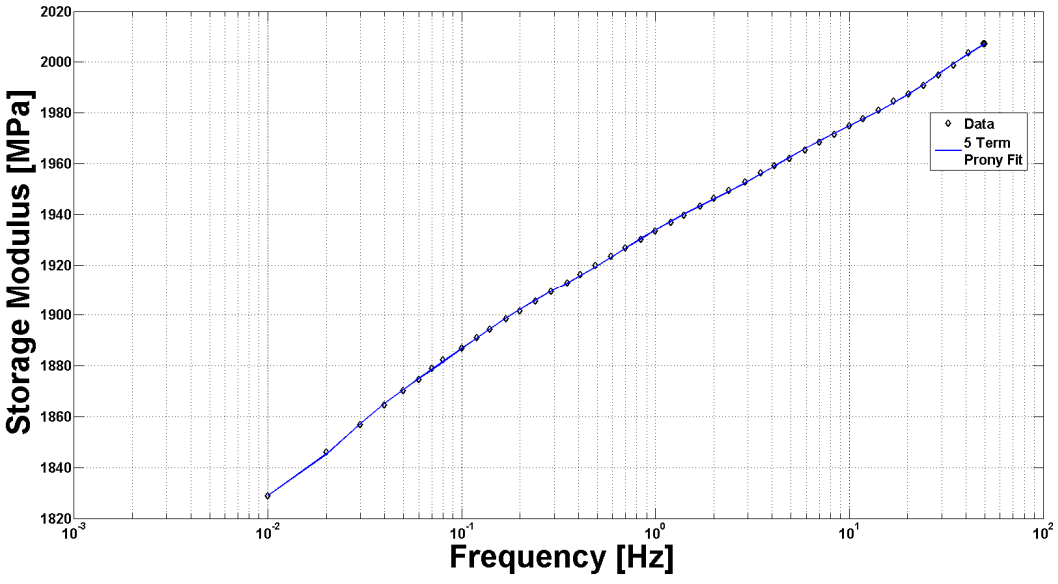

Figure 4.38 Viscoelastic data of the neat resin epoxy system fit with a 5 term Prony series expansion.

Table 4.13 Prony series coefficients for epoxy viscoelastic material properties.

Parameter	Value
E_o [MPa]	2020.22
e_1	0.0272
e_2	0.0217
e_3	0.0158
e_4	0.0170
e_5	0.0178
τ_1	7.3135
τ_2	0.0050
τ_3	0.0363
τ_4	0.2231
τ_5	1.3048

As the material under study was a continuous fiber composite, it was paramount in the micromechanics modeling of the stiffening effect to ensure that the axial dimension of the 3-Dimensional unit cell was not influencing the results. To this end, the effect that the aspect ratio (RVE axial length/fiber diameter) of the unit cells had was investigated. Figure 4.39 shows the calculated improvement in fiber misalignment (MA) ($\Delta\theta$) as a function of aspect ratio for several applied macroscopic stress levels, for a CFC RVE with a volume fraction of fibers of 60%, and initial fiber misalignment of 1 degree.

Several key observations were made from Figure 4.39. Most importantly, from these micromechanics analyses, the hypothesis that misaligned fibers align themselves in the direction of macroscopic loading was confirmed. Moreover, it was found that the improvement in alignment with the axial direction converged as the aspect ratio of the unit cell analyzed increased; for this reason, the geometry of all further analyses was set

to an aspect ratio of 20. Also, the improvement in alignment clearly increased with increasing applied stress levels, as had previously been postulated.

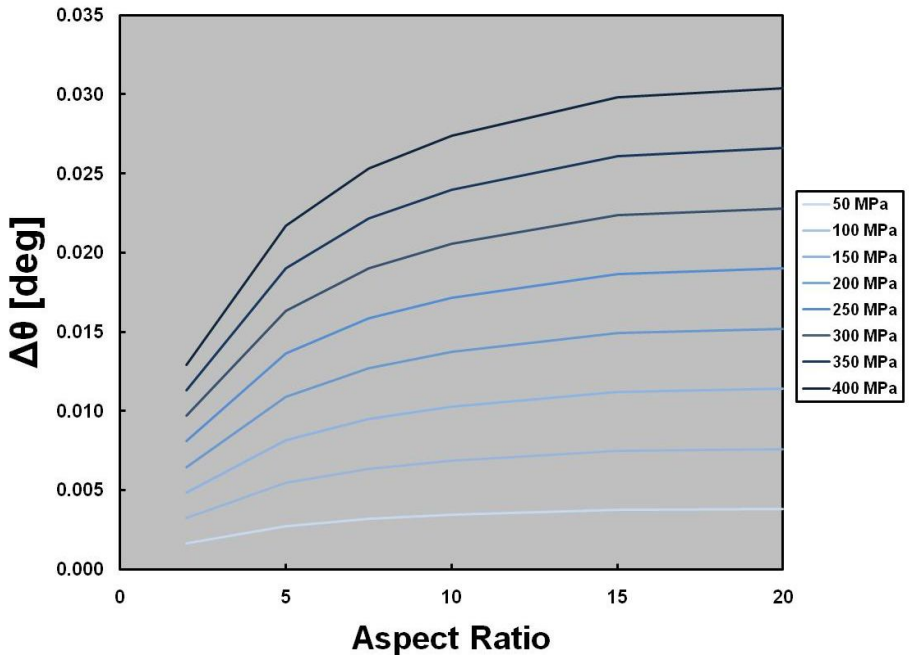

Figure 4.39 Improvement in fiber misalignment as a function of aspect ratio for several harmonically varying applied stress levels.

The combined effects of initial fiber misalignment, and applied macroscopic stress on a CFC RVE with 65% v_f are shown in the surface plot of Figure 4.40. From Figure 4.40, it was clear that poorly aligned fibers subjected to large stress amplitudes would align themselves to the greatest extent, while decreases in either of the variables would lead to less improvement in alignment. Similar results were obtained for all volume fractions of fibers. The analogous plot for the GFC RVE is shown in Figure 4.41. In light of the maximum stress experienced by each composite, the amount of harmonic stress applied to the respective RVE's was reduced for the GFC (Table 4.8).

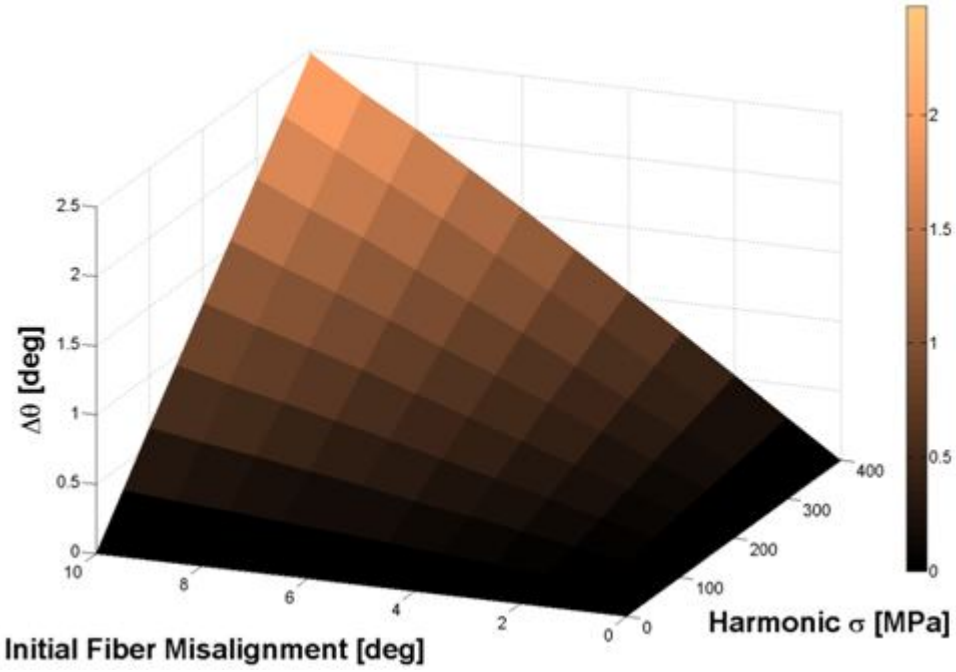

Figure 4.40 Surface plot showing the calculated improvement in fiber alignment as a function of the applied stress, and initial fiber misalignment for a CFC RVE with 65% v_f.

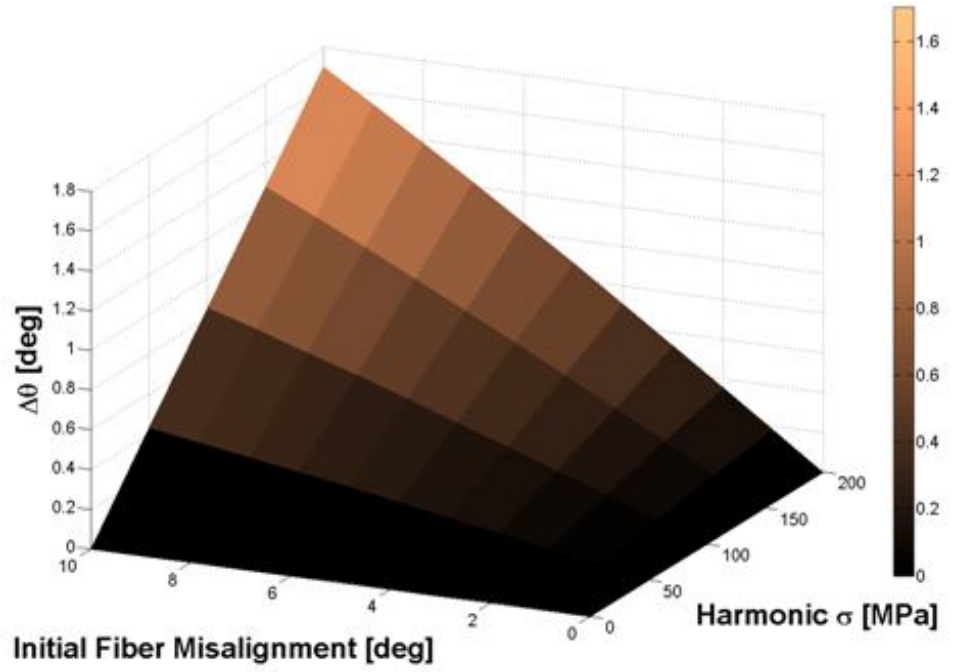

Figure 4.41 Surface plot showing the calculated improvement in fiber alignment as a function of the applied stress, and initial fiber misalignment for a GFC RVE with 65% v_f.

When comparing Figure 4.40 and Figure 4.41 it was clear that misaligned glass fibers were able to align themselves to a greater extent at equivalent stress amplitudes in comparison to carbon fibers, for equivalent stress amplitudes. As glass fibers are significantly less stiff in the axial direction than are carbon fibers, less axial constraint was provided by neighboring fibers enabling greater alignment.

Figure 4.42 shows the effect that the volume fraction of fibers had on the improvement in fiber alignment for several initial misalignment levels for the CFC; similar results were found for the GFC. It was found that as the volume fraction of fibers increased, the amount of alignment decreased. This is explained from the fact that as volume fraction of fibers increases, inter-fiber spacing decreases, effectively increasing axial constraint from neighboring fibers and restricting the amount of alignment that the fibers could obtain.

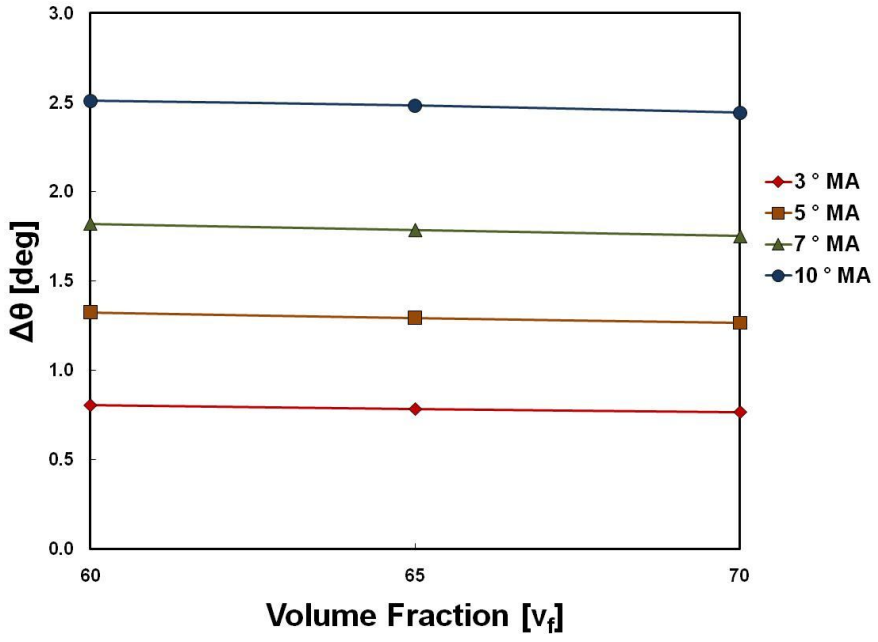

Figure 4.42 Effect of v_f on the improvement in fiber alignment for various levels of fiber misalignment.

Finally, the effect that excitation frequency of the system had on the improvement in fiber alignment was evaluated for a CFC RVE with v_f = 60%, stress amplitude of 300 MPa, and an initial fiber misalignment of 1.0 degrees. From Figure 4.43 it was observed that the excitation frequency did affect the improvement in fiber alignment, albeit a nearly negligible effect. Clearly the dependence of the epoxies' stiffness on excitation frequency had a negligible effect on the ability of the stiff fibers to align in the compliant matrix. Similar results were found for all volume fractions of fibers, initial fiber misalignments, stress amplitudes, as well as the GFC.

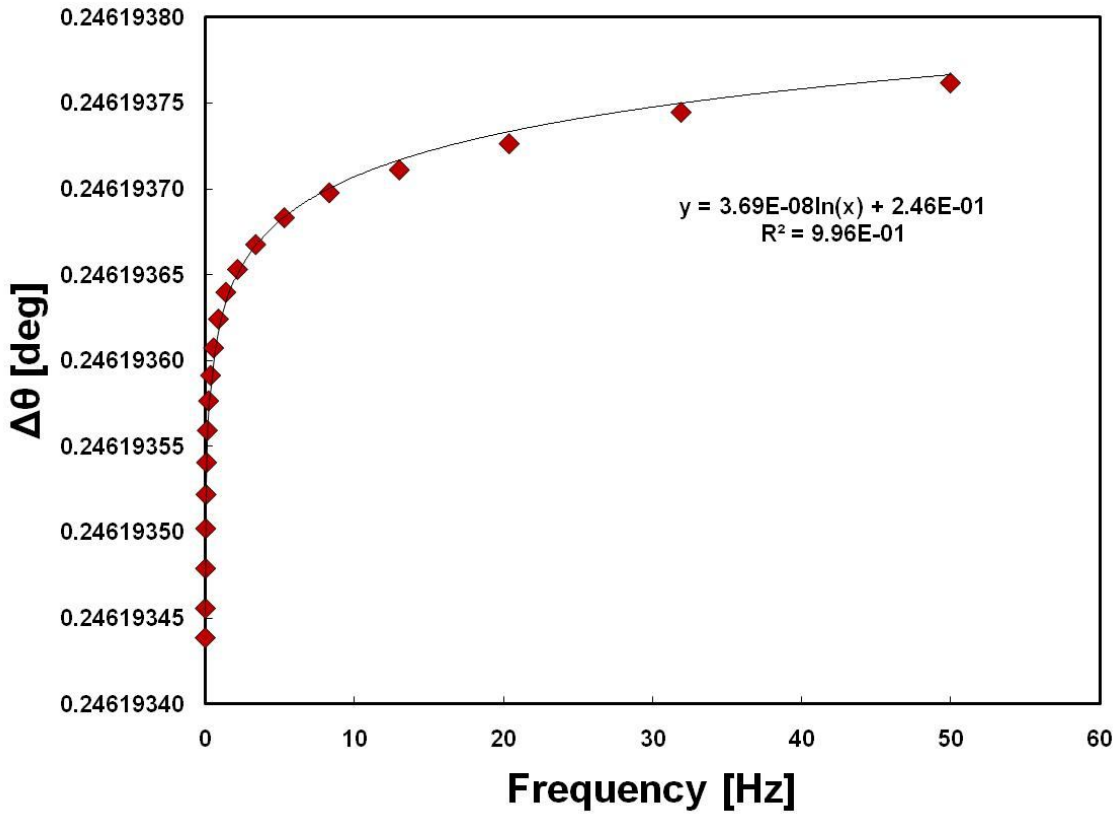

Figure 4.43 Effect of frequency on improvement in fiber alignment.

From the perspective of the micromechanics analyses of this section, a number of the experimental observations for the "Wear-in" region may be explained. Before the composite was cyclically loaded, the microstructure of the composite was such that fibers were not perfectly aligned with the axial direction, to a lesser or greater extent. As cyclic loading began and steady state was achieved, misaligned fibers were able to improve their alignment a certain amount ($\Delta\theta$), which was shown to be a function of the macroscopic stress level as well as the initial amount of misalignment. As the loading condition was flexure, and an axial stress gradient was present in both the CFC and the GFC (with a discontinuity at the interface of the two), fibers further from the center of the material were able to align themselves to a greater extent. However, as was evidenced in Figure 4.40 and Figure 4.41, as the fibers improved their respective alignment with the axial direction, the rate at which they would continue to align decreased. If given enough time before substantial damage began accumulating in the composite, the material's stiffness would plateau, as was experimentally observed for the stress amplitudes in which significant axial stress was present, but damage accumulation did not prematurely commence (σ_3 and σ_4, Figure 4.13).

4.3 Summary of unaged fatigue behavior

The fatigue performance of the hybrid composite material in an unaged condition was evaluated via a rotating beam test protocol. A rotating beam test protocol was found favorable, as it allowed for evaluation of the effect that a multi-axial loading condition had on the failure mechanisms of the composite. It was found that at lower stress amplitudes (with a correspondingly reduced amount of highly transversely stressed area) axial failures were dominant, manifested in the small shape parameters of the corresponding cycles to failure Weibull distributions. At larger stress amplitudes (with a correspondingly larger amount of highly transversely stressed area) the failure mechanism became mixed mode between transverse compression and axial failure. This change in failure mode was evidenced by the considerably sharper cycles to failure Weibull distributions.

Fatigue behavior of the material was found to occur in 2 distinct regions, the first of which was termed a "Wear-in" region. As the composite was initially cycled, the axial stiffness of the hybrid composite increased. The increase in stiffness positively correlated with the maximum axial bending stress. It was postulated that the improvement in stiffness was attributed to misaligned fibers improving their alignment with the axial direction, under the influence of an applied tensile stress. This conjecture was confirmed via the micromechanics analyses of section 4.2.4, in which it was found that fibers were able to improve their alignment with the axial direction to a greater extent under greater applied stress levels. In addition fibers with poorer alignment were able to improve their alignment at a greater rate. The micromechanics modeling

predicted that as fibers improved their alignment the rate at which the stiffness of the hybrid composite was changing would eventually plateau, as was experimentally observed. Finally, by accounting for the viscoelastic nature of the epoxy resin, it was determined that the dependency that the epoxy's stiffness had on frequency had a negligible effect on the improvement in fiber alignment.

From a macromechanics perspective, the finite element model of the experimental set-up proved to be a valuable tool. The tuned model was developed assuming a volume fraction of fibers taken from the literature, and was subsequently used to evaluate the "Wear-in" effect. Through this study, an equivalent volume fraction of fibers was calculated. The calculated values were in good agreement with more recently published values of the volume fraction of fibers for each of the composite materials; in the more recent study, the volume fraction of fibers was actually measured, whereas in the former study the volume fraction of fibers was estimated based upon manufacturing parameters.

The second portion of fatigue life was termed the damage accumulation portion. It was observed that damage was accumulated in a 2 stage fashion. In the initial portion of damage accumulation the relationship between damage and number of cycles was linear, whereas during the second stage of damage accumulation, the relationship between the two variables became exponential in nature. For both stages, damage accumulation rates increased with increasing stress amplitude. Finally, a Basquin relationship adequately described the Wohler curve of the hybrid composite material.

5. THE EFFECT OF THERMAL AGING IN AN OXIDATIVE ENVIRONMENT

One of the primary advantages of the ACCC conductor design is that it is not thermally restricted to operating temperatures of ~100 °C. By incorporating carbon fibers into the load bearing member of the conductor design, sag at elevated temperatures is mitigated, allowing utility companies to transmit greater amounts of electricity to meet consumer demand during heavy load periods. However, in transmitting greater amounts of power the temperature on the transmission line will increase due to resistive heating.

This fact brings into question what effect prolonged exposure to elevated temperatures will have on the hybrid composite material's mechanical properties. Of primary concern to the author was how elevated temperature exposure would affect the fatigue performance of the hybrid composite material. A fair amount of information may be found in the literature with respect to the effect that elevated temperatures has on quasi-static mechanical properties (Lowe, Fox and Otieno-Alego 2002) (Barjasteh, Kar and Nutt 2011). However, to the author's knowledge the present study is the first to consider the effect that prolonged elevated temperature exposure has on the fatigue behavior of a composite material. In addition, the quasi-static flexure strength as a function of aging time was evaluated, as were microstructural changes during the aging process.

5.1 Methods

5.1.1 Thermal exposure

Hybrid composite cores directly from the pultrusion process were provided by a manufacturer. Specimens were cut too a length of 406.4 mm on an abrasive diamond saw; the ends of these specimens were then sealed using a silicone based adhesive. Specimens were placed in an atmospheric oven and the temperature was linearly ramped from room temperature to the aging temperature of 180 ± 2 °C at 5 °C/min for 3, 6, and 12 months. Reports of the glass transition temperature of the hybrid composite material have ranged considerably between 187 and 225 °C (EPRI 2010), (Bosze, et al. 2006), (Barjasteh, Kar and Nutt 2011). Suffice it to say that the aging temperature in this study caused accelerated aging, but was below reported literature values of T_g. Furthermore, as will be shown in section 5.2.2, the value of T_g is not a clearly defined value, but rather a range of temperatures, which is strongly influenced by the method in which the T_g is measured. A conservative approach for determining T_g is proposed, which may change the manufacturers' recommendation for maximum continual operating temperature.

Each time specimens were removed from the oven, the temperature was linearly ramped down to 25 °C at a rate of 5 °C/min in order to avoid creating significant residual stress within the composite as a result of the mismatch in thermal expansion coefficients. The aged composites then had 25.4 mm removed from each end using the same diamond abrasive blade in order to eliminate any potential of axial thermal oxidation of the composite.

Schoeppner et al. studied the anisotropic aging behavior of carbon fiber/PMR-15 composites, and concluded that thermal oxidation penetrated to a far greater extent in the 0° direction of a composite as compared to the 90° direction (Schoeppner, Tandon and Ripberger 2007). Keeping in mind the service environment of a transmission line, predominantly transverse thermal oxidation is expected, thus justifying eliminating any material that had the potential of experiencing axial thermal oxidation. To characterize the extent of transverse thermal oxidation, dark field optical microscopy of polished cross-sections was performed. Twenty-five measurements of the oxidation layer were made on two different specimens for each aging condition. Scanning Electron Microscopy was also performed on the oxidized surfaces of the GFC, to qualitatively evaluate the effect that thermal oxidation had on the surface of the hybrid composite.

5.1.2 Volumetric relaxation

Previous studies on the aging of polymers, and polymer matrix composites have shown that exposure to elevated temperatures results in mass loss of the polymer (Struik 1978), (Lowe, Fox and Otieno-Alego 2002), (Akay and Spratt 2008), (EPRI 2010), (Barjasteh, Kar and Nutt 2011), (Barjatesh, et al. 2009), (EPRI 2009). In the case of polymer matrix composites, this mass loss is (in general) associated only with the polymer, as the reinforcing fibers are thermally stable at the aging temperatures considered in this work (Bowles, et al. 1993), (Tsuji, McManus and Bowles 2000), (Kamvouris, et al. 1997). Struik, and Gentz et al. observed that in addition to the mass loss of the polymer, there is an associated loss in volume, or volumetric relaxation (Struik 1978), (Gentz, Benedikt, et al. 2004). For PMR-15 and PMRII-50, Gentz noted that

length relaxation was strongly influenced by both aging environment, as well as aging temperature (Gentz, Benedikt, et al. 2004), (Gentz 2004). For this work, the aging process included thermal oxidation (chemical aging) as well as volumetric relaxation (physical aging).

Gentz et al. have shown that a stretched exponential function (the so-called "Kohlrausch" function) describes the normalized length relaxation process of thermorheologically simple polymers (Gentz 2004). The normalized function for length relaxation is given by

$$\frac{L(t)}{L(0)} = e^{\left[-\left(\frac{t}{\tau}\right)^{\beta}\right]} \tag{5.1}$$

where L(t) is the length at time t, L(0) is the initial isothermal equilibrium length, t is time, τ is the associated relaxation time for an isothermal aging temperature, and β is a length relaxation fractional exponent that may take on values between 0 and 1. A consequence of a polymer being thermorheologically simple, is that for aging temperatures below the glass transition temperature of the polymer, there is only one dominant relaxation. Hence, β will take on a single value for various isothermal aging temperatures. That is to say, at various isothermal aging temperatures the shape of the volumetric relaxation curve will only be affected by the change in the relaxation time. If one linearizes the Arrhenius equation, the result yields

$$\ln(\tau) = \frac{\Delta H}{RT} + \ln(\tau_0) \tag{5.2}$$

in which ΔH is the activation energy, R is the universal gas constant, T is temperature, and τ_0 is a material constant, from which the activation energy of the aging process may be determined.

A Netzch© 402C dilatometer was used to measure the length relaxation of the hybrid composite. Specimens were sectioned off to a length of 5.1 mm with a water-cooled diamond abrasive blade, and then conditioned in an oven at 80 °C for 72 hours in order to eliminate any water that had been absorbed. Specimens were then placed into the dilatometer in such an orientation as to measure the transverse dimensional relaxation (alternately referred to as volumetric relaxation, or shrinkage) of the hybrid composite as shown in Figure 5.1. As relaxation of the composite is only associated with volumetric relaxation of the polymer, and not the reinforcing fibers, measuring the transverse volumetric relaxation is far more appropriate than measuring the axial relaxation (Daniels, Luo and Sun 2001).

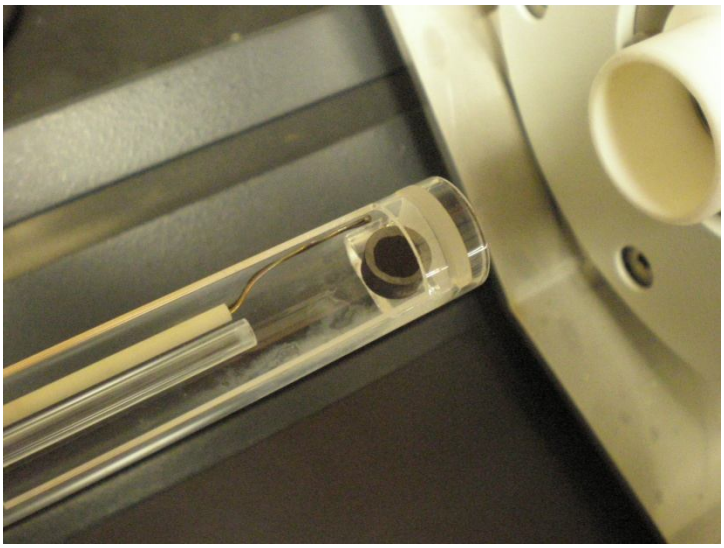

Figure 5.1 Hybrid composite specimen oriented in the dilatometer chamber to measure the transverse dimensional relaxation.

Specimens were heated to 240 °C (~15 °C above the highest reported T_g) at a rate of 5 °C/min, and held for 10 minutes to erase any previous thermal history. The specimens were then quenched to their isothermal aging temperature at a rate 5 °C/min, and held for 500 hours. For the first 60 minutes of the isothermal portion of the test, data were sampled at 2 samples/minute, while for the remainder of the test data were sampled at 0.5 samples/minute.

5.1.3 Static flexure strength

A four point loading configuration was used to test all specimens (Figure 5.2); the test was developed based upon ASTM standard D4476, with a few key modifications. First, the saddled loading pins had a minimum inner diameter of 7/3 the size of the diameter of the test specimens (25.3 mm). This geometry is 4.67 times larger than the recommended pin diameter of ASTM D4476.

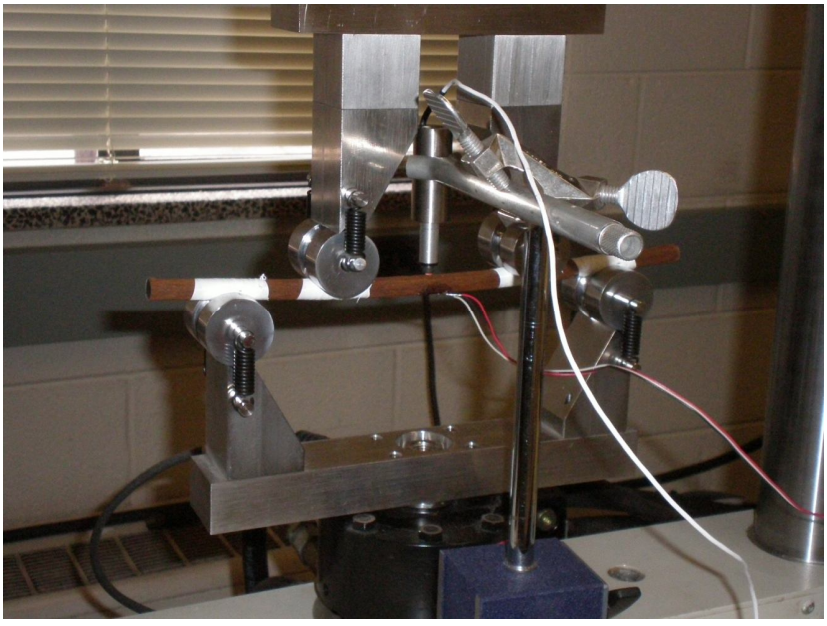

Figure 5.2 Four point loading configuration used for evaluating the flexure strengths of the hybrid composite at different aging times.

A finite element model of the four point bending experiment was developed to assess the effect that pin diameter had on the transverse contact stresses present in the specimen under test (Figure 5.3). One of the primary issues associated with the flexure testing of unidirectional composite materials is transverse crushing of the material at the loading pins. Hence, evaluation of the contact stresses enabled the selection of an appropriate pin geometry in order to obtain material failures.

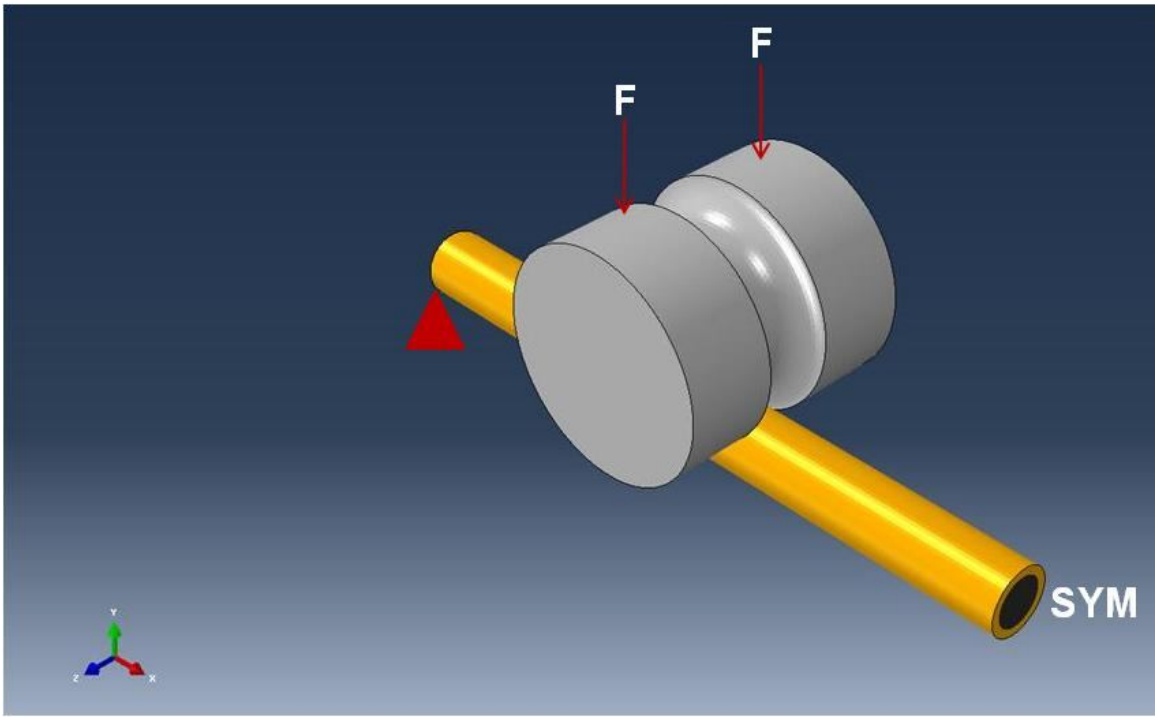

Figure 5.3 Schematic of the finite element model with a loading pin which had a minimum diameter of 7/3 the outer diameter of the hybrid composite.

Both the GFC and CFC were modeled as transversely isotropic materials, with the material properties given in Table 4.2. The axial length of the composite was 101.6 mm, while the transverse dimensions were the same as the nominal geometry model of Chapter 4. The loading pin was modeled as a rigid body, thus not requiring a material

property definition. Two minimum inner diameters of the loading pin were considered; the geometry of ASTM D4476 with a minimum diameter of ½ the diameter of the test specimen (4.75 mm), and a larger pin geometry in which the minimum diameter was 7/3 that of the test specimen (22.17 mm).

Rigid-deformable contact between the pin and GFC was modeled with a hard penalty based contact definition. Additionally, an initial *TIE constraint was imposed between the specimen and the loading pin to expedite convergence of the non-linear problem. Due to symmetry considerations, only one-half of the true geometry was considered in the finite element model; appropriate boundary conditions were applied to account for the symmetry plane. Boundary conditions for the model are shown schematically in Figure 5.3. A representative load of 889.6 N was applied in a uniformly distributed manner to the rigid loading pins. As both composite material definitions were transversely isotropic linear elastic the transverse state of stress linearly scaled to the magnitude of applied load, enabling extrapolation to higher applied loads. A static implicit finite element formulation was considered for all analyses.

Additionally, Teflon® tape was lightly wrapped around the composite specimens at each location that would be contacted by a loading pin to more evenly distribute the contact stresses and reduce friction. Through these two modifications, it was anticipated that transverse crushing at the loading pins would be eliminated, and consistent material failures would be achieved. Obtaining true material failures was the only way that the effect of aging on the static flexure strength of the hybrid composite could be appropriately evaluated. Five specimens for each aging condition were tested, with the

exception that 2 specimens were tested that had been aged for 9 months. An auxiliary LVDT was used to measure the mid-span deflection of specimens, in order to characterize the effective axial modulus of the hybrid composite material. A loading rate of 3 mm/min was used to approximate a quasi-static loading; load and mid-span deflection data were sampled at 20 Hz for all tests.

5.1.4 Fatigue testing

Aged specimens were cut with a diamond abrasive blade to their final test length of 71.1 mm. In the location that the specimens were to be cut, Teflon® tape was used to prevent exposed and loose glass fibers from significant fraying. Tests were run in accordance with the procedure described in section 4.1.1. Three stress amplitudes (identified σ_2, σ_3, and σ_4 in Chapter 4) for each aging condition were considered (identified as σ_1, σ_2, and σ_3 in this chapter) for comparison to the fatigue behavior of the unaged specimens of Chapter 4.

5.1.5 Micromechanics modeling of fatigue damage initiation

Considering the fatigue failure characteristics of the unaged specimens (Figure 4.26) in which only the GFC accumulated fatigue damage, as well as the forthcoming fatigue failure morphologies of the aged hybrid composite specimens, a need for understanding the failure mechanisms was clear. Initially it appeared as though a paradigm was observed, in which the material which was subjected to a smaller maximum axial stress amplitude (the GFC) accumulated fatigue damage, while the material subjected to a substantially larger stress amplitude remained undamaged (the CFC). In light of the discussion of section 2.1.3 on fatigue damage of composite materials initiating as matrix

damage, the distribution of axial stress within the epoxy matrix during fatigue loading was in need of characterization. To this end, 3-Dimensional viscoelastic representative volume element finite element models were developed. As the distribution of matrix stress is known to be a factor of several parameters (e.g. – v_f, fiber packing arrangement, stress amplitude, etc.) several variants of the RVEs were developed.

When considering the orientation of fibers in a unidirectional composite material, the two most common fiber packing arrangements are square and hexagonal packed (Hull and Clyne 1996). While these packing arrangements are idealized, and not often perfectly observed in true composite systems, they do provide insight into the effect that packing arrangement has on the distribution of stresses. Thus, unit cells consisting of both square and hexagonally packed fibers were developed. Perfect bonding was assumed between the fiber and matrix, and a range of volume fraction of fibers between 50% and 75% were considered[1]. Illustrative square and hexagonal packed RVEs with a volume fraction of fibers of 65% are shown in Figure 5.4 Figure 5.5, respectively. From both figures it can be seen that the entire mesh consisted of hexahedral elements, which were fully integrated for all analyses.

[1] Note: the theoretical packing limit for a square packing arrangement is 78.5 %, while for a hexagonally packed system the theoretical packing limit is 90.7%.

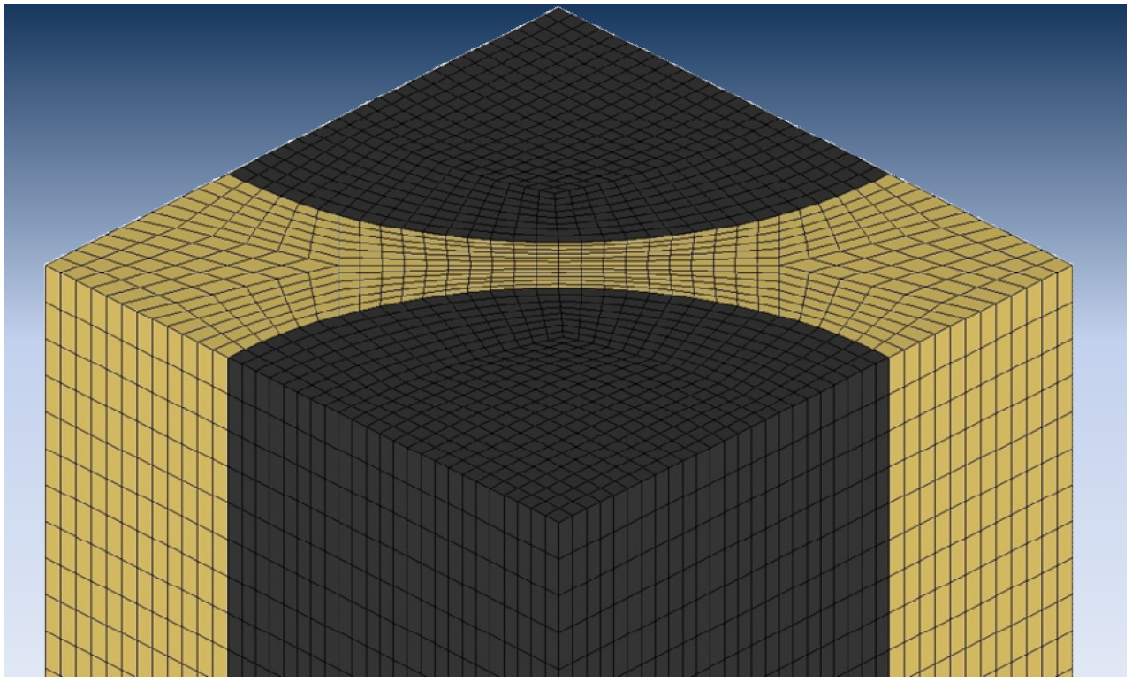

Figure 5.4 Representative square packed RVE with $v_f = 65\%$.

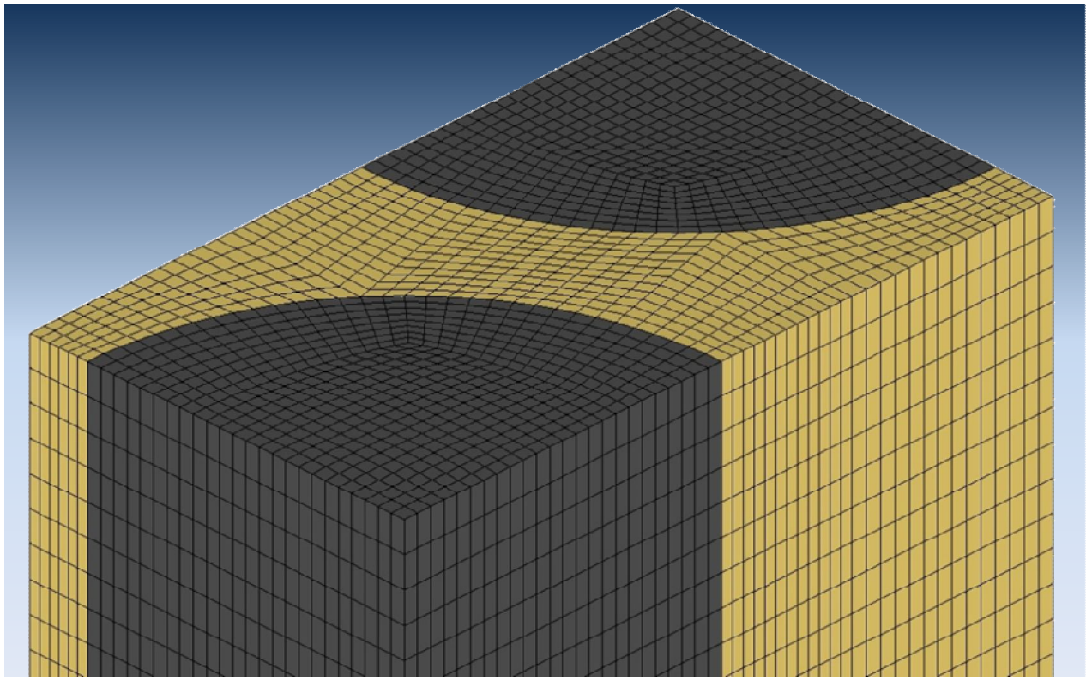

Figure 5.5 Representative hexagonal packed RVE with $v_f = 65\%$.

Periodic boundary conditions were applied to the RVEs via equation (2.1). For the CFC RVEs, transversely isotropic elastic material properties were assigned to the carbon fibers; material properties are summarized in Table 4.4. For the GFC RVEs, isotropic material properties were taken from (Hull and Clyne 1996), in which E = 76 GPa, ν = 0.22, and ρ = 2500 kg/m^3. For the epoxy matrix, ρ = 1200 kg/m^3 and ν = 0.40 for all analyses. The viscoelastic frequency dependent stiffness data of the neat resin epoxy specimens of section 4.2.4 was also used in this study. In addition, the frequency dependent viscoelastic response of specimens that had been aged in an atmospheric oven at 180 °C for 3 and 6 months were incorporated into the RVE models to account for aging (J. Middleton 2012); 12 month specimens were not considered for reasons that will be elaborated upon in section 5.2.5. For all CFC RVEs the diameter of the carbon fibers were modeled as 7 μm, while for the GFC RVEs the diameter of the glass fibers were modeled as 20 μm.

Direct steady state dynamics analyses were performed in Abaqus® 6.9-2, allowing the transient response of the RVEs to a harmonically varying applied force to be determined. Such an analysis is directly applicable to the fully reversed fatigue loading of section 5.1.4, and allows for the viscoelastic nature of the epoxy resin to be accounted for. For all analyses in which frequency was not a variable, the excitation frequency was 31 Hz, to match the experimental test frequency. To investigate the effect that the 3 stress amplitudes had on the state of stress within the epoxy matrix, the maximum macro stress at the outer fibers for each material was determined; these values were shown previously, but are once again presented for convenience in Table 5.1. An axial concentrated load, in

accordance with the stress amplitudes of Table 5.1 and the cross-sectional area of the respective RVE, was applied to a "dummy" node that had been coupled to the free surface of the RVE to which the axial stress was to be applied. Nodes on the opposite face of the RVE were constrained in the axial direction, while the node on the center of that face was additionally constrained in the transverse directions to eliminate the rigid body modes.

Table 5.1 Summary of the maximum axial macro stresses within the outer fibers for each composite material.

Stress Amplitude	σ_{MAX} CFC [MPa]	σ_{MAX} GFC [MPa]
σ_1	219.9	99.5
σ_2	274.8	124.3
σ_3	329.8	149.2

5.2 Results and Discussion

5.2.1 90° thermal oxidation

Dark field microscopy revealed that the transverse thermal oxidation mechanism for the hybrid composite was a self-limiting process, as had previously been reported (Barjatesh, et al. 2009). The oxidation layer was identified via Dark Field micrographs as the darker region on the surface of the hybrid composite, separating the bulk GFC and the potting epoxy. Representative micrographs of the oxidized layer are shown in Figure 5.6 through Figure 5.9, while Figure 5.10 shows the progression of the oxidation layer thickness as a function of aging time. The data were found to be in reasonable agreement with previous observations made of the hybrid composite material in which the oxidation layer was measured via nano-hardness (Barjatesh, et al. 2009).

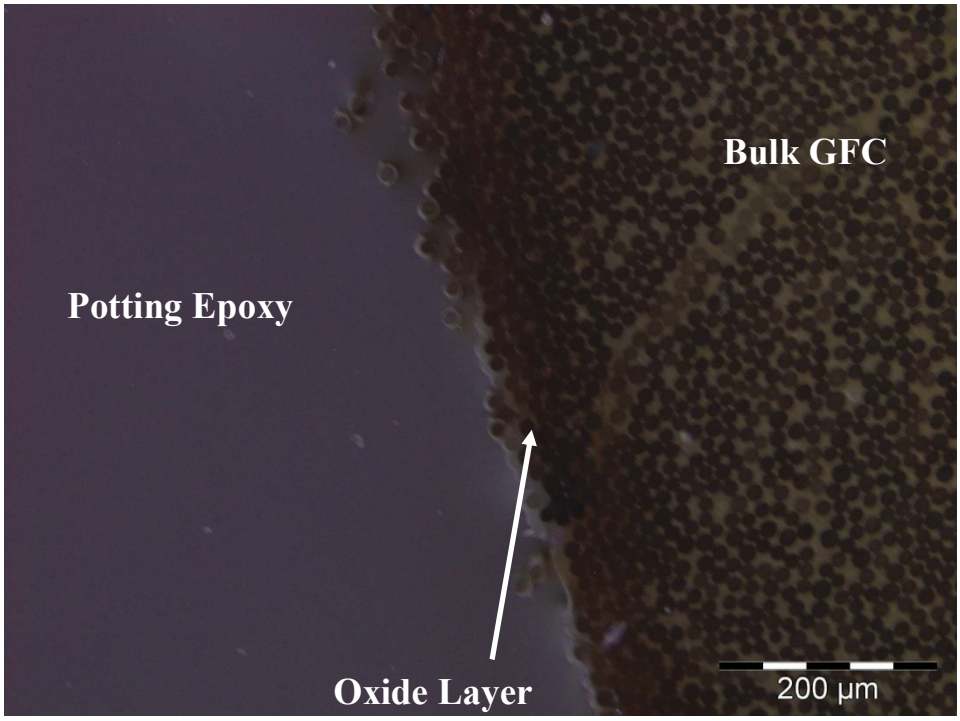

Figure 5.6 Dark field micrograph of a specimen aged at 180 °C for 3 months.

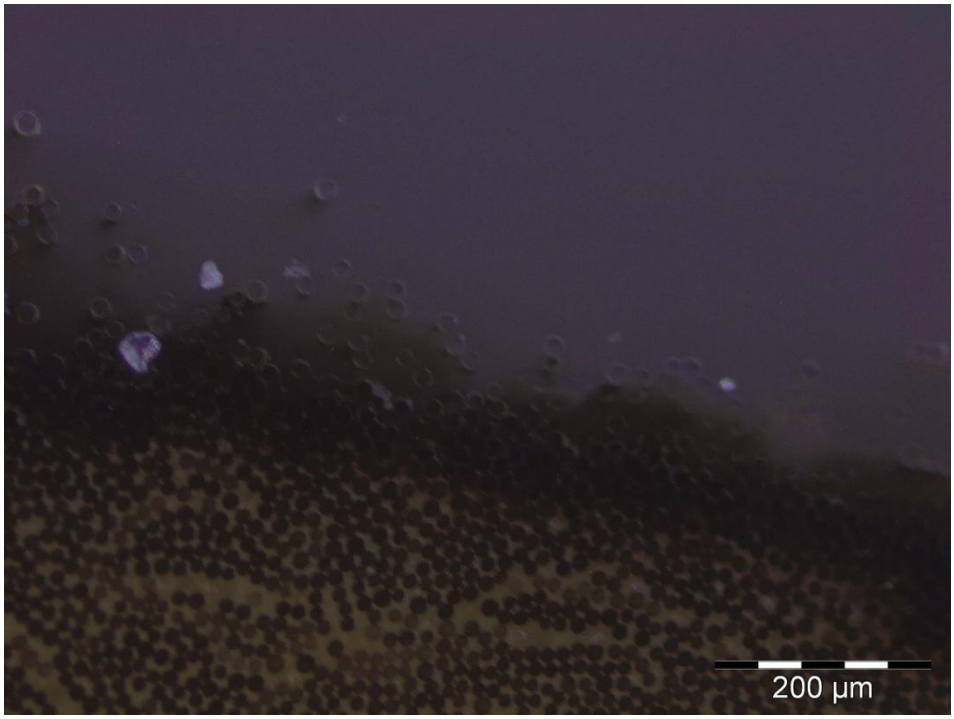

Figure 5.7 Dark field micrograph of a specimen aged at 180 °C for 6 months.

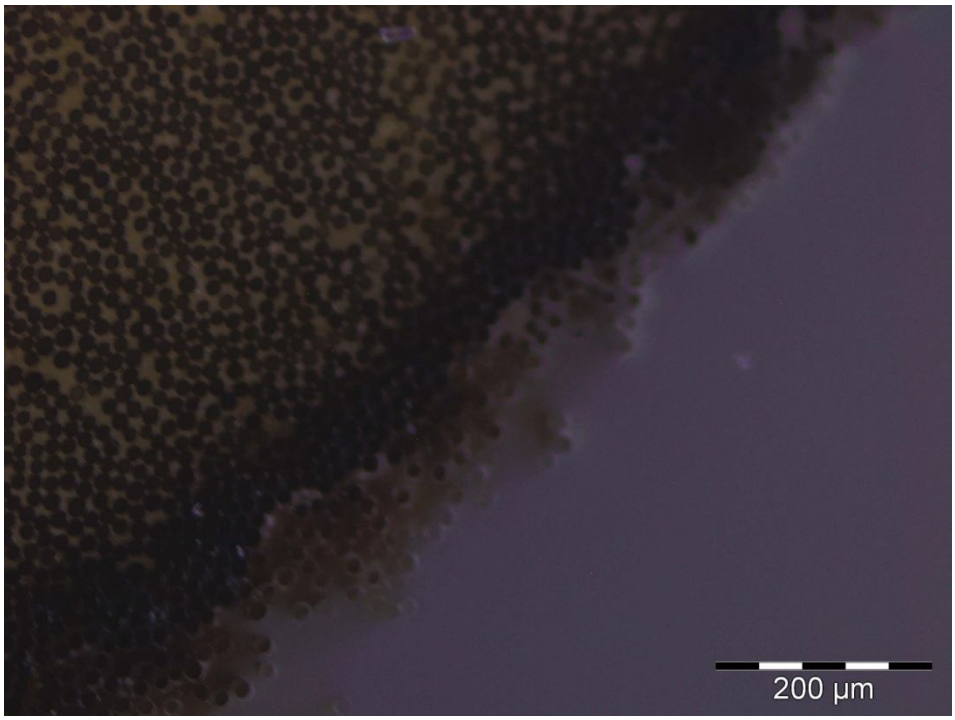

Figure 5.8 Dark field micrograph of a specimen aged at 180 °C for 9 months.

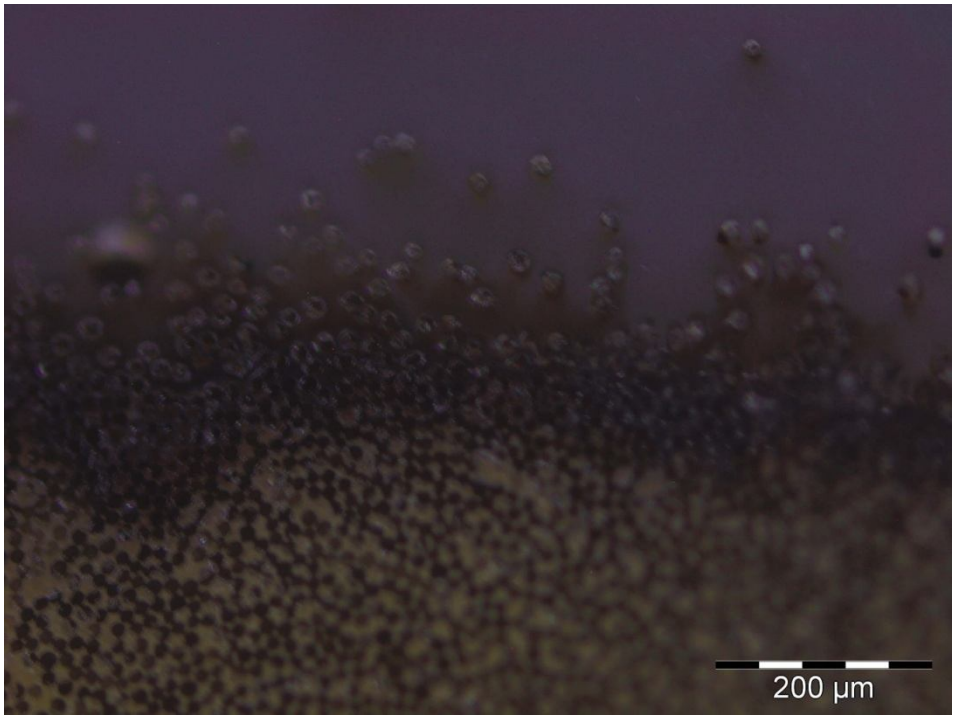

Figure 5.9 Dark field micrograph of a specimen aged at 180 °C for 12 months.

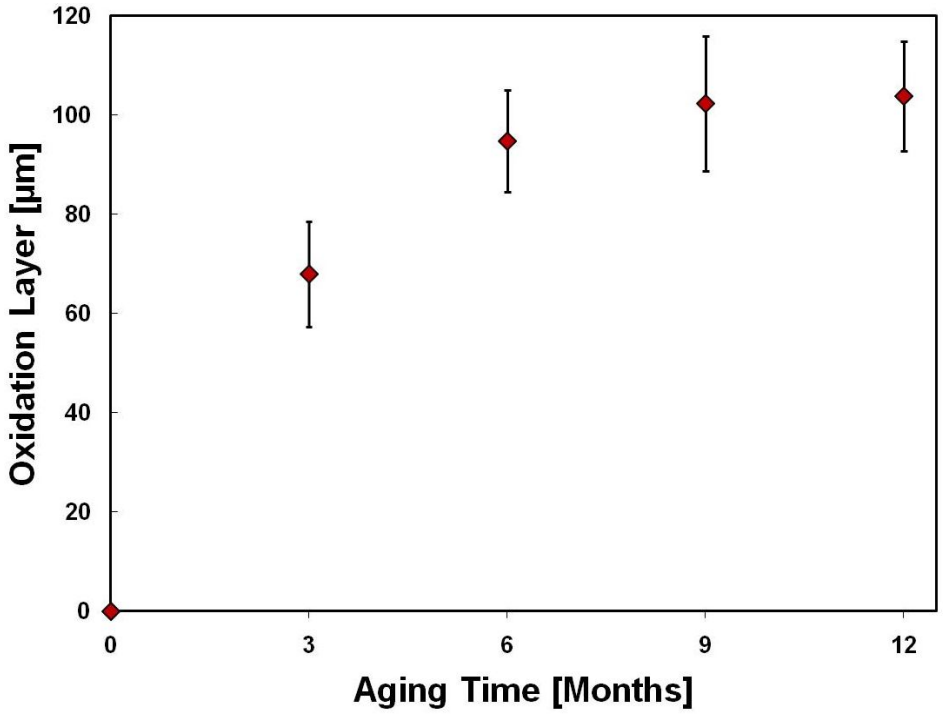

Figure 5.10 Thermal oxidation layer thickness as a function of aging time for an aging temperature of 180 °C.

A primary issue with determining the thickness of the oxidation layer stemmed from the fact that for the aged specimens, glass fibers had become loose on the surface due to thermal oxidation. Thus, a clearly defined edge was not distinguishable, making estimation of the oxidation layer inexact. To further investigate surface degradation of the aged hybrid composites scanning electron microscopy of the transverse surfaces of aged specimens was performed. Low magnification micrographs for specimens in an unaged condition, and aged for 3, 6, and 12 months at 180 °C are shown in Figure 5.11 through Figure 5.14, respectively. Analogous micrographs at higher magnification are shown in Figure 5.15 through Figure 5.18.

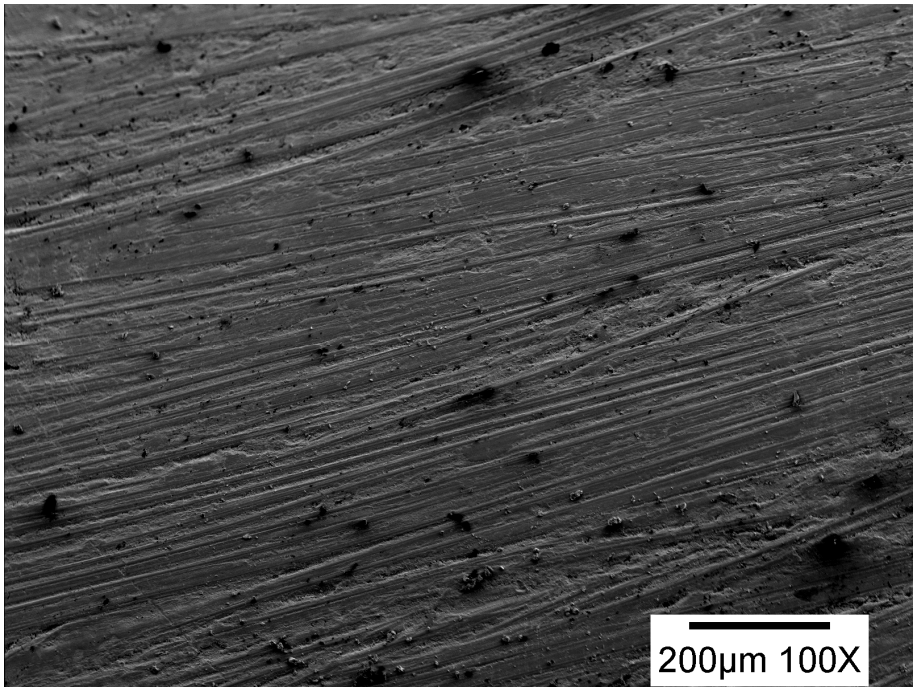

Figure 5.11 Low magnification SEM micrograph of the surface of a hybrid composite that had not been exposed to elevated temperatures.

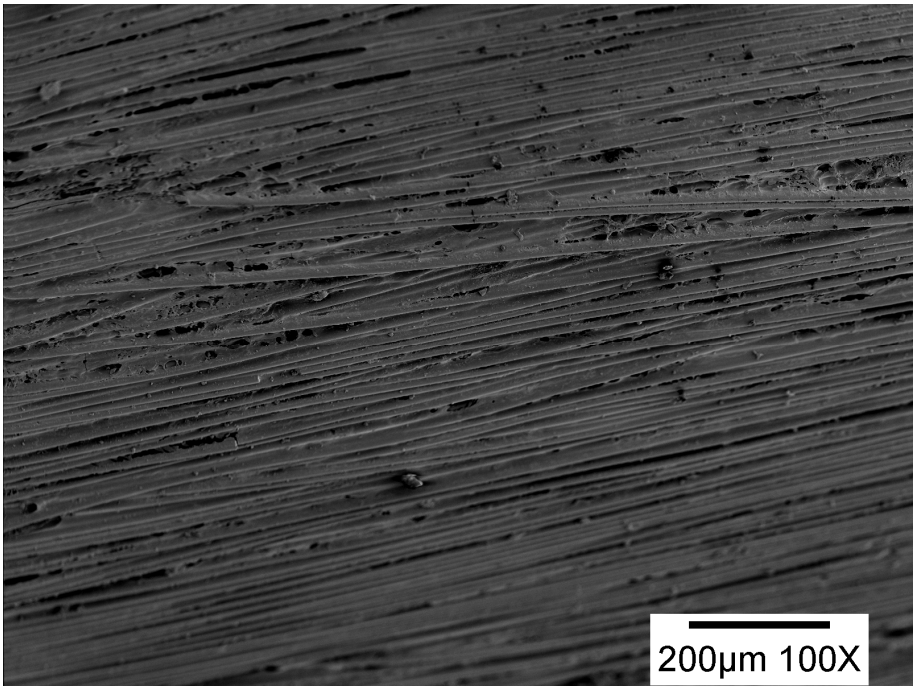

Figure 5.12 Low magnification SEM micrograph of the surface of a hybrid composite that had been aged at 180 °C for 3 months.

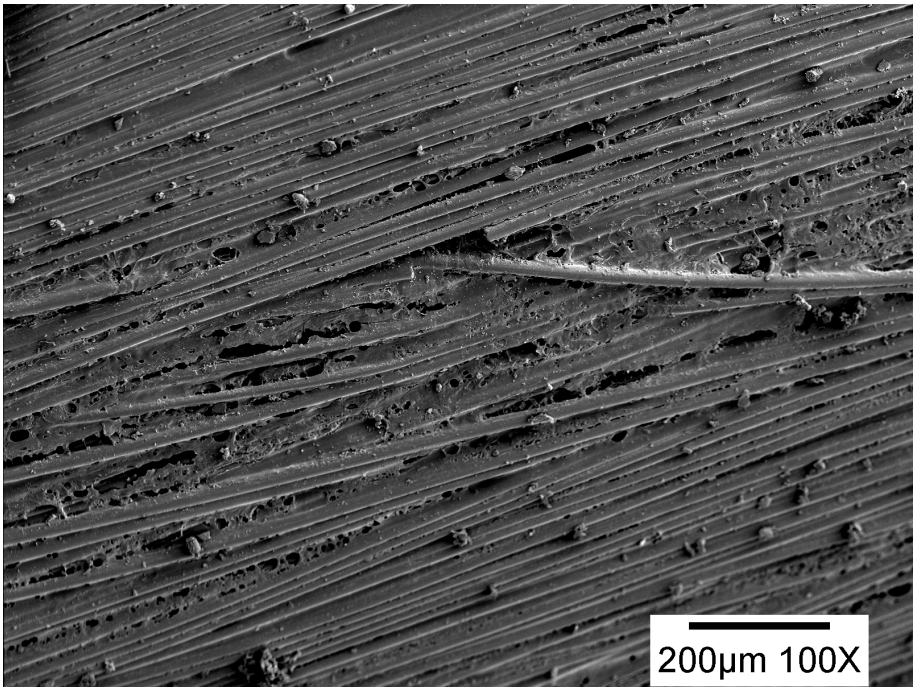

Figure 5.13 Low magnification SEM micrograph of the surface of a hybrid composite that had been aged at 180 °C for 6 months.

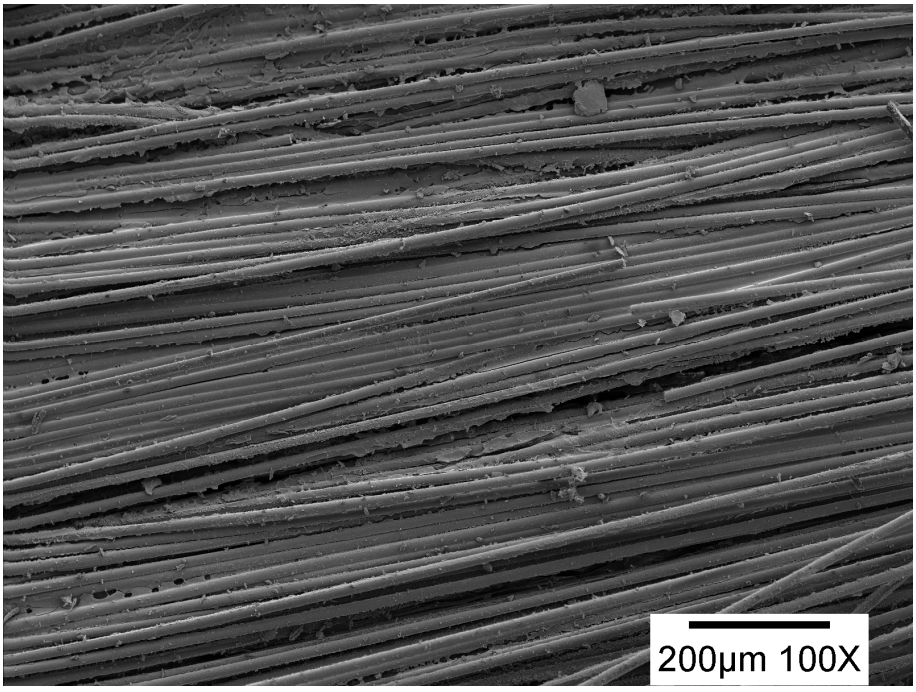

Figure 5.14 Low magnification SEM micrograph of the surface of a hybrid composite that had been aged at 180 °C for 12 months.

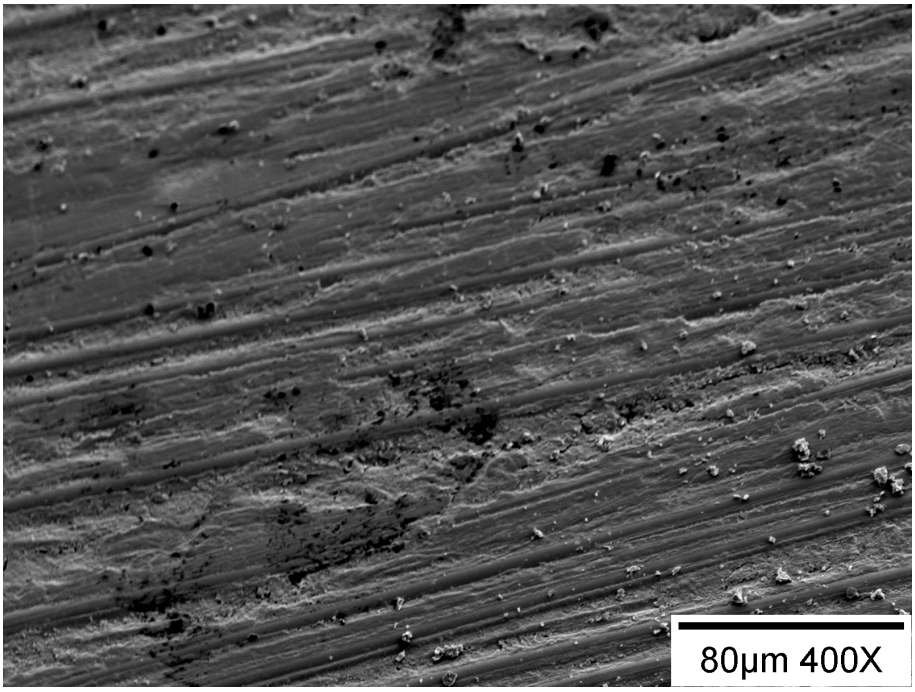

Figure 5.15 High magnification SEM micrograph of the surface of a hybrid composite that had not been exposed to elevated temperatures.

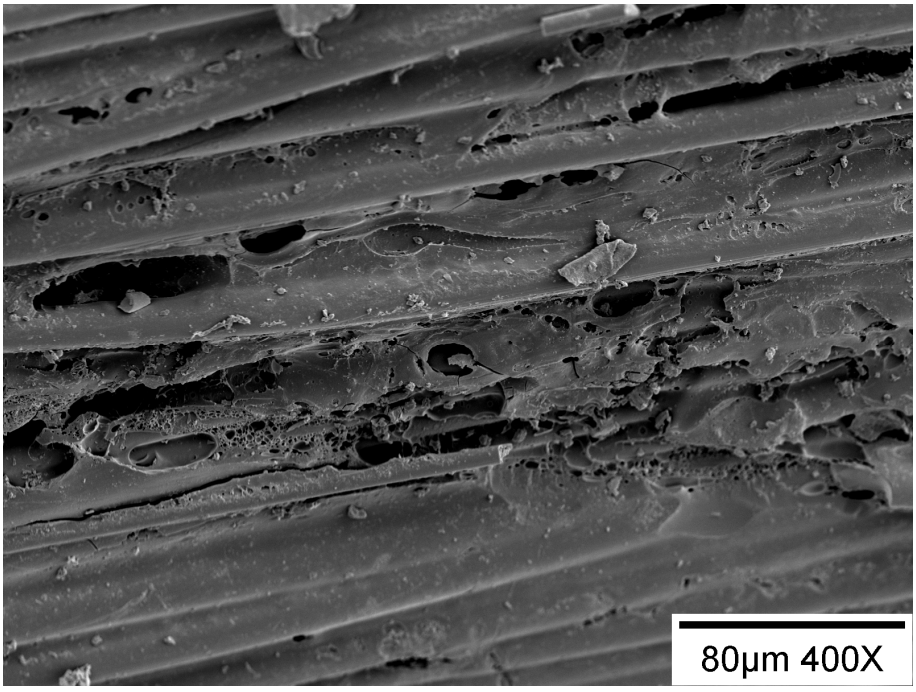

Figure 5.16 High magnification SEM micrograph of the surface of a hybrid composite that had been aged at 180 °C for 3 months.

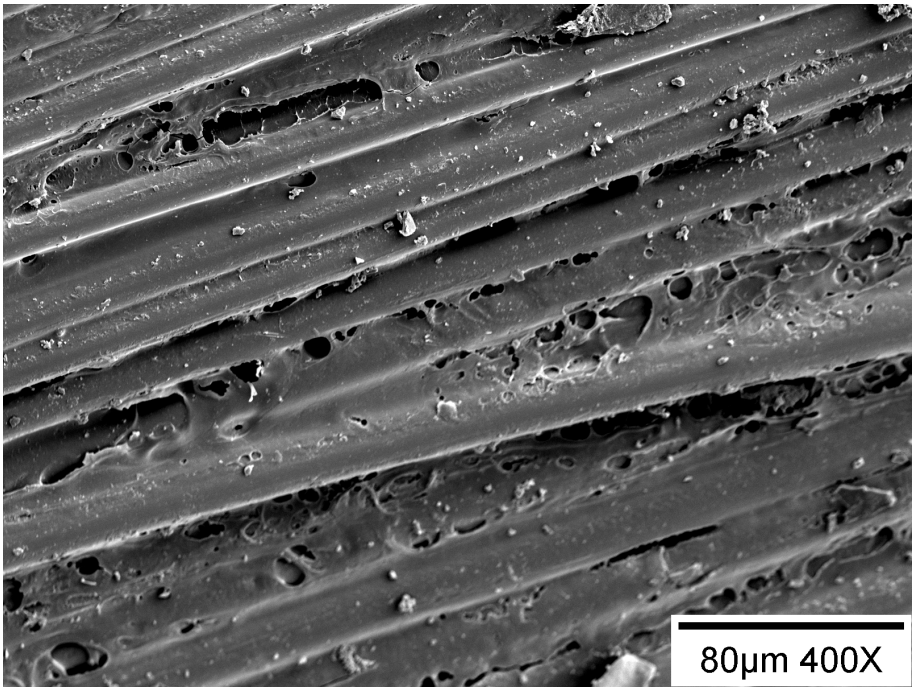

Figure 5.17 High magnification SEM micrograph of the surface of a hybrid composite that had been aged at 180 °C for 6 months.

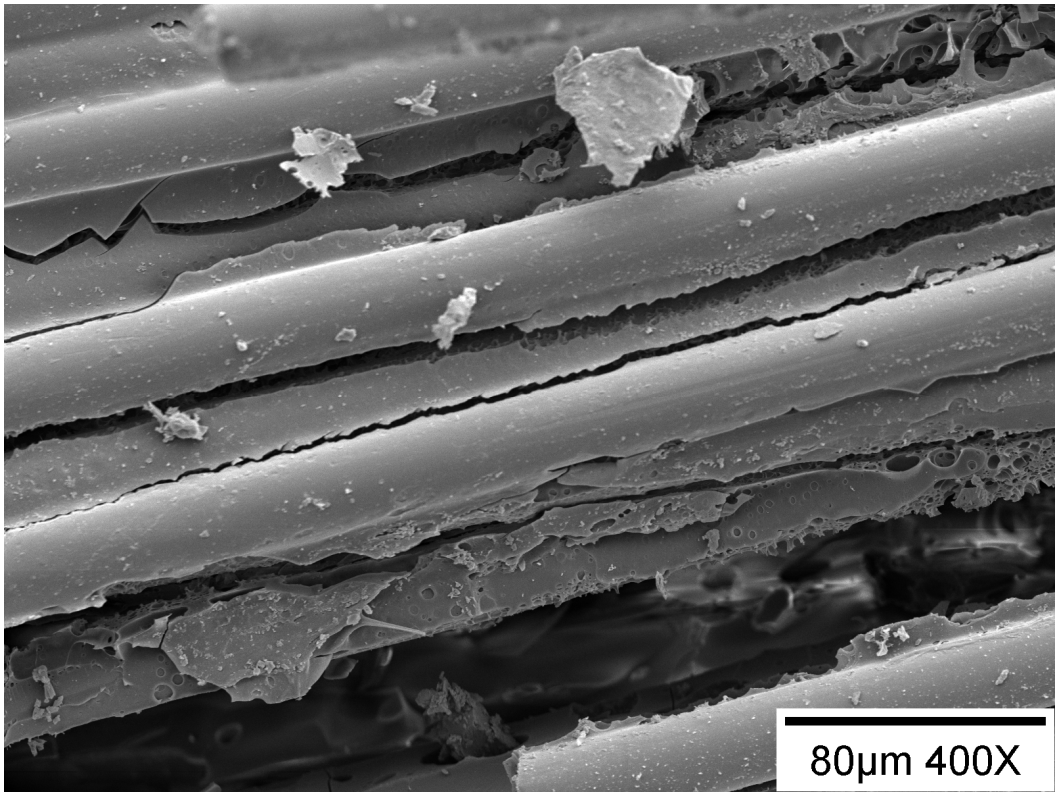

Figure 5.18 High magnification SEM micrograph of the surface of a hybrid composite that had been aged at 180 °C for 12 months.

From the SEM micrographs it was clear that as aging time increased so too did the amount of exposed glass fibers on the surface of the hybrid composite. For the 3 month aging condition, the only distinguishable difference from the unaged specimens was the loss of the thin polymer layer on the surface. At 6 months aging time, individual glass fibers were identifiable into the depths of the surface and the epoxy matrix had become porous in nature. The 12 month aged specimens exhibited pronounced matrix porosity, fiber/matrix debonding on the surface, and individual glass fibers into the depth of the surface were observed. SEM observations confirmed that a substantial amount of polymer had been lost on the surface of the hybrid composite at extend aging times.

5.2.2 Volumetric relaxation

Figure 5.19 shows the raw data for an isothermal aging temperature of 180 °C fit with equation (5.1). The best fit parameters were determined using a non-linear least squares regression algorithm. From the data, a β value of 0.58 was determined, which was found to well describe all other isothermal aging temperature curves, indicating that the polymer of the hybrid composite could be treated as thermorheologically simple.

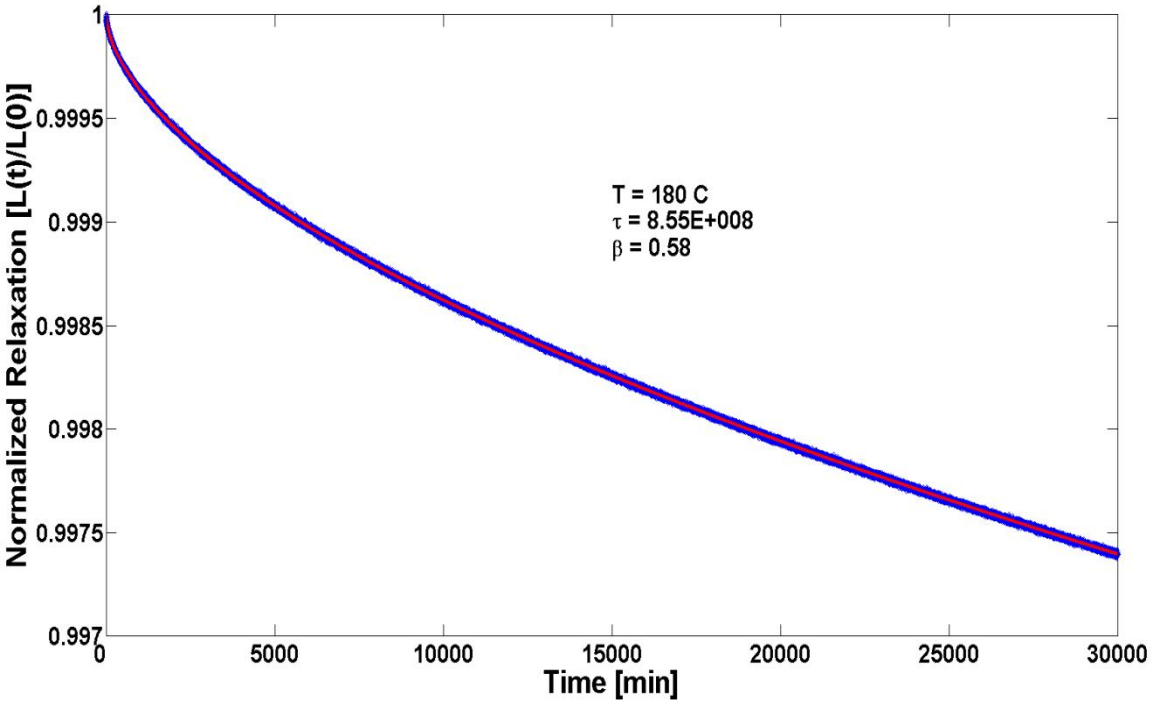

Figure 5.19 Normalized relaxation curve for an isothermal aging temperature of 180 °C.

Figure 5.20 provides the normalized transverse relaxation curves as a function of time for isothermal aging temperatures of 165 °C, 170 °C, 180 °C, 185 °C, and 195 °C.

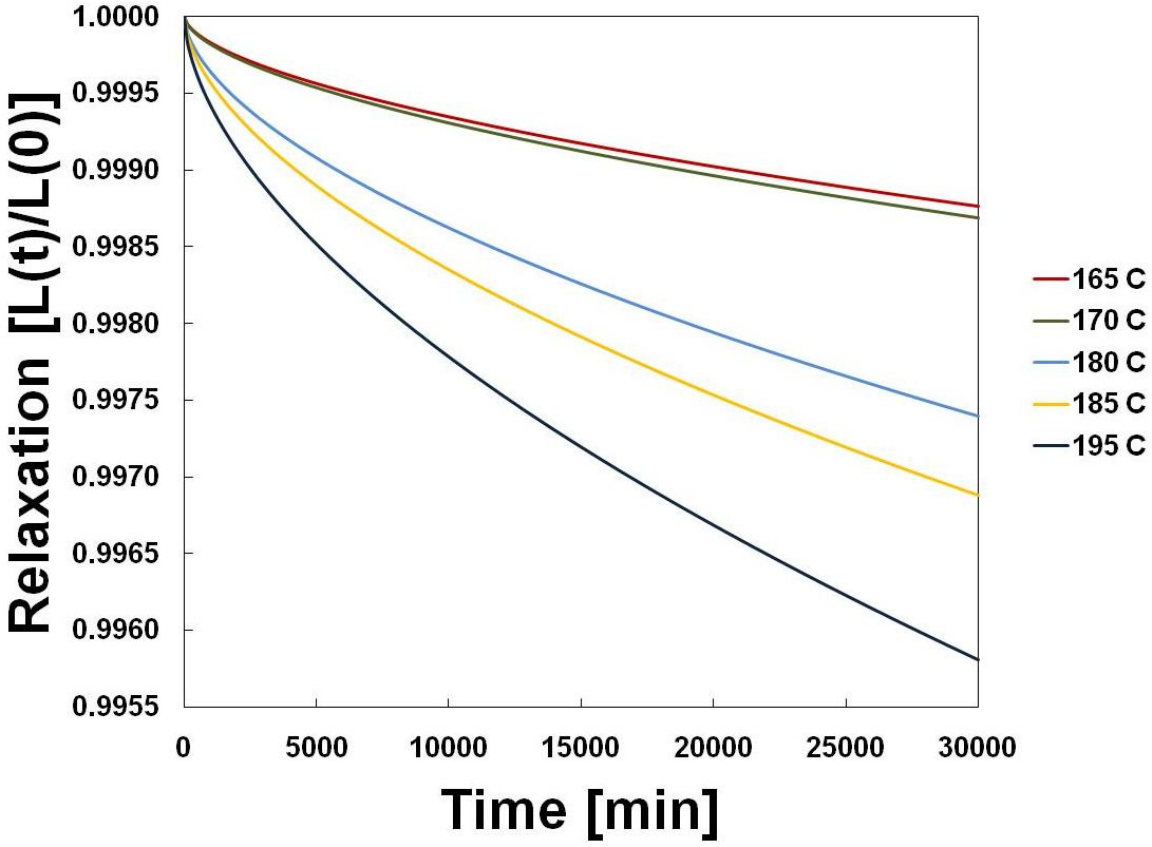

Figure 5.20 Normalized transverse relaxation data for several isothermal aging temperatures.

Clearly as the isothermal aging temperature increased, so too did the amount of relaxation. The activation energy for the aging processes (chemical and physical) was then found from an Arrhenius plot (Figure 5.21). The activation energy for the process was found to be 1.89kJ/mol; such a relationship accommodates the potential for a time-temperature equivalence, the consequence of which will be elaborated upon at the conclusion of this chapter. Moreover, the activation energy is substantially below what is required for covalent bond breaking. The activation energy is consistent with the amount of energy required for secondary bond breakage, and conformational changes.

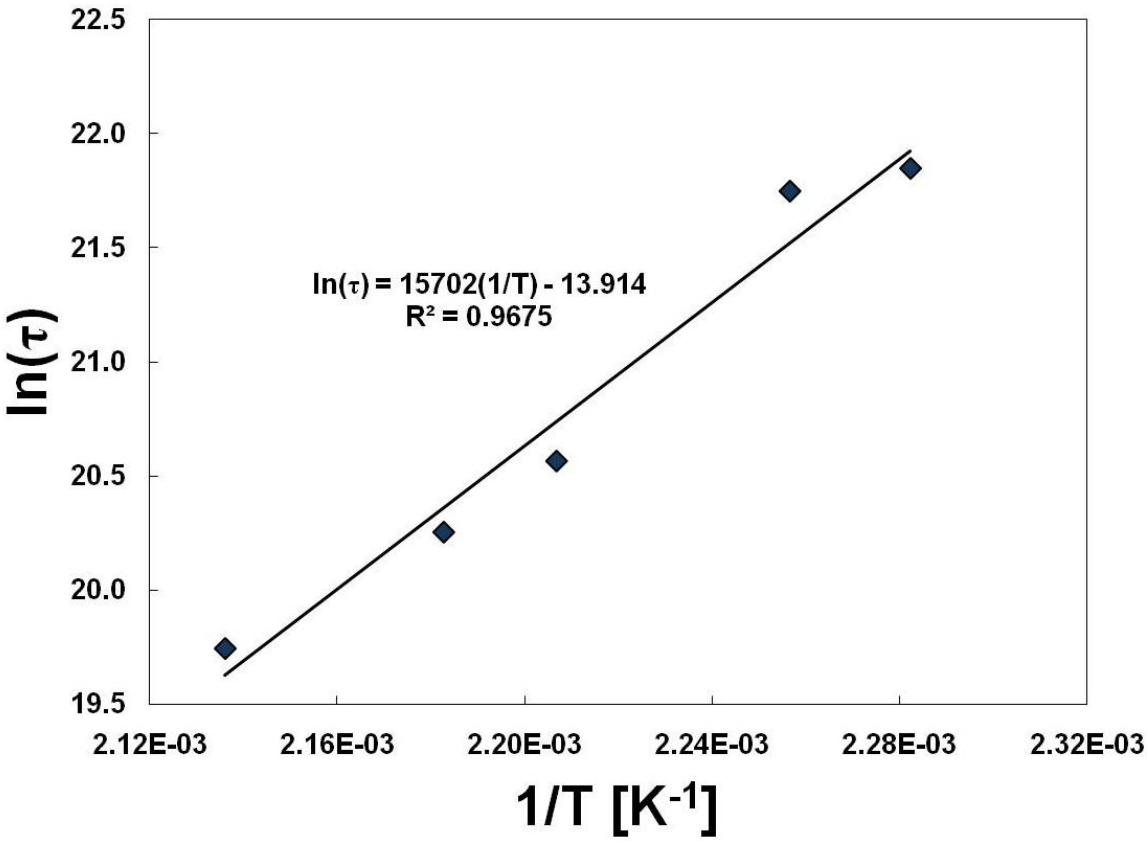

Figure 5.21 Arrhenius plot for activation energy determination of the aging processes.

Currently, the only reported values of glass transition temperature in the literature have been measured via Dynamic Mechanical Analysis (DMA), from which the peak in tan(δ) has been used to define the glass transition temperature (EPRI 2010), (Bosze, et al. 2006), (Barjasteh, Kar and Nutt 2011). In this test, the peak in tan(δ) roughly corresponds to a one decade drop in either the axial storage modulus or shear storage modulus, which is used to define the glass transition temperature. An alternative means of defining the glass transition temperature is the temperature at which the phase transformation from the glassy to the rubbery phase occurs. A common means of measuring such a phase transformation temperature is through the use of a dilatometer, in

which the rate of expansion of the material with respect to temperature is measured. The temperature at which the rate of expansion increases is defined as the glass transition temperature (Gentz 2004).

Commonly in polymer composites, the transition is not sharply defined, in which case one fits the data of the glassy state with a line, and the data of the rubbery state with a separate line; the intersection point of the two lines is then defined as the glass transition temperature (Gentz 2004). An example phase transformation plot for the hybrid composite is shown in Figure 5.22. The glass transition temperature of the hybrid composite was measured in this manner 5 times, with a mean T_g of 154.1 °C, with a standard deviation 1.8 °C.

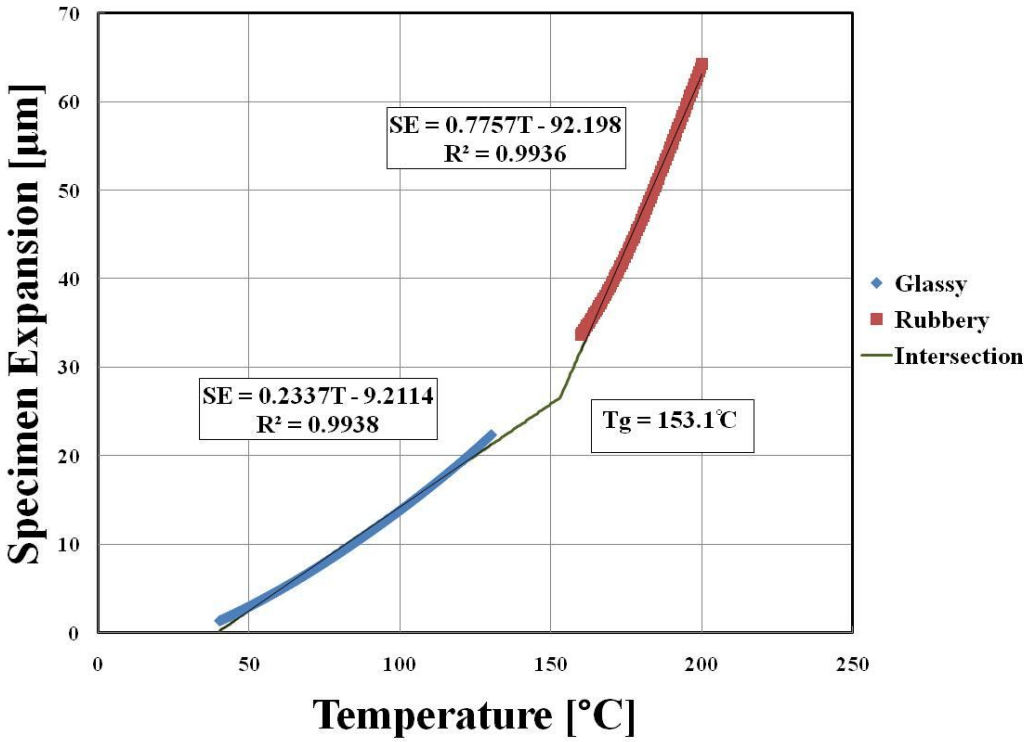

Figure 5.22 Glass transition temperature measurement via dilatometry.

From the measurements of the glass transition temperature via dilatometric measurement, it appears that the reported values of T_g measured via DMA result in a non-conservative estimate of the glass transition temperature. Such discrepancies in the value of T_g as a result of differing measurement techniques (or even different test parameters using the same measurement technique) are quite common (Perkin Elmer 2008). Generally, an accepted standard practice for measuring T_g in a particular industry is agreed upon, and then adopted throughout the industry. At the end of this chapter guidelines with respect to a conservative measurement of the glass transition temperature will be provided, in light of the data presented from this section.

5.2.3 Static flexure strength

Figure 5.23 compares the transverse stress field distributions for both pin geometries considered. It was found that at equivalent applied forces, the larger loading pin diameter reduced the contact stresses by 62.7%. Additionally, the degree of localization of the transverse stress field was substantially reduced by the larger loading pin geometry.

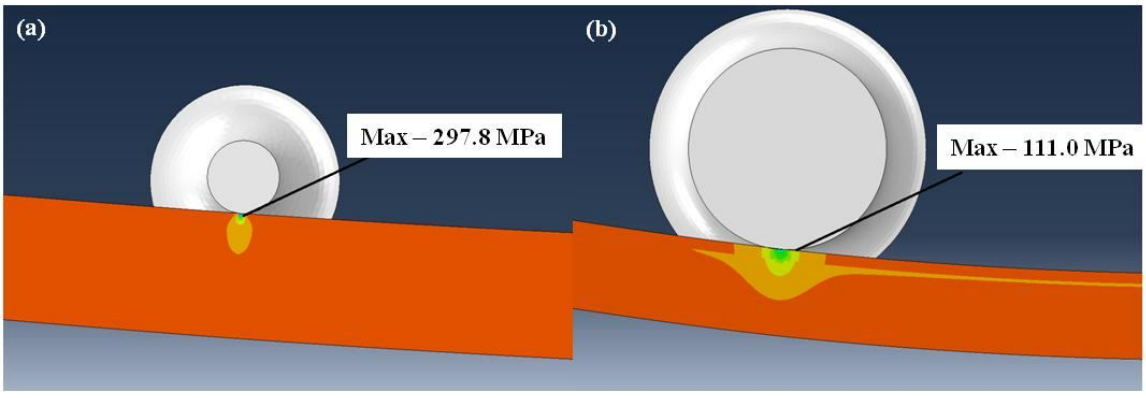

Figure 5.23 Comparison of the transverse stress field distributions for (a) a pin geometry with a minimum inner diameter of ½ that of the test specimen, and (b) a pin geometry with a minimum inner diameter of 7/3 that of the test specimen.

Hence, by reducing the contact stresses (and the degree of localization) at the loading pins the probability of transverse crushing at the load pins for equivalent applied loads could be substantially reduced, resulting in the possibility of obtaining legitimate material failures (as opposed to boundary condition driven failures). A true material failure was highly desirable for evaluating the effect that thermal exposure in an atmospheric environment had on the quasi-static flexural strength of the hybrid composites.

A plot of the flexural response for a hybrid composite that had been aged at 180 °C for 3 months is shown in Figure 5.24; the material's response was linear elastic up to failure. Plots for all specimens may be found in Appendix C. A typical failed specimen is shown in Figure 5.25, from which it is observed that failure of the material initiated in the mid-plane and was shear stress driven. This failure morphology is representative for all aging conditions.

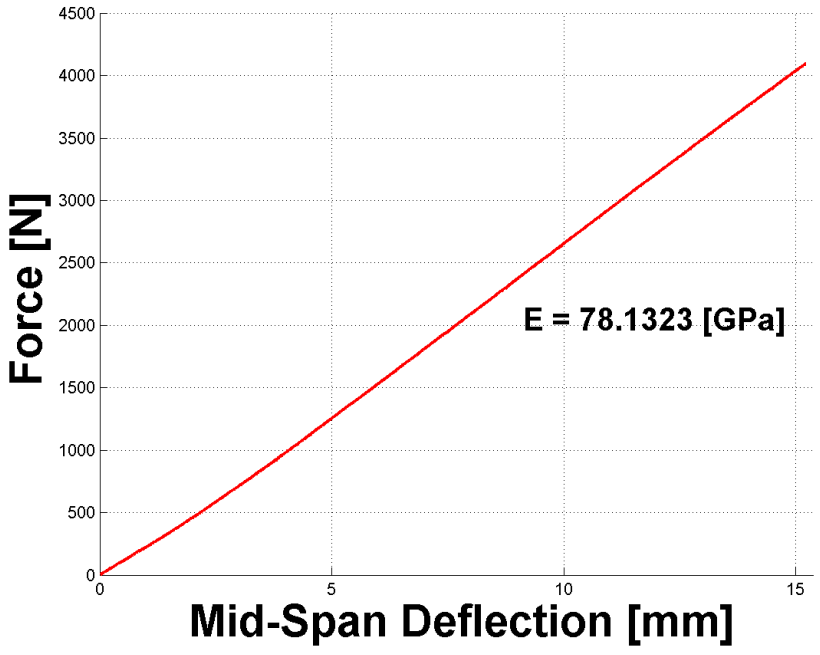

Figure 5.24 Flexural response of a hybrid composite specimen that had been aged at 180 °C for 3 months.

Figure 5.25 Typical flexural failure of the hybrid composite material.

The issue of shear driven failures during flexure loading in unidirectional composites is well known, and often unavoidable. In an attempt to avoid shear driven failures ASTM test method D4476 recommends that rod specimens are sectioned in half (ASTM 2003). As doing such would substantially change the geometry, and properties (especially when evaluating aging behavior) of the hybrid composite, it was decided to accept the shear driven failures of the test, while loosely terming the test a "flexure" test due to the 4 point loading configuration. By allowing a shear driven failure the test was more sensitive to changes in matrix) dominated properties (e.g. – shear strength), which should be the most severely affected by thermal exposure (Gentz 2004).

The effect that aging time had on the flexural load at failure and the mid-span deflection at failure are shown in Figure 5.26. From Figure 5.26 it is observed that the strength of the composite, as well as the elastic limit decreased with time. Up to 9 months aging time, moderate reduction in the flexural strength of the composite was observed. However, the mean flexural strength of the hybrid composites that had been aged at 180 °C for 12 months was reduced by 74% when compared to the mean flexural strength of unaged composites.

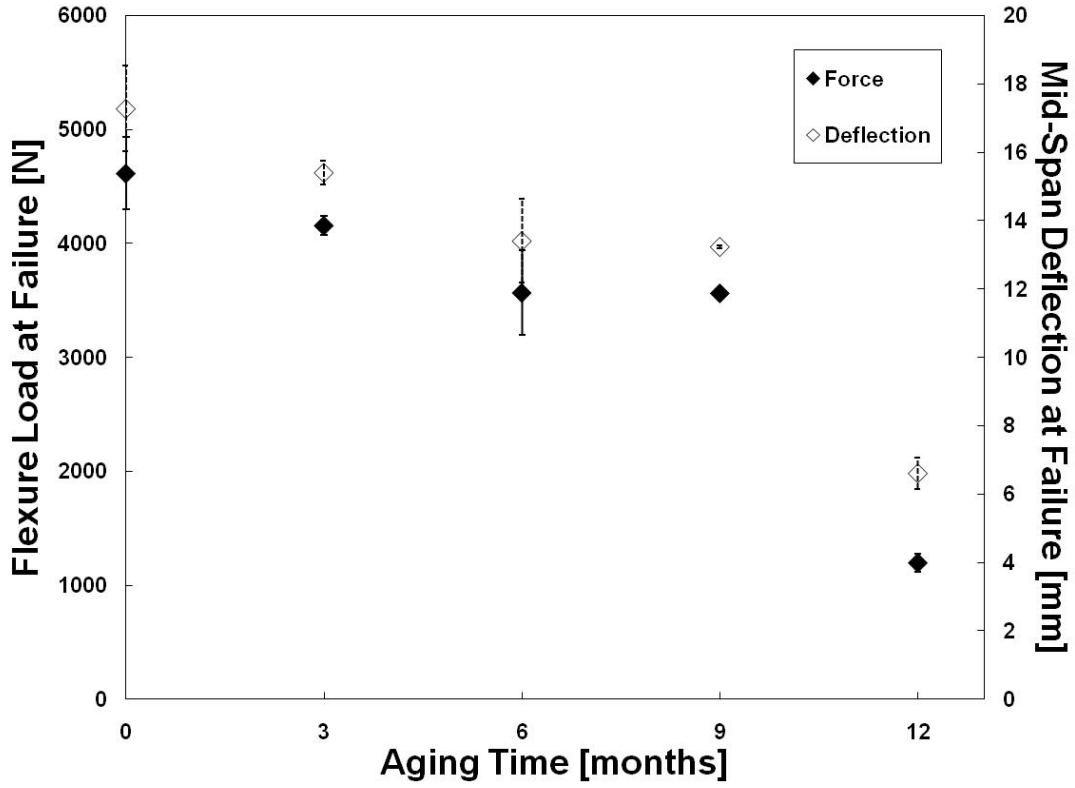

Figure 5.26 The effect of aging time at 180 °C on the flexure strength and elastic limit of the hybrid composite.

Additionally, the effective axial flexural modulus of the material was calculated based upon the first 500 data points of the load vs. mid-span deflection curve. The effect that aging time had on effective axial flexural modulus is shown in Figure 5.27. Up to 9 months aging time, the effective axial flexural modulus was unaffected, however, at 12 months aging time a 16% reduction was observed in the mean effective axial flexural modulus in comparison to the unaged composites. Figure 5.26 and Figure 5.27 suggest that a substantial change occurred to the micro-structure of the composite between 9 and 12 months aging time at 180 °C. This conjecture will be further supported in section 5.2.4 in which the micro-structure of the aged composite specimens was investigated via scanning electron microscopy.

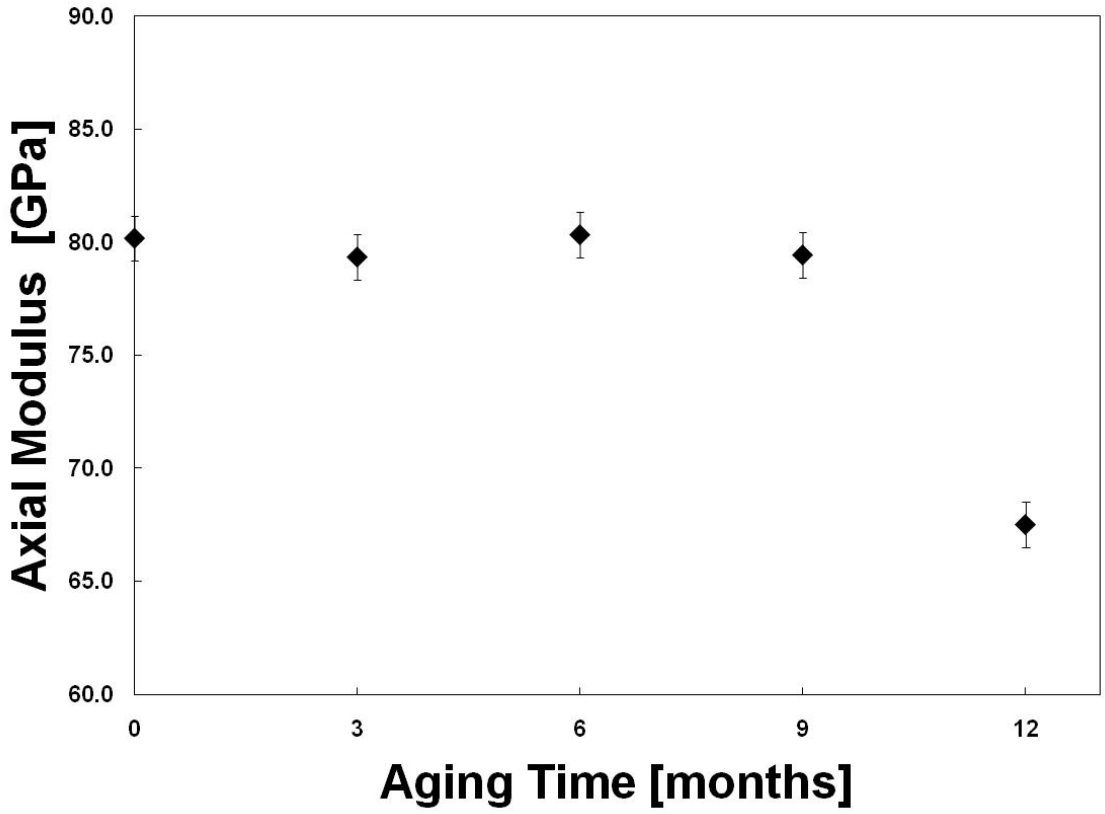

Figure 5.27 The effect of aging time at 180 °C on the effective axial flexural modulus of the hybrid composite.

5.2.4 Aged fatigue behavior

Using the definition of Damage, as defined by equation (4.1), comparative Damage vs. the number of cycles for the three stress amplitudes, at all aging times is shown in Figure 5.28 through Figure 5.30. Once again for all stress amplitudes and aging conditions, it was observed that damage was accumulated in a two stage fashion. For the 3 month aged specimens Damage was accumulated in a more or less linear fashion with respect to cycles in Stage I (equation (4.2))

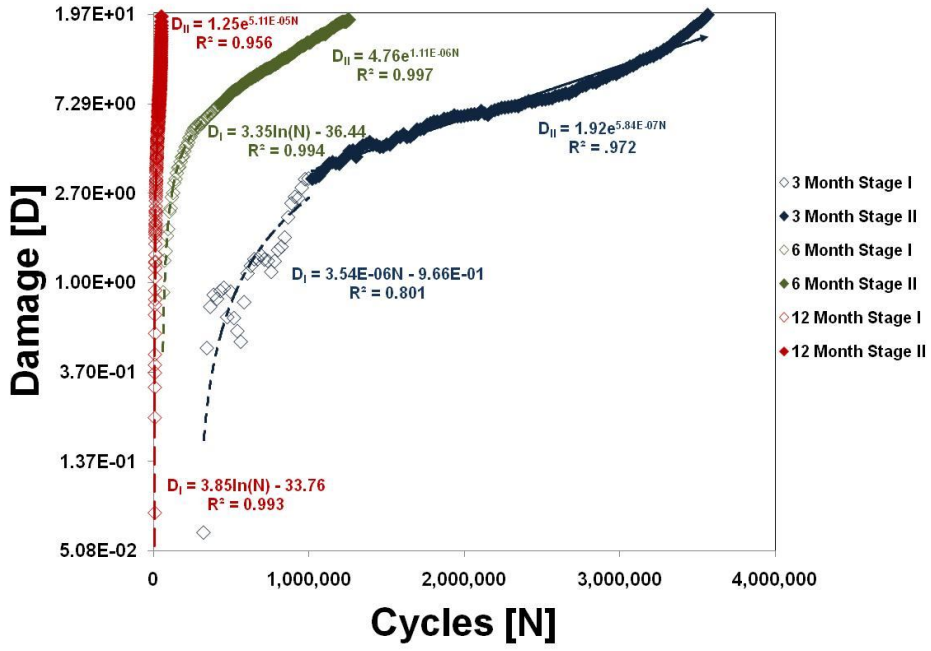

Figure 5.28 Damage vs. Number of cycles for σ_1 for 3 month aged (blue), 6 month aged (green), and 12 month aged (red) specimens. Note: y-axis is natural logarithmically scaled.

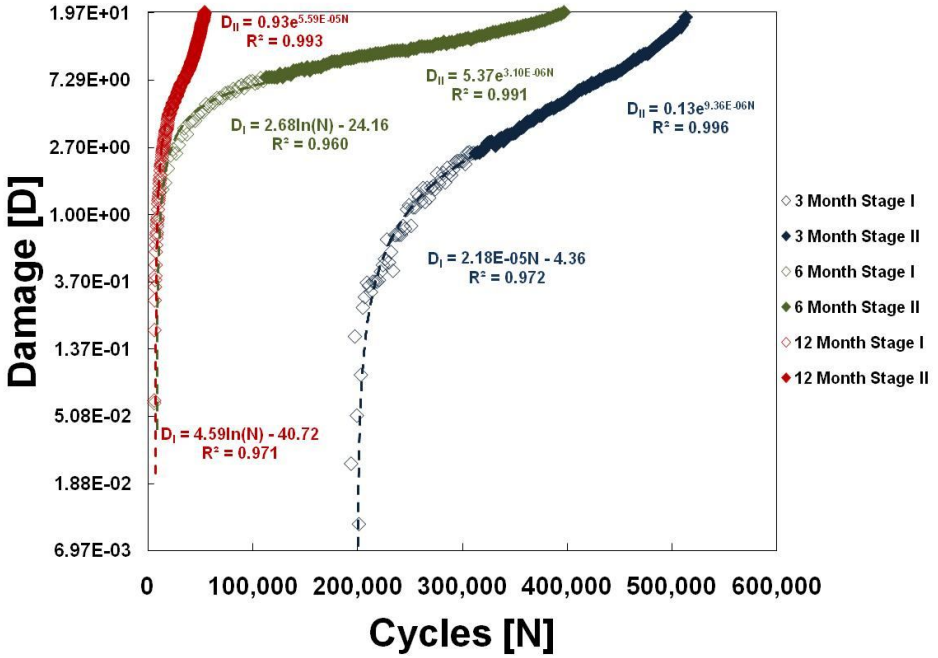

Figure 5.29 Damage vs. Number of cycles for σ_2 for 3 month aged (blue), 6 month aged (green), and 12 month aged (red) specimens. Note: y-axis is natural logarithmically scaled.

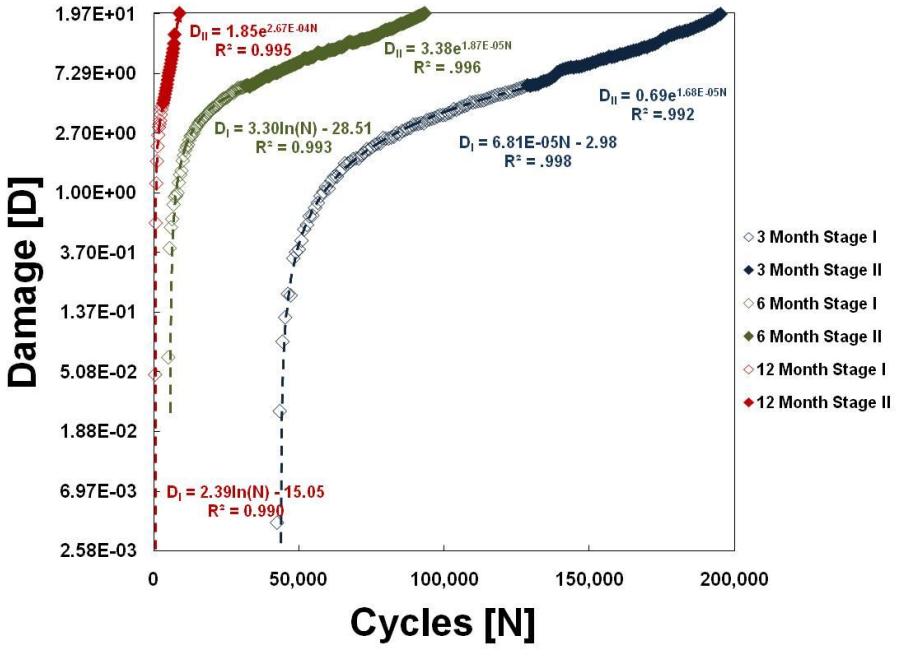

Figure 5.30 Damage vs. Number of cycles for σ_3 for 3 month aged (blue), 6 month aged (green), and 12 month aged (red) specimens. Note: y-axis is natural logarithmically scaled.

Interestingly, for the 6, and 12 month aged specimens the relationship between damage accumulation and number of cycles was best described by a natural logarithmic function in Stage I

$$D_I = \chi \ln(N) - \phi . \qquad (5.3)$$

in which χ and ϕ are once again material and stress amplitude dependent parameters. The natural logarithmic nature of damage accumulation during Stage I for the 6 and 12 month aged specimens was attributed to the crushing of the exposed glass fibers on the surface of the specimens (Figure 5.13, Figure 5.14, Figure 5.17, and Figure 5.18). Initially, as the glass fibers were crushed damage was accumulated at an accelerated rate. As the number of exposed glass fibers which had been crushed increased (reducing the amount of loosely bound glass fibers on the surface of the composite), the rate of damage

accumulation was retarded until Stage II damage accumulation commenced. The result, evidenced in Figure 5.28 through Figure 5.30, was a clear change in concavity of the damage curve between Stages I and II for the 6 and 12 month aged specimens; this change in concavity was absent for the 3 month aged specimens in which Stage I had a linear damage relationship, and therefore possessed a second derivative value of zero.

For all aging conditions an exponential relationship best described the relationship between Damage and number of cycles during Stage II damage accumulation (of the form of equation (4.3)). Damage curves for all aging conditions and stress amplitudes may be found in Appendix D. Table 5.2 summarizes the values for the material parameters that best fit the aged fatigue data using equations (4.2), (4.3), and (5.3).

Table 5.2 Summary of the material parameters for the Damage models described in equations (4.2), (4.3), and (5.3); reported mean [±1 standard deviation].

		3 Month		6 Month		12 Month	
		α	β	χ	φ	χ	φ
Stage I	σ_1	5.40E-6 [± 3.03E-6]	2.11 [± 1.87]	2.69 [± 0.81]	27.76 [± 9.28]	3.89 [± 0.65]	34.56 [± 8.00]
	σ_2	1.94E-5 [± 7.13E-6]	3.57 [± 2.95]	2.96 [± 0.46]	27.55 [± 5.52]	4.48 [± 1.87]	38.32 [± 17.63]
	σ_3	8.60E-5 [± 1.65E-5]	1.93 [± 1.47]	3.59 [± 0.81]	30.97 [± 9.18]	3.45 [± 1.91]	26.89 [± 17.83]
		κ	λ	κ	λ	κ	λ
Stage II	σ_1	1.70 [± 1.74]	1.23E-6 [± 9.66E-7]	5.10 [± 1.91]	1.16E-6 [± 5.14E-7]	4.07 [± 2.15]	1.56E-5 [± 1.44E-5]
	σ_2	0.37 [± 0.35]	8.52E-6 [± 5.07E-6]	4.62 [± 1.89]	4.82E-6 [± 1.50E-6]	2.41 [± 1.96]	6.95E-5 [± 5.64E-5]
	σ_3	1.41 [± 0.85]	1.59E-5 [± 4.07E-6]	4.38 [± 0.83]	1.44E-5 [± 2.47E-6]	1.29 [± 0.85]	2.71E-4 [± 1.96E-4]

Work was also done to investigate the rate at which damage was accumulated. To this end, the Incremental Polynomial Method approach taken in Chapter 4 was again utilized to numerically calculate the rate of change of damage accumulation with respect to cycles for all Stage II data (equations 4.4 – 4.6). The relationship between damage accumulation rate and the number of cycles was also found to be of the form of equation (4.7). Figure 5.31 shows the effect that aging had on the damage accumulation rate, for σ_1. No statistically significant difference existed between damage accumulation rates for the 3 and 6 month aging condition, but for the 12 month aging condition the damage accumulation rate was found to be an order of magnitude greater. Similar trends held for the other 2 stress amplitudes, as is shown in Figure 5.32 and Figure 5.33.

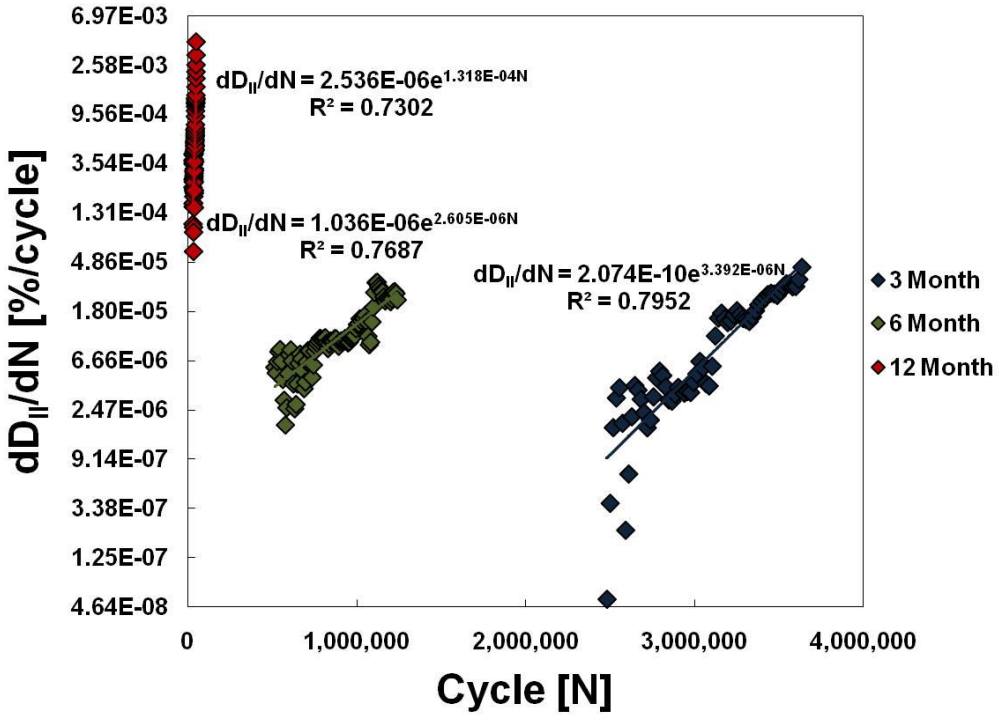

Figure 5.31 Representative rate of damage accumulation as a function of the number of cycles for all aging times subjected to σ_1.

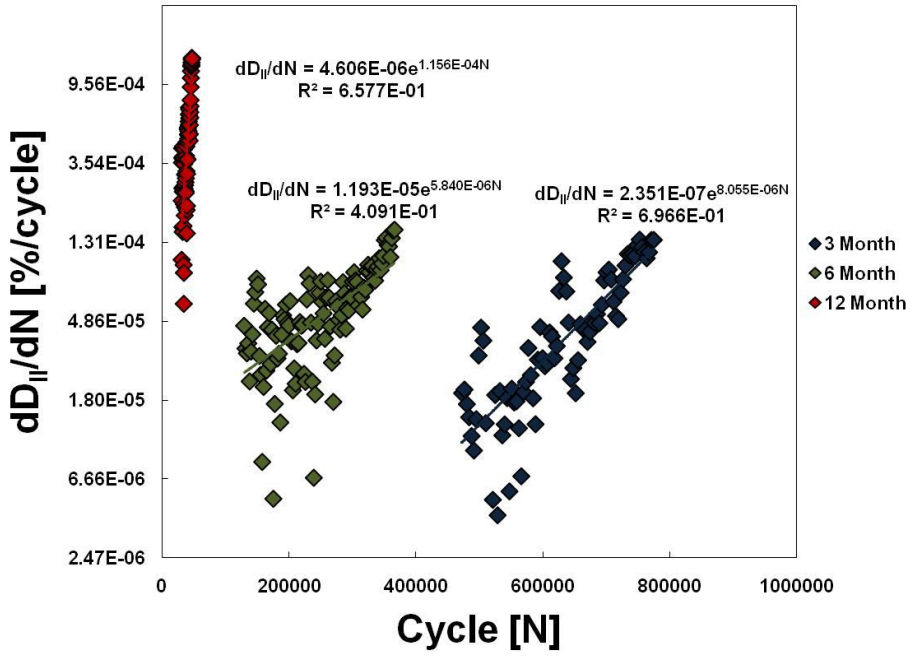

Figure 5.32 Representative rate of damage accumulation as a function of the number of cycles for all aging times subjected to σ_2.

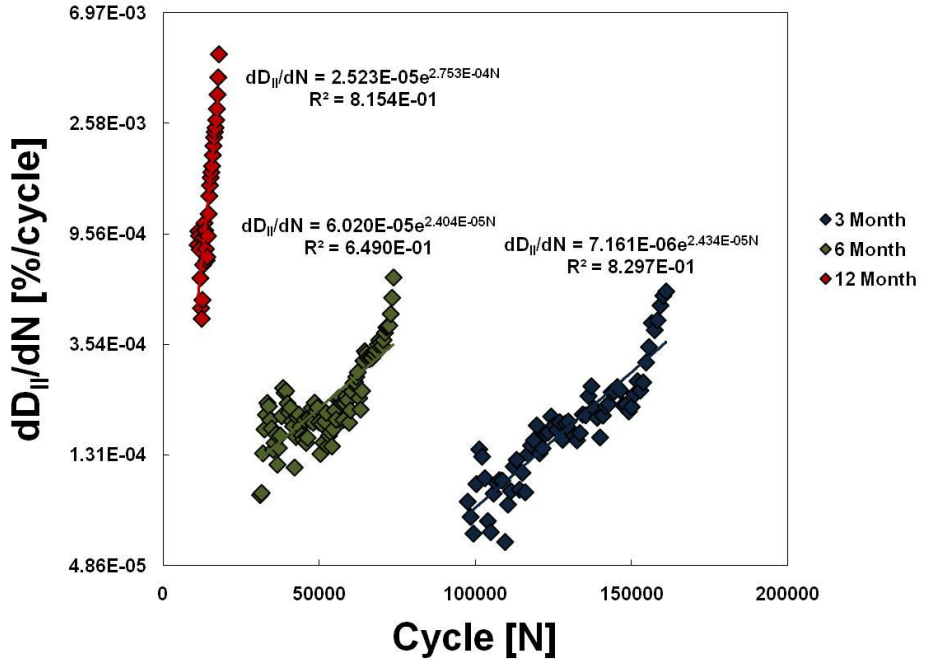

Figure 5.33 Representative rate of damage accumulation as a function of the number of cycles for all aging times subjected to σ_3.

In addition, the effect that the various stress amplitudes had on specific aging times was investigated, as is shown in Figure 5.34 through Figure 5.36; a clear stress amplitude dependence was observed for the rate term (η) at all aging times. Analogous to the unaged fatigue behavior, larger stress amplitudes resulted in greater damage accumulation rates. Damage accumulation rate material parameters for all aging conditions are summarized in Table 5.3.

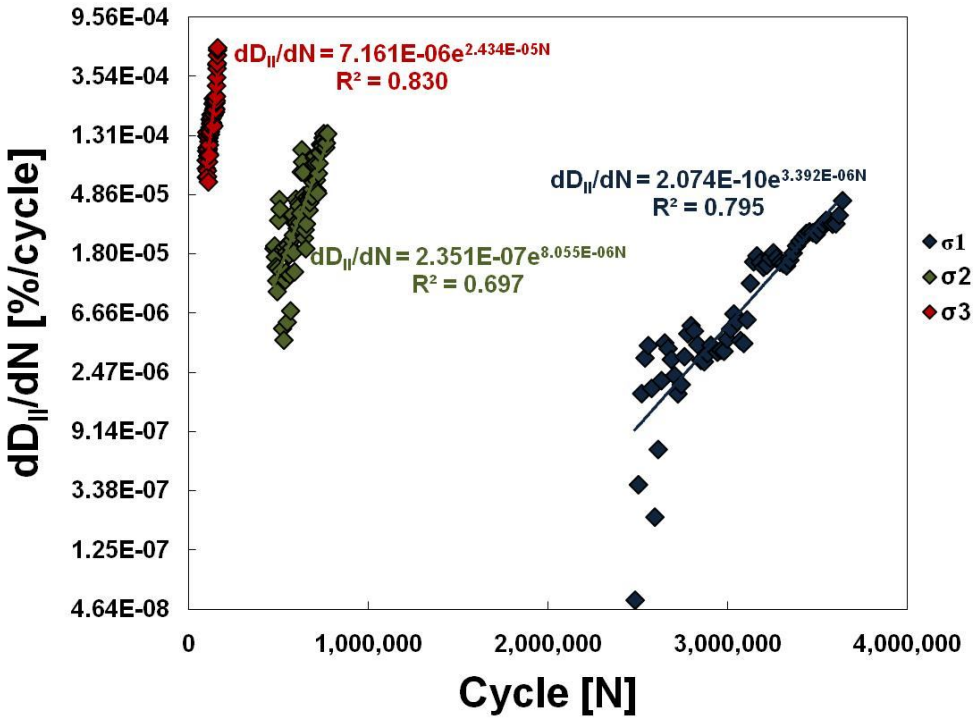

Figure 5.34 The effect of stress amplitude on the rate of damage accumulation for specimens aged at 180 °C for 3 months.

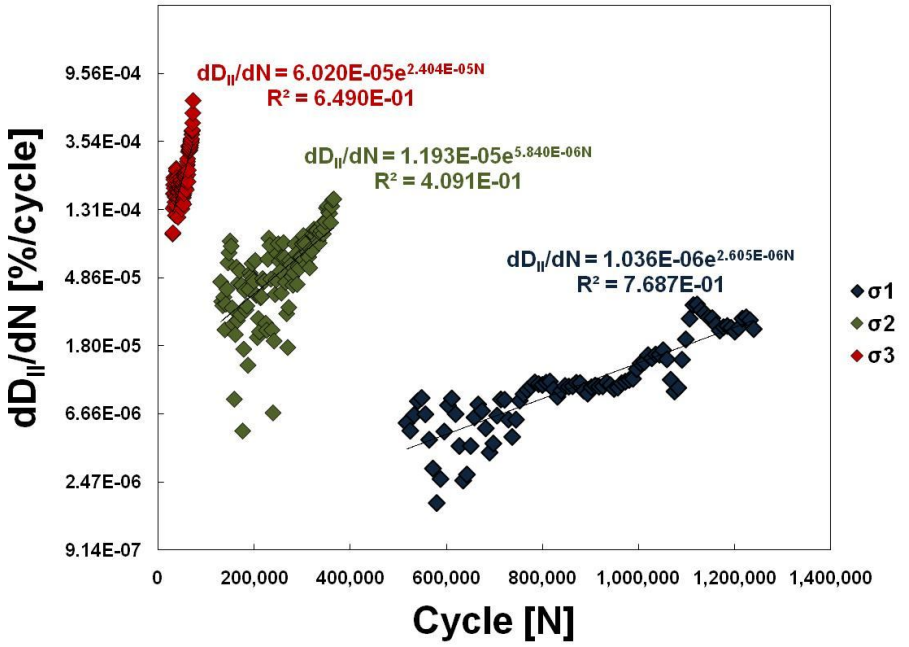

Figure 5.35 The effect of stress amplitude on the rate of damage accumulation for specimens aged at 180 °C for 6 months.

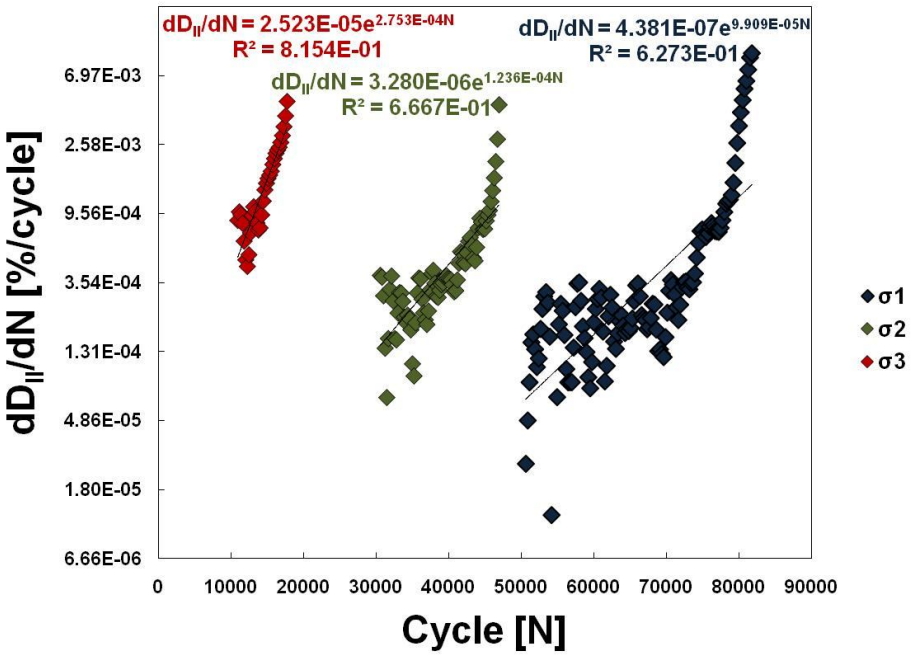

Figure 5.36 The effect of stress amplitude on the rate of damage accumulation for specimens aged at 180 °C for 12 months.

Table 5.3 Summary of the material parameters for the Damage accumulation rate model of equation (4.7); reported mean [±1 standard deviation].

	3 Month		6 Month		12 Month	
	γ	η	γ	η	γ	η
σ_1	8.97E-7 [± 1.04E-6]	1.84E-6 [± 1.24E-6]	4.55E-6 [± 3.34E-6]	1.57E-6 [± 7.07E-7]	1.35E-5 [± 2.60E-5]	4.46E-5 [± 4.05E-5]
σ_2	1.64E-6 [± 3.00E-6]	9.46E-6 [± 3.38E-6]	1.79E-5 [± 1.51E-5]	6.77E-6 [± 6.51E-6]	3.69E-5 [± 7.27E-5]	1.46E-4 [± 1.31E-4]
σ_3	1.44E-5 [± 1.27E-5]	1.98E-5 [± 7.49E-6]	6.01E-5 [± 2.70E-5]	1.58E-5 [± 7.25E-6]	1.43E-4 [± 1.80E-4]	3.32E-4 [± 1.82E-4]

Figure 5.37 shows the Wöhler plots for the 3, 6, and 12 month aged specimens, in addition to the unaged S-N data of Chapter 4. Once again the maximum bending stress within the GFC (σ_{BGFC}) was plotted on the ordinate, to maintain consistency with Chapter 4. Cycles to failure (N_f) was defined as a 20% reduction in initial stiffness.

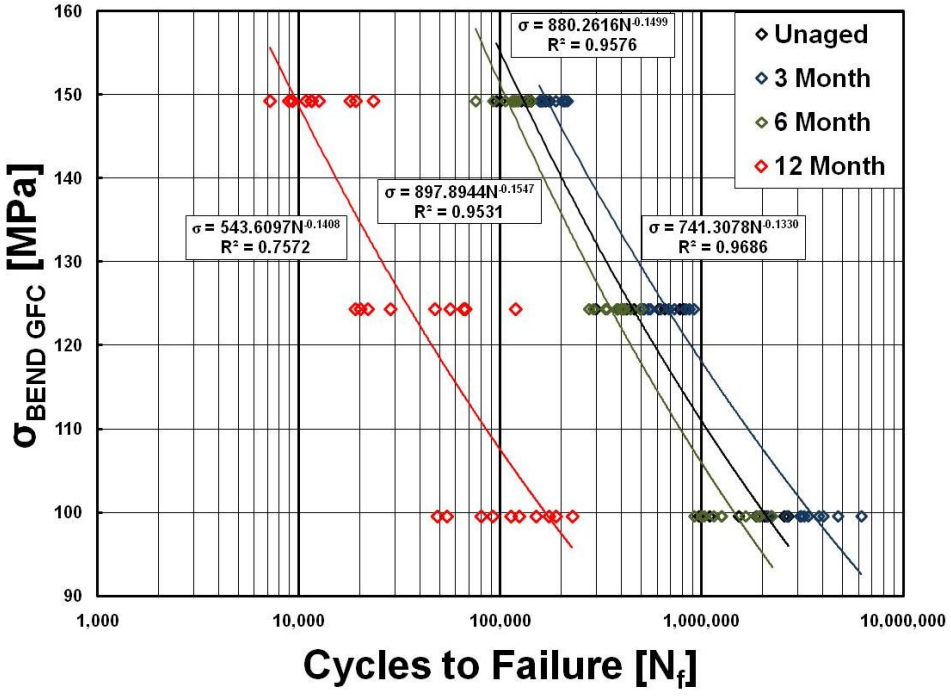

Figure 5.37 Wöhler plots for unaged (black), 3 month aged (blue), 6 month aged (green), and 12 month aged (red) specimens.

From Figure 5.37, it was observed that the 3 month aged specimens showed moderately improved fatigue performance with respect to cycles to failure when compared to the unaged data. Conversely, the 6 month aged specimens exhibited decreased fatigue performance with respect to cycles to failure in comparison to the unaged specimens. Further reduction in N_f was found for the 12 month aged specimens. The data for each stress amplitude and aging condition were fit with a two parameter Weibull distribution, and the appropriateness of fit was evaluated with a Kolmogorov-Smirnoff goodness of fit test at the 5% significance level (Haldar and Mahadevan 2000). Table 5.4 summarizes the scale (w) and shape (k) parameter for each Weibull distribution, while Figure 5.38 through Figure 5.46 show the Weibull distribution CDF fits for all three stress amplitudes and aging times. Similar to the unaged fatigue data, a narrowing of the failure distributions was observed with increasing stress amplitude was observed for the 3 and 6 month aged specimens. This trend indicated that axial failures remained dominant at the lower stress amplitude, and that a mixed mode failure again controlled the larger stress amplitudes. Conversely for the 12 month aged specimens marked variability was prevalent for all stress amplitudes. Such variability indicates substantial microstructure degradation had occurred to the 12 months aged specimens.

Table 5.4 Summary of Weibull distribution cycles to failure parameters for the 3, 6, and 12 month aged specimens.

	3 Month		6 Month		12 Month	
	w	**k**	**w**	**k**	**w**	**k**
σ_1	4,022,505	3.39	1,598,947	3.55	141,769	2.42
σ_2	735,751	5.15	406,402	6.38	57,882	1.86
σ_3	193,480	9.40	122,018	7.53	14,927	2.86

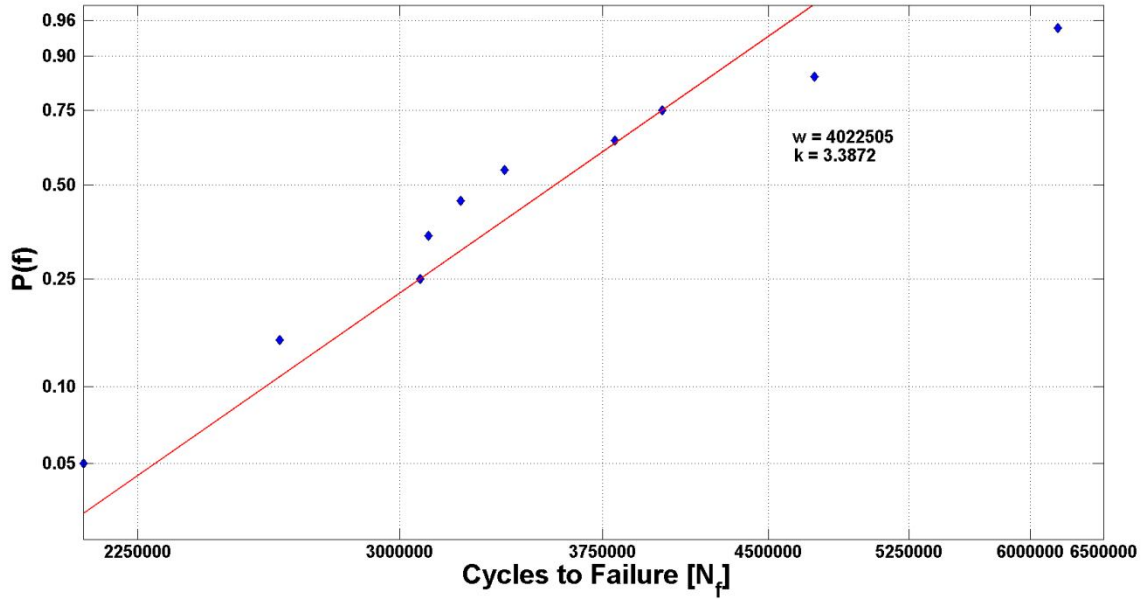

Figure 5.38 Weibull CDF for σ_1 for specimens aged at 180 °C for 3 months; w = 4,022,505, k = 3.39.

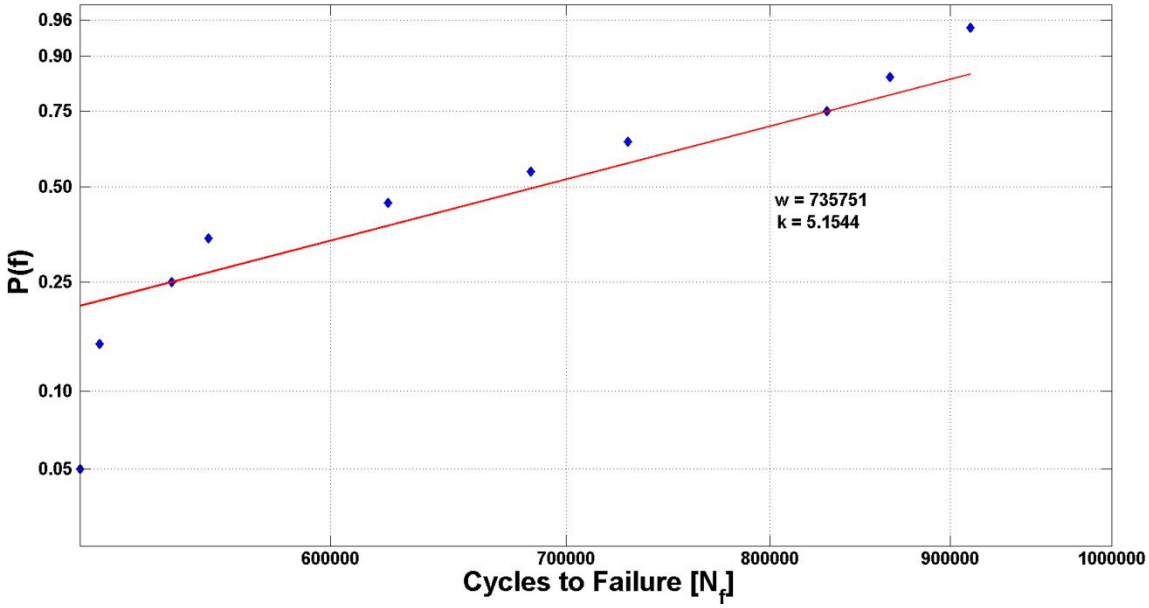

Figure 5.39 Weibull CDF for σ_2 for specimens aged at 180 °C for 3 months; w = 735,751, k = 5.15.

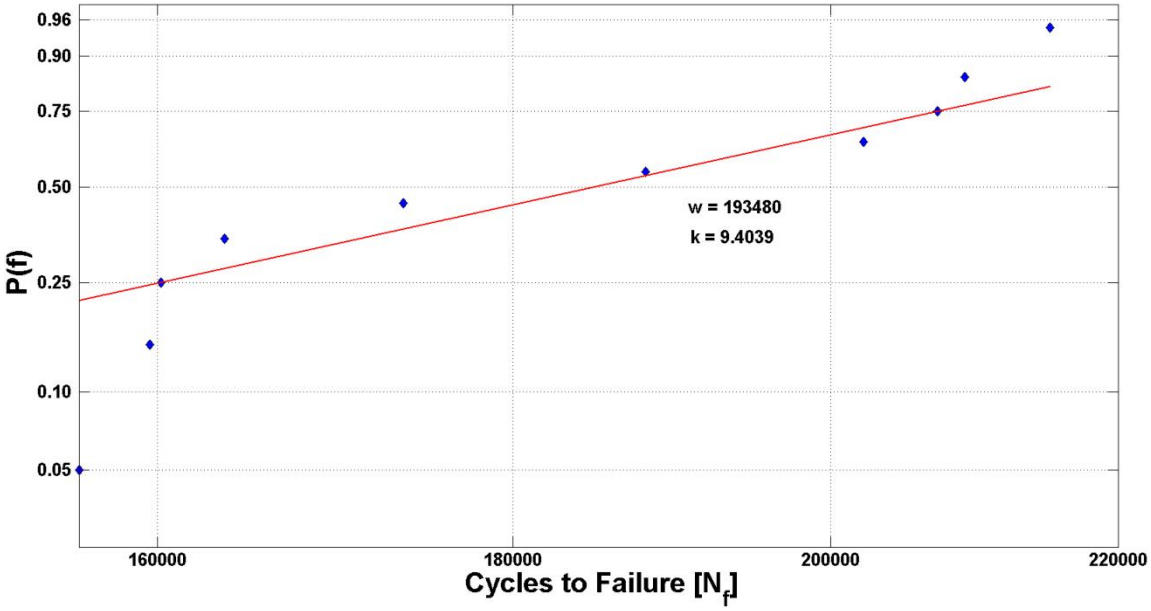

Figure 5.40 Weibull CDF for σ_3 for specimens aged at 180 °C for 3 months; w = 193,480, k = 9.40.

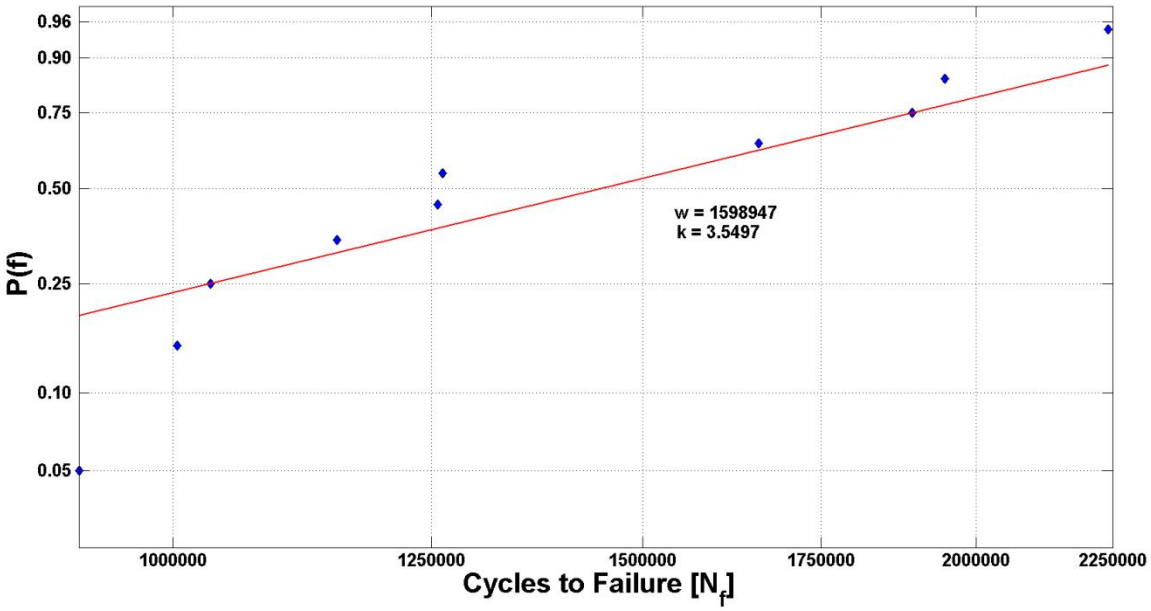

Figure 5.41 Weibull CDF for σ_1 for specimens aged at 180 °C for 6 months; w = 1,598,947, k = 3.54.

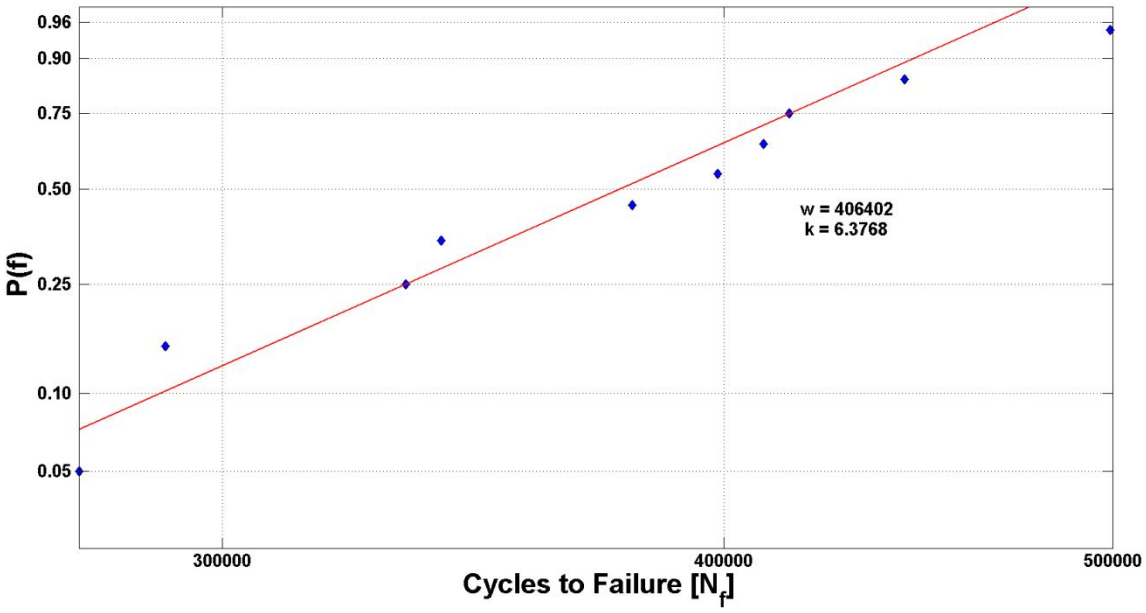

Figure 5.42 Weibull CDF for σ_2 for specimens aged at 180 °C for 6 months; w = 406,402, k = 6.38.

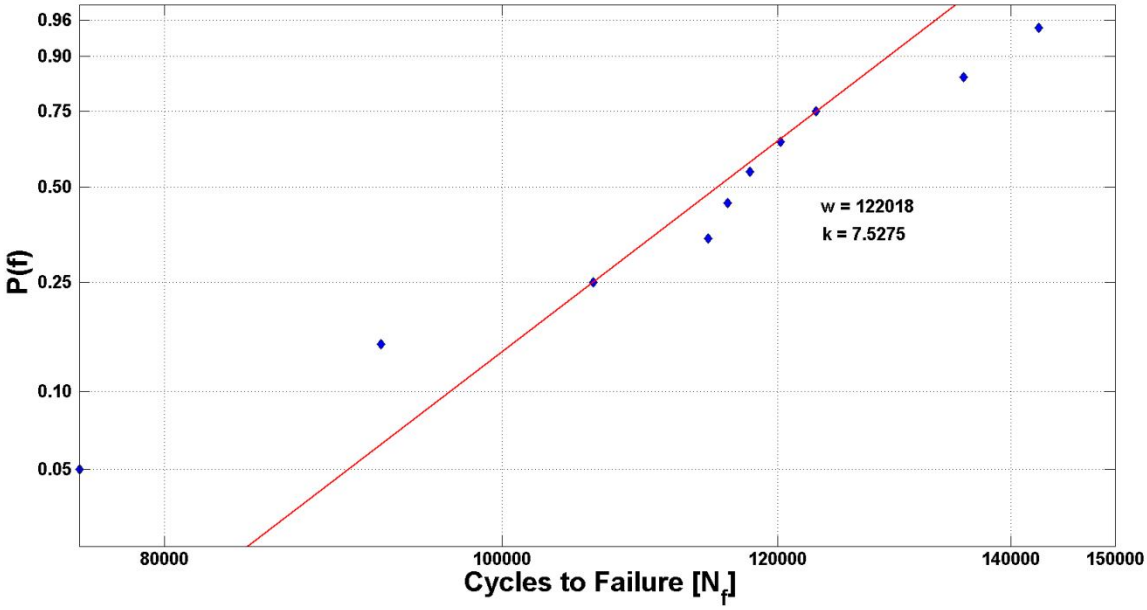

Figure 5.43 Weibull CDF for σ_3 for specimens aged at 180 °C for 6 months; w = 122,018, k = 7.5275.

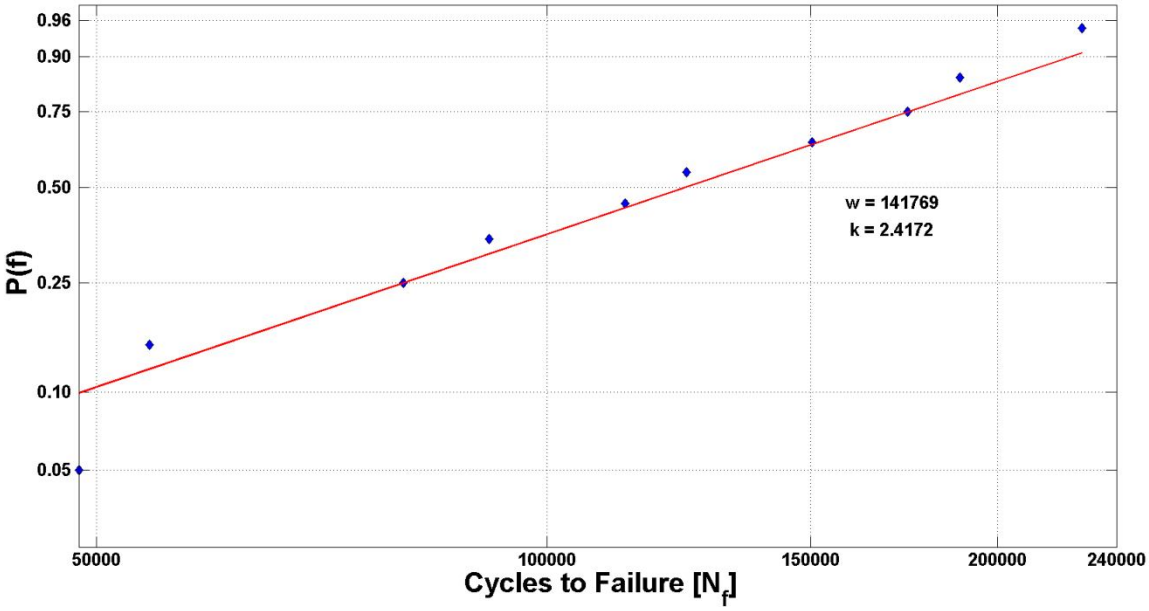

Figure 5.44 Weibull CDF for σ_1 for specimens aged at 180 °C for 12 months; w = 141,769, k = 2.42.

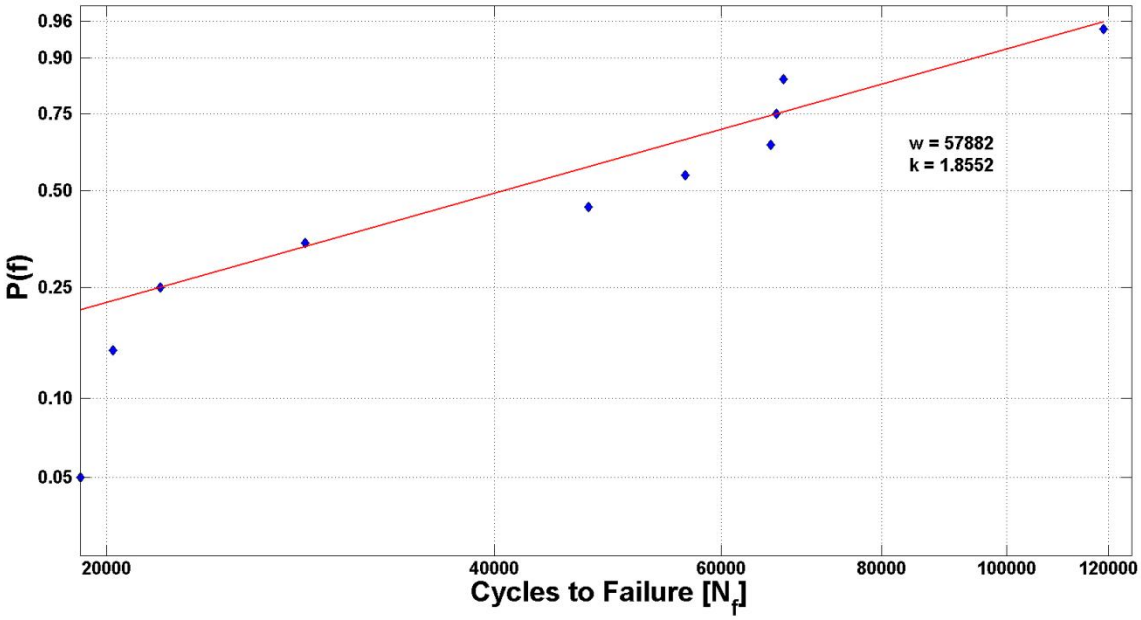

Figure 5.45 Weibull CDF for σ_2 for specimens aged at 180 °C for 12 months; w = 57,882, k = 1.86.

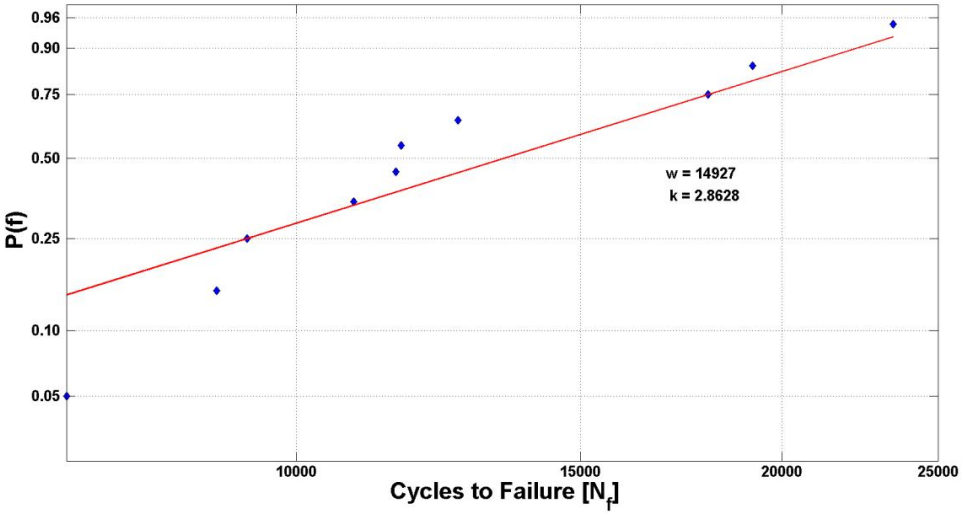

Figure 5.46 Weibull CDF for σ_3 for specimens aged at 180 °C for 12 months; w = 14,927, k = 2.86.

The Stage II damage accumulation rate term (λ) and the rate of damage accumulation rate term (η) were found to well describe the evolution of fatigue performance with respect to observed changes in micro-structure as the composite was aged at elevated temperature(Figure 5.47 and Figure 5.48).

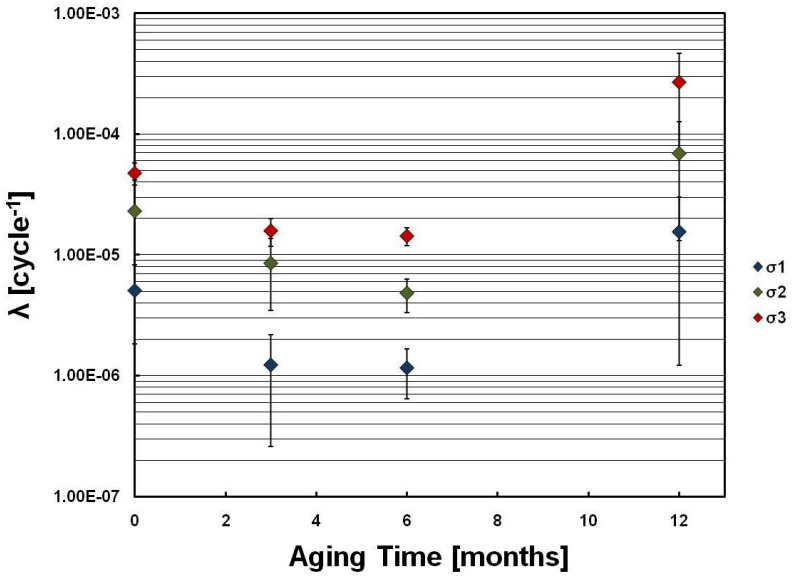

Figure 5.47 Damage accumulation rate term (λ) for all 3 stress amplitudes as a function of aging time; ±1 standard deviation error bars shown.

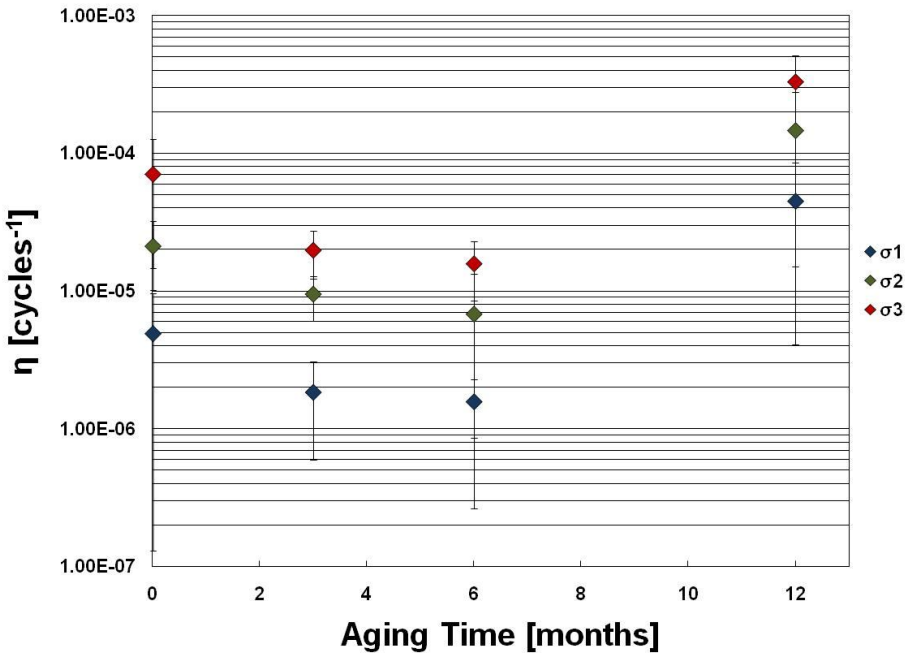

Figure 5.48 Rate of damage accumulation rate term (η) for all 3 stress amplitudes as a function of aging time; ±1 standard deviation error bars shown.

It was observed that the Damage accumulation rate term decreased for all stress amplitudes for aging times of 3 and 6 months, but showed a drastic increase at 12 months aging time. From this data, it is proposed that at short (3 months), and intermediate (6 months) aging times fiber/matrix interfacial properties, as well as matrix mechanical properties have improved, resulting in an improved resistance to damage accumulation. This is confirmed in Figure 5.49 and Figure 5.50 via Scanning Electron Microscopy, in which the fiber/matrix interfaces of both the GFC and CFC appear to be well intact.

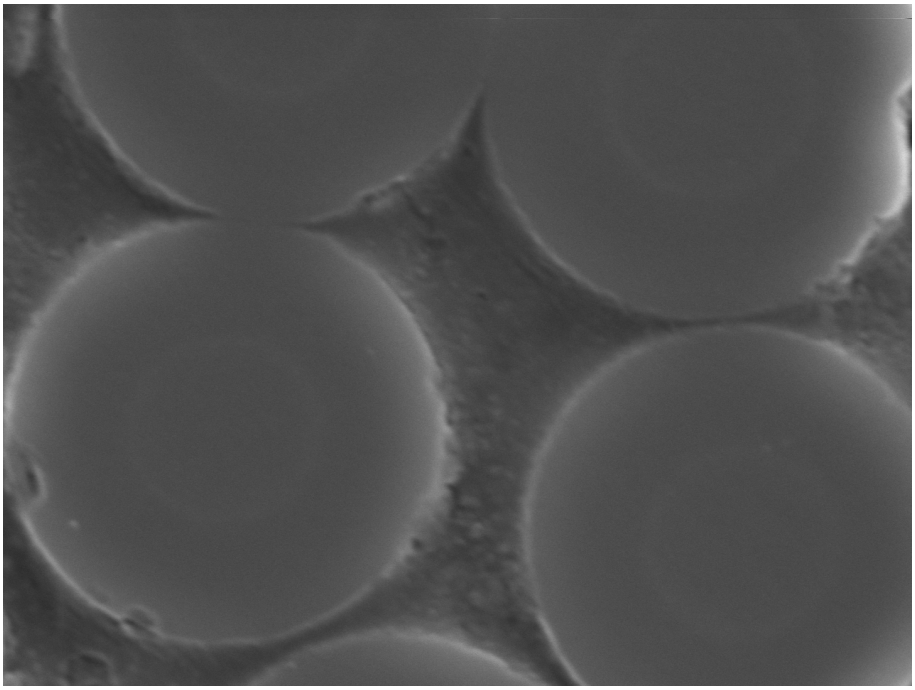

Figure 5.49 SEM micrograph of the representative CFC microstructure for specimens aged at 180 °C for 3 and 6 months time.

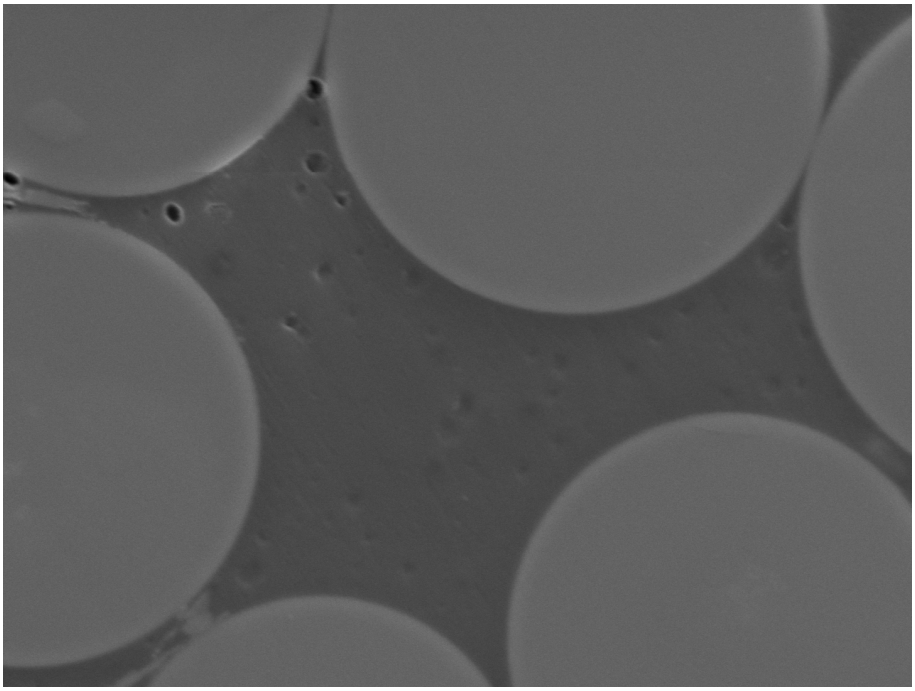

Figure 5.50 SEM micrograph of the representative GFC microstructure for specimens aged at 180 °C for 3 and 6 months time.

For the 3 months aging time, thermo-oxidation had not substantially degraded the surface of the composite and the interfacial and matrix material properties of the bulk had substantially improved, allowing for the improved cycles to failure performance. At 6 months aging time surface degradation had increased due to thermo-oxidation, while the bulk of the composite remained relatively unaffected, resulting in modestly decreased cycles to failure performance. For the extended aging condition (12 months), surface degradation had progressed, but more importantly volumetric shrinkage caused a substantial amount of fiber/matrix degradation to have occurred (Figure 5.51 and Figure 5.52). The extent to which physical aging had occurred at 12 months aging time resulted in drastically reduced cycles to failure data, as well as an order of magnitude increase in the rate at which damage was accumulated.

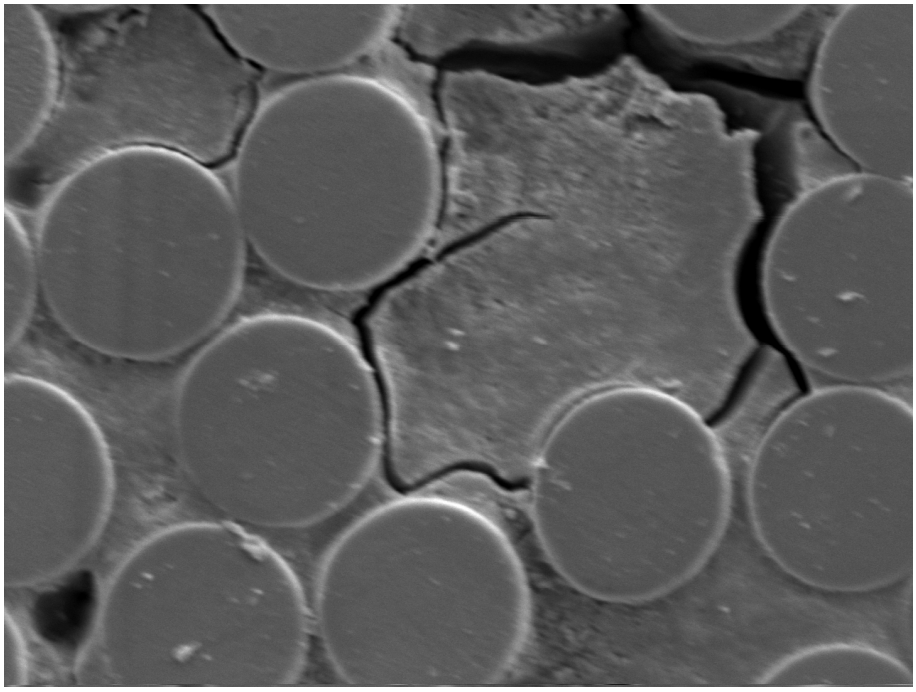

Figure 5.51 SEM micrograph of the representative CFC microstructure for specimens aged at 180 °C for 12 months time.

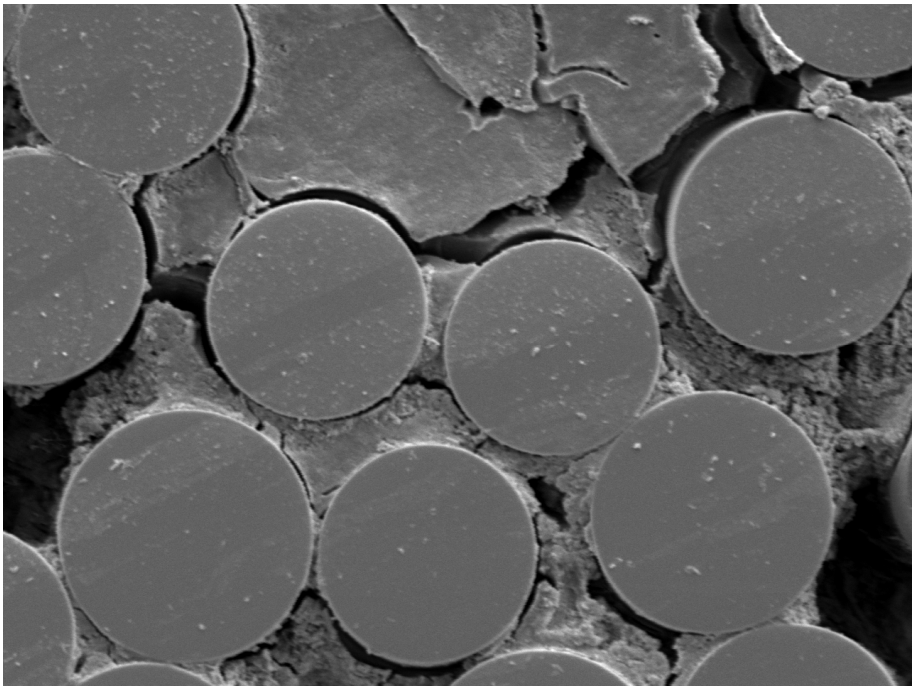

Figure 5.52 SEM micrograph of the representative GFC microstructure (in the bulk of the material, away from the oxidation layer) for specimens aged at 180 °C for 12 months time.

The difference in the two aging mechanisms was also found to affect the failure morphology of the aged specimens. As with the unaged specimens that had failed in fatigue loading (Chapter 4, Figure 4.26), fatigue damage was only evidenced in the GFC for the specimens that had been aged for 3 and 6 months (Figure 5.53 and Figure 5.54). Up to 6 months aging time not enough physical aging had occurred to degrade the bulk of the hybrid composite, only surface degradation due to thermal oxidation was evidenced.

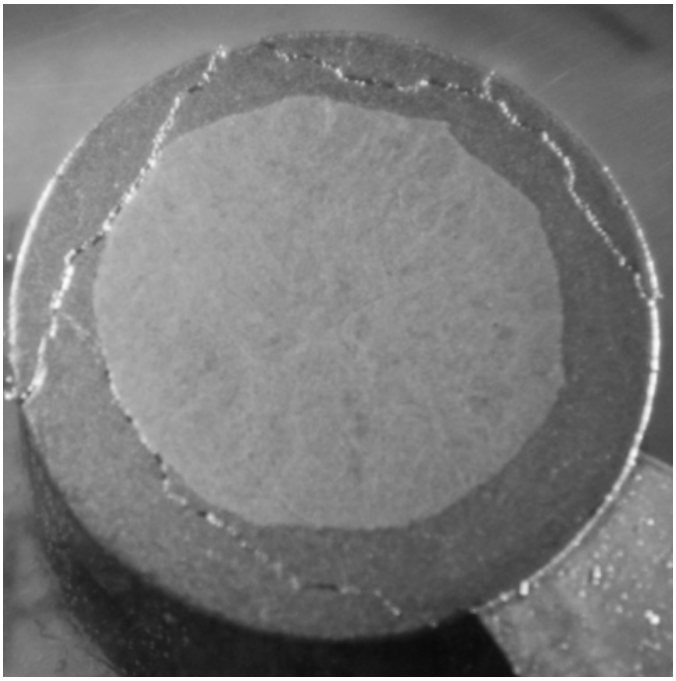

Figure 5.53 Representative transverse cross-section of a fatigue failed specimen that had been aged at 180 °C for 3 months.

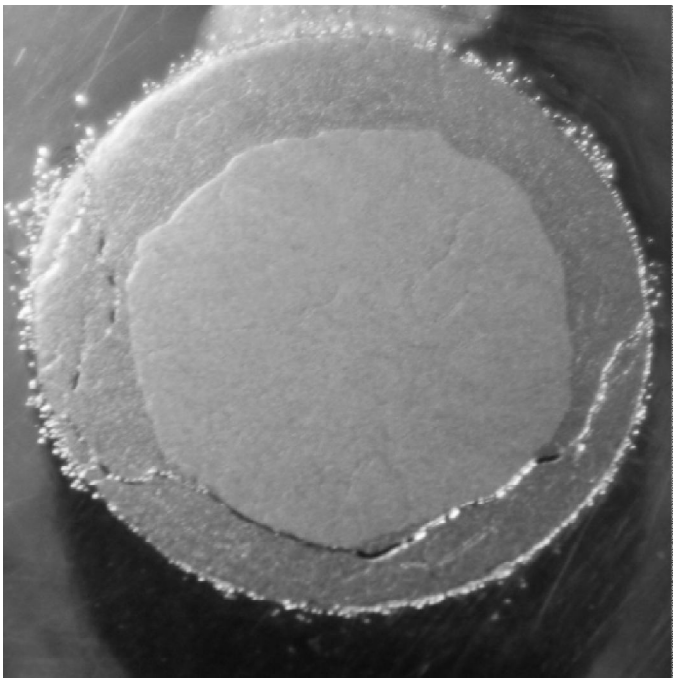

Figure 5.54 Representative transverse cross-section of a fatigue failed specimen that had been aged at 180 °C for 6 months.

However, for the 12 month aged specimens, fatigue damage was found to have accumulated in both the CFC and the GFC. Because enough physical aging had occurred such that residual stress built up within the epoxy matrix of the bulk composite, substantial fiber/matrix debonding of both composites had occurred (Figure 5.55). Hence, at 12 months aging time, enough physical aging had occurred to compromise the micro-structure of the bulk of the hybrid composite, which was evidenced by the fatigue damage in the CFC. The associated damage mechanisms that resulted in this interesting failure morphology are the focus of the forthcoming section, which investigated damage initiation via micromechanics modeling.

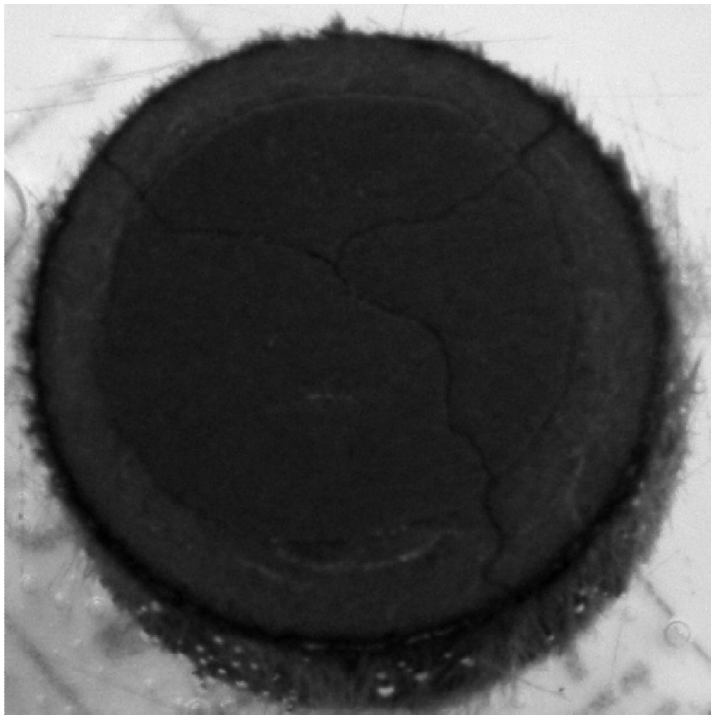

Figure 5.55 Representative transverse cross-section of a fatigue failed specimen that had been aged at 180 °C for 12 months.

5.2.5 Micromechanics of fatigue damage initiation

Figure 5.56 provides the DMA storage modulus data for specimens in the unaged, 3 and 6 month thermal aging condition (180 °C in an atmospheric oven), as well as the Prony series fit of the respective data. A 5 term Prony series was adequate in fitting all storage modulus curves, all coefficients are summarized in Table 5.5. It is clear from Figure 5.56 that as the neat resin epoxy specimens aged, embrittlement had occurred over the entire frequency range considered in this work.

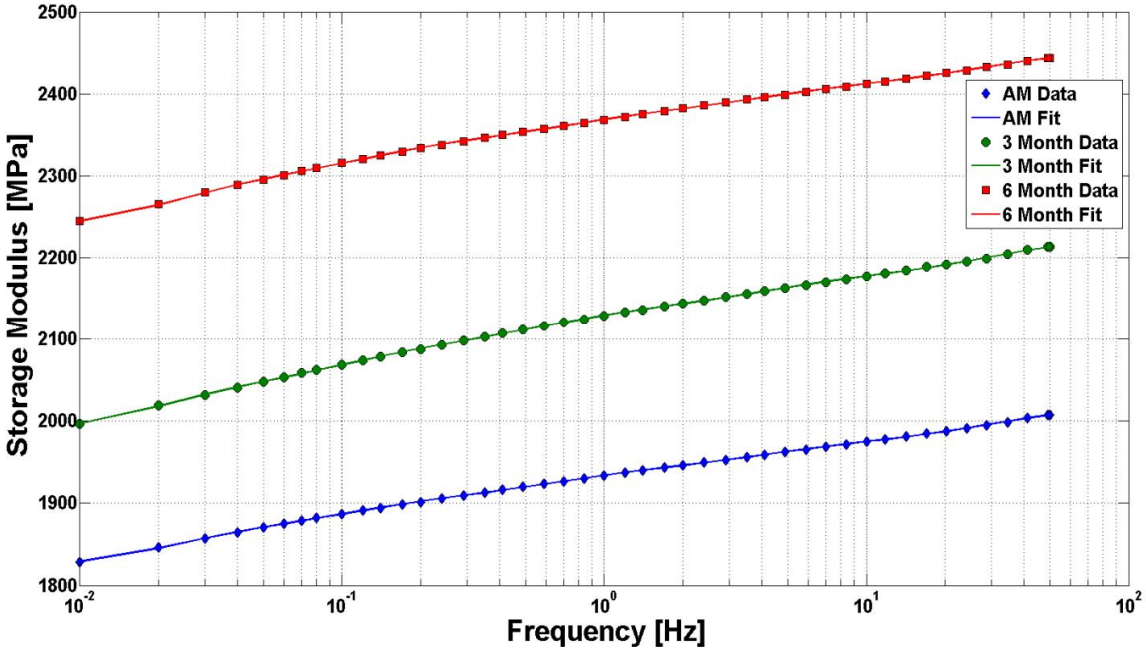

Figure 5.56 Storage modulus as a function of frequency, with the corresponding 5 term Prony series fit for specimens aged 0, 3 and 6 months.

Table 5.5 Summary of all Prony series coefficients used for viscoelastic material property definition, fit from the DMA data.

	0 Months	3 Months	6 Months
E_0 [MPa]	2020.22	2227.32	2455.00
e_1	0.0272	0.0293	0.0281
e_2	0.0217	0.0215	0.0167
e_3	0.0158	0.0174	0.0131
e_4	0.0170	0.0219	0.0184
e_5	0.0178	0.0197	0.0143
τ_1	7.3135	8.2457	7.2069
τ_2	0.0050	0.0050	0.0053
τ_3	0.0363	0.0380	0.0351
τ_4	0.2231	1.4203	1.2015
τ_5	1.3048	0.2482	0.1973

Representative stress field contours of the axial stress for square and hexagonally packed RVEs for an unaged CFC with a $v_f = 65\%$, subjected to σ_3 are shown in Figure 5.57 and Figure 5.58, respectively. Similar stress field distributions were observed for the GFC, all volume faction of fibers, stress amplitudes, and aging conditions. Clearly the axial stress within the reinforcing fiber will be considerably higher, necessitating for this work that full scale be set as the maximum axial stress within the epoxy matrix, with all values above such mapping to gray (Figure 5.57 and Figure 5.58). In agreement with the observations of Eshelby (Eshelby 1957), the stress within the elliptical inclusions (circular fibers) was uniform for all analyses. The maximum axial stress within the epoxy

matrix occurred in-between the fibers, signifying that the interaction of the stress field between inclusions was concentrating the local state of axial stress.

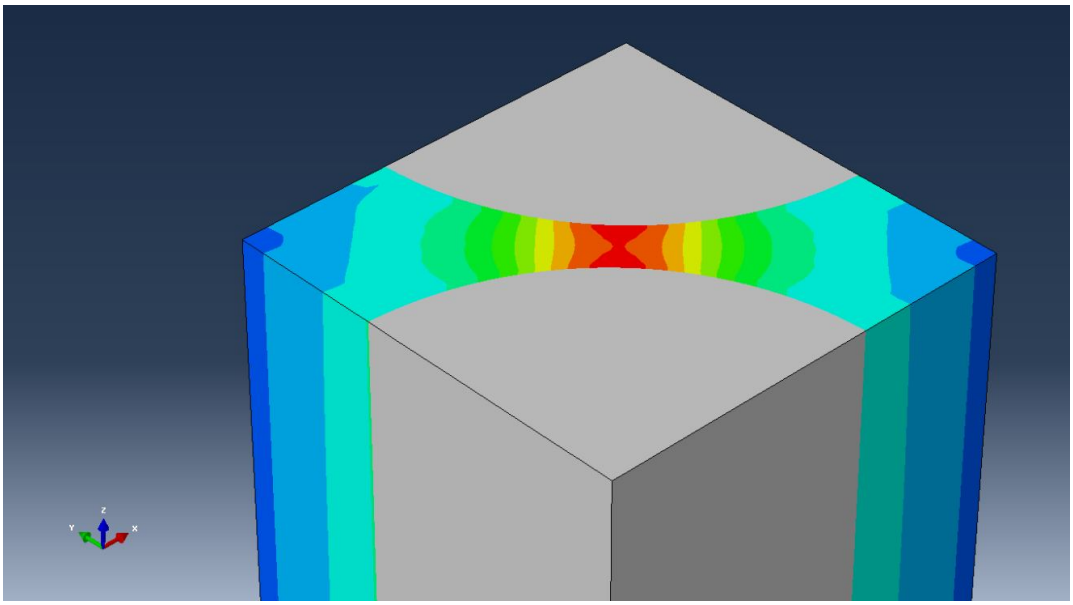

Figure 5.57 Axial stress field distribution for a square packed CFC RVE with $v_f = 65\%$.

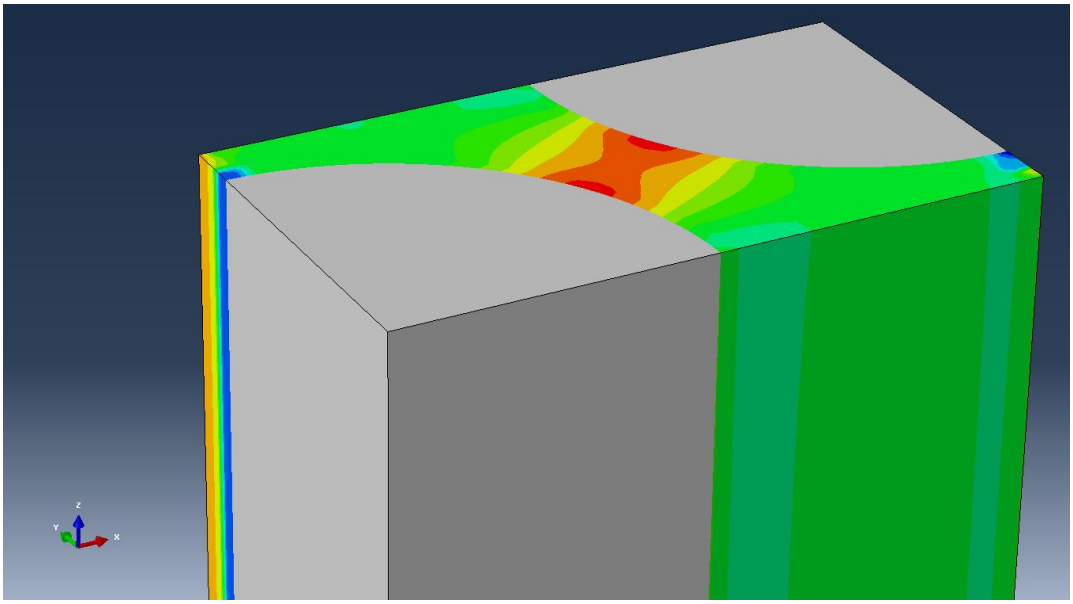

Figure 5.58 Axial stress field distribution for a hexagonal packed CFC RVE with $v_f = 65\%$.

The effect that the volume fraction of fibers had on the axial stress for the unaged CFC RVEs that had been subjected to σ_3 is shown in Figure 5.59, while Figure 5.60 presents the analogous results for the GFC. Several important conclusions can be made from these two figures. Most obviously, even though the macro stress on the GFC was less than that of the CFC, the axial stress within the epoxy matrix was higher in the GFC. We attribute this to the fact that carbon fibers are ~3x stiffer in the axial direction in comparison to the glass fibers. Thus, a far greater amount of the axial stress was carried by the carbon fibers in comparison to the glass fibers, enabling the matrix material of the CFC to remain at a considerably reduced state of stress in comparison to the GFC. This is the primary reason that fatigue damage was evidenced only in the GFC, and not the CFC of the hybrid composite.

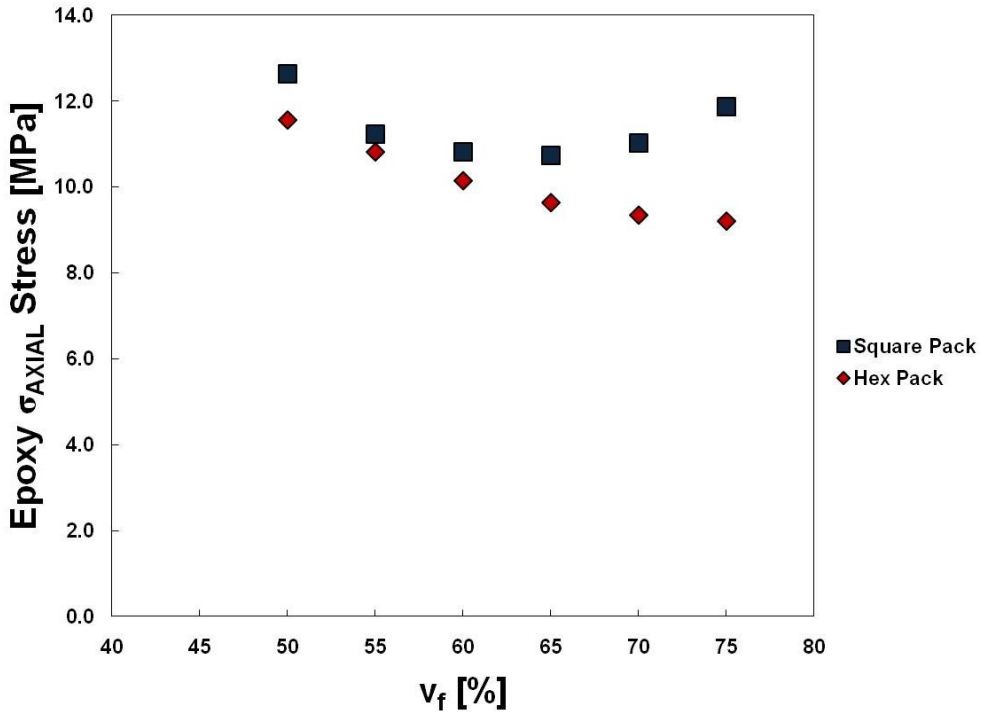

Figure 5.59 Maximum axial stress as a function of v_f for the unaged CFC RVEs subjected to σ_3.

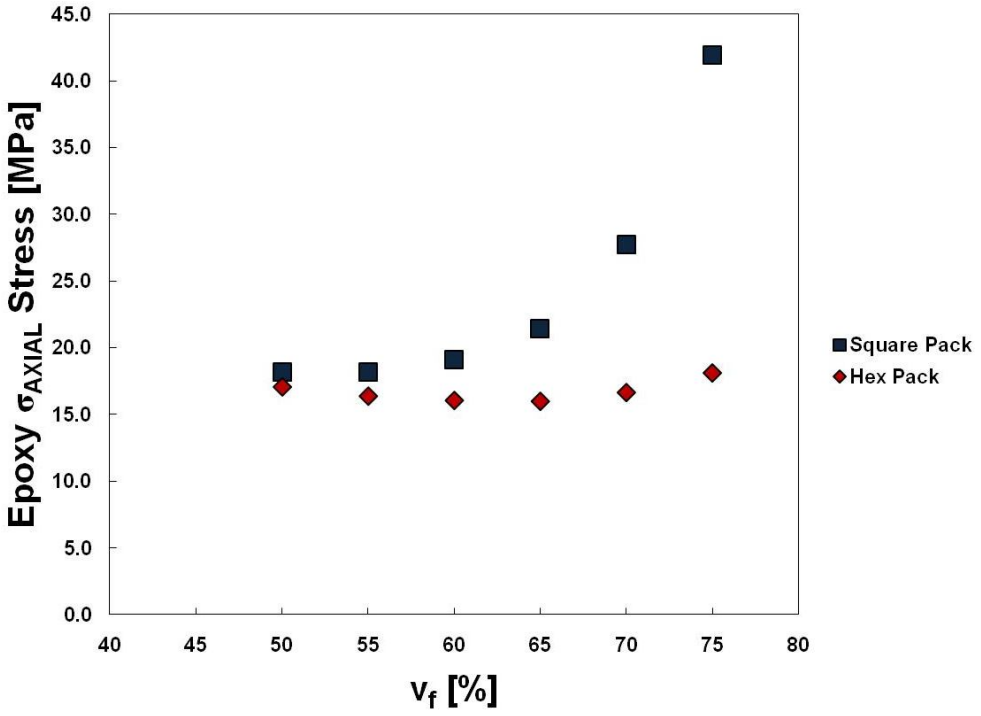

Figure 5.60 Maximum axial stress as a function of v_f for the unaged GFC RVEs subjected to σ_3.

Moreover, these analyses provide general insight into the experimental observations of others that carbon fiber reinforced composites perform in a superior manner in fatigue loading in comparison to glass fiber reinforced composites (see (Boller 1964),(Jones, et al. 1984)). By reducing the state of stress within the matrix material, considerably higher stress amplitudes can be achieved with carbon fiber reinforced composites before fatigue damage initiates.

Also from Figure 5.59, it was observed that the packing arrangement and the volume fraction of fibers impacted the maximum axial stress within the CFC. For both the square and hexagonal packed arrays, the axial stress initially decreased as v_f became larger than 50%. For the square packing arrangement a minimum stress occurred at ~68% v_f. A minimum was not observed for the hexagonal packed RVEs for the range of v_f

considered in this work, although a minimum was being approached, nearing 75% v_f. From a load share perspective (making the "iso-strain" assumption of the Voigt model) and neglecting stress field interaction, the stress within the fiber and matrix will be proportional to the respective area fraction of each material of a transverse cross-section, as well as the ratio of stiffness between the two materials. Hence, at lower volume fractions the axial stress within the matrix was greater because the area fraction of matrix material was higher. Conversely, as the v_f increased, the area fraction of matrix material decreased, decreasing the axial stress. The decline persisted until the inter-fiber spacing decreased enough, with increasing v_f, that the stress field interaction between neighboring fibers became significant enough to amplify the axial stress.

Similar observations held for the GFC, with the exception being that for the square packing arrangement, axial stress was continually increasing for the range of v_f considered in this work. Because glass fibers are significantly less stiff than carbon fibers, the ratio of matrix stiffness to fiber stiffness is considerably higher in the GFC, reducing the value of v_f in which a minimum axial stress would be observed in the matrix. Interestingly for the GFC, due to the lower stiffness of the glass fibers, and the small inter-fiber spacing that occurs at v_f = 75% in a square packing arrangement, a pronounced stress field interaction occurred, significantly amplifying the axial stress. This signifies that in a true composite system with a large v_f, that neighboring fibers having a small inter-fiber spacing will have a much higher probability of initiating fatigue damage within the matrix, than would fibers having a greater (and uniform) inter-fiber spacing.

To investigate the effect that thermal aging had on the state of stress within the unaged epoxy matrix, aged RVEs were analyzed by replacing the viscoelastic material properties of the epoxy material with the measured viscoelastic response of aged neat resin samples (Figure 5.56 and Table 5.5). As a representative case RVEs of the CFC and GFC with $v_f = 65\%$, subjected to σ_3 were considered. Figure 5.61 shows that as the hybrid composite aged, the axial state of stress of the epoxy within both composites increased. With the epoxy at higher levels of axial stress, one would expect fatigue damage to accumulate earlier in life, causing a reduction in N_f. This was observed for the 6 month aged fatigue specimens of section 5.2.4.

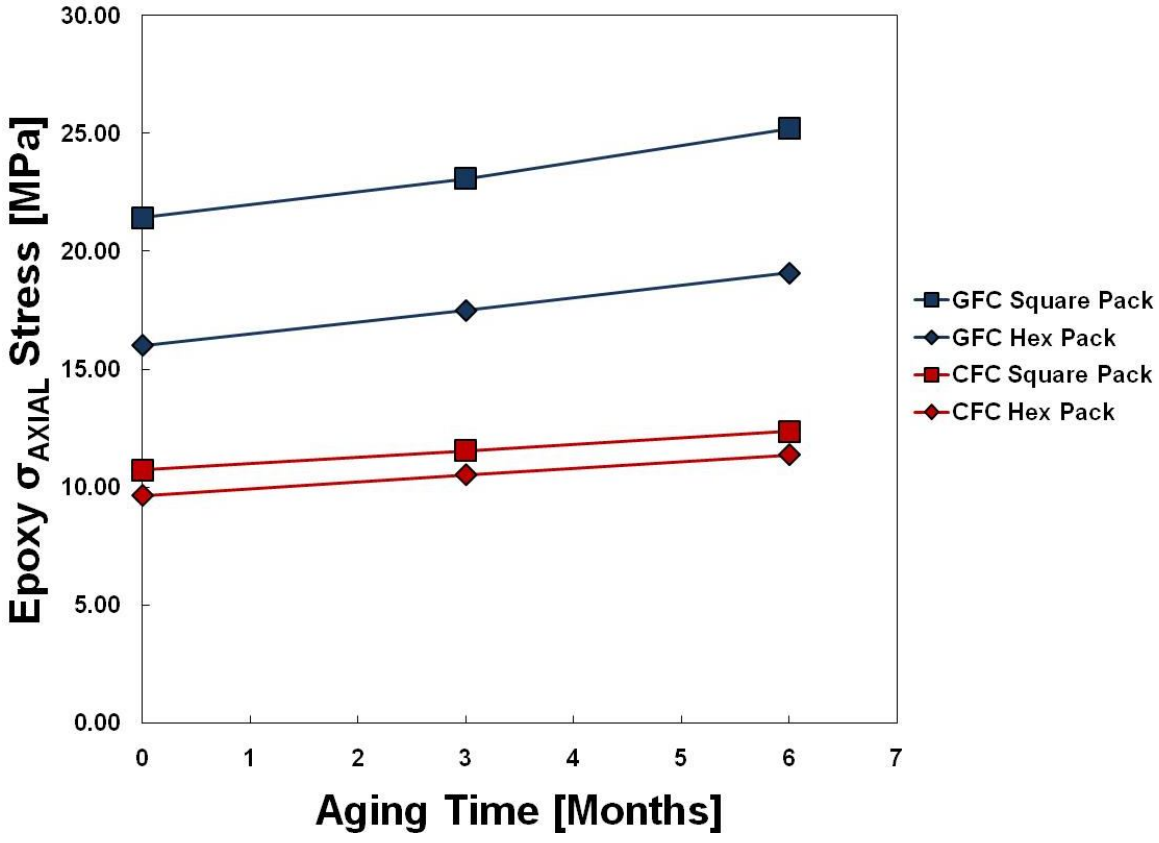

Figure 5.61 Maximum axial stress within the epoxy matrix as a function of aging time for the GFC and the CFC subjected to σ_3, considering both types of packing arrangements, for a $v_f = 65\%$.

As was previously discussed, for the 3 month aged specimens a post-cure effect had been observed, resulting in an increase in N_f. With the epoxy stiffening at 3 months, the axial stress within the epoxy of the composite would have increased, promoting a reduction in fatigue life. However, as others have observed, post-cure also results in enhanced toughness and inter-laminar shear strength (see (Lowe, Fox and Otieno-Alego 2002), (Akay and Spratt 2008)), negating the effects of the slightly higher state of stress within the epoxy matrix, and facilitating the modest improvement in N_f. Additionally, the neat resin specimens of this study were subjected to a full cure cycle, and were therefore not expected to undergo the degree of post-cure that the pultruded composites did.

Through RVE modeling, Gentz et al. highlighted the consequence of aging and the associated volumetric relaxation on the state of residual stress within the matrix material of a CF/PMR15 composite system (Gentz, Benedikt, et al. 2004), (Benedikt, et al. 2004), (Gentz 2004). These observations were quite important, and can certainly be anticipated to contribute to the state of stress within the epoxy material reported in this work. Unfortunately, long-term and elevated temperature viscoelastic material properties of the matrix material were not available, thus the effects of volumetric shrinkage could not be incorporated into the models. Additionally, to fully quantify the effect that aging had on the composites, the evolution of interfacial properties and fracture toughness of the epoxy would need to be known. Currently these are unknown parameters, and for this reason, the 12 month aging condition was not considered. Due to the substantial degradation of

the 12 month aged composites, the undamaged RVE approach adopted in this section was not appropriate.

The effect that the various stress amplitudes had on the state of stress within the unaged epoxy matrix for the CFC and the GFC can be seen in Figure 5.62 and Figure 5.63, respectively. Figure 5.62 and Figure 5.63 are surface plots in which, v_f and stress amplitude are independent variables, and the axial stress within the epoxy matrix is the response variable for the respective square packed, unaged RVE. As expected, the stress within the epoxy matrix increased with increasing stress amplitude for all volume fractions. Similar observations were made for the hexagonal packing arrangement, and all aging conditions.

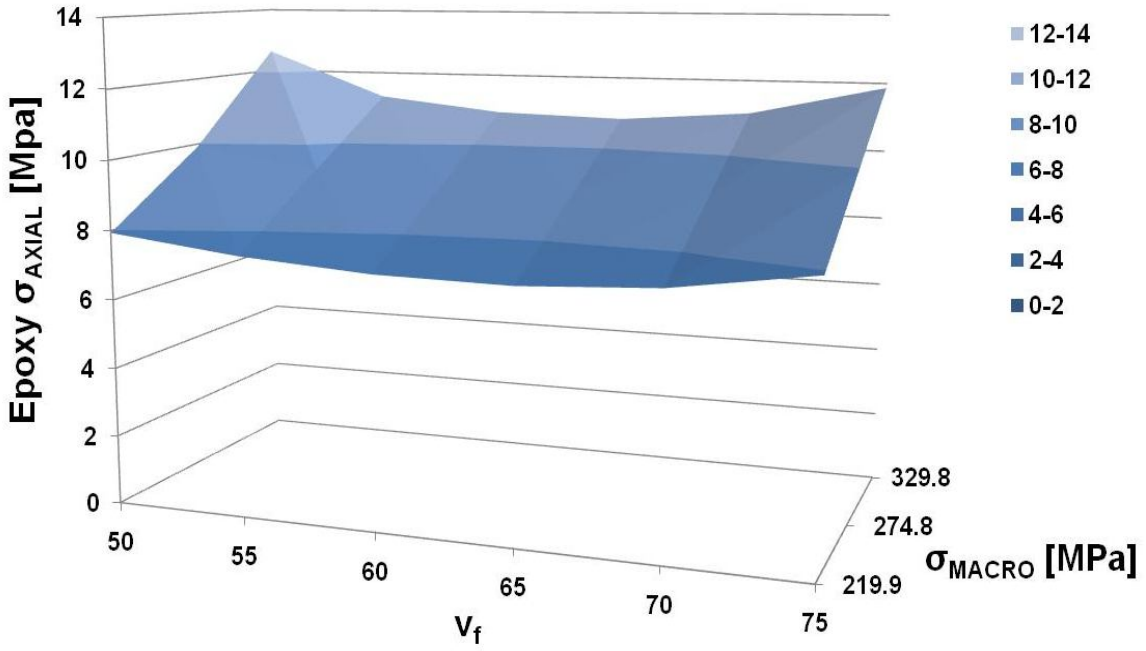

Figure 5.62 Surface plot for the CFC square packed RVE showing the effect that the stress amplitude and v_f had on the maximum axial stress within the unaged epoxy.

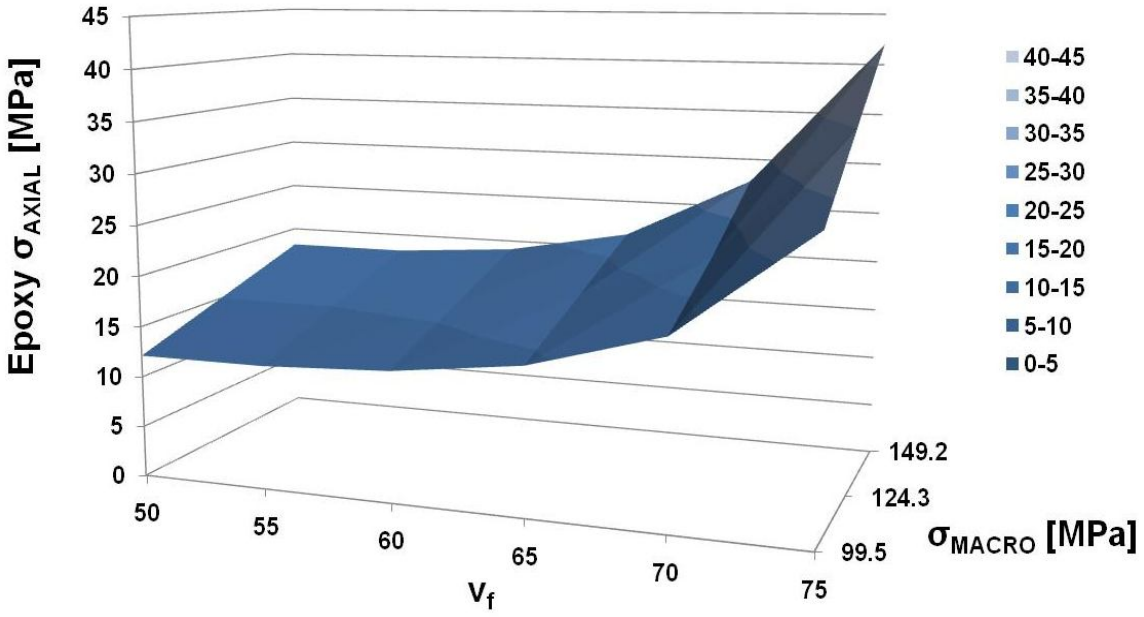

Figure 5.63 Surface plot for the GFC square packed RVE showing the effect that the stress amplitude and v_f had on the maximum axial stress within the unaged epoxy.

In looking at a slice of the surface plot (v_f = 65%) we see that a linear relationship existed between the maximum macro stress applied to each composite, and the axial stress within the epoxy matrix (Figure 5.64). From this perspective, it was clear why fatigue life was shortened at higher stress amplitude loading; due to the fact that the matrix material was more highly stressed, fatigue damage was able to accumulate with a fewer number of applied cycles. For all stress amplitudes the stress within the epoxy matrix was markedly higher for the GFC as compared to the CFC, for reasons previously discussed. Also, from Figure 5.64 it was observed that the maximum axial stress within the epoxy was increasing at an increased rate with respect to the applied stress amplitude for the GFC in comparison to the CFC. This supports the experimental observations of others that the slope of the S-N line for glass fiber reinforced composites is steeper than for carbon fiber reinforced composites (Boller 1964), (Jones, et al. 1984).

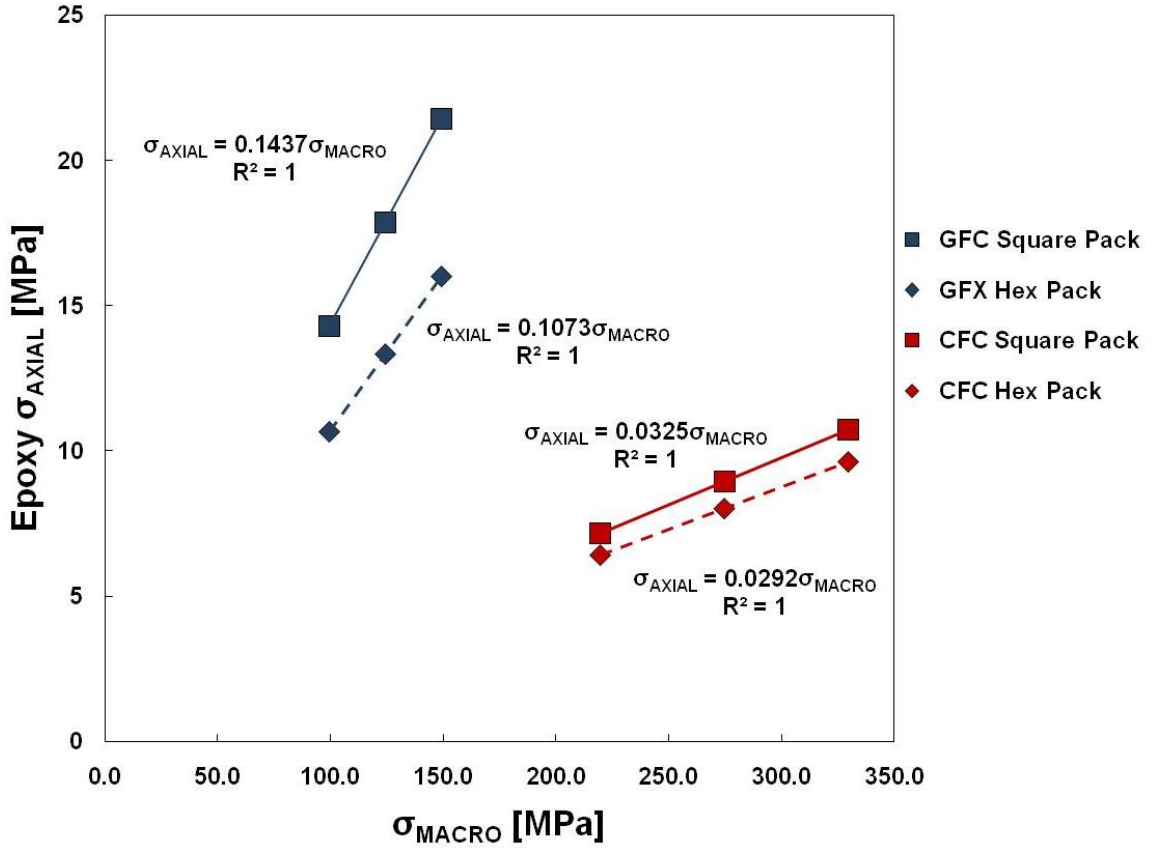

Figure 5.64 Maximum axial stress within the unaged epoxy matrix as a function of the macro stress amplitude for each composite (v_f = 65%).

Finally, the effect that frequency had on the state of stress within the epoxy matrix was evaluated. A frequency range between 0.01 and 50 Hz was considered, to evaluate the importance of the viscoelastic nature of the epoxy resin. Results for the unaged GFC square packed RVE (v_f = 65%, subjected to σ_3) are shown in Figure 5.65; similar trends held for both materials, all v_f's, stress amplitudes, and packing arrangements. From Figure 5.65 it was observed that the excitation frequency did have an effect on the maximum stress within the epoxy matrix, albeit a nearly negligible effect. The relationship between maximum stress and frequency was natural logarithmic in nature;

however, the increase in axial stress was only 0.00091% over the entire frequency range considered, for this particular example. For this heavily cross-linked high temperature epoxy, it appears that the excitation frequency has an almost negligible effect on the state of stress within the matrix material.

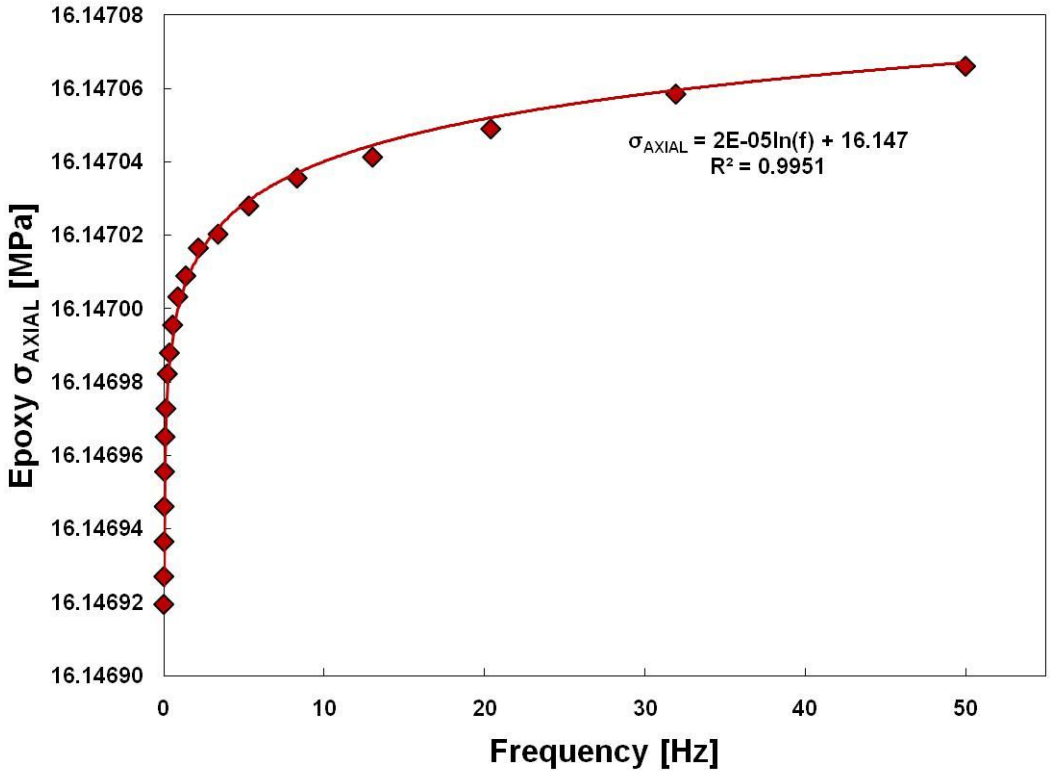

Figure 5.65 Maximum axial stress within the unaged epoxy matrix as a function of excitation frequency for the hexagonal packed GFC (v_f = 65%) subjected to the σ_3 stress amplitude.

The understanding of frequency dependency on fatigue life found in the literature (Kharrazi and Sarkani 2001) is supported by the present work. We conclude that the dependency of stiffness of the matrix material on frequency has minimal impact on the state of stress during cyclic loading. Rather, in looking at tan(δ) as a function of frequency for the unaged epoxy resin (as a representative example), an understanding of

the so-called "autogenous heating" effect can be gained (Figure 5.66). At lower frequencies, the matrix is highly "lossy," but cycles are not accumulated fast enough temporally to allow heat to build. At intermediate frequencies, the heat generated due to hysteretic losses causes a marginal increase in temperature, enabling stress to relax out of the matrix material, and promoting increased fatigue life. At higher frequencies, heat is generated faster than it can be dissipated to the surroundings allowing unstable heating and reduced fatigue life.

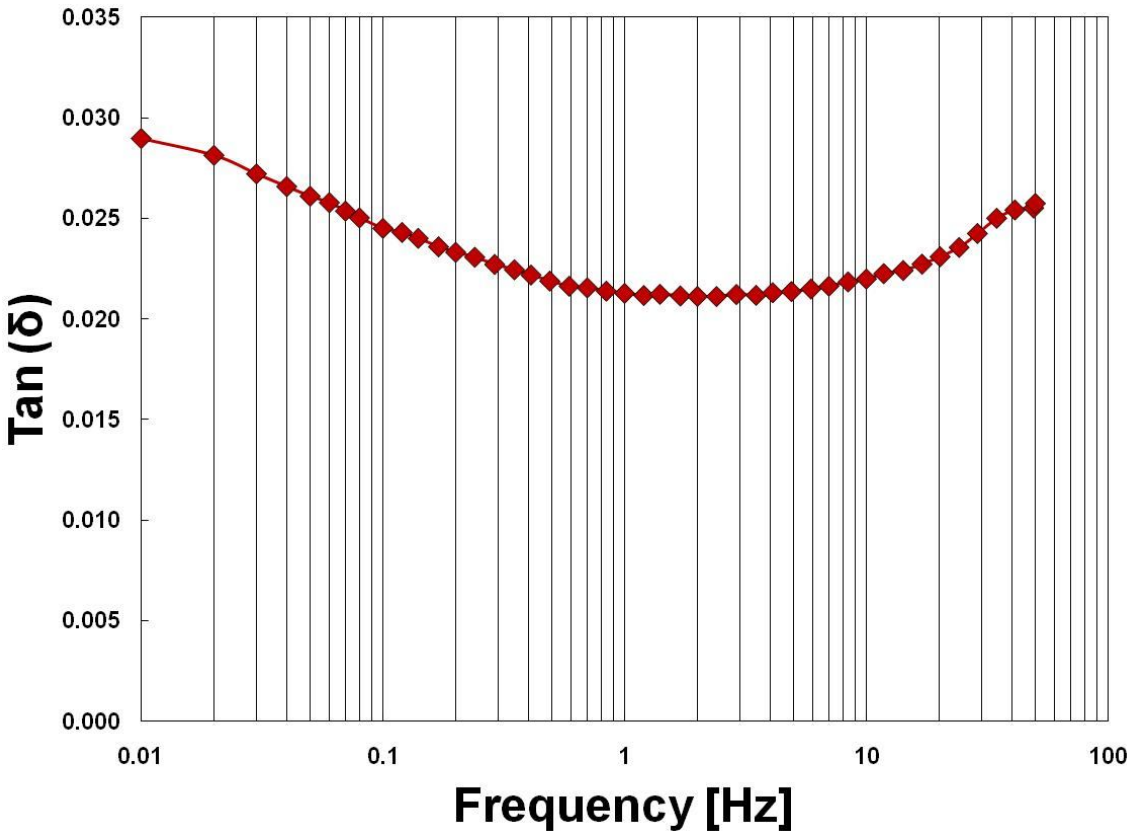

Figure 5.66 Tan(δ) as a function of frequency for the unaged neat resin epoxy specimen.

5.3 Summary of aged fatigue behavior

The effect of thermal aging on the flexural performance of a hybrid polymer matrix composite material was evaluated. It was found that exposure to 180 °C for 3 months resulted in improved fatigue performance of the composite, with mildly diminished static flexure strength. Aging for 6 months resulted in moderately degraded fatigue performance and a further reduction in flexure strength, while severely reduced performance (both static and fatigue) for 12 months aging time was found. The mild improvement in fatigue performance for 3 month aged specimens was attributed to post-cure of the epoxy resin and improved interfacial properties, while the diminished performance for the 6 month aged specimens was attributed to thermal oxidation. The drastic reduction in properties for the 12 month aging condition was primarily attributed to volumetric shrinkage. At 12 months aging time, it was found that volumetric relaxation had caused a significant amount of damage to both the GFC and the CFC, hindering load transfer between fibers. As a consequence, substantial reductions in flexure strength and an order of magnitude increase in the rate of Damage accumulation were observed, as well as severely reduced N_f at all stress amplitudes. Moreover, fatigue damage was observed in the CFC for the 12 month aging condition, whereas it had only occurred within the GFC for aging times up to 6 months.

The experimental observation with respect to the unique failure morphology of the fatigue specimens that had been aged up to 6 months time at 180 °C were explained through 3-Dimensional viscoelastic representative volume element models. Such models were to investigate the initiation of fatigue damage within the hybrid polymer matrix

composite material. From these analyses, it was explained why fatigue failure of the hybrid polymer matrix composite was restricted to the GFC for specimens aged up to 6 months. Even though the GFC was at a lower macro-axial stress than the CFC, the stress within the epoxy matrix was markedly higher and facilitated fatigue damage. The effect that thermal aging had on the predicted axial stress within the matrix from the RVEs was evaluated via DMA analysis of aged neat resin specimens. Axial stress within the epoxy positively correlated with aging time, to a degree explaining the experimental observations. The neat resin specimens of this study were fully cured, and thus did not capture the post cure effect found in the hybrid composite specimens at 3 months aging time. For both composite systems and equivalent v_f's, a hexagonal packing arrangement resulted in a reduced state of stress in comparison to a square fiber packing arrangement. In generalizing the results of this work to the body of knowledge on fatigue of polymer matrix composites, insight was gained into the reasons for superior fatigue performance of carbon fiber reinforced composites in comparison to glass fiber reinforced composites.

Finally, the isothermal aging behavior of the hybrid composite material was evaluated via length dilatometry. It was found that the volumetric relaxation of the material was well described by a stretched exponential function. Several isothermal temperatures were evaluated, enabling the use of an Arrhenius plot to determine the activation energy. Moreover, from the dilatometric measurements a means of measuring the glass transition temperature was shown based upon the phase transformation of the polymer which resulted in a conservative estimate of T_g. In light of the reduction in fatigue performance when exposed to elevated temperature for extended aging times, in conjunction with the

considerably greater dimensional stability of the hybrid composite system at lower temperatures, a re-evaluation of the maximum operating temperature of the next generation transmission line may be in order.

6. DAMAGE MECHANISM IDENTIFICATION

From the perspective of the experimental work of the previous 2 chapters, an ability to identify the particular damage mechanisms that were occurring to the hybrid composite material as a function of stress level, number of accumulated cycles, etc would be extremely valuable. Such a technique would ideally be non-destructive in nature, and would preferably be able to accomplish damage mechanism identification *in situ* without the necessity of removing the part from service. For this purpose, broadband acoustic emission monitoring was identified as an ideal candidate. Based upon the wave propagation modes excited by the particular failure mechanism that has occurred within the hybrid composite material, the frequency spectra of the broadband acoustic emission will be significantly affected, enabling damage mechanism identification.

Furthermore, the ability to identify which material the damage has occurred within is highly desirable, particularly in light of the fatigue failure morphologies shown in Chapters 4 and 5. The GFC is included in the hybrid composite core transmission line design primarily to prevent a galvanic couple between the CFC and the conducting aluminum strands. However, it was shown in Chapters 4 and 5, that the GFC is the material that accumulates the vast majority of damage during fully reversed fatigue loading. Given that aging time/temperature remained low enough, transverse crack growth through the GFC as a result of fatigue loading resulted in a direct electric path between the CFC and the conducting aluminum strands. Thus, it would be highly

advantageous to be able to identify when the GFC was sustaining damage to classify when further inspection, repair, or decommissioning would be necessary. In addition, the ability to recognize when the CFC was sustaining substantial damage is equally advantageous in identifying when the possibility of a catastrophic structural failure is imminent.

The ability to predict the resultant waveform from a given acoustic emission source has, until recently, been confined to simplistic geometries and/or exceedingly restrictive assumptions (e.g. – infinite media, etc.). Through the rapid improvements in personal computational capabilities, a few researchers have employed finite element techniques to determine the waveforms that result from various sources (see (Gary and Hamstad 1994), (Hamstand, O' Gallagher and Gary 1999), (Jong 2006), (Sause and Horn 2010)). The advantage of the finite element approach in modeling stress wave propagation is in its' ability to account for relatively complex part geometries, which inherently facilitate geometric spreading and boundary reflections. In this study, an explicit 3-Dimensional finite element model was developed to study the spectral content that resulted from the simulation of the most common forms of damage mechanisms that occur in unidirectional polymer matrix composite materials (i.e. – fiber fracture, matrix cracking, and fiber/matrix interfacial failure). From the finite element modeling, a classification scheme capable of differentiating between failure mechanisms, as well as which material the damage originated from was developed. The classification scheme was applied to experimental acoustic emission data from quasi-static flexure testing, confirming the effectiveness of the proposed model.

6.1 Methods

6.1.1 Numeric modeling

A 3-Dimensional numeric model was developed to simulate the most common types of damage mechanisms that occur in unidirectional polymer matrix composite materials (i.e. – matrix cracking, fiber/matrix debonding, and fiber fracture). Sause and Horn have shown the utility of 3-Dimensional finite element modeling of damage mechanisms in determining the associated wave modes that are excited for a plate-type unidirectional carbon fiber composite (Sause and Horn 2010). Through 3-dimensional finite element modeling, geometric reflections and dispersion are inherently taken into account for any arbitrary geometry. Based upon the frequency characteristics of the signal, which are a direct result of the wave modes excited, the particular damage mechanism may then be classified.

To characterize the acoustic emission spectral signatures for damage events within the hybrid composite rod of the present study, a Drake sized (9.50 mm outer diameter, 7.10 mm CFC diameter) composite was considered. The anisotropic material properties of both the GFC and the CFC were calculated via equation (2.34), assuming a volume fraction of fibers of 60%. The density of each material was determined from a rule of mixtures calculation, again assuming a volume fraction of fibers of 60% and no void content; densities of 1560 kg/m^3 for the CFC and 2039 kg/m^3 for the GFC were assigned. From symmetry considerations a 1/8 volume model was developed with the appropriate boundary conditions applied to the symmetry planes (Figure 6.1). The axial length of the rod was 127.0 mm.

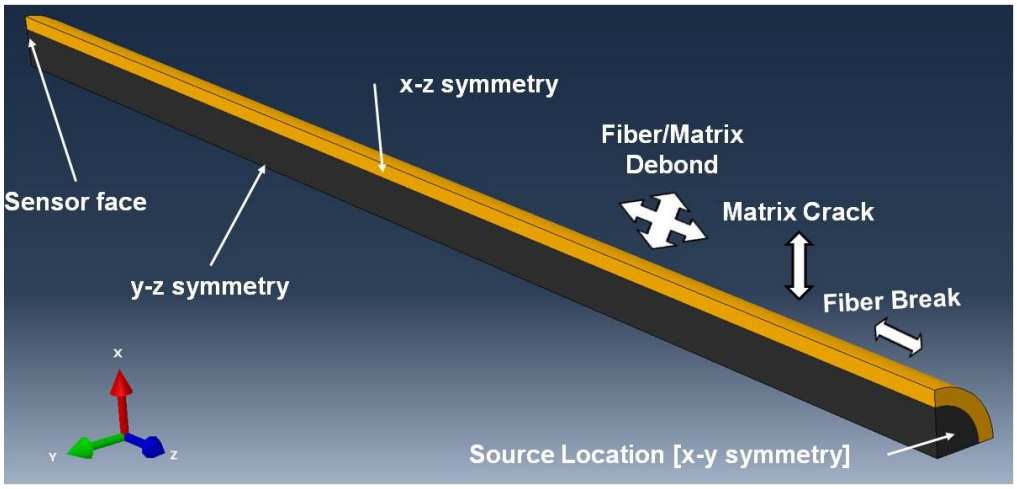

Figure 6.1 Schematic showing the finite element set-up, with the various simulated damage mechanisms.

Hamstad, O' Gallagher, and Gary initially showed that the depth at which a particular acoustic emission event occurs greatly affects the spectral content of the signal for a homogeneous and isotropic media (Hamstad, O' Gallagher and Gary 2002). For this reason, several depths of sources were considered. The origin of the coordinate system was placed at the center of the specimen, and sources were simulated in both the GFC and the CFC at various depths as shown in Figure 6.2.

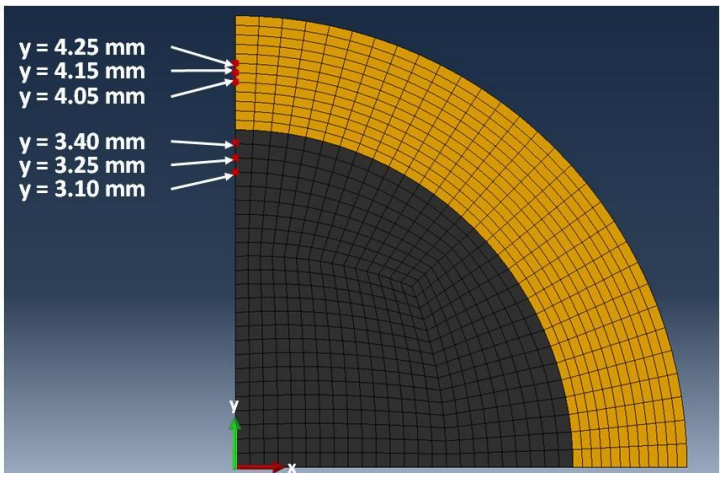

Figure 6.2 Transverse cross-section of the hybrid composite showing depth locations at which acoustic emission sources were modeled.

The entire mesh consisted of first order reduced integration hexahedral elements, with a nominal characteristic element length of 147 μm. The reduced integration element formulation was found preferable, as the elements were less stiff in bending, and thus did not absorb as much of the low frequency energy as was found to be the case with the fully integrated elements. Such a fine mesh resolution was found necessary in order for the solution to have converged. Axial velocities on the end opposite of the excitation location were sampled at 25.0 MHz.

To numerically simulate the physical sensor, axial wave velocities at nodal locations were sampled on the face of the CFC opposite of the excitation source (Figure 6.3). Axial nodal velocities (v_Z) were only taken from the CFC, as the diameter of the CFC closely approximated the diameter of the piezoelectric element of the transducer used in the present study. An average axial wave velocity (V_Z), most representative of what the AE transducer would sense, was calculated at each time step by numeric evaluation of the surface integral

$$V_Z(t) = \frac{1}{A_{SENSOR}} \iint v_Z(x, y, t)\,dx\,dy \qquad (6.1)$$

The use of an acoustic emission transducer with a piezoelectric element that has a diameter less than the diameter of the CFC was imperative in this study. Because of the reduced bandwidth of the GFC, if the acquired signal had contributions from the GFC, the frequency of the signal would have been "weighted down," potentially eliminating the ability to differentiate signals.

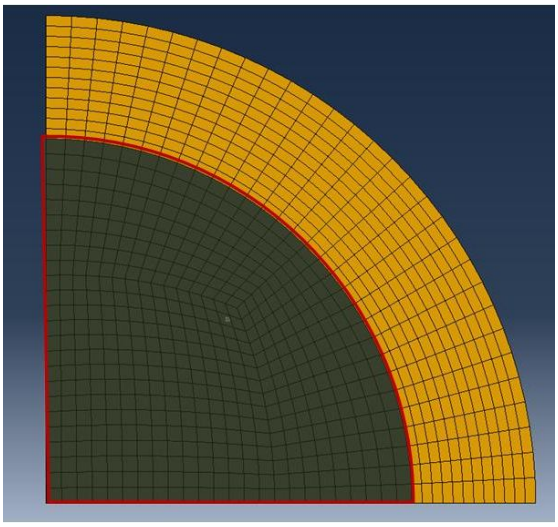

Figure 6.3 Schematic showing the sensor used to evaluate the aperture effect (outlined in red).

Analyses were allowed to run up to the point at which the first reflection off of the x-y symmetry plane boundary condition would have occurred assuming the ideal extensional wave velocity of the CFC; that is to say, analyses were allowed to run as if an ideal extensional wave were allowed to traverse the axial length 3 times in order to avoid false reflections. Experimentally, the test piece was considerably longer and reflections off of the axial faces did not occur during signal acquisition.

All numeric velocity signals were filtered with a fourth order Butterworth band pass filter, with the pass band between 80 and 1500 kHz. The high pass portion of the filter was higher than what is generally used experimentally, but was necessary for the numeric signals in order to compare them to the experimental signals. Experimentally, commercial broadband piezoelectric transducers (even high quality transducers) are not sensitive to frequencies below ~20 kHz, and their sensitivity is not flat below ~100 kHz. Thus, in order to be able to characterize the experimental signals from the numeric

calculations, a greater high pass filter was necessary. Sause and Horn have remarked on this necessity as well in their study of simulating acoustic emission signals in plate type unidirectional carbon fiber composites (Sause and Horn 2010).

Damage mechanisms were simulated by applying a concentrated force to a node, in order to simulate the desired damage mechanism. Forces were applied in directions, in which energy release would have occurred for a given damage mechanism, and are shown schematically in Figure 6.1. As an example, a fiber fracture in the unidirectional composite would have resulted in energy being released in the axial (z) direction. It should be pointed out that the in-plane direction of energy release used to simulate matrix cracking was arbitrarily chosen, and was only done so as to maintain consistency with the symmetry boundary condition being applied to the y-z symmetry plane.

The so-called sharp end function was used to prescribe the temporal shape of the acoustic emission source, and is given by

$$F(t) = \begin{cases} 0 & t < 0 \\ 1 - \dfrac{erf(t_2 - t_1)}{erf(t_2)} & 0 \le t \le \tau \\ 1 & t > \tau \end{cases} \tag{6.2}$$

where t_1 and t_2 are defined as

$$\begin{aligned} t_1 &= t\sqrt{a} \\ t_2 &= \tau\sqrt{a} \\ a &= -\frac{\ln(0.5)}{\left(\frac{3\tau}{8}\right)^2} \end{aligned} \tag{6.3}$$

in which τ is the rise time of the source (Hamstad 2011). For all analyses in which the rise time of the source was not a variable under study, a rise time of 300 ns was used. To

investigate the effect that duration of the rise time had, rise times of 50 ns, and 500 ns were also considered. A normalized sharp end function is shown in Figure 6.4.

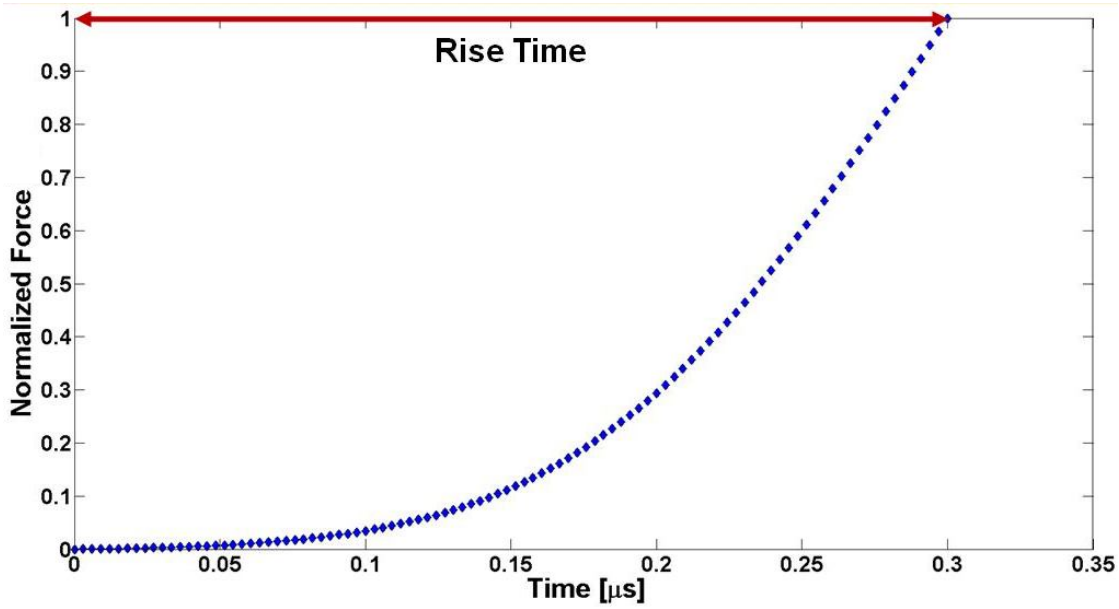

Figure 6.4 Normalized source function, having a sharp end temporal shape.

All analyses were performed in Abaqus 6.9.2 using an explicit time integration formulation. It was believed that the explicit formulation would be considerably more computationally efficient than an implicit formulation. The explicit formulation operates with a lumped mass matrix (as opposed to a consistent mass matrix), and thus does not require the construction, and subsequent solution of a tangent stiffness matrix within the discritized dynamic equilibrium equations. With an implicit formulation, as the problem size increases, i.e. – the degrees of freedom within the problem increases, having to solve the increasingly large system of linear equations results in reduced computational efficiency, as well as the need for considerable computational facilities (physical memory) for intermediate data storage. However, in the explicit formulation, the solution

of the element acceleration vector is trivial, increasing the computational efficiency of the method for large problems, while also reducing the necessary physical memory. A representative case was considered to compare the computational efficiency of the explicit formulation to that of the implicit formulation.

6.1.2 Experimental acoustic emission signal acquisition

Experimental acoustic emission signals were obtained during the quasi-static four point flexure testing of the aged hybrid composite specimens of section 5.2.3. Broadband acoustic waveforms were recorded for two specimens at each aging condition (except in the case of the 9 months aging condition, as there were an insufficient number of specimens). The center-center pin dimensions of the 4 point loading fixture are shown schematically in Figure 6.5, and result in what is commonly referred to as a "quarter point set-up." Test specimens were cut to a length of 279.4 mm, allowing for adequate overhang past the outer loading pins to couple the acoustic emission transducers to the specimens using custom holding cases as shown in Figure 6.6.

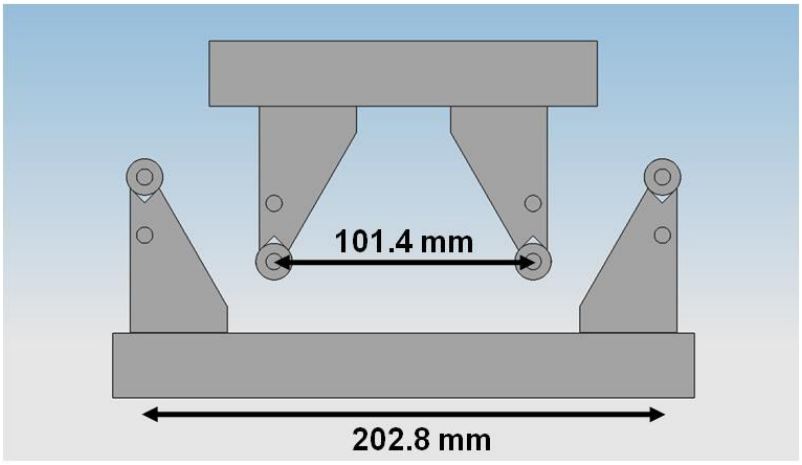

Figure 6.5 Schematic and pertinent dimensions for signal propagation of the 4 point bend fixture.

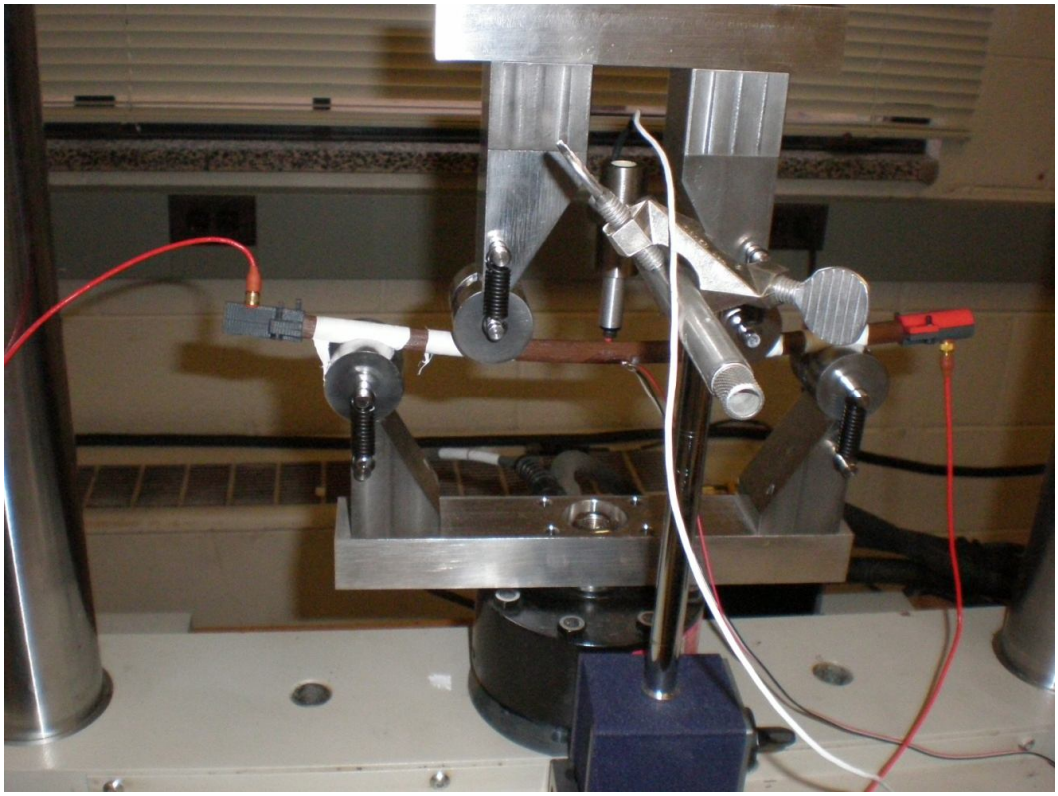

Figure 6.6 4 point loading configuration with a specimen under test, and acoustic emission transducers coupled to the axial faces of both ends of the hybrid composite rod.

Digital Wave Corporations B-1025 wideband transducers were used for signal acquisition. Signals from the transducers were fed into PA2040G/A preamplifiers, and waveforms were captured with a 2 channel FTM4000 signal acquisition unit that fed into a personal computer. Pre-trigger, signal, and acquisition parameters are summarized in Table 6.1. Acoustic emissions from the specimen under test were transmitted to the sensor through the use of vacuum grease.

Table 6.1 Summary of acquisition parameters

Parameter	Pre-trigger	AE Signal	Signal Acquisition
Threshold [mV]	100	N/A	100
Gain [dB]	42	36	N/A
High Pass Filter [kHz]	20	20	20
Low Pass Filter [kHz]	4000	4000	1500

Signals were acquired at a sampling rate of 25 MHz; a total of 2048 data points were acquired, with 256 pre-trigger points also being acquired to allow for a "clean front end" of the waveform. Tests were run to 80% of the mean flexure load at failure for the 3 specimens of the respective aging condition previously tested, as to avoid damaging transducers. At 80% of the mean load at failure, loading was paused for 60 seconds while the transducers were removed, and then loading re-commenced to failure.

Post-test, signals were processed in 2 different ways. The first processing method resulted in only signals which occurred within the inner span. These signals were identified by evaluating the difference in time (Δt) between distinguishable features on the extensional portion of the wave for both channels. Based upon the measured wave velocity of 7.32 mm/μs, and the inner span distance of 101.4 mm, the Δt had to be less than or equal to 13.9 μs for the event to be considered as having occurred within the gage. The second processing method accepted all signals which could be identified as having occurred between the outer spans (i.e. $-\ \Delta t \leq 27.7$ μs). All experimental signals were passed through a 4^{th} order Butterworth band pass filter, with the pass band between 20 and 1500 kHz.

From a deformation and damage accumulation perspective, the two sets of signals should have contained substantially different information. For a 4 point loading configuration, the portion of the composite between the inner span is subjected to a uniform (and maximum) bending moment with no shear. The portions of the composite between the outer load pins and the inner load pins are subjected to a constant shear loading, with the applied moment linearly increasing from 0 to the maximum applied moment between the outer and inner load pins. Hence a far greater number of matrix cracking and fiber/matrix debonding signals would be expected from the second set of signals. Furthermore, it was hoped that insight into the aging process could be gained by identifying the various damage mechanisms and the composite material from which the events were occurring.

6.2 Results and Discussion

6.2.1 Numeric Results and Discussion

The origin of an acoustic emission signal is associated with a local release of energy. From the perspective of the newly formed crack surface, one would expect the crack surface to be displaced a given amount δ, and after initial release of the energy the displacement of the newly formed crack surfaces would vibrate until the stiffness of the surrounding material had damped out the oscillatory component of displacement. In the finite element modeling of acoustic emission sources, there are two approaches that may then be taken. Sause and Horn elected to prescribe displacements of the crack surface, and then allow decay of displacements of the crack surface (Sause and Horn 2010). Alternatively, as was the approach of this work, one may prescribe a force at the crack surface related to the expected energy release of the deformation mechanism. If the displacements at the crack surface are then monitored, it can be shown that the methods are equivalent to one another. As evidence of this, representative cases for both composite materials and all 3 damage mechanisms that have occurred at depths of y = 4.15 mm, and 3.25 mm are presented. Defining the magnitude quantity of total displacement as

$$u_r = \sqrt{u_x^2 + u_y^2 + u_z^2}. \tag{6.4}$$

Figure 6.7 presents u_r as a function of time for all 3 damage mechanisms occurring at a depth of y = 4.15 mm (GFC), while Figure 6.8 presents the same plot for events occurring at a depth of y = 3.25 mm (CFC).

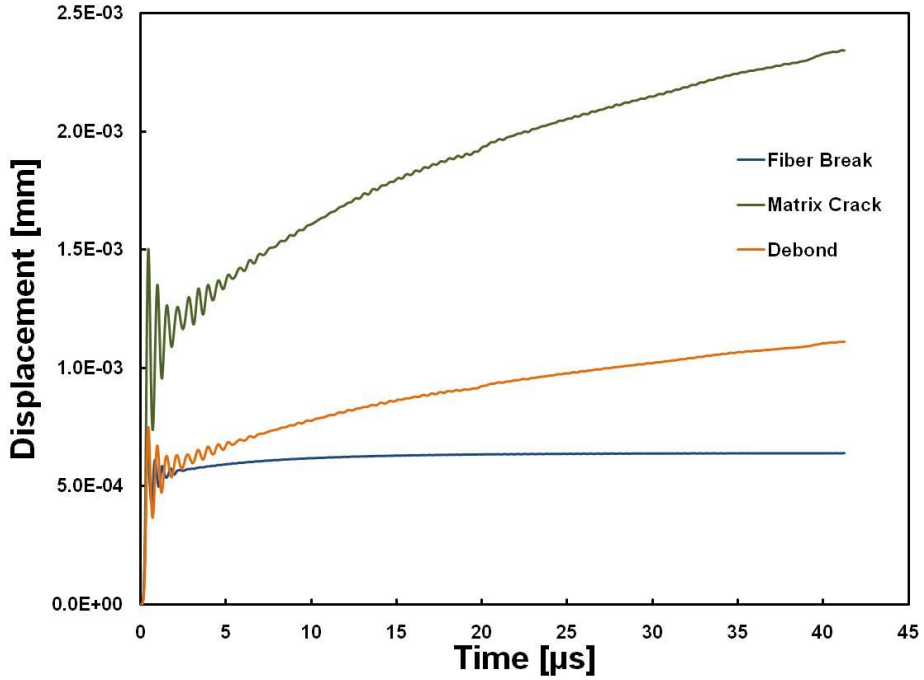

Figure 6.7 Displacement magnitude (u_r) of the crack surface for events occurring at a depth of y = 4.15 mm (GFC).

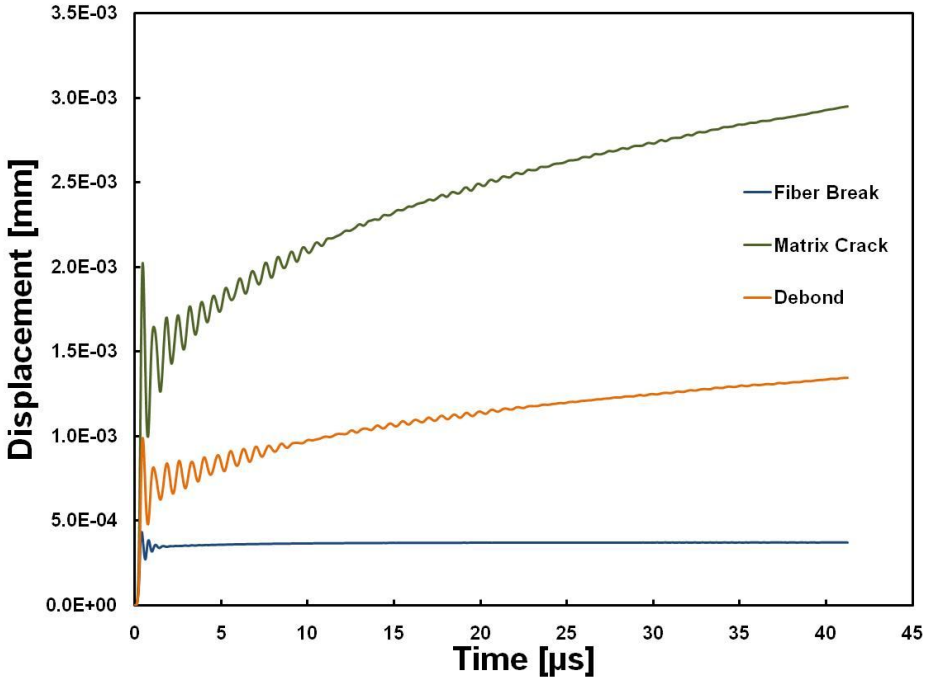

Figure 6.8 Displacement magnitude (u_r) of the crack surface for events occurring at a depth of y = 3.25 mm (CFC).

For both materials, the behavior of the crack surface was quite similar in that after initial excitation, initial oscillations of the crack surface occurred while decaying out and tending towards the final value of displacement for the crack surface. As both composites are substantially stiffer in the axial directions than in the transverse directions the crack surface was able to obtain equilibrium considerably faster for fiber fractures as compared to fiber/matrix debonding, and matrix cracking events. In addition, since the GFC is stiffer in the transverse direction, the crack surface vibrations were found to decay out moderately quicker when compared to that of the CFC for matrix cracking and debonding events.

Figure 6.9 provides the spectra for fiber fracture events that occurred at various depths, while Figure 6.10 and Figure 6.11 show the analogous plots for matrix cracking and fiber/matrix debonding events, respectively. As previously mentioned, a dominant amount of energy was found to occur between 100 and 300 kHz for all simulated deformation mechanisms. Moreover, signal differentiation (i.e. – what type of deformation mechanism occurred, and which material it occurred in) could be achieved by evaluating where respective portions of energy within the spectra were located.

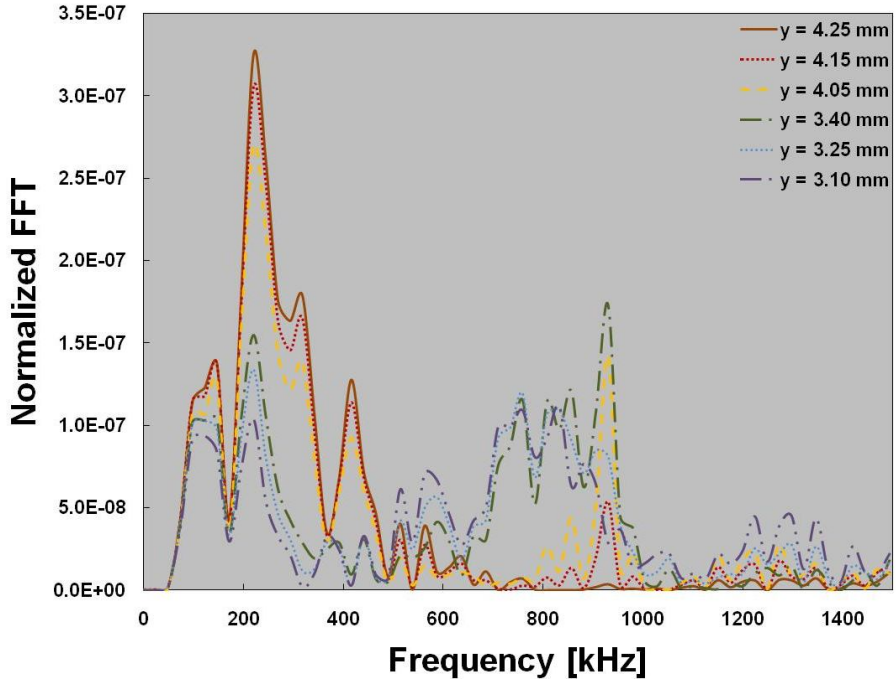

Figure 6.9 Spectra for a fiber fracture event that occurred at various depths with a propagation distance of 127.0 mm, and a source rise time of 300 ns.

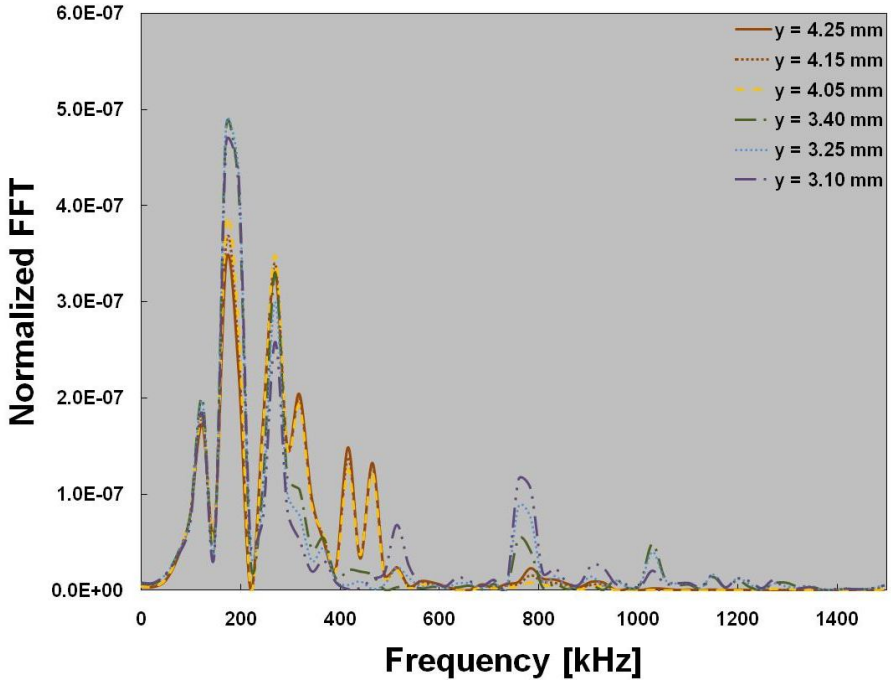

Figure 6.10 Spectra for a matrix cracking event that occurred at various depths with a propagation distance of 127.0 mm, and a source rise time of 300 ns.

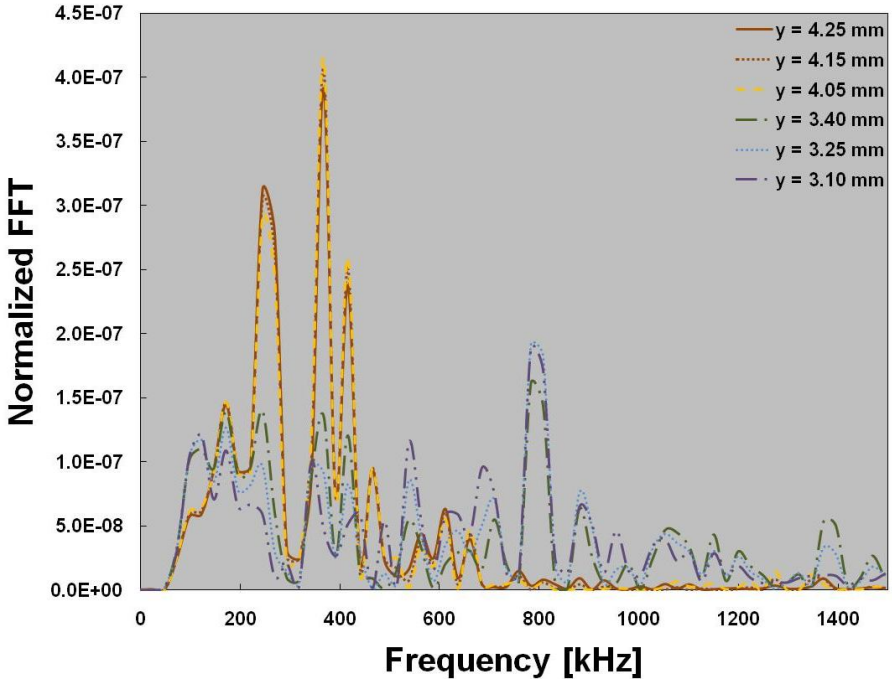

Figure 6.11 Spectra for a fiber/matrix debonding event that occurred at various depths with a propagation distance of 127.0 mm, and a source rise time of 300 ns.

A few studies have used particular frequency contributions of acoustic emission signals in the attempt of differentiating between various damage mechanisms in composite materials, with varying levels of success. De Groot, Winjen, and Janssen used various coupon geometries, in an attempt to assign particular frequency ranges to specific deformation mechanisms (de Groot, Wijnen and Janssen 1995). In their study, the assumption must be made that particular specimen geometries will only exhibit a particular deformation mechanism. For example, in that work, it was postulated that unidirectional specimens tensile tested in a 90° orientation will primarily exhibit matrix cracking. However, no mention with respect to fiber/matrix debonding is given, which would certainly also be anticipated from such a test geometry. Moreover, no rational

with respect to the fundamental nature as to why a given failure mechanism should result in particular frequencies being excited is provided.

Jong used information about the symmetry (or anti-symmetry, as the case had it) and attenuation characteristics of acquired acoustic emission signals to investigate transverse matrix cracking of unidirectional carbon fiber/epoxy composites, as well as hybrid carbon and glass fiber/epoxy matrix composites (carbon fibers were oriented in a 0° direction, while the glass fibers were oriented in the 90° direction) (Jong 2006). In addition, Jong used 2-Dimensional finite element modeling in an attempt to provide a fundamental explanation with respect to the frequencies excited by specific deformation mechanisms. Because of the 2-Dimensional nature of his models, boundary reflections were not able to be accounted for, potentially limiting the utility of the method. In addition, others have observed that the depth at which a source occurs has a pronounced effect upon the wave modes excited, a variable not addressed in Jong's work.

Sause and Horn developed a 3-Dimensional finite element model to study the spectral content of the dynamic stress waves that propagated in a unidirectional carbon fiber/epoxy matrix composite material as a result of the occurrence of the most common deformation mechanisms (Sause and Horn 2010). Because of the 3-Dimensional nature of the model, boundary reflections and geometric spreading of the wave were inherently accounted for. In addition, the geometry of the acoustic emission transducer was accounted for in their work. From their study, they concluded that the respective wave modes excited by a particular simulated deformation mechanism could be applied to experimental signal classification. Application of their method to several coupon

geometries resulted in outstanding agreement between simulation and experiment, providing AE users with a signal classification scheme for plate type geometries which originated from a fundamental basis (Sause and Horn 2010).

Examination of the spectra shown in Figure 6.9 through Figure 6.11 lend optimism to the idea that information about specific spectral energy could allow differentiation between deformation mechanisms, as well as which material the event occurred in. To realize the technique, the concept of partial power (PP) was used, and is defined as

$$PP_i = \frac{\int_{f_1}^{f_2} U^2(f)df}{\int_{0kHz}^{1500\,kHz} U^2(f)df} \tag{6.5}$$

where $U^2(f)$ is the magnitude of the Fourier transform of the signal U(t), and f_1 and f_2 take on various values dependent upon the i^{th} partial power being investigated. For this hybrid composite and geometry, 3 Partial Powers were defined with frequency ranges as defined in Table 6.2. Integration of the numerator and denominator of equation (6.5) are evaluated numerically.

Table 6.2 Definition of frequency bounds for PP1-PP3.

Partial Power	f_1 [kHz]	f_2 [kHz]
PP_1 [%]	0	200
PP_2 [%]	300	500
PP_3 [%]	700	1500

Figures 6.12 through 6.14 show plots of PP_1 vs. PP_2, PP_1 vs. PP_3, and PP_2 vs. PP_3, respectively. From the plots, well defined clustering of different deformation mechanisms is clearly observed for a majority of deformation cases. However, in all 3 cases differentiation between 2 deformation mechanisms appears improbable.

Fortunately, the ambiguous deformation mechanisms are different in the different Partial Power spaces, implying that in a 3 space, the deformation mechanisms should be clearly identifiable.

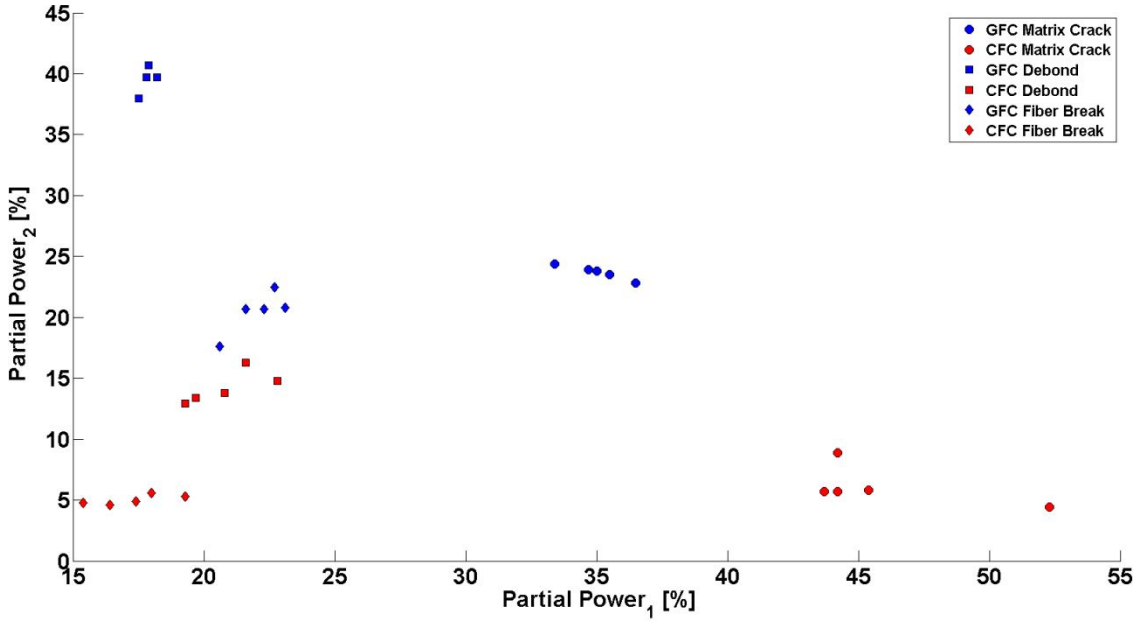

Figure 6.12 Partial Power$_1$ vs. Partial Power$_2$ for all simulated deformation mechanisms.

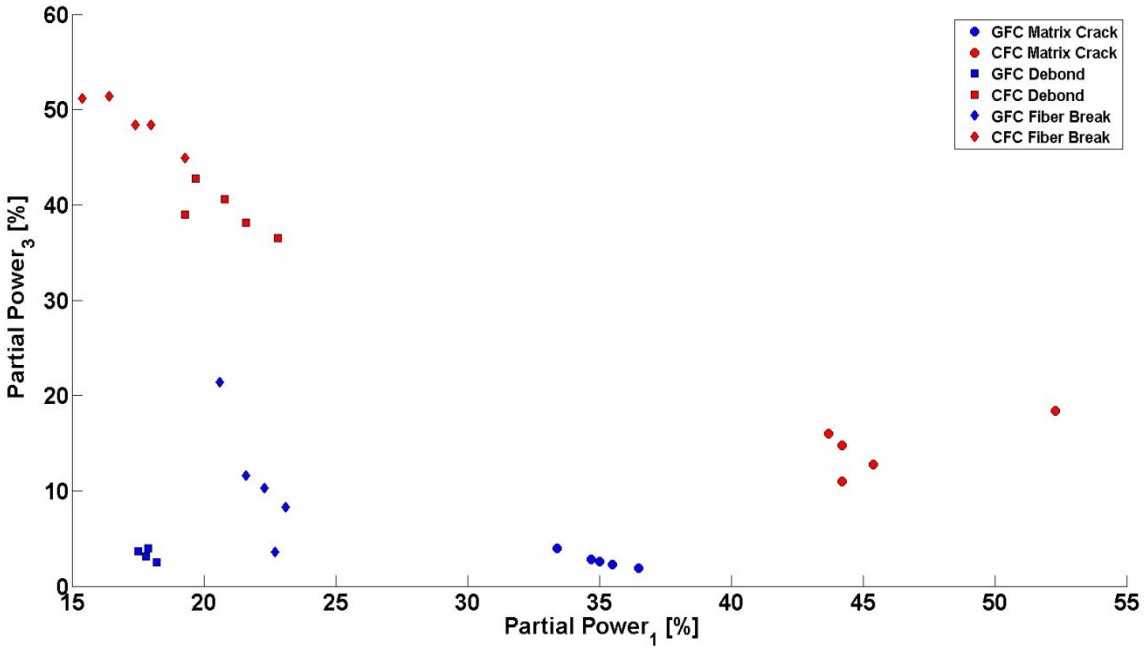

Figure 6.13 Partial Power$_1$ vs. Partial Power$_3$ for all simulated deformation mechanisms.

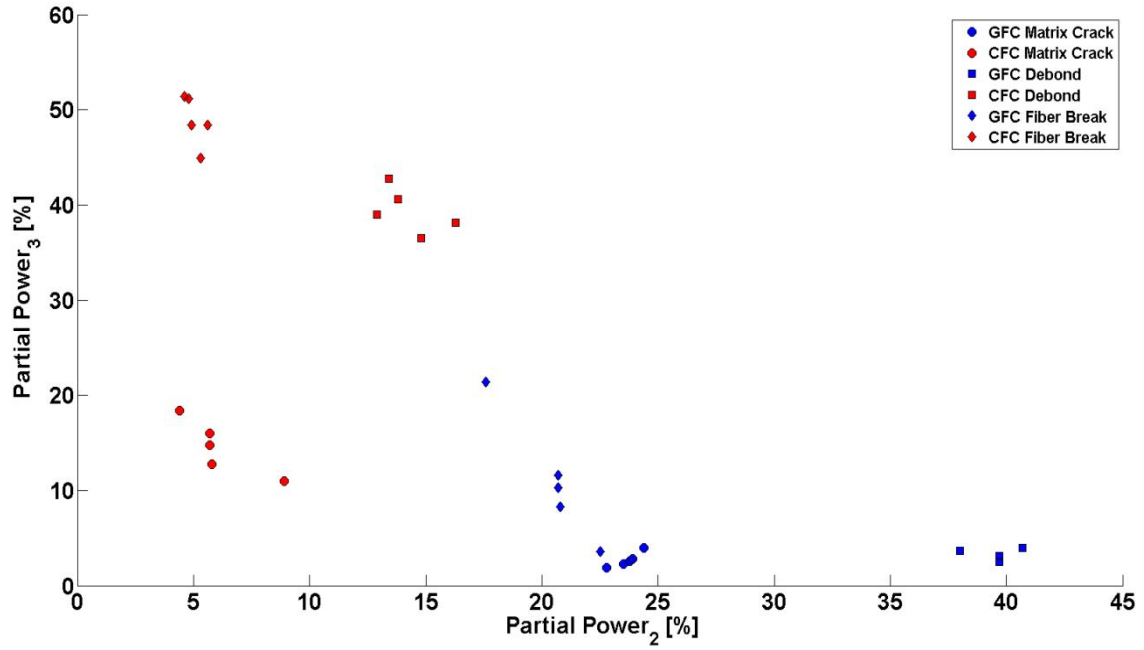

Figure 6.14 Partial Power$_2$ vs. Partial Power$_3$ for all simulated deformation mechanisms.

Figure 6.15 shows all simulated signals from the parametric depth study plotted with their respective partial powers (1-3) oriented in an orthogonal manner, from which it was clear that signals from different damage mechanisms and materials of origin clustered together, in this particular 3-Dimensioned Partial Power space. By assigning appropriate portions of the Partial Power space clear differentiation between deformation mechanisms, as well as which material the event occurred in could be achieved. Such analysis of experimental signals could then lend insight into the state of damage within the hybrid composite as a function of loading.

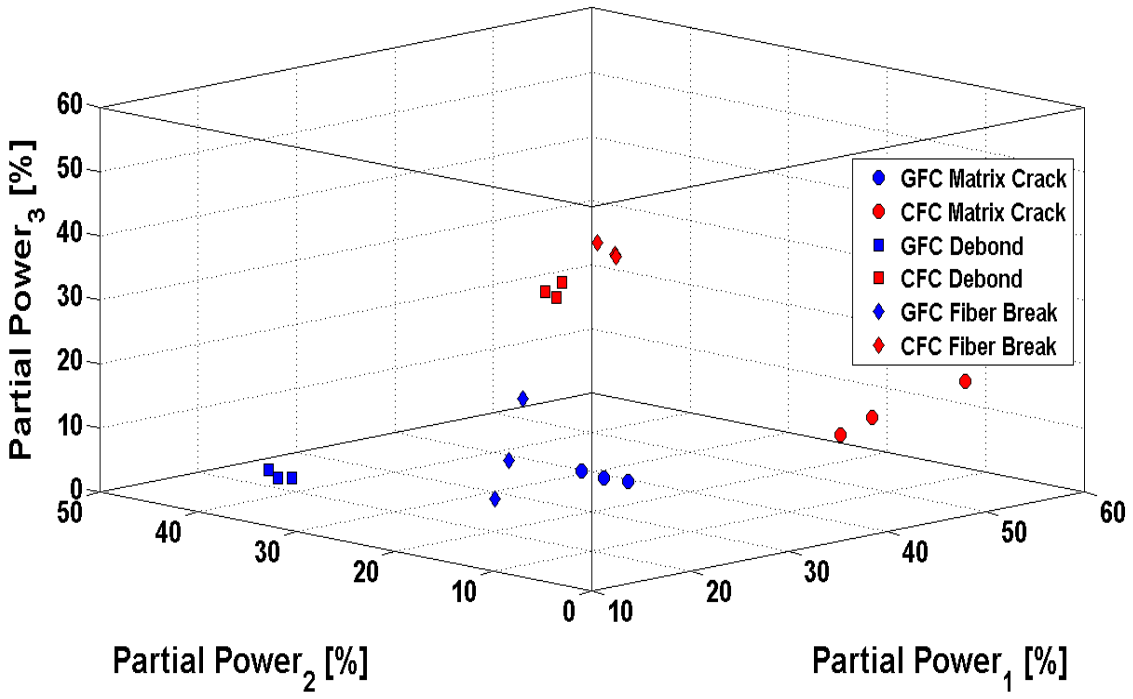

Figure 6.15 Plot of partial power values for all simulated signals, which had variable depths, a propagation distance of 127.0 mm, and a source rise time of 300 ns.

To evaluate the effect that source rise time had on the spectral content of the simulated deformation mechanisms, source rise times of 50 ns, 300 ns, and 500 ns were investigated for depths of y = 4.15 mm (GFC), and y = 3.25 mm (CFC). Figure 6.16

through Figure 6.18 show the effect of the considered source rise times on spectral content for fiber fracture, matrix cracking events, and fiber/matrix debonding events, respectively. It was found that shorter rise times tended to accentuate the higher frequency content of the signal. Conversely, longer simulated rise times exhibited diminished high frequency characteristics, but emphasized low frequency contributions of the signal. With respect to characterization of the experimental signals, it is expected that actual source rise times will be variable (and deformation mechanism specific), and that the effect will cause mild spreading in the Partial Power space, but will have a largely minimal impact on signal classification.

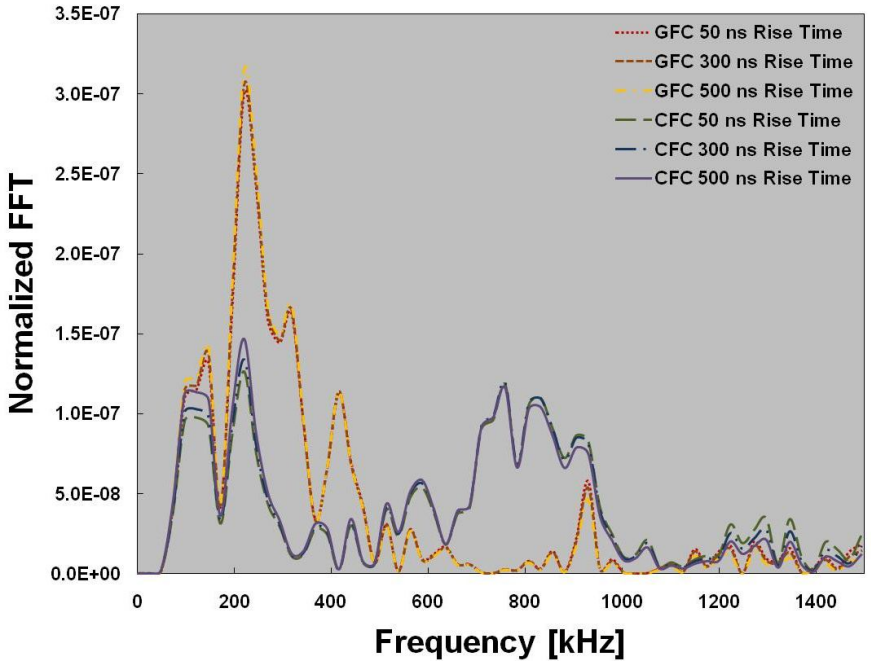

Figure 6.16 Effect of source rise time on the spectral content of simulated fiber fracture events which occurred at a depth of y = 4.15 mm (GFC) and y = 3.25 mm (CFC), with a propagation distance of L = 127.0 mm.

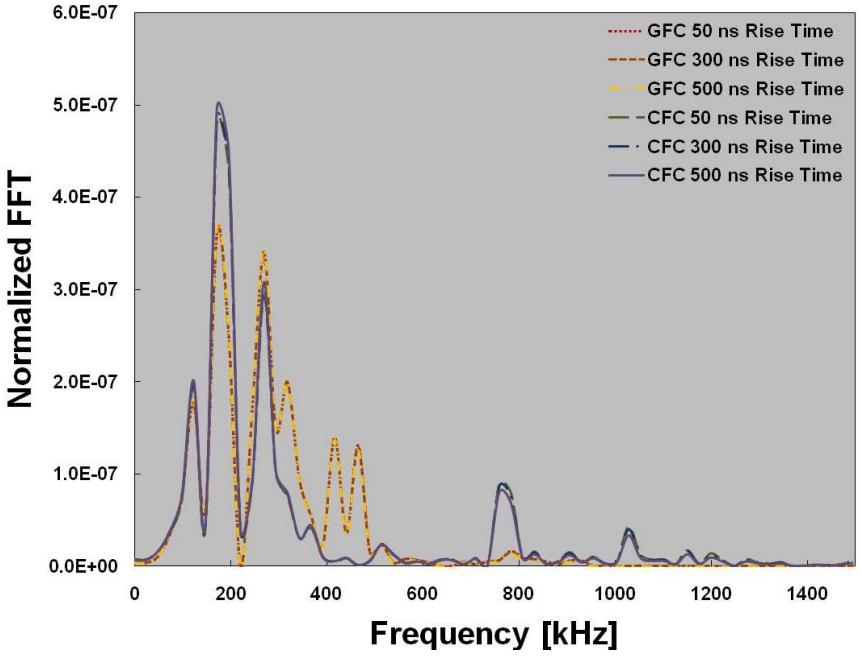

Figure 6.17 Effect of source rise time on the spectral content of simulated matrix cracking events which occurred at a depth of y = 4.15 mm (GFC) and y = 3.25 mm (CFC), with a propagation distance of L = 127.0 mm.

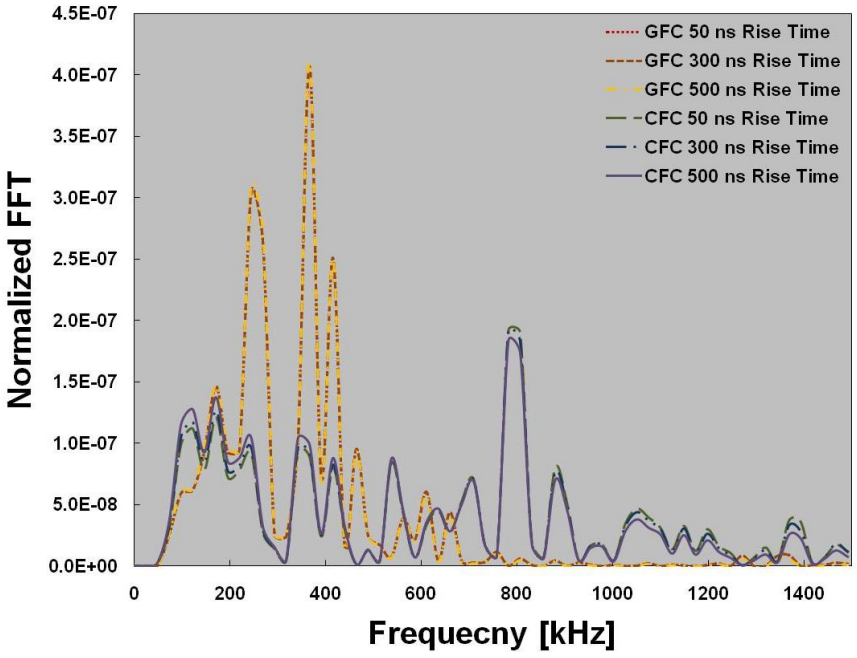

Figure 6.18 Effect of source rise time on the spectral content of simulated fiber/matrix debonding events which occurred at a depth of y = 4.15 mm (GFC) and y = 3.25 mm (CFC), with a propagation distance of L = 127.0 mm.

By incorporating the additional signals from the rise time parametric study to the plot of partial powers (Figure 6.15), a clearer picture of the signal identification regions could be assigned, (Figure 6.19). Thus, from the simulation of acoustic emission events of this section, a signal classification scheme for experimental waveforms is proposed and summarized in Table 6.3.

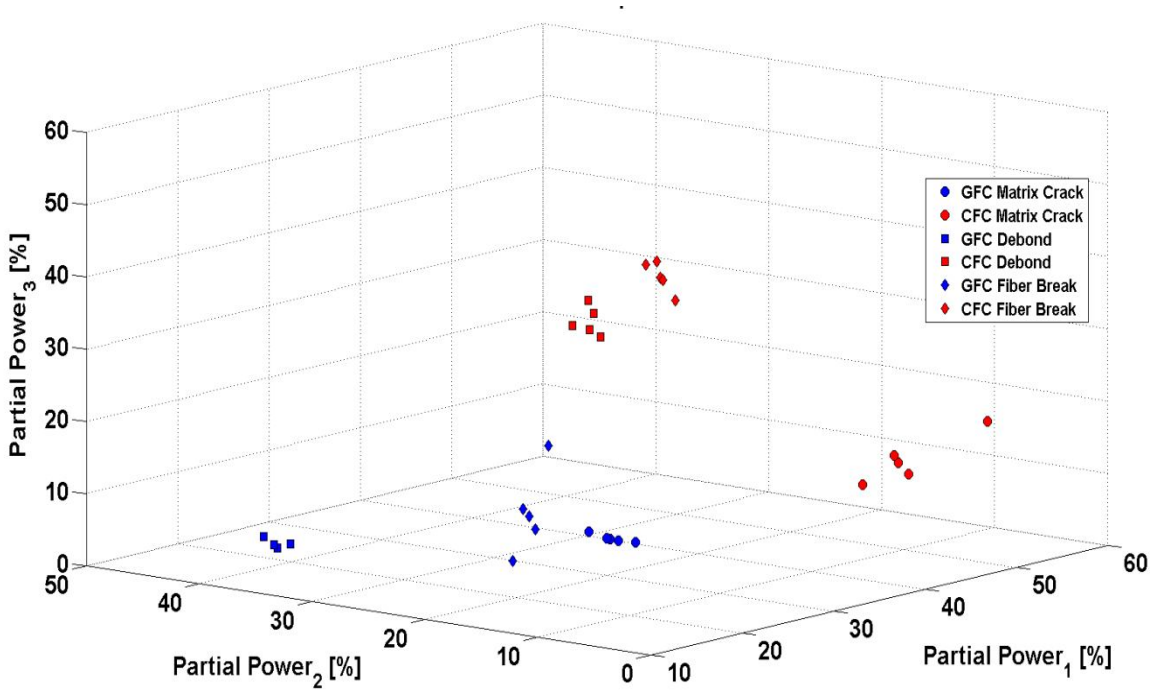

Figure 6.19 Plot of partial power values for all depth and rise time parametric study simulated signals.

Table 6.3 Spectral characteristics of simulated deformation mechanisms.

Deformation Mechanism	Spectral Characteristics
CFC fiber fracture	Moderate PP_1 Minimal PP_2 Strong PP_3
CFC matrix cracking	Strong PP_1 Minimal to Moderate PP_2 Minimal to Moderate PP_3
CFC fiber/matrix debonding	Minimal to Moderate PP_1 Moderate PP_2 Moderate to Strong PP_3
GFC fiber fracture	Minimal to moderate PP_1 Moderate PP_2 Moderate PP_3
GFC matrix cracking	Minimal to Moderate PP_1 Minimal to Moderate PP_2 Minimal PP_3
GFC fiber/matrix debonding	Minimal to Moderate PP_1 Strong PP_2 Minimal PP_3

To validate that the explicit time integration scheme was far more computationally efficient than the implicit integration scheme, a coarse mesh model was considered. The coarse mesh was considered in order to accommodate reasonable run times for the implicit analysis. A mesh (consisting of a total of 97,632 degrees of freedom) was used to simulate a fiber fracture which occurred at a depth of y = 4.15 mm (simulation of a glass fiber fracture); the exact same analysis was run in parallel using the explicit and implicit integration scheme on an 8 processor Linux workstation which has a total of 20 GB of physical memory. To allow for a stable solution, the time step in the explicit integration scheme was limited to 4.0E-9 seconds, while the maximum time step (allowing for a sampling rate of 25 MHz) of 4.0E-8 seconds was used for the implicit analysis. The explicit analysis completed in 2.85 seconds of total CPU time, while the

implicit analysis took 5,689.1 seconds of total CPU time. The solutions for both analyses were identical when comparing the axial velocity of the sensor face, however, the solution was incorrect as too coarse of a mesh was considered.

As was previously mentioned, the coarse mesh was considered to allow for reasonable computational times of the implicit model. Using the explicit formulation, analyses using the converged mesh (which had a total of 2,337,339 degrees of freedom) completed in ~38 minutes, while initial execution of the implicit analysis using the converged mesh resulted in an estimated 3.7 days to complete. These observations highlight the fact that, in general, for larger models explicit analyses execute in a far more computationally efficient manner (Abaqus 2009).

6.2.2 Experimental results, waveform classification, and discussion

From a parametric AE perspective, conclusions with respect to the effect of prolonged elevated temperature exposure could be drawn. Representative cumulative events versus load curves for specimens aged in air for 3, 6, and 12 months at 180 °C are shown in Figure 6.20. In agreement with the observations of section 5.2.3 that increased aging time resulted in diminished strength, it was found that the onset of significant acoustic emission (i.e. – the "knee" in the cumulative events vs. load curve) also decreased with increased aging time. Hence, at longer aging times, specimens began accumulating substantial damage at lower load levels.

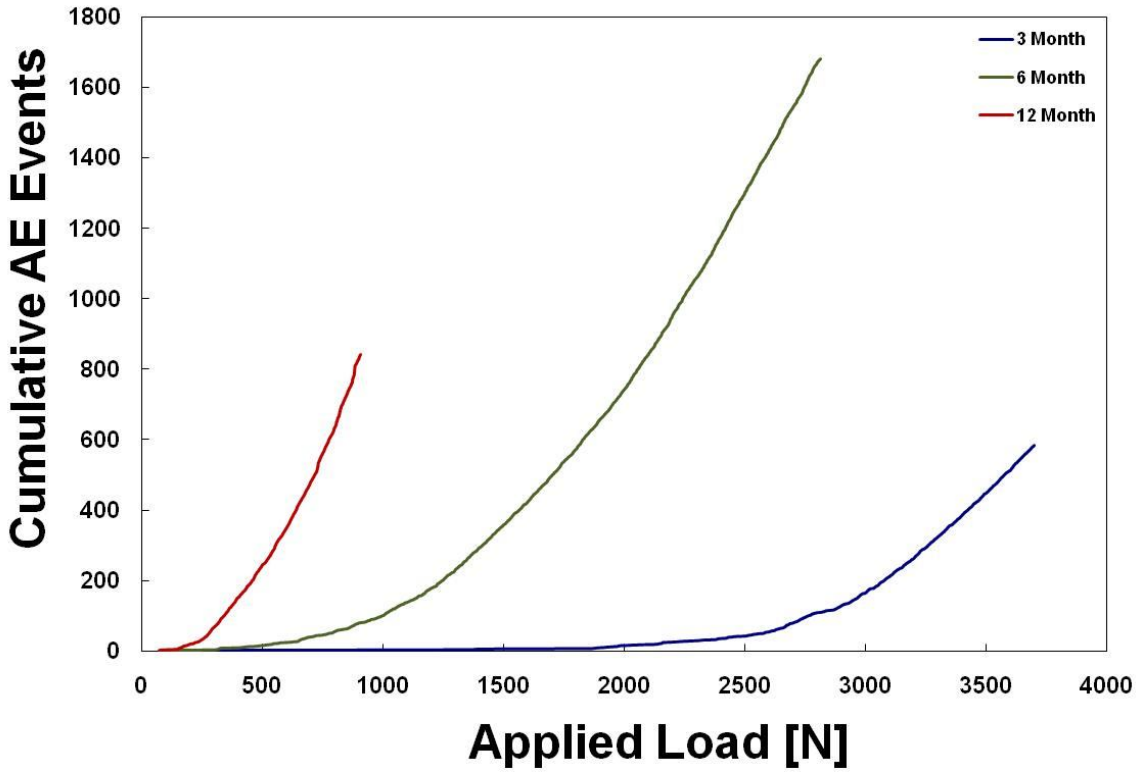

Figure 6.20 Representative cumulative events vs. load curves in flexure loading for aged specimens.

To validate the deformation mechanism classification scheme proposed in section 6.2.1, waveforms were recorded during flexure loading of select aged specimens from the work presented in section 5.2.3. Post-processing of these waveforms was described in section 6.2.1, in which the respective partial powers of each event were calculated. Figure 6.21 through Figure 6.23 present the Partial Power space plots for specimens aged for 3, 6, and 12 months, in which only events that occurred within the inner span were accepted.

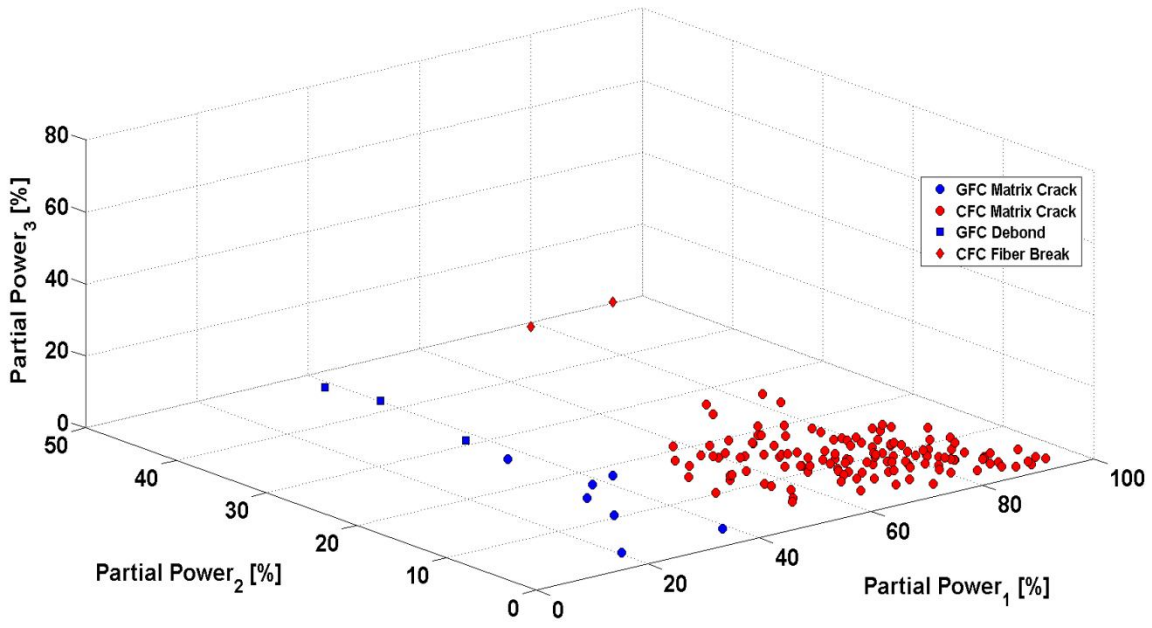

Figure 6.21 Partial Power space plot for a 3 month aged specimen during flexure loading, in which only gage events were accepted.

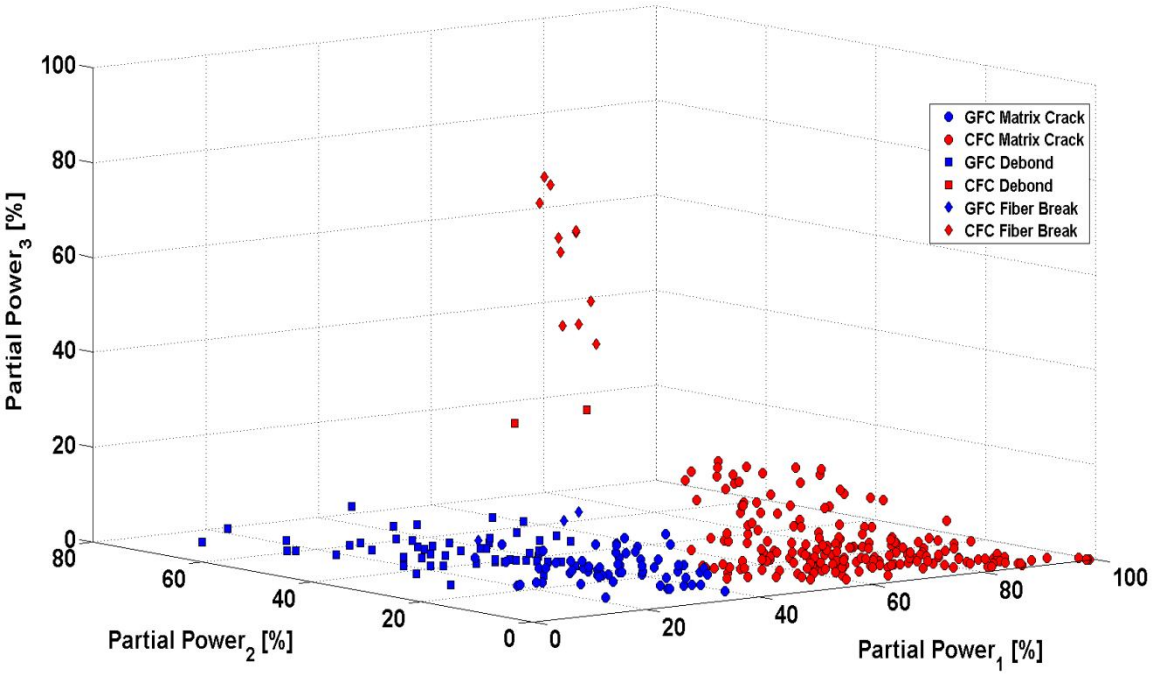

Figure 6.22 Partial Power space plot for a 6 month aged specimen during flexure loading, in which only gage events were accepted.

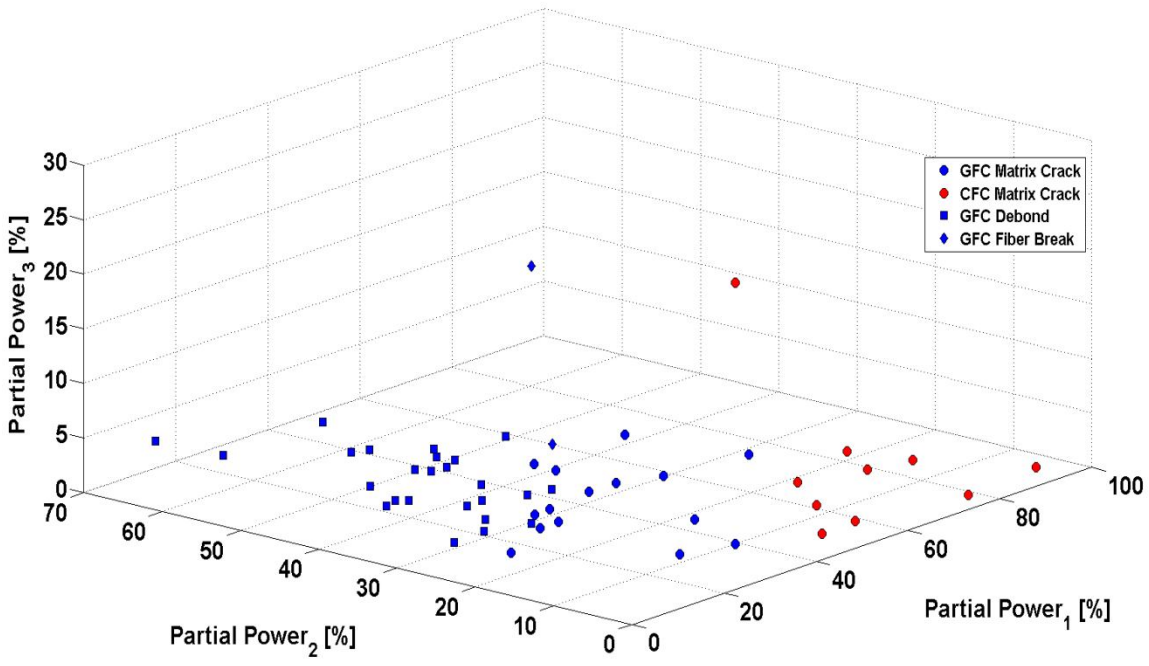

Figure 6.23 Partial Power space plot for a 12 month aged specimen during flexure loading, in which only gage events were accepted.

From Figure 6.21 through Figure 6.23 it is clear that the classification scheme is quite effective in distinguishing between the respective deformation mechanisms, as well as the material of origin. Moreover, the most frequently occurring deformation mechanism for the 3 month aging condition was CFC matrix cracking. At 3 months aging time neither chemical, nor physical aging had occurred to a substantial extent. However, upon removing specimens from the aging oven, a greater amount of residual stress is expected to be imparted into the matrix material of the CFC due the greater mismatch in thermal expansion coefficients between the fiber and matrix material, when compared to the GFC. Additionally, the CFC is under a considerably higher state of stress than is the GFC during flexure loading, resulting in a greater probability of matrix cracking events occurring.

Interestingly, a shift in the proportionality of event occurrence was observed between the 3 months aging time, and aging times greater than that. After 3 months aging time, thermal oxidation had deteriorated the surface of the GFC to a far greater extent, creating a far greater number of sites for matrix cracking and fiber matrix/debonding events to occur. At that point matrix cracking and fiber/matrix debonding of the GFC and matrix cracking of the CFC were virtually equally observed deformation mechanisms. This observation supports the findings from sections 5.2.3 and 4, and highlights the fact that the matrix material of the GFC was the most degraded material at extended aging times, and was therefore the most susceptible to damage.

In addition, recall that the transducers were removed at 80% of the mean load at failure as to avoid damaging the acoustic emission transducers, explaining the comparative absence of fiber fracture events. Substantial and localized fiber fracture events were only expected nearing ultimate failure loads (Scott, et al. 2011). Moreover, the fewer number of events for the 12 month aged specimens should not be interpreted as an indictment of lack of damage occurring. Rather, it must be recognized that failure loads for the 12 month aged specimens were drastically reduced, causing the reduced number of events, especially in fiber fracture occurrences because loads did not become substantial enough to facilitate fiber fracture.

As an alternative means of analyzing the acoustic waveforms emanating during 4 point flexure loading, events which occurred between the outer spans were evaluated as well. It was anticipated that events which occurred between the outer spans, but outside of the inner span would be predominantly shear failure driven, and result in a far greater

number of matrix cracking and interfacial failures. Figure 6.24 through Figure 6.26, which show the Partial Power space plots in which events that occurred between the outer spans were accepted for specimens aged 3, 6, and 12 months, respectively, confirm the aforementioned supposition.

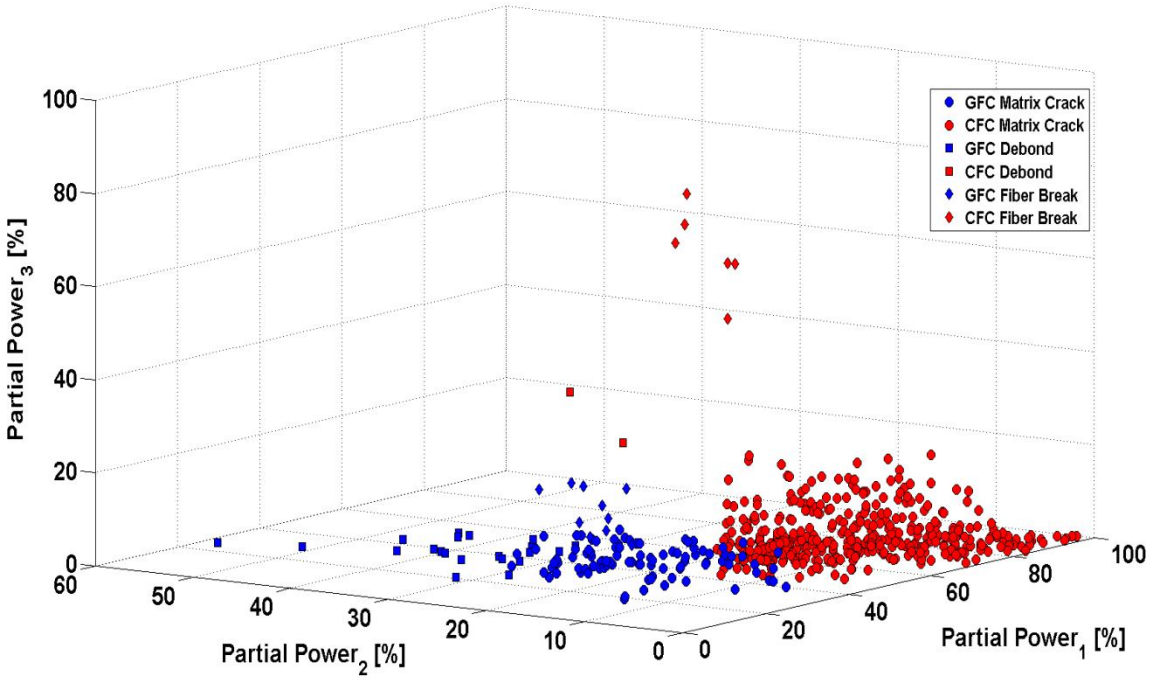

Figure 6.24 Partial Power space plot for a 3 month aged specimen during flexure loading, in which events which occurred between the outer spans were considered valid.

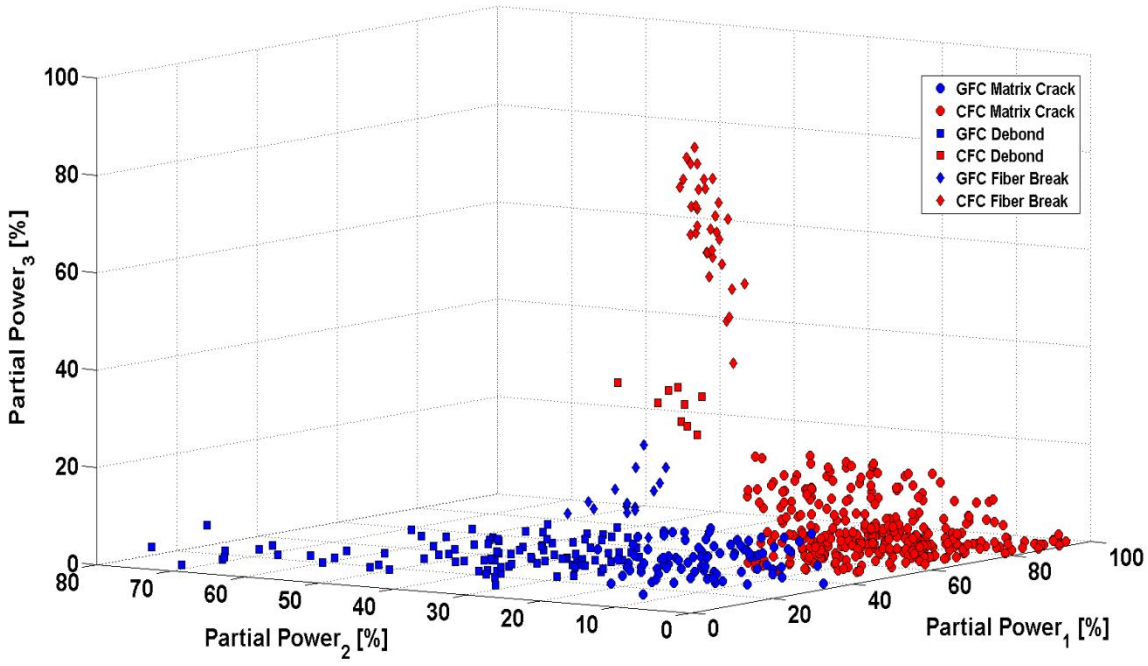

Figure 6.25 Partial Power space plot for a 6 month aged specimen during flexure loading, in which events which occurred between the outer spans were considered valid.

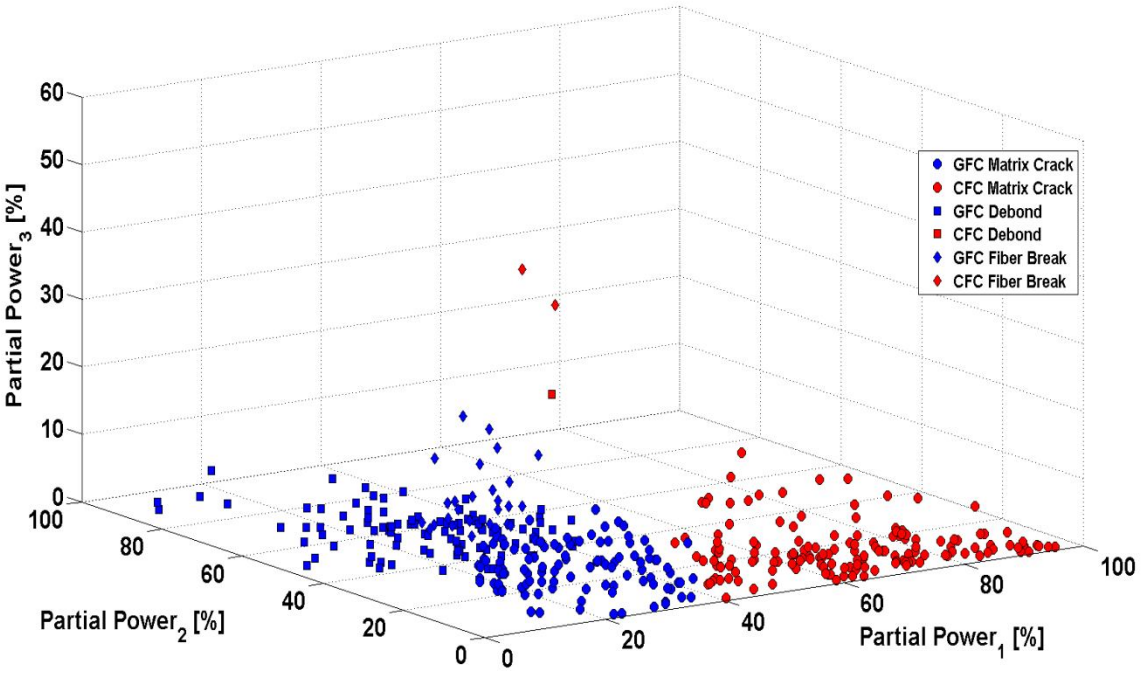

Figure 6.26 Partial Power space plot for a 12 month aged specimen during flexure loading, in which events which occurred between the outer spans were considered valid.

Under the influence of shear loading, matrix cracking and fiber/matrix interfacial failure increased substantially, for all aging conditions considered. When considering events from the second processing method, it was again observed that at 3 months aging time CFC matrix cracking was the most commonly observed deformation mechanism, while matrix cracking and fiber/matrix debonding of the GFC became more common place at the longer aging times. Such conclusions once again highlight the fact that the GFC was subjected to 2 different aging mechanisms, whereas the CFC was only subjected to one form of aging. Finally, from all of the experimental data it was observed that a comparatively few number of CFC fiber/matrix debonding events were observed, which speaks towards the manufacturing quality of the pultruded hybrid polymer matrix composite material.

6.3 Conclusions regarding damage mechanism identification

It has been shown that 3-dimensional finite element modeling may be used to develop a classification scheme capable of distinguishing deformation mechanisms, as well as the material of origin for the signal from a unidirectional polymer matrix hybrid composite material with rod type geometry. Moreover, the explicit finite element formulation was shown to provide a far more computationally efficient time integration scheme than implicit formulations for the purposes of simulating acoustic emission events. Thus, an explicit integration scheme is ideally suited for the dynamic study of stress wave propagation of structure, and sub-structure sized parts.

Fiber fracture, matrix cracking, and fiber/matrix debonding were numerically simulated, and the resulting axial motion of the waveform on the opposite face was extracted. Based upon the spectral characteristics of the simulated signals, the deformation mechanism, as well as the material of origin of the signal could be differentiated via the method of a 3-Dimensioned Partial Power space. The proposed method was used to evaluate the occurrence of deformation mechanisms in aged hybrid composite specimens, from which the efficacy of the method was confirmed. Moreover, the method emphasized that with increased aging time that the matrix material of the embrittled composite material became more susceptible to accumulating shear induced damage (i.e. – matrix cracking, and interfacial failure). The proposed identification scheme could readily be applied to damage identification during fatigue loading when considering a mean stress, or variable amplitude loading, which would greatly benefit the technology.

7. CONCLUDING REMARKS

A concise summary of the milestone contributions of the present work is included below. Following the synopsis, a discussion of the merits and obstacles for implementing polymer matrix composite materials' in transmission line design is presented from the perspective of the author.

From this work, several substantial contributions have been made to the further understanding of the physical behavior of a particular hybrid polymer matrix composite material. Said contributions include:

- Evaluation of the fatigue behavior of the hybrid composite rod subjected to a fully reversed state of axial stress (in the presence of constant transverse compression). From this investigation it was found that the GFC was the material that accumulated a majority of fatigue damage. Semi-empirical damage accumulation relationships were developed from the experimental data.
- An increase in material stiffness upon initial cyclic loading of the pultruded hybrid composite was observed experimentally, and explained via micromechanics modeling. The observed phenomenon was attributed to misaligned fibers aligning themselves in the direction of applied loading.

- The flexure properties (both in static and fatigue loading) of the hybrid composite subjected to an elevated temperature of 180 °C which is near, but below T_g, as a function of aging time was investigated. Static flexure performance was found to be a monotonically decreasing function with respect to time. The fatigue performance of the hybrid composite increased with respect to cycles to failure performance and damage resistance for short aging times (3 months). This observation was attributed to an enhancement in the fiber/matrix interfacial properties. Intermediate exposure (6 months) resulted in mildly diminished cycles to failure performance, but maintained an increased level of damage accumulation resistance in comparison to the unaged hybrid composite. The slight reduction in cycles to failure performance was attributed to the surface effect of thermal oxidation. Prolonged exposure (12 months) resulted in significantly diminished cycles to failure performance, and damage accumulation resistance. The significant degradation in both fatigue metrics was attributed predominantly to physical aging of the epoxy matrix material which occurred throughout the bulk of the composite, and the associated deterioration in microstructural integrity.
- A conservative means of measuring the glass transition temperature was shown to under-predict T_g by approximately 30°C, in comparison to values reported in the literature.
- The isothermal aging behavior of the hybrid composite material was measured at temperatures below T_g (as measured via DMA techniques). A stretched

exponential function was shown to well describe the aging behavior with respect to time. In addition, it was shown that an Arrhenius relationship can be used for determination of the activation energy of the aging process.

- A fundamental understanding of why the GFC was the material that failed during fatigue loading was gained through steady state dynamics representative volume element modeling.
- A quasi-static "flexure" test was developed that resulted in true material failures (i.e. – failures which were not initiated by crushing underneath the loading pins). "Flexure" is used in quotations, as the failure is shear driven, but is nevertheless suitable for evaluating the aging performance of the pultruded hybrid composite rods.
- A damage identification scheme based upon broadband acoustic emission techniques was developed, capable of classifying common unidirectional polymer matrix composite failure mechanisms, as well as the material of origin of the damage event for the hybrid composite rod geometry.

New transmission line designs based upon a hybrid polymer matrix composite material provide increased power delivery capabilities, while also offering a more efficient means of transmitting electricity during normal operating conditions. Such capabilities are drastically needed within the US, as well as globally.

However, as is the view of the author, a few challenges remain before the technology will gain wide spread acceptance. Most importantly, the concerns with respect to diminished fatigue performance when exposed to elevated temperatures due to physical

aging of the hybrid composite material must be addressed. From the isothermal aging study, it was conclusively shown that the hybrid composite maintains dimensional stability to a far greater extent at equivalent aging times when the aging temperature was reduced. A thorough understanding of the aging time/temperature dependence of the hybrid composite material would go a long way in the safe design of transmission lines based upon this technology.

As previously mentioned, more knowledge on the fatigue performance of the hybrid composite is necessary. The effects of mean stress, variable amplitude loading, and load sequence effects must be understood for the safe implementation of the technology.

Finally, a few isolated "incidents," have occurred during installation of the composite core transmission lines within the past few years. During the analysis of the failures it became evident that these incidents were (in the opinion of the author) a result of localized transverse damage that resulted from dynamic impact. This issue is commonplace in the aerospace industry where a regular design variable for composite laminates is compression after impact, and open-hole compression after impact; this leads into the final two sets of challenges for the technology that the author perceives.

First, the impact damage tolerance of the hybrid composite material must be understood. The effect that impact has on the fatigue performance of the hybrid composite remains a critical knowledge gap (and is suspected to be the cause of the most notarized failure). Second, a viable non-destructive evaluation technique, capable of detecting flaw sizes on the order of 1 μm, or smaller, in either of the composite materials must be developed. At present time acousto-ultrasonics, phased array ultrasonics, and

computed tomography appear to be the most suitable techniques, each with their own issues in need of resolving to see the concept come to fruition.

REFERENCES

Abaqus. *Abaqus Theory Manual.* Providence, 2009.

Aboudi, J. *Mechanics of Composite Materials, A Unified Micromechanical Approach.* Amsterdam: Elsevier Science Publishers, 1991.

Adam, T, N Gathercole, H Reiter, and B Harris. "Life prediction for fatigue of T800/5245 carbon-fibre composites: II varibale-amplitude loading." *International Journal of Fatigue* 16 (1994): 533-547.

Akay, M, and G Spratt. "Evaluation of thermal ageing of carbon fibre reinforced bismaleimide." *Composites Science and Technology* 68 (2008): 3081-3086.

Alawar, A, E Bosze, and S Nutt. "A composite core conductor for low sag at high temperatures." *IEEE Transactions on Power Delivery* 20, no. 3 (2005): 2193-2199.

ASTM. "D4476 - 03 Standard test method for flexural properties of fiber reinforced pultruded plastic rods." West Conshohocken: ASTM International, 2003.

ASTM. "E647-00 Standard Test Method for Measurement of Fatigue Crack Growth Rate." West Conshohocken: ASTM International, 2000.

Barjasteh, E, N Kar, and S Nutt. "Effect of filler on thermal aging of composites for next-generation power lines." *Composites Part A*, 2011: accepted for publication.

Barjatesh, E, E Bosze, Y Tsai, and S Nutt. "Thermal aging of fiberglass/carbon-fiber hybrid composites." *Composites Part A* 40 (2009): 2038-2045.

Beaumont, P, and B Harris. "The effect of environment on fatigue and crack-propagation in carbon-fibre reinforced epoxy resin." *Proceedings of an International Conference on Carbon Fibers: Their Composites and Applications.* London: Plastics Institute, 1972. 283-291.

Benedikt, B, et al. "X-ray diffraction experiments on aged graphite fiber/polyimide composites with embedded aluminum inclusion." *Composites Part A* 35 (February 2004): 667-681.

Boller, K. "Fatigue characteristics of reinforced-plastics laminates subjected to axial loading." *Modern Plastics* 41 (1964): 145-150; 188.

Bonora, Nicola, and Andrew Ruggiero. "Micromechanical modeling of composites with mechanical interface - Part 1: Unit cell model development and manufacturing process effects." *Composites Science and Technology* 66 (2006): 314-322.

Bosze, E, A Alawar, O Bertschger, Y Tsai, and S Nutt. "High-temperature strength and storage modulus in unidirectional hybrid composites." *Composites Science and Technology* 66 (2006): 1963-1969.

Bowles, K, D Jayne, Leonhardt, and T. "Isothermal aging effects on PMR-15 resin." *SAMPE Quarter*, 1993: 2-9.

Burks, Brian, Daniel Armentrout, Jon Buckley, Mark Baldwin, and Maciej Kumosa. "Hybrid composite rods subjected to excessive bending loads." *Composites Science and Technology* 69, no. 15-16 (2009): 2625-32.

Burks, Brian, James Middleton, and Maciej Kumosa. "Impact of geometric variability on the flexural properties of the ACCC/TW conductor core." Fort Collins: International Conference on Overhead Transmission Lines, 2010. 436-443.

Burks, Brian, James Middleton, Daniel Armentrout, and Maciej Kumosa. "Effect of excessive bending on residual tensile strength of hybrid composite rods." *Composites Sceince and Technology* 70 (2010): 1490-1496.

Chugtai, A, D Smith, and M Kumosa. "Chemical analysis of a field-failed composite suspension insulator." *Composites Science and Technology* 58, no. 10 (1998): 1641-1647.

Claren, Rodolfo, and Giorgio Diana. "Dynamic Strain Distribution on Loaded Stranded Cables." *IEEE Transactions on Power Apparatus andSystems* 88, no. 11 (November 1969): 1678-1676.

Claren, Rodolfo, and Giorgio Diana. "Mathematical Analysis of Transmission Line Vibration." *IEEE Transaction on Power Apparatus and Systems* 88, no. 12 (1969).

Daniels, I, J Luo, and Z Sun. *Constitutive Behavior and Damage Characterization of High Temperature Polymer Composites.* Arlington: AFOSR, 2001.

de Groot, P, P Wijnen, and R Janssen. "Real-time frequency determination of acoustic emission for different fracture mechanisms in carbon/epoxy composites." *Composites Science and Technology* 55 (1995): 405-412.

Dickson, R, G Fernando, T Adam, H Reiter, and B Harris. "Fatigue behavious of hybrid composites Part 2: Carbon-glass hybrids." *Journal of Materials Science* 24 (1989): 227-233.

EIA. "Annual Energy Outlook 2011." Washington D.C., 2010.

EPRI. *Aging assesment of a composite core high-temperature low-sag (HTLS) conductor.* Palo Alto: Elextric Power Research Institute, 2009.

EPRI. *Endurance test on two carbon fiber composite core conductors.* Palo Alto: Electric Power Research Institute, 2010.

EPRI. *EPRI Transmission Line Reference Book: Wind-Induced Conductor Motion 2nd Edition.* Palo Alto, CA: Electric Power Research Institute, 2009.

EPRI. *High-Temperature, Low-Sag Transmission Conductors.* Palo Alto, CA: Electric Power Research Institute, 2002.

Eshelby, J. "The determination of the elastic field of an ellipsoidal inclusion, and related problems." *Proceedings of the Royal Society* A241 (1957): 376-396.

Gary, J, and M Hamstad. "On the far-field structure of waves generated by a pencil lead break on a thin plate." *Journal of Acoustic Emission* 12, no. 3/4 (1994): 157-170.

Gathercole, N, H Reiter, T Adam, and B Harris. "Life prediction for fatigue of T800/5245 carbon-fibre composites: I. Constant-amplitude loading." *International Journal of Fatigue* 16 (1994): 523-532.

Gentz, M. *Polyimide composites at elevated temperatures.* Denver: University of Denver, PhD Dissertation, 2004.

Gentz, M, B Benedikt, J Sutter, and M Kumosa. "Residual stresses in unidirectional graphite fibers/polyimide composites as a function of aging." *Composites Science and Technology* 64 (February 2004): 1671-1677.

Haldar, A, and S Mahadevan. *Probability, Reliability, and Statistical Methods in Engineering Design.* New York: John Wiley and Sons, Inc., 2000.

Halpin, J, and S Tsai. *Environmental factors in composite design.* AFML-TR-67-423, Air Force Materials Laboratory Technical Report, 1967.

Hamstad, M. "Re-examination of NIST acoustic emission absolute sensor calibration: Part II - Finite element modeling of acoustic emission signal from glass capillary fracture." *Journal of Acoustic Emission* 29 (2011): 175-183.

Hamstad, M, A O' Gallagher, and J Gary. "A wavelet transform applied to acoustic emission signals: Part 2: Source location." *Journal of Acoustic Emission* 20 (2002): 62-82.

Hamstad, M, A O' Gallagher, and J Gary. "Modeling of buried acoustic emission monopole and dipole sources with a finite element technique." *Journal of Acoustic Emission* 17, no. 3/4 (1999): 97-110.

Harris, B. "Fatigue and accumulation of damage in reinforced plastics." *Composites*, 1977: 214-220.

Harris, B ed. *Fatigue of Composites.* Cambridge: Woodhead Publishing Limited, 2003.

Harris, B, N Gathercole, J Reiter, and Adam T. "Fatigue of carbon-fibre-reinforced plastics under block loading conditions." *Composites Part A: Applied Science and Manufacturing* A28 (1997): 327-337.

Hofer, K, M Stander, and L Bennet. *Polymer Engineering Science* 18 (1978): 120-127.

Hull, D, and T Clyne. *An Introduction to Composite Materials 2nd Ed.* Cambridge: Cambridge University Press, 1996.

Hwang, W, and K Han. "Fatigue of composites - Fatigue modulus concept and life prediction." *Journal of Composite Materials* 20 (1986): 154-165.

Jones, C, R Dickson, T Adam, H Reiter, and B Harris. "The environmental fatigue behaviour of reinforced plastics." *Proceedings of the Royal Society* A396 (1984): 315-338.

Jong, H. "Transverse cracking in a cross-ply composite laminate - Detection in acoustic emission and source characterization." *Journal of Composite Materials* 40, no. 1 (2006): 37-69.

Kamvouris, J, G Roberts, J Pereira, and C Rabzak. "Chemical and Physical aging effects in PMR-15 neat resin." *ASTM STP* 1302 (1997): 243-258.

Kaynak, Cevdet, and Onur Mat. "Uniaxial fatigue behavior of filament-wound glass-fiber/epoxy composite tubes." *Composites Science and Technology* 61 (2001): 1833-1840.

Kharrazi, M, and S Sarkani. "Frequency-dependent fatigue damage accumulation in fiber-reinforced plastics." *Journal of Composite Materials* 35, no. 21 (2001): 1924-1953.

Kim, H, and L Ebert. "Flexural fatigue behaviour of unidirectional fiberglass composites." *Fiber Science and Technology* 14 (1981): 3-20.

Kraus, J, and Hagedron. "Aeolian vibrations: wind energy input evaluated from measurements on an energized line." *IEEE Transactions on Power Delivery* 6, no. 3 (1991): 1264-1270.

Kumosa, L, D Armentrout, and M Kumosa. "An evaluation of the critical conditions for the initiation of stress corrosion cracking in unidirectional E-glass/polymer composites." *Composites Science and Technology* 61, no. 4 (2001): 615-623.

Lafarie-Frenot, MC, C Henaff-Gardin, and D Gamby. "Matrix cracking induced by cyclic ply stressses in composite laminates." *Composites Science and Technology* 61 (2001): 2327-2336.

Lambert, J, AR Chambers, I Sinclair, and SM Spearing. "3D damage characterization and the role of voids in the fatigue of wind turbine blade materials." *Composites Science and Technology* 72 (2012): 337-343.

Lerner, Eric. "What's wrong with the Electric Grid?" *The Industrial Physicist*, 2003: 8-13.

Liu, W, Y Hu, and T Belytschko. "Multiple Quadrature Underintegrated Finite Elements." *International Journal for Numerical Methods in Engineering* 37, no. 17 (1994): 3263-3289.

Lowe, A, B Fox, and V Otieno-Alego. "Interfacial ageing of high temperature carbon/bismaleimide composites." *Composites Part A* 33 (2002): 1289-1292.

Madsen, K, H Nielsen, and O Tingleff. *Methods for non-linear least squares problems 2nd Edition.* 2004.

Manjunatha, CM, S Spenger, AC Taylor, and AJ Kinloch. "The tensile fatigue behavior of a glass-fiber reinforced plastic composite using a hybrid-toughened epoxy matrix." *Journal of Composite Materials* 44, no. 17 (2010): 2095-2109.

Middleton, J. *Thermal aging of a cycloaliphatic epoxy resin.* Annual Sponsor Update, Denver: University of Denver, 2012.

Middleton, J, T Wells, B Burks, and M Kumosa. *Effect of Ozone on select physical properties of a high temperature epoxy.* Annual Update, Mechanical and Materials Engineering, University of Denver, Denver, CO: in Prepartion, 2011.

Middleton, James, et al. "The effect of ozone exposure at room temperature on polymer degradation in polymer matrix composite conductors." *Polymer Degradation and Stability*, in preparation, 2012.

Mori, T, and K Tanaka. "Average stress in matrix and average elastic energy of materials with misfitting inclusions." *Acta Metallurgica* 21 (1973): 571-574.

Mura, T. *Micromechanics of Defects in Solids 2nd Edition.* Dordecht: Martinus Nijhoff Publishers, 1987.

NCDC, National Climactic Data Center. *www.noaa.gov.* August 20, 2008. http://lwf.ncdc.noaa.gov/oa/climate/online/ccd/avgwind.html (accessed March 15, 2011).

Neddleman, A, and V Tvergaard. "Comparison of crystal plasticity and isotropic hardening predictions for metal-matrix composites." *ASME Journal of Applied Mechanics* 60 (1993): 70-76.

NERC. "2008-2017 Regional and National Peak Demand and Energy Forecasts Bandwidths." Princeton, NJ, 2008.

Newaz, G. "Influence of matrix material on flexural fatigue performance of unidirectional composites." *Composites Science and Technology*, 1985: 199-214.

Owen, M, and S Morris. *Proceedings of an International Conference on Carbon Fibers: Their Composites and Applications.* London: Plastics Institute, 1972.

Perkin Elmer. *Introduction to Dynamic Mechanical Analysis.* Waltham: Perkin Elmer Inc., 2008.

Poffenbreger, James, and R. Swart. "Differential Displacement and Dynamic Conductor Strain." *IEEE Transactions on Power Apparatus and Systems* 84, no. 4 (1965): 281-289.

Ramberg, W, and W Osgood. "Description of stress-strain curves by three parameters." *Technical Note No. 902* (National Advisory Comittee for Aeronautics), 1943.

Ramey, G, and J Townsend. "Effects of clamps on fatigue of ACSR conductors." *ASCE Journal of the Energy Division* 107 (1981): 103-110.

Ramey, G, R Brunair, and R Duncan. "An experimental evaluation of S-N curves and validity of Miner's cumulative damage hypothesis for an ACSR conductor." *IEEE Transactions on Power Delivery* 3, no. 3 (July 1988): 1131-1140.

Reifsnider, K, and R Jamison. "Fracture of fatigue-loaded composite laminates." *International Journal of Fatigue*, 1982: 187-197.

Rupnowski, P, and M Kumosa. "Meso- and micro-stress analysis in an 8HS graphite/polyimide woven composite subjected to biaxial in-plane loads at room temperature." *Composites Science and Technology* 63 (2003): 785-7999.

Sause, MGR, and S Horn. "Simulation of acoustic emission in planar carbon fiber reinforced plastic specimens." *Journal of Nondestructive Evaluation* 29 (2010): 123-142.

Schoeppner, G, G Tandon, and E Ripberger. "Anisotropic odixation and weight loss in PMR-15 composites." *Composites Part A* 38 (2007): 890-904.

Scott, A, M Mavrogordato, P Wright, I Sinclair, and M Spearing. "In Situ fracture measurement in carbon-epoxy laminates using high resolution computed tomography." *Composites Science and Technology* 71 (2011): 1471-1477.

Sinha, Nadan, and P Hagerdon. "Wind-excited overhead transmission lines: Estimation of connection stresses at junctions." *Journal of Sound and Vibration* 301 (2007): 400-409.

Stephens, RI, A Fatemi, RR Stephens, and H Fuchs. *Metal Fatigue in Engineering 2nd Edition.* New York: John Wiley and Sons Inc., 2001.

Struik, Leindert. *Physical aging in amorphous polymers and other materials.* Amsterdam: Elsevier Scientific Publishing Company, 1978.

Sturgeon, J. "Fatigue testing of carbon-fibre-reinforced plastics." *Proceedings of the 28th Annual Technical Conference of Reinforced Plastics/Composites Inst of SPI.* New York: Society for Plastics Industry, 1975. paper 12B.

Sun, C, and R Vaidya. "Prediction of composite properties from a representative volume element." *Composites Science and Technology* 56 (1996): 171-179.

Suquet, P. "Elements of homogenization theory for inelastic solid mechanics." In *Homogenization Techniques for Composite Media*, by E Sanches-Palencia and A (Eds.) Zaoui, 194-275. Berlin: Springer-Verlag, 1987.

Tanimoto, Toshio, and Sadao Amijima. "Progressive nature of fatigue damage of glass fiber reinforced plastics." *Journal of Composite Materials* 9 (1975): 380-390.

Towo, A, and M Ansell. "Fatigue of sisal fibre reinforced composites: Constant-life diagrams and hysteresis loop capture." *Composites Science and Technology* 68 (2008): 915-924.

Tsuji, L, H McManus, and K Bowles. "Mechanical properties of degraded PMR-15 resin." *ASTM STP 2000* 1357 (2000): 3-17.

Van Paepegem, W, K De Geyter, P Vanhooymissen, and J Degrieck. "Effect of friction on the hysteresis loops from three-point bending fatigue tests of fibre-reinforced composites." *Composite Structures* 72, no. 2 (2006): 212-217.

Vastag, B. "White House pushes policies to upgrade nation's aging electrical grid." *Washington Post*, June 13, 2011.

Verma, H, and P Hagerdon. "Wind induced vibrations of long electrical overhead transmission line spans: a modified approach." *Wind and Structures* 8, no. 2 (2005): 89-106.

Wolfrum, J, S Eibl, and L Lietch. "Rapid evaluation of long-term thermal degradation of carbon fibre epoxy composites." *Composites Science and Technology* 69, no. 3-4 (2009): 523-530.

Xia, Zihui, Yunfa Zhang, and Fernand Ellyin. "A unified periodical boundary conditions for representative volume elements of composites and applications." *International Journal of Solids and Structures* 40 (2003): 1907-1921.

Zhang, Yunfa, Zihui Xia, and Fernand Ellyin. "Nonlinear viscoelastic micromechanical analysis of fibre-reinforced polymer laminates with damage evolution." *International Journal of Solids and Structures* 42 (2005): 591-604.

APPENDIX A – FATIGUE DAMAGE CURVES OF UNAGED SPECIMENS

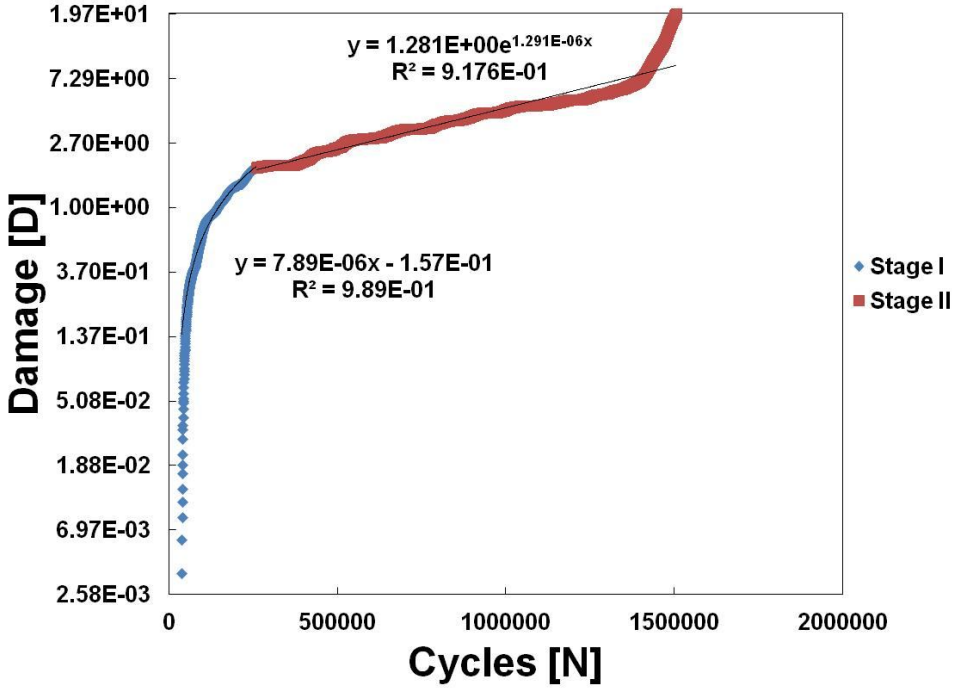

Figure A 1 - Damage curve of σ_2 - specimen 1.

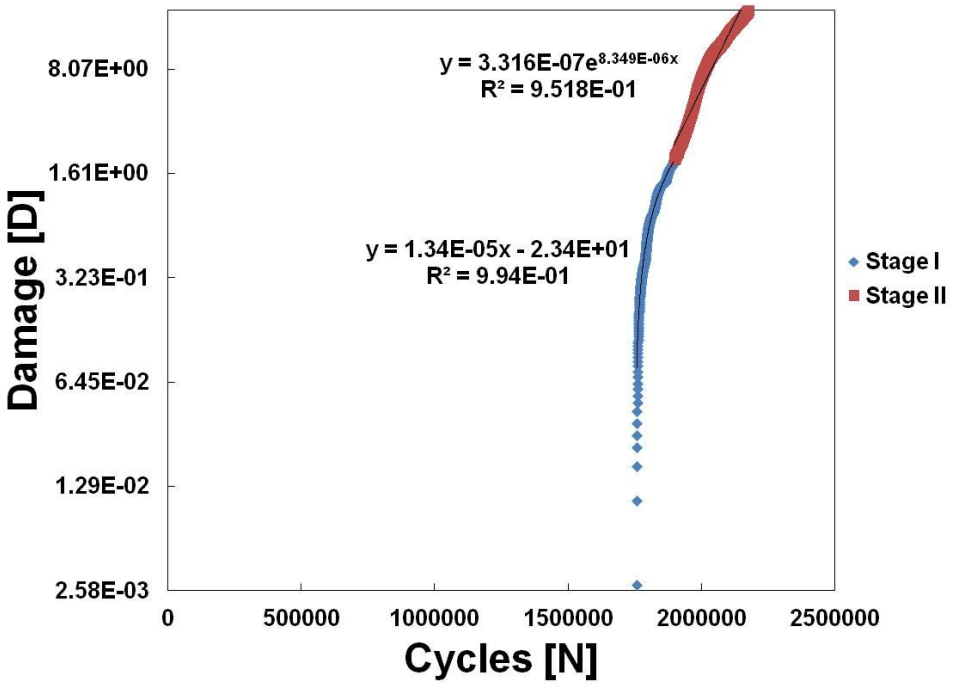

Figure A2 - Damage curve of σ_2 - specimen 2.

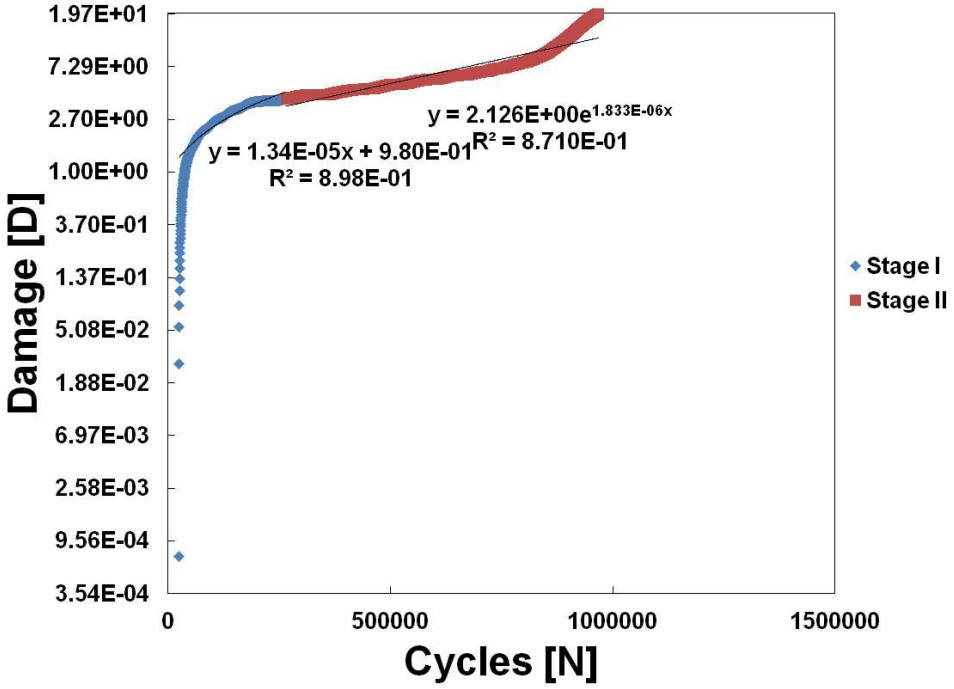

Figure A3 - Damage curve of σ_2 - specimen 3.

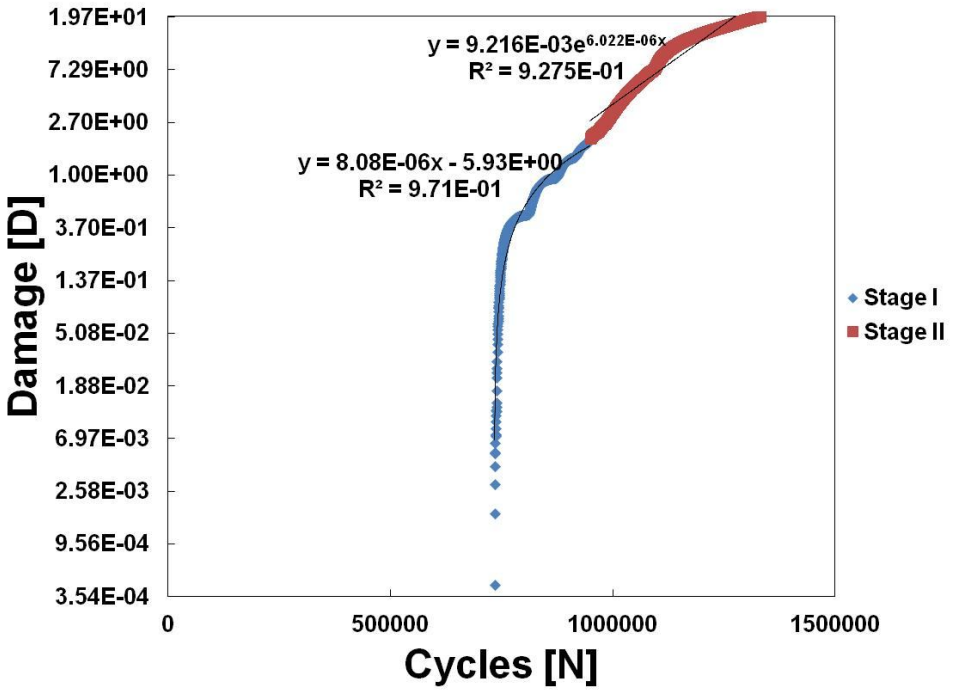

Figure A4 - Damage curve of σ_2 - specimen 4.

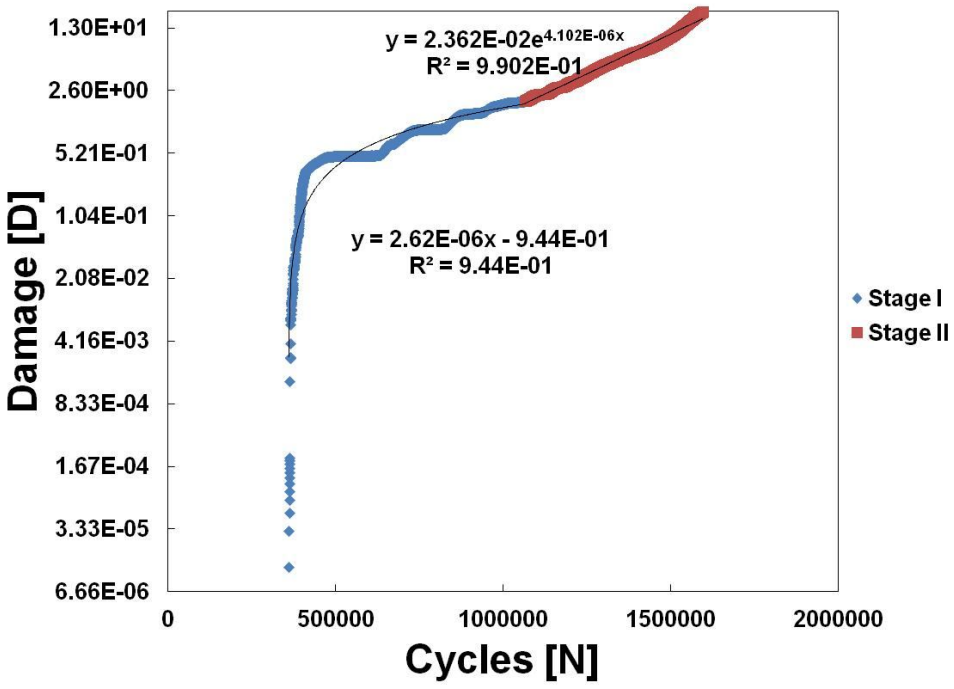

Figure A5 - Damage curve of σ_2 - specimen 5.

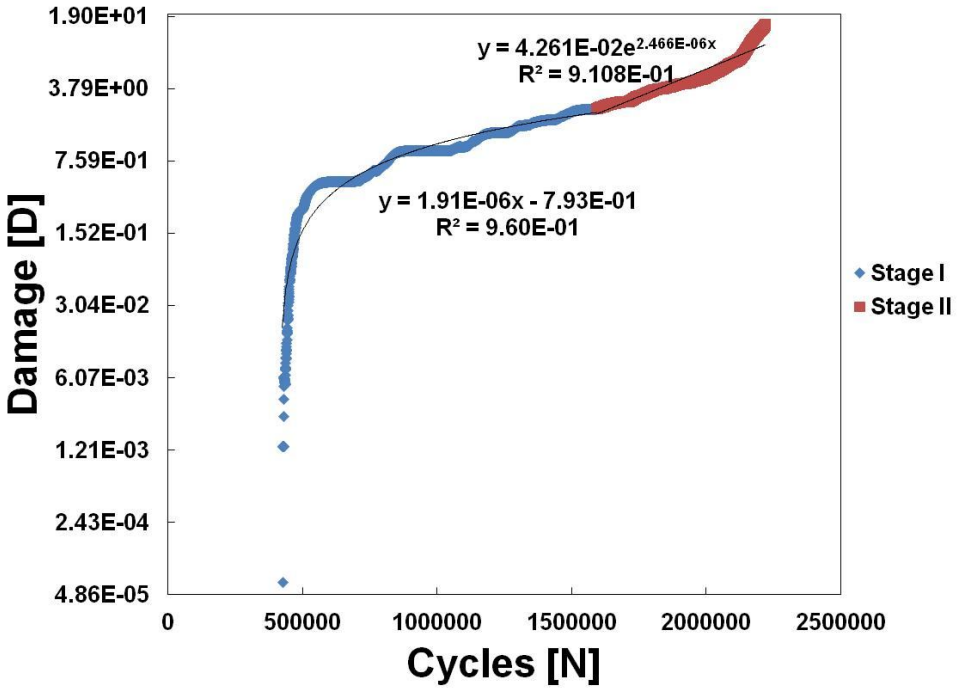

Figure A6 - Damage curve of σ_2 - specimen 6.

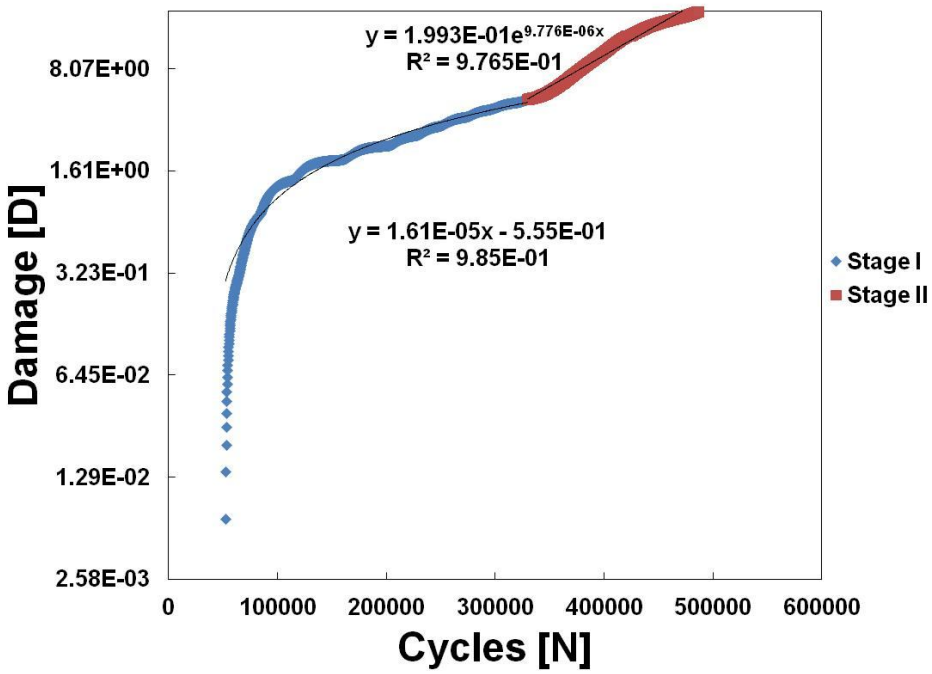

Figure A7 - Damage curve of σ_2 - specimen 7.

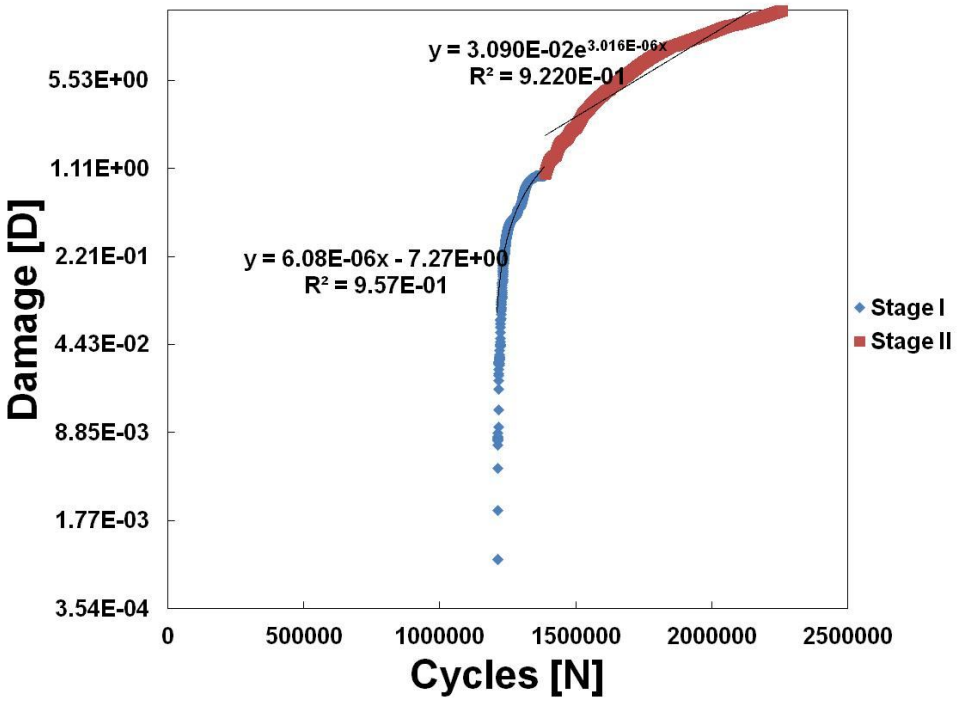

Figure A8 - Damage curve of σ_2 - specimen 8.

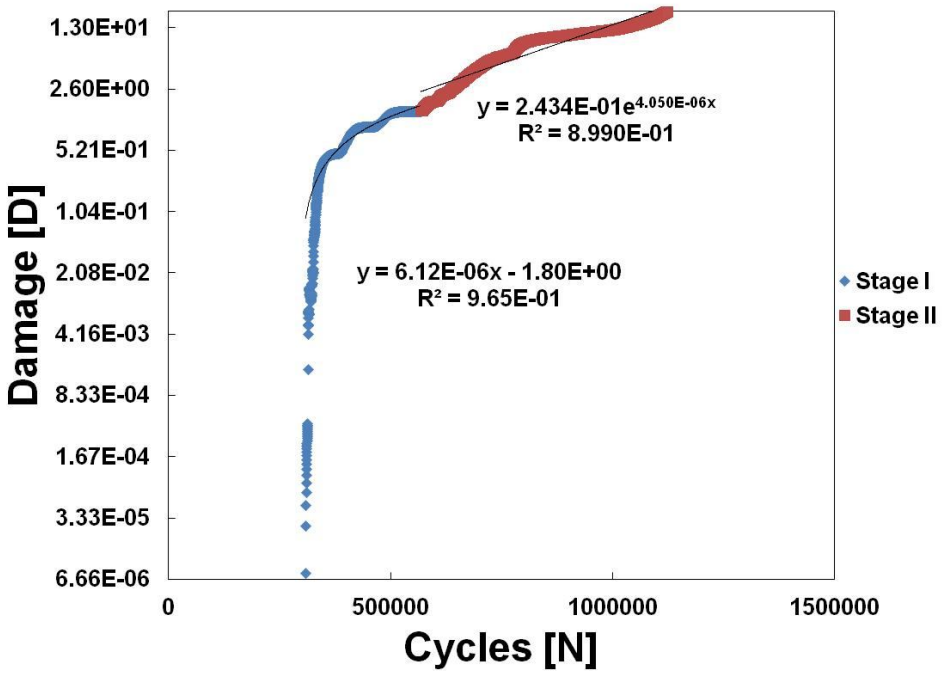

Figure A9 - Damage curve of σ_2 - specimen 9.

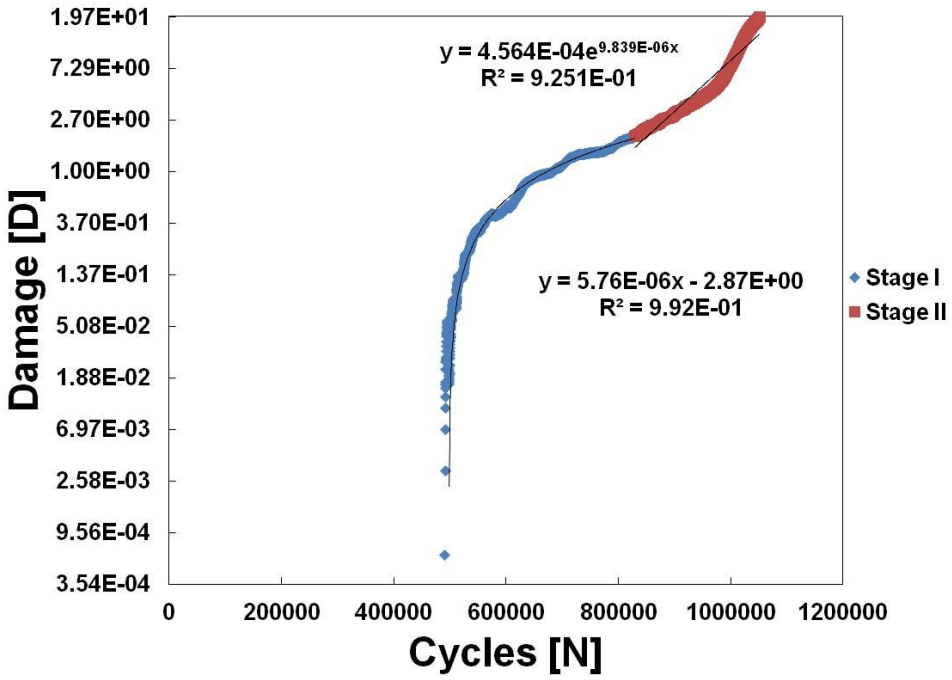

Figure A10 - Damage curve of σ_2 - specimen 10.

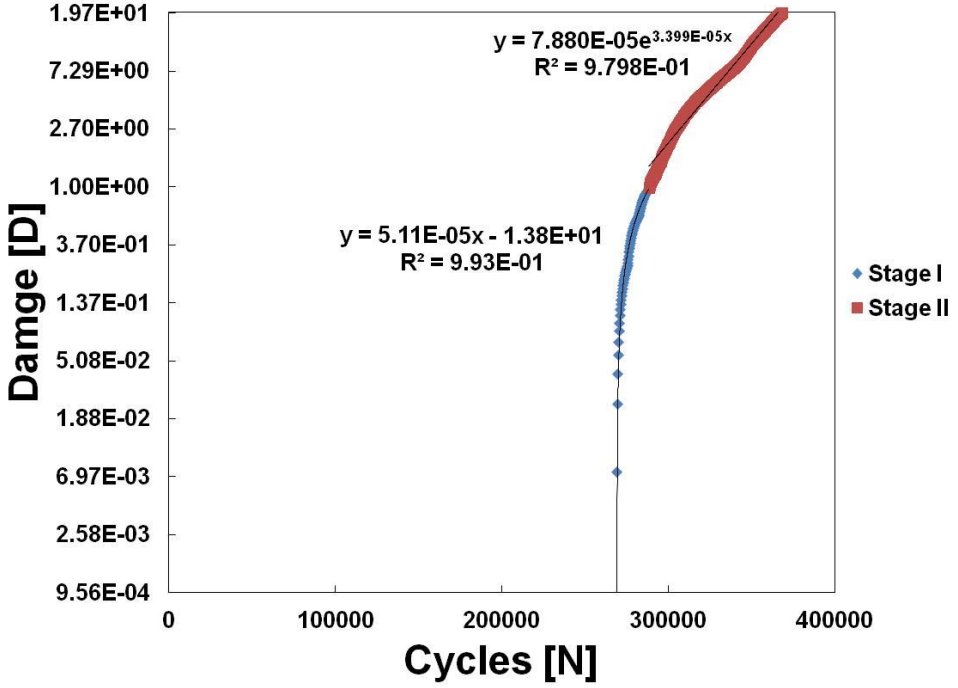

Figure A11 - Damage curve of σ_3 - specimen 1.

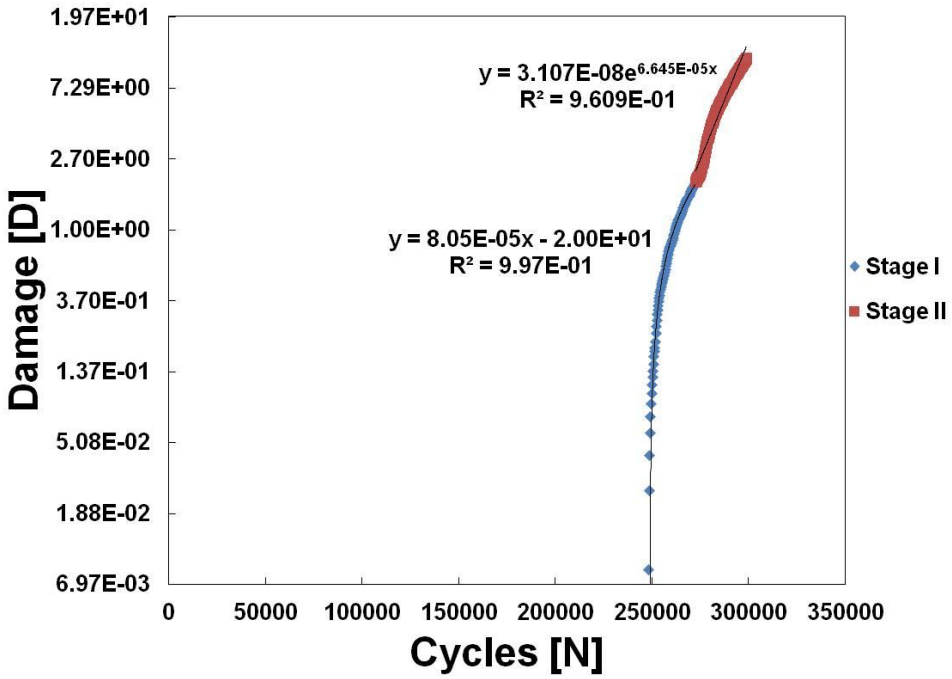

Figure A12 - Damage curve of σ_3 - specimen 2.

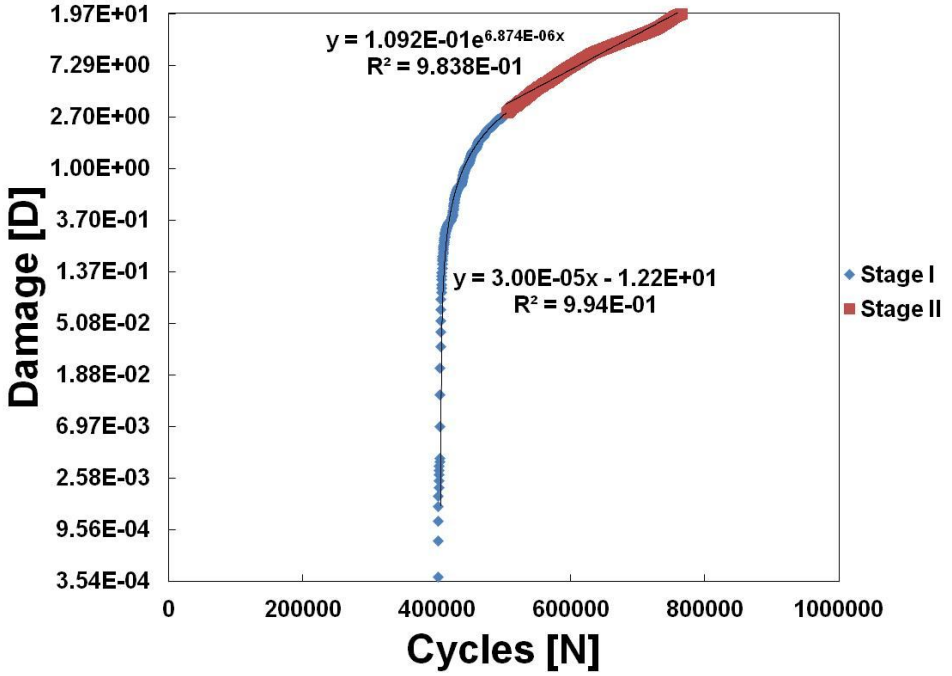

Figure A13 - Damage curve of σ_3 - specimen 3.

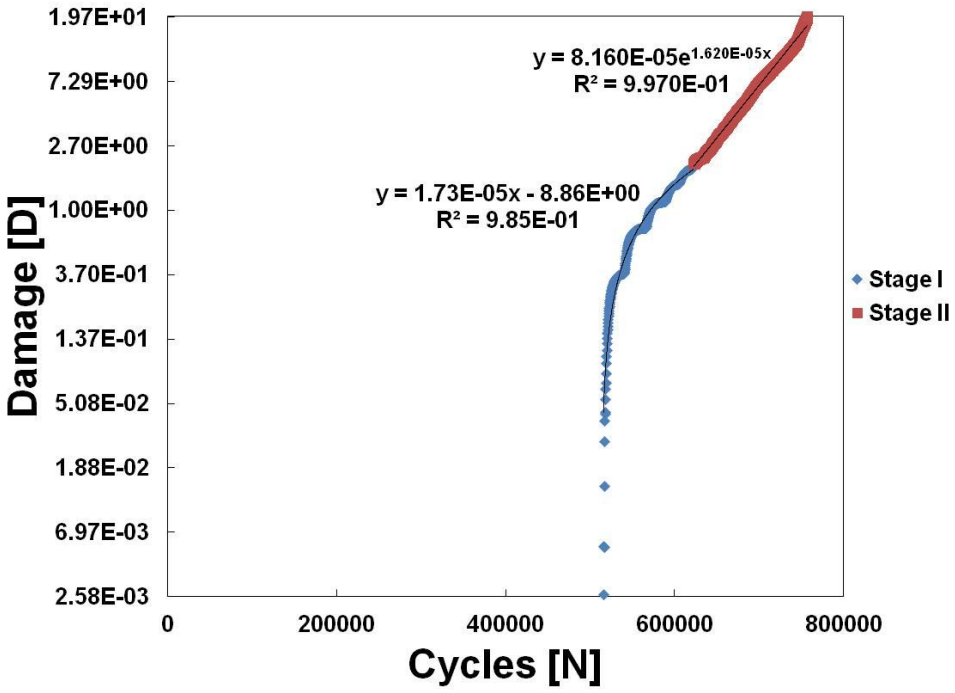

Figure A14 - Damage curve of σ_3 - specimen 4.

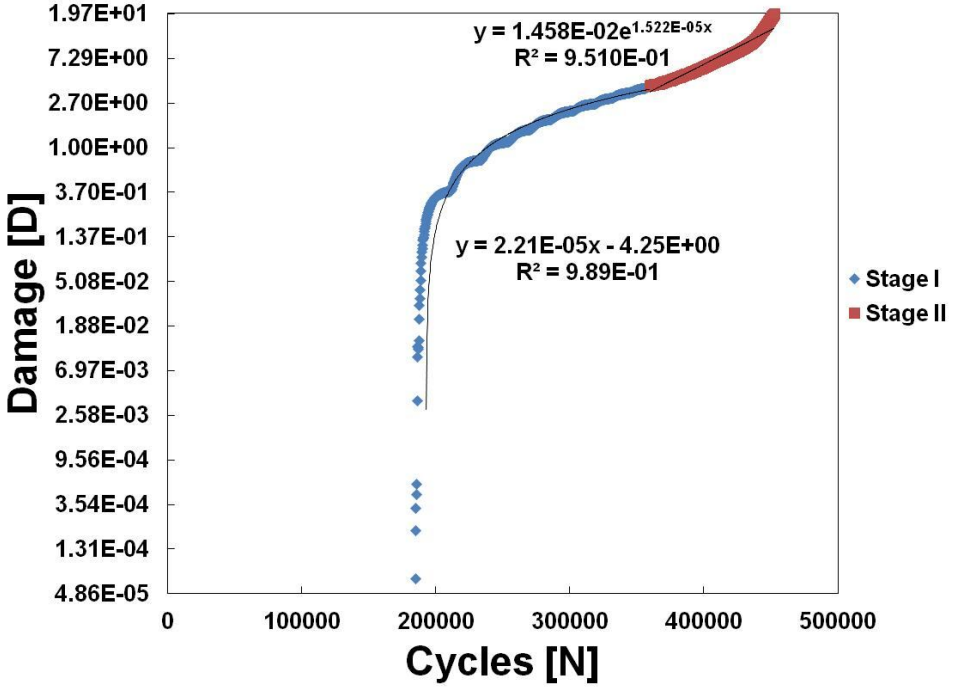

Figure A15 - Damage curve of σ_3 - specimen 5.

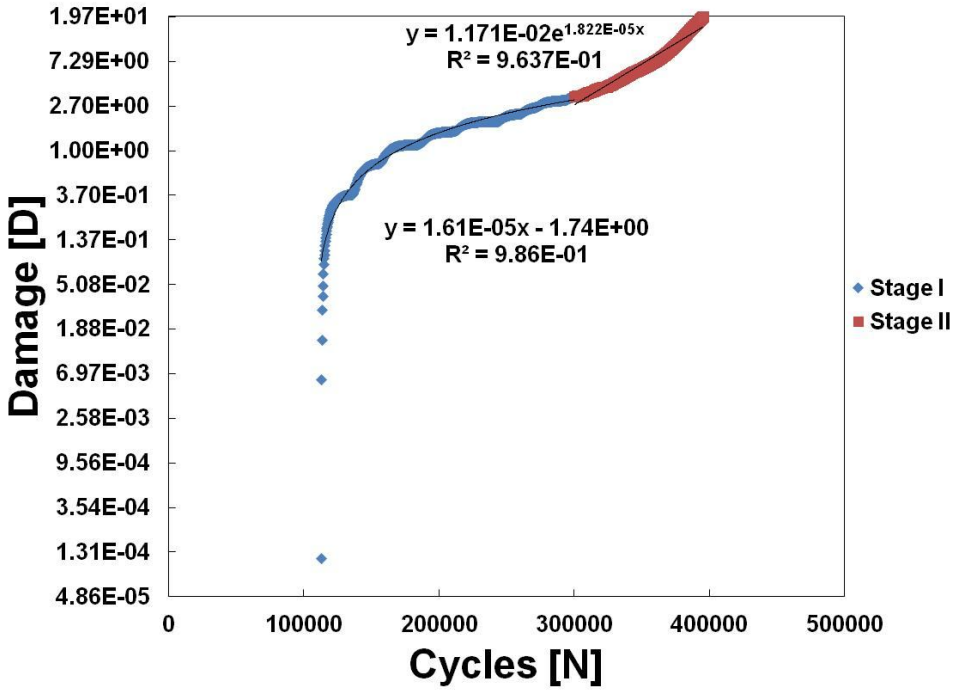

Figure A16 - Damage curve of σ_3 - specimen 6.

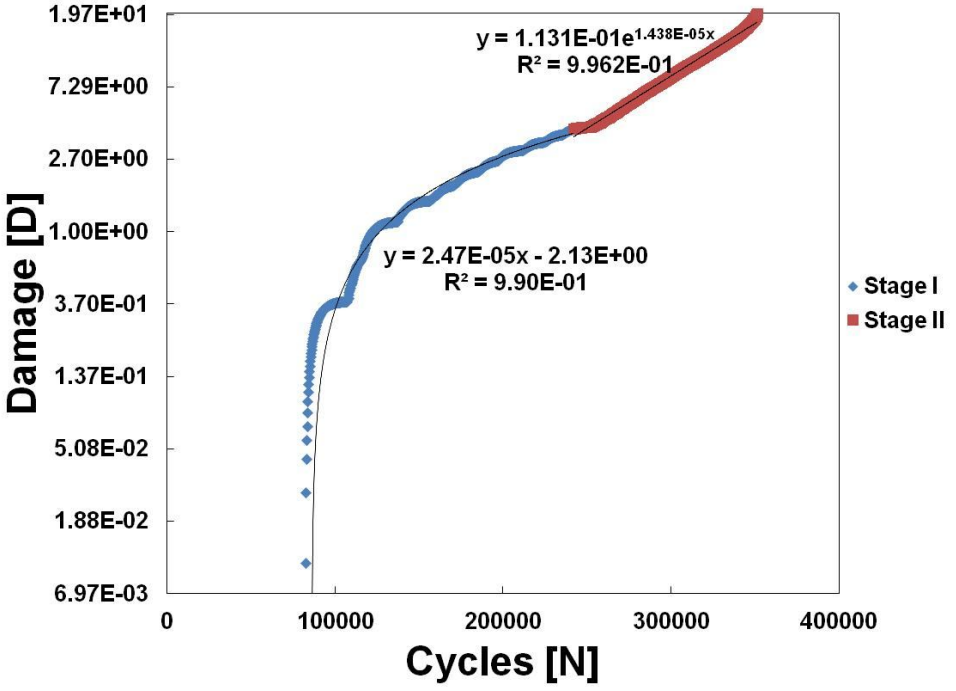

Figure A17 - Damage curve of σ_3 - specimen 7.

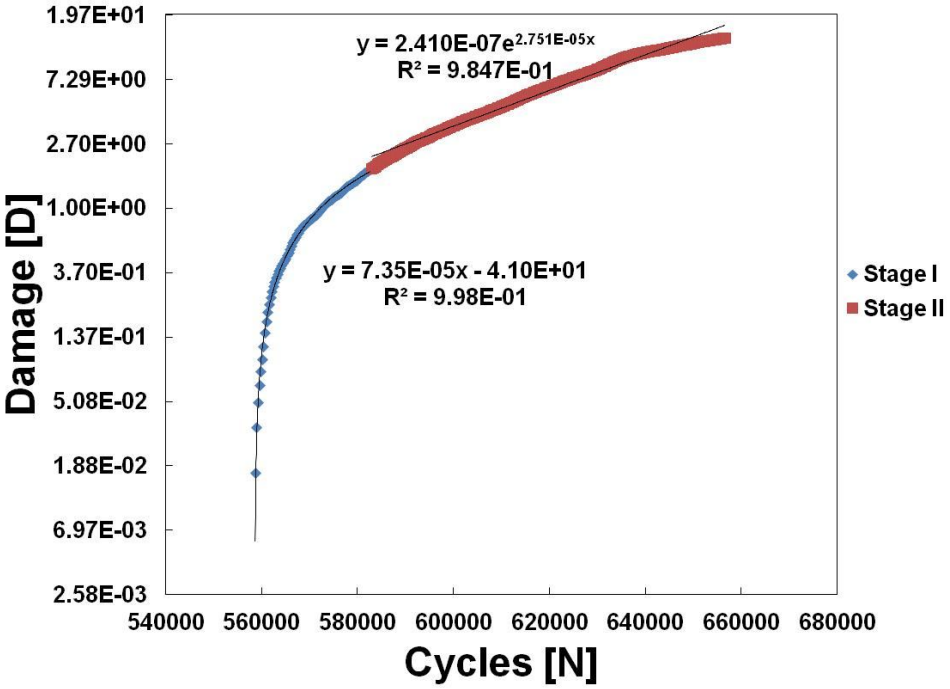

Figure A18 - Damage curve of σ_3 - specimen 8.

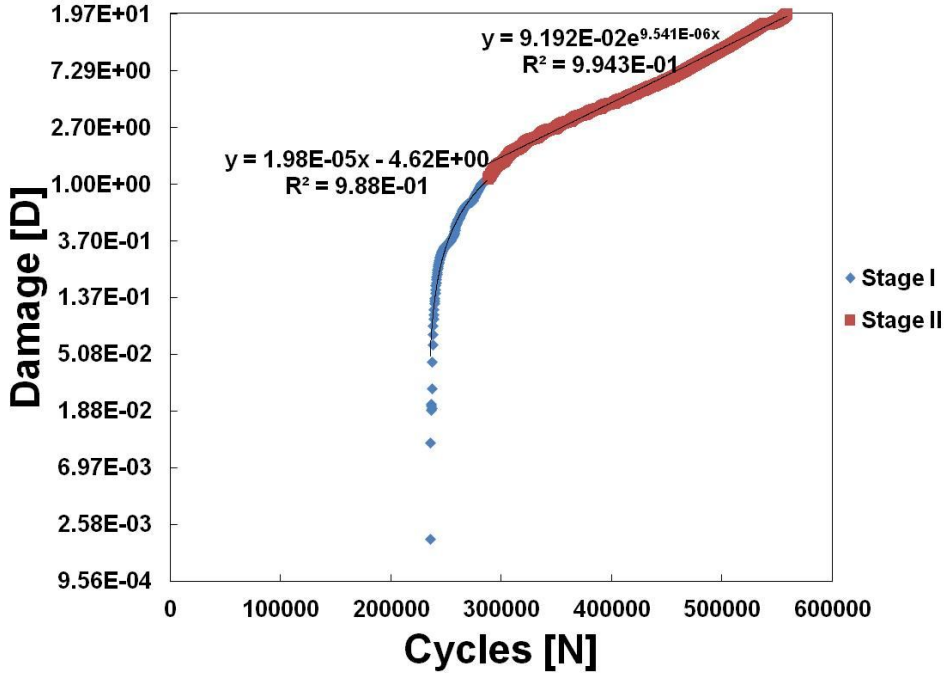

Figure A19 - Damage curve of σ_3 - specimen 9.

σ_3 - specimen 10 Damage curve was not available due to DASU failure.

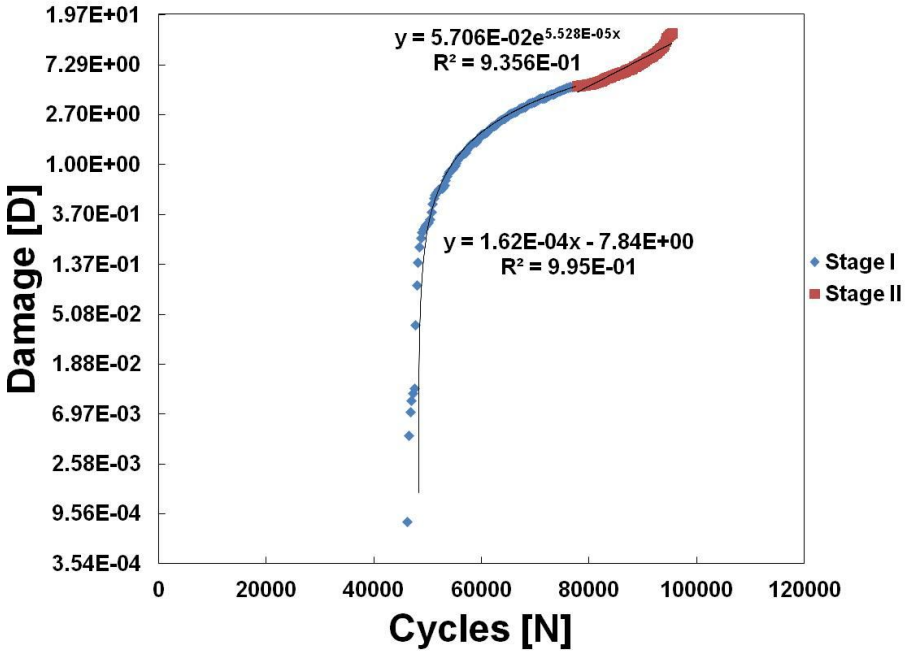

Figure A20 - Damage curve of σ_4 - specimen 1.

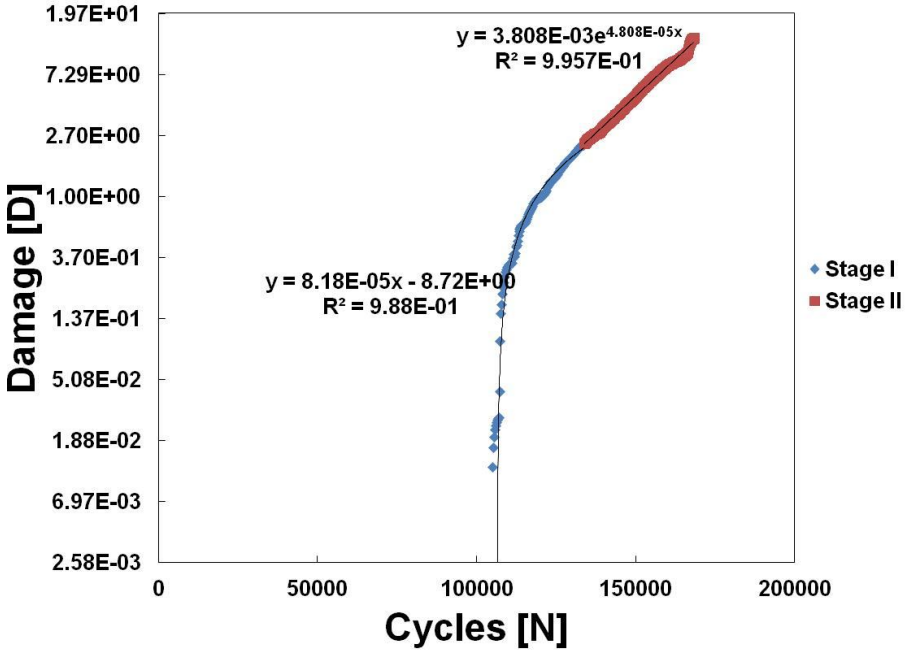

Figure A21 - Damage curve of σ_4 - specimen 2.

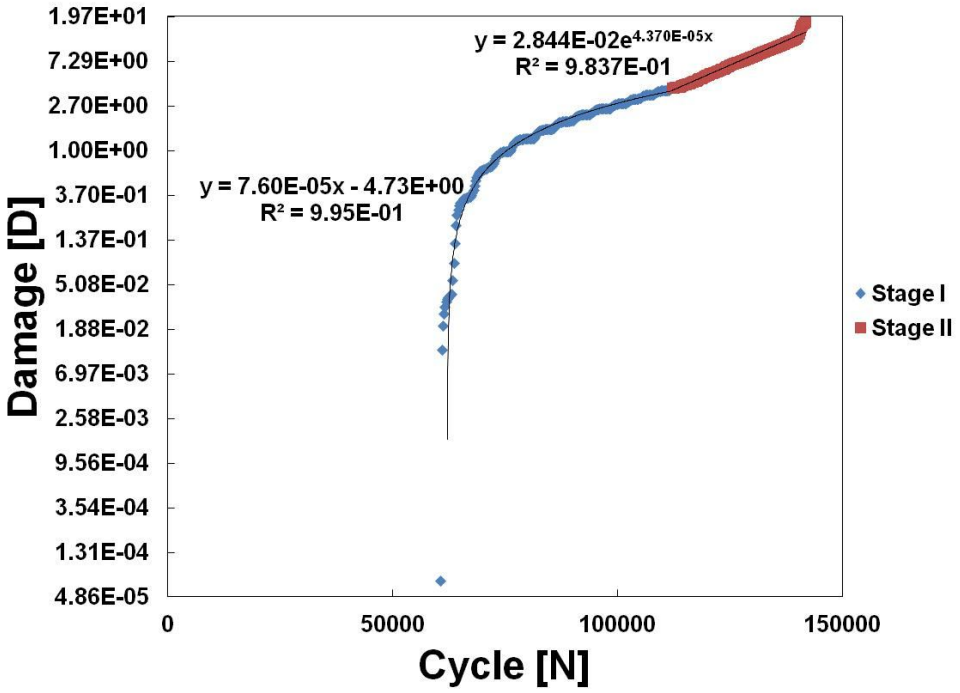

Figure A22 - Damage curve of σ_4 - specimen 3.

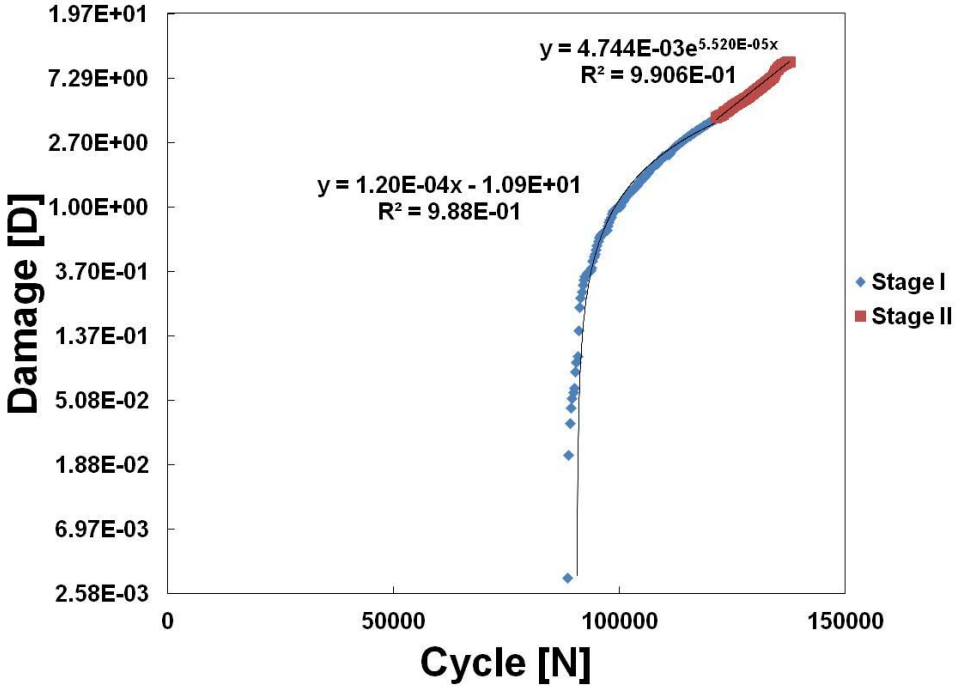

Figure A23 - Damage curve of σ_4 - specimen 4.

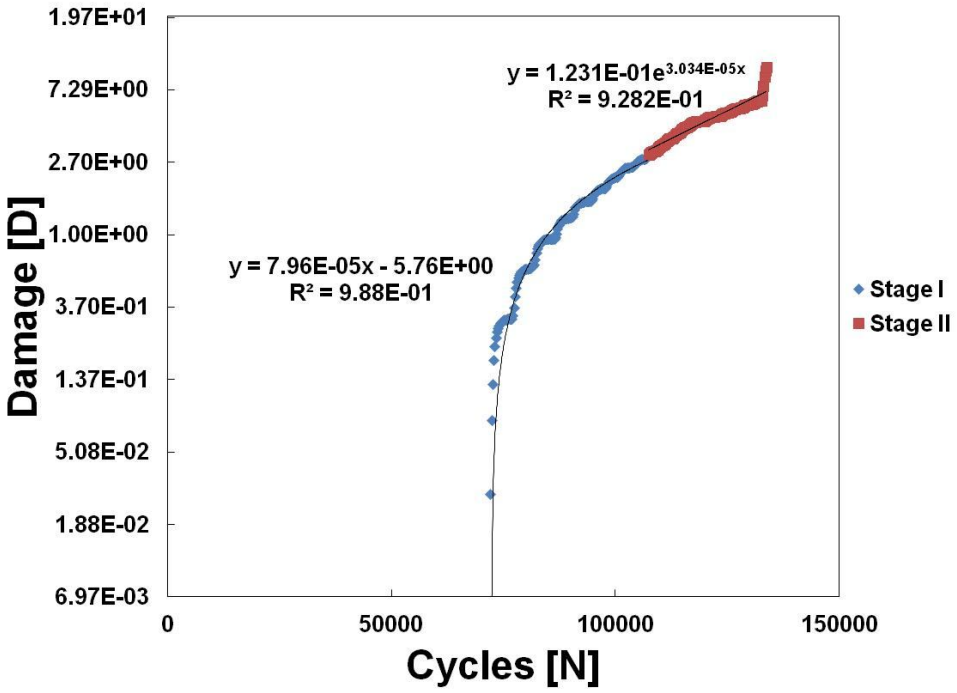

Figure A24 - Damage curve of σ_4 - specimen 5.

σ_4 - specimen 6 Damage curve was not available due to DASU failure.

σ_4 - specimen 7 Damage curve was not available due to DASU failure.

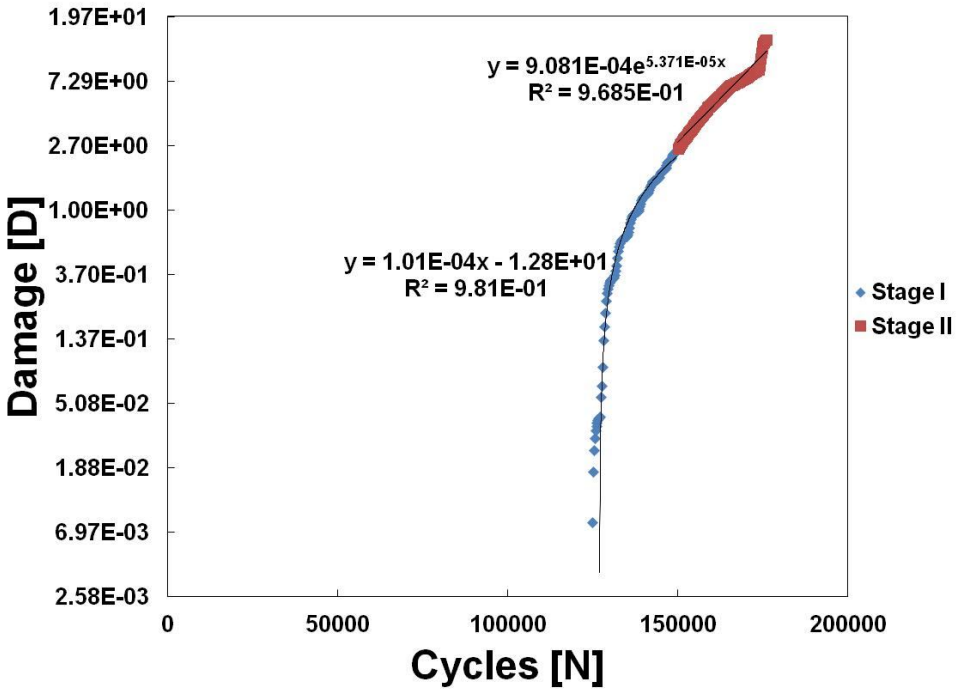

Figure A 25 - Damage curve of σ_4 - specimen 8.

σ_4 - specimen 9 Damage curve was not available due to DASU failure.

σ_4 - specimen 10 Damage curve was not available due to DASU failure.

APPENDIX B – FATIGUE DAMAGE ACCUMULATION RATE CURVES FOR UNAGED SPECIMENS

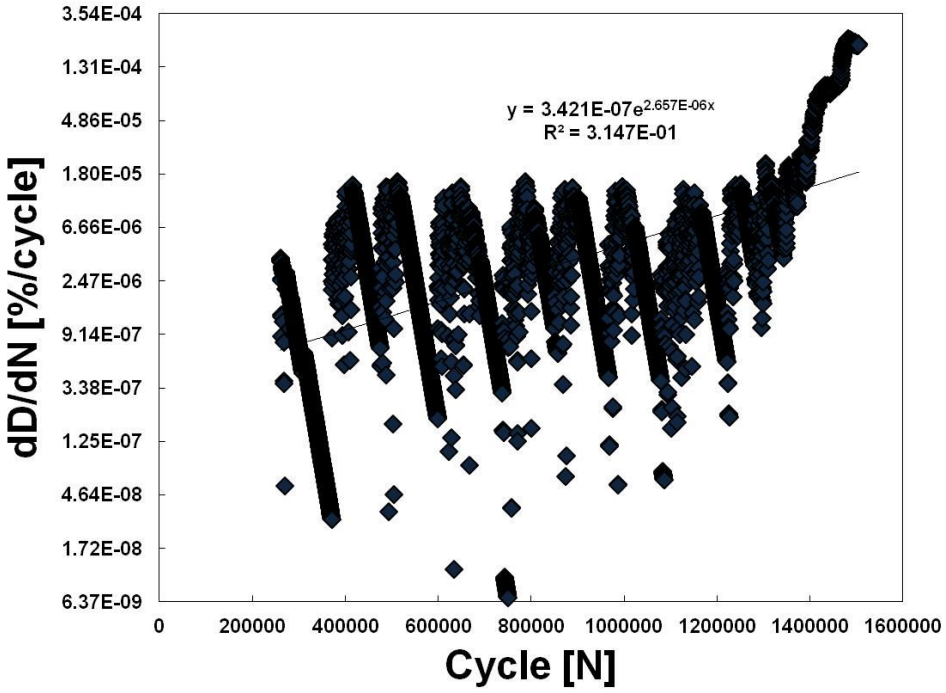

Figure B 1 - Rate of damage accumulation curve of σ_2 - specimen 1.

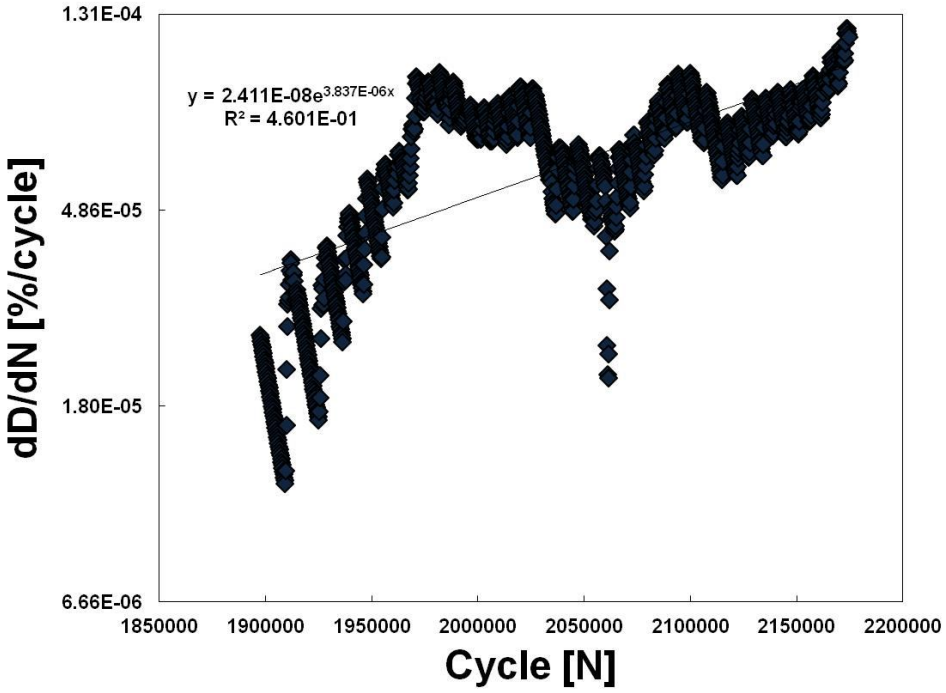

Figure B 2 - Rate of damage accumulation curve of σ_2 - specimen 2.

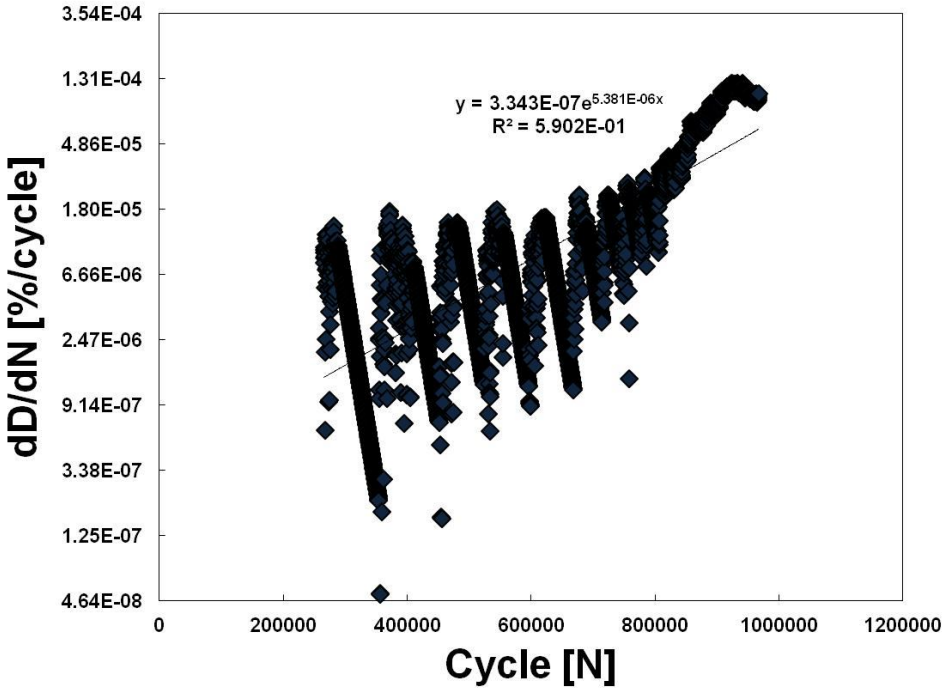

Figure B 3 - Rate of damage accumulation curve of σ_2 - specimen 3.

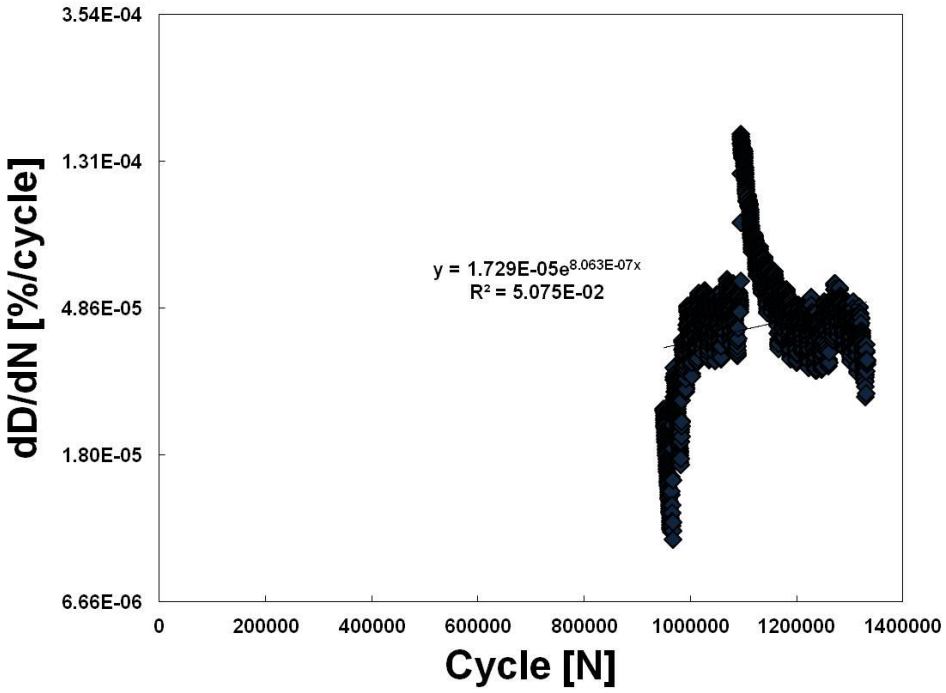

Figure B 4 - Rate of damage accumulation curve of σ_2 - specimen 4.

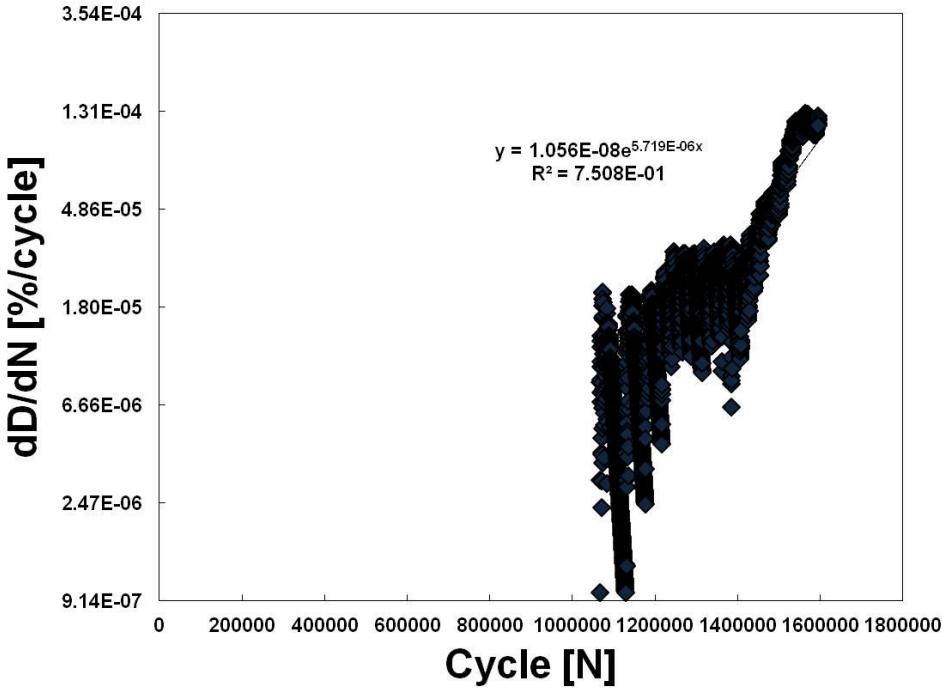

Figure B 5 - Rate of damage accumulation curve of σ_2 - specimen 5.

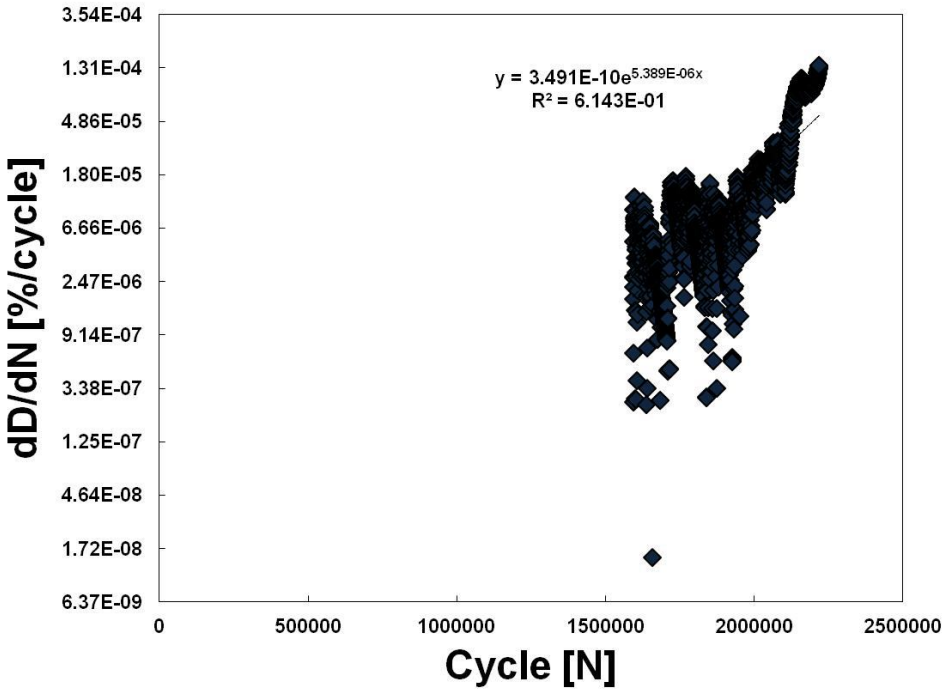

Figure B 6 - Rate of damage accumulation curve of σ_2 - specimen 6.

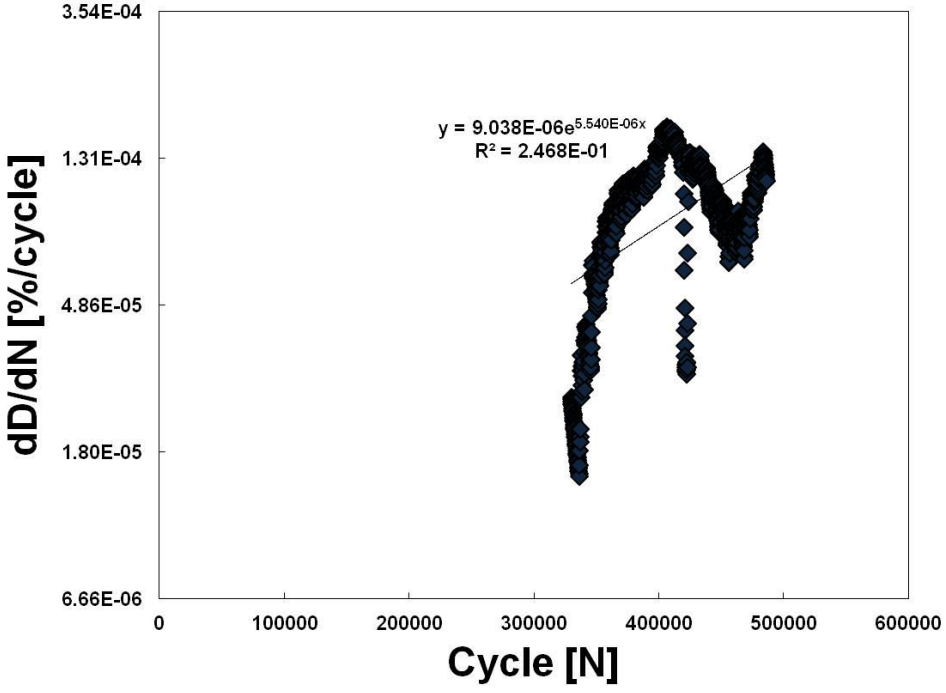

Figure B 7 - Rate of damage accumulation curve of σ_2 - specimen 7.

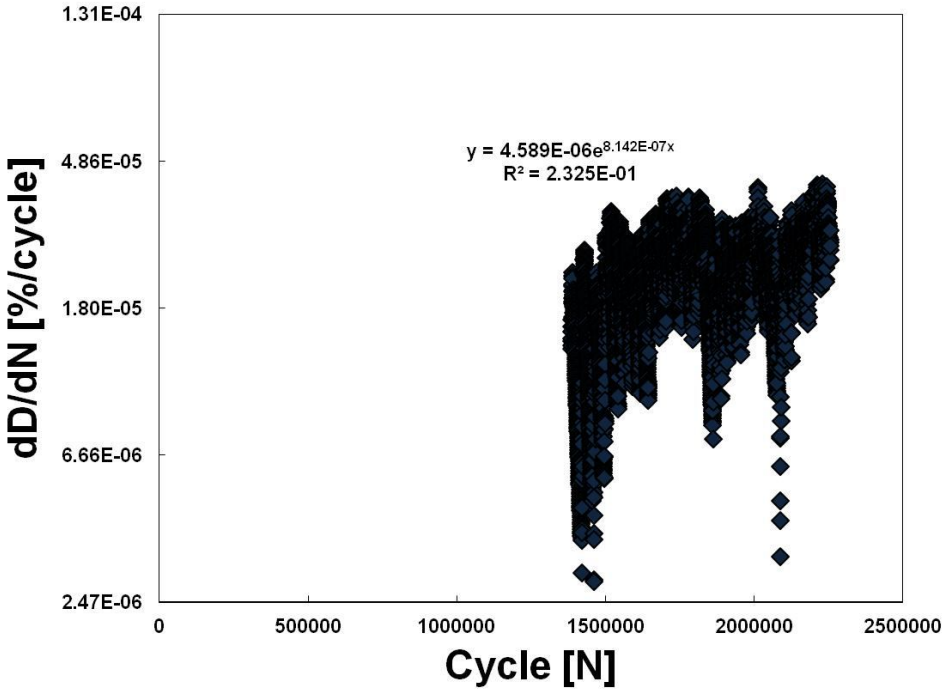

Figure B 8 - Rate of damage accumulation curve of σ_2 - specimen 8.

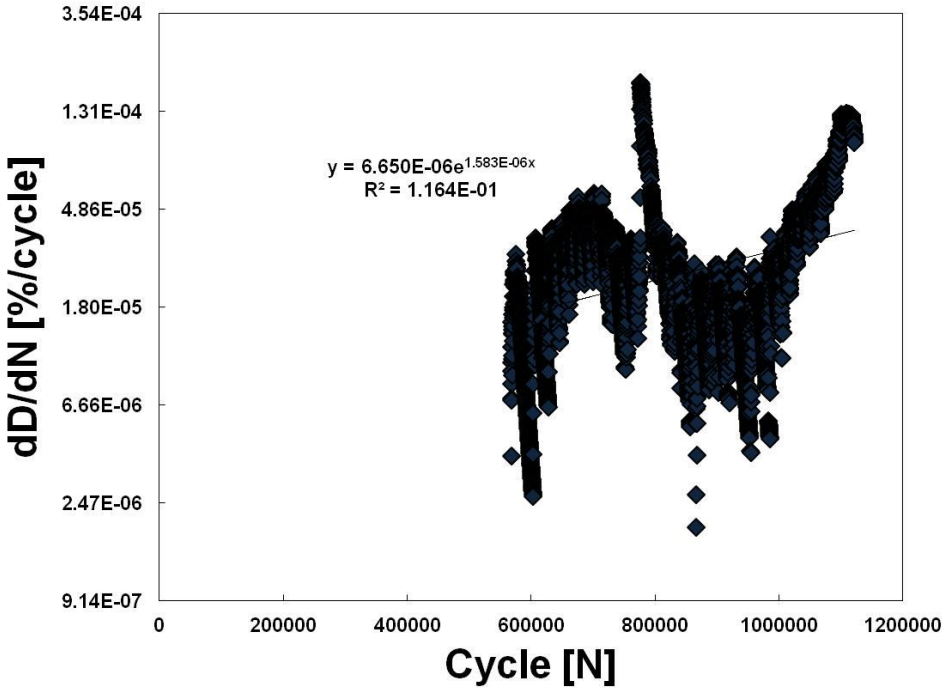

Figure B 9 - Rate of damage accumulation curve of σ_2 - specimen 9.

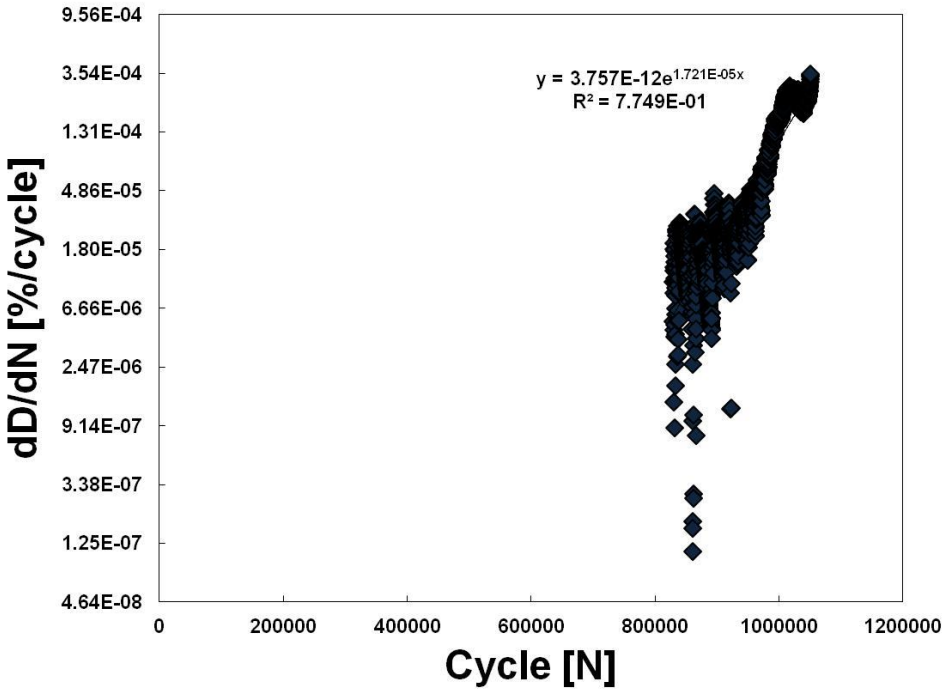

Figure B 10 - Rate of damage accumulation curve of σ_2 - specimen 10.

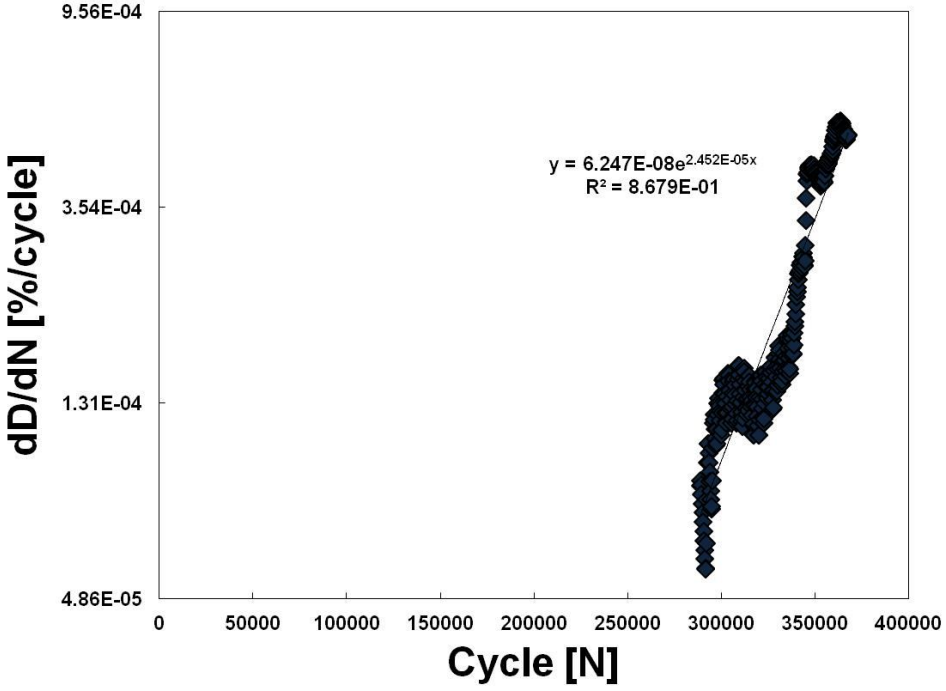

Figure B 11 - Rate of damage accumulation curve of σ_3 - specimen 1.

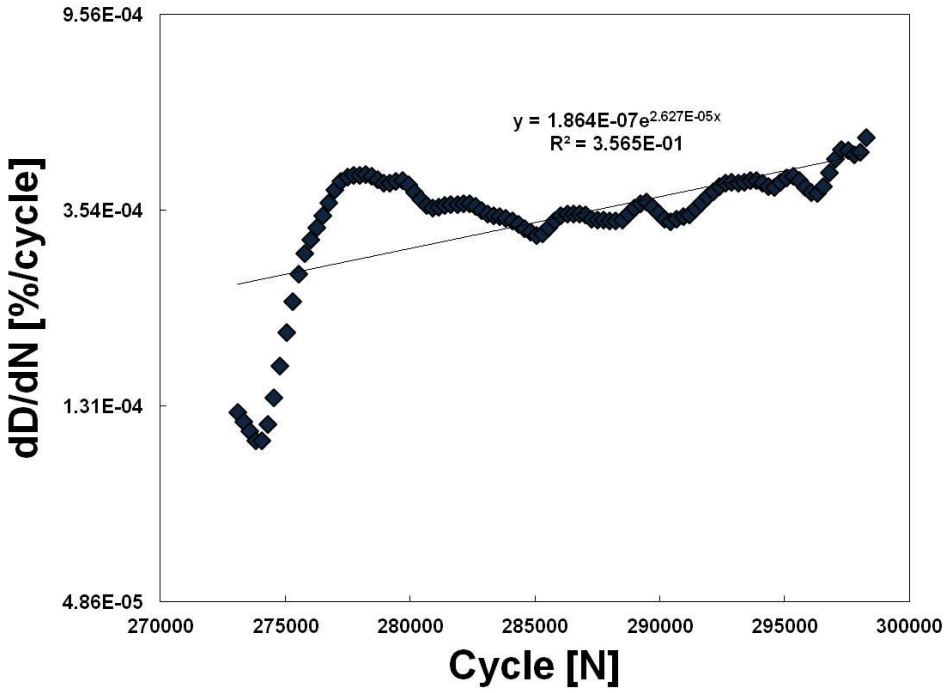

Figure B 12 - Rate of damage accumulation curve of σ_3 - specimen 2.

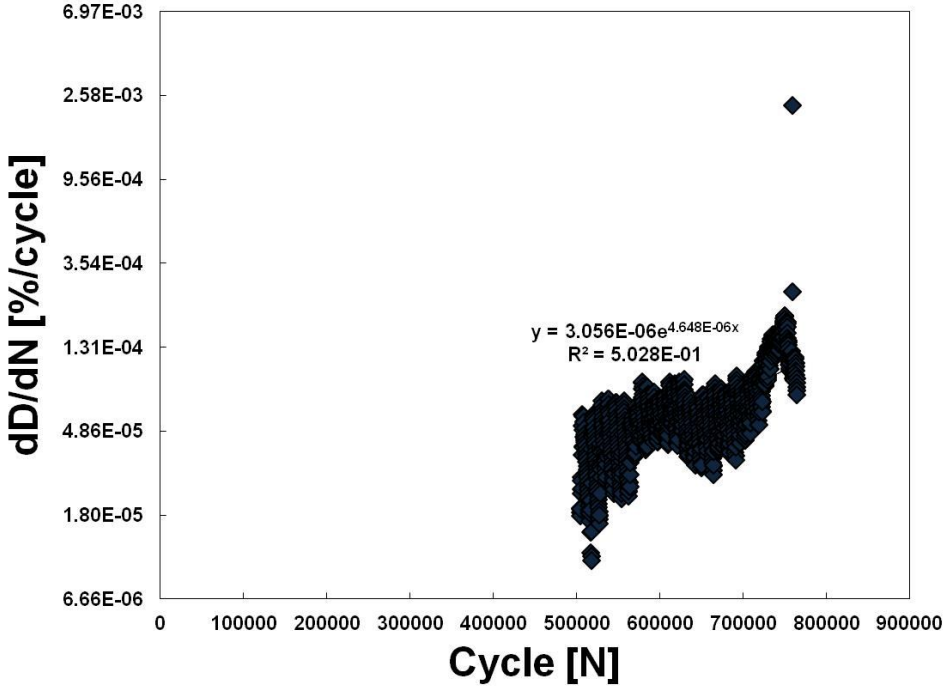

Figure B 13 - Rate of damage accumulation curve of σ_3 - specimen 3.

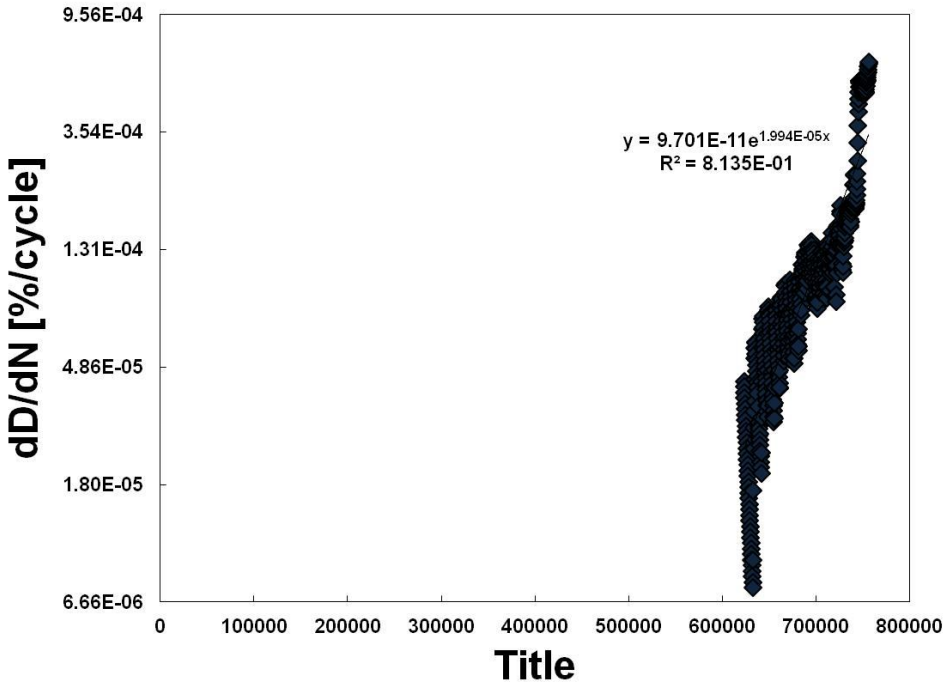

Figure B 14 - Rate of damage accumulation curve of σ_3 - specimen 4.

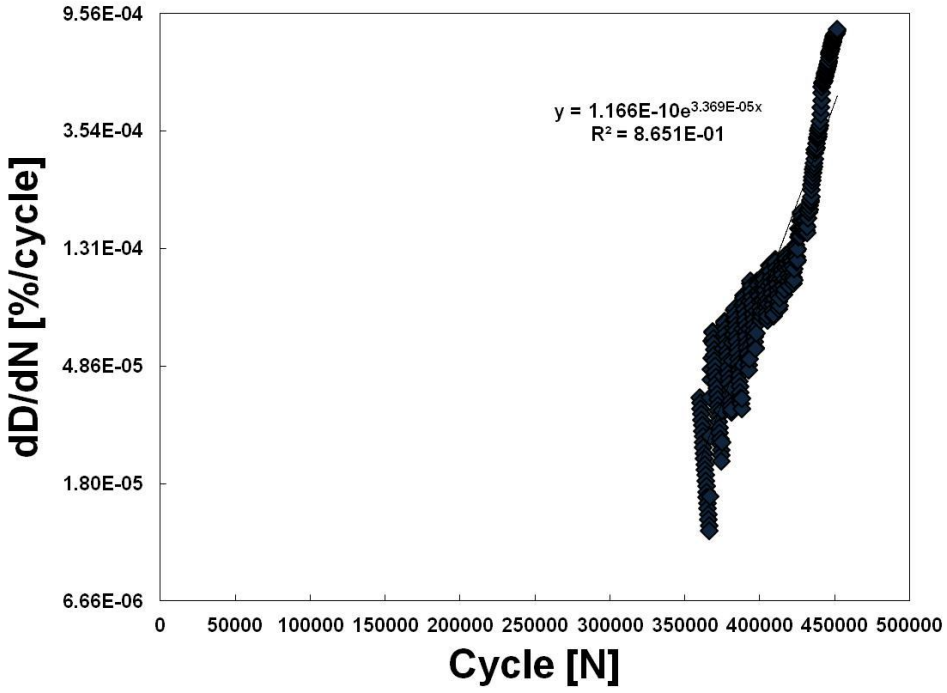

Figure B 15 - Rate of damage accumulation curve of σ_3 - specimen 5.

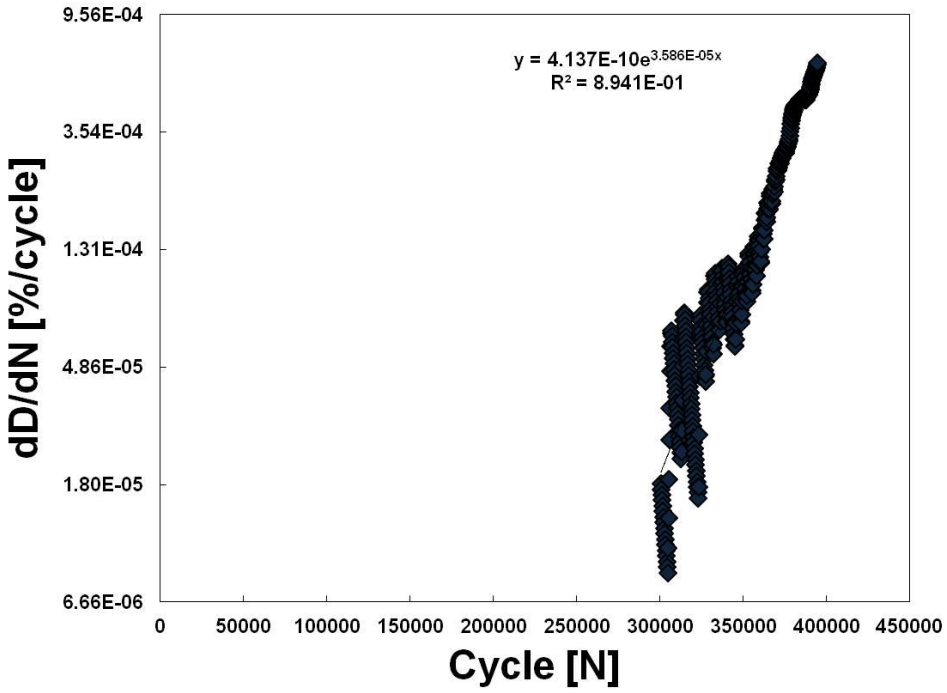

Figure B 16 - Rate of damage accumulation curve of σ_3 - specimen 6.

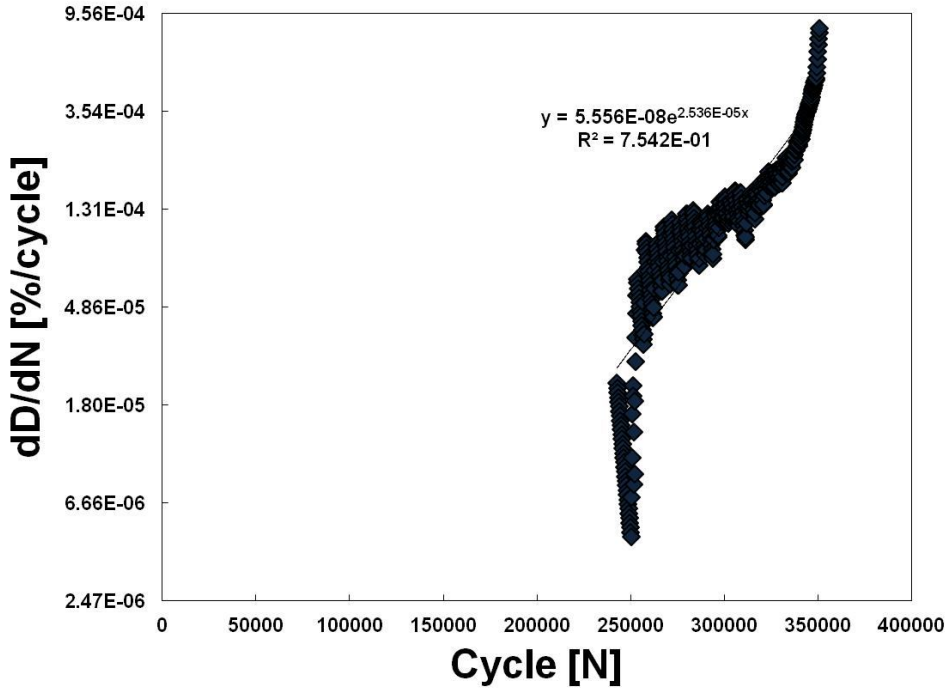

Figure B 17 - Rate of damage accumulation curve of σ_3 - specimen 7.

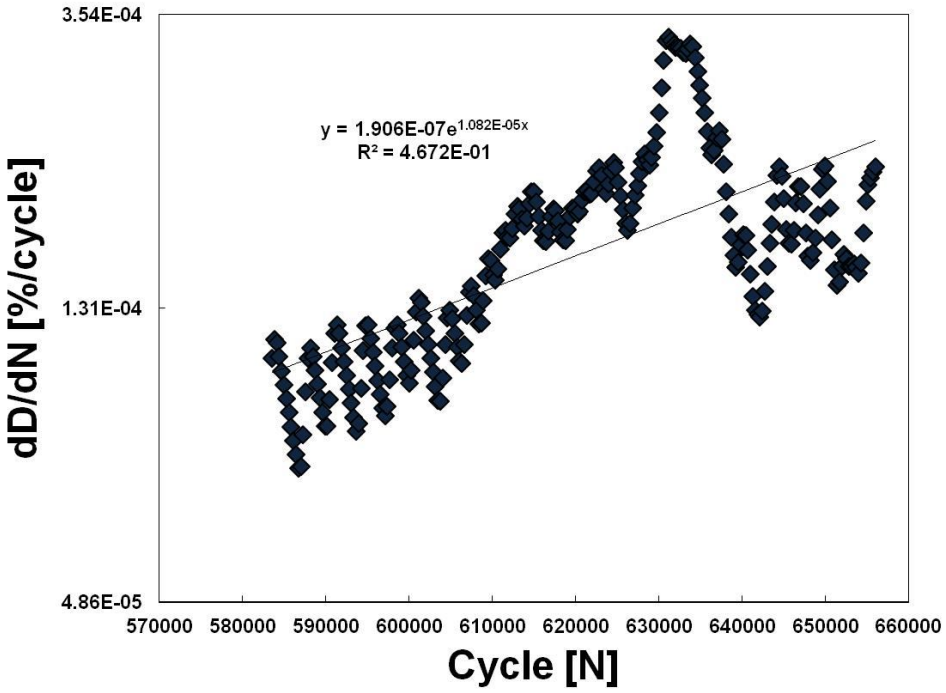

Figure B 18 - Rate of damage accumulation curve of σ_3 - specimen 8.

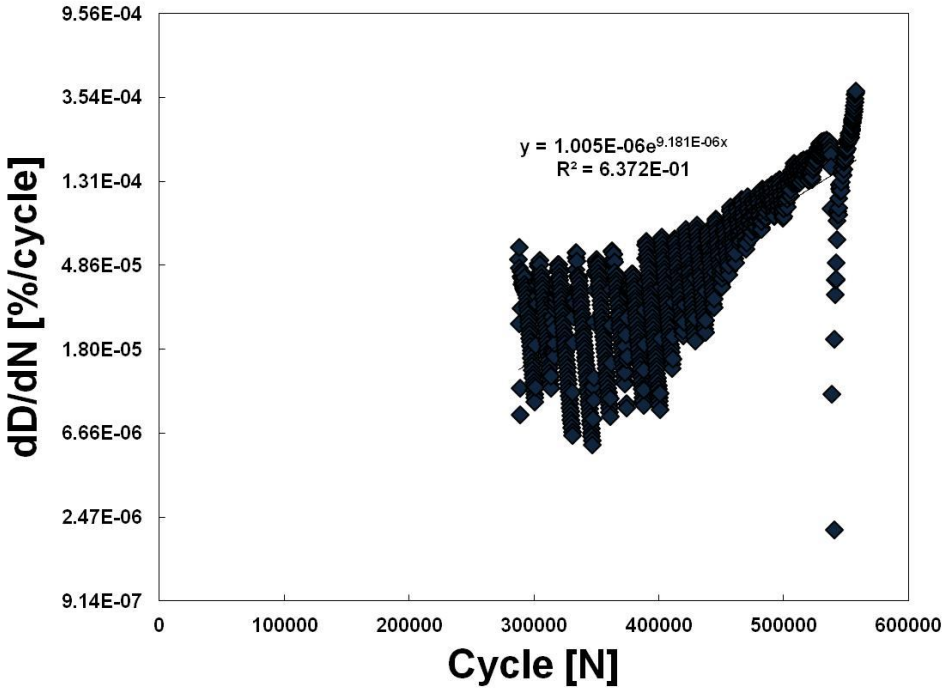

Figure B 19 - Rate of damage accumulation curve of σ_3 - specimen 9.

σ_3 - specimen 10 rate of damage accumulation curve was not available due to DASU failure.

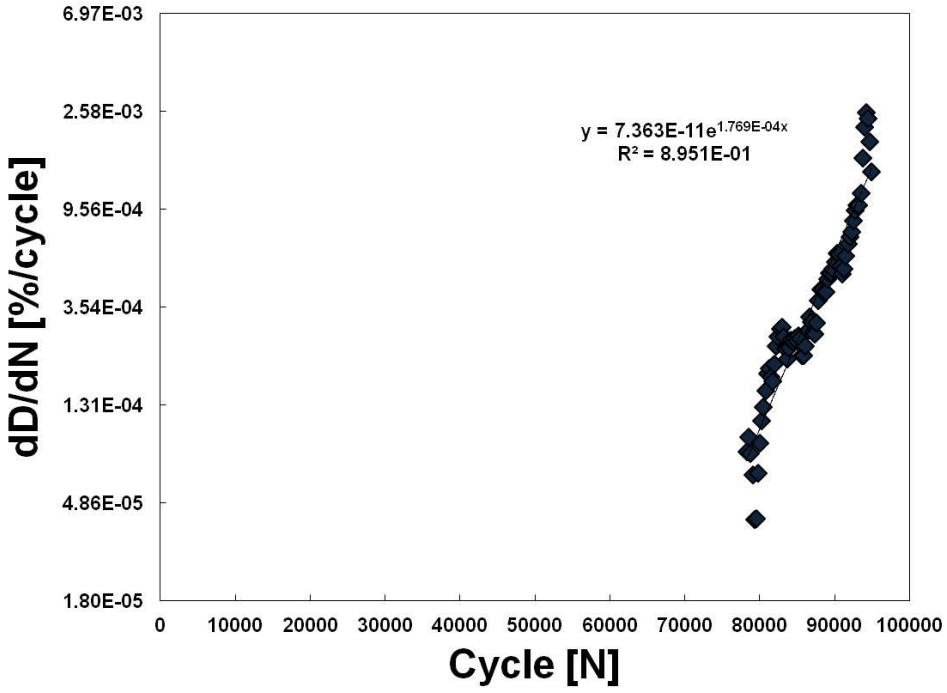

Figure B 20 - Rate of damage accumulation curve of σ_4 - specimen 1.

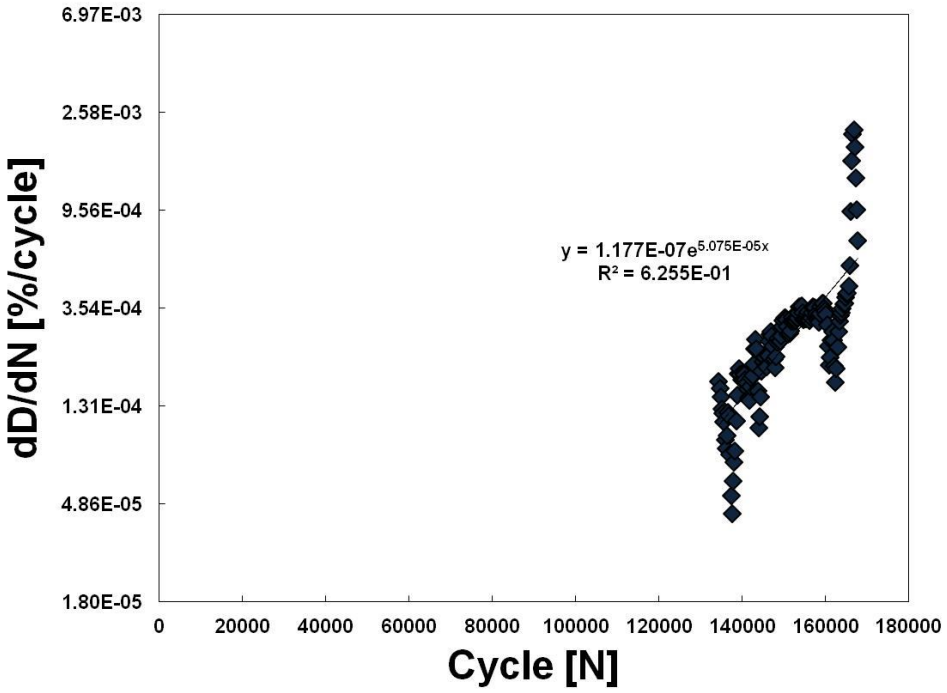

Figure B 21 - Rate of damage accumulation curve of σ_4 - specimen 2.

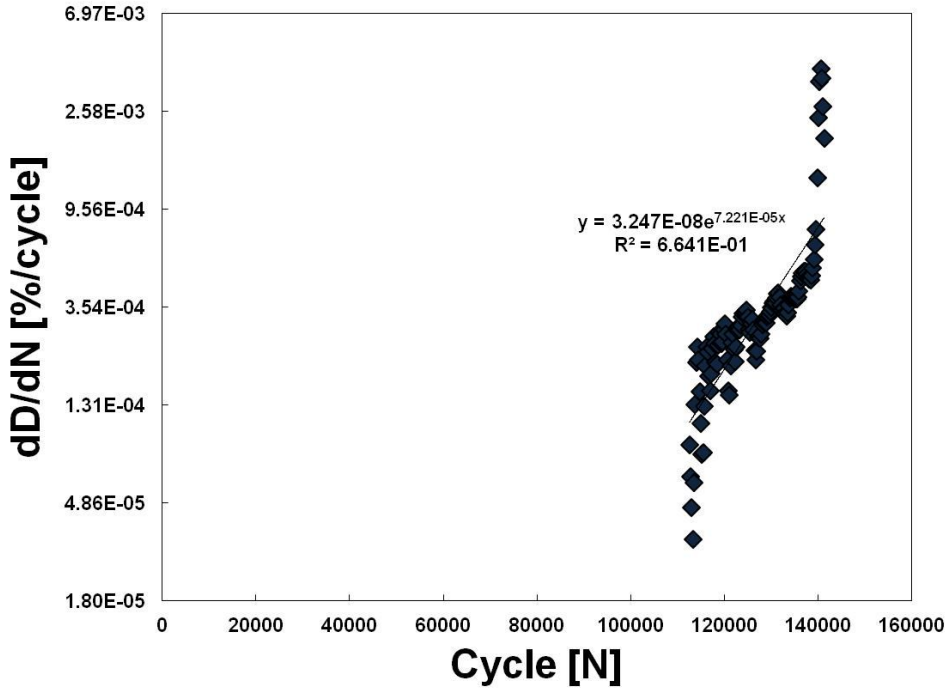

Figure B 22 - Rate of damage accumulation curve of σ_4 - specimen 3.

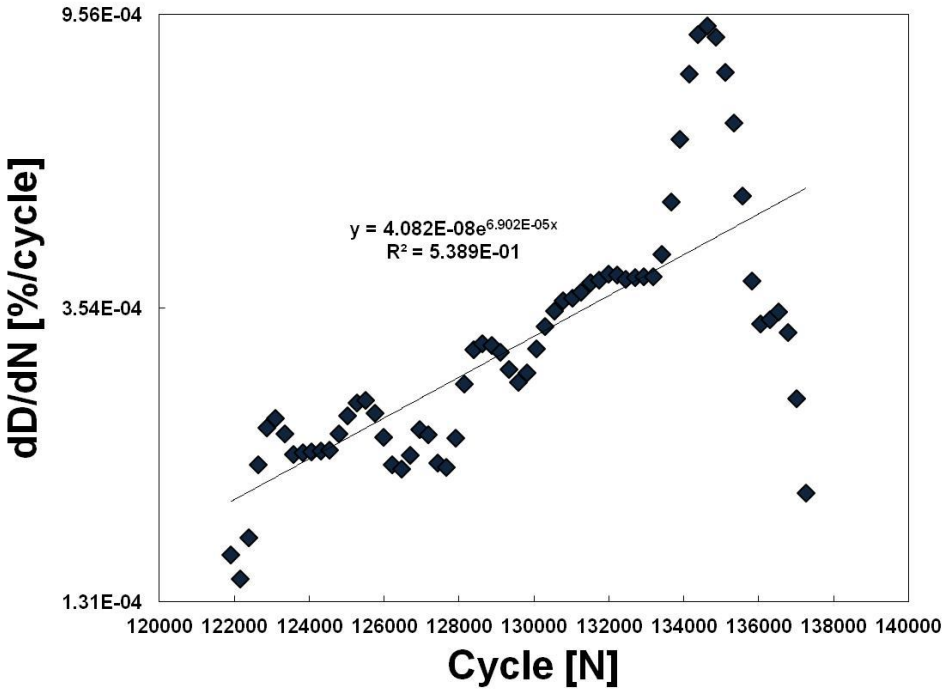

Figure B 23 - Rate of damage accumulation curve of σ_4 - specimen 4.

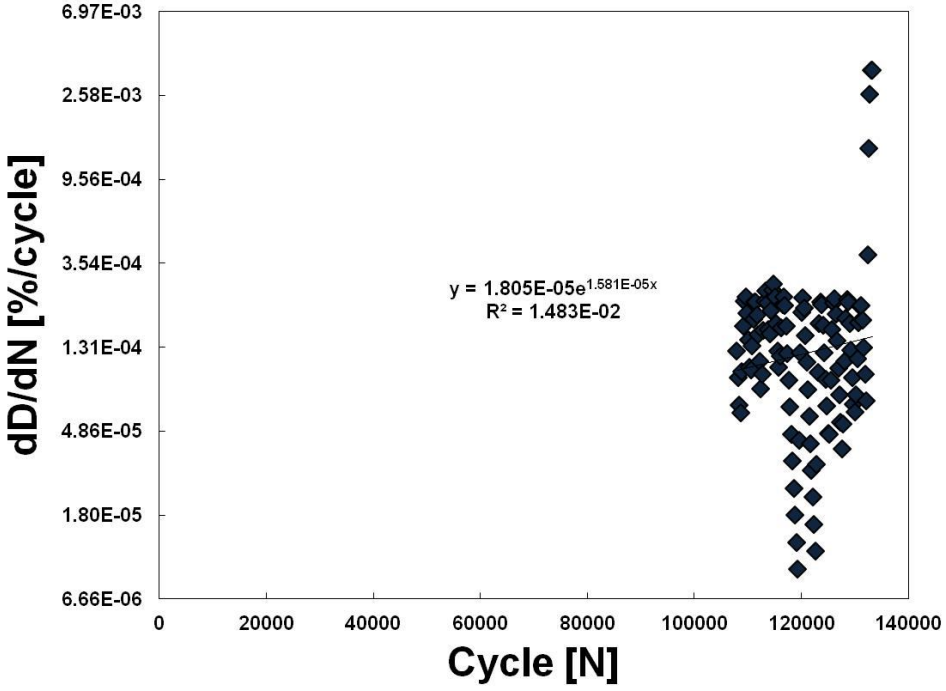

Figure B 24 - Rate of damage accumulation curve of σ_4 - specimen 5.

σ_4 - specimen 6 rate of damage accumulation curve was not available due to DASU failure.

σ_4 - specimen 7 rate of damage accumulation curve was not available due to DASU failure.

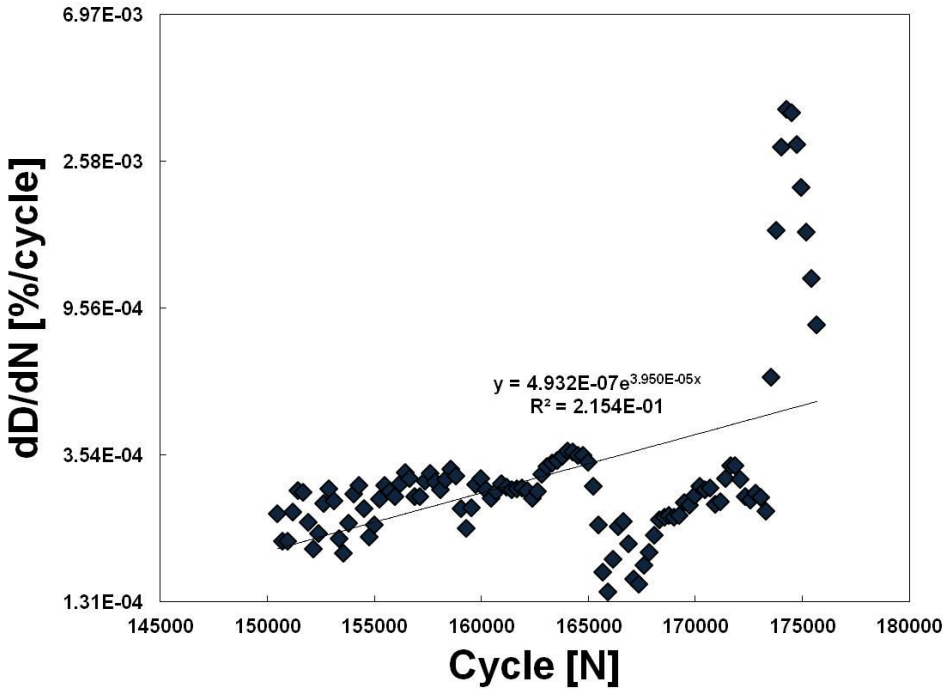

Figure B 25 - Rate of damage accumulation curve of σ_4 - specimen 8.

σ_4 - specimen 9 rate of damage accumulation curve was not available due to DASU failure.

σ_4 - specimen 10 rate of damage accumulation curve was not available due to DASU failure.

σ_5 - specimen 1 rate of damage accumulation curve was not available due to DASU failure.

σ_5 - specimen 2 rate of damage accumulation curve was not available due to DASU failure.

σ_5 - specimen 3 rate of damage accumulation curve was not available due to DASU failure.

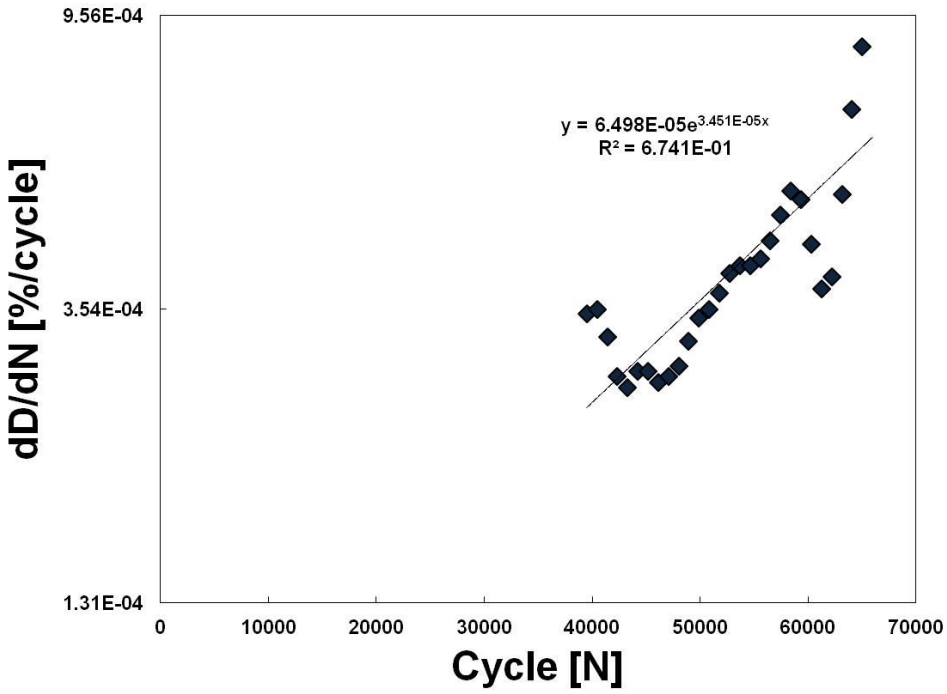

Figure B 26 - Rate of damage accumulation curve of σ_5 - specimen 4.

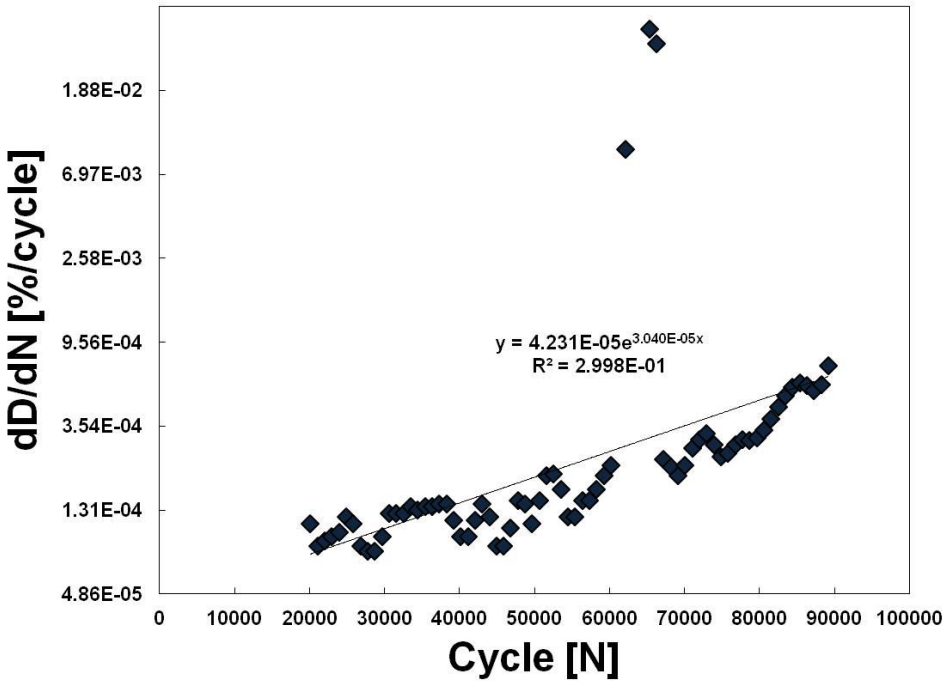

Figure B 27 - Rate of damage accumulation curve of σ_5 - specimen 5.

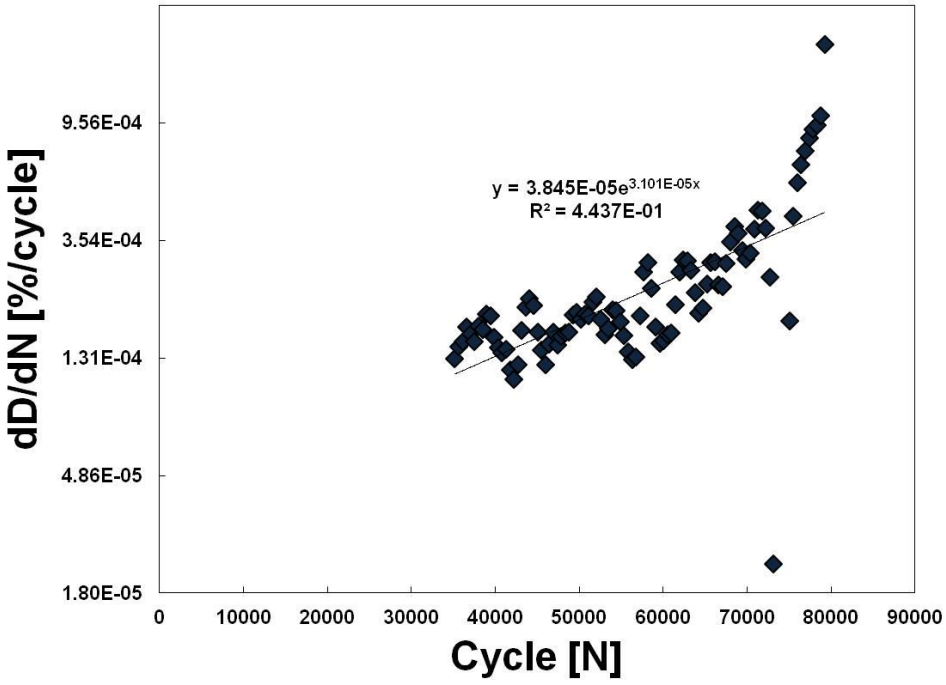

Figure B 28 - Rate of damage accumulation curve of σ_5 - specimen 6.

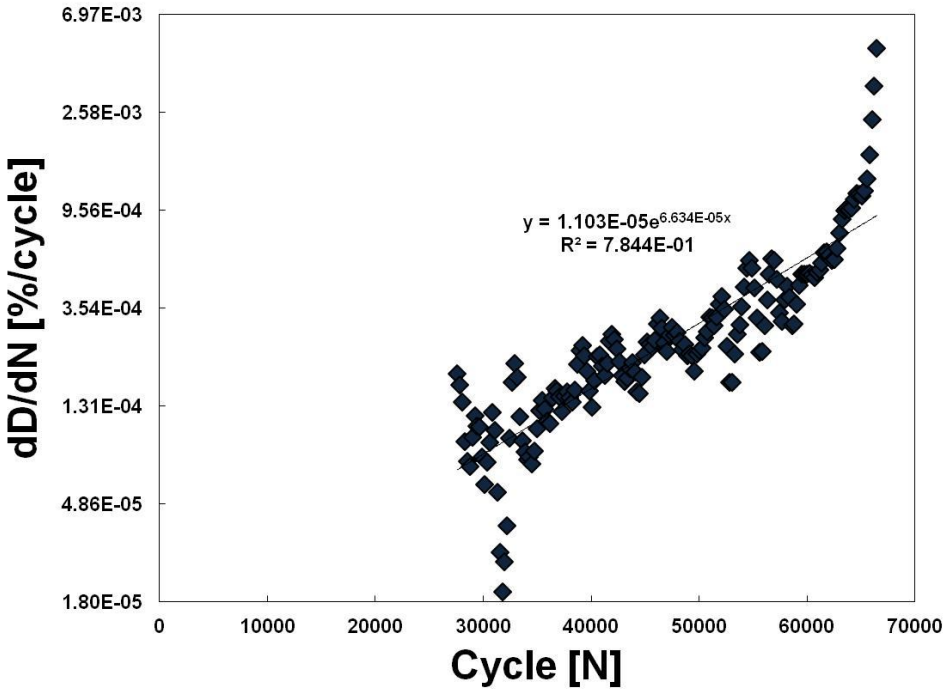

Figure B 29 - Rate of damage accumulation curve of σ_5 - specimen 7.

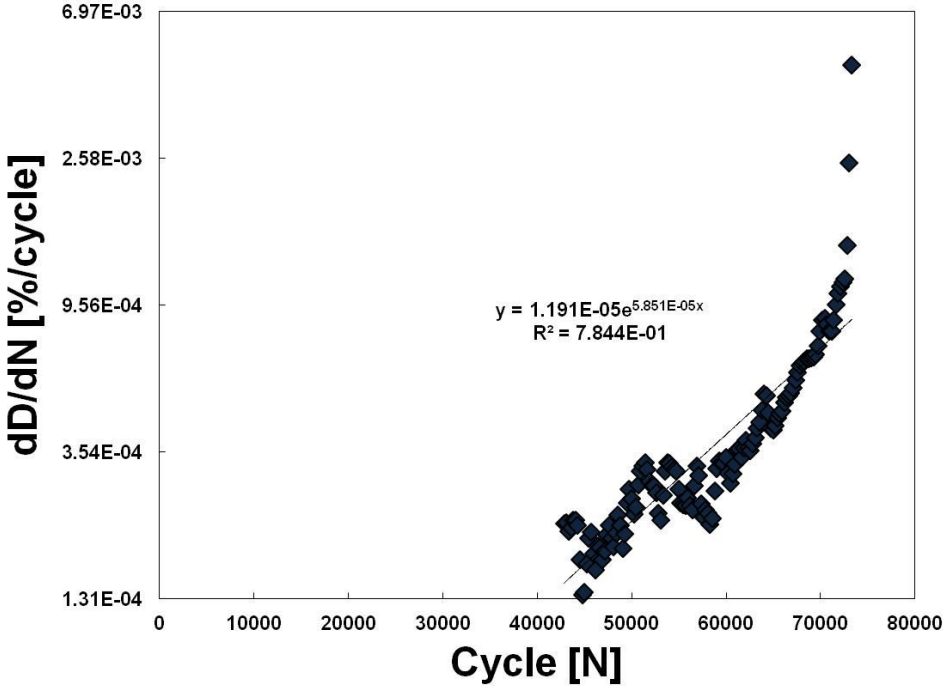

Figure B 30 - Rate of damage accumulation curve of σ_5 - specimen 8.

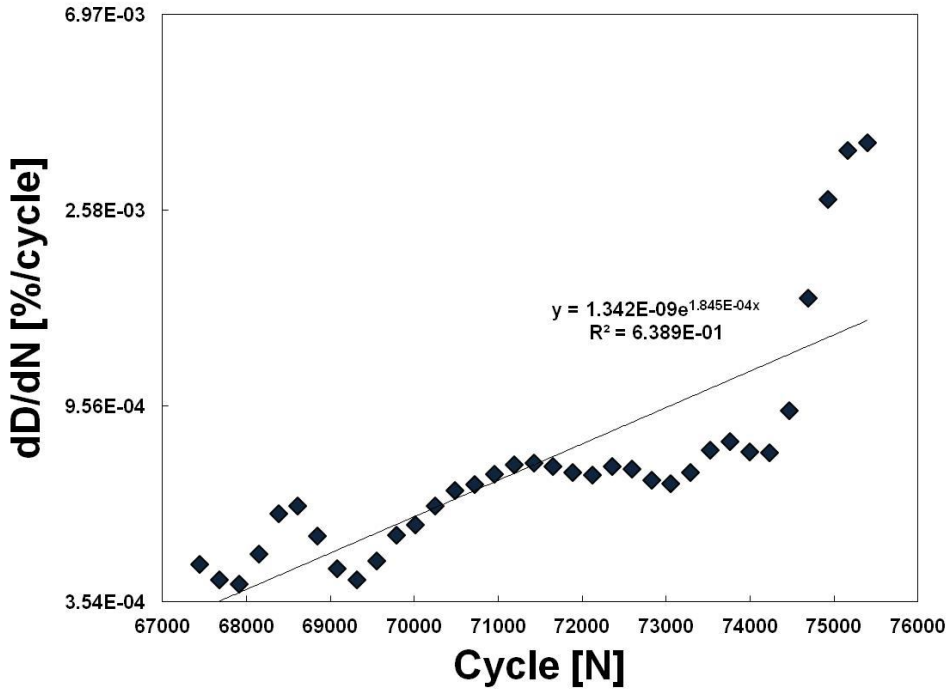

Figure B 31 - Rate of damage accumulation curve of σ_5 - specimen 9.

σ_5 - specimen 10 rate of damage accumulation curve was not available due to DASU failure.

APPENDIX C – QUASI-STATIC LOAD VS. MID-SPAN DEFLECTION PLOTS FOR AGED SPECIMENS

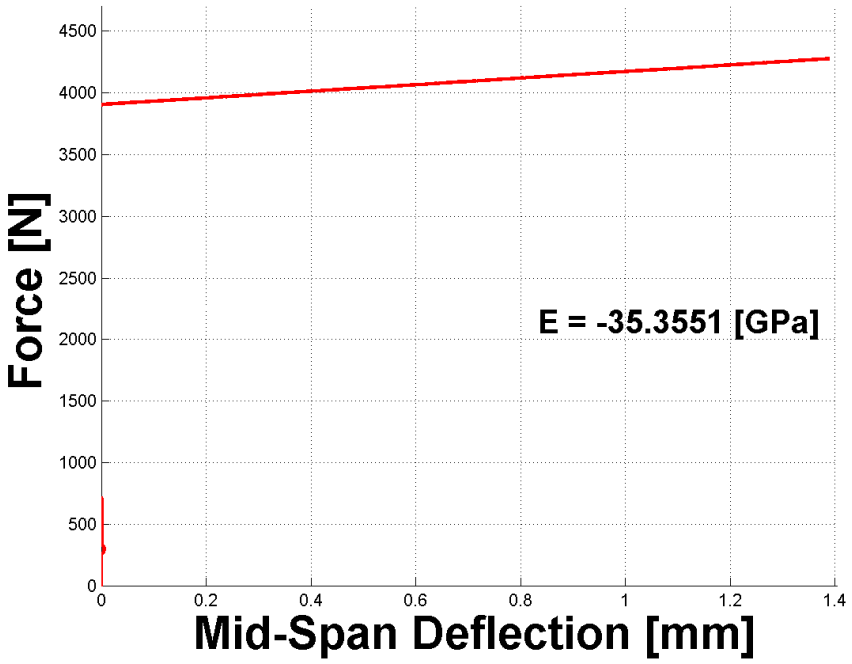

Figure C 1 – Load vs. mid-span deflection for Specimen 1 that had been aged at 180 °C for 3 months. Note: the LVDT hung up during the test, invalidating the effective axial modulus measurement, however, the strength value remained valid.

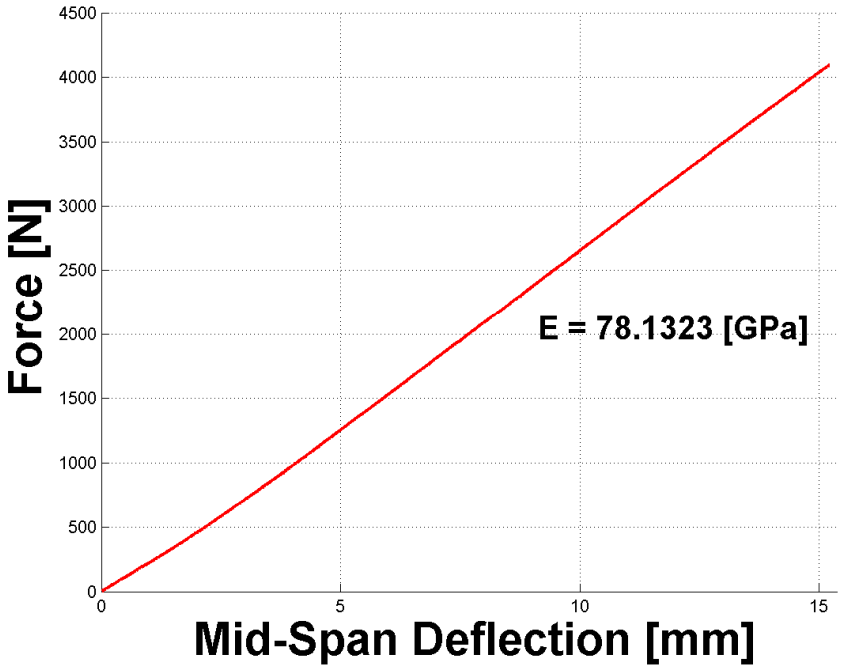

Figure C 2 - Load vs. mid-span deflection for Specimen 2 that had been aged at 180 °C for 3 months.

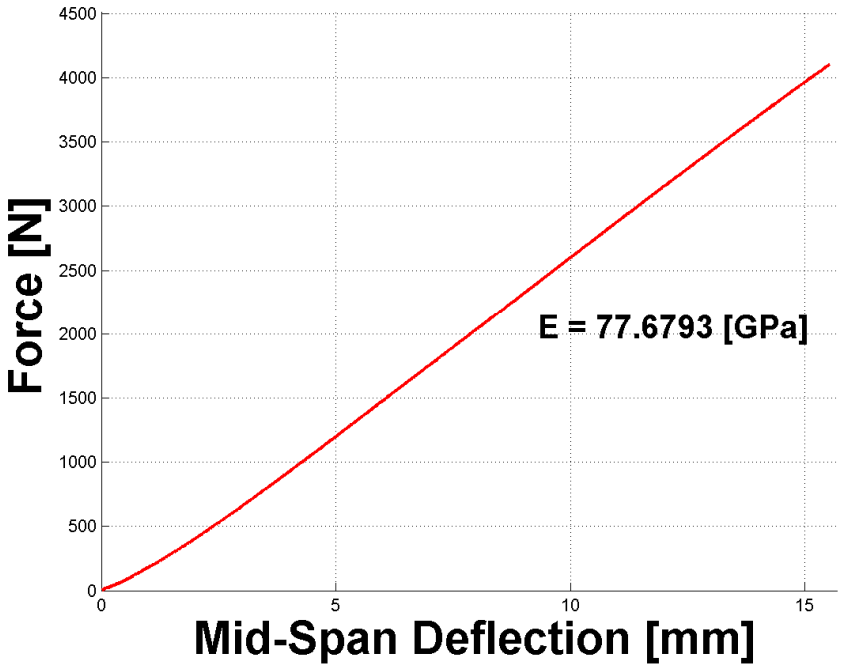

Figure C 3 - Load vs. mid-span deflection for Specimen 3 that had been aged at 180 °C for 3 months.

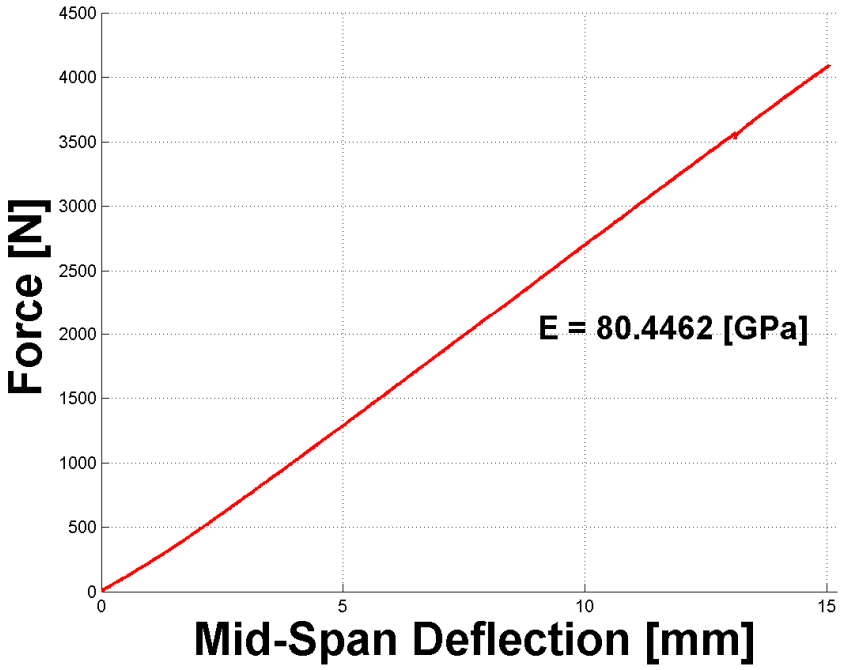

Figure C 4 - Load vs. mid-span deflection for Specimen 4 that had been aged at 180 °C for 3 months.

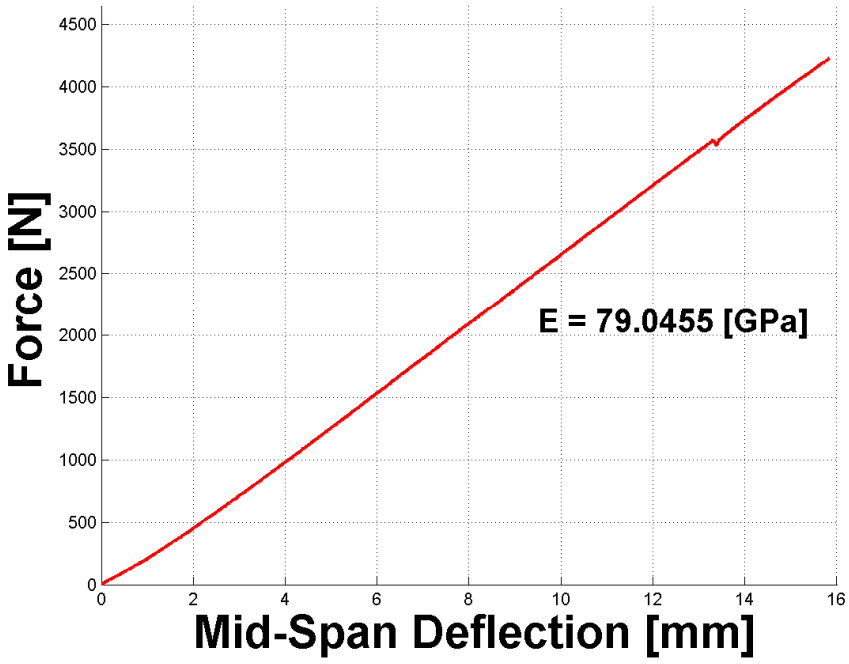

Figure C 5 - Load vs. mid-span deflection for Specimen 5 that had been aged at 180 °C for 3 months.

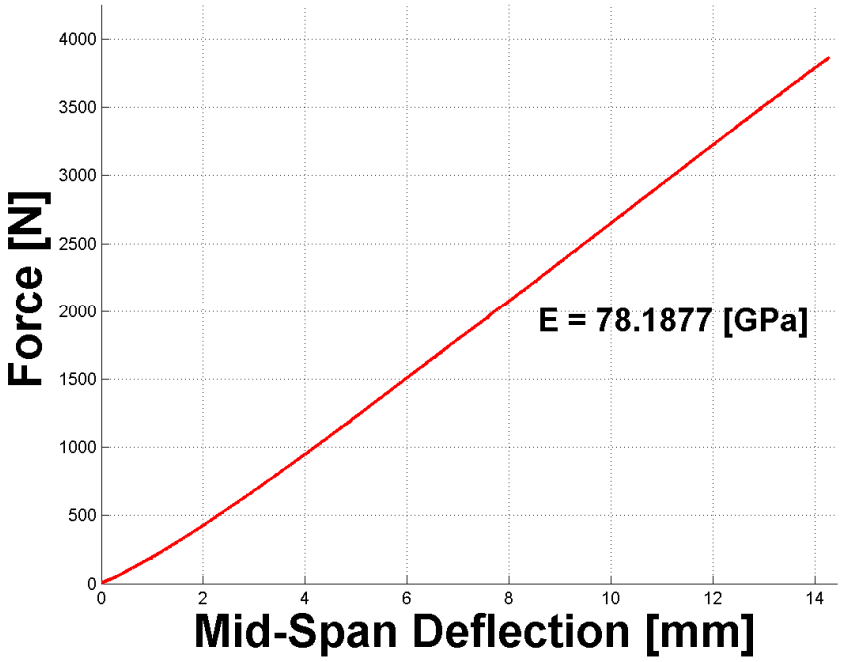

Figure C 6 - Load vs. mid-span deflection for Specimen 1 that had been aged at 180 °C for 6 months.

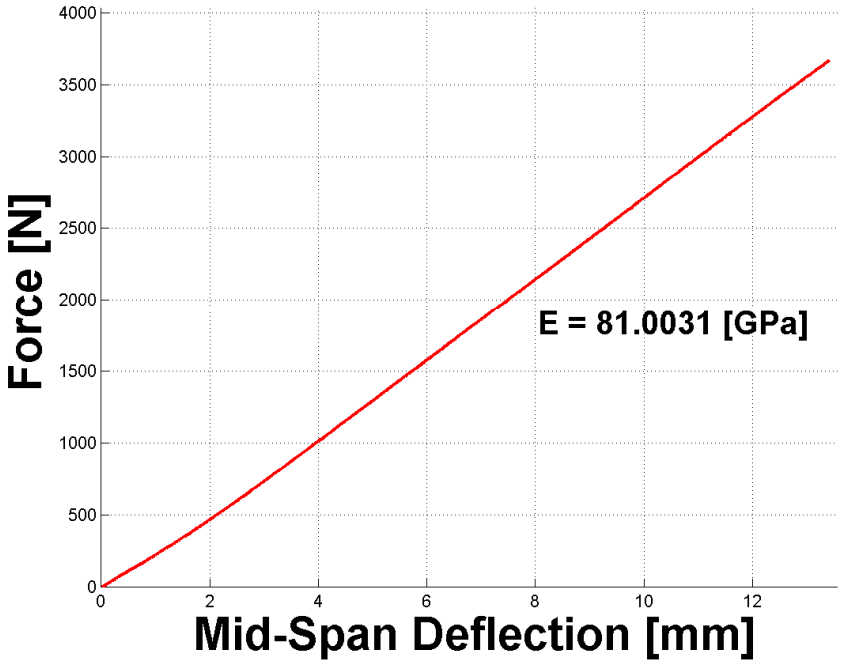

Figure C 7 - Load vs. mid-span deflection for Specimen 2 that had been aged at 180 °C for 6 months.

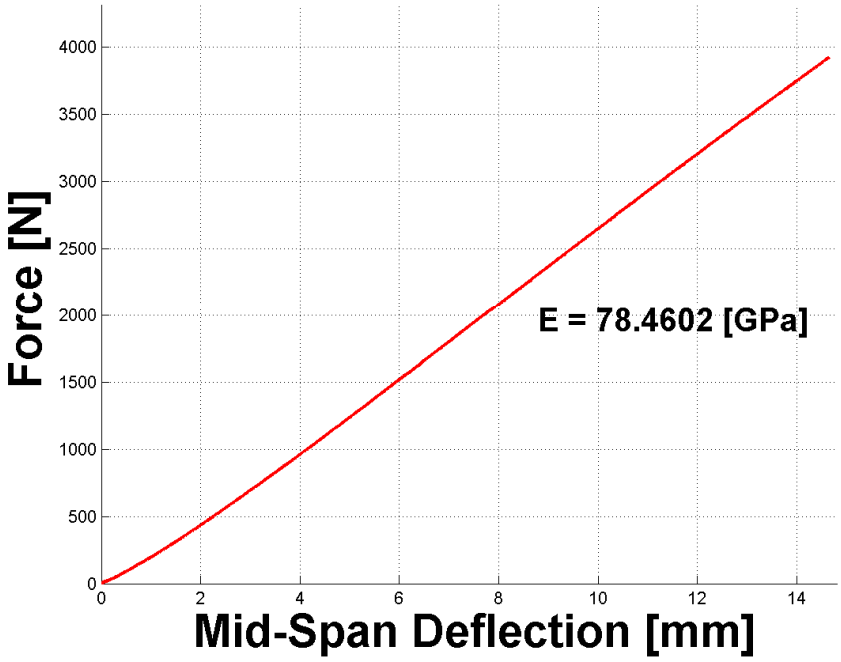

Figure C 8 - Load vs. mid-span deflection for Specimen 3 that had been aged at 180 °C for 6 months.

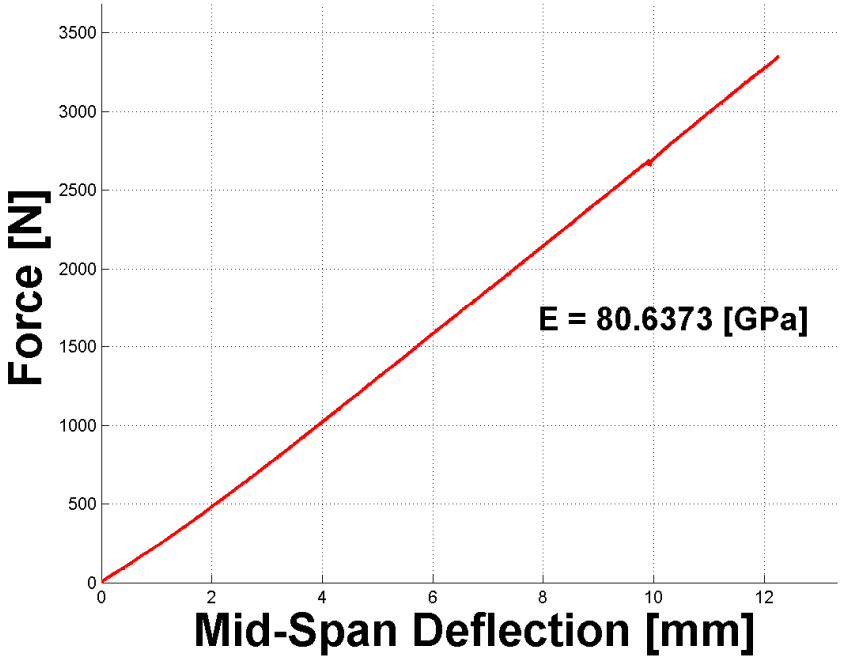

Figure C 9 - Load vs. mid-span deflection for Specimen 4 that had been aged at 180 °C for 6 months.

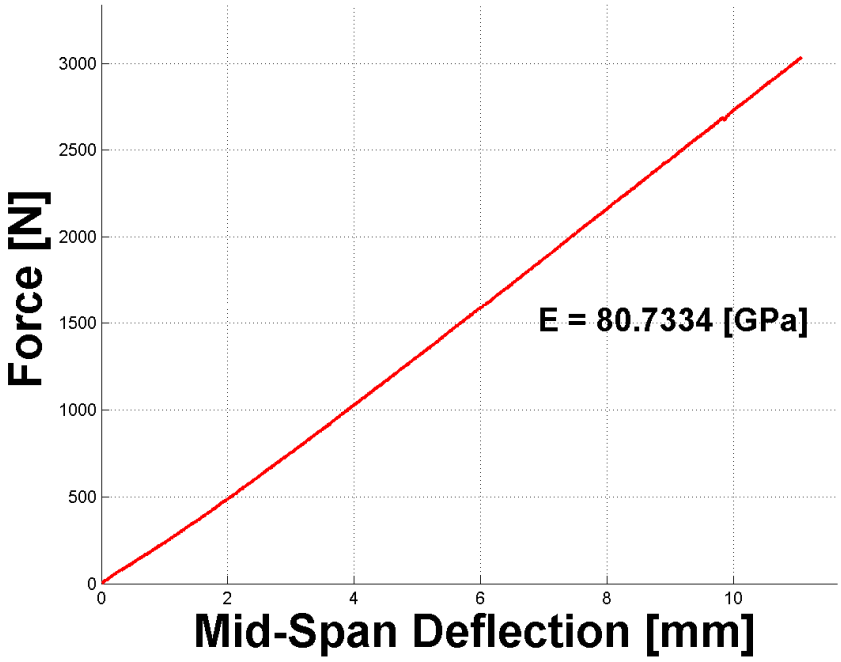

Figure C 10 - Load vs. mid-span deflection for Specimen 5 that had been aged at 180 °C for 6 months.

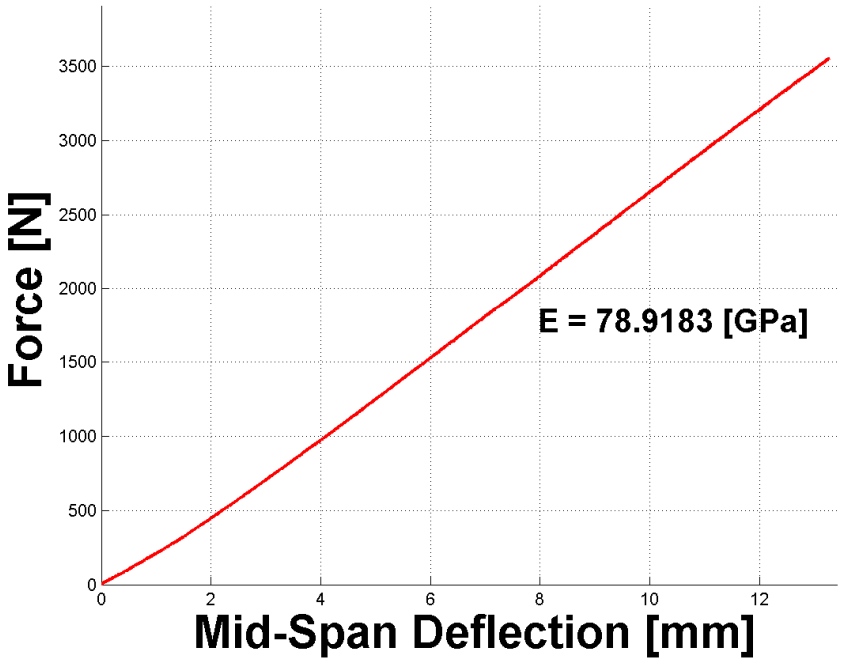

Figure C 11 - Load vs. mid-span deflection for Specimen 1 that had been aged at 180 °C for 9 months.

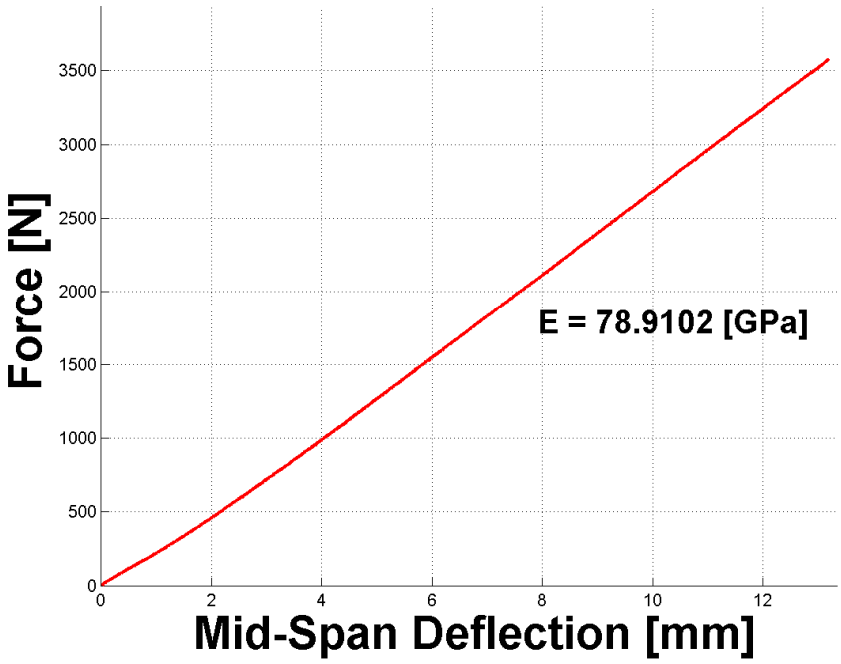

Figure C 12 - Load vs. mid-span deflection for Specimen 2 that had been aged at 180 °C for 9 months.

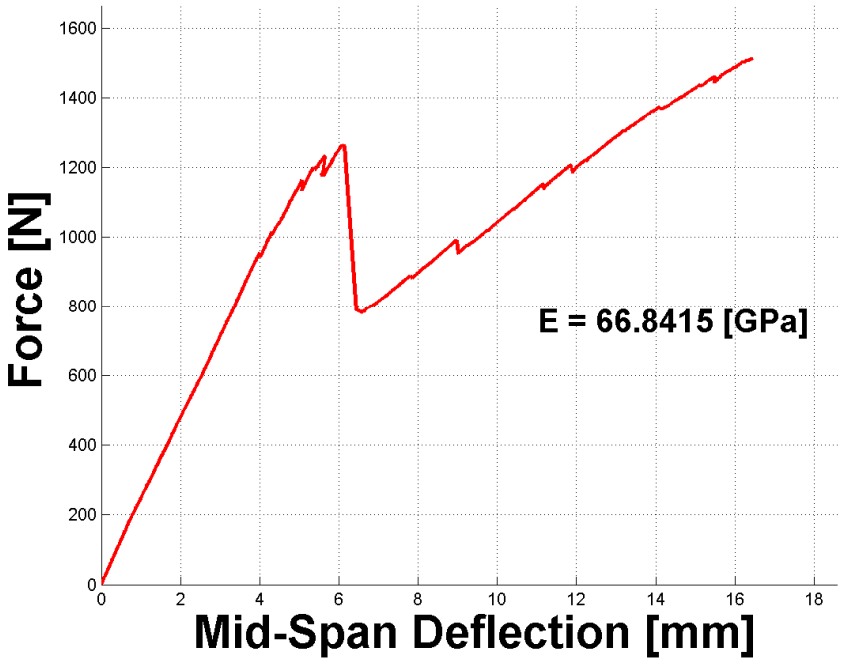

Figure C 13 - Load vs. mid-span deflection for Specimen 1 that had been aged at 180 °C for 12 months.

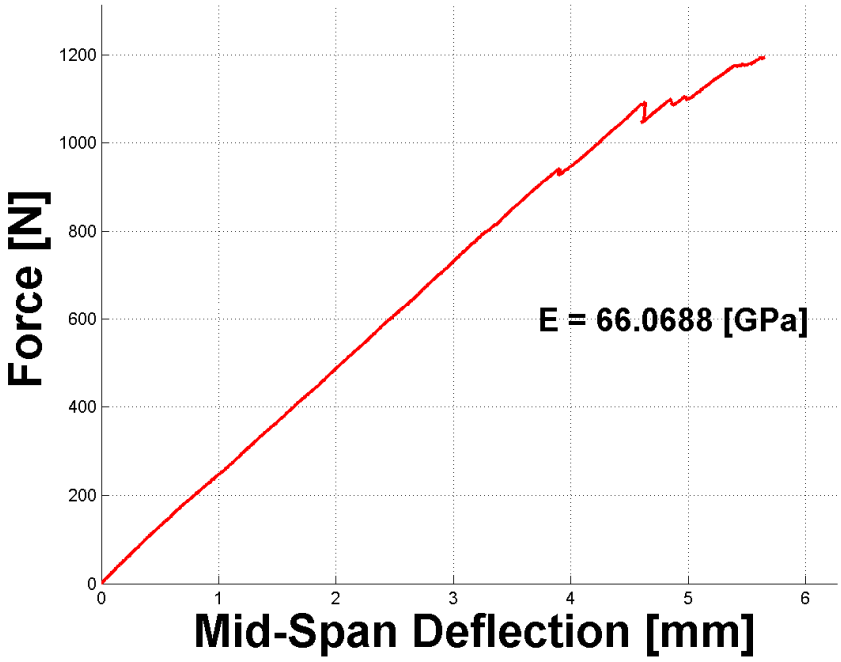

Figure C 14 - Load vs. mid-span deflection for Specimen 2 that had been aged at 180 °C for 12 months.

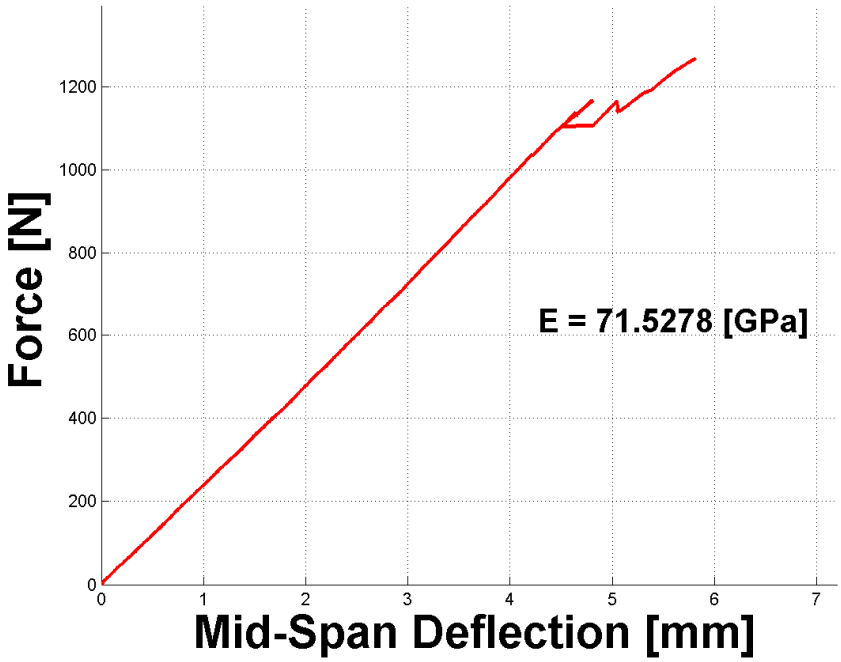

Figure C 15 - Load vs. mid-span deflection for Specimen 3 that had been aged at 180 °C for 12 months.

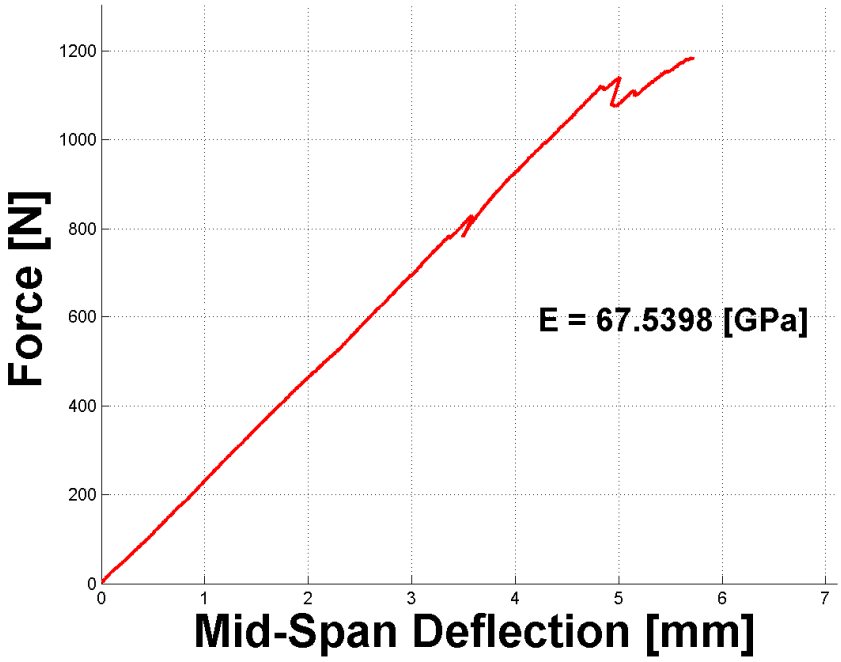

Figure C 16 - Load vs. mid-span deflection for Specimen 4 that had been aged at 180 °C for 12 months.

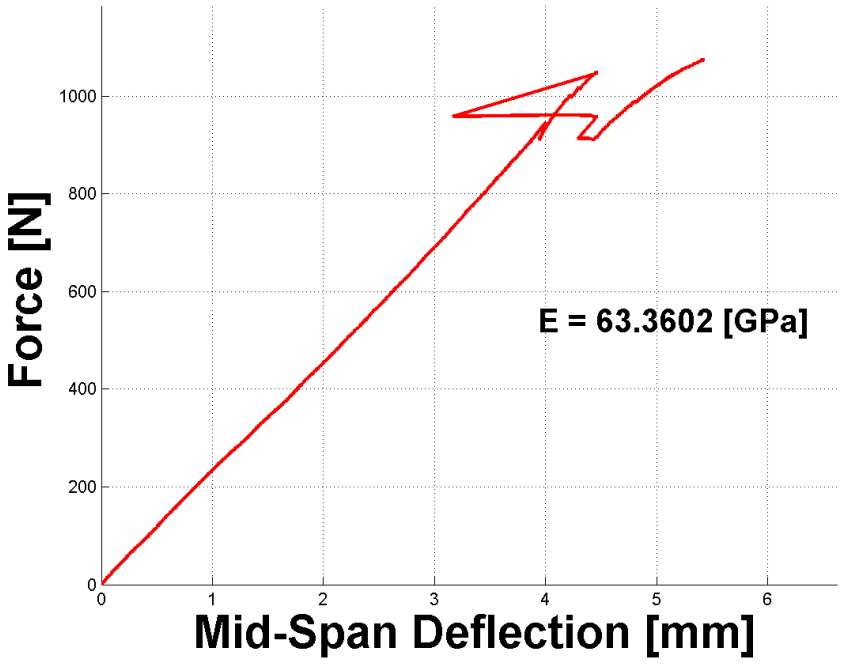

Figure C 17 - Load vs. mid-span deflection for Specimen 5 that had been aged at 180 °C for 12 months.

APPENDIX D - FATIGUE DAMAGE CURVES OF AGED SPECIMENS

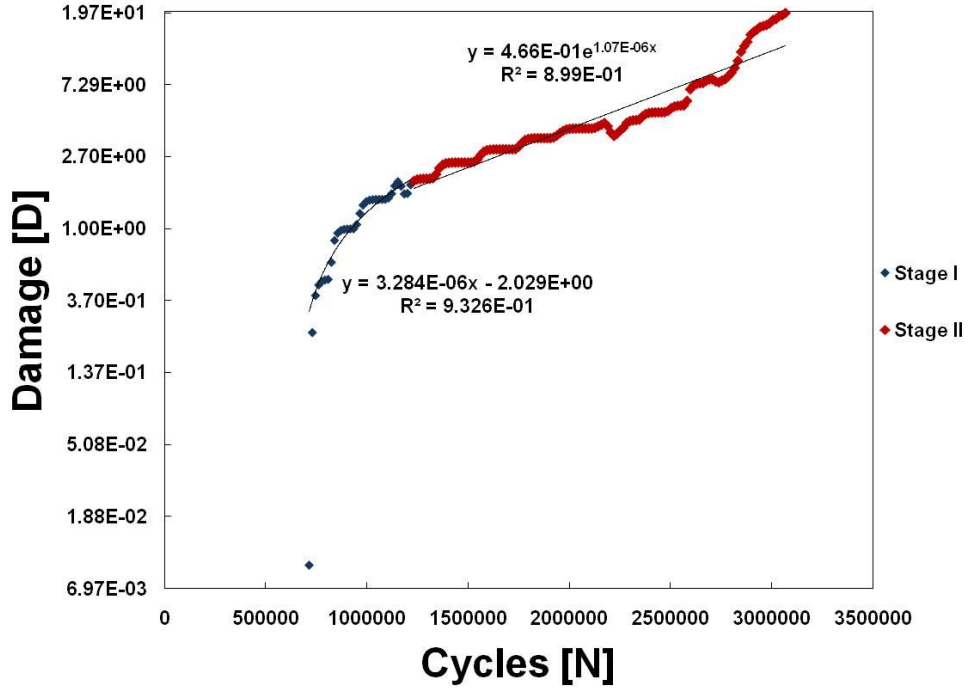

Figure D 1 – Damage curve of 3 month aged σ_1 – specimen 1.

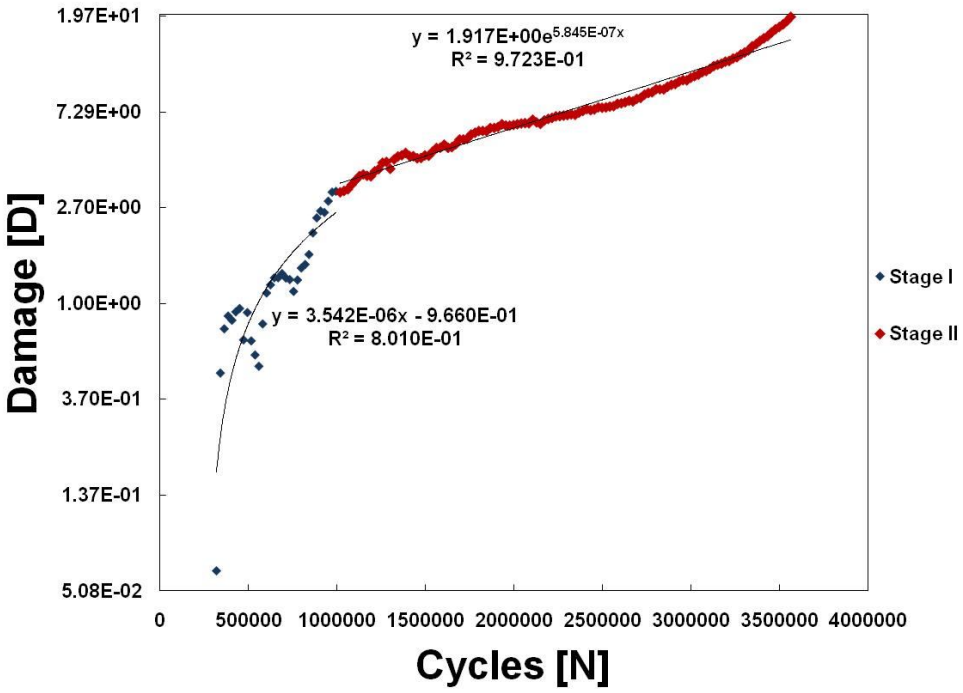

Figure D 2 - Damage curve of 3 month aged σ_1 – specimen 2.

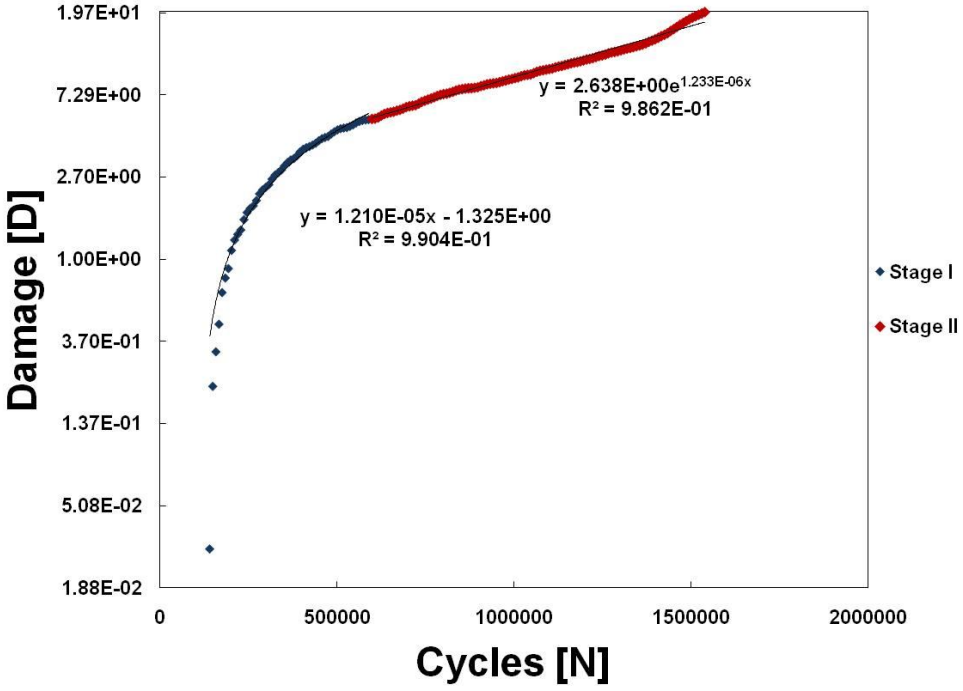

Figure D 3 - Damage curve of 3 month aged σ_1 – specimen 3.

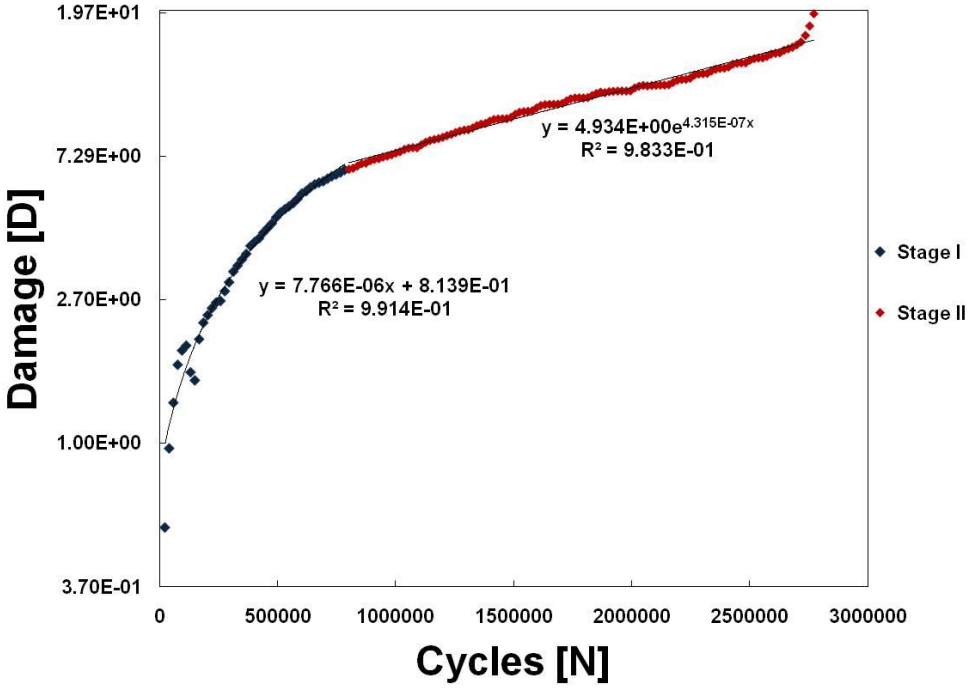

Figure D 4 - Damage curve of 3 month aged σ_1 – specimen 4.

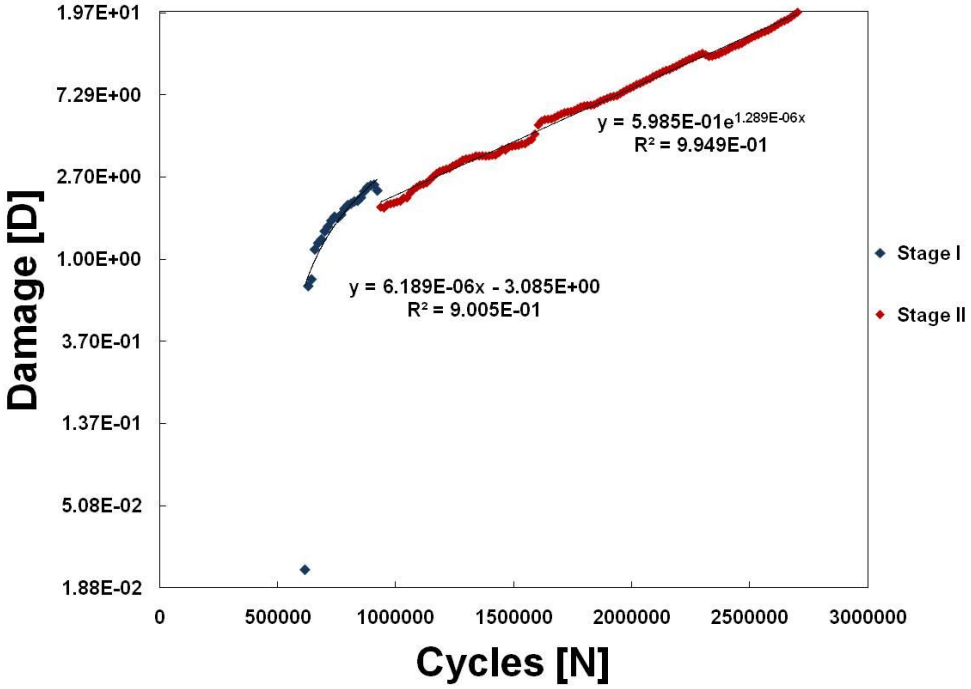

Figure D 5 - Damage curve of 3 month aged σ_1 – specimen 5.

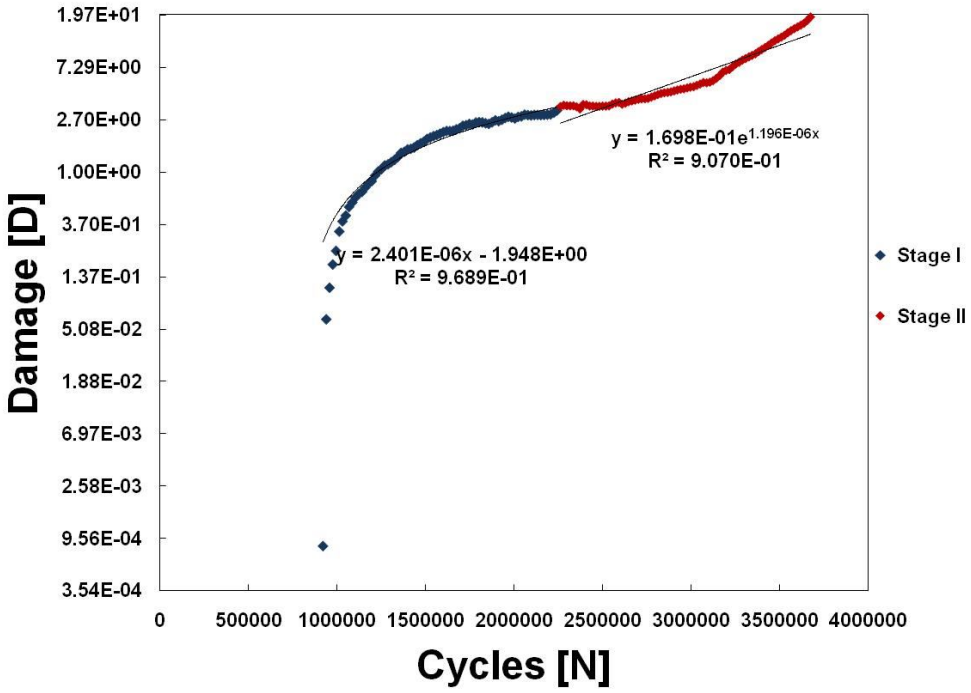

Figure D 6 - Damage curve of 3 month aged σ_1 – specimen 6.

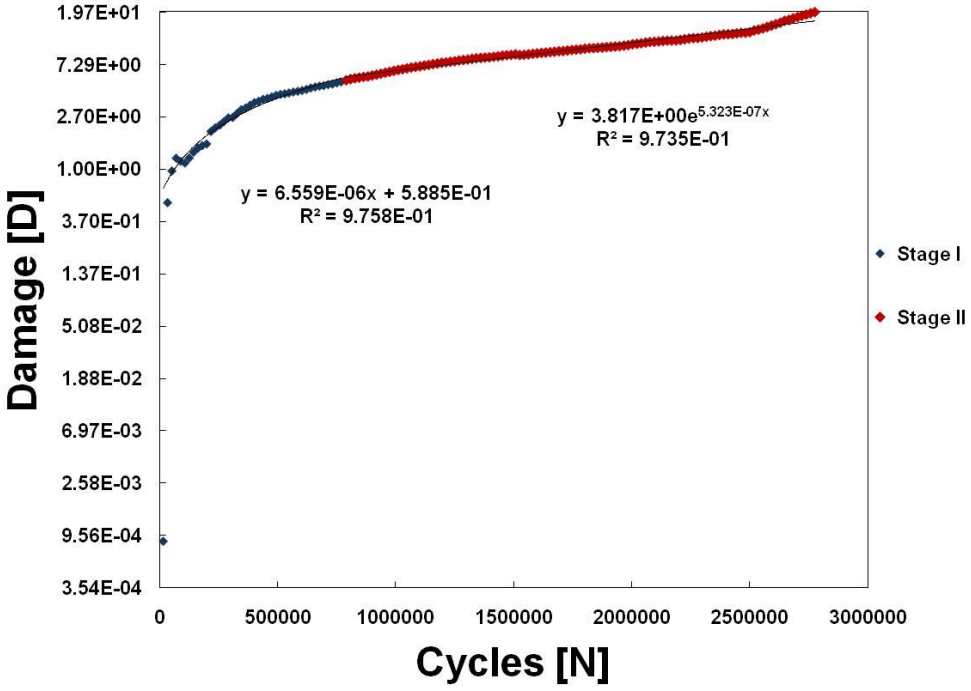

Figure D 7 - Damage curve of 3 month aged σ_1 – specimen 7.

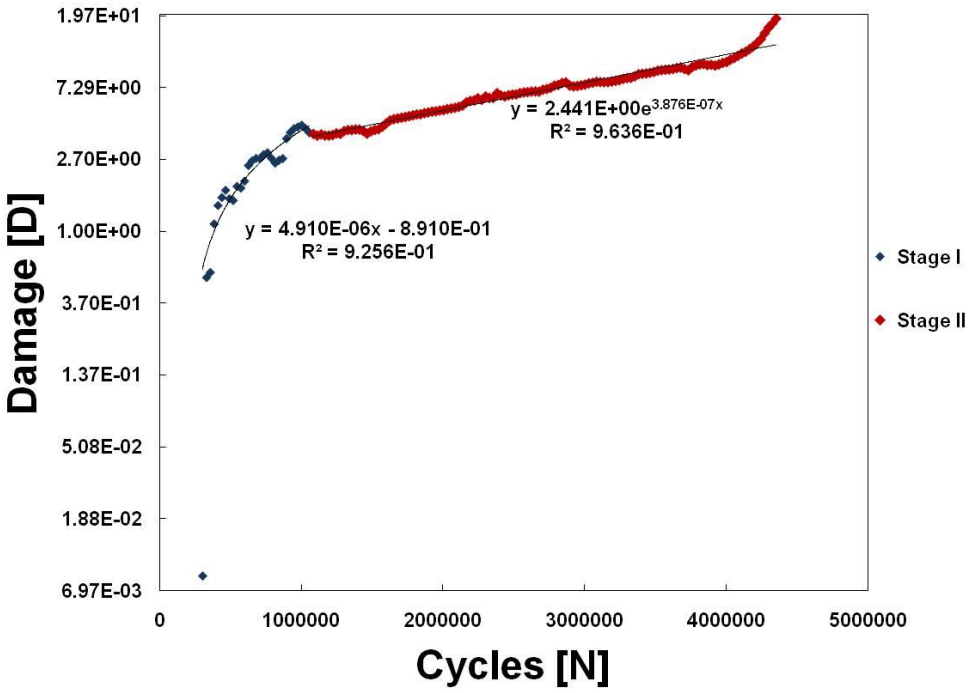

Figure D 8 - Damage curve of 3 month aged σ_1 – specimen 8.

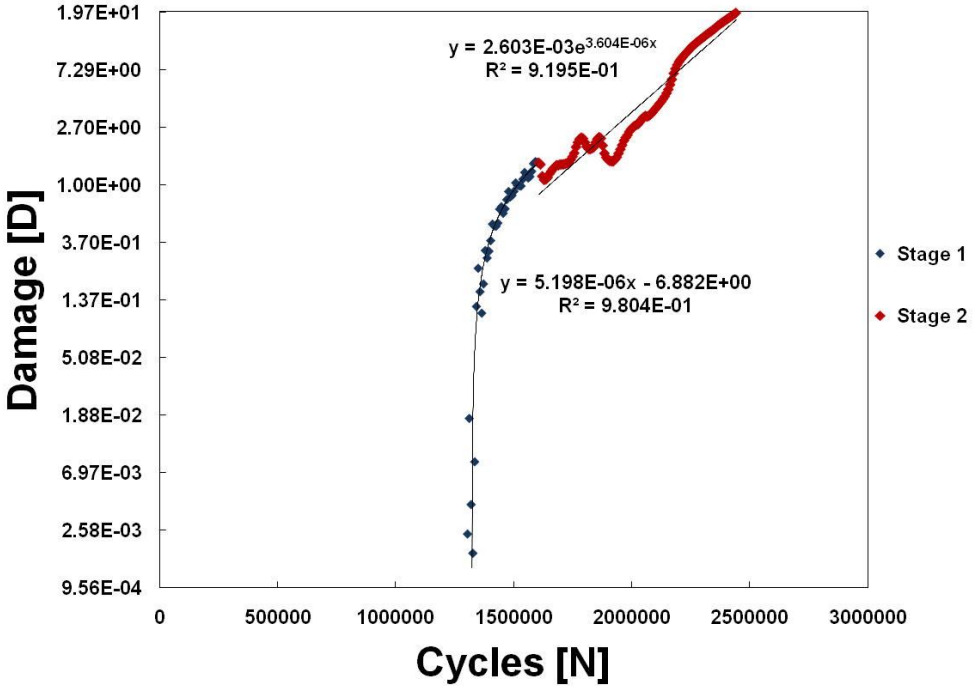

Figure D 9 - Damage curve of 3 month aged σ_1 – specimen 9.

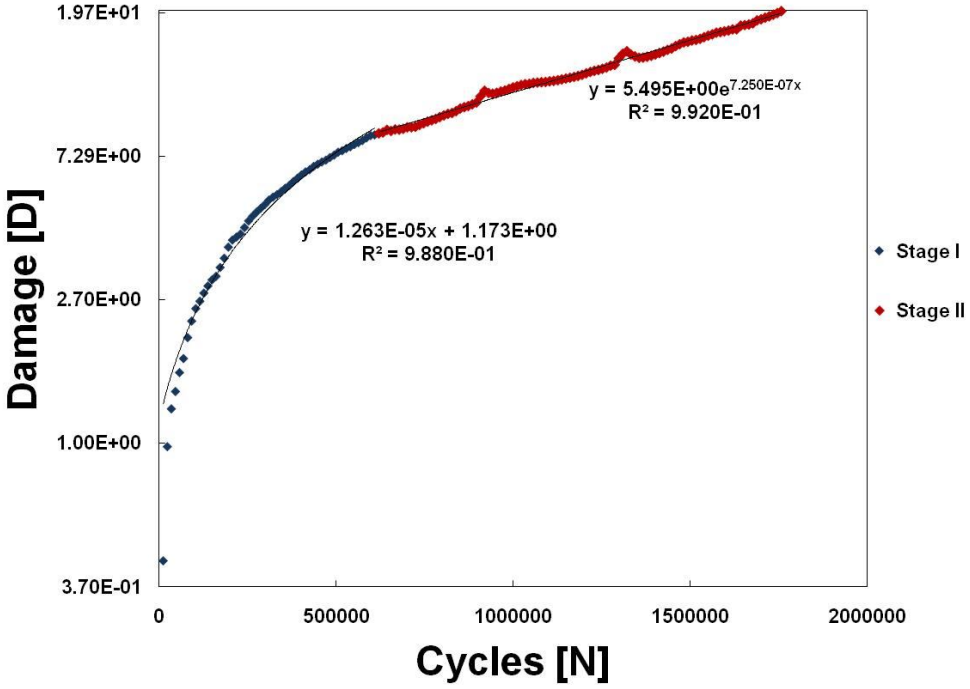

Figure D 10 - Damage curve of 3 month aged σ_1 – specimen 10.

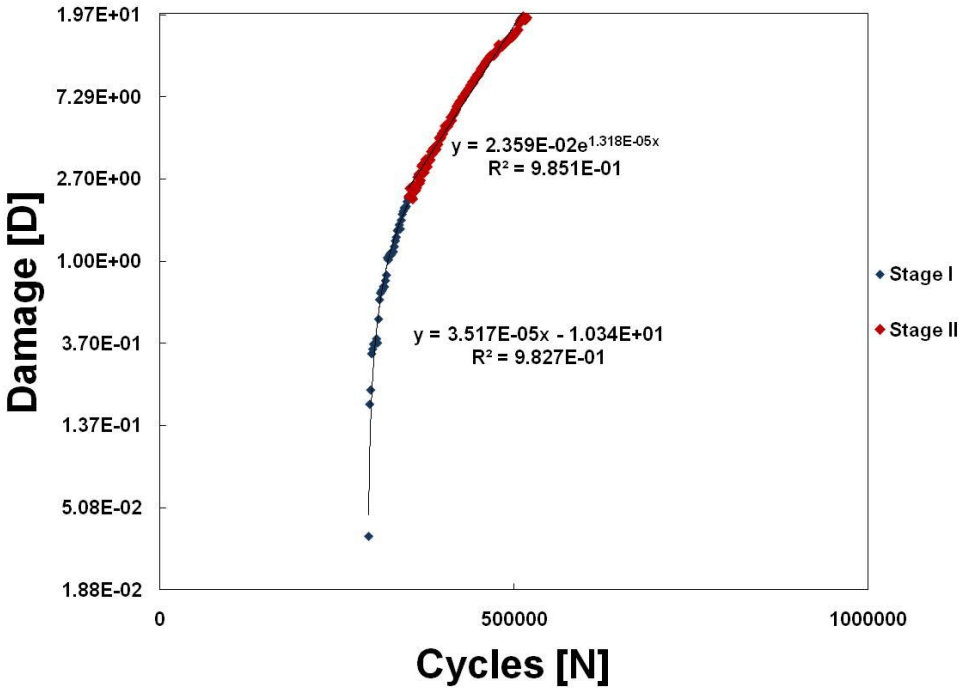

Figure D 11 - Damage curve of 3 month aged σ_2 – specimen 1.

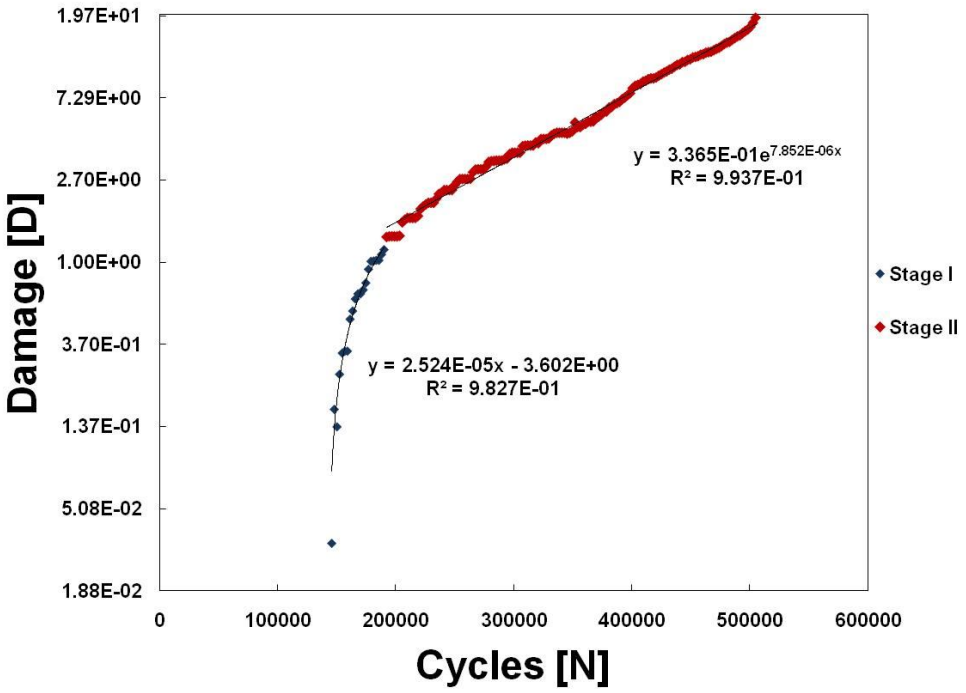

Figure D 12 - Damage curve of 3 month aged σ_2 – specimen 2.

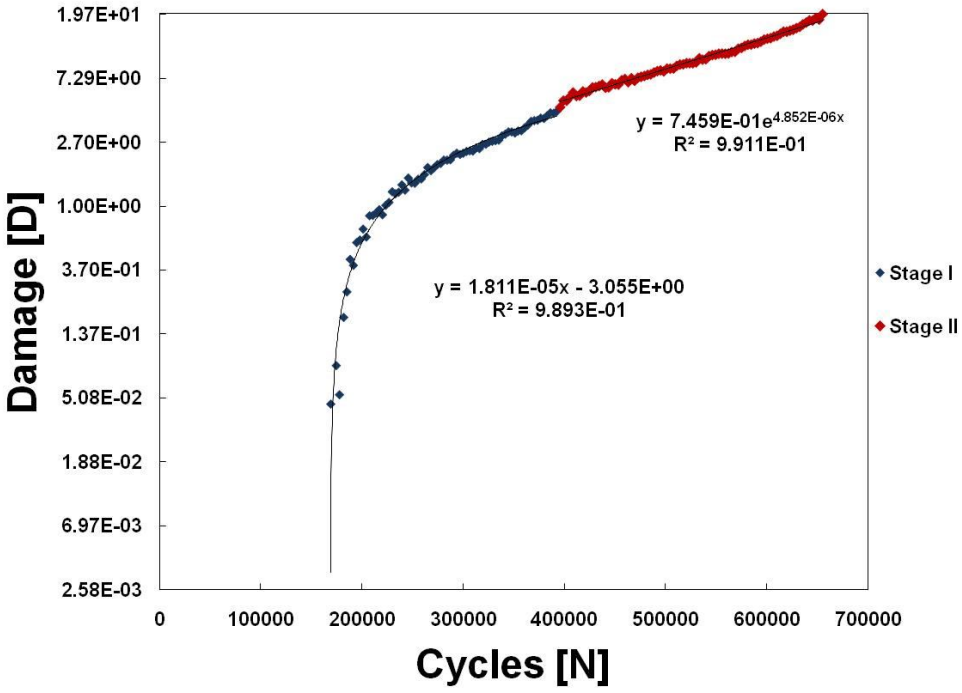

Figure D 13 - Damage curve of 3 month aged σ_2 – specimen 3.

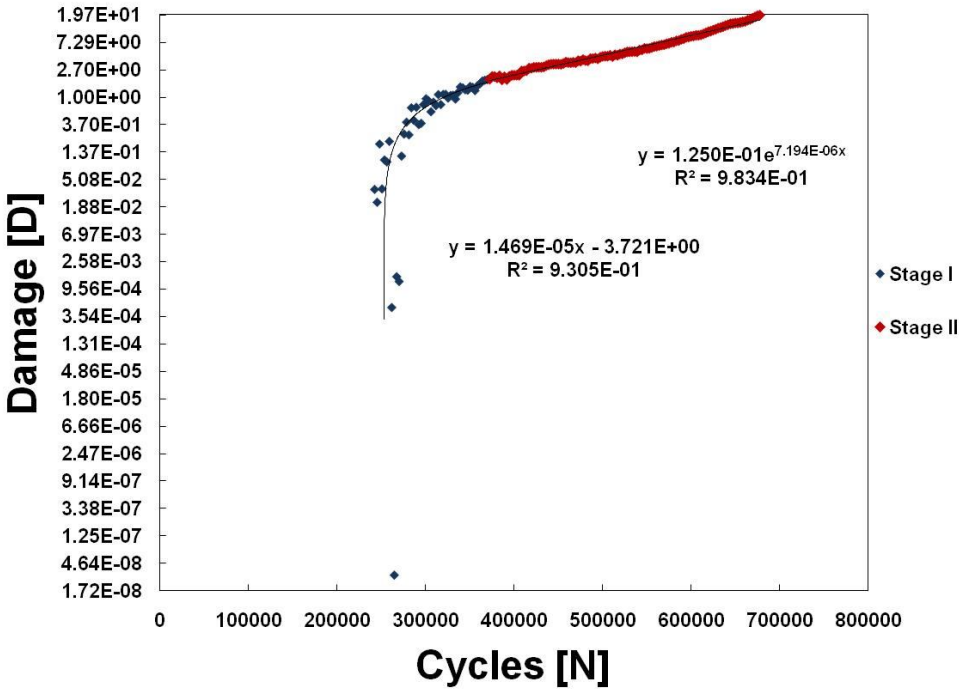

Figure D 14 - Damage curve of 3 month aged σ_2 – specimen 4.

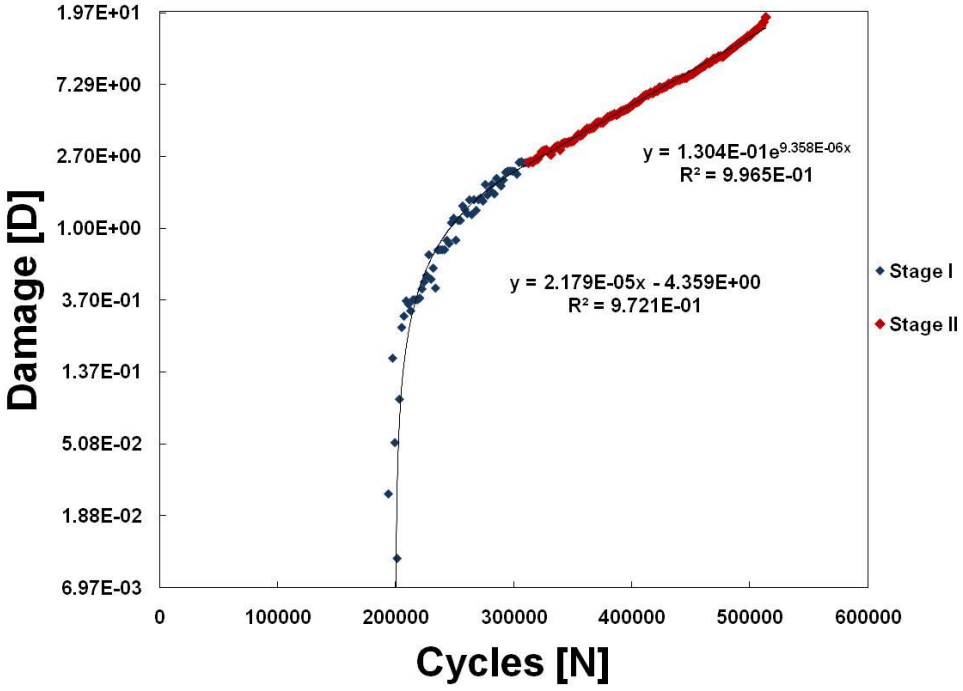

Figure D 15 - Damage curve of 3 month aged σ_2 – specimen 5.

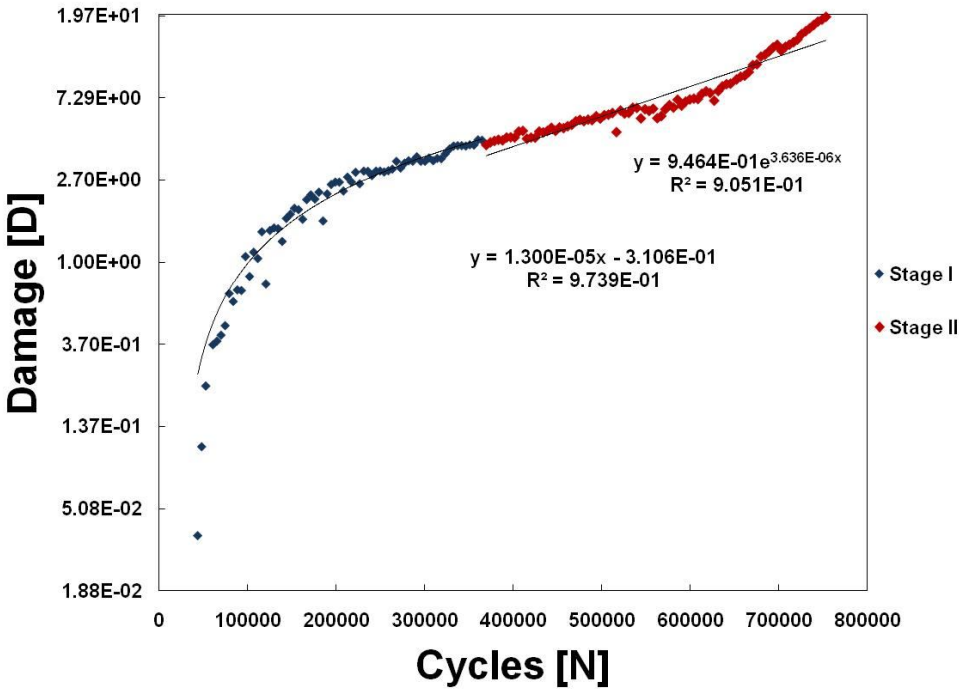

Figure D 16 - Damage curve of 3 month aged σ_2 – specimen 6.

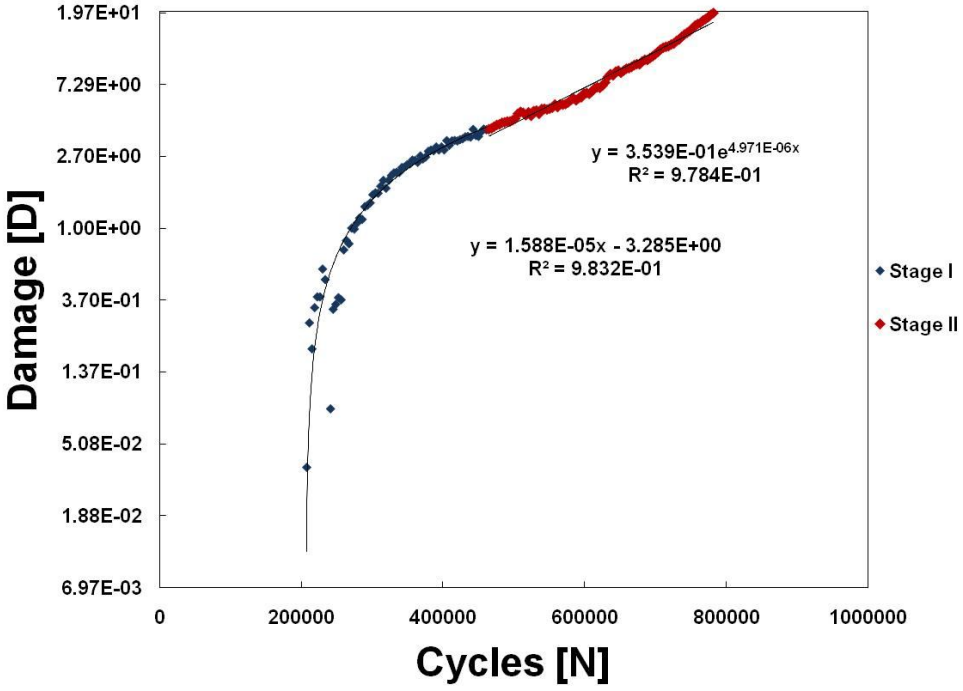

Figure D 17 - Damage curve of 3 month aged σ_2 – specimen 7.

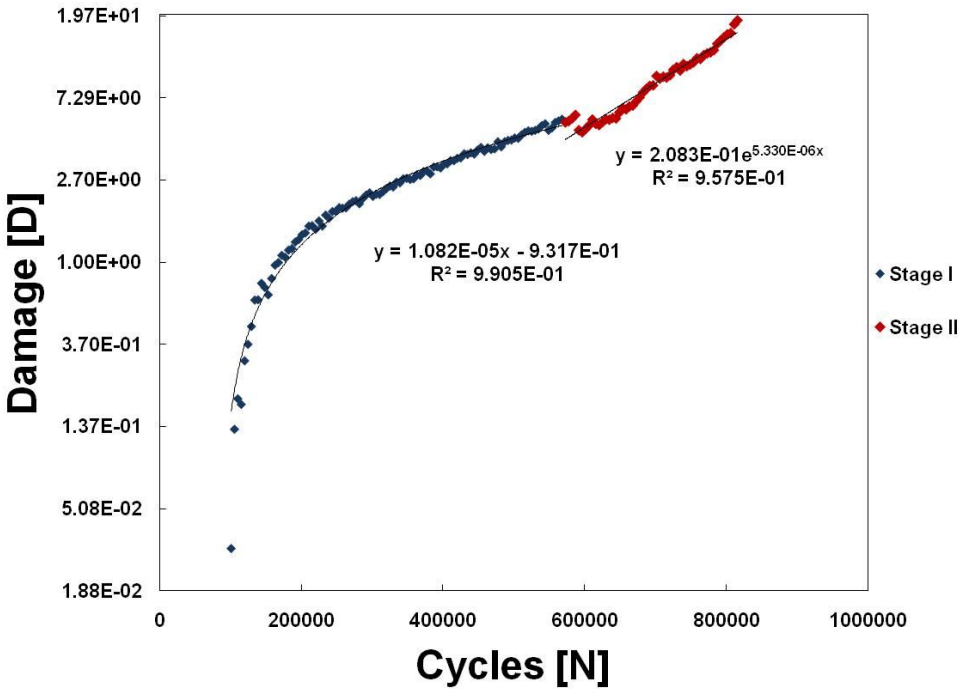

Figure D 18 - Damage curve of 3 month aged σ_2 – specimen 8.

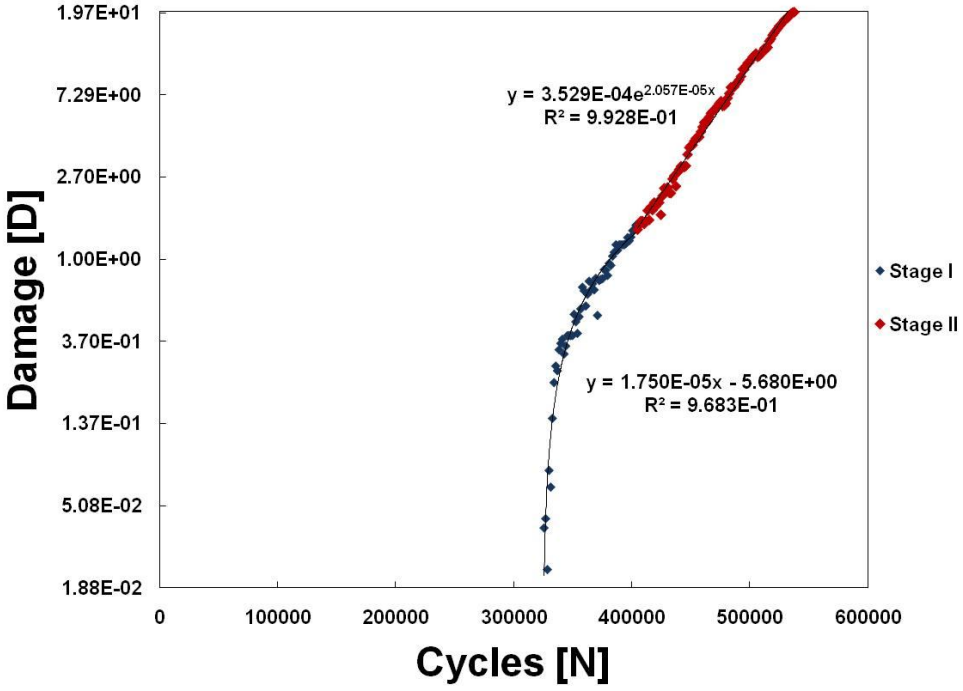

Figure D 19 - Damage curve of 3 month aged σ_2 – specimen 9.

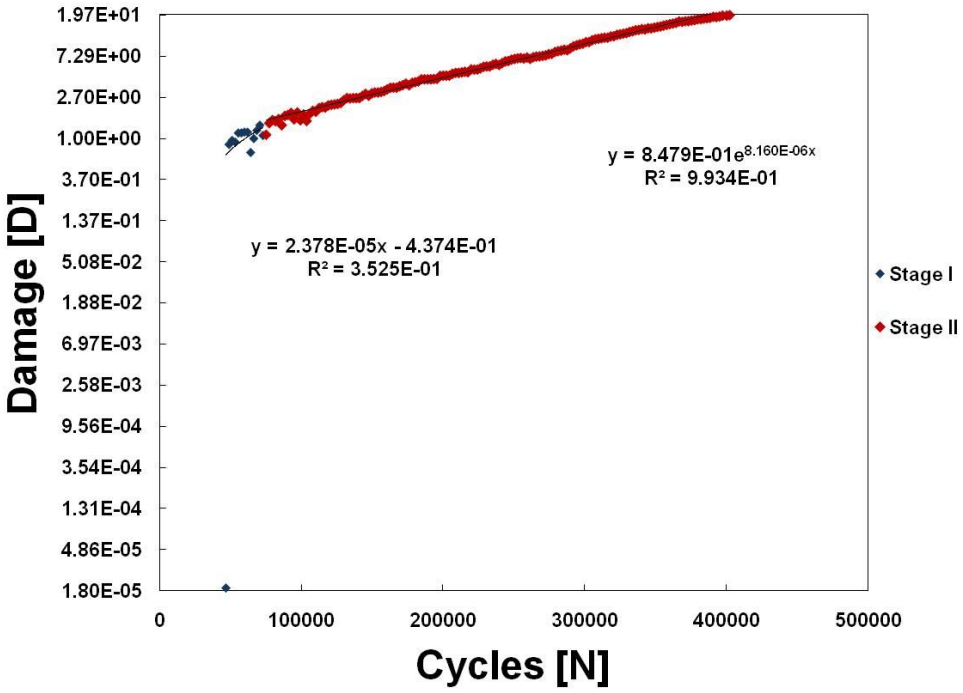

Figure D 20 - Damage curve of 3 month aged σ_2 – specimen 10.

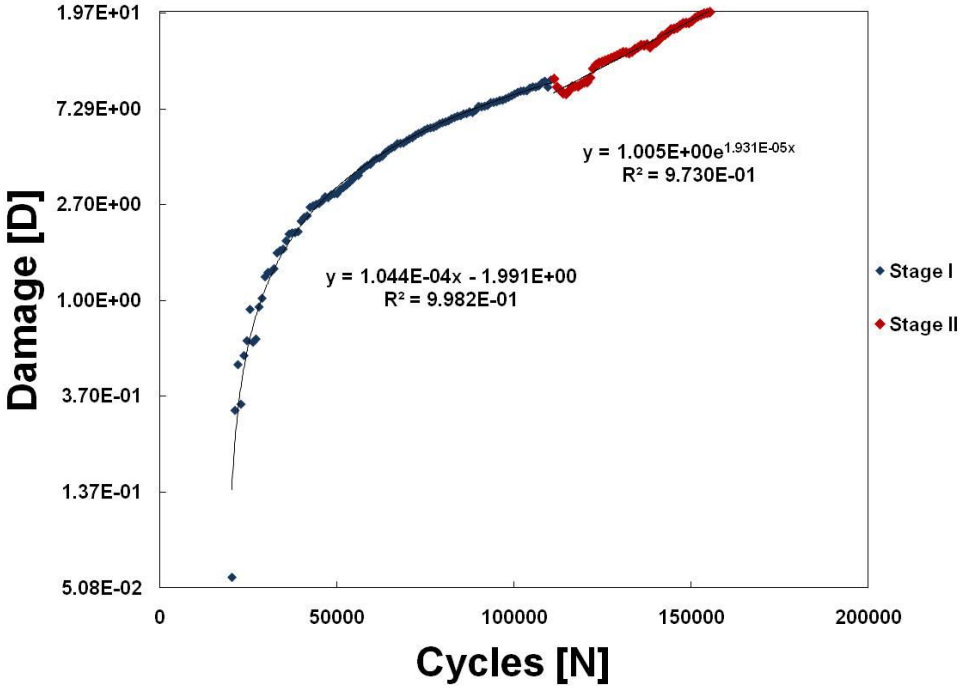

Figure D 21 - Damage curve of 3 month aged σ_3 – specimen 1.

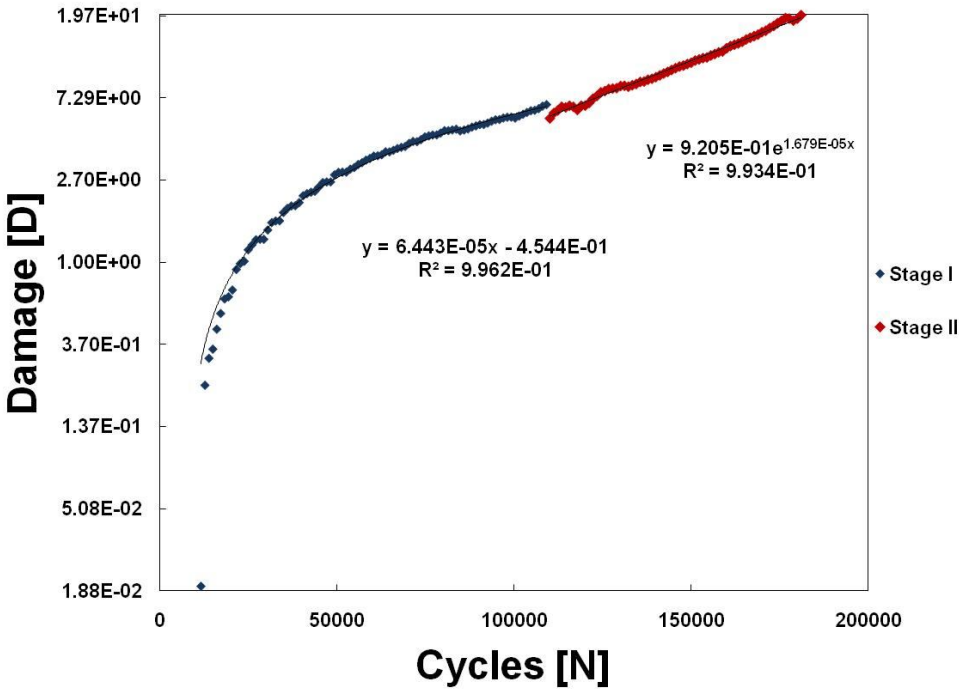

Figure D 22 - Damage curve of 3 month aged σ_3 – specimen 2.

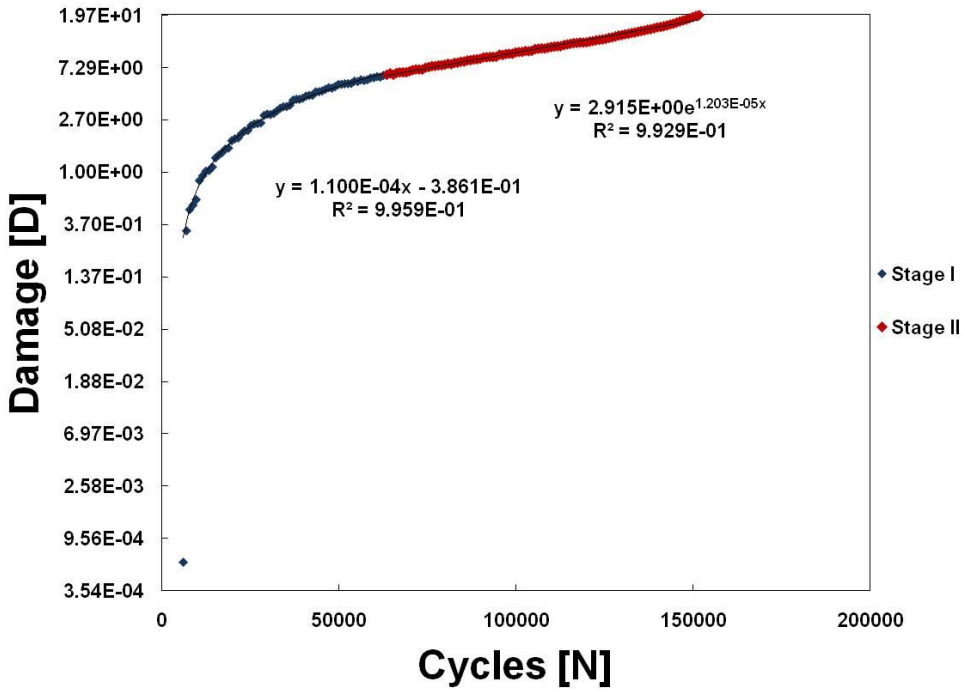

Figure D 23 - Damage curve of 3 month aged σ_3 – specimen 3.

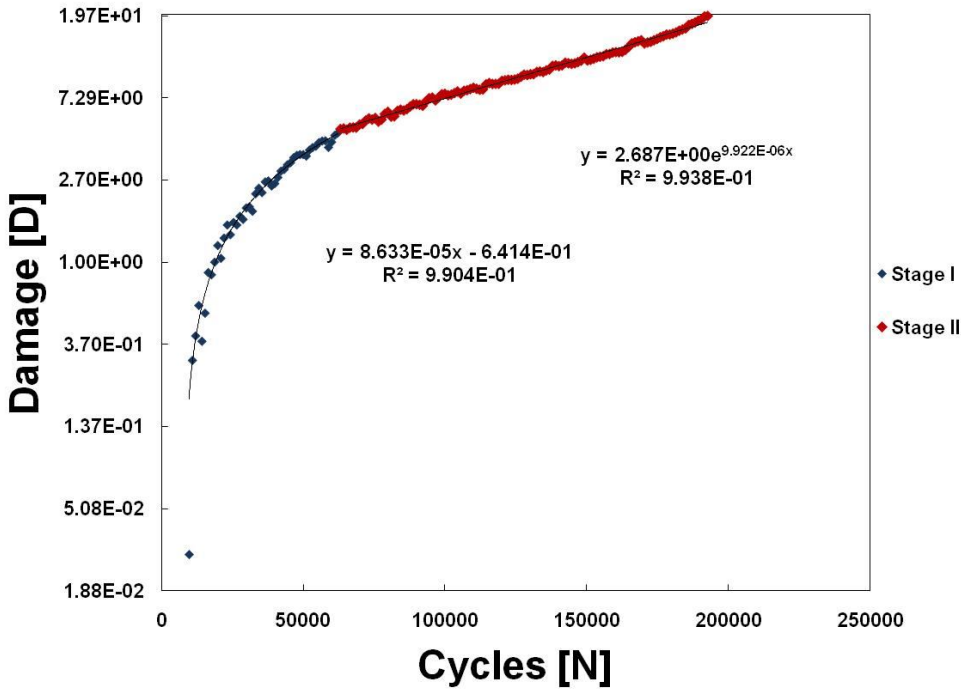

Figure D 24 - Damage curve of 3 month aged σ_3 – specimen 4.

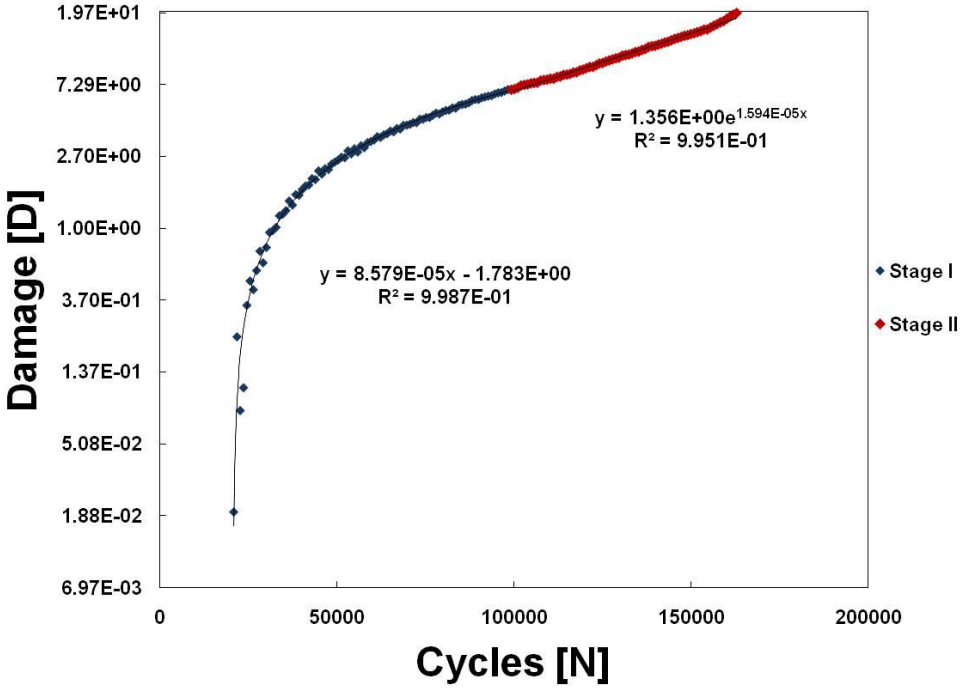

Figure D 25 - Damage curve of 3 month aged σ_3 – specimen 5.

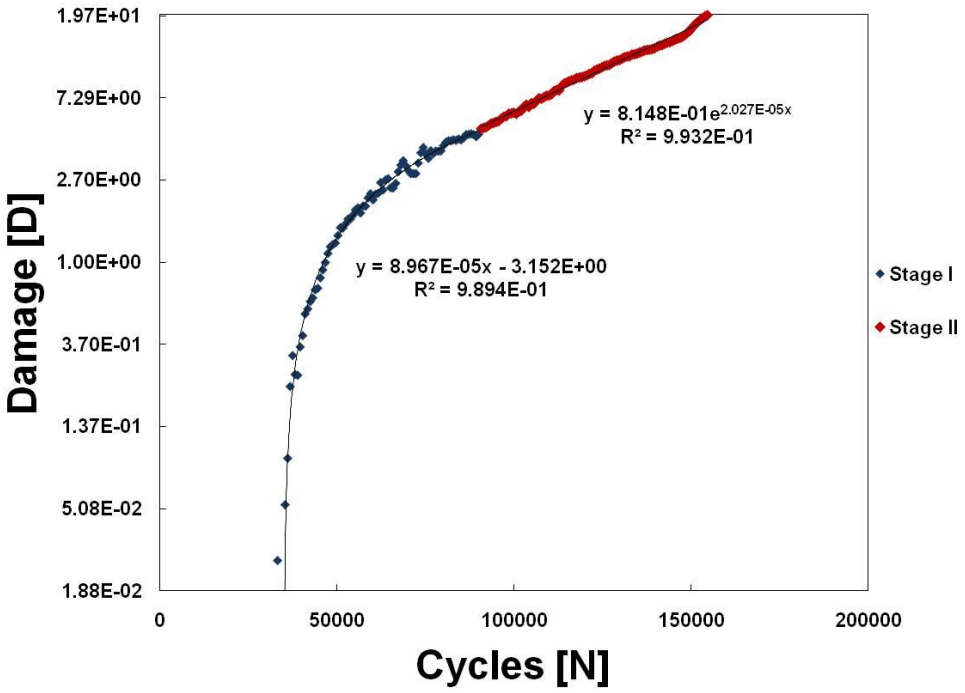

Figure D 26 - Damage curve of 3 month aged σ_3 – specimen 6.

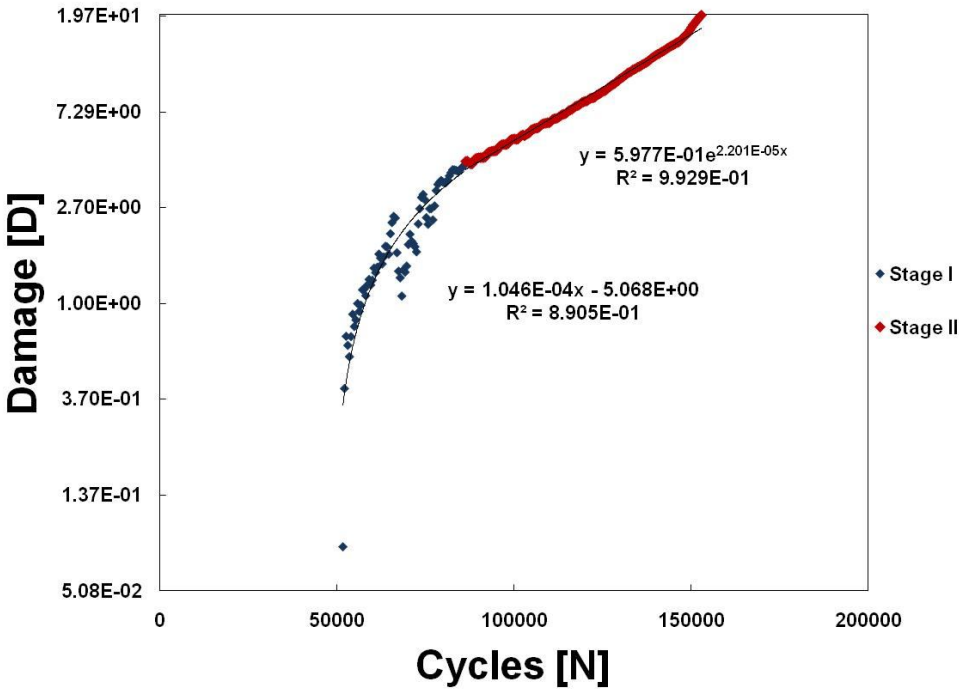

Figure D 27 - Damage curve of 3 month aged σ_3 – specimen 7.

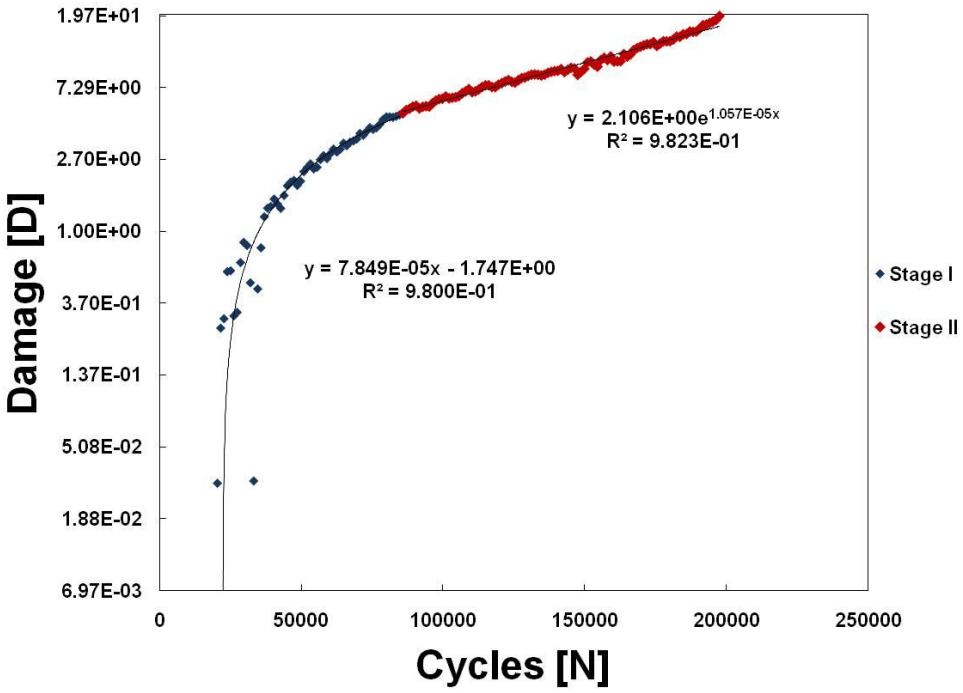

Figure D 28 - Damage curve of 3 month aged σ_3 – specimen 8.

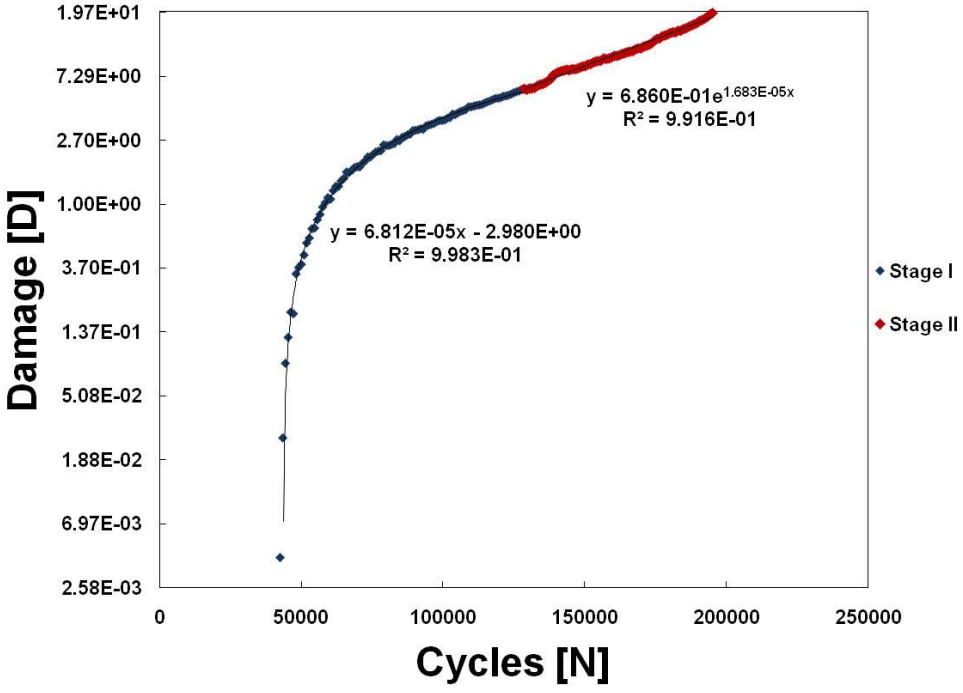

Figure D 29 - Damage curve of 3 month aged σ_3 – specimen 9.

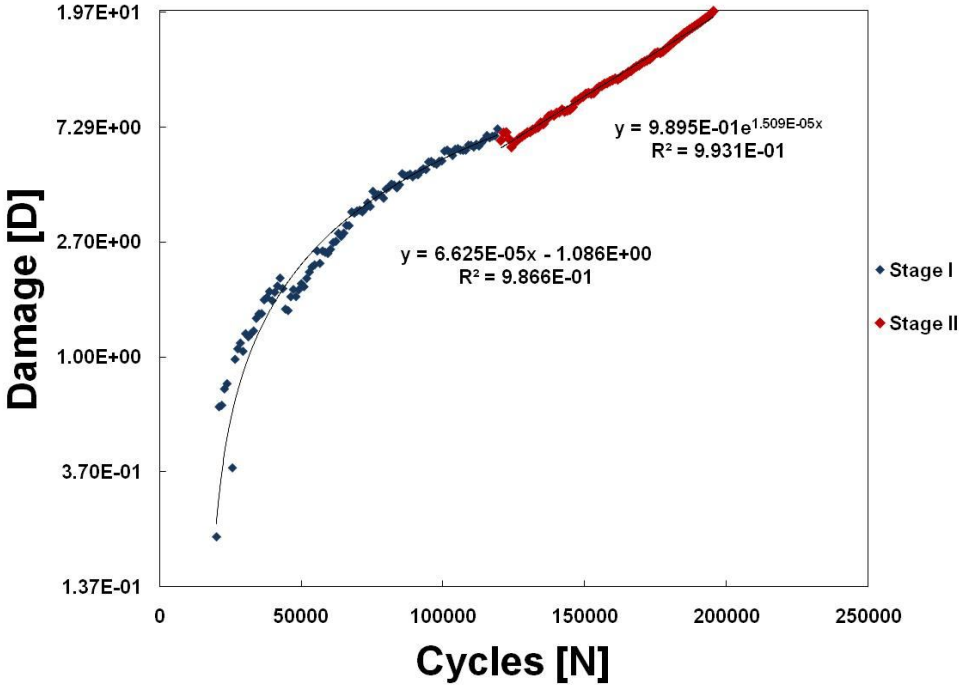

Figure D 30 - Damage curve of 3 month aged σ_3 – specimen 10.

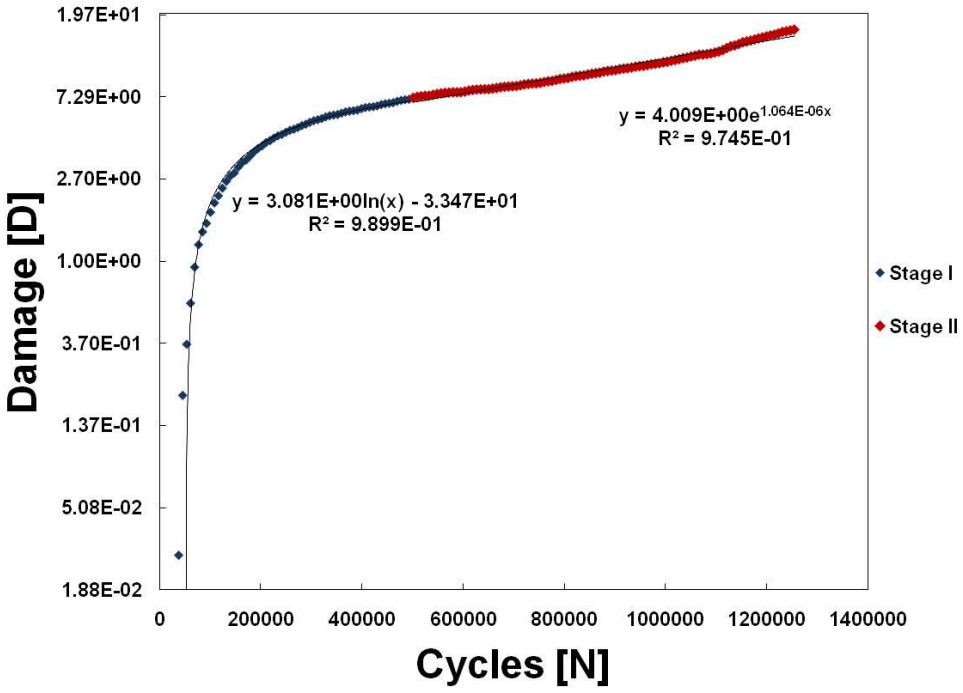

Figure D 31 - Damage curve of 6 month aged σ_1 – specimen 1.

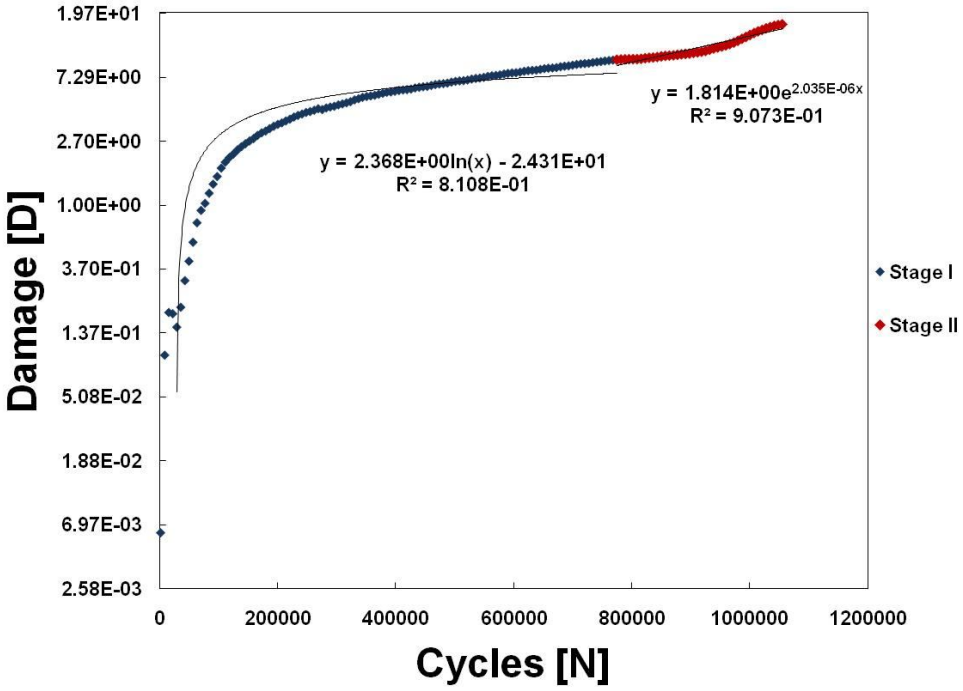

Figure D 32 - Damage curve of 6 month aged σ_1 – specimen 2.

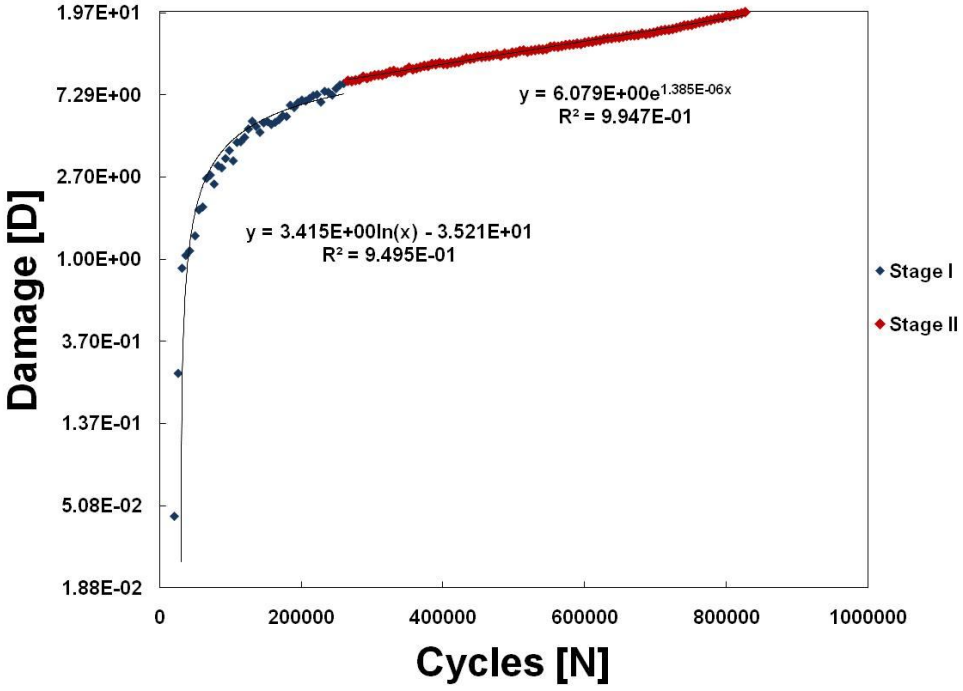

Figure D 33 - Damage curve of 6 month aged σ_1 – specimen 3.

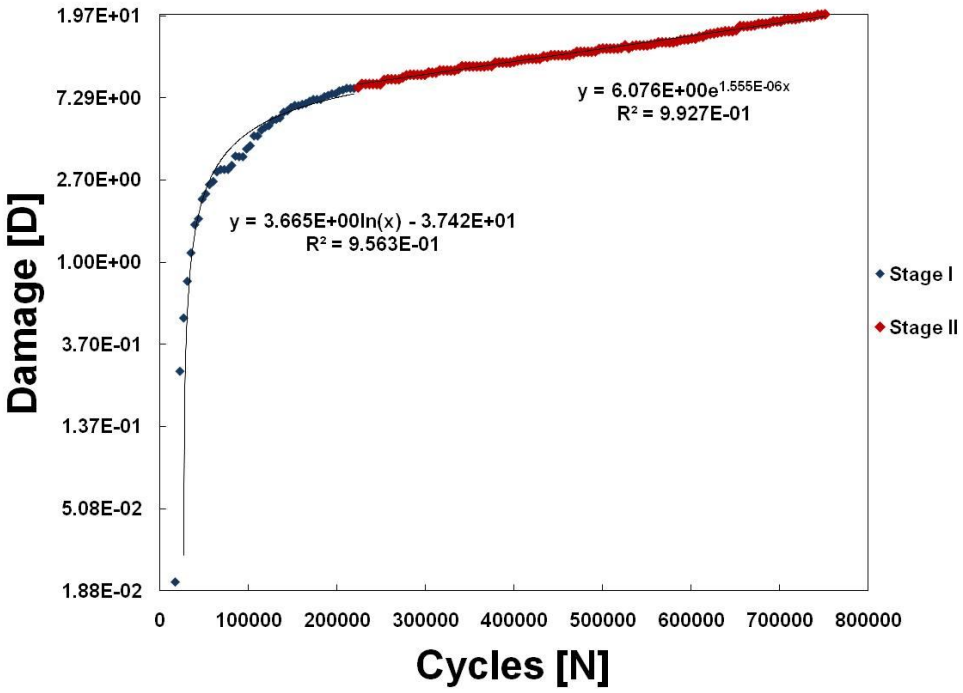

Figure D 34 - Damage curve of 6 month aged σ_1 – specimen 4.

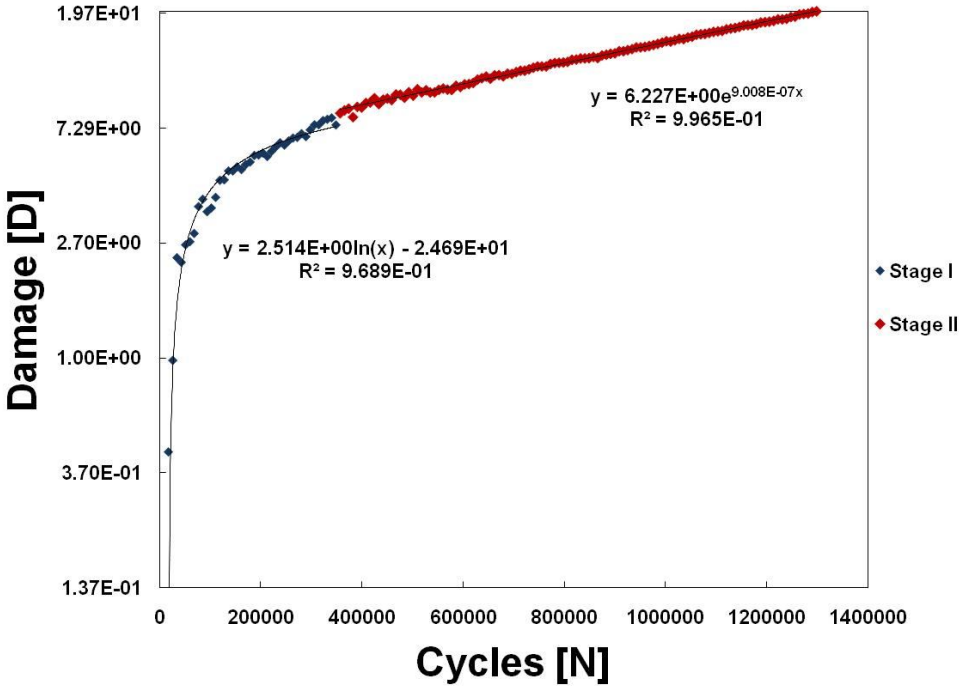

Figure D 35 - Damage curve of 6 month aged σ_1 – specimen 5.

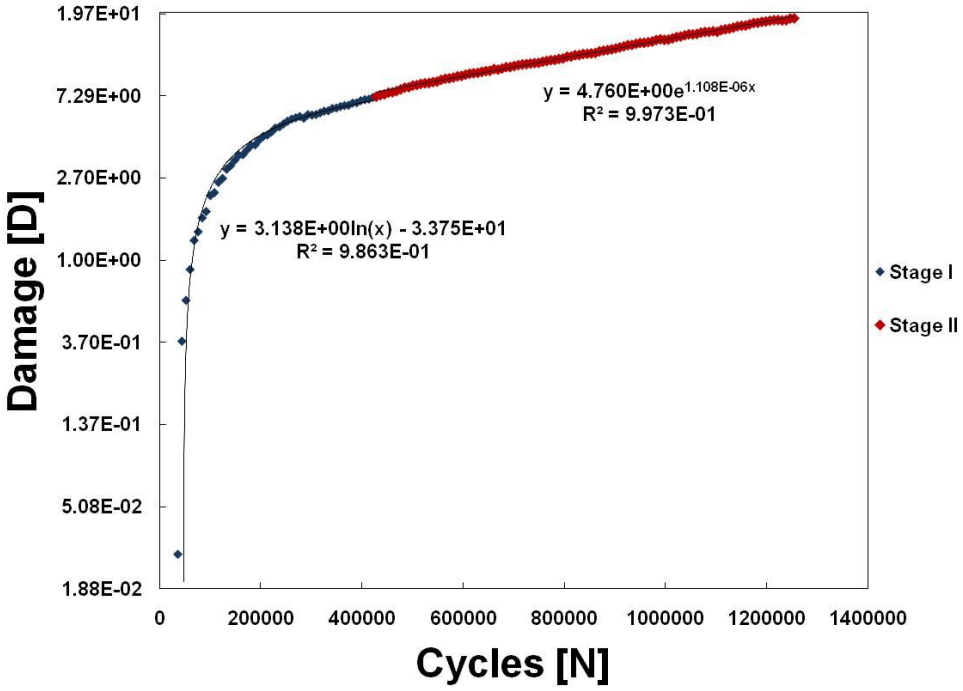

Figure D 36 - Damage curve of 6 month aged σ_1 – specimen 6.

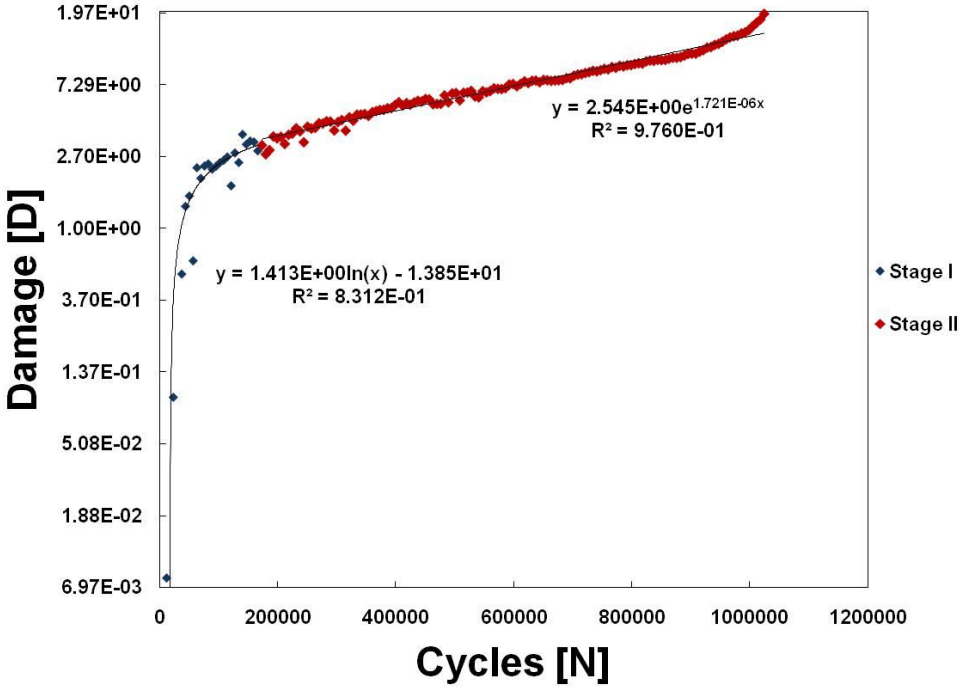

Figure D 37 - Damage curve of 6 month aged σ_1 – specimen 7.

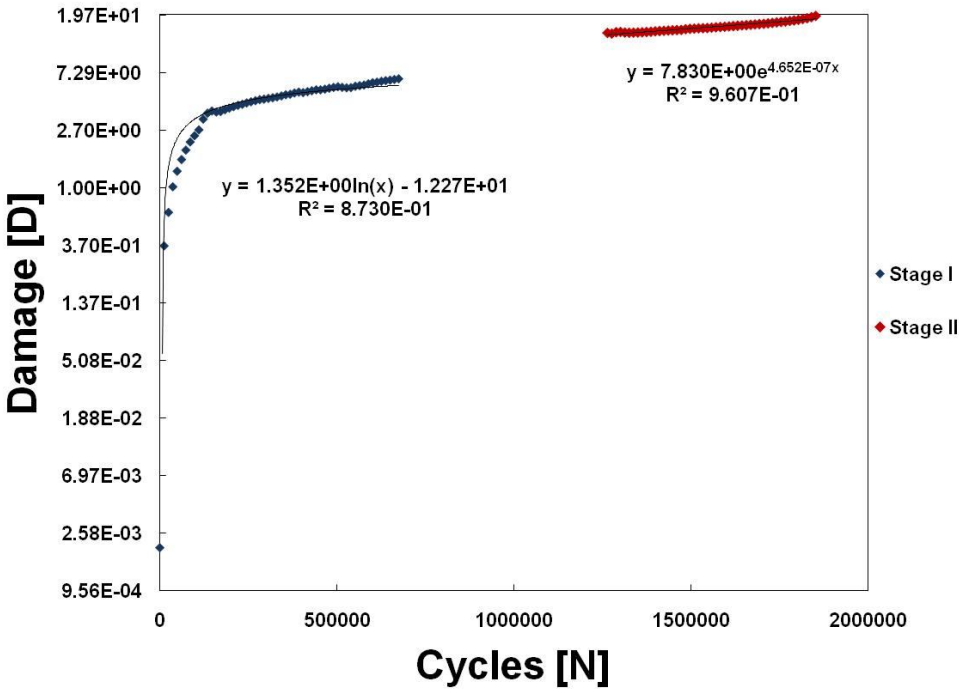

Figure D 38 - Damage curve of 6 month aged σ_1 – specimen 8.

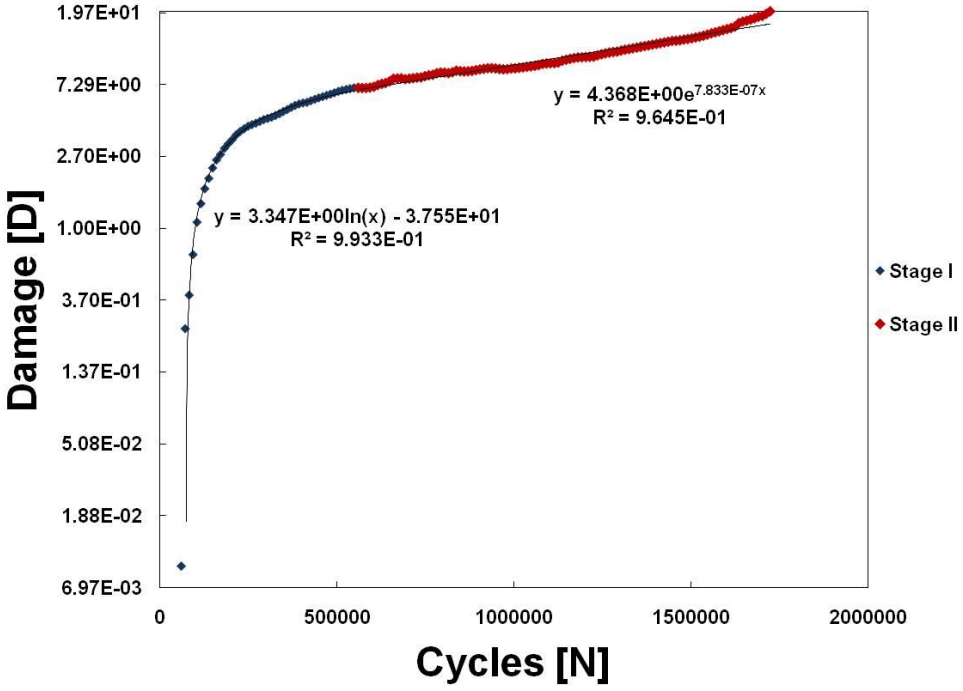

Figure D 39 - Damage curve of 6 month aged σ_1 – specimen 9.

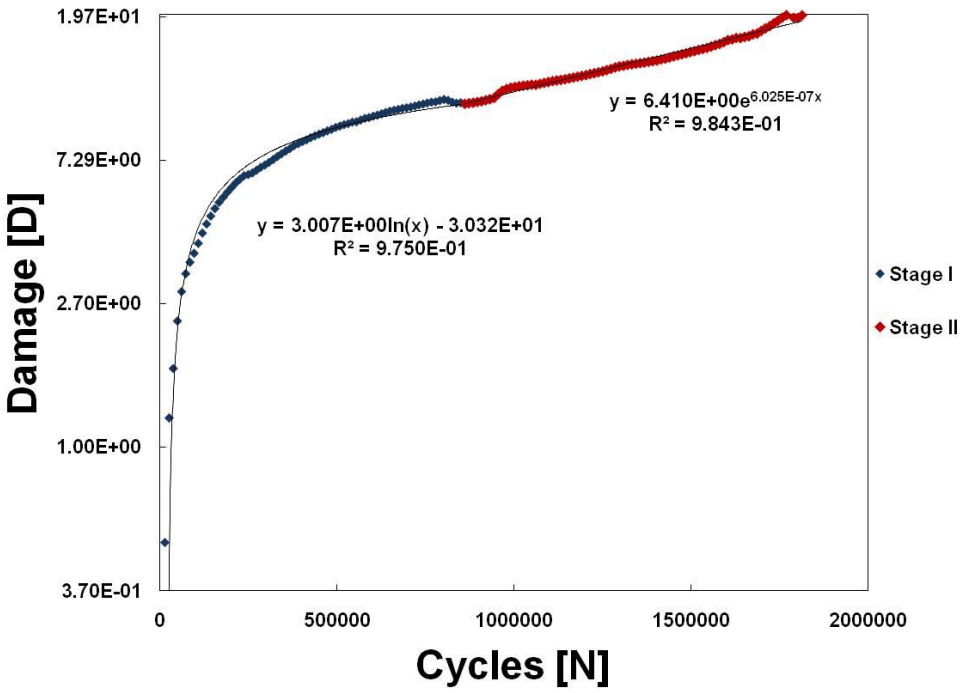

Figure D 40 - Damage curve of 6 month aged σ_1 – specimen 10.

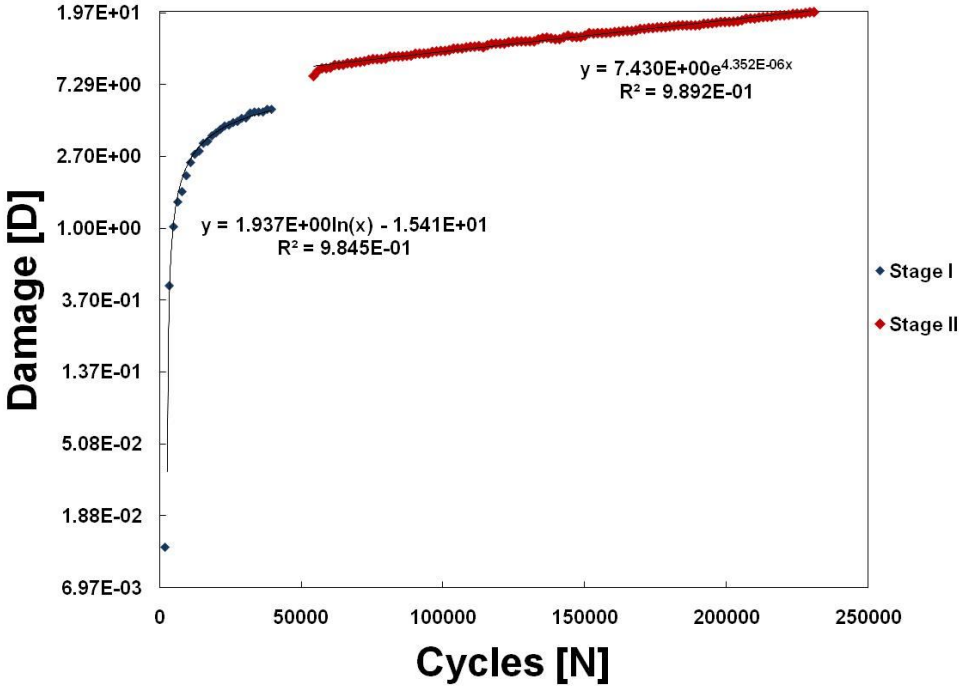

Figure D 41 - Damage curve of 6 month aged σ_2 – specimen 1.

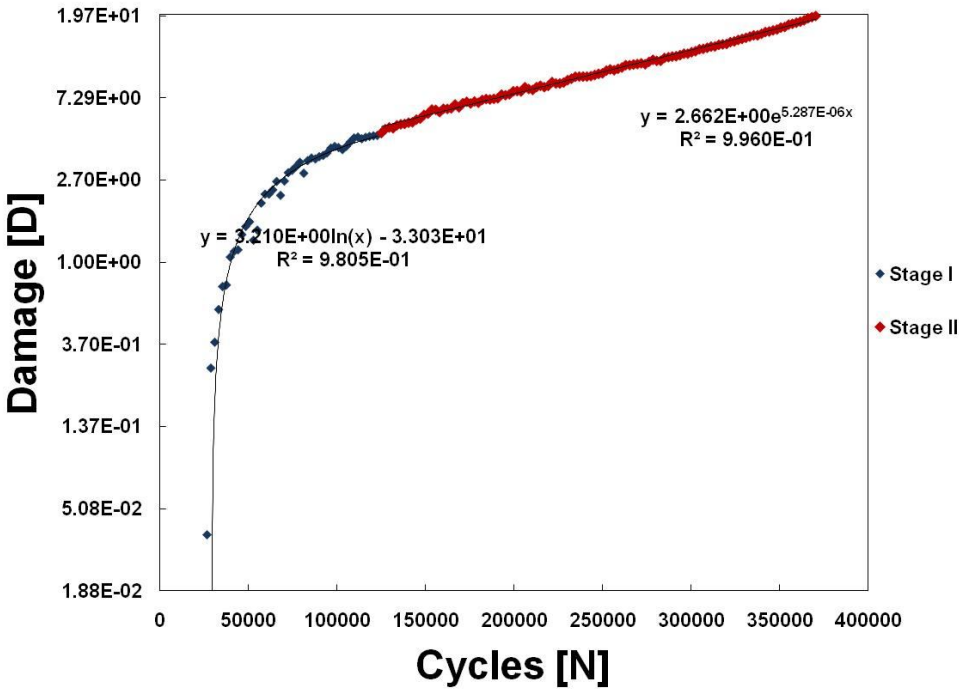

Figure D 42 - Damage curve of 6 month aged σ_2 – specimen 2.

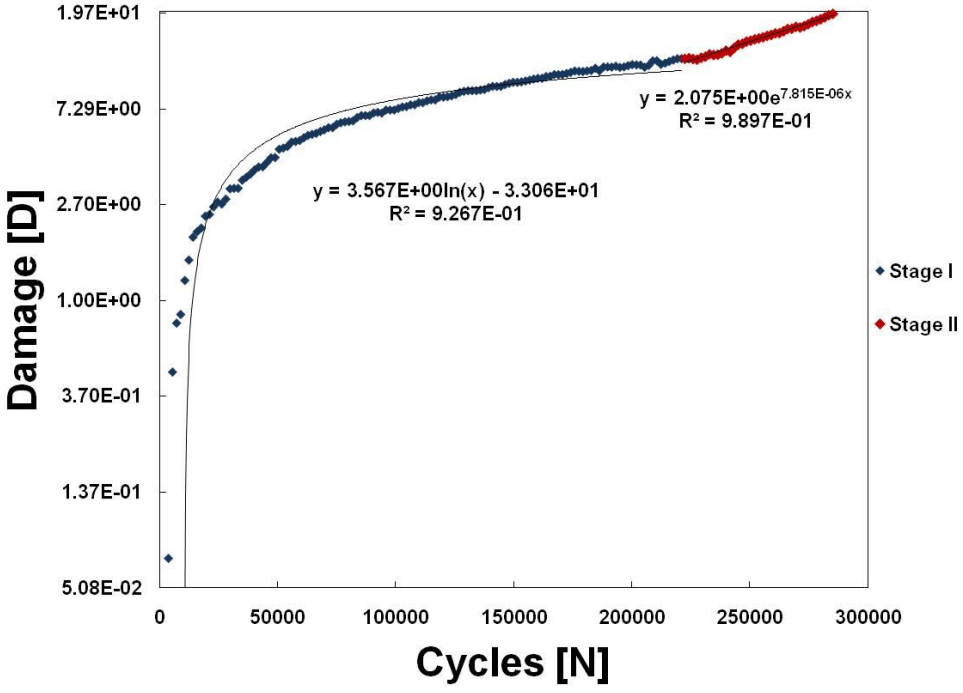

Figure D 43 - Damage curve of 6 month aged σ_2 – specimen 3.

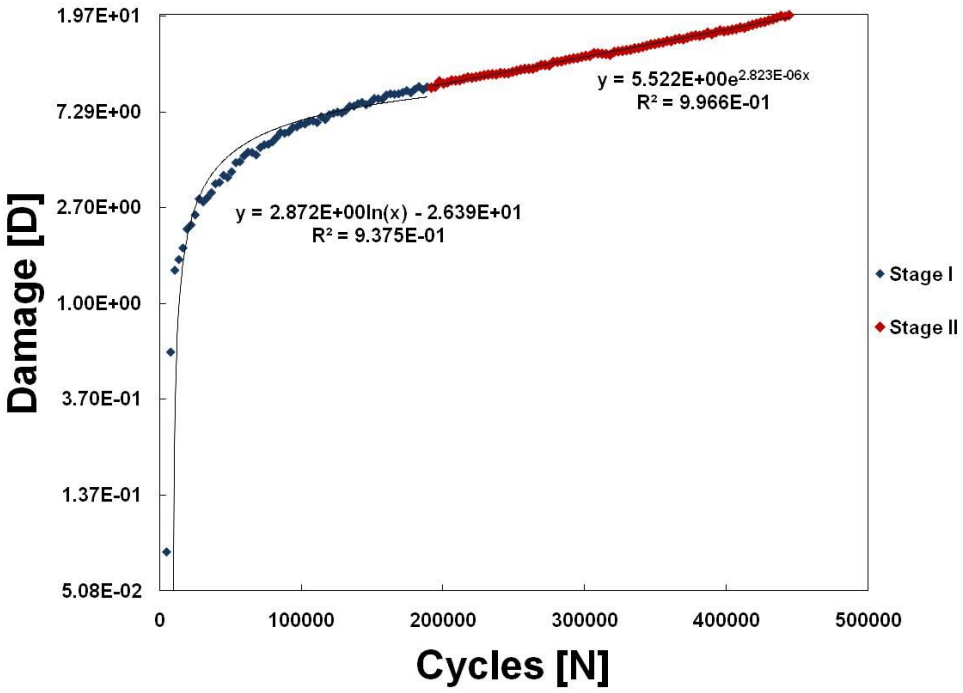

Figure D 44 - Damage curve of 6 month aged σ_2 – specimen 4.

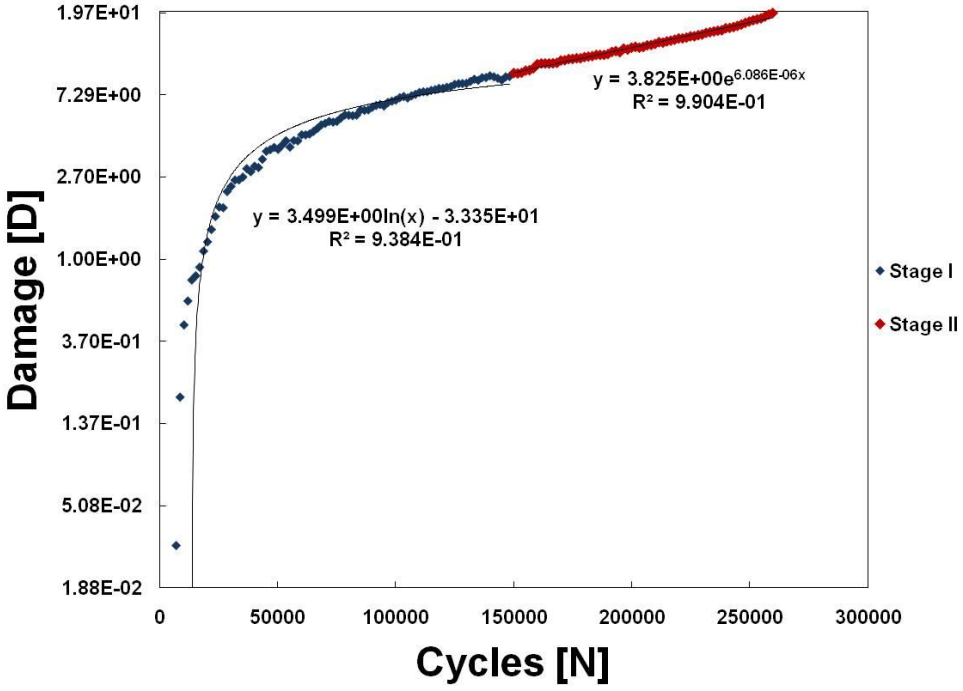

Figure D 45 - Damage curve of 6 month aged σ_2 – specimen 5.

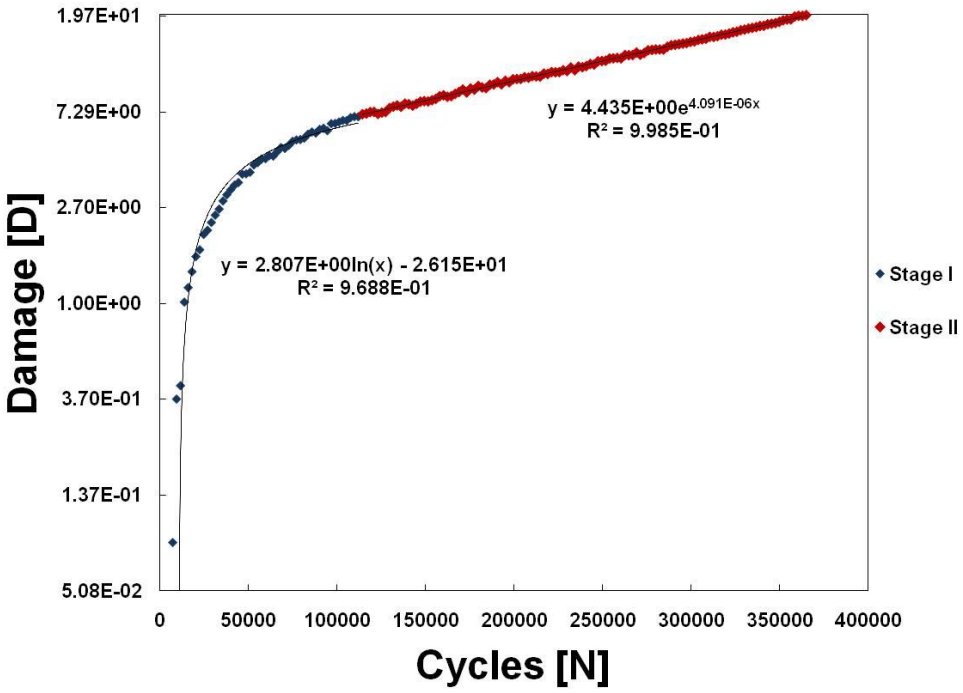

Figure D 46 - Damage curve of 6 month aged σ_2 – specimen 6.

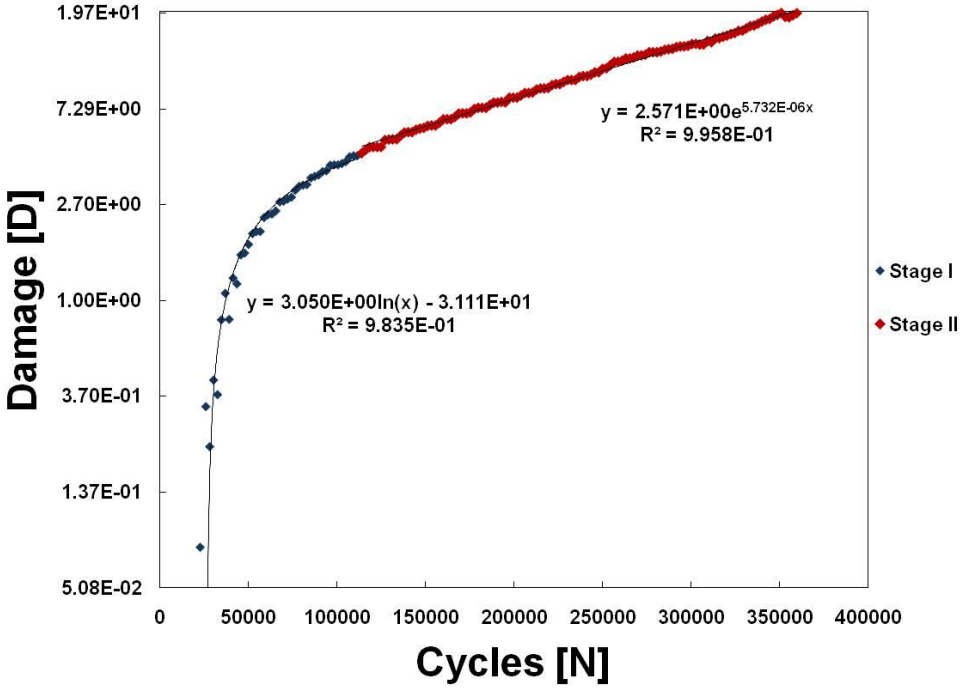

Figure D 47 - Damage curve of 6 month aged σ_2 – specimen 7.

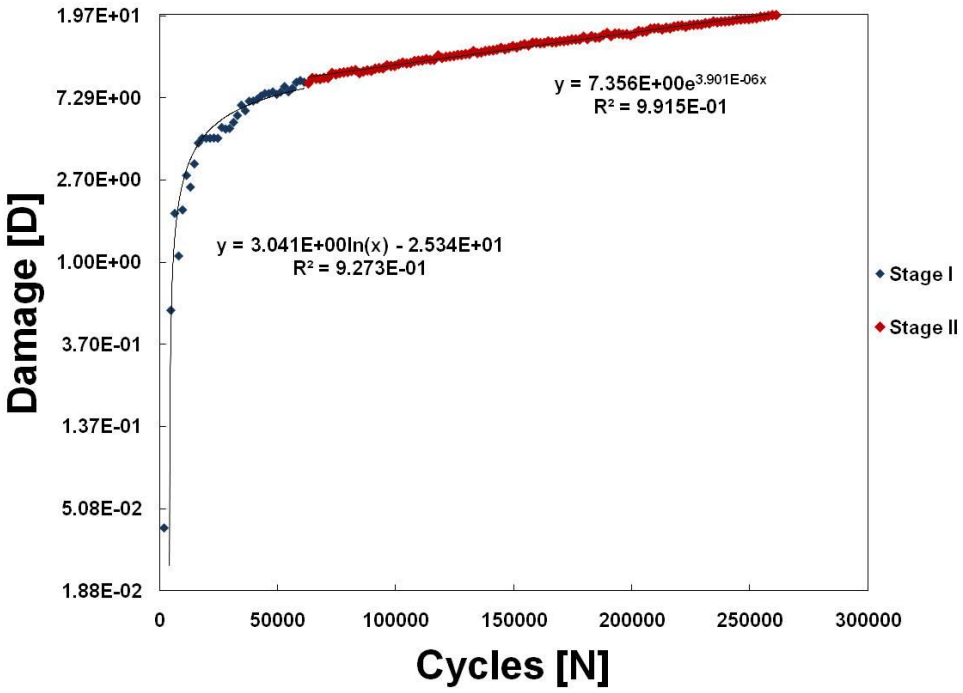

Figure D 48 - Damage curve of 6 month aged σ_2 – specimen 8.

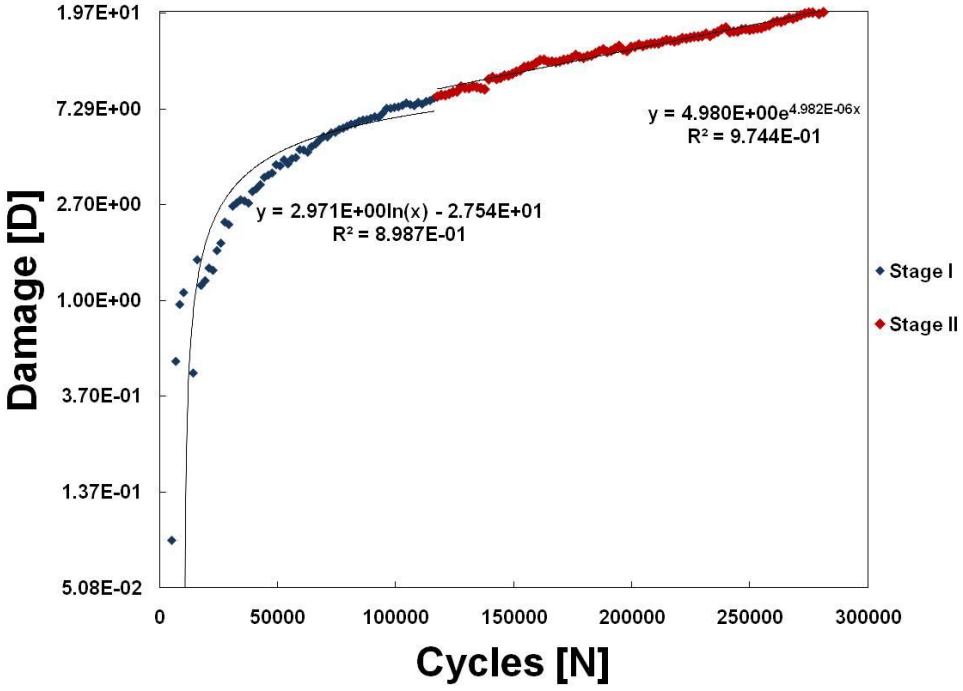

Figure D 49 - Damage curve of 6 month aged σ_2 – specimen 9.

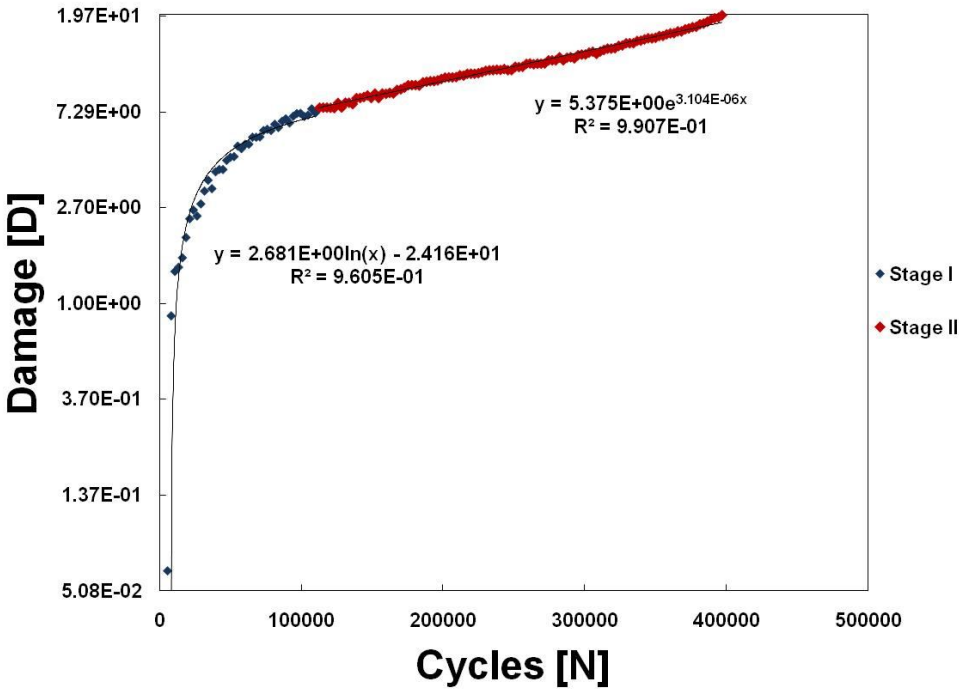

Figure D 50 - Damage curve of 6 month aged σ_2 – specimen 10.

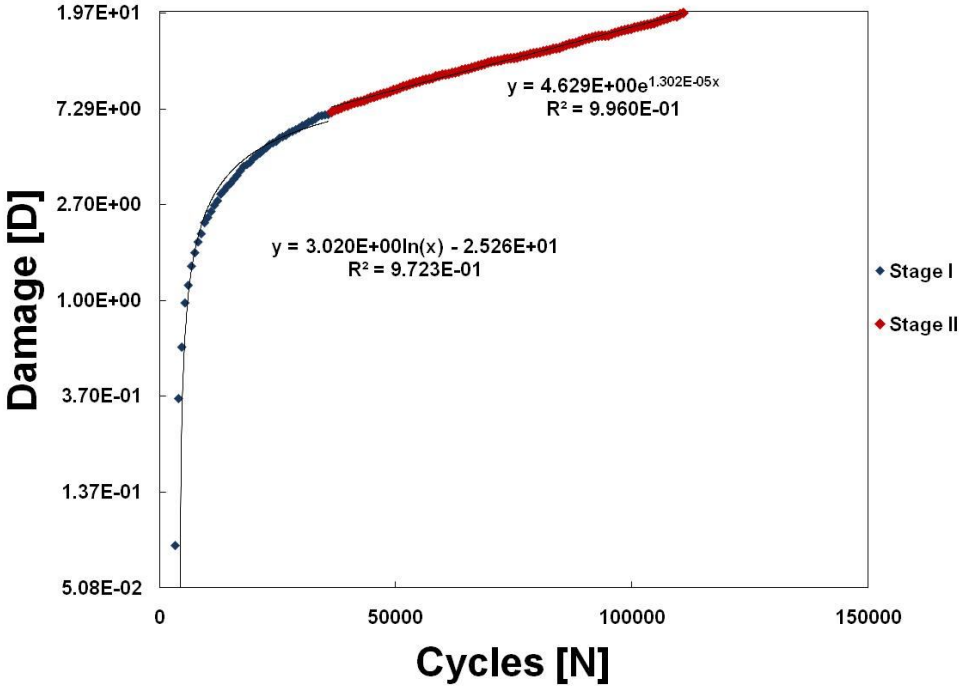

Figure D 51 - Damage curve of 6 month aged σ_3 – specimen 1.

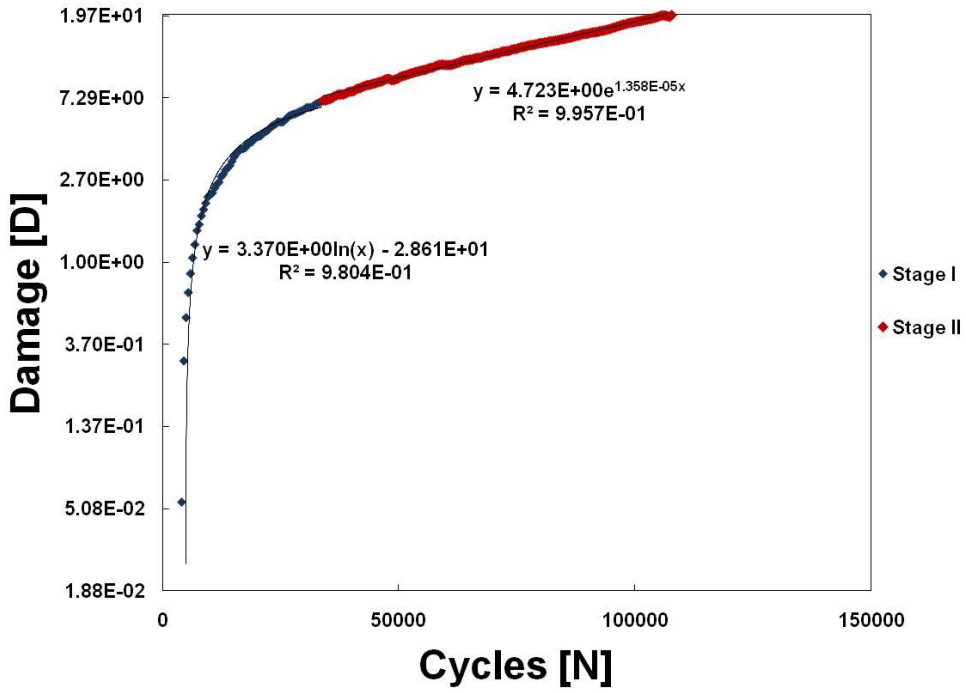

Figure D 52 - Damage curve of 6 month aged σ_3 – specimen 2.

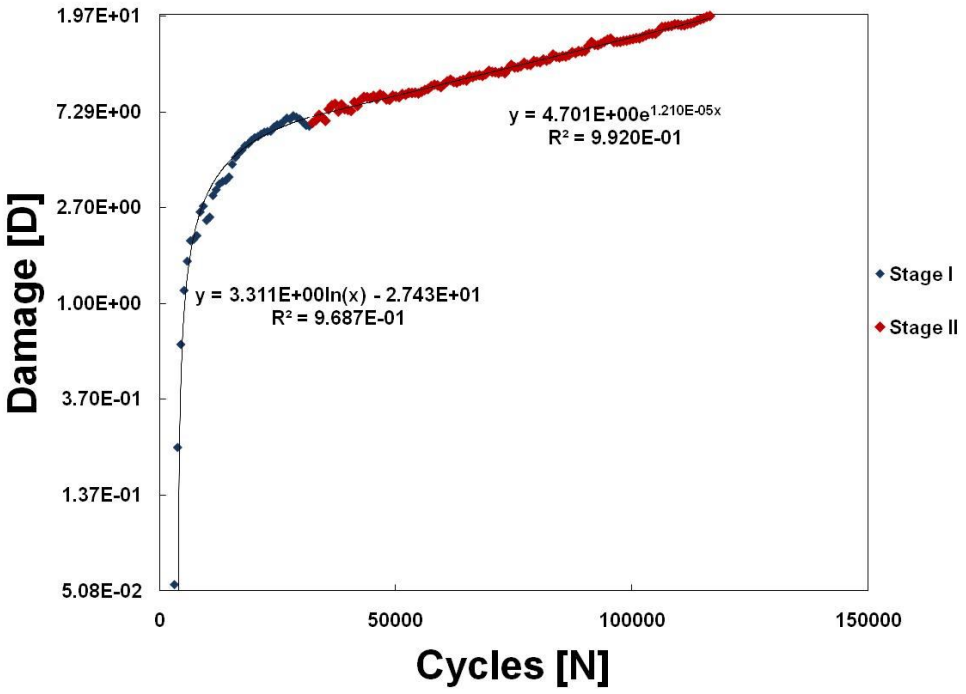

Figure D 53 - Damage curve of 6 month aged σ_3 – specimen 3.

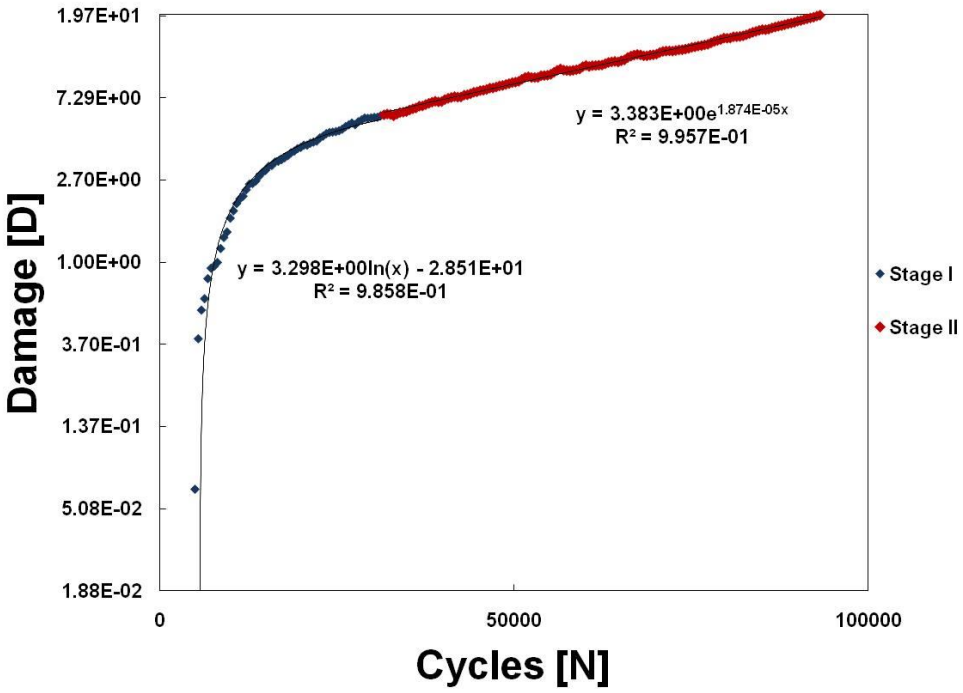

Figure D 54 - Damage curve of 6 month aged σ_3 – specimen 4.

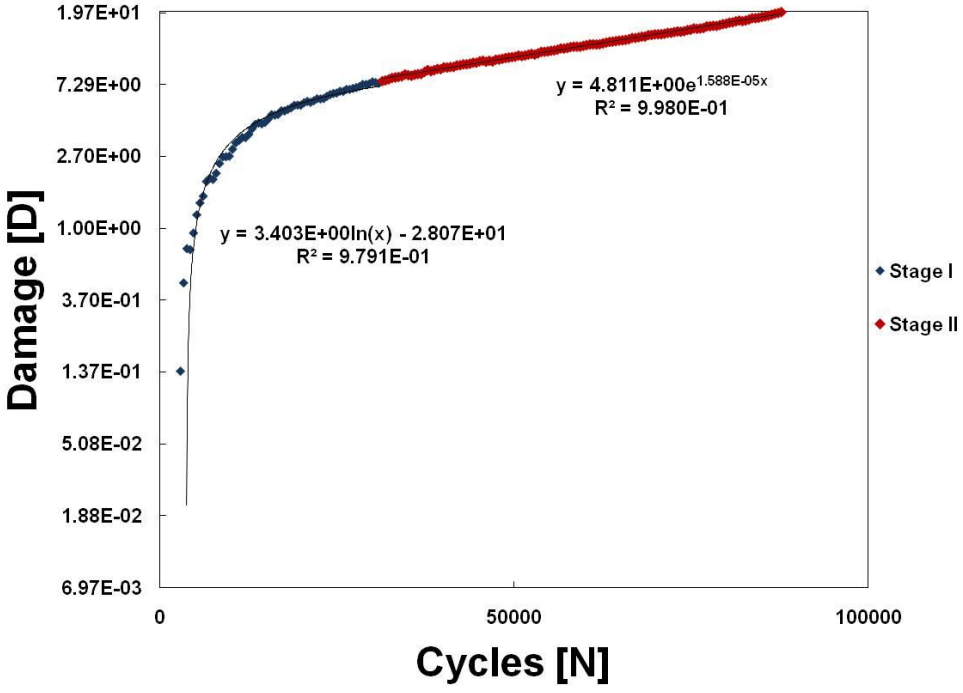

Figure D 55 - Damage curve of 6 month aged σ_3 – specimen 5.

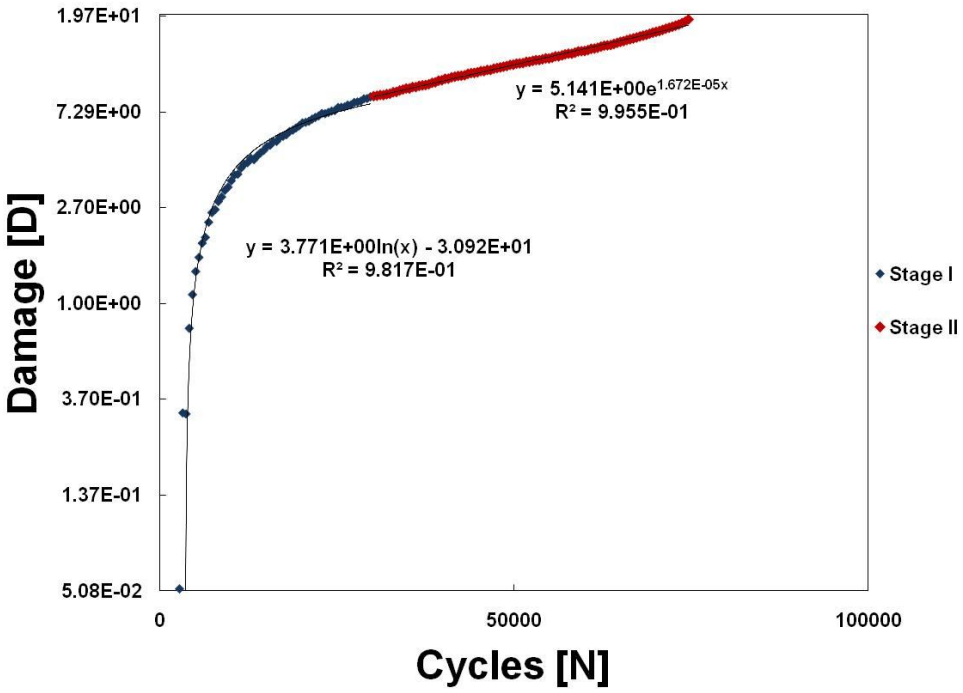

Figure D 56 - Damage curve of 6 month aged σ_3 – specimen 6.

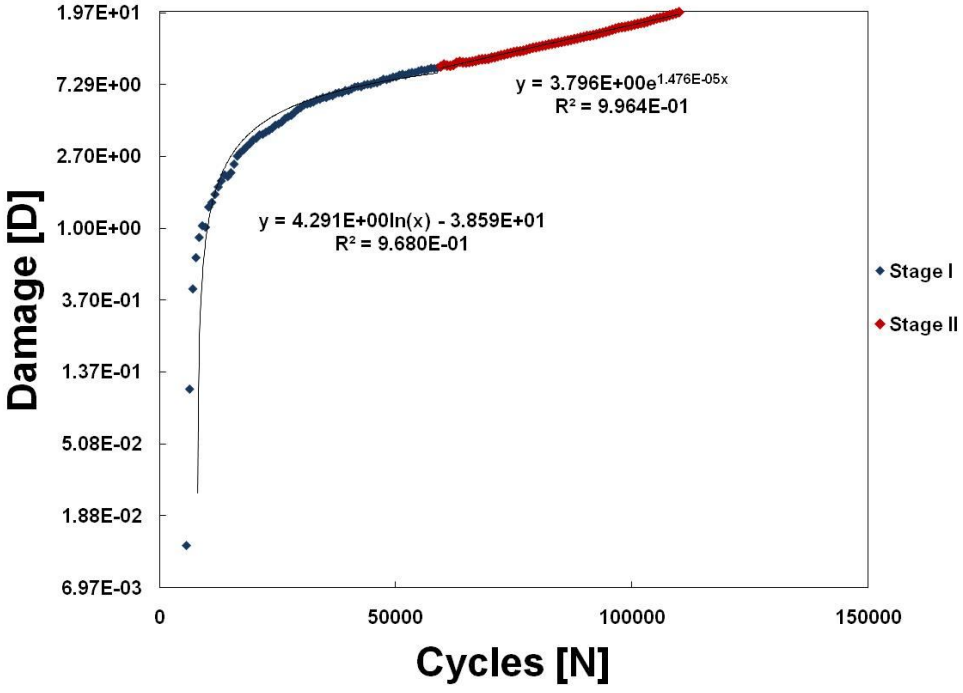

Figure D 57 - Damage curve of 6 month aged σ_3 – specimen 7.

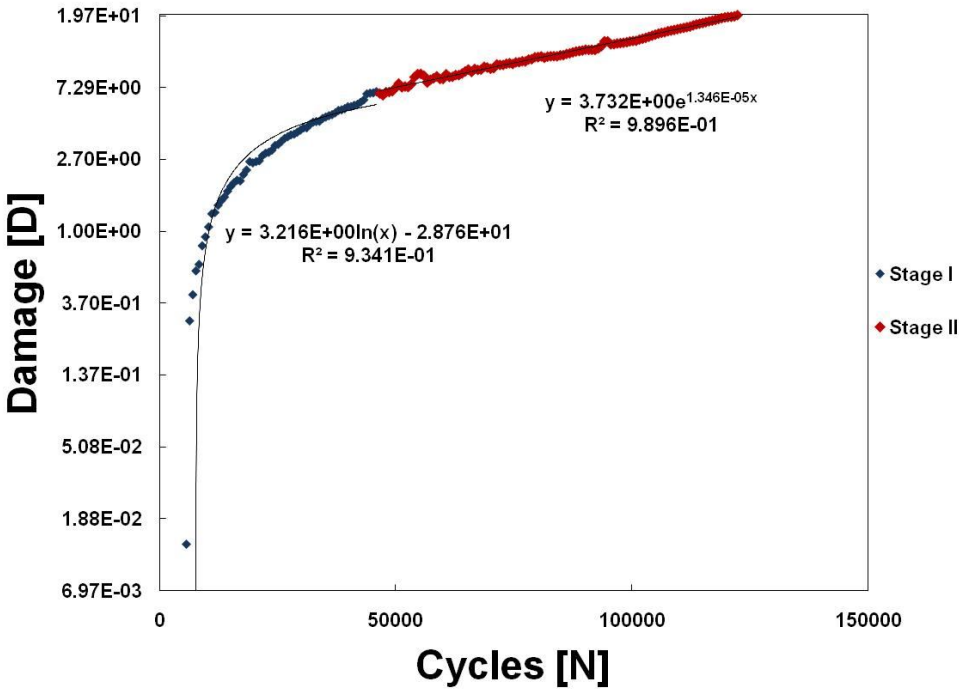

Figure D 58 - Damage curve of 6 month aged σ_3 – specimen 8.

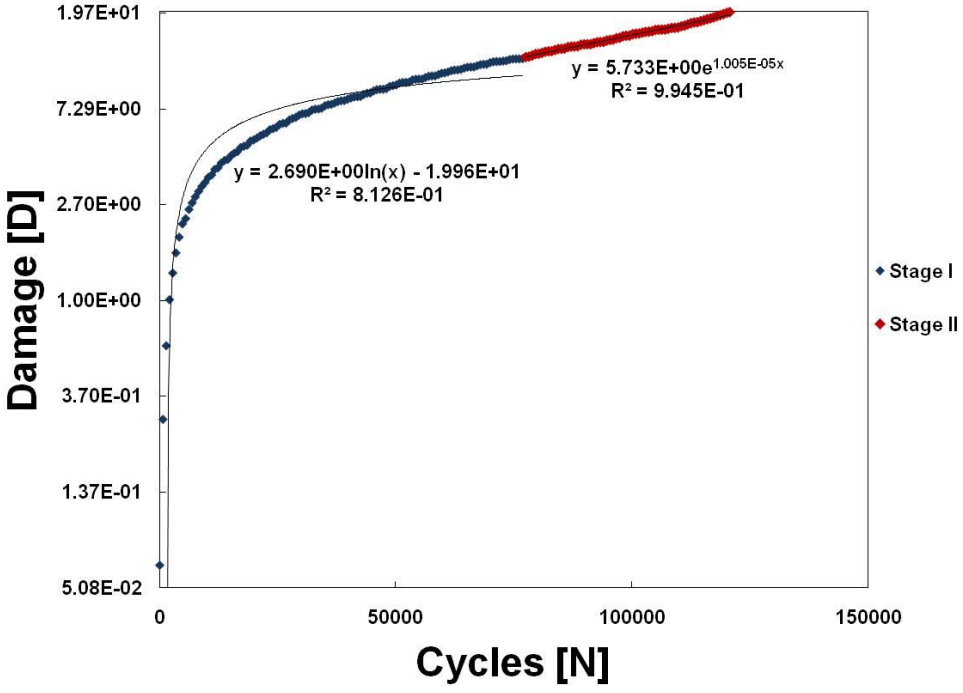

Figure D 59 - Damage curve of 6 month aged σ_3 – specimen 9.

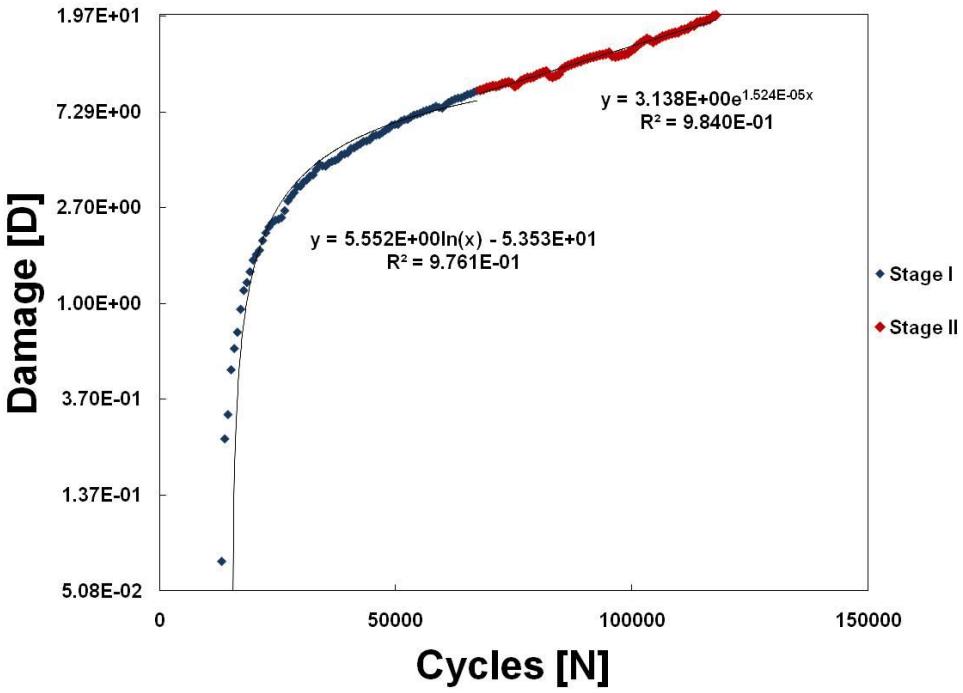

Figure D 60 - Damage curve of 6 month aged σ_3 – specimen 10.

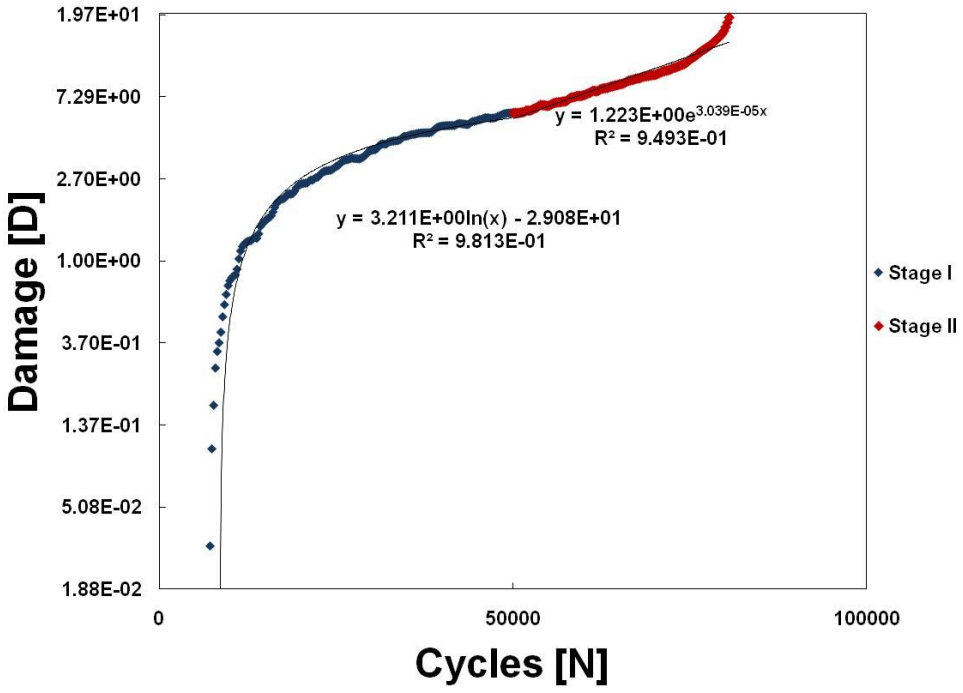

Figure D 61 - Damage curve of 12 month aged σ_1 – specimen 1.

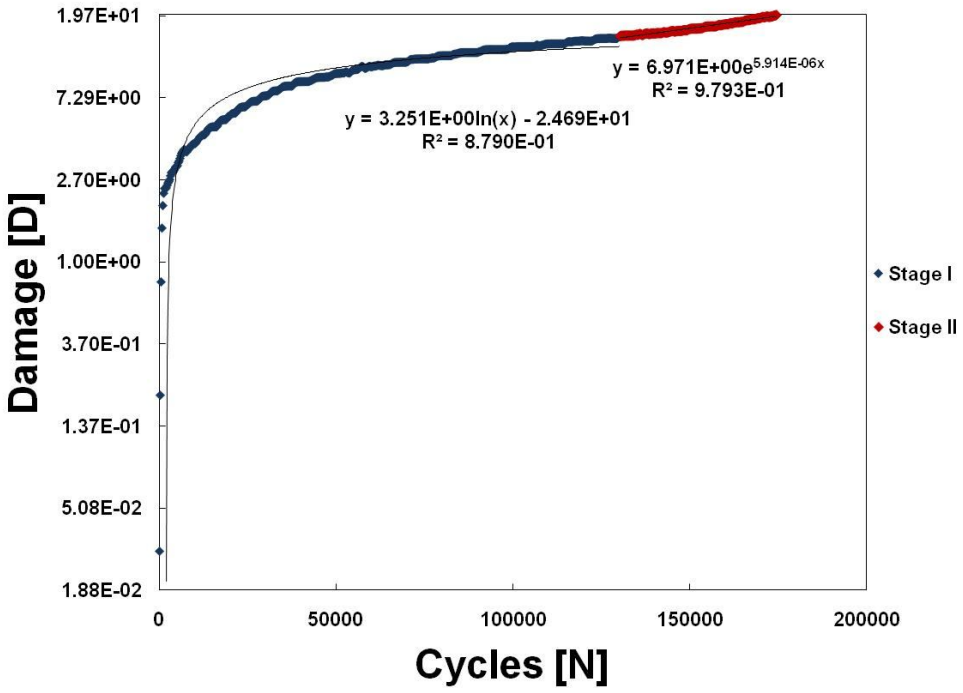

Figure D 62 - Damage curve of 12 month aged σ_1 – specimen 2.

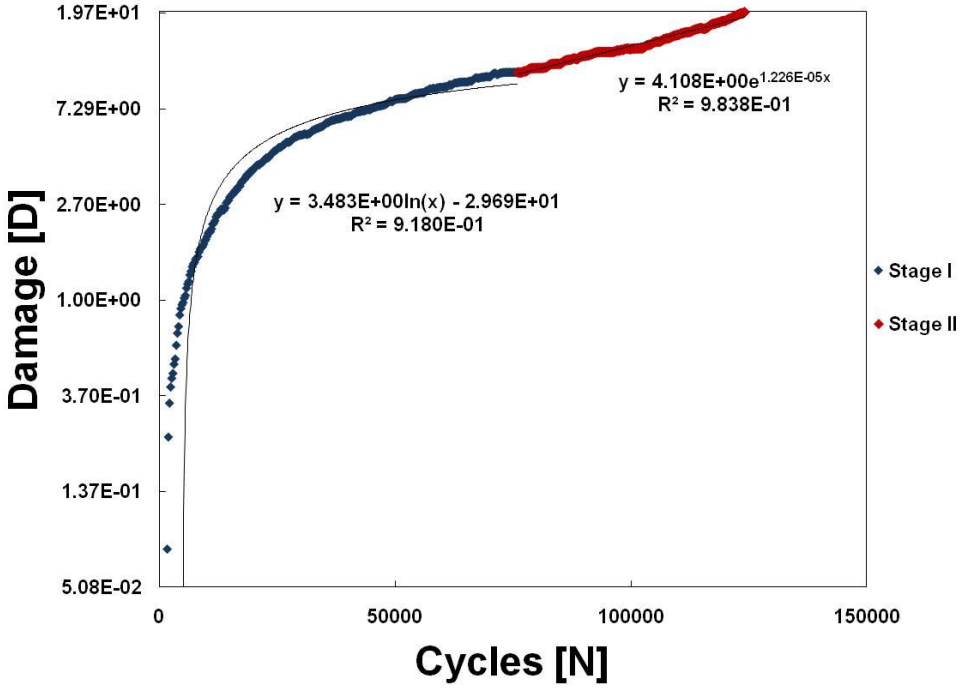

Figure D 63 - Damage curve of 12 month aged σ_1 – specimen 3.

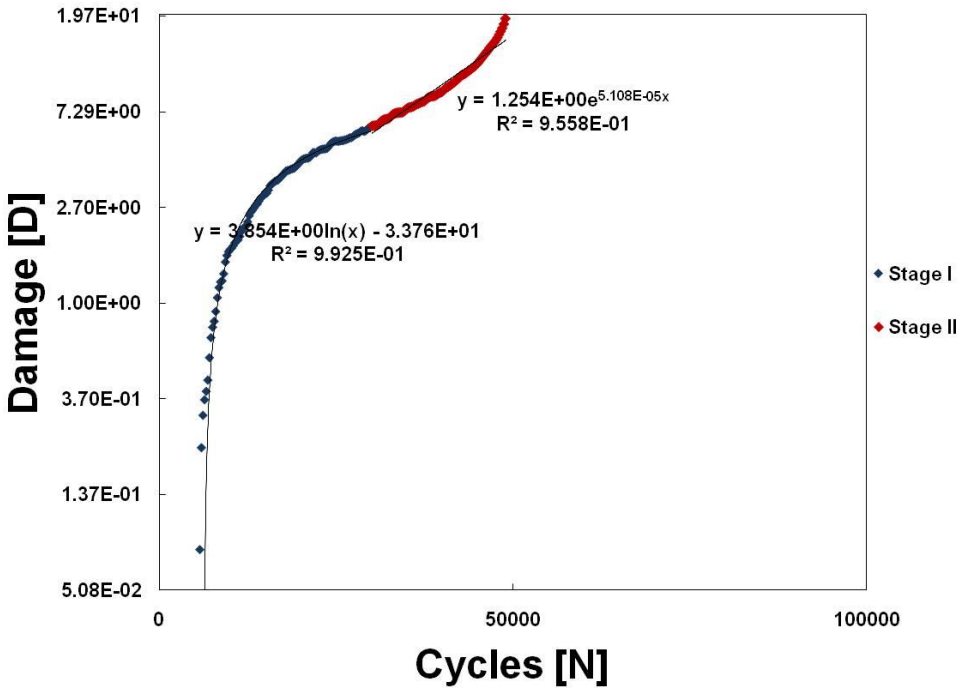

Figure D 64 - Damage curve of 12 month aged σ_1 – specimen 4.

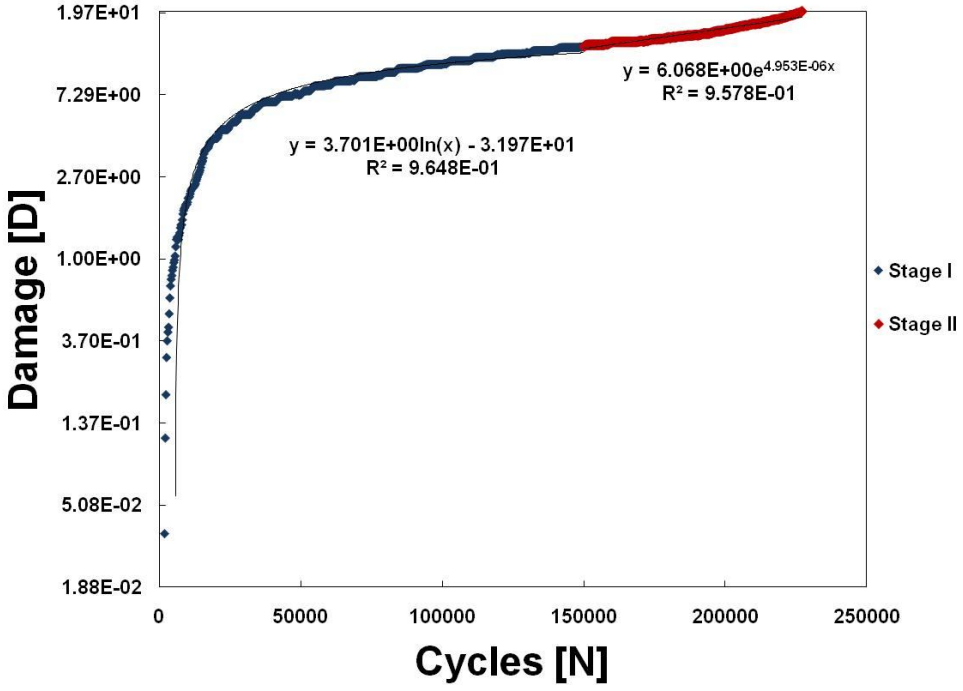

Figure D 65 - Damage curve of 12 month aged σ_1 – specimen 5.

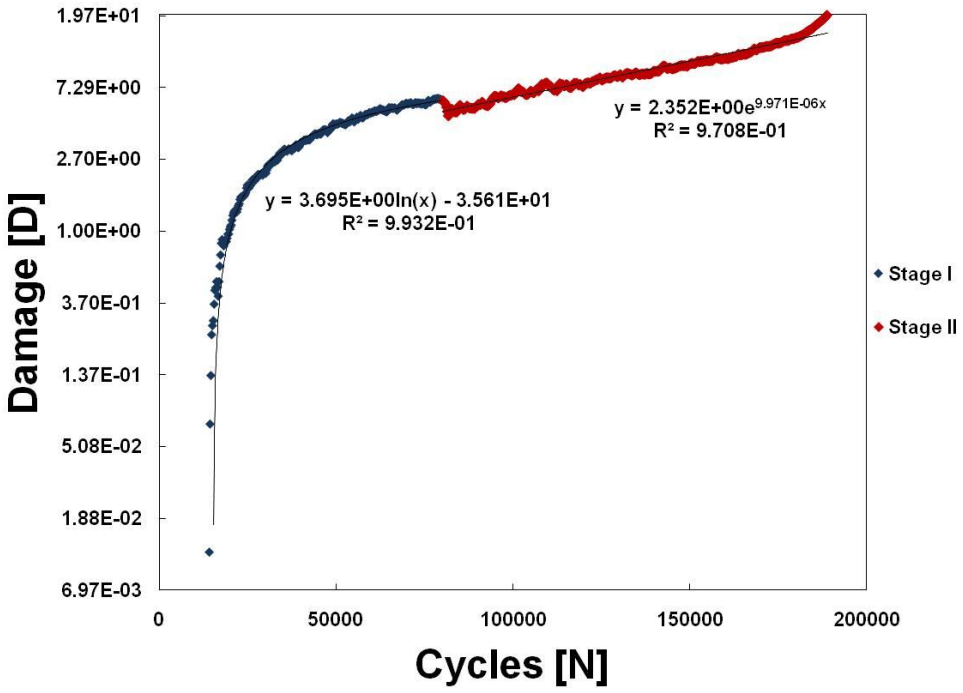

Figure D 66 - Damage curve of 12 month aged σ_1 – specimen 6.

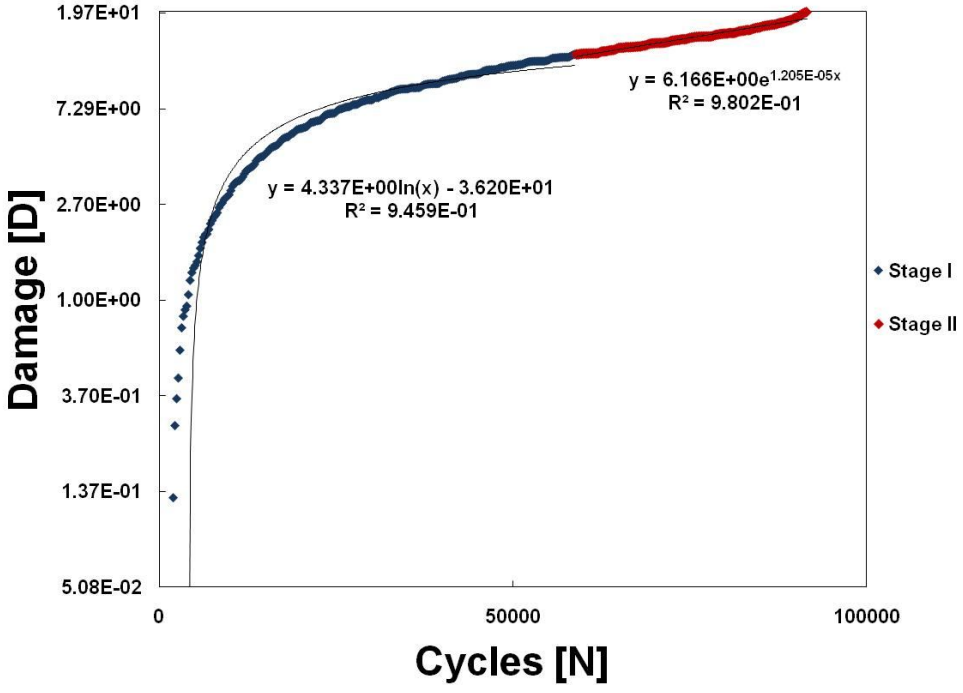

Figure D 67 - Damage curve of 12 month aged σ_1 – specimen 7.

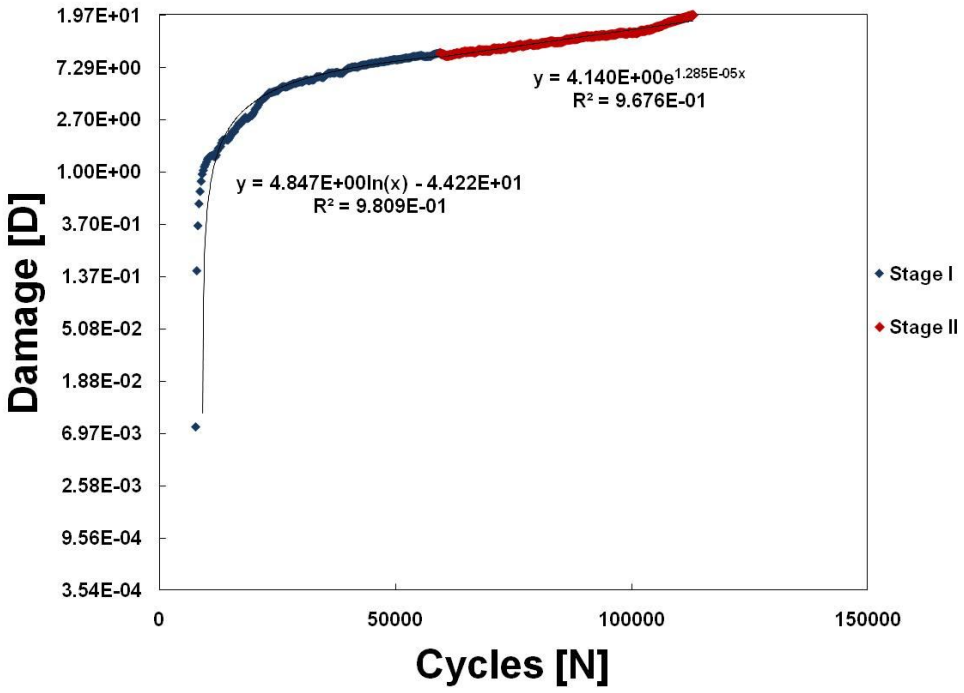

-

Figure D 68 - Damage curve of 12 month aged σ_1 – specimen 8.

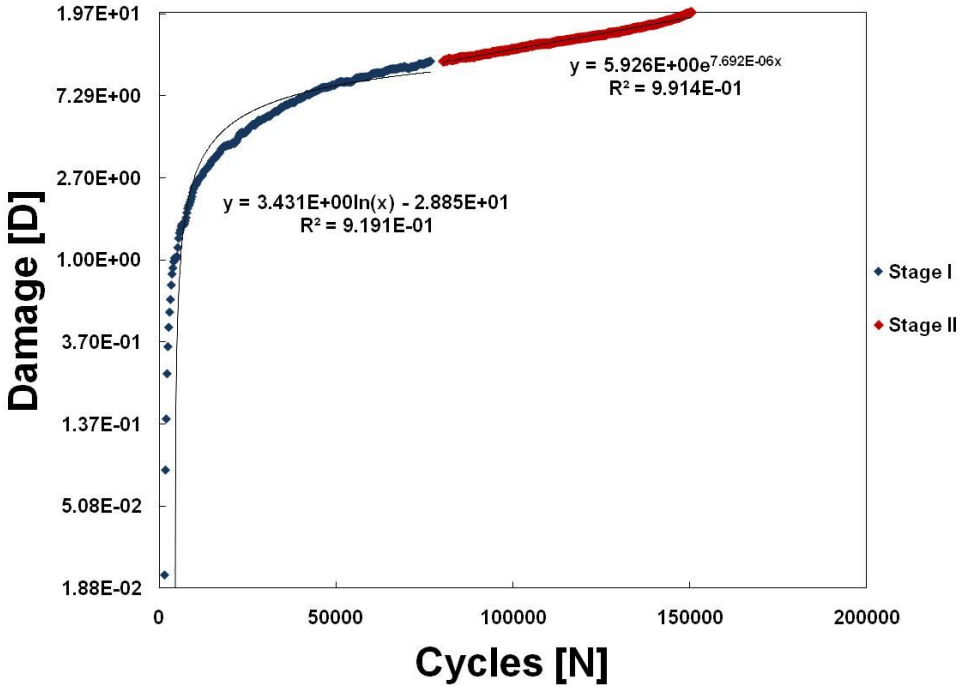

Figure D 69 - Damage curve of 12 month aged σ_1 – specimen 9.

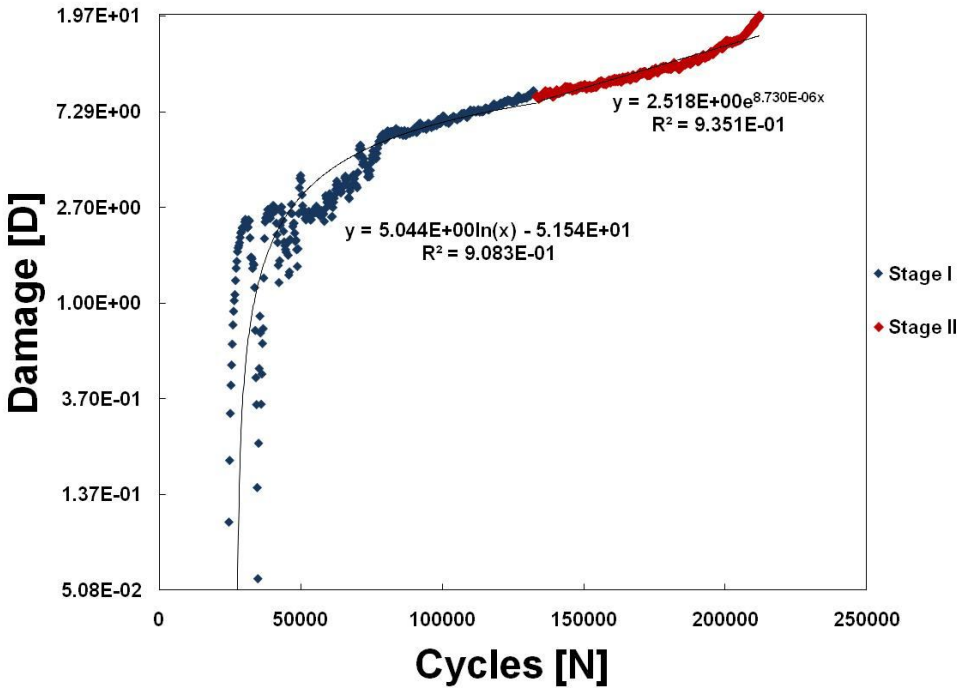

Figure D 70 - Damage curve of 12 month aged σ_1 – specimen 10.

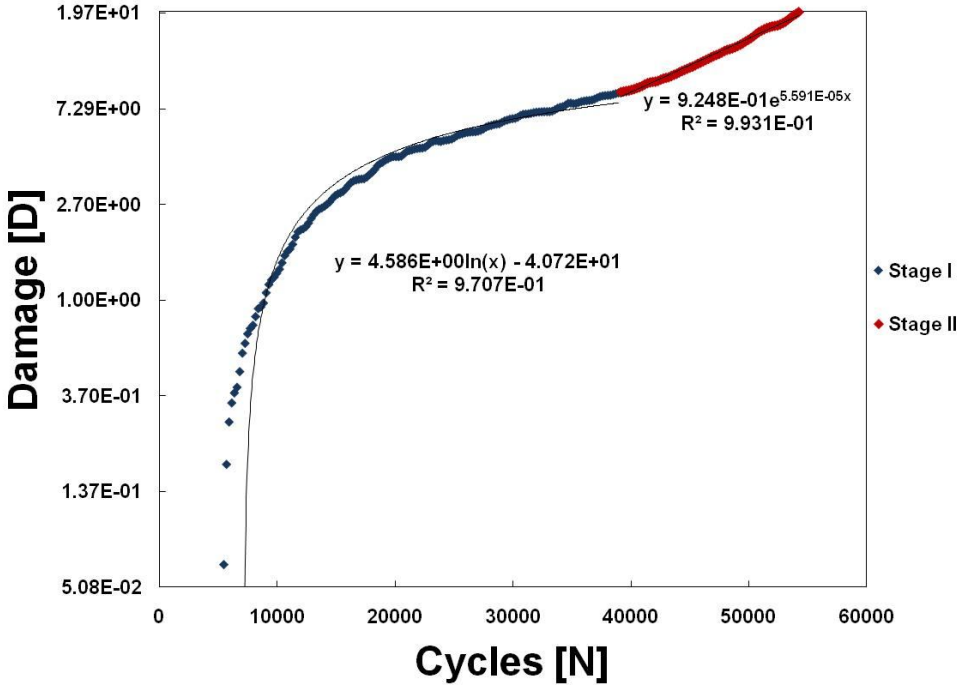

Figure D 71 - Damage curve of 12 month aged σ_2 – specimen 1.

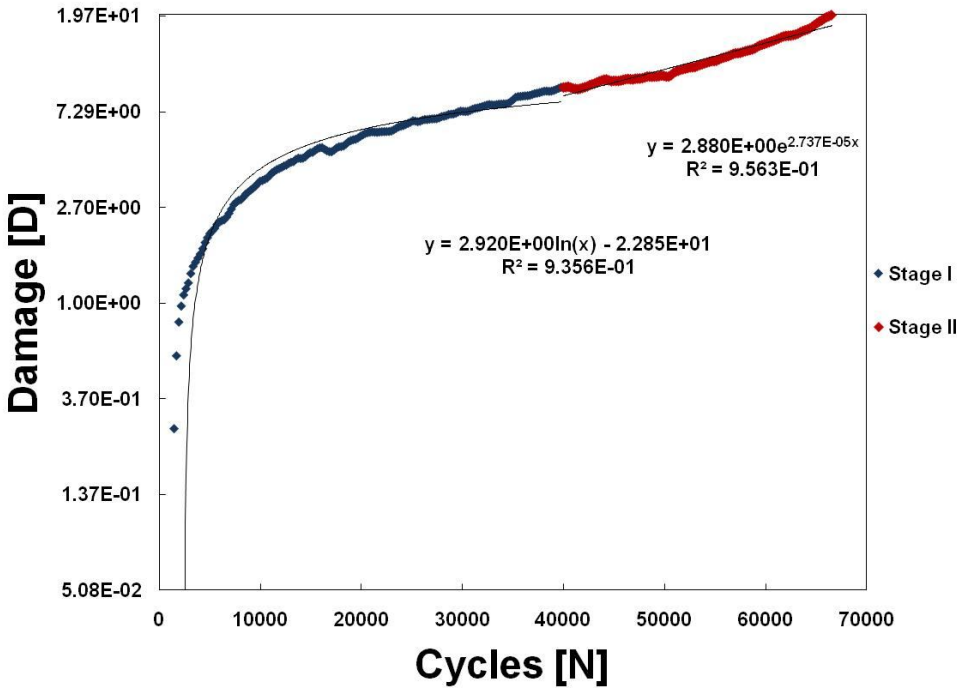

Figure D 72 - Damage curve of 12 month aged σ_2 – specimen 2.

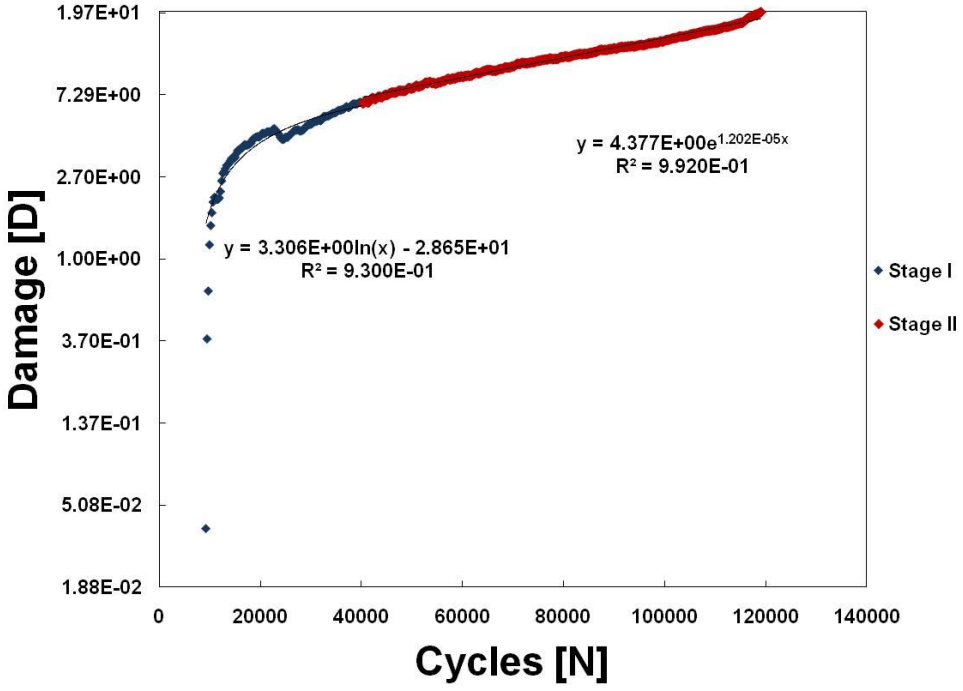

Figure D 73 - Damage curve of 12 month aged σ_2 – specimen 3.

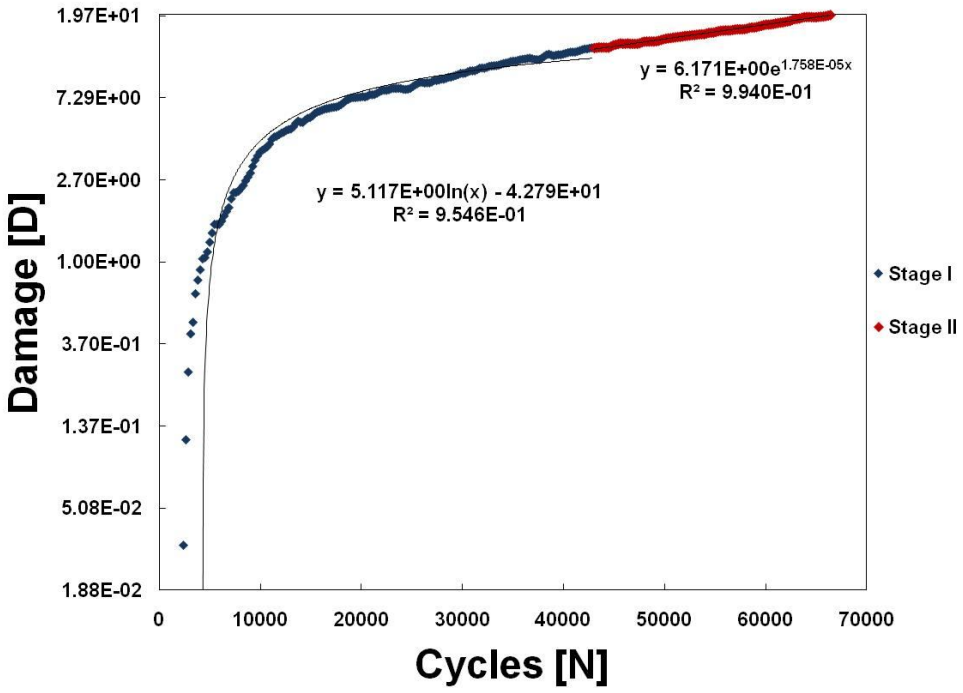

Figure D 74 - Damage curve of 12 month aged σ_2 – specimen 4.

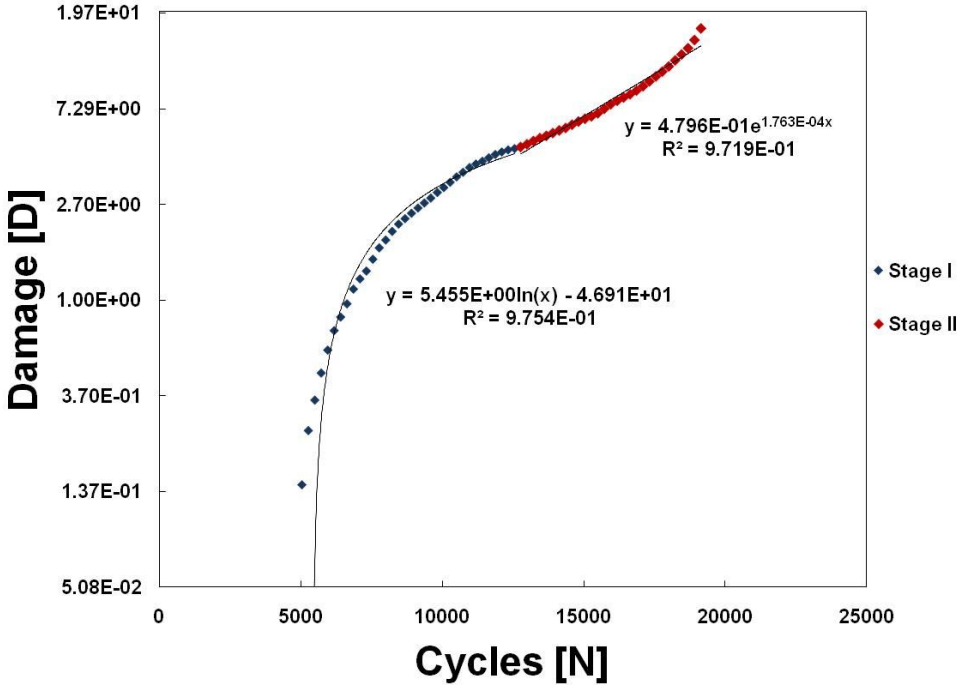

Figure D 75 - Damage curve of 12 month aged σ_2 – specimen 5.

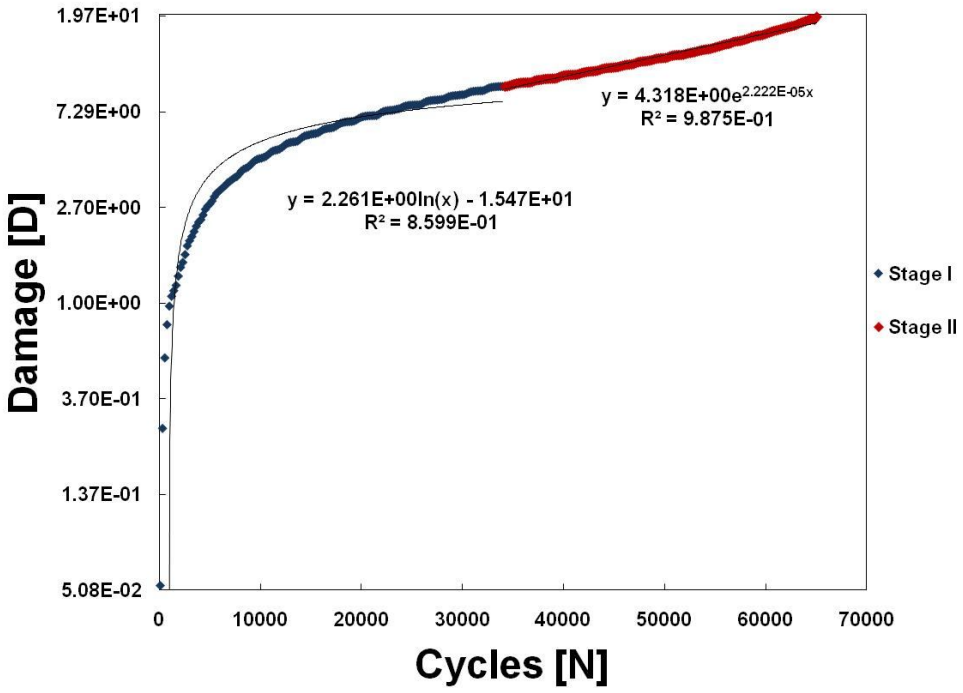

Figure D 76 - Damage curve of 12 month aged σ_2 – specimen 6.

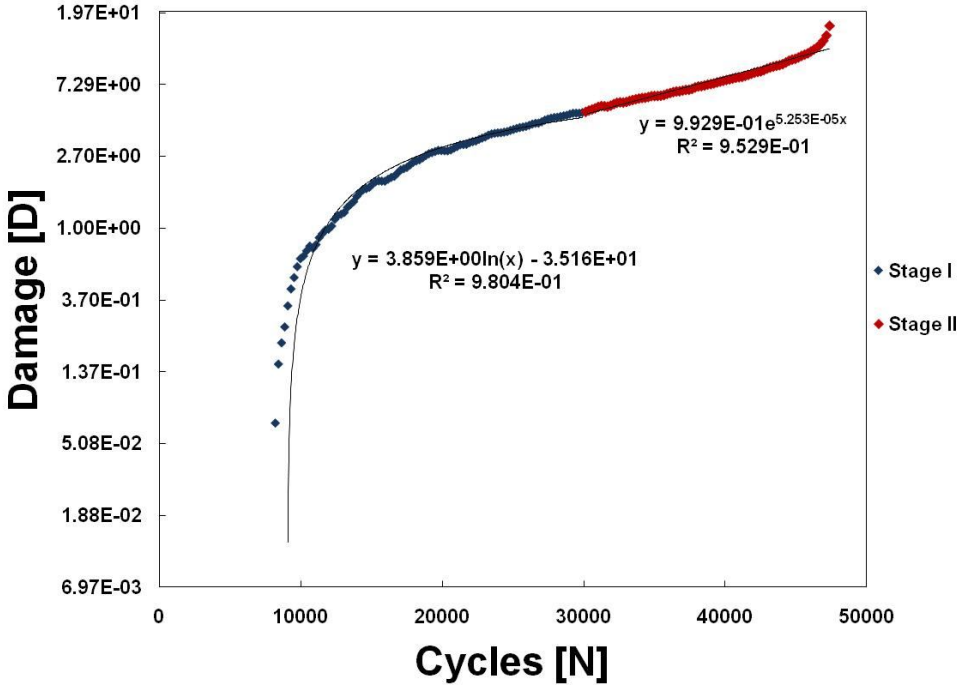

Figure D 77 - Damage curve of 12 month aged σ_2 – specimen 7.

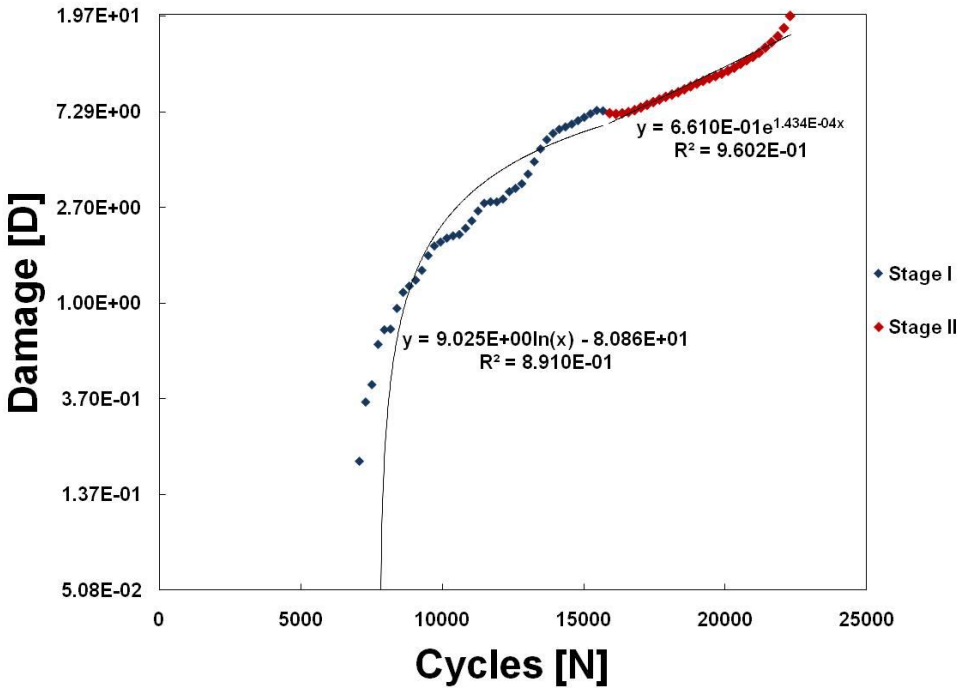

Figure D 78 - Damage curve of 12 month aged σ_2 – specimen 8.

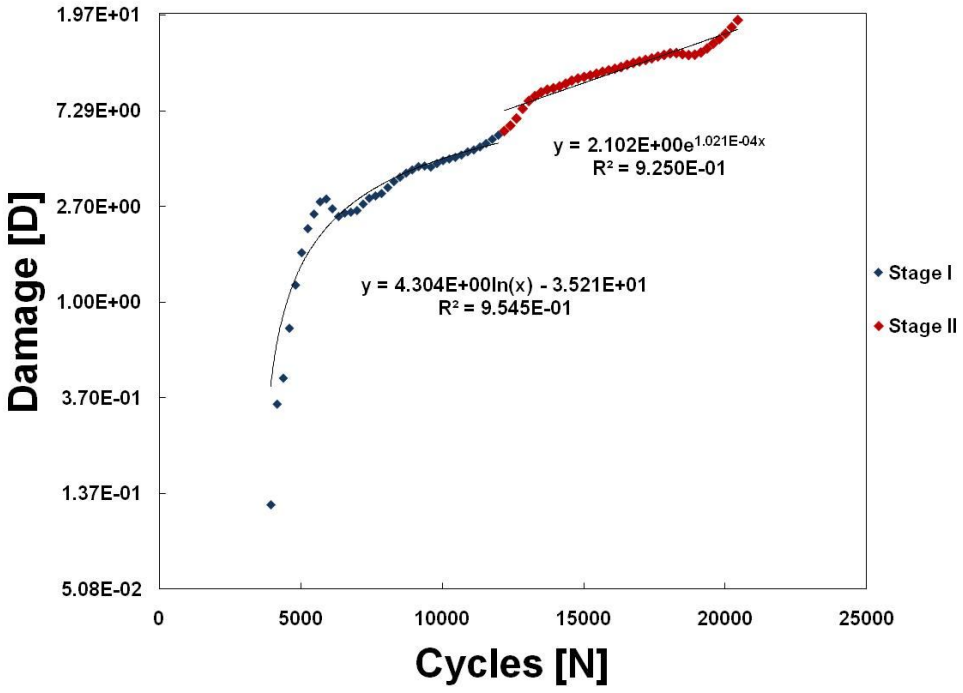

Figure D 79 - Damage curve of 12 month aged σ_2 – specimen 9.

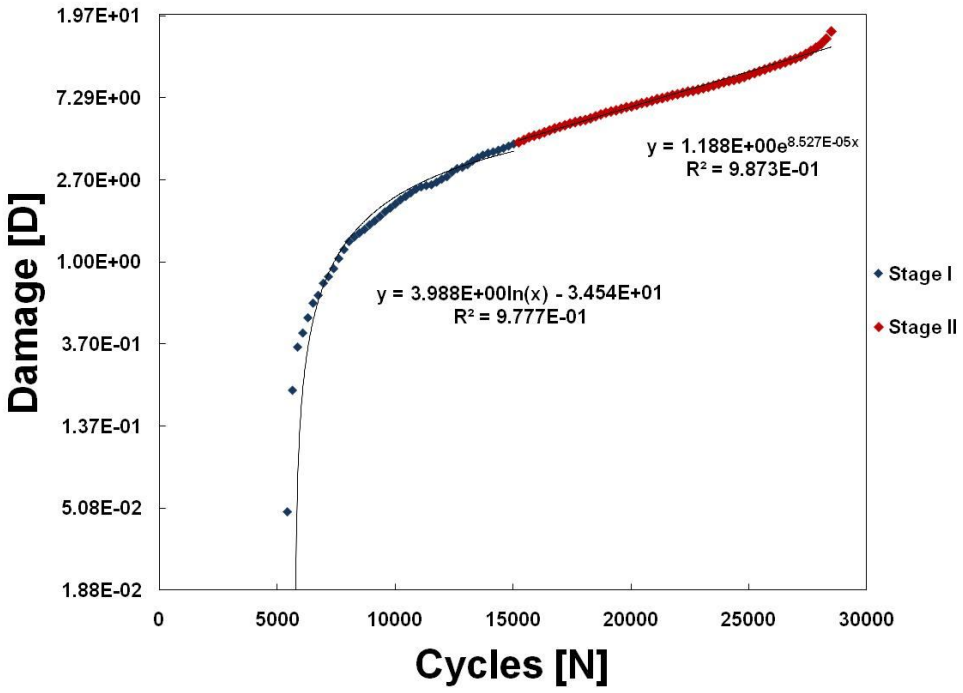

Figure D 80 - Damage curve of 12 month aged σ_2 – specimen 10.

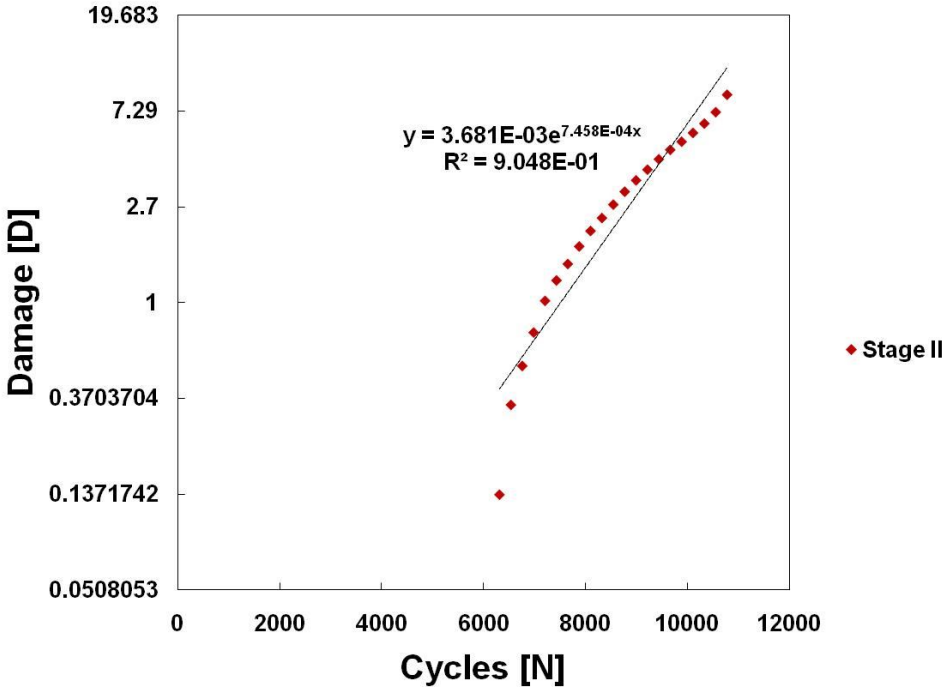

Figure D 81 - Damage curve of 12 month aged σ_3 – specimen 1.

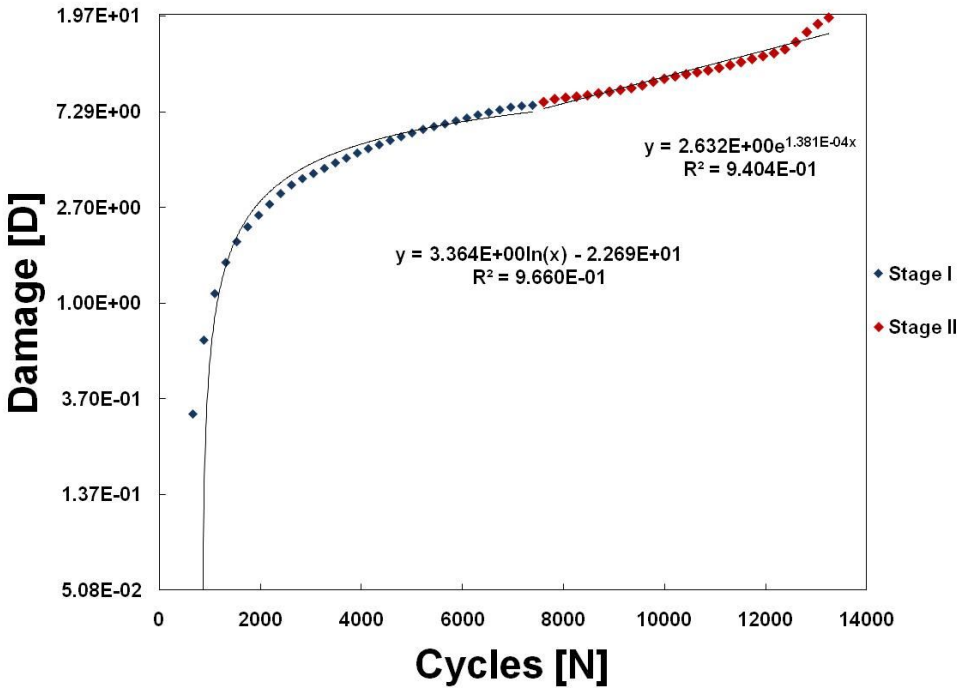

Figure D 82 - Damage curve of 12 month aged σ_3 – specimen 2.

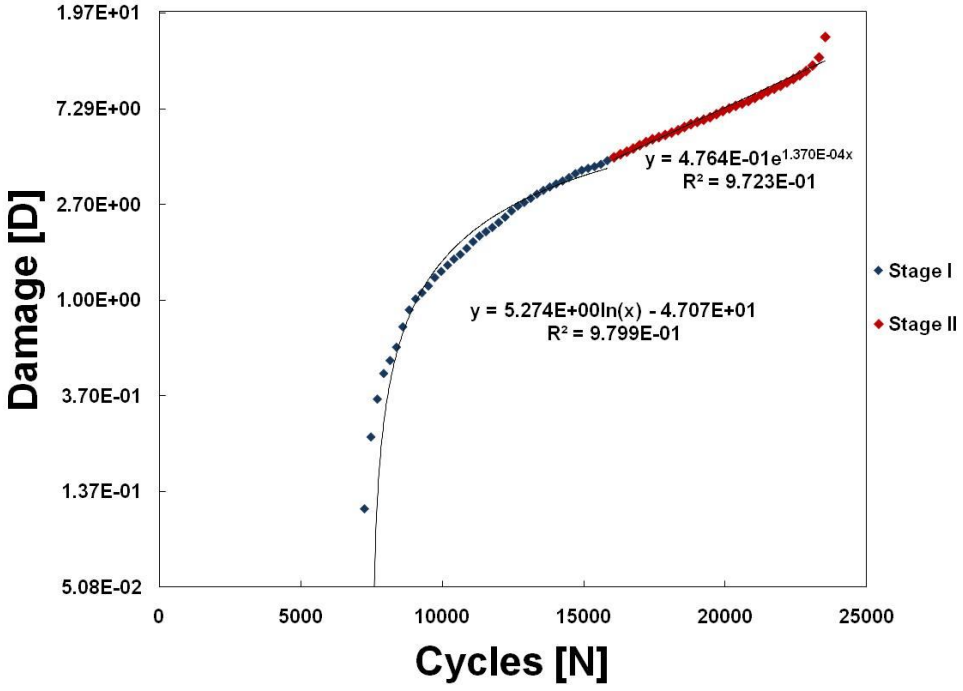

Figure D 83 - Damage curve of 12 month aged σ_3 – specimen 3.

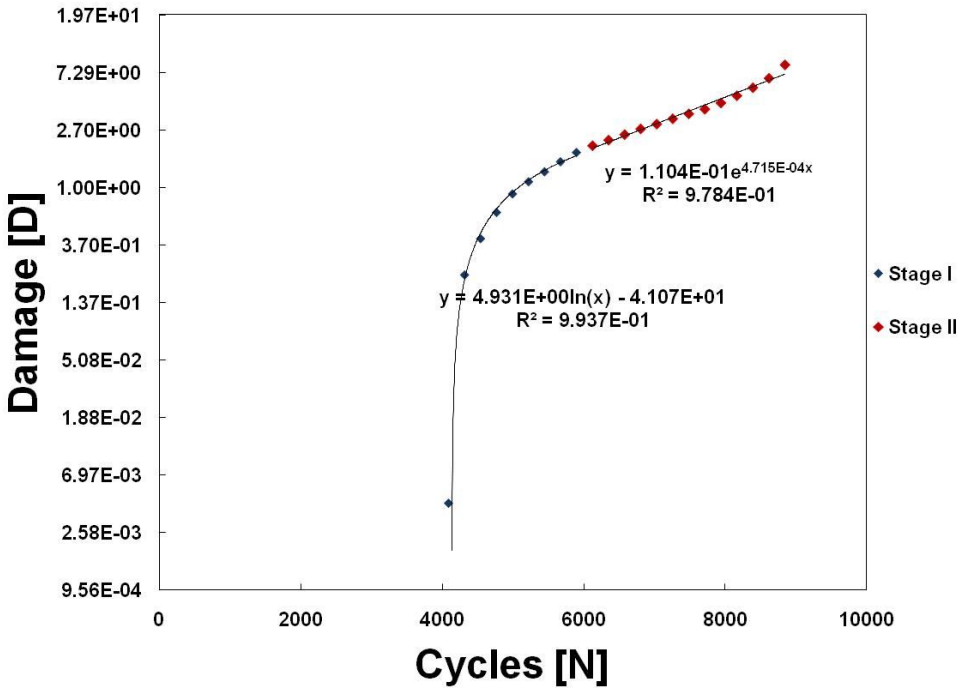

Figure D 84 - Damage curve of 12 month aged σ_3 – specimen 4.

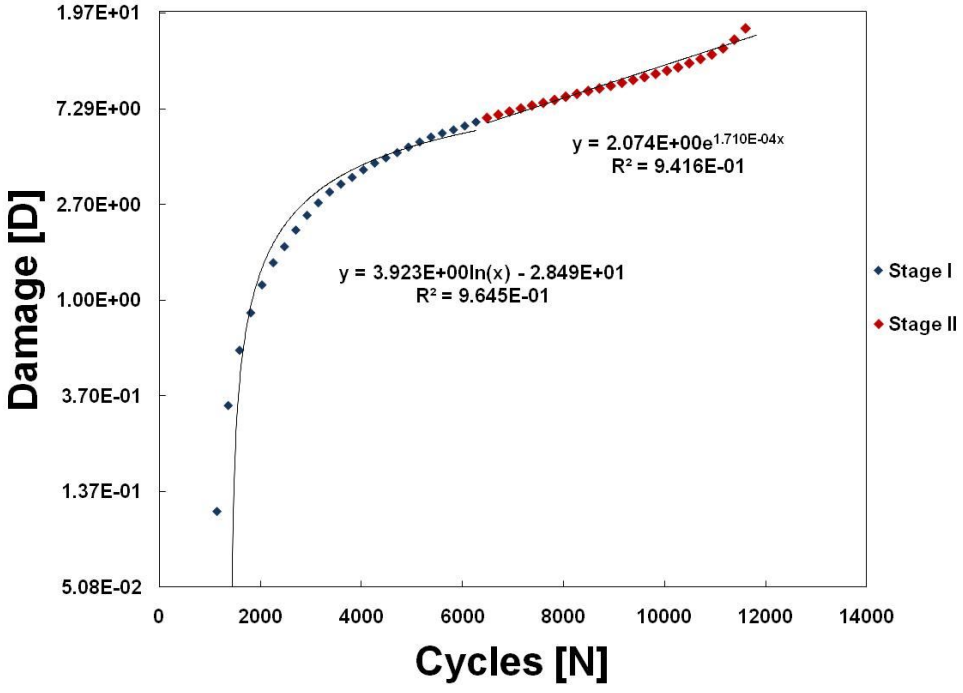

Figure D 85 - Damage curve of 12 month aged σ_3 – specimen 5.

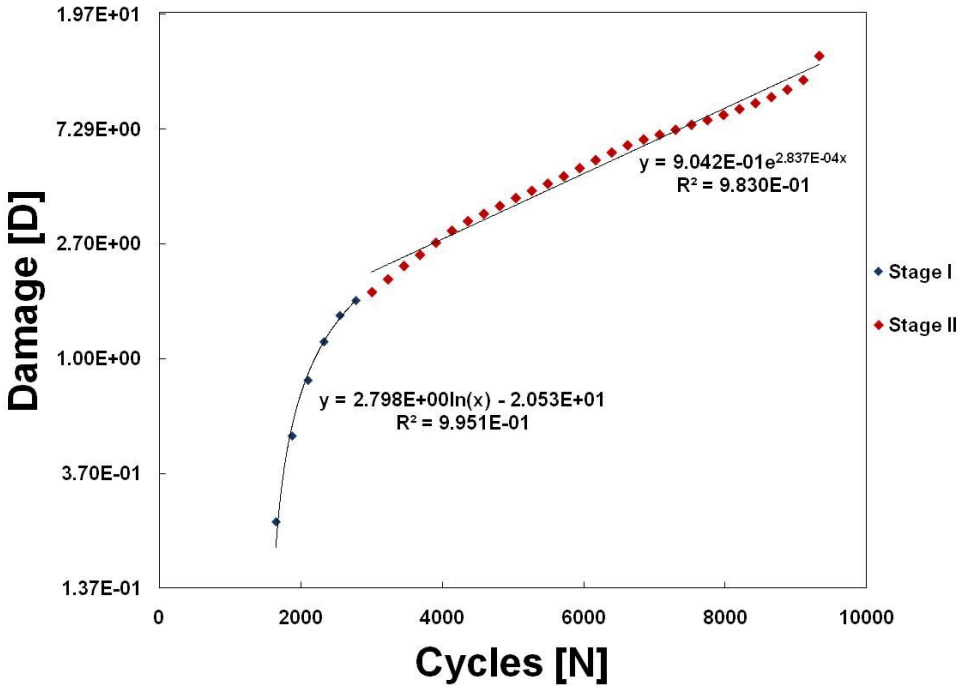

Figure D 86 - Damage curve of 12 month aged σ_3 – specimen 6.

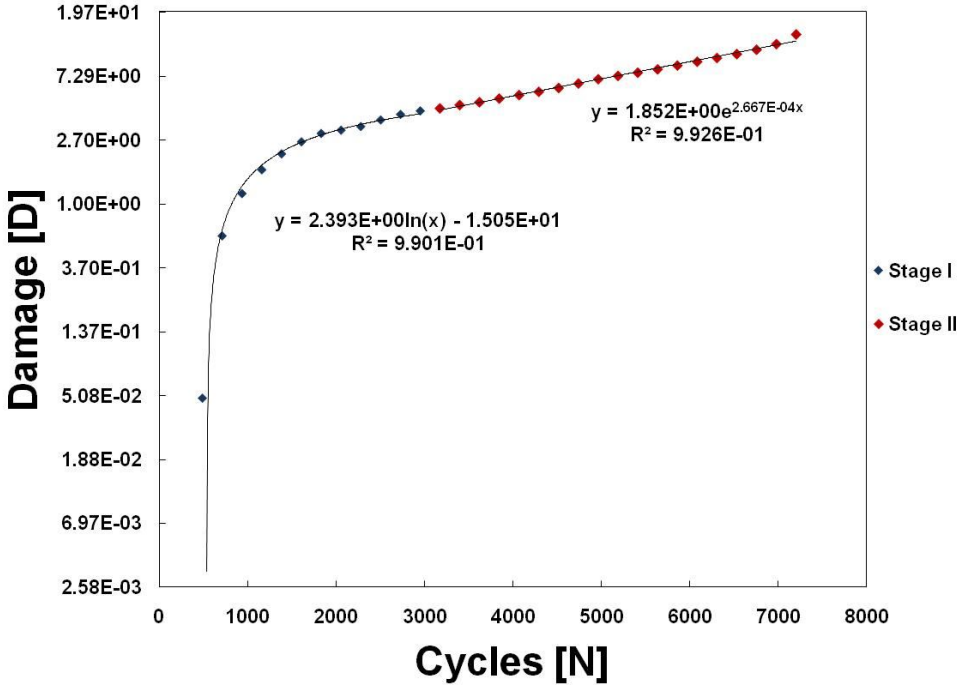

Figure D 87 - Damage curve of 12 month aged σ_3 – specimen 7.

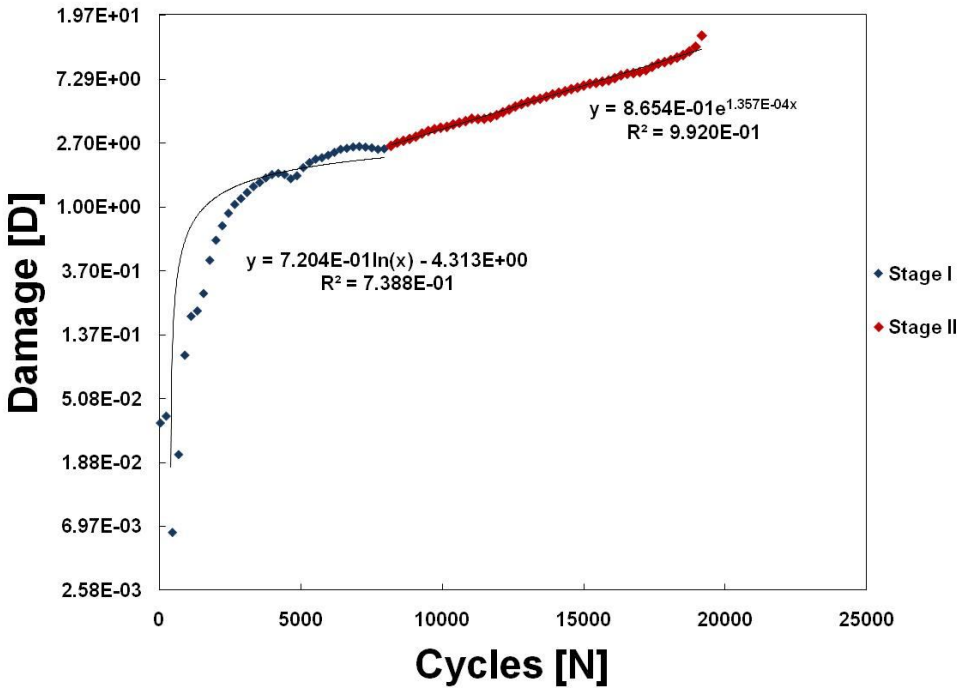

Figure D 88 - Damage curve of 12 month aged σ_3 – specimen 8.

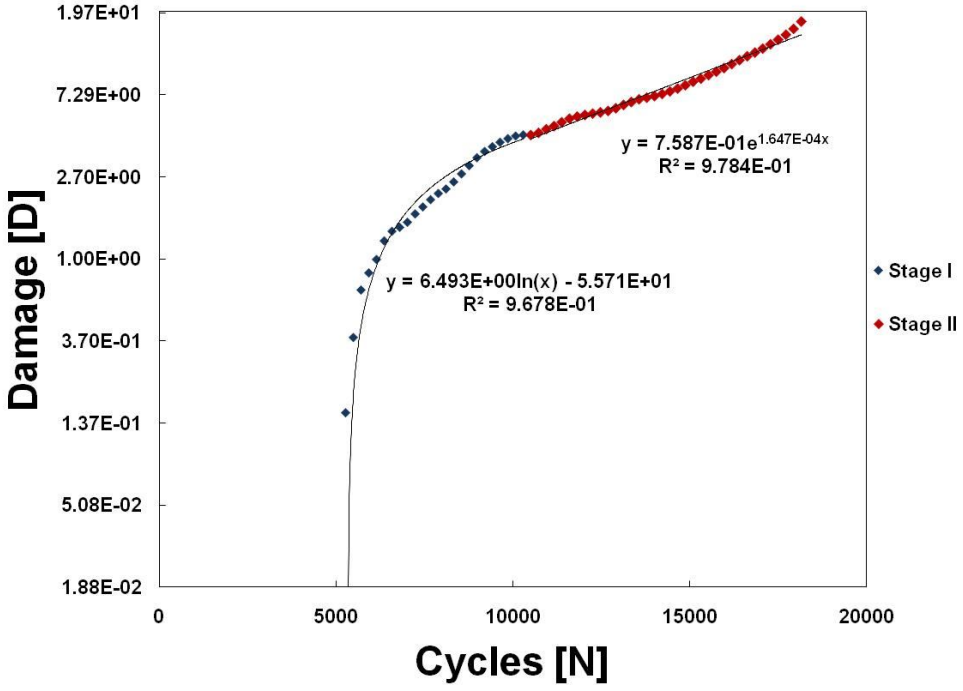

Figure D 89 - Damage curve of 12 month aged σ_3 – specimen 9.

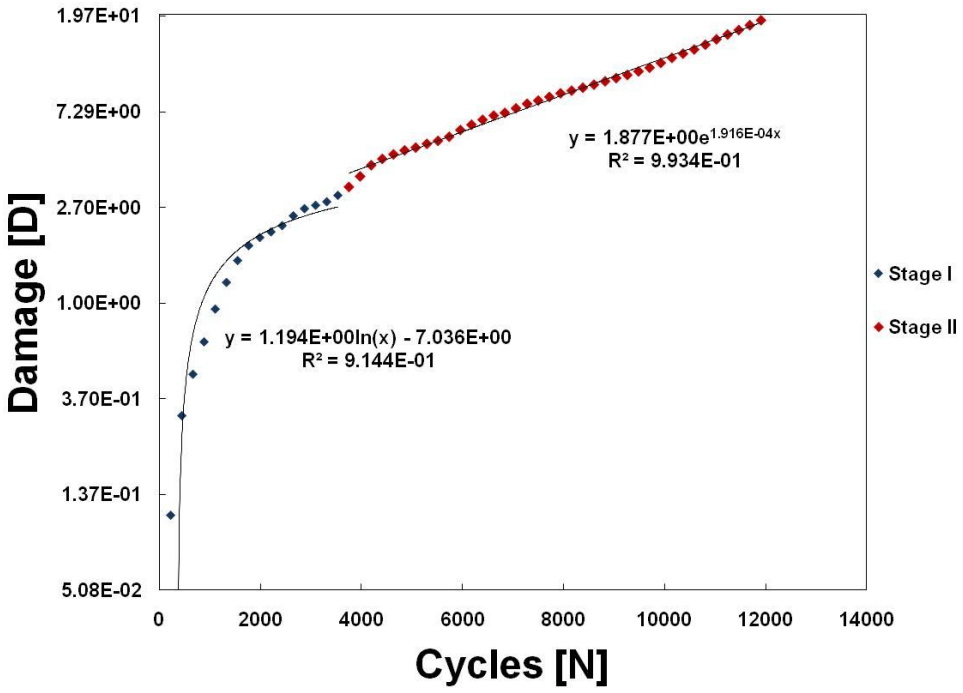

Figure D 90 - Damage curve of 12 month aged σ_3 – specimen 10.

APPENDIX E - FATIGUE DAMAGE ACCUMULATION RATE CURVES FOR AGED SPECIMENS

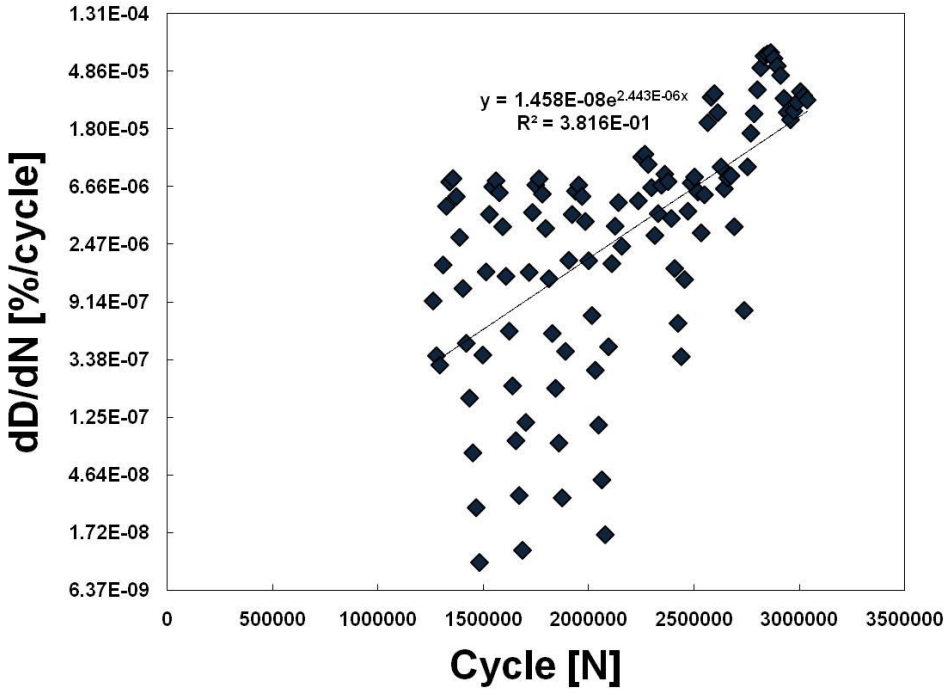

Figure E 1 – Rate of Damage accumulation of 3 month aged σ_1 – specimen 1.

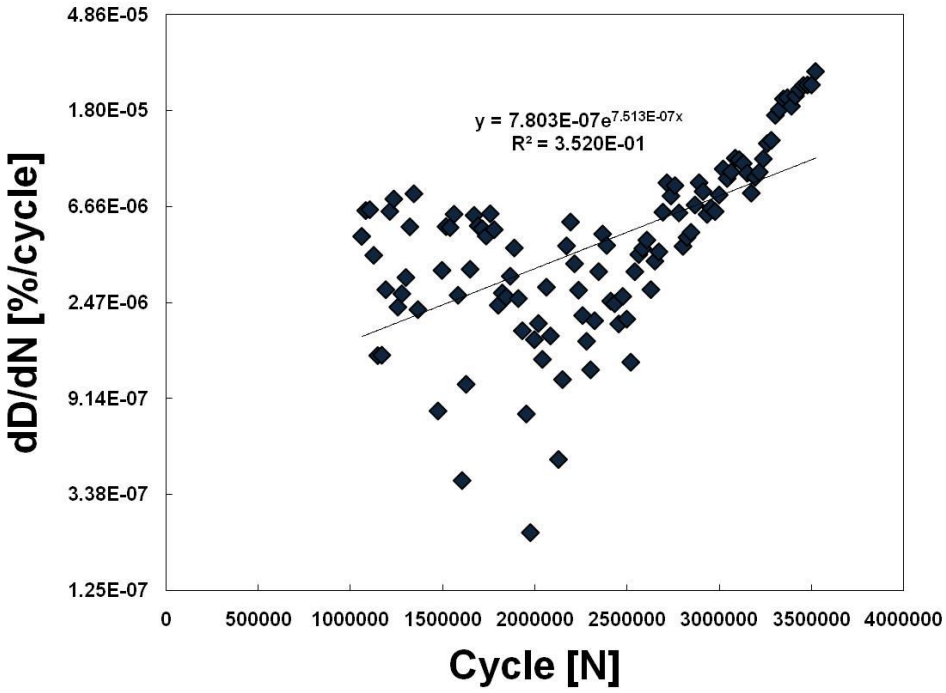

Figure E 2 - Rate of Damage accumulation of 3 month aged σ_1 – specimen 2.

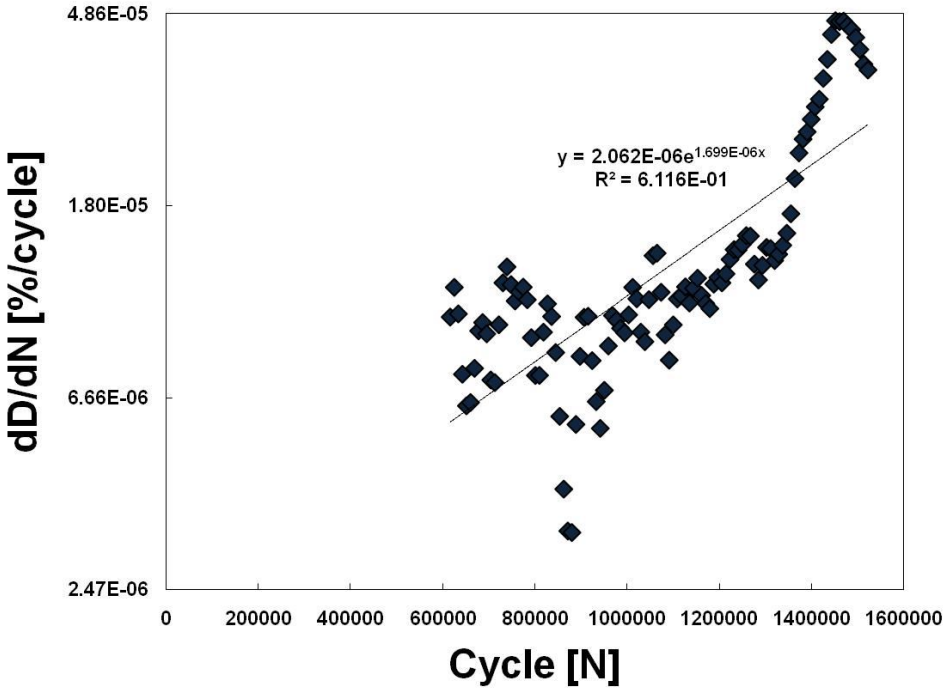

Figure E 3 - Rate of Damage accumulation of 3 month aged σ_1 – specimen 3.

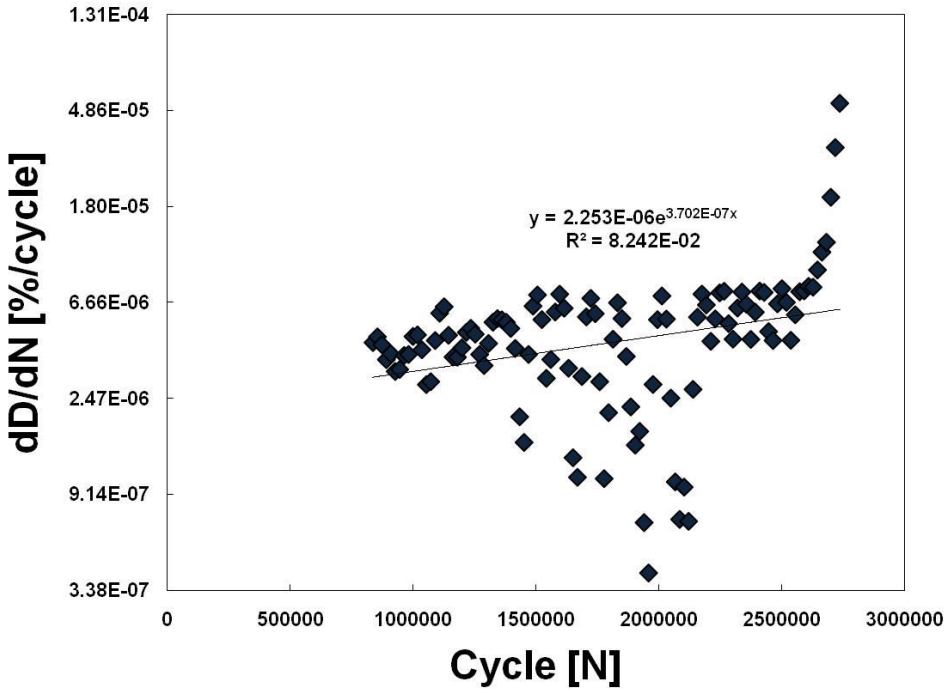

Figure E 4 - Rate of Damage accumulation of 3 month aged σ_1 – specimen 4.

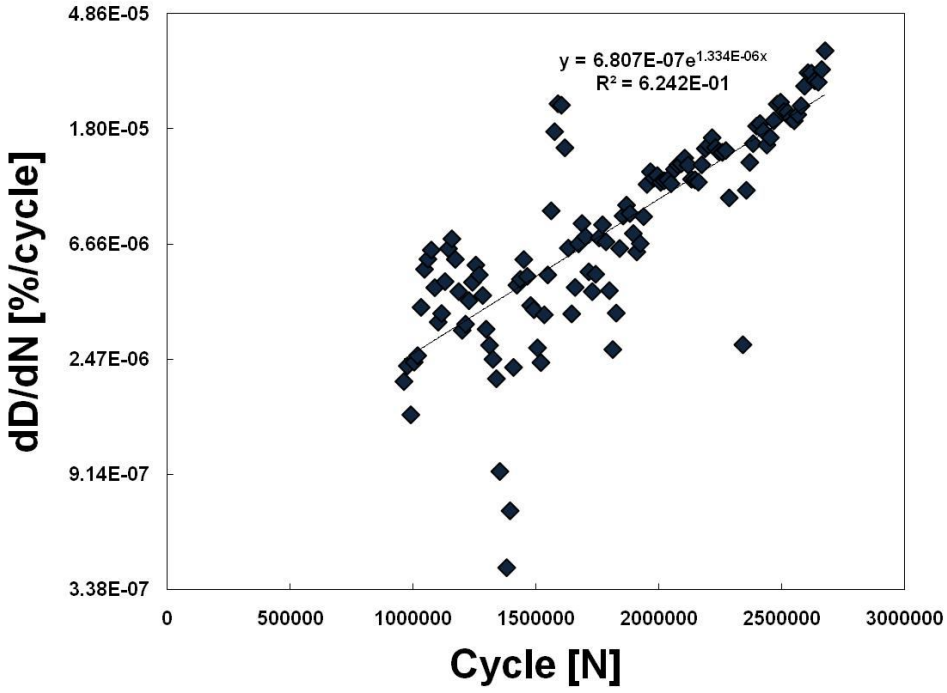

Figure E 5 - Rate of Damage accumulation of 3 month aged σ_1 – specimen 5.

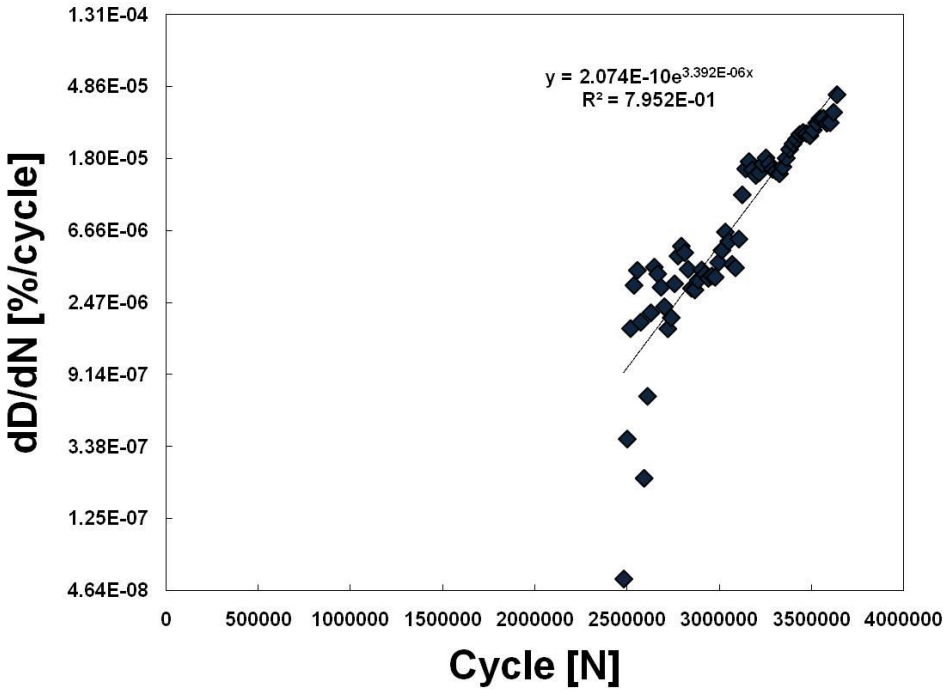

Figure E 6 - Rate of Damage accumulation of 3 month aged σ_1 – specimen 6.

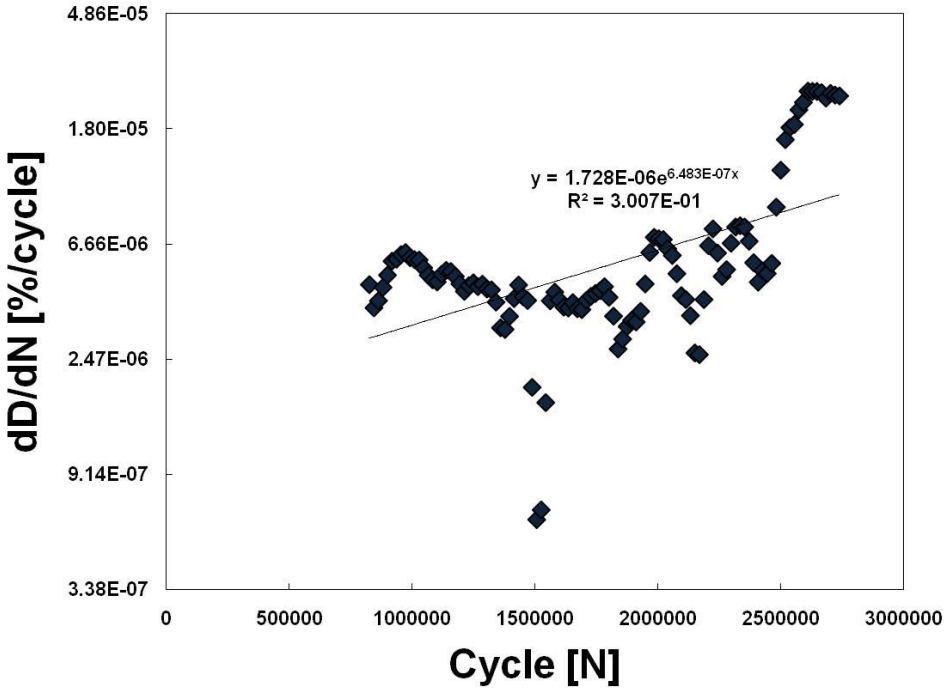

Figure E 7 - Rate of Damage accumulation of 3 month aged σ_1 – specimen 7.

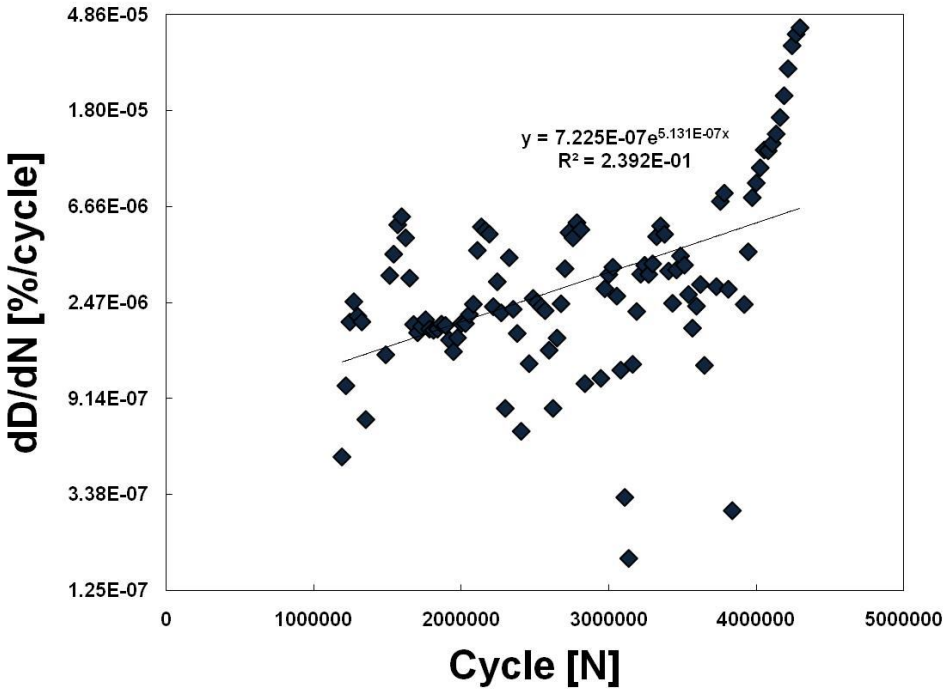

Figure E 8 - Rate of Damage accumulation of 3 month aged σ_1 – specimen 8.

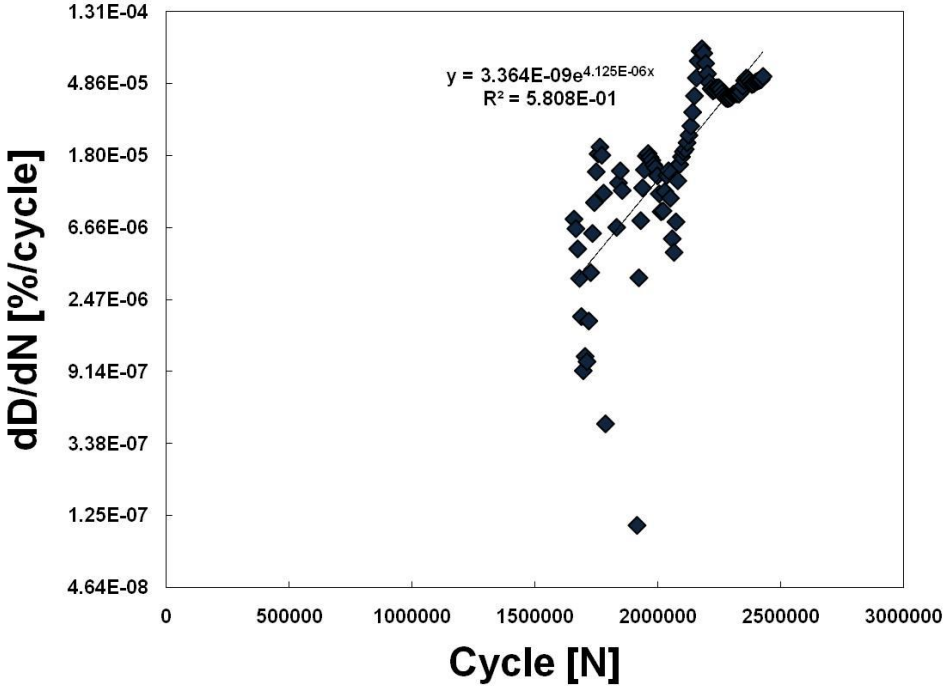

Figure E 9 - Rate of Damage accumulation of 3 month aged σ_1 – specimen 9.

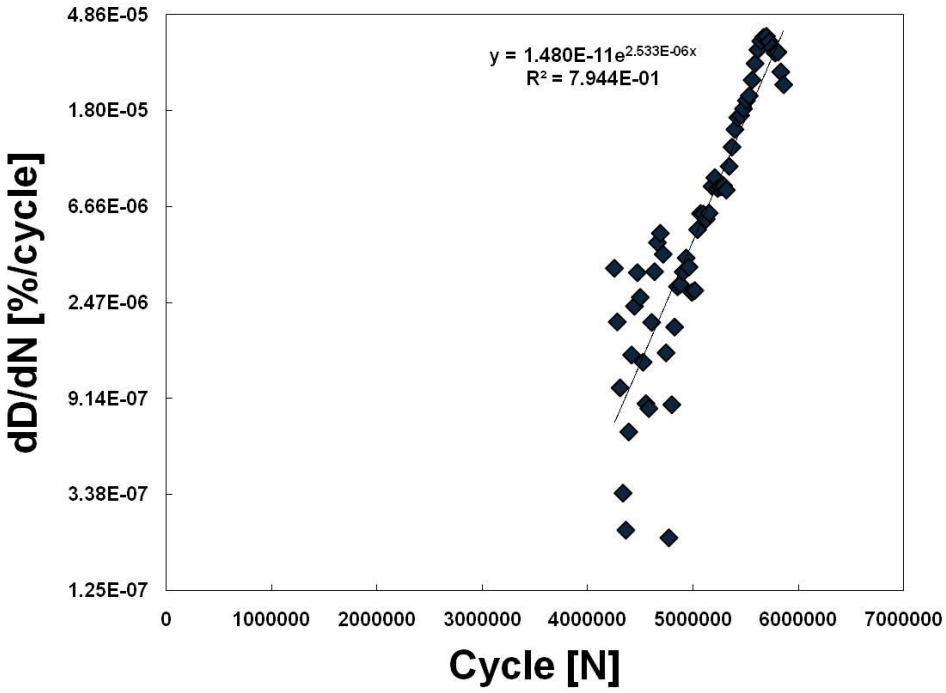

Figure E 10 - Rate of Damage accumulation of 3 month aged σ_1 – specimen 10.

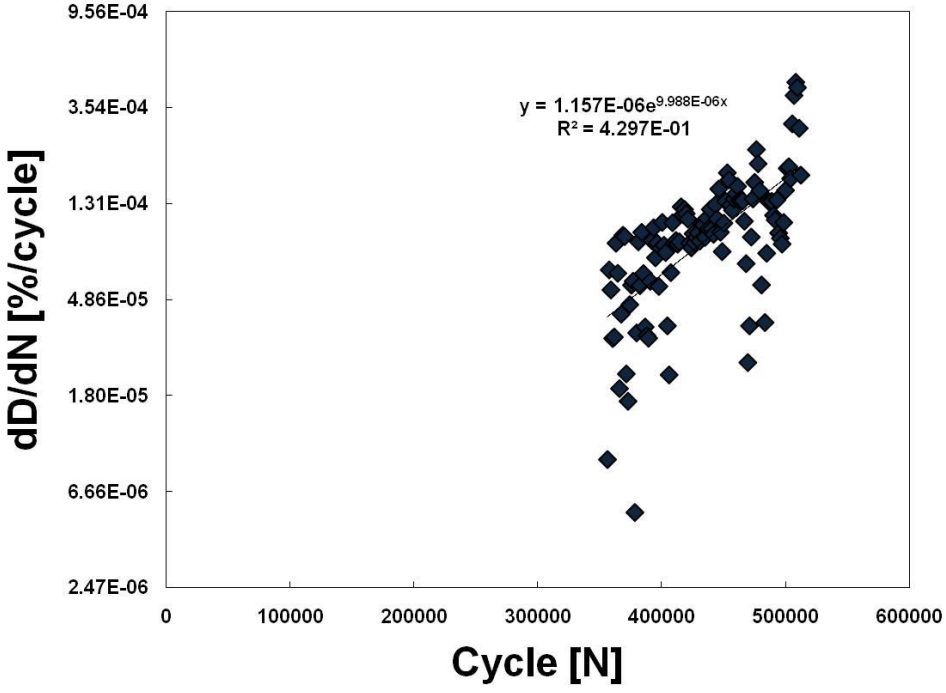

Figure E 11 - Rate of Damage accumulation of 3 month aged σ_2 – specimen 1.

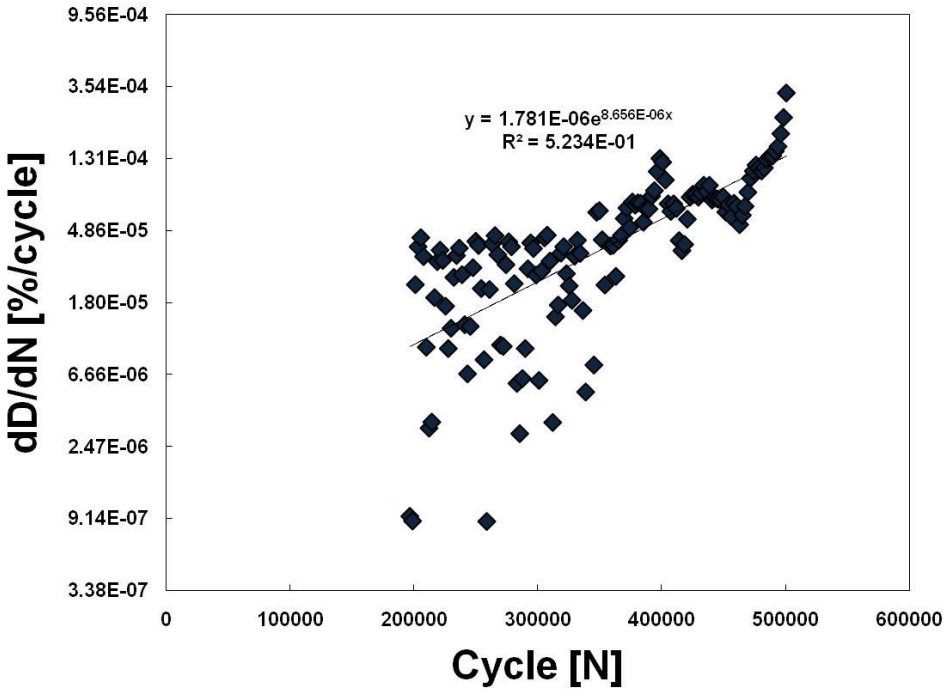

Figure E 12 - Rate of Damage accumulation of 3 month aged σ_2 – specimen 2.

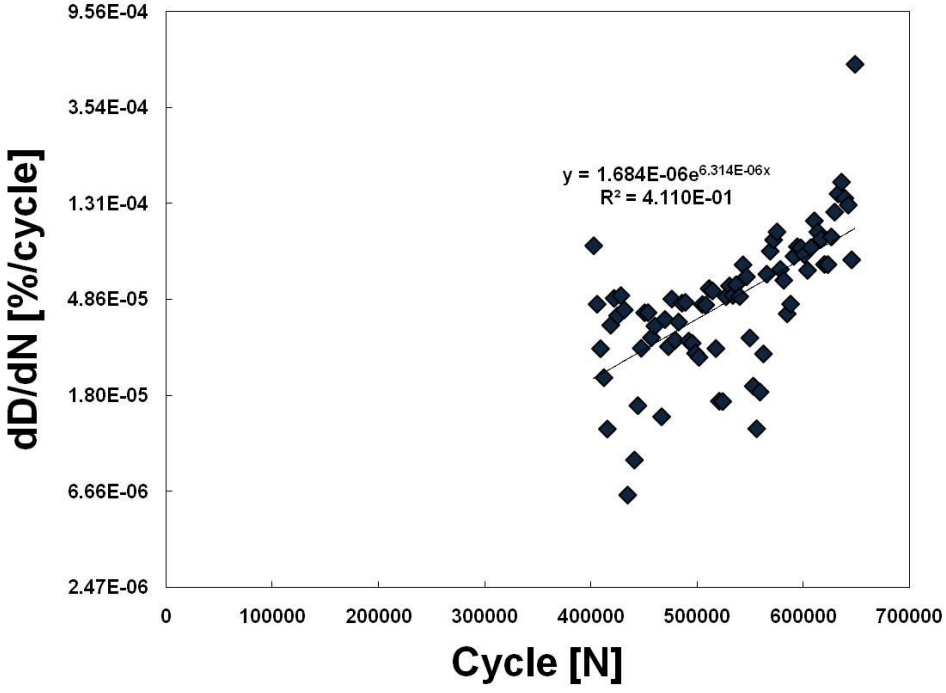

Figure E 13 - Rate of Damage accumulation of 3 month aged σ_2 – specimen 3.

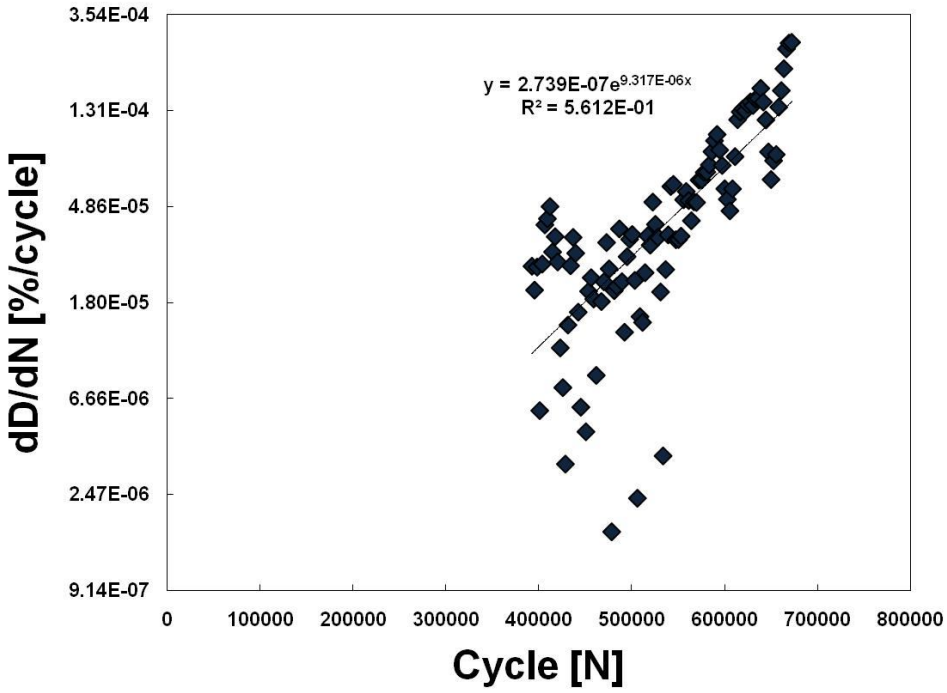

Figure E 14 - Rate of Damage accumulation of 3 month aged σ_2 – specimen 4.

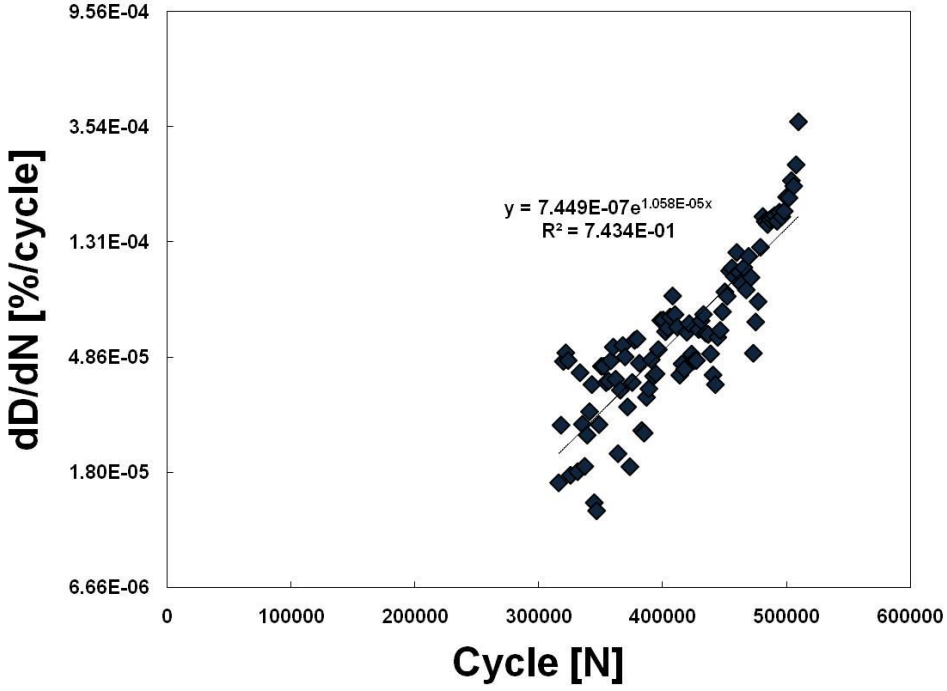

Figure E 15 - Rate of Damage accumulation of 3 month aged σ_2 – specimen 5.

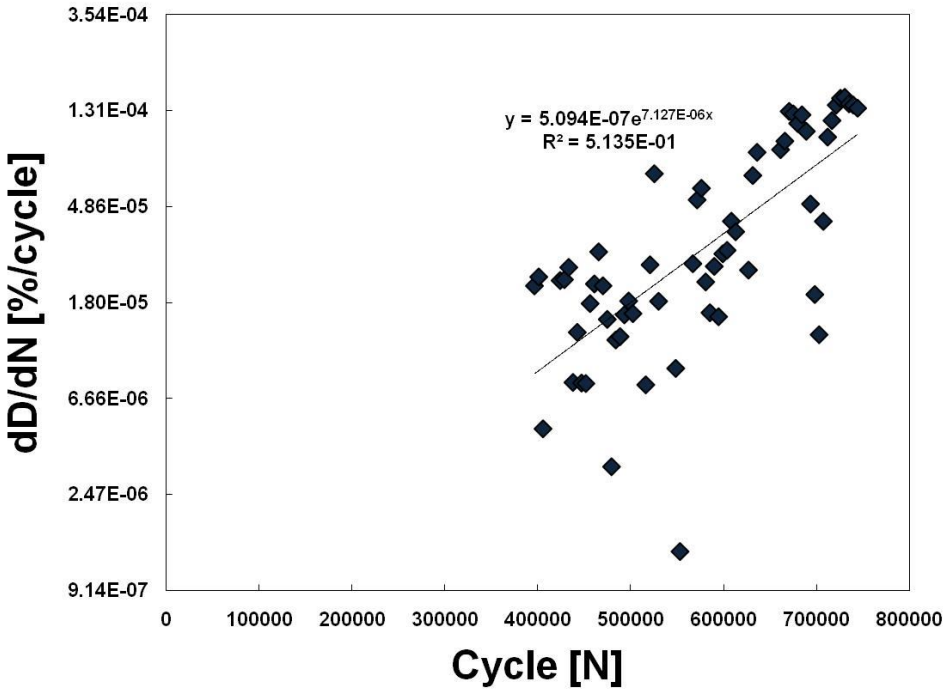

Figure E 16 - Rate of Damage accumulation of 3 month aged σ_2 – specimen 6.

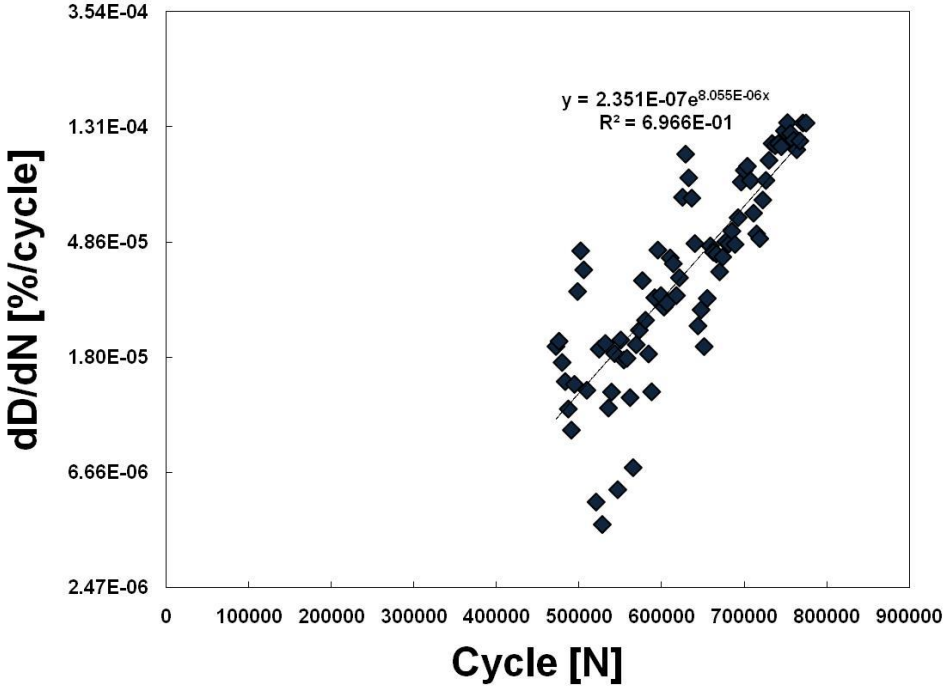

Figure E 17 - Rate of Damage accumulation of 3 month aged σ_2 – specimen 7.

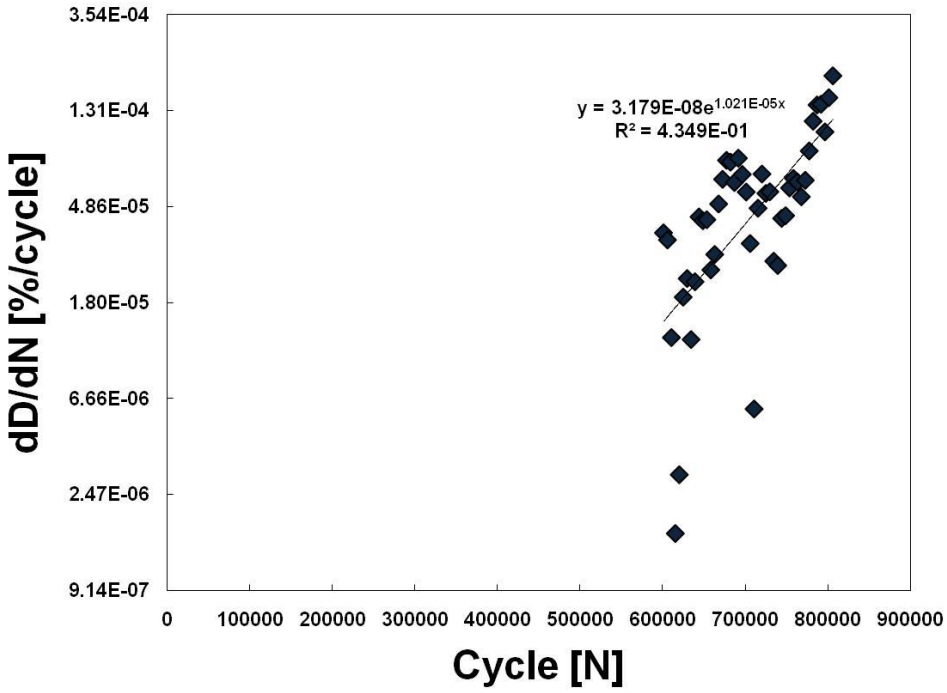

Figure E 18 - Rate of Damage accumulation of 3 month aged σ_2 – specimen 8.

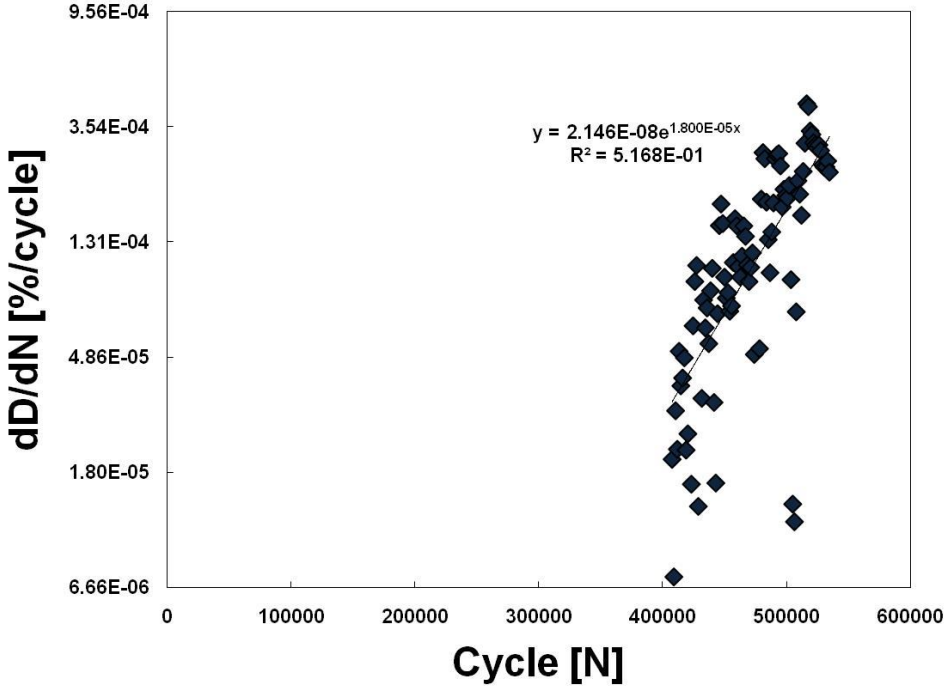

Figure E 19 - Rate of Damage accumulation of 3 month aged σ_2 – specimen 9.

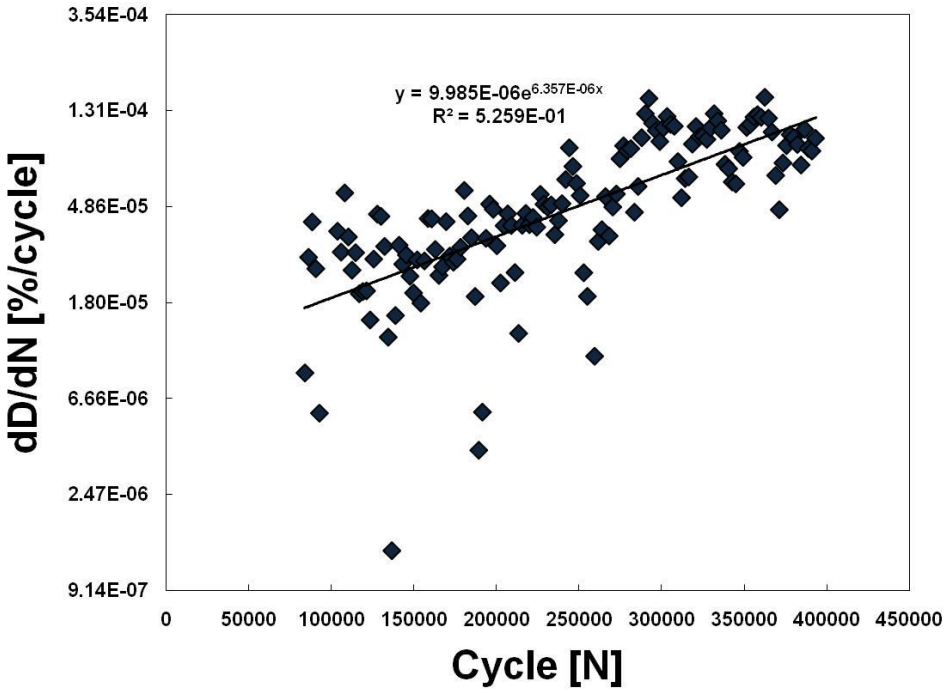

Figure E 20 - Rate of Damage accumulation of 3 month aged σ_2 – specimen 10.

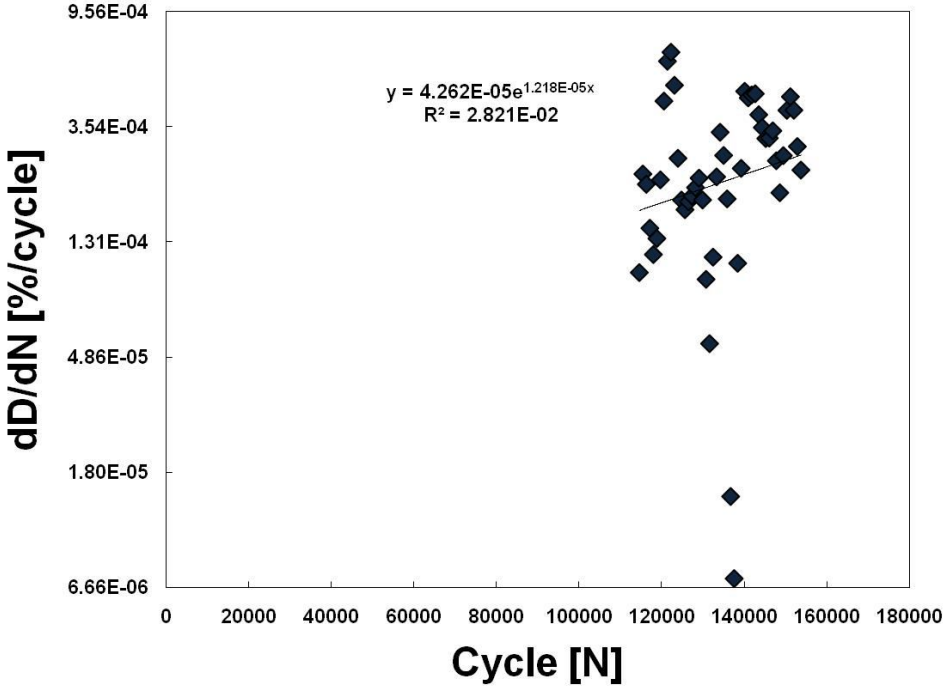

Figure E 21 - Rate of Damage accumulation of 3 month aged σ_3 – specimen 1.

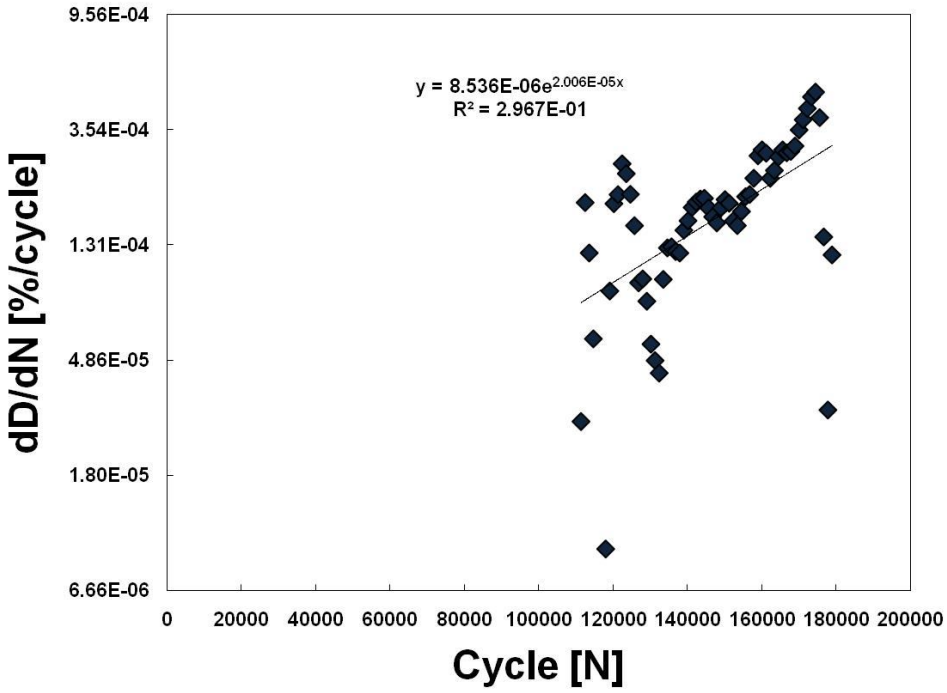

Figure E 22 - Rate of Damage accumulation of 3 month aged σ_3 – specimen 2.

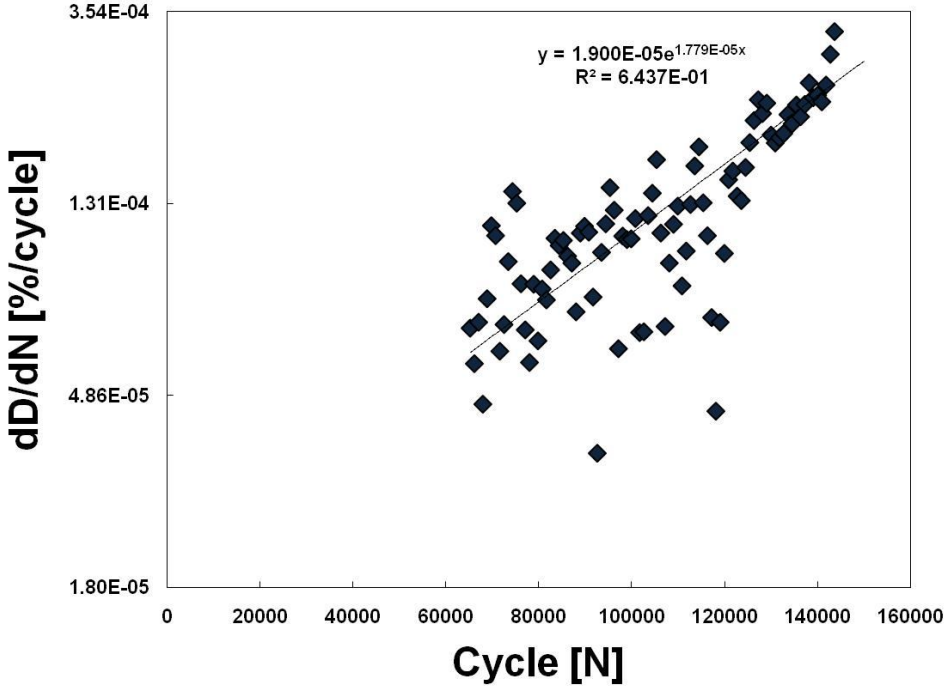

Figure E 23 - Rate of Damage accumulation of 3 month aged σ_3 – specimen 3.

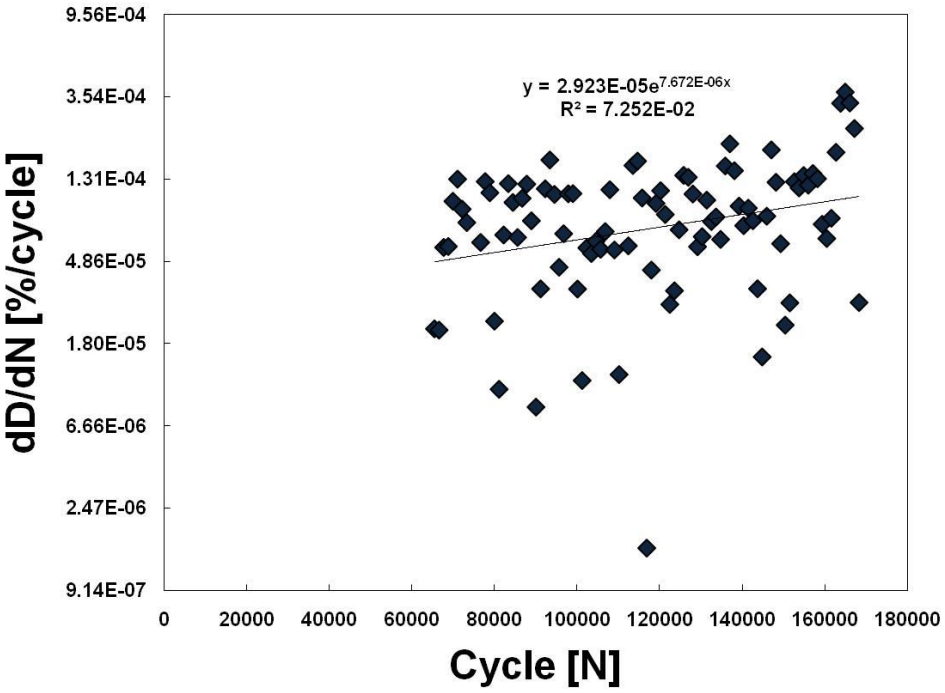

Figure E 24 - Rate of Damage accumulation of 3 month aged σ_3 – specimen 4.

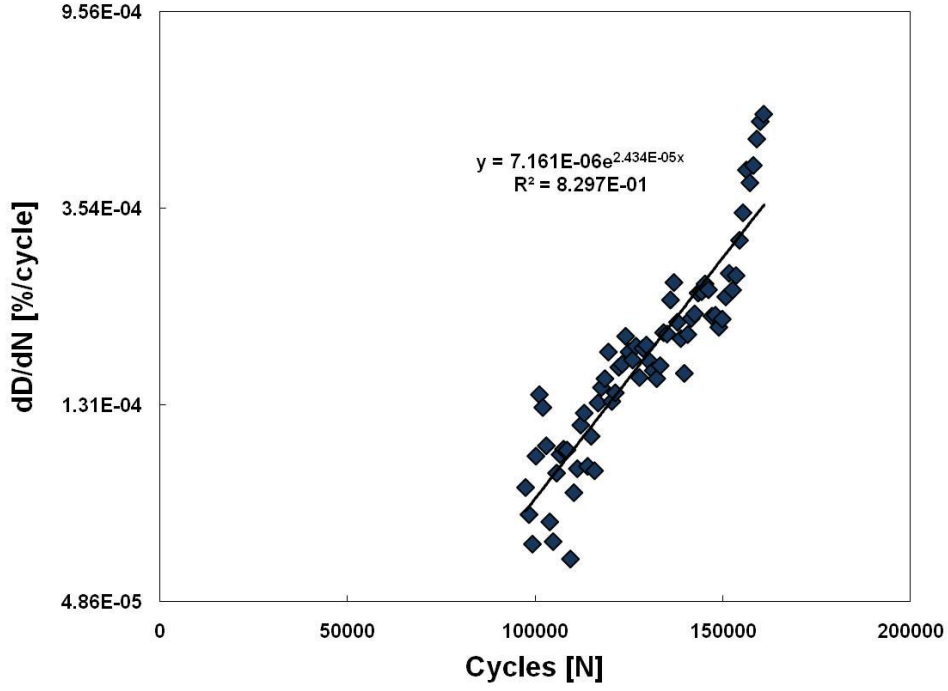

Figure E 25 - Rate of Damage accumulation of 3 month aged σ_3 – specimen 5.

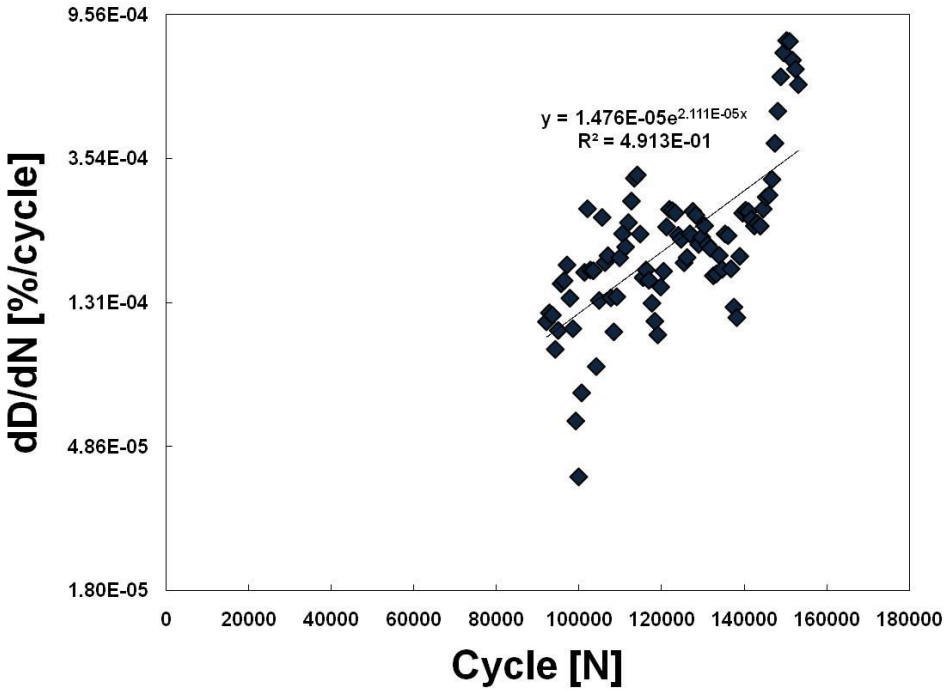

Figure E 26 - Rate of Damage accumulation of 3 month aged σ_3 – specimen 6.

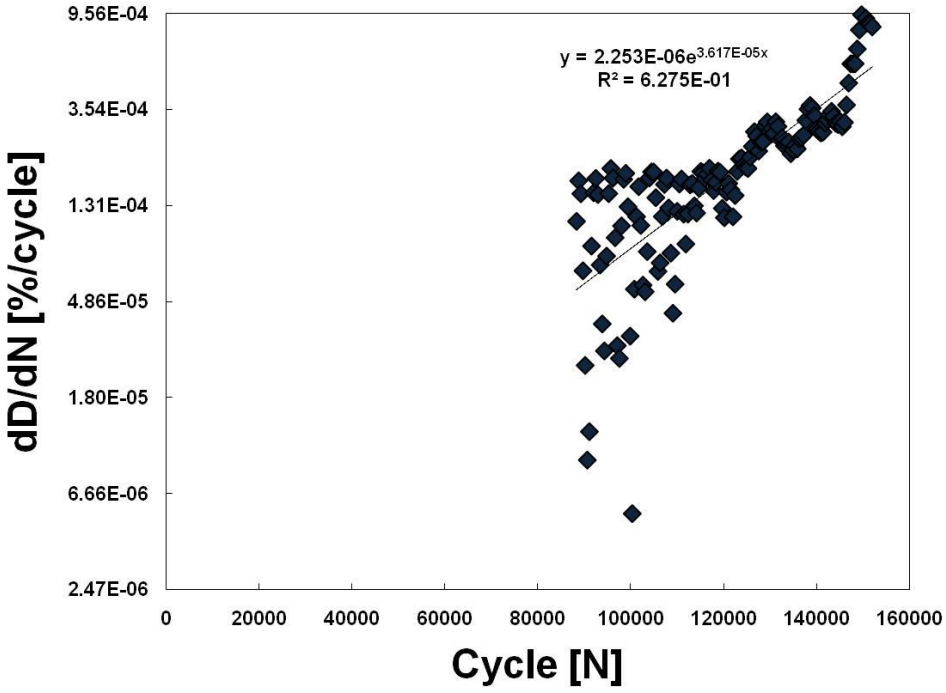

Figure E 27 - Rate of Damage accumulation of 3 month aged σ_3 – specimen 7.

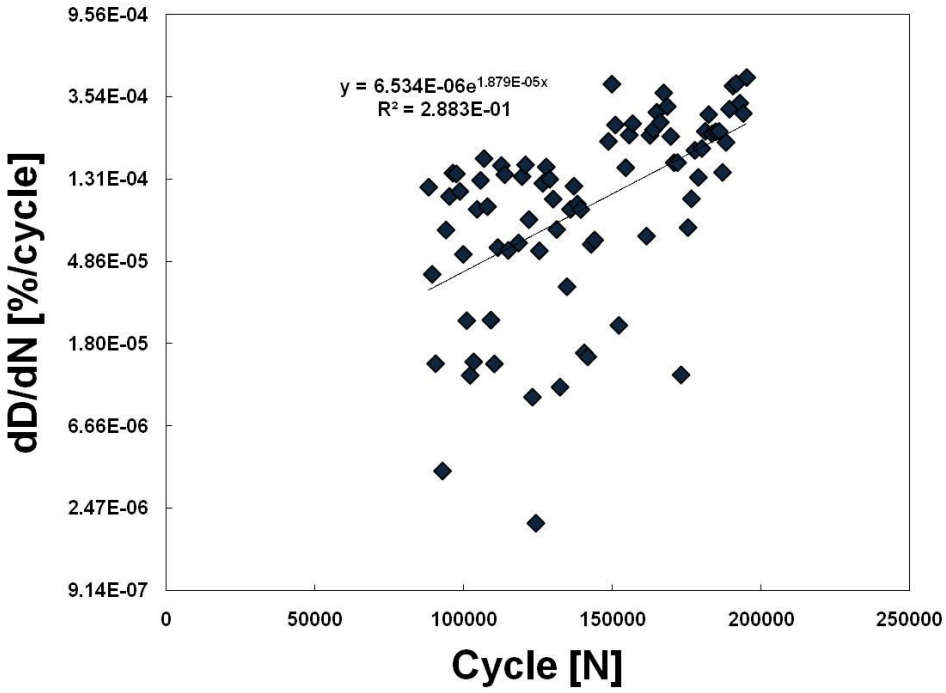

Figure E 28 - Rate of Damage accumulation of 3 month aged σ_3 – specimen 8.

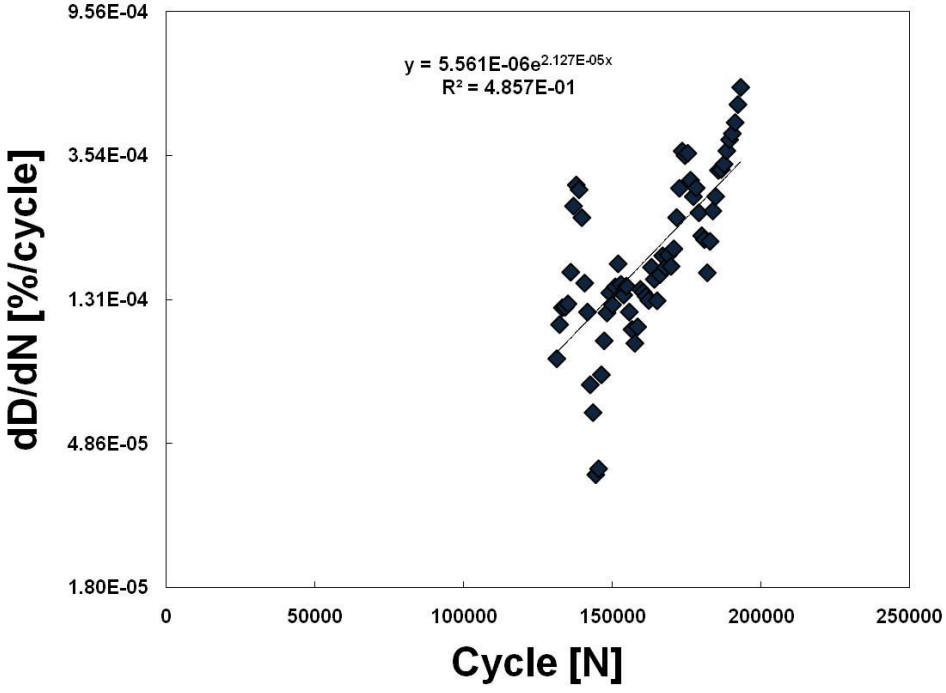

Figure E 29 - Rate of Damage accumulation of 3 month aged σ_3 – specimen 9.

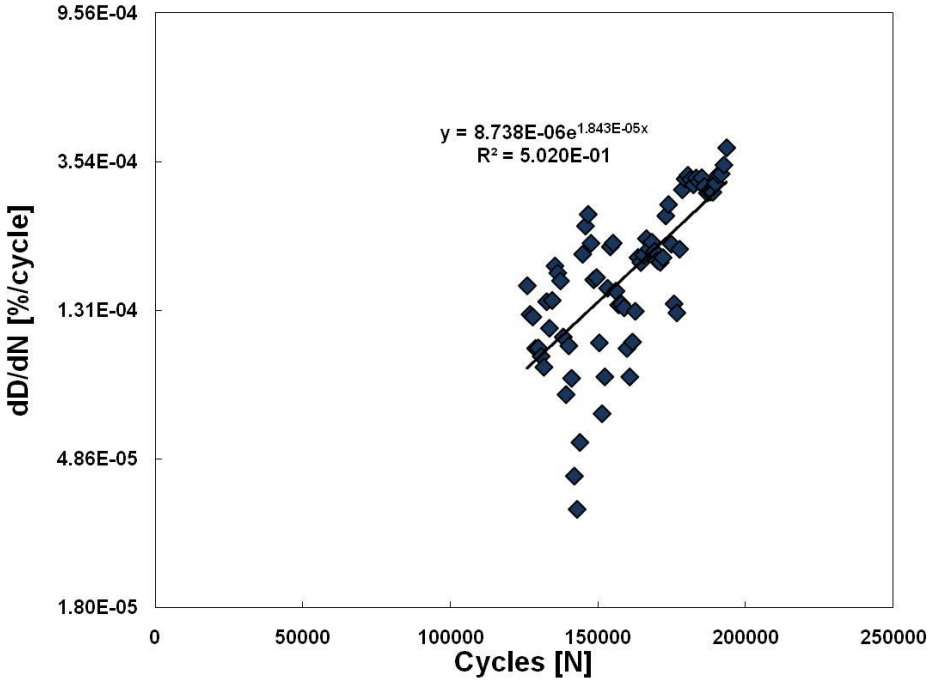

Figure E 30 - Rate of Damage accumulation of 3 month aged σ_3 – specimen 10.

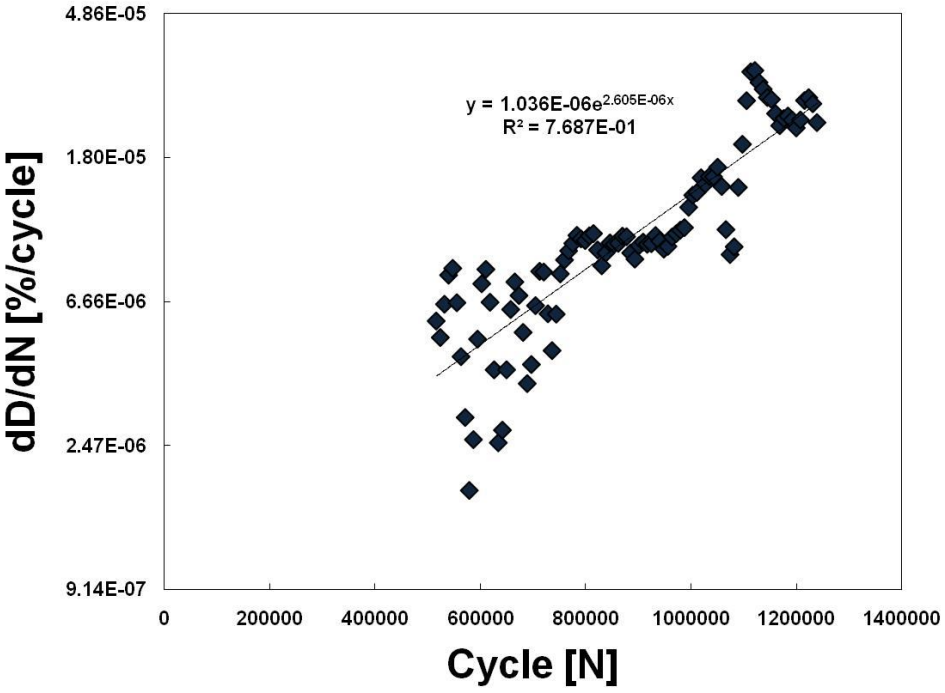

Figure E 31 - Rate of Damage accumulation of 6 month aged σ_1 – specimen 1.

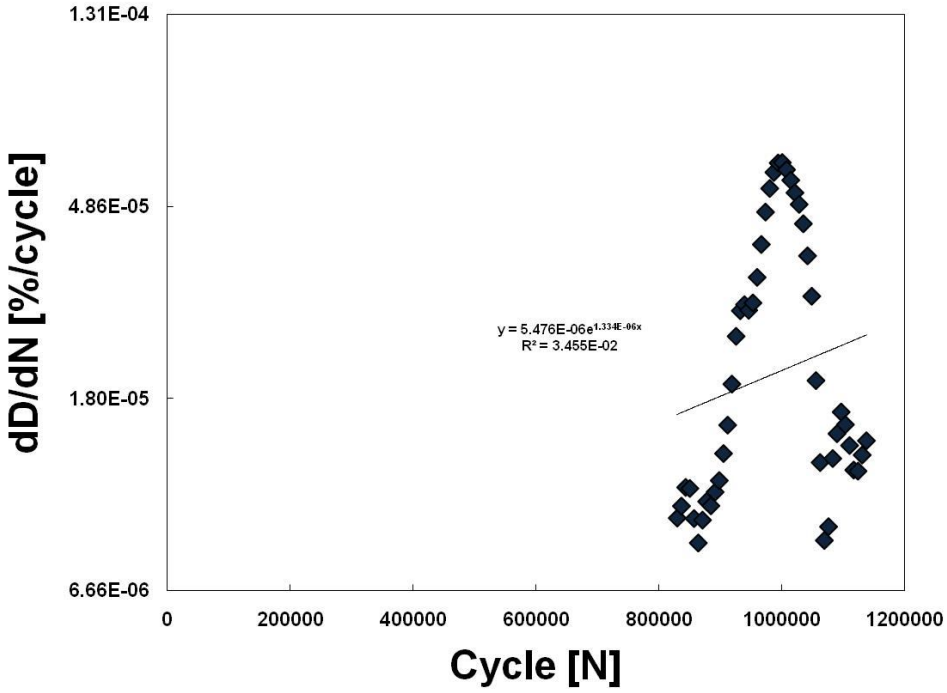

Figure E 32 - Rate of Damage accumulation of 6 month aged σ_1 – specimen 2.

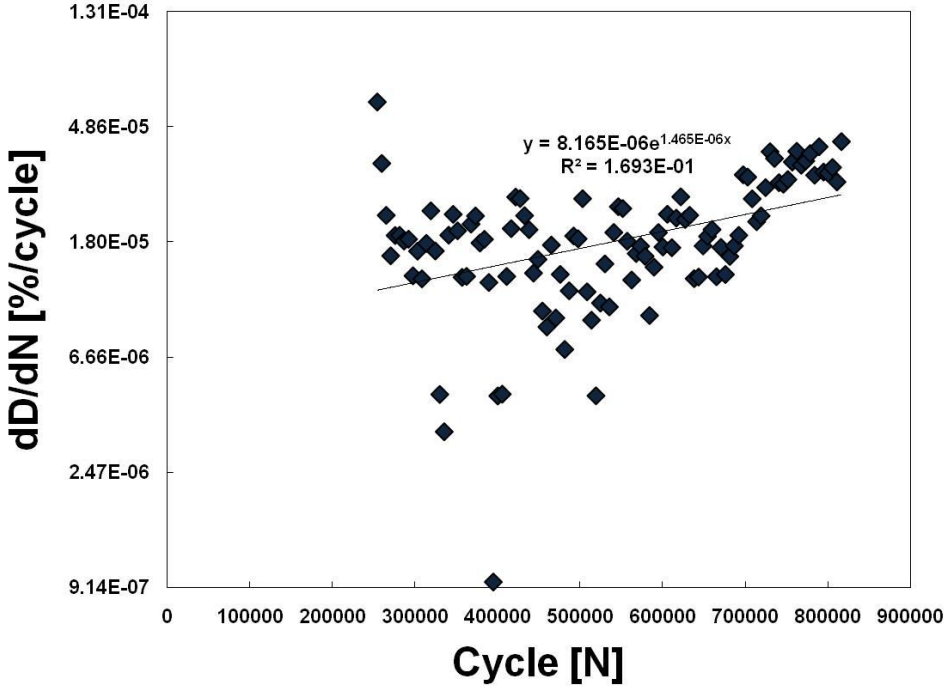

Figure E 33 - Rate of Damage accumulation of 6 month aged σ_1 – specimen 3.

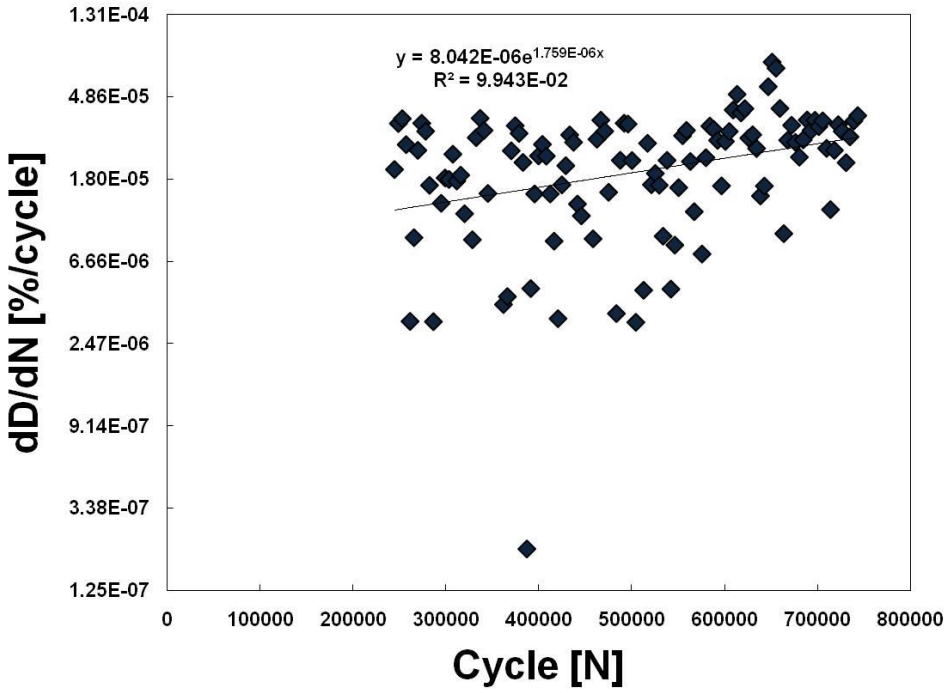

Figure E 34 - Rate of Damage accumulation of 6 month aged σ_1 – specimen 4.

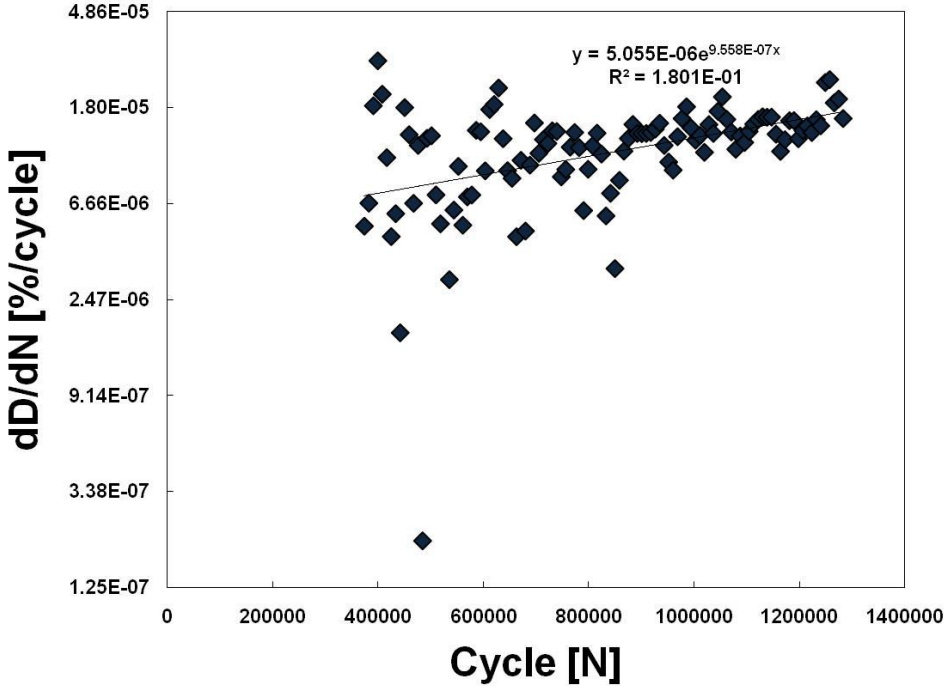

Figure E 35 - Rate of Damage accumulation of 6 month aged σ_1 – specimen 5.

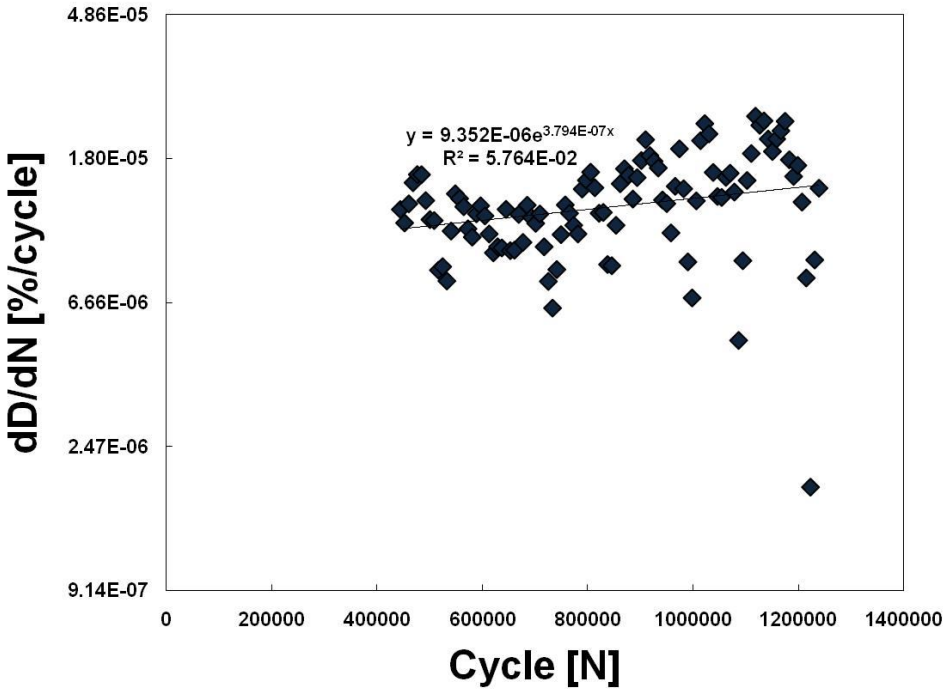

Figure E 36 - Rate of Damage accumulation of 6 month aged σ_1 – specimen 6.

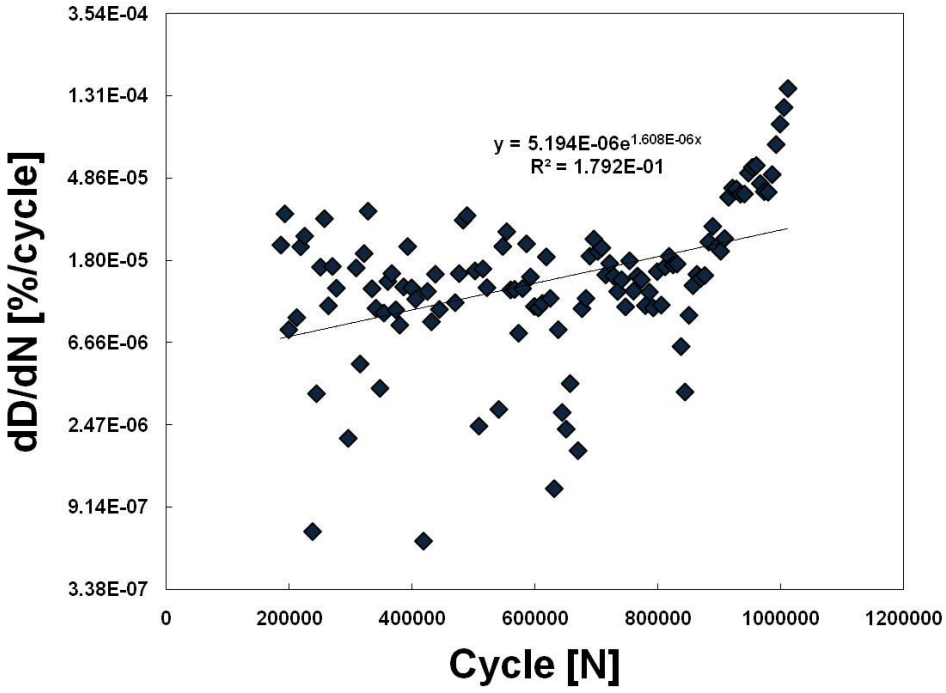

Figure E 37 - Rate of Damage accumulation of 6 month aged σ_1 – specimen 7.

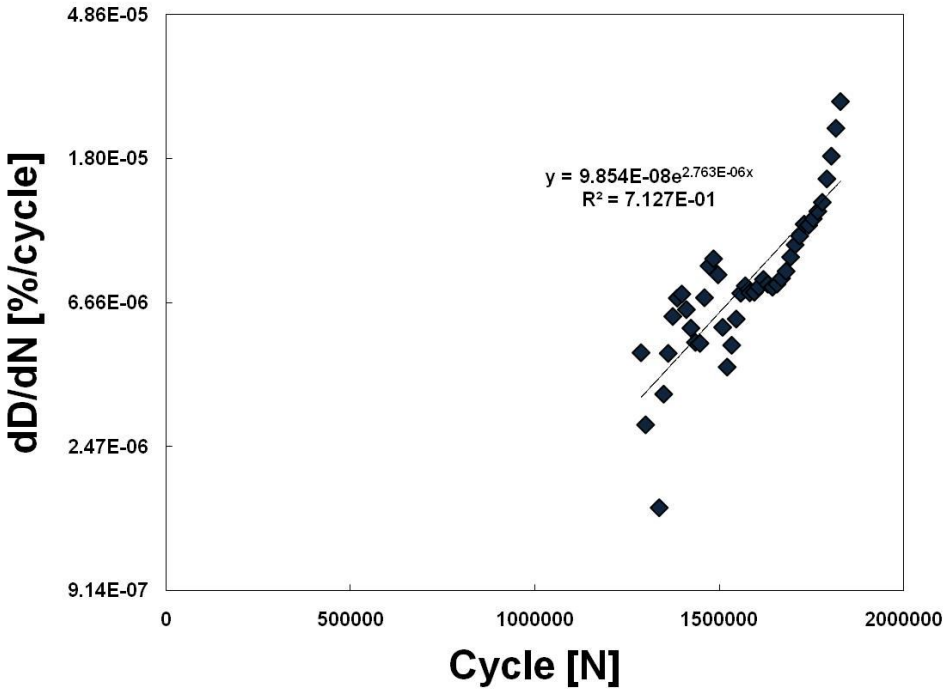

Figure E 38 - Rate of Damage accumulation of 6 month aged σ_1 – specimen 8.

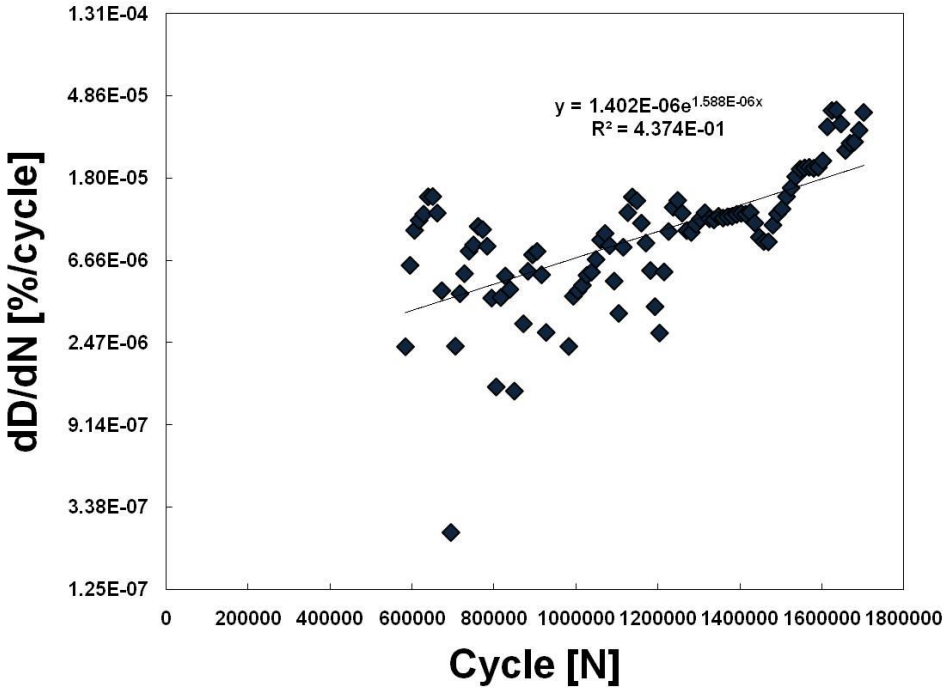

Figure E 39 - Rate of Damage accumulation of 6 month aged σ_1 – specimen 9.

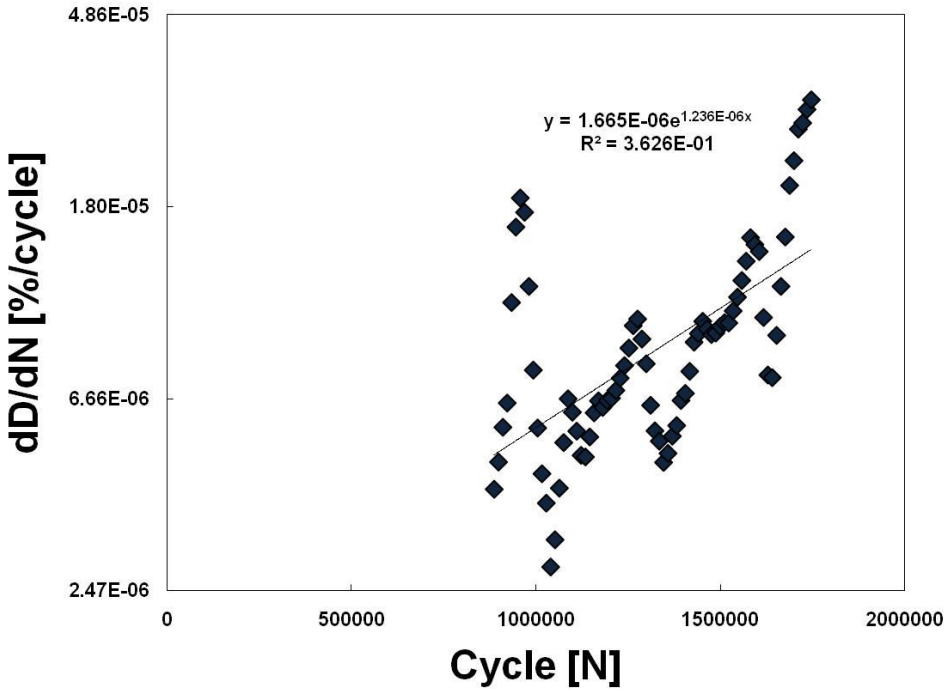

Figure E 40 - Rate of Damage accumulation of 6 month aged σ_1 – specimen 10.

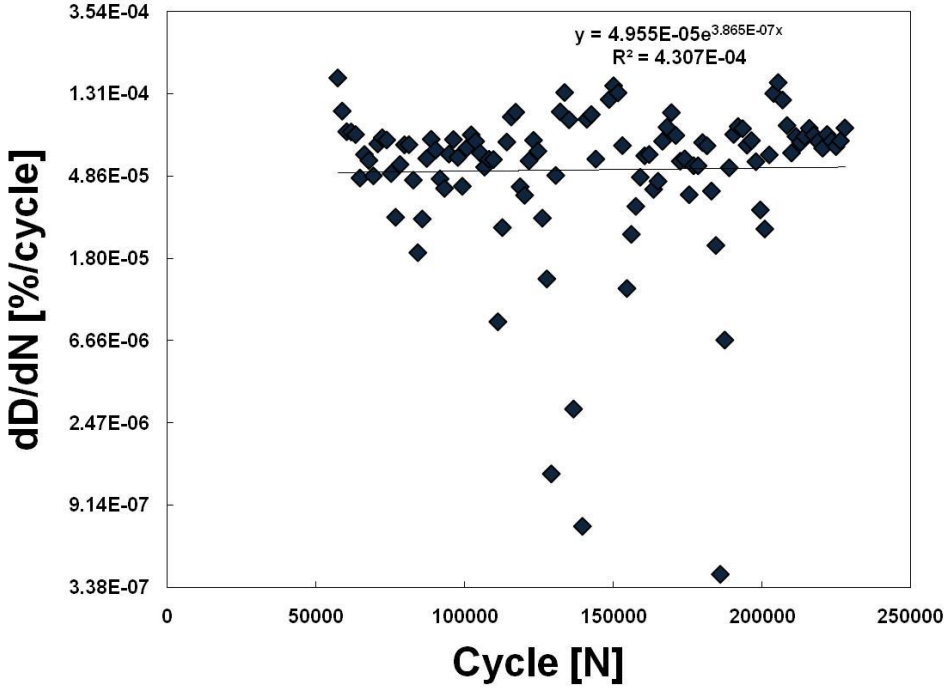

Figure E 41 - Rate of Damage accumulation of 6 month aged σ_2 – specimen 1.

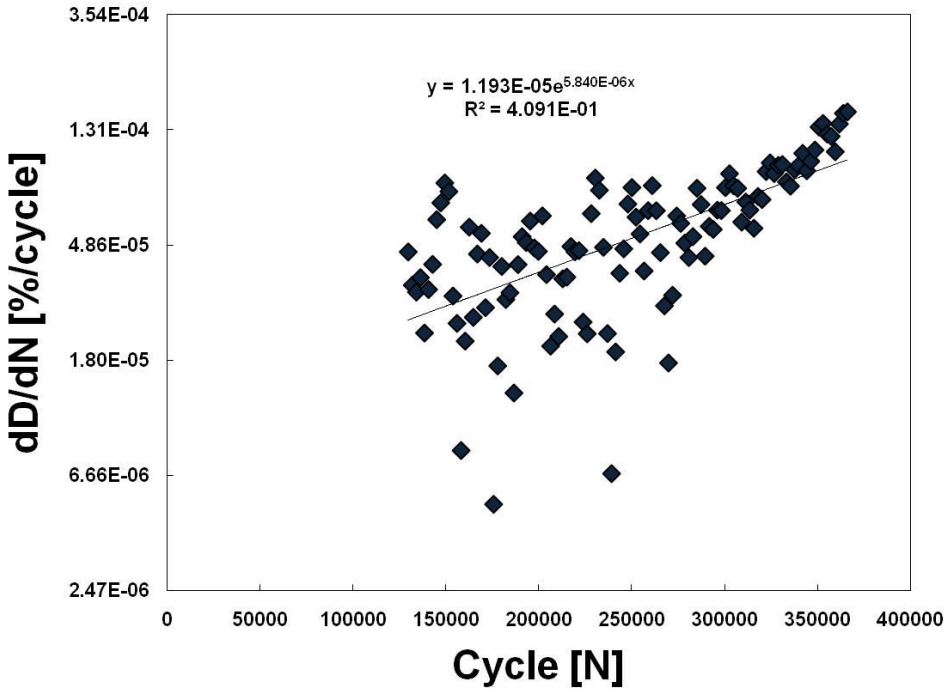

Figure E 42 - Rate of Damage accumulation of 6 month aged σ_2 – specimen 2.

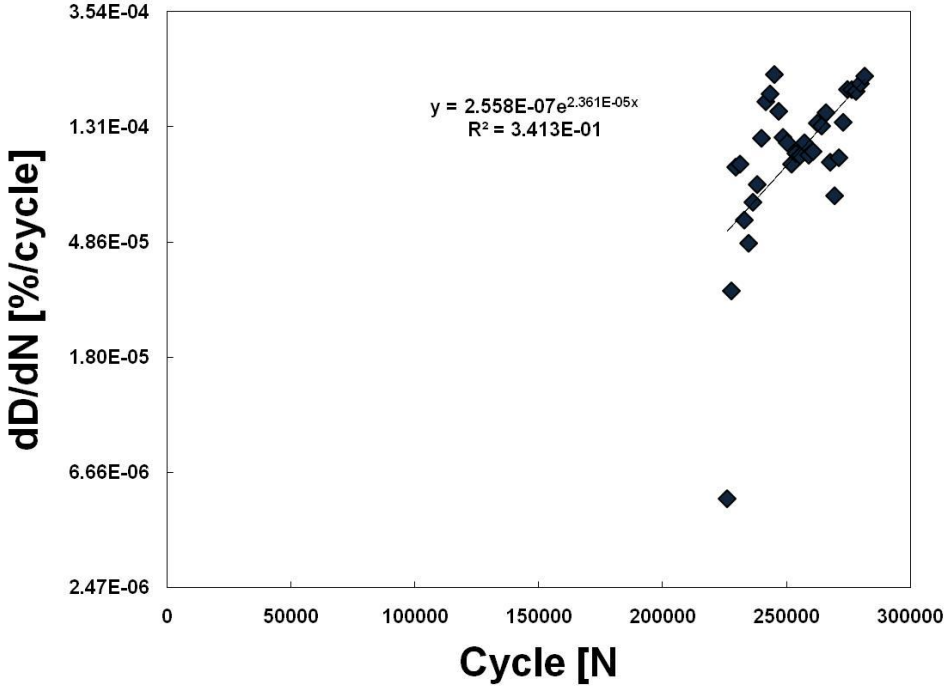

Figure E 43 - Rate of Damage accumulation of 6 month aged σ_2 – specimen 3.

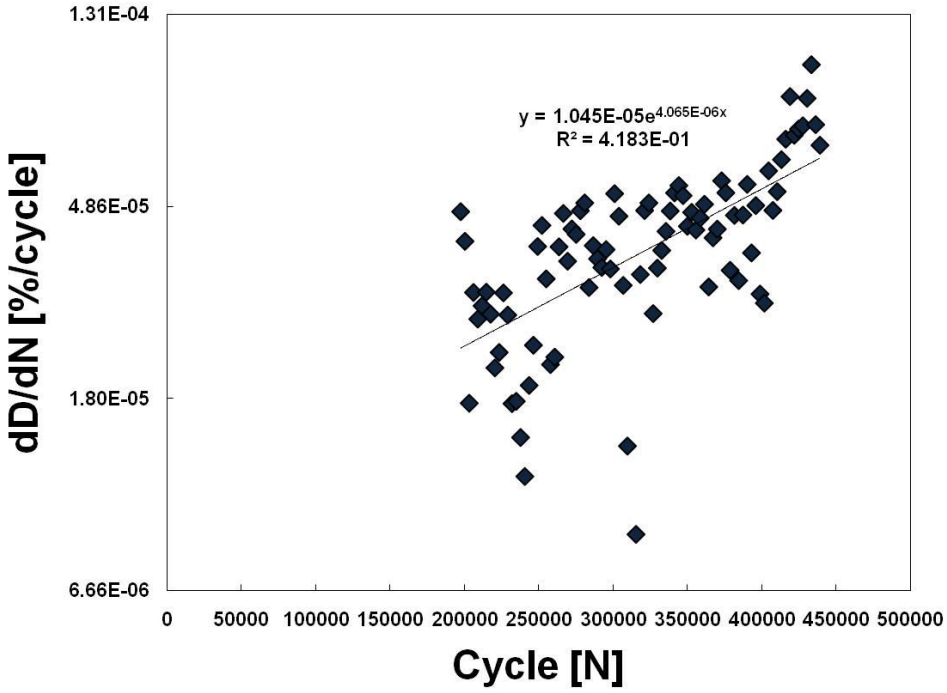

Figure E 44 - Rate of Damage accumulation of 6 month aged σ_2 – specimen 4.

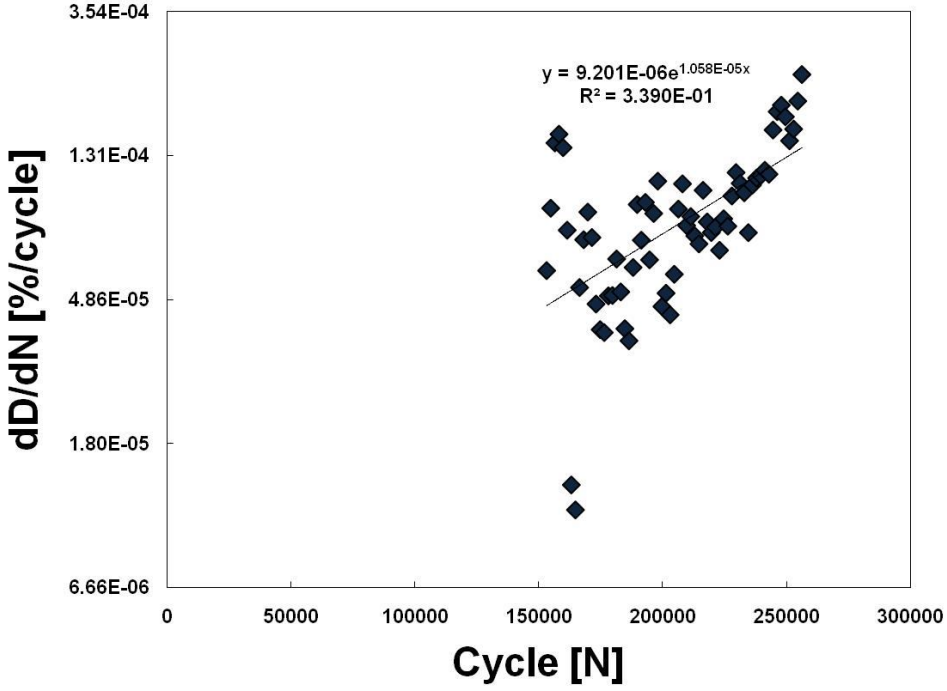

Figure E 45 - Rate of Damage accumulation of 6 month aged σ_2 – specimen 5.

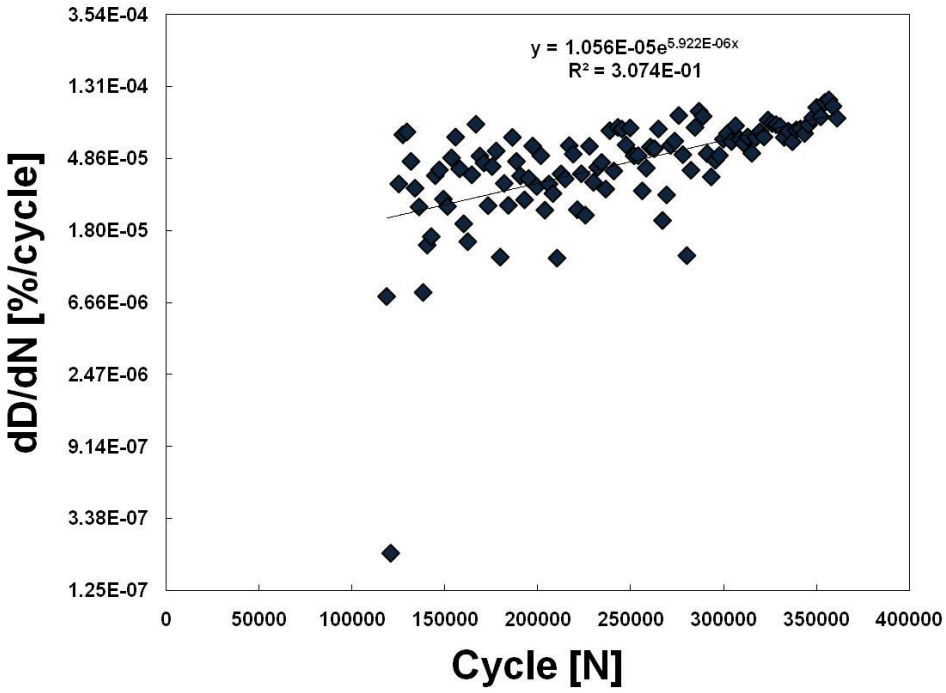

Figure E 46 - Rate of Damage accumulation of 6 month aged σ_2 – specimen 6.

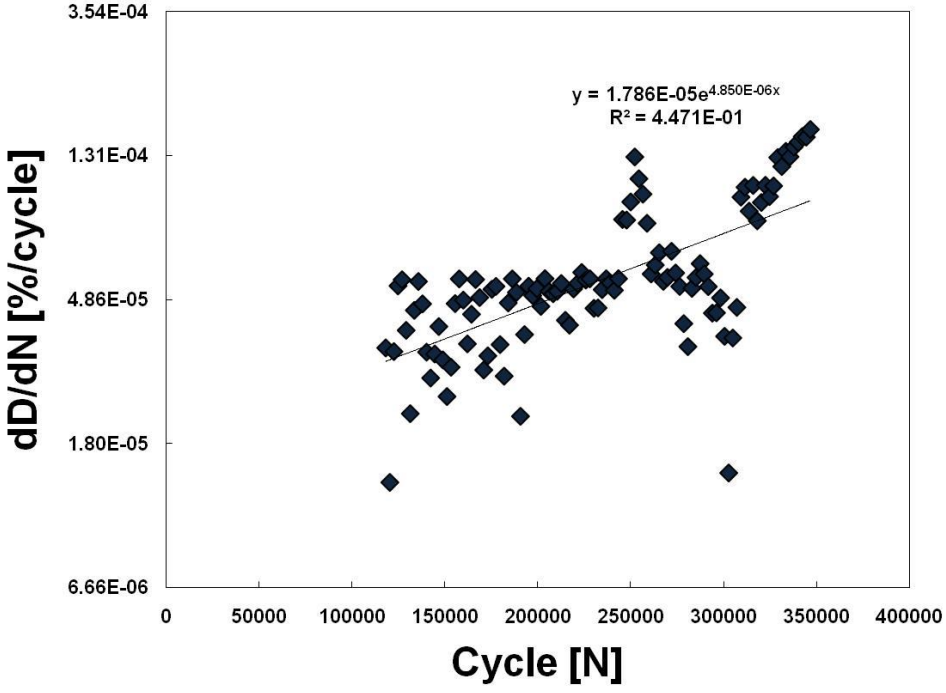

Figure E 47 - Rate of Damage accumulation of 6 month aged σ_2 – specimen 7.

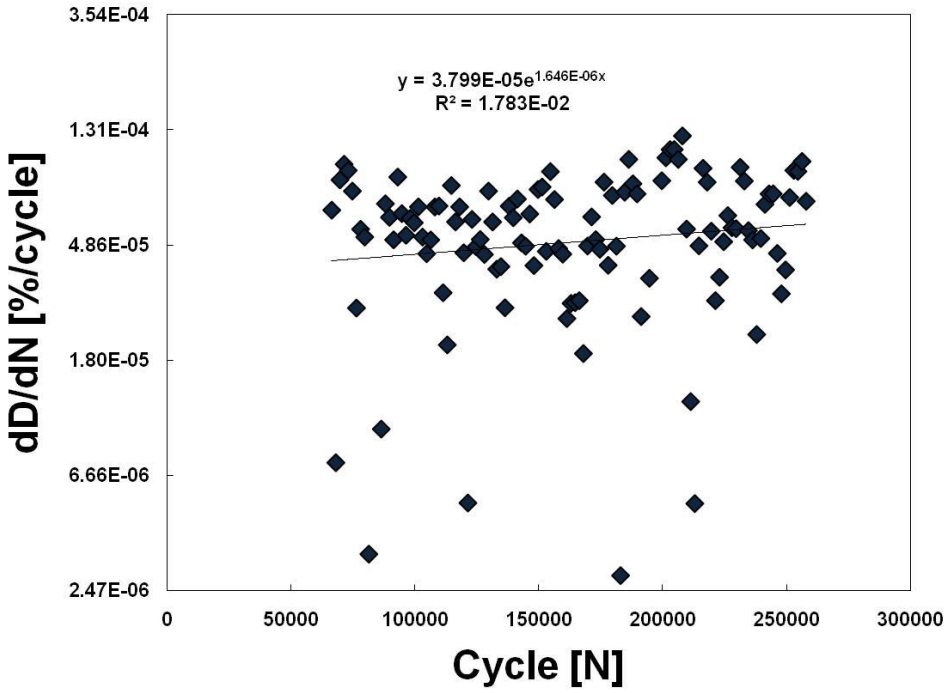

Figure E 48 - Rate of Damage accumulation of 6 month aged σ_2 – specimen 8.

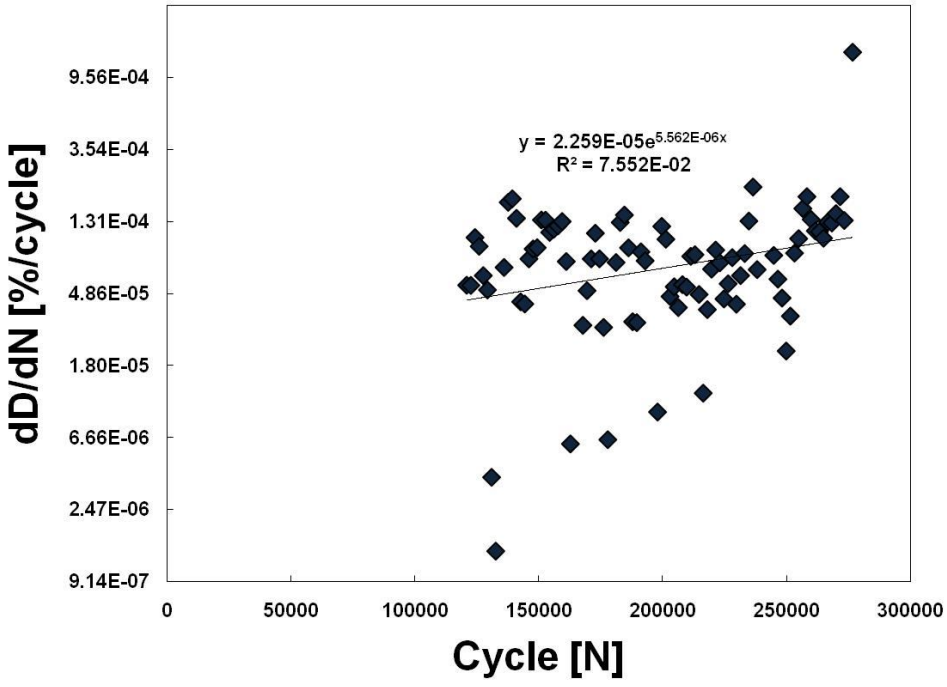

Figure E 49 - Rate of Damage accumulation of 6 month aged σ_2 – specimen 9.

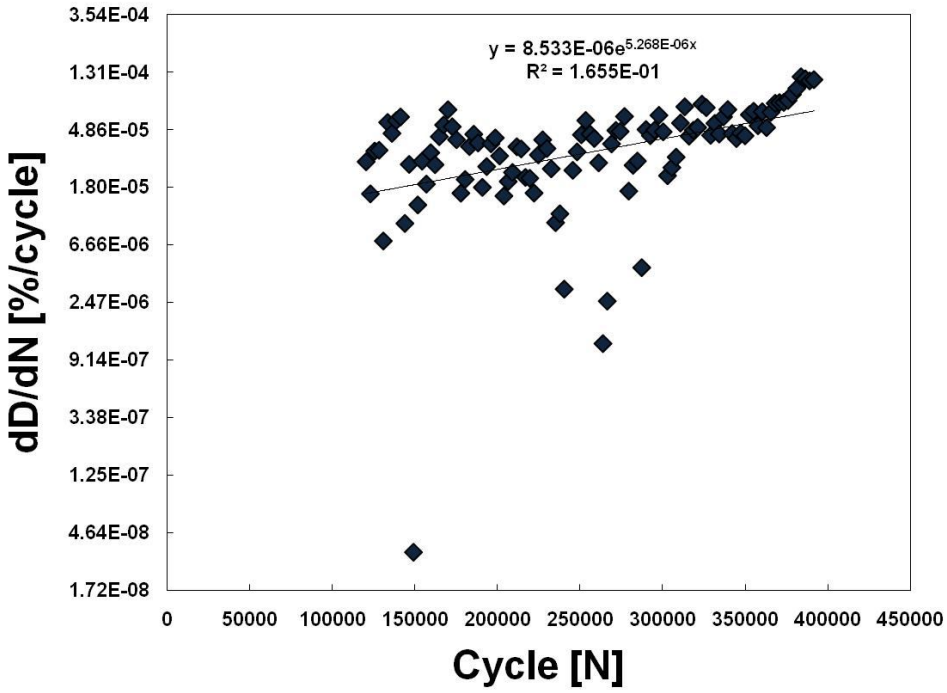

Figure E 50 - Rate of Damage accumulation of 6 month aged σ_2 – specimen 10.

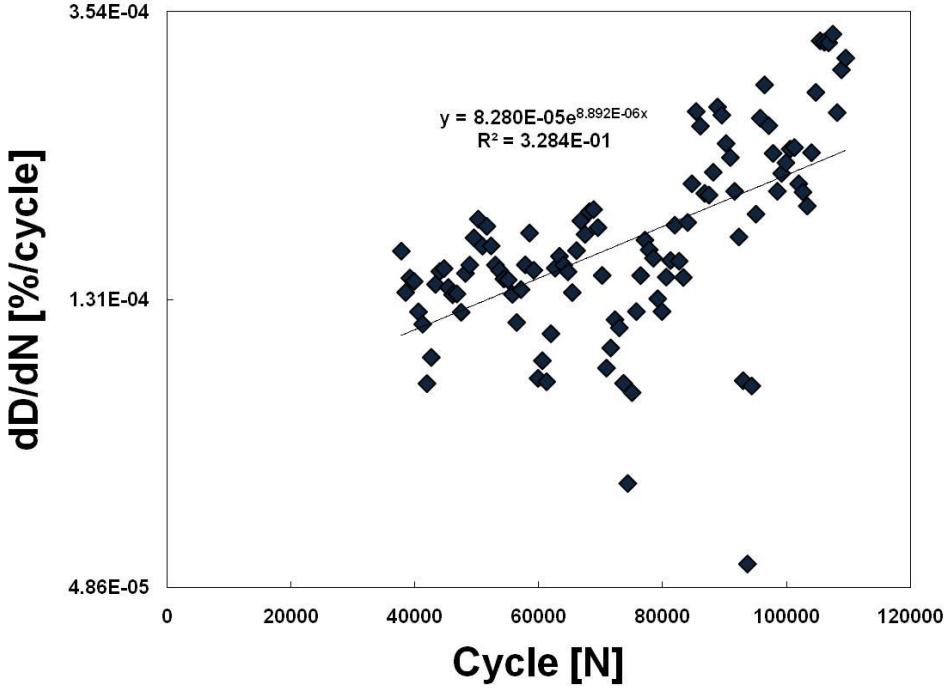

Figure E 51 - Rate of Damage accumulation of 6 month aged σ_3 – specimen 1.

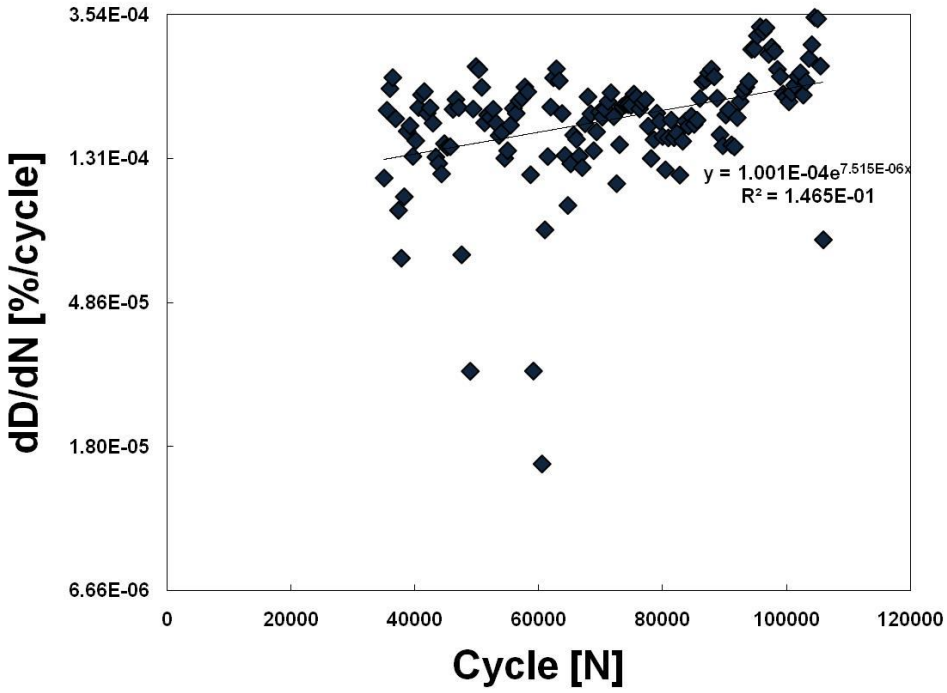

Figure E 52 - Rate of Damage accumulation of 6 month aged σ_3 – specimen 2.

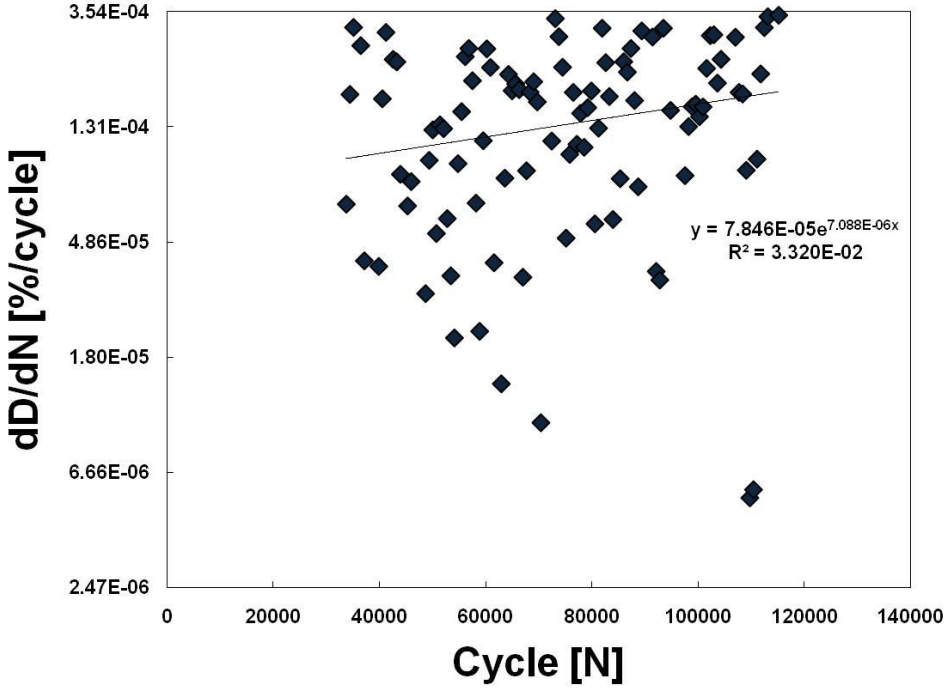

Figure E 53 - Rate of Damage accumulation of 6 month aged σ_3 – specimen 3.

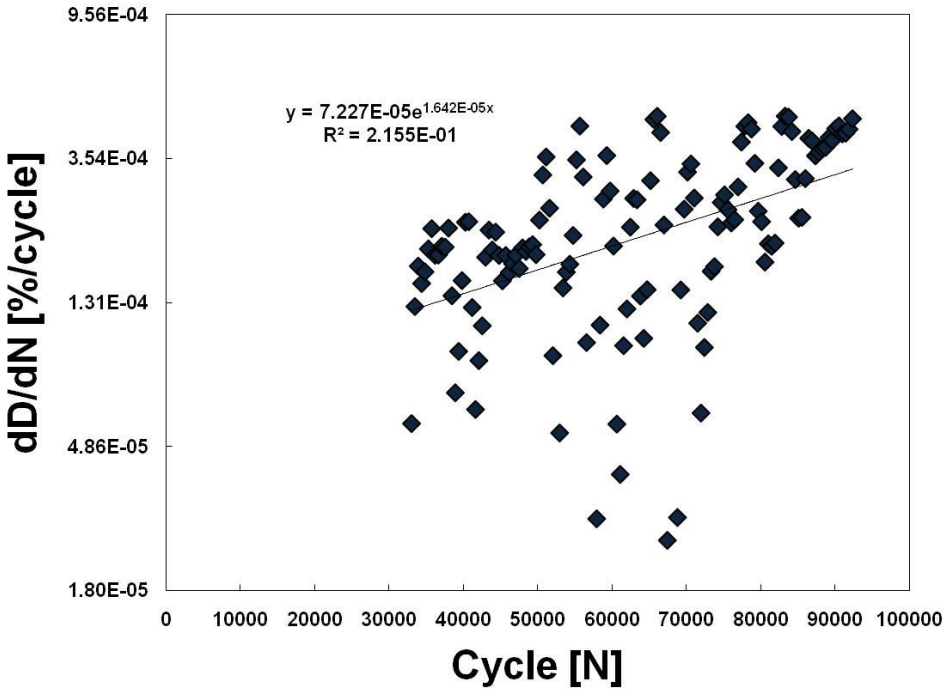

Figure E 54 - Rate of Damage accumulation of 6 month aged σ_3 – specimen 4.

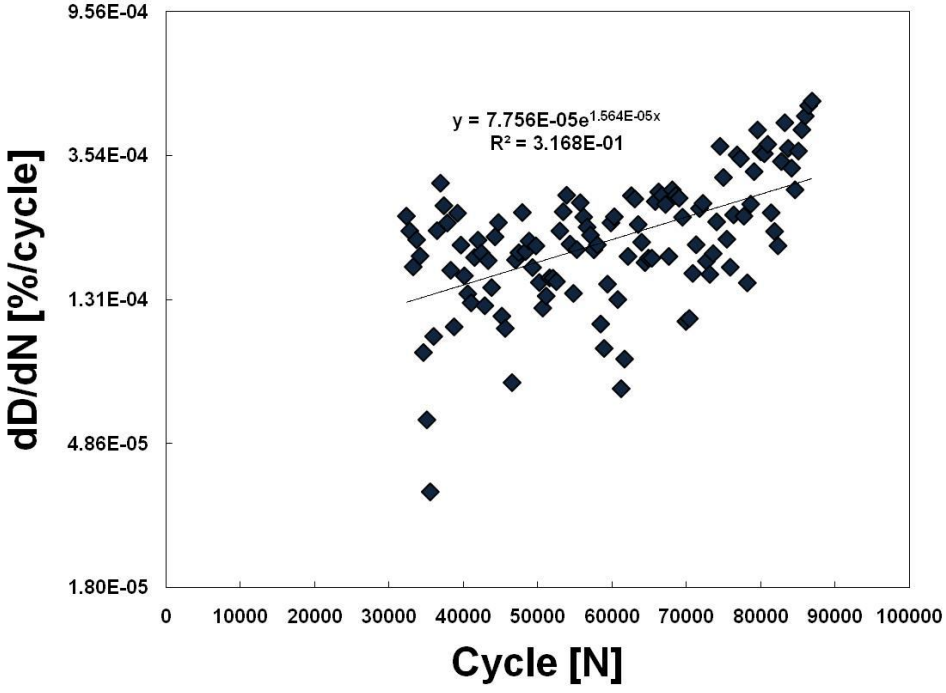

Figure E 55 - Rate of Damage accumulation of 6 month aged σ_3 – specimen 5.

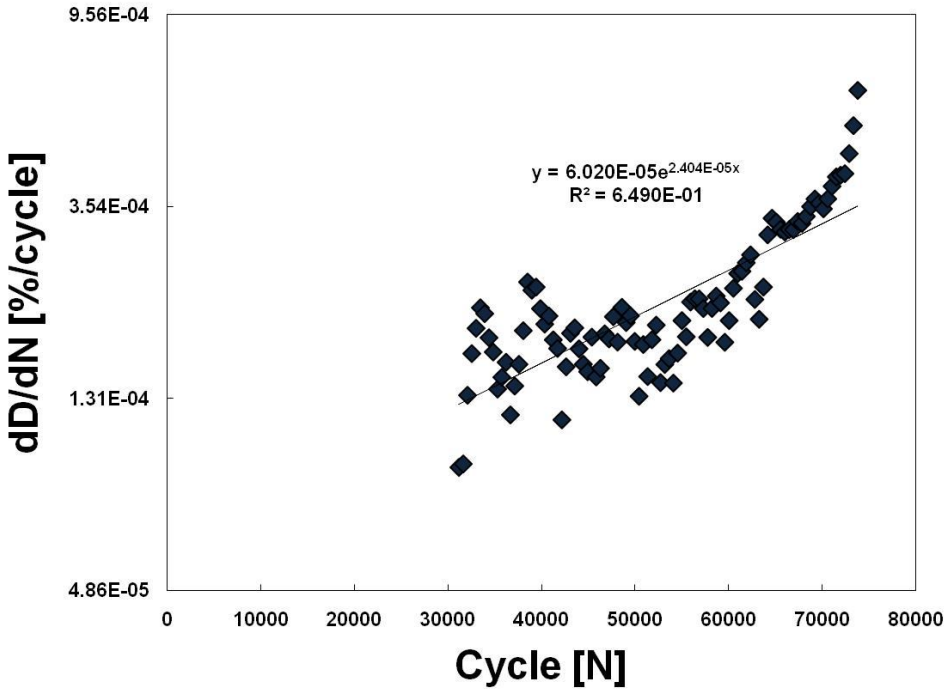

Figure E 56 - Rate of Damage accumulation of 6 month aged σ_3 – specimen 6.

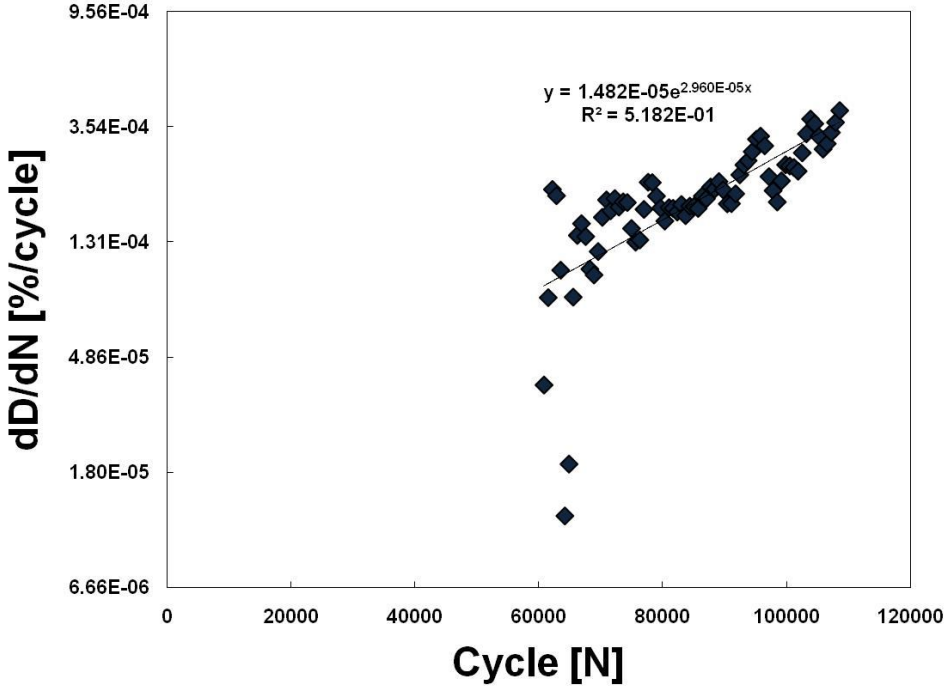

Figure E 57 - Rate of Damage accumulation of 6 month aged σ_3 – specimen 7.

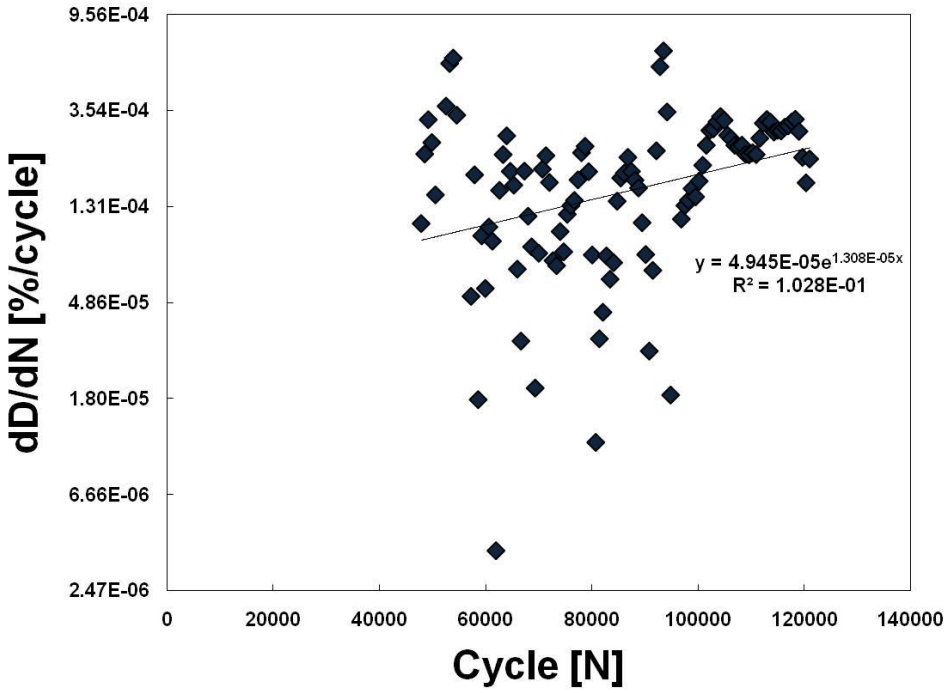

Figure E 58 - Rate of Damage accumulation of 6 month aged σ_3 – specimen 8.

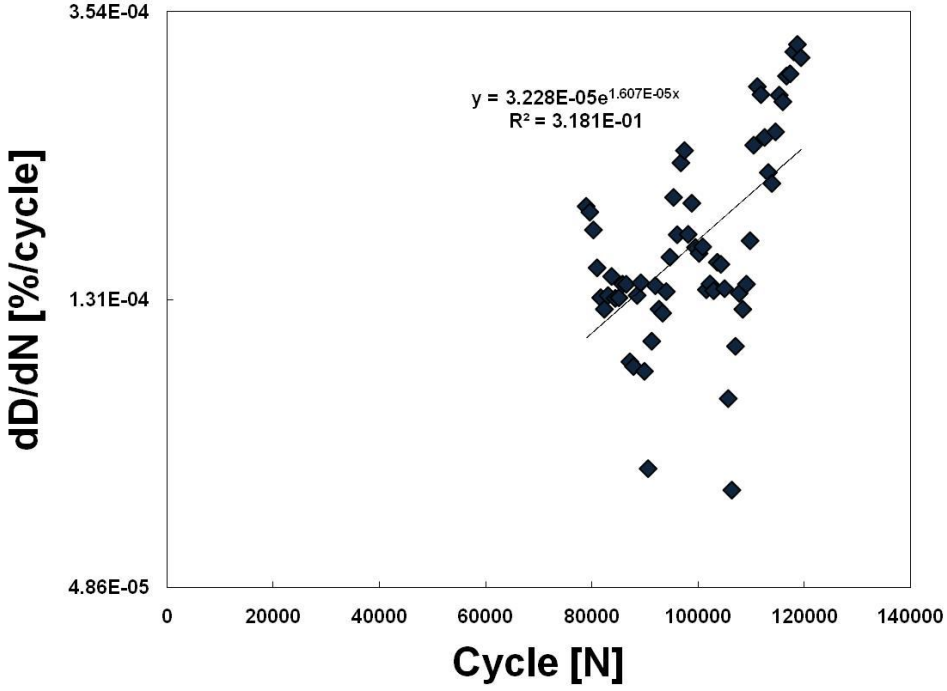

Figure E 59 - Rate of Damage accumulation of 6 month aged σ_3 – specimen 9.

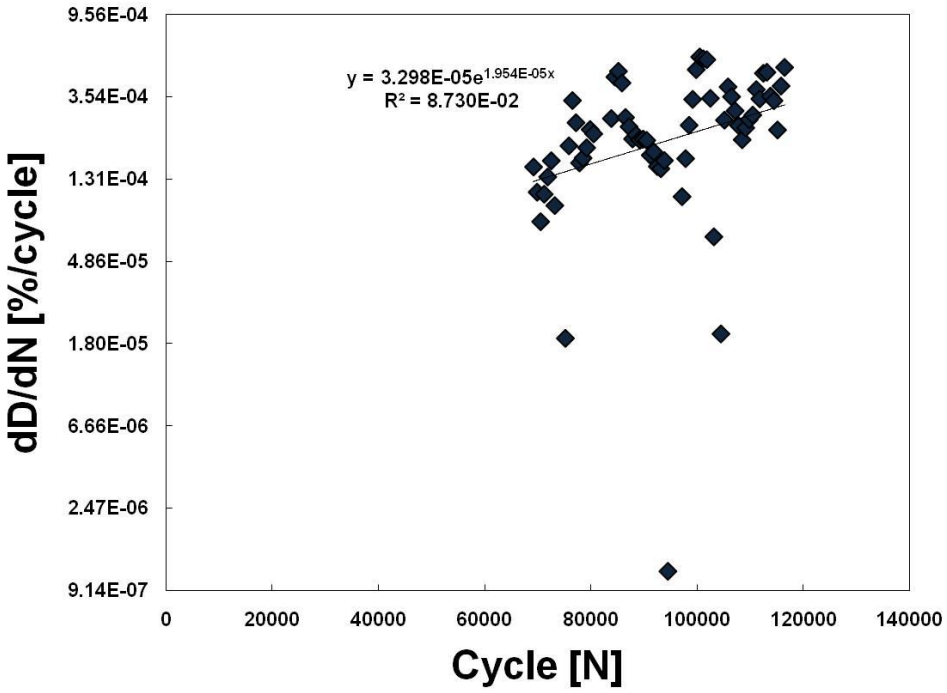

Figure E 60 - Rate of Damage accumulation of 6 month aged σ_3 – specimen 10.

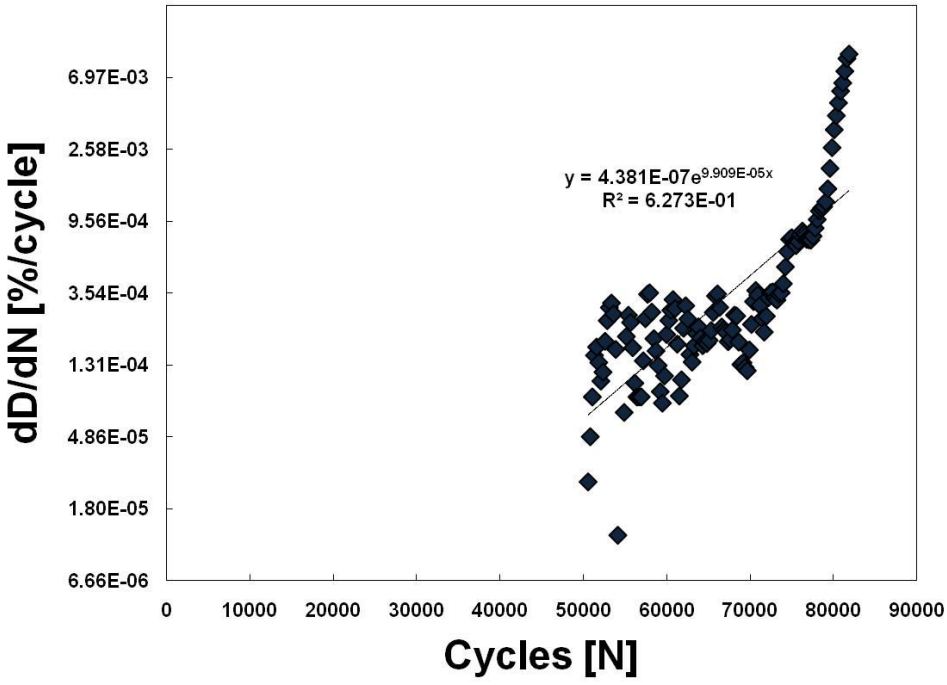

Figure E 61 - Rate of Damage accumulation of 12 month aged σ_1 – specimen 1.

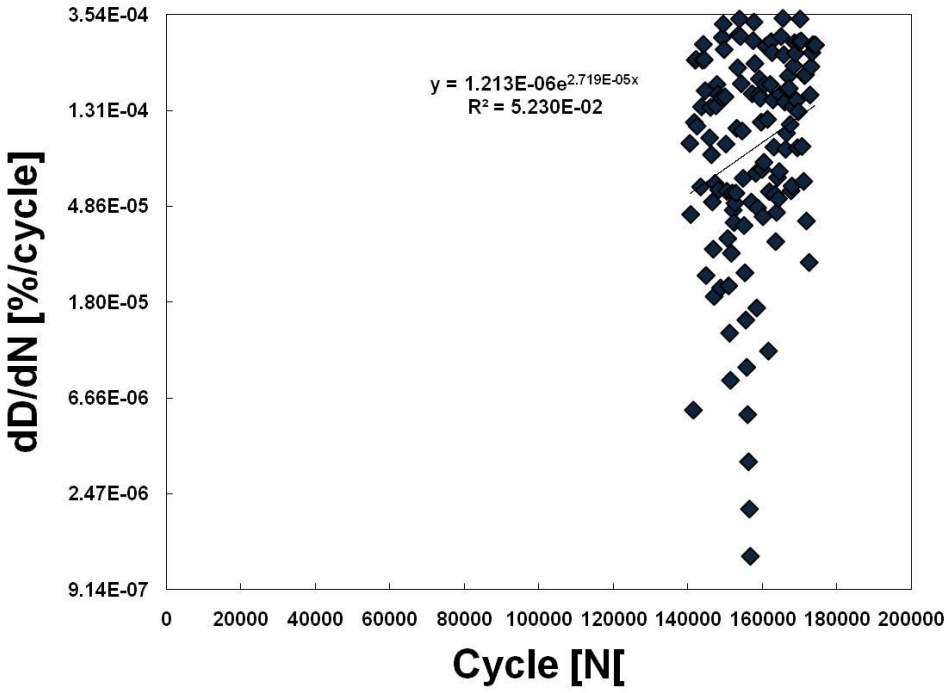

Figure E 62 - Rate of Damage accumulation of 12 month aged σ_1 – specimen 2.

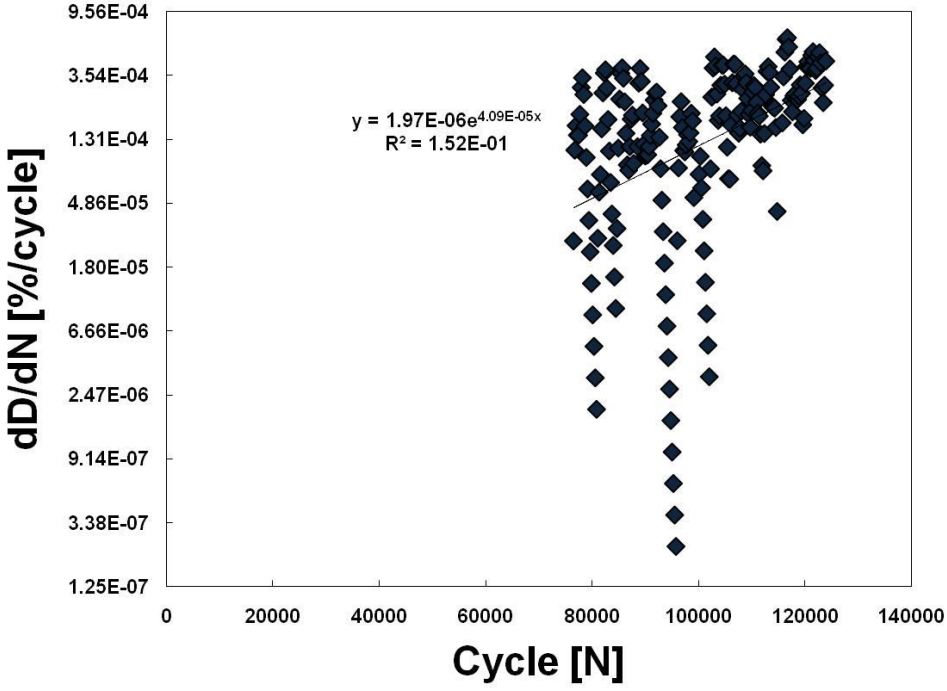

Figure E 63 - Rate of Damage accumulation of 12 month aged σ_1 – specimen 3.

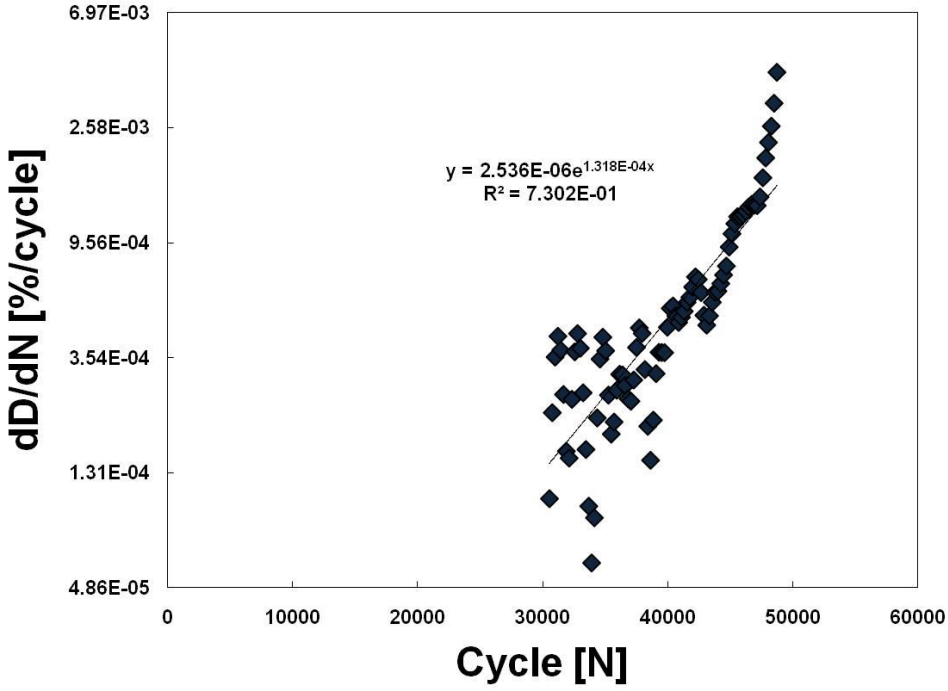

Figure E 64 - Rate of Damage accumulation of 12 month aged σ_1 – specimen 4.

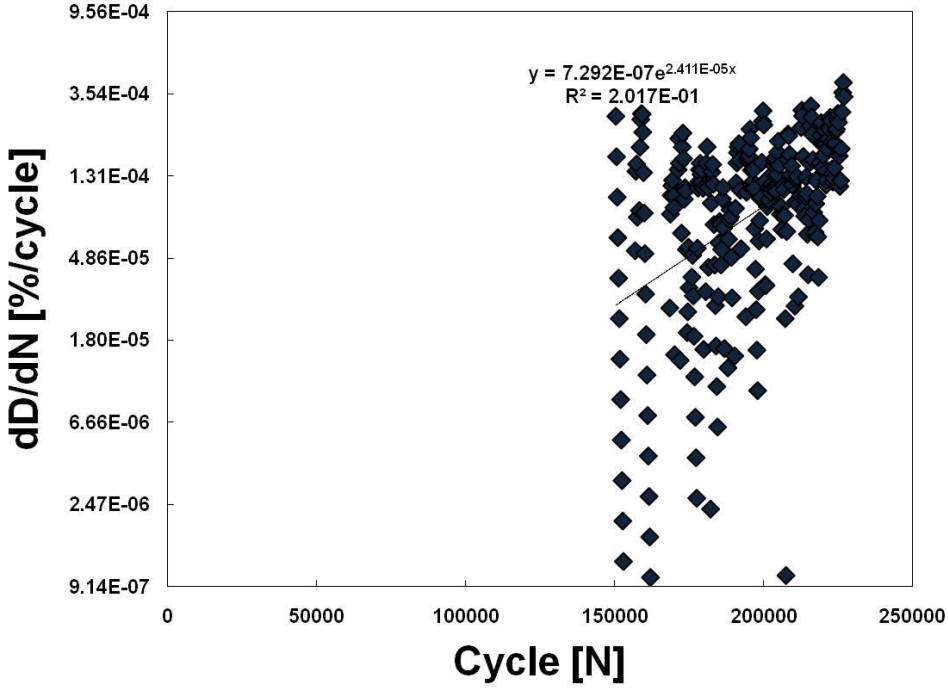

Figure E 65 - Rate of Damage accumulation of 12 month aged σ_1 – specimen 5.

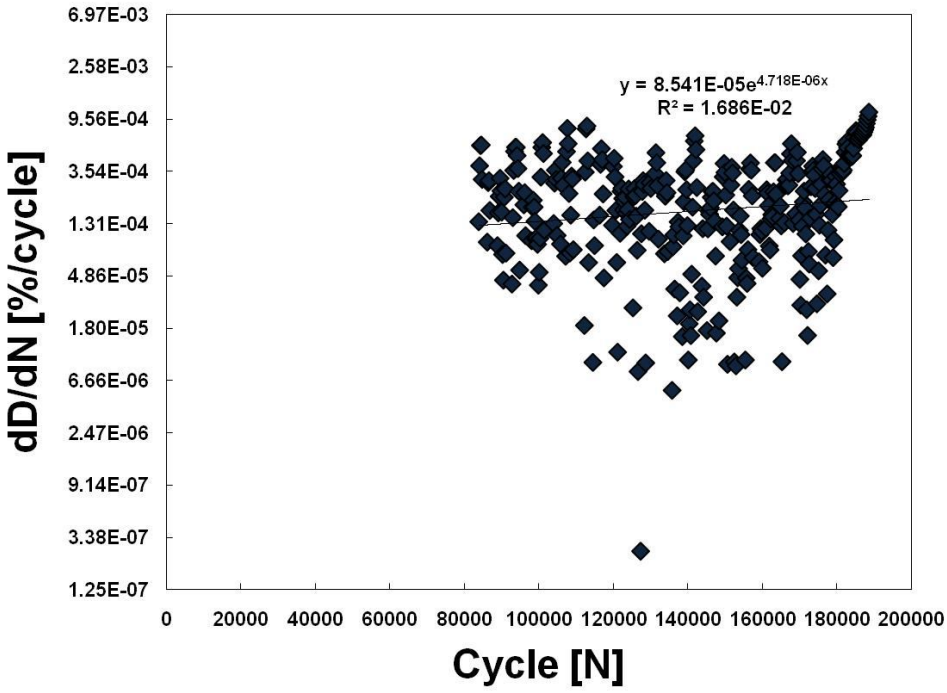

Figure E 66 - Rate of Damage accumulation of 12 month aged σ_1 – specimen 6.

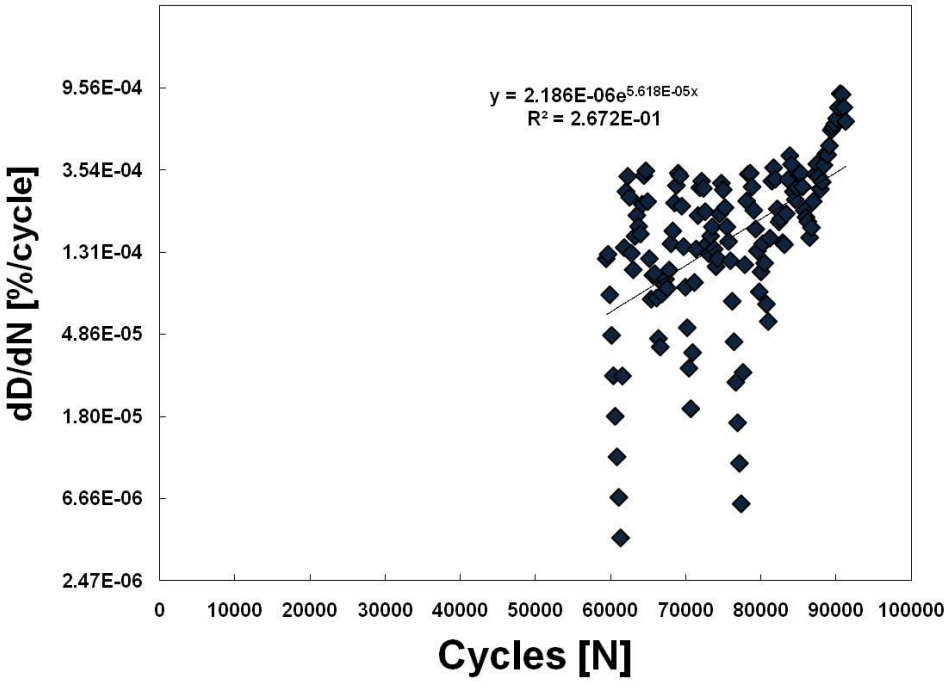

Figure E 67 - Rate of Damage accumulation of 12 month aged σ_1 – specimen 7.

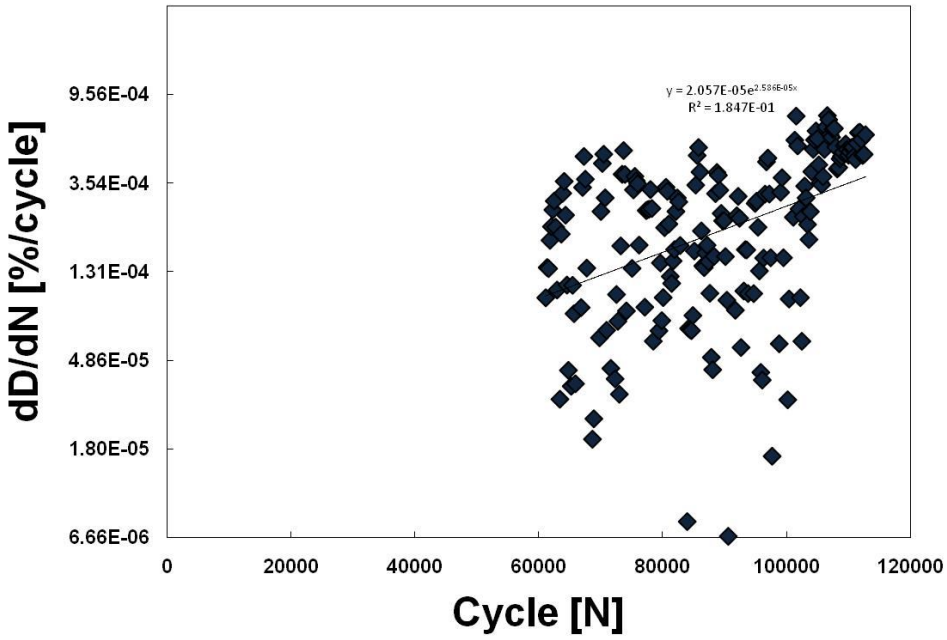

Figure E 68 - Rate of Damage accumulation of 12 month aged σ_1 – specimen 8.

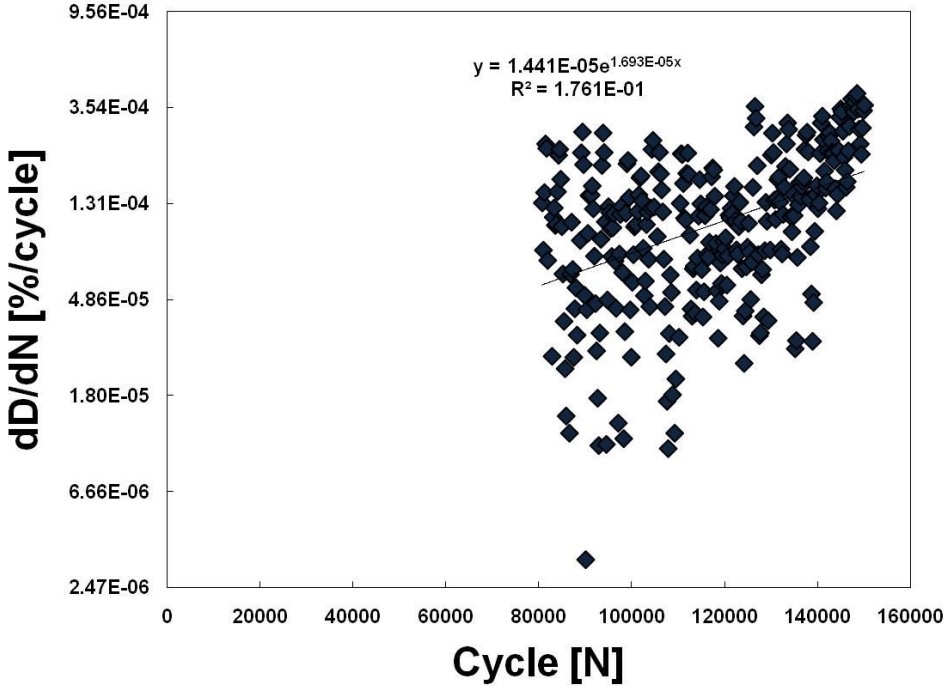

Figure E 69 - Rate of Damage accumulation of 12 month aged σ_1 – specimen 9.

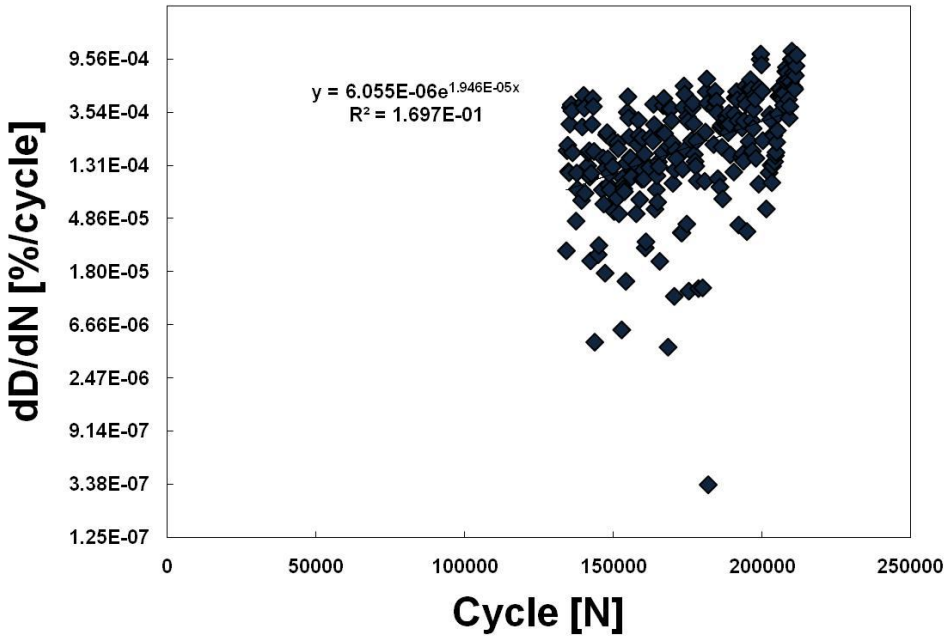

Figure E 70 - Rate of Damage accumulation of 12 month aged σ_1 – specimen 10.

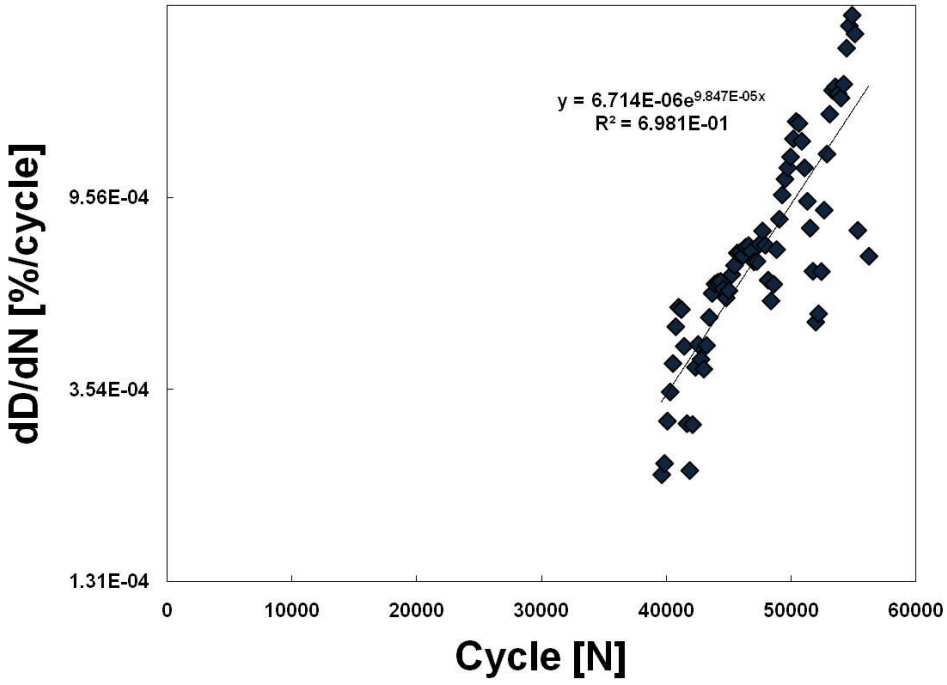

Figure E 71 - Rate of Damage accumulation of 12 month aged σ_2 – specimen 1.

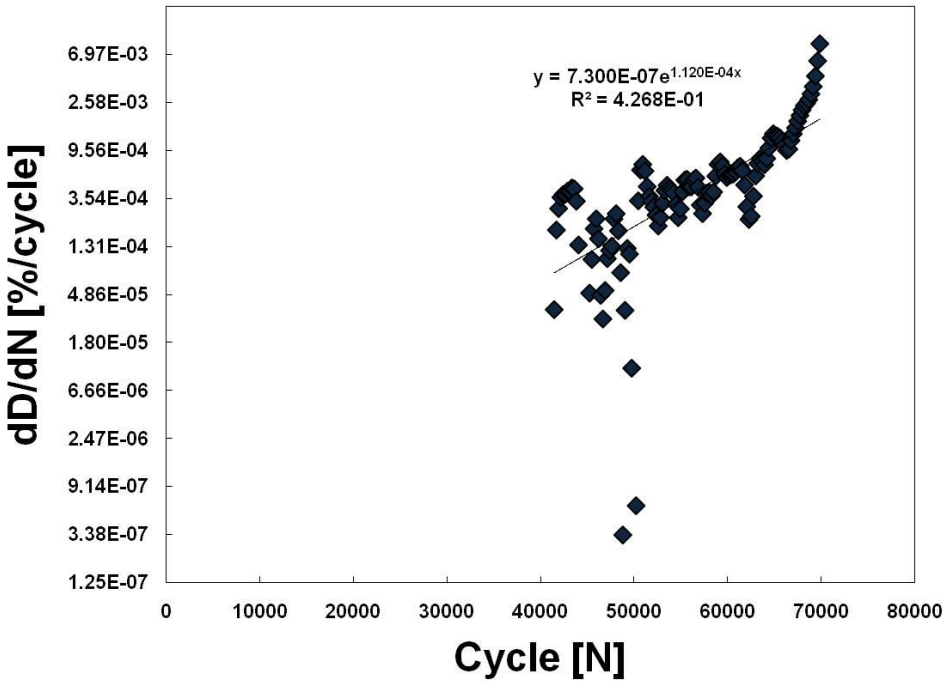

Figure E 72 - Rate of Damage accumulation of 12 month aged σ_2 – specimen 2.

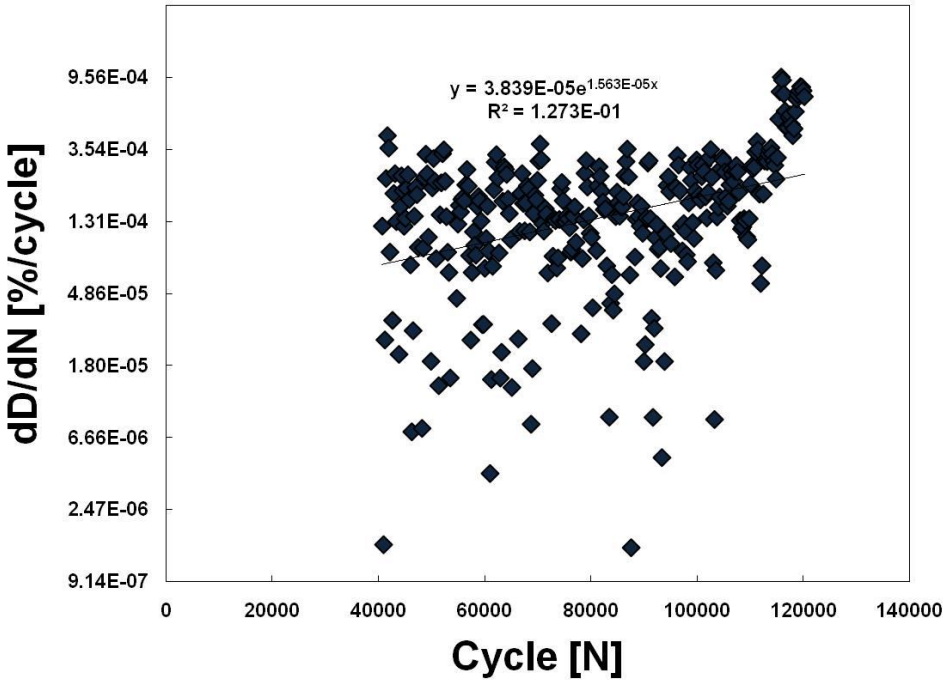

Figure E 73 - Rate of Damage accumulation of 12 month aged σ_2 – specimen 3.

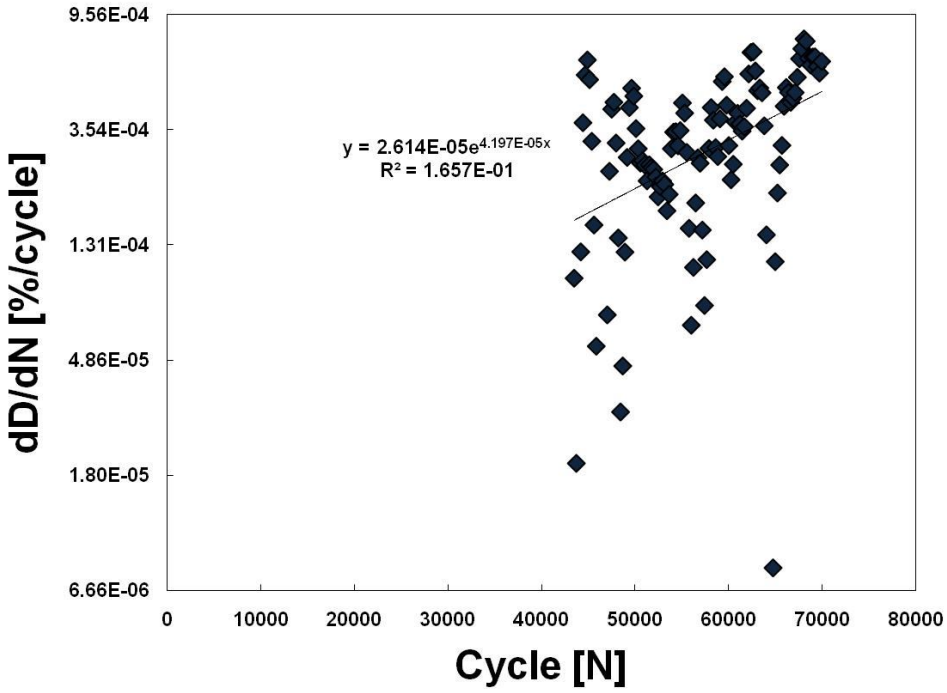

Figure E 74 - Rate of Damage accumulation of 12 month aged σ_2 – specimen 4.

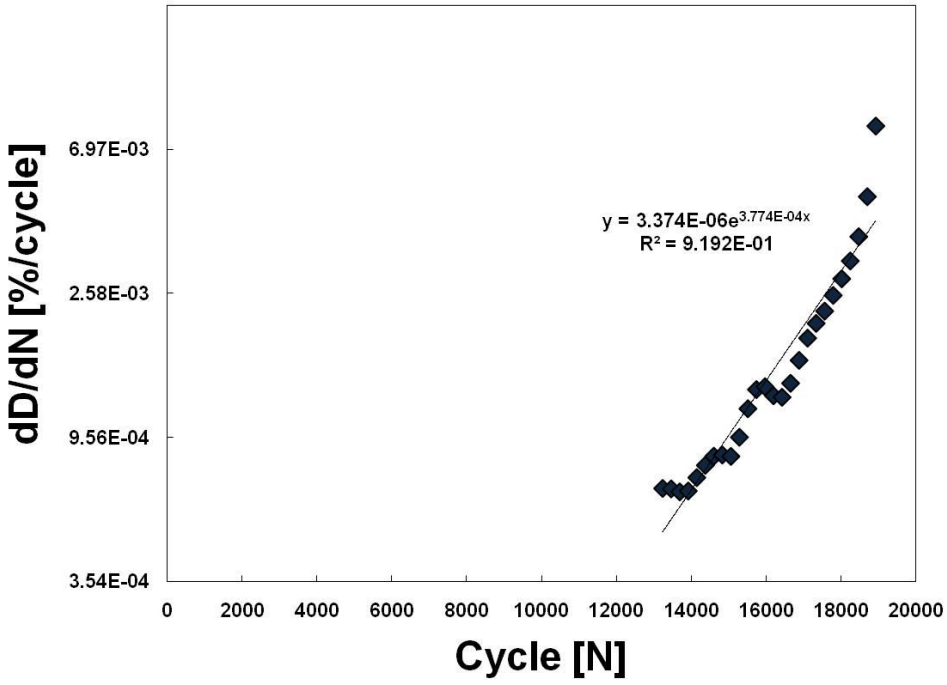

Figure E 75 - Rate of Damage accumulation of 12 month aged σ_2 – specimen 5.

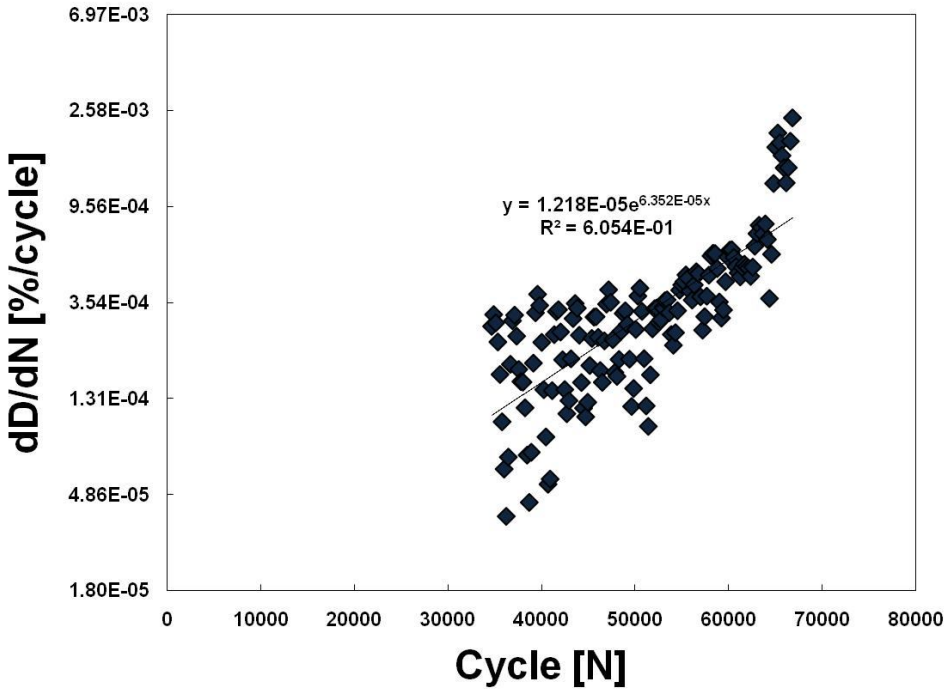

Figure E 76 - Rate of Damage accumulation of 12 month aged σ_2 – specimen 6.

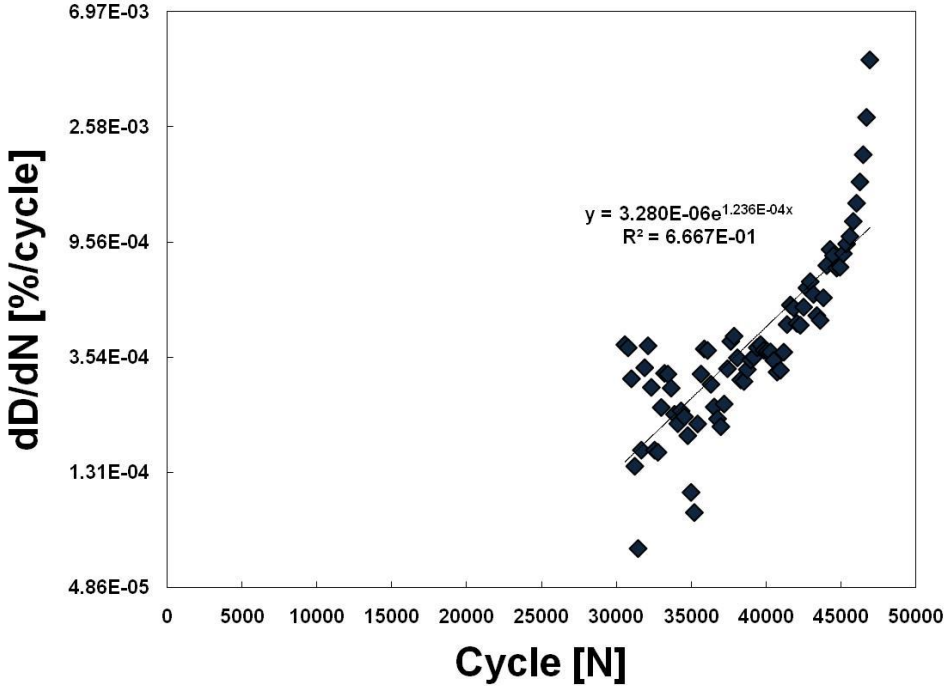

Figure E 77 - Rate of Damage accumulation of 12 month aged σ_2 – specimen 7.

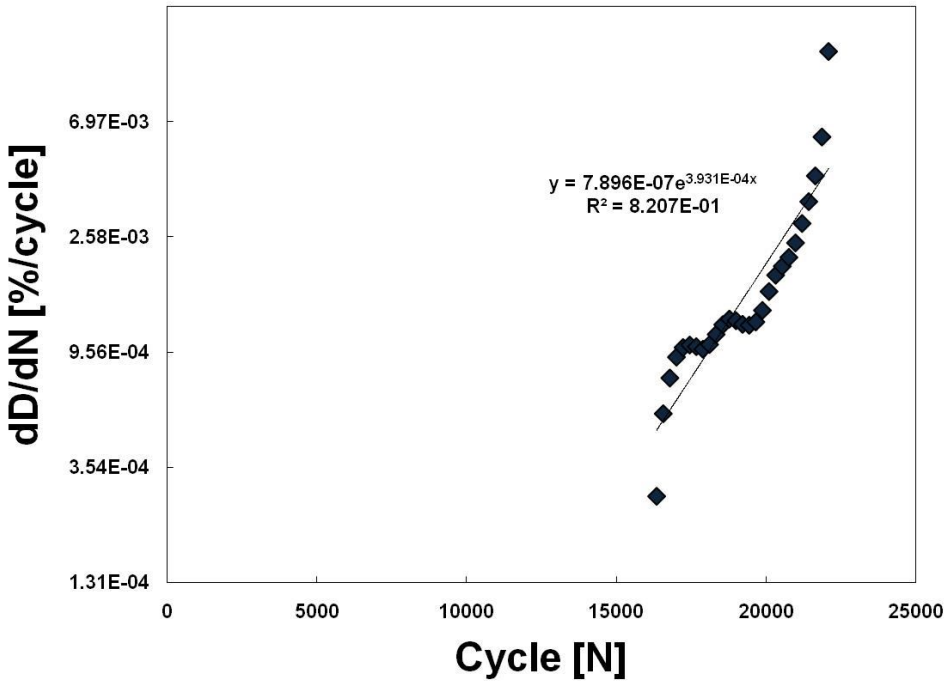

Figure E 78 - Rate of Damage accumulation of 12 month aged σ_2 – specimen 8.

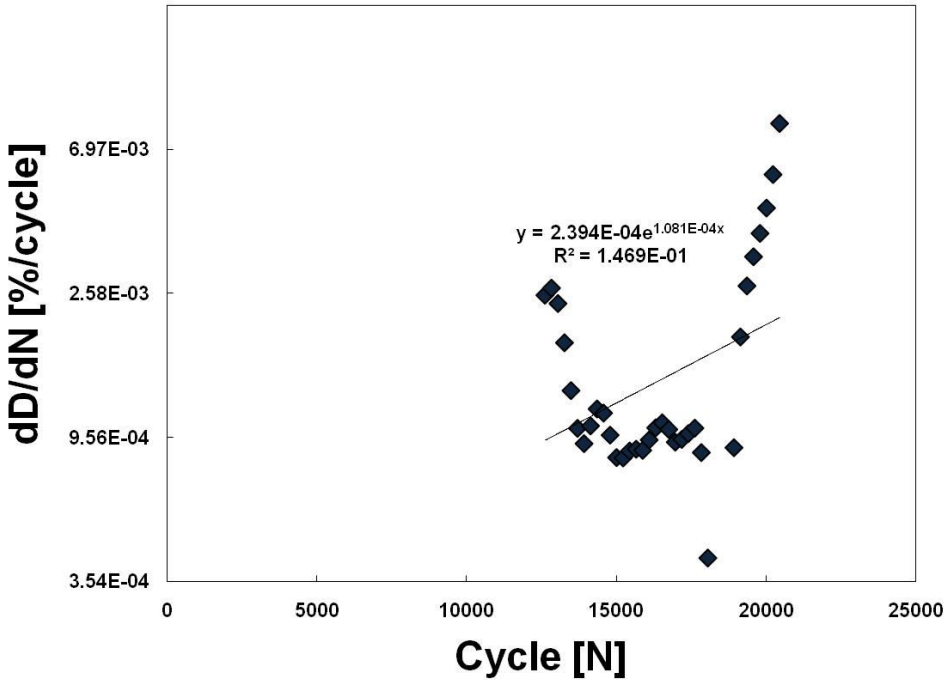

Figure E 79 - Rate of Damage accumulation of 12 month aged σ_2 – specimen 9.

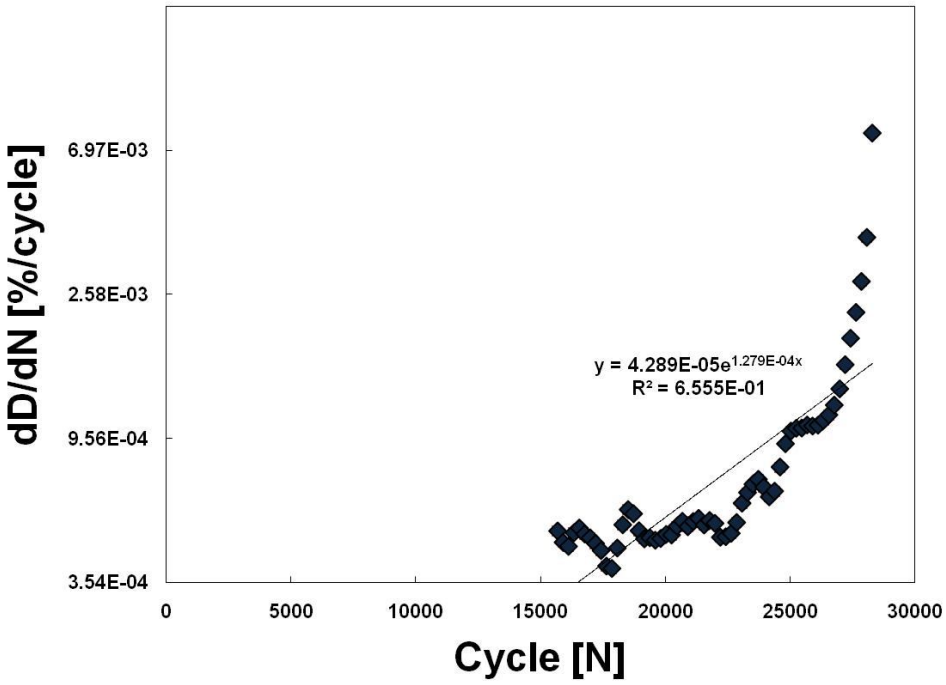

Figure E 80 - Rate of Damage accumulation of 12 month aged σ_2 – specimen 10.

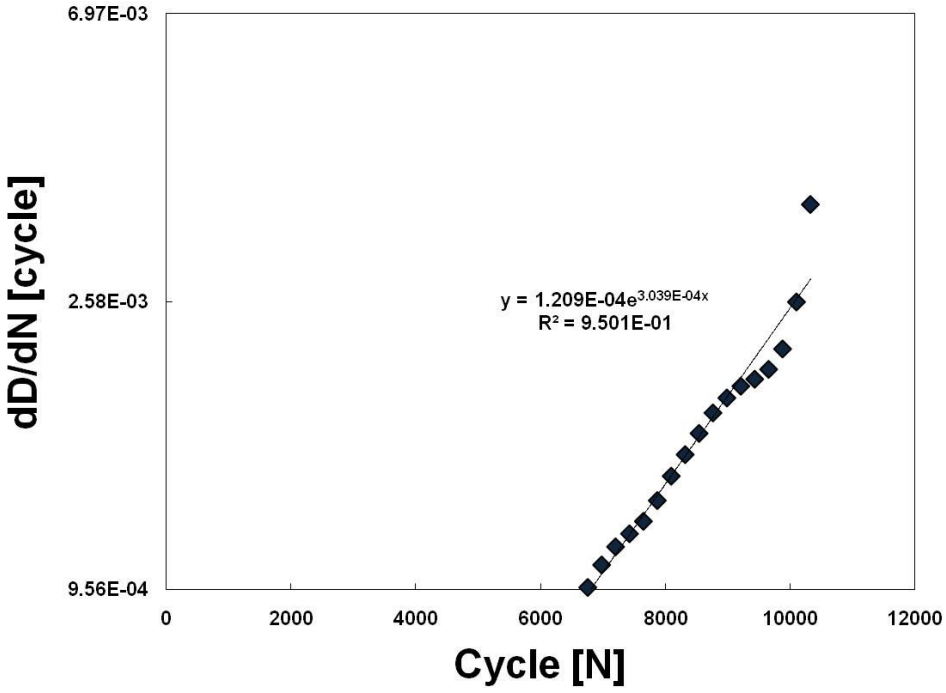

Figure E 81 - Rate of Damage accumulation of 12 month aged σ_3 – specimen 1.

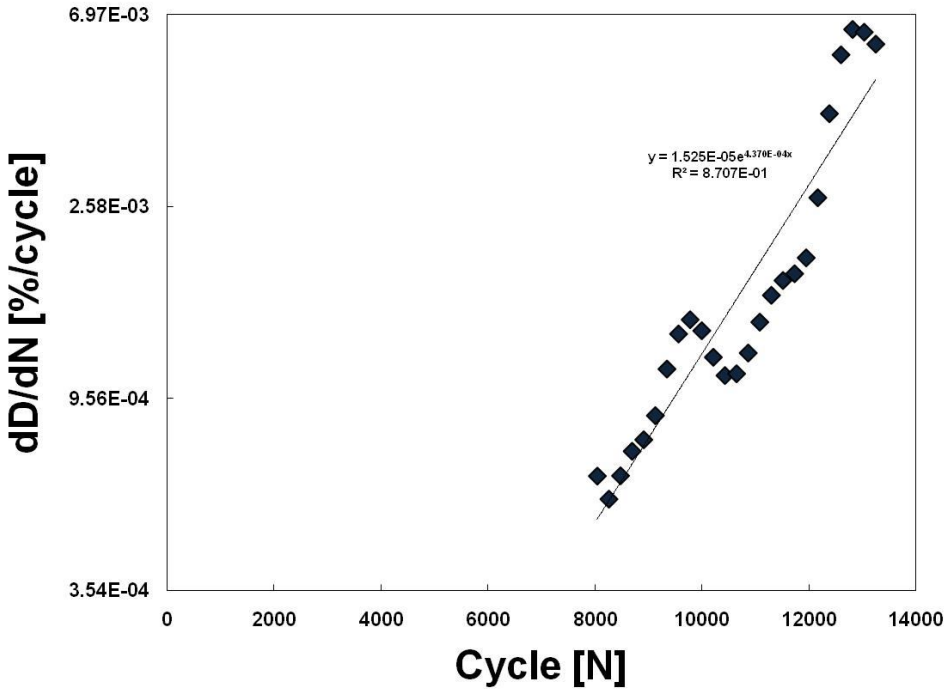

Figure E 82 - Rate of Damage accumulation of 12 month aged σ_3 – specimen 2.

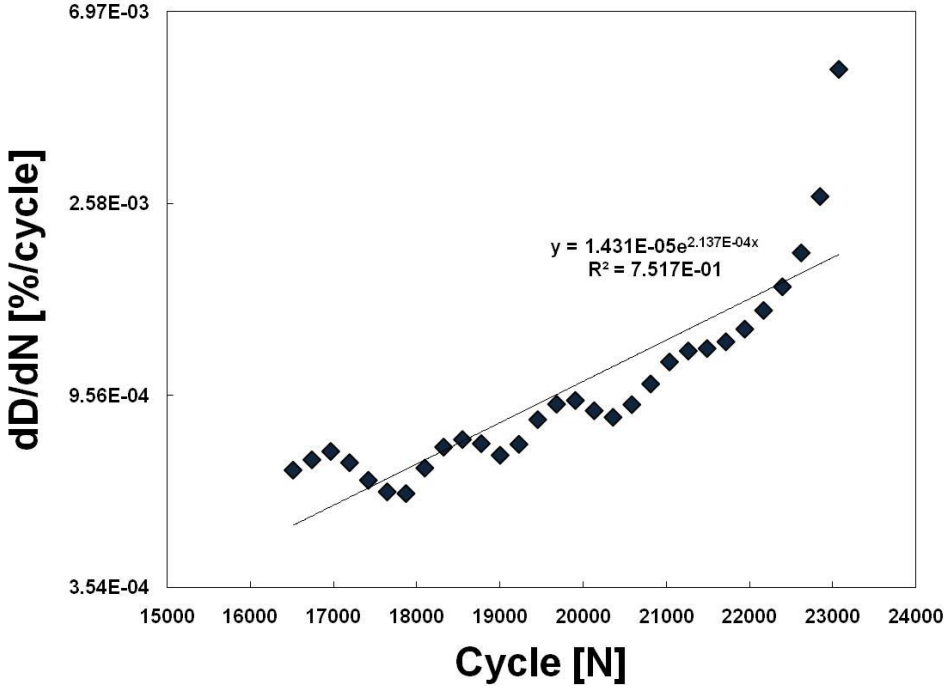

Figure E 83 - Rate of Damage accumulation of 12 month aged σ_3 – specimen 3.

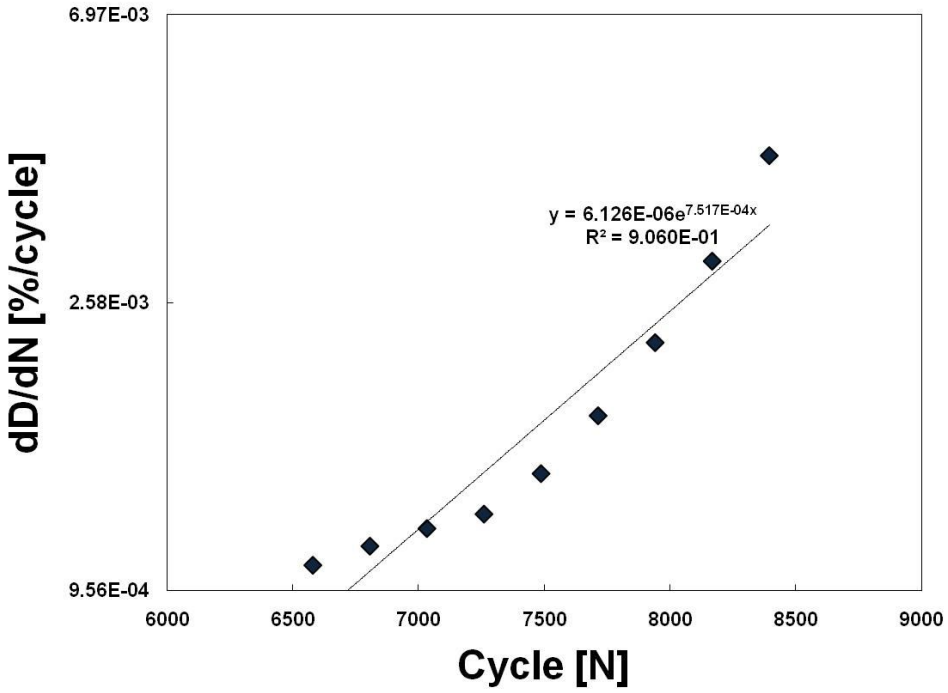

Figure E 84 - Rate of Damage accumulation of 12 month aged σ_3 – specimen 4.

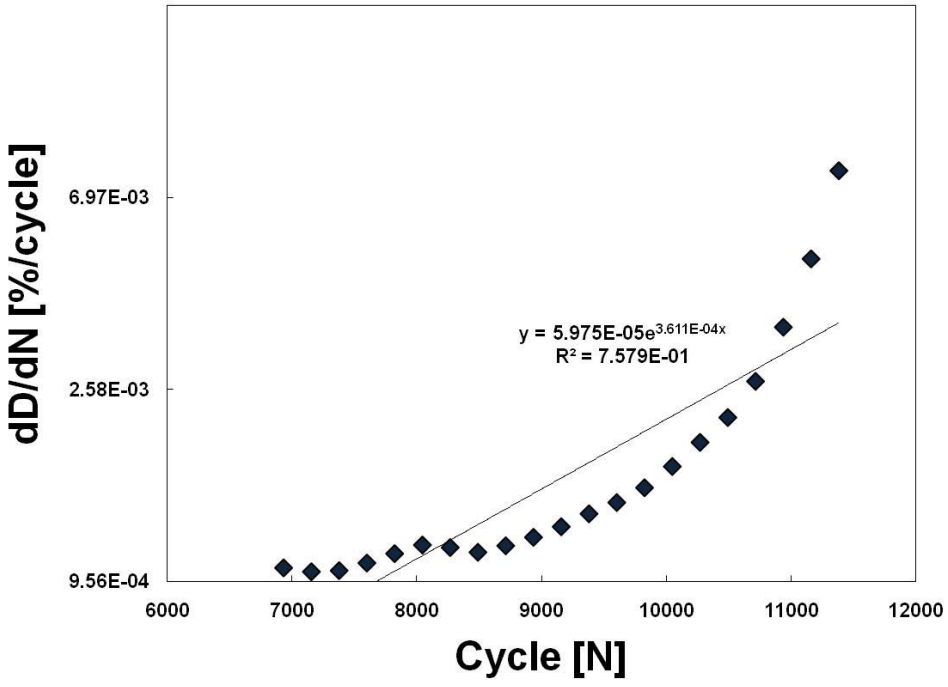

Figure E 85 - Rate of Damage accumulation of 12 month aged σ_3 – specimen 5.

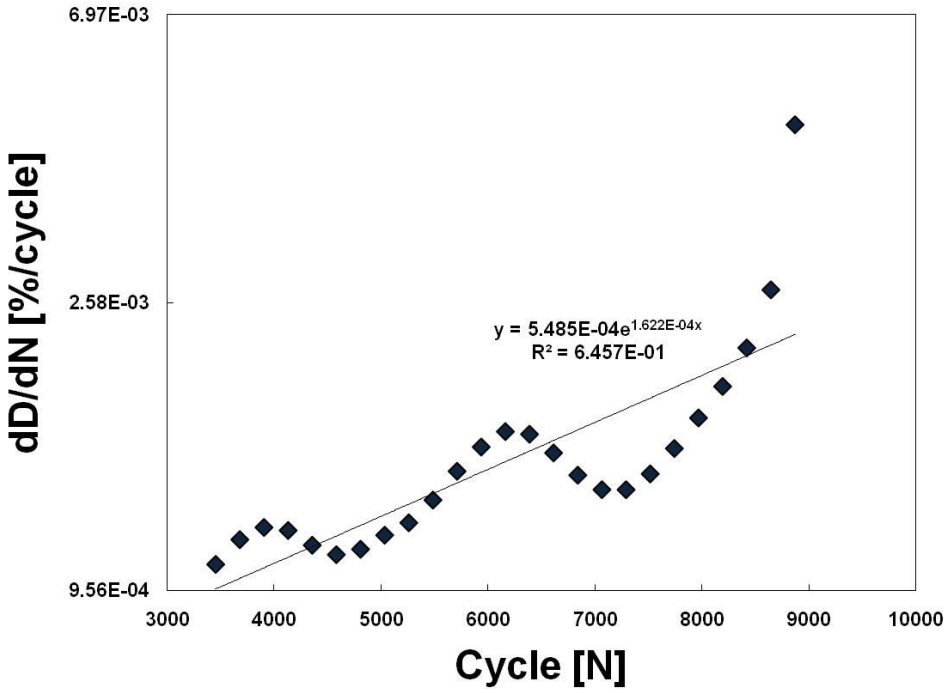

Figure E 86 - Rate of Damage accumulation of 12 month aged σ_3 – specimen 6.

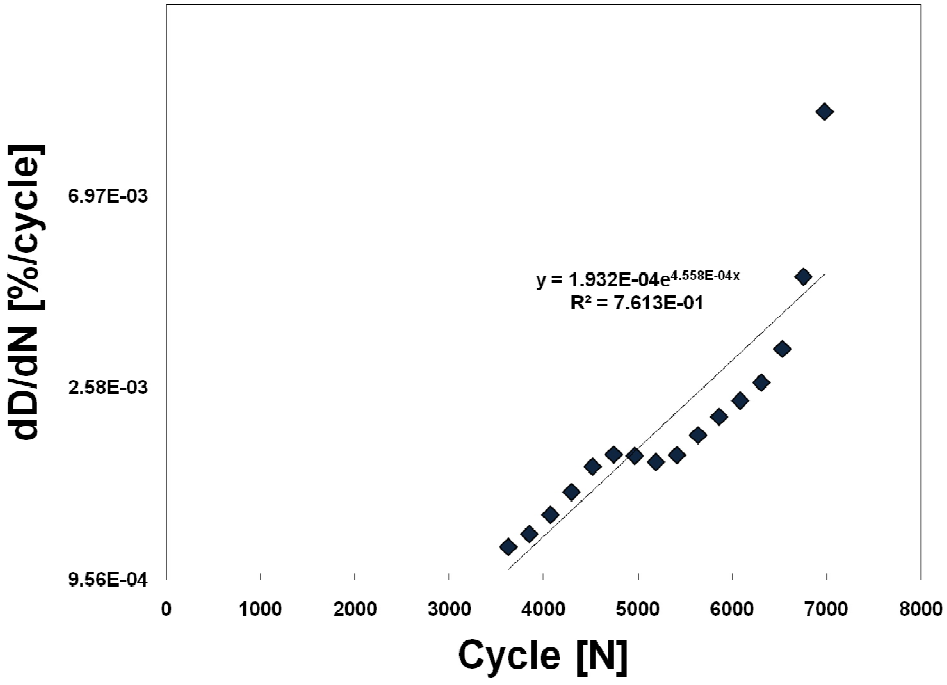

Figure E 87 - Rate of Damage accumulation of 12 month aged σ_3 – specimen 7.

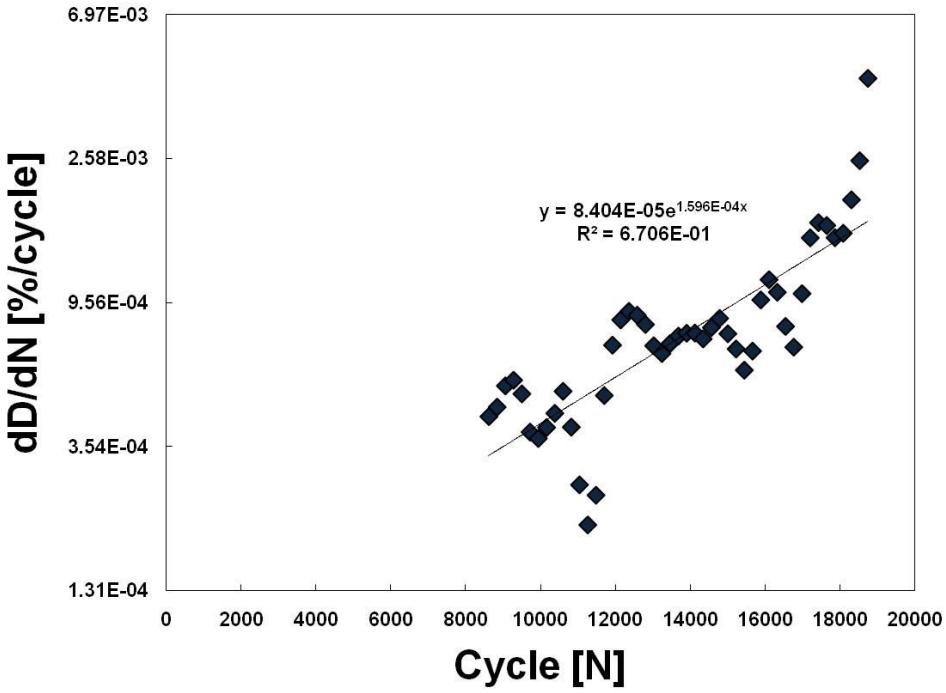

Figure E 88 - Rate of Damage accumulation of 12 month aged σ_3 – specimen 8.

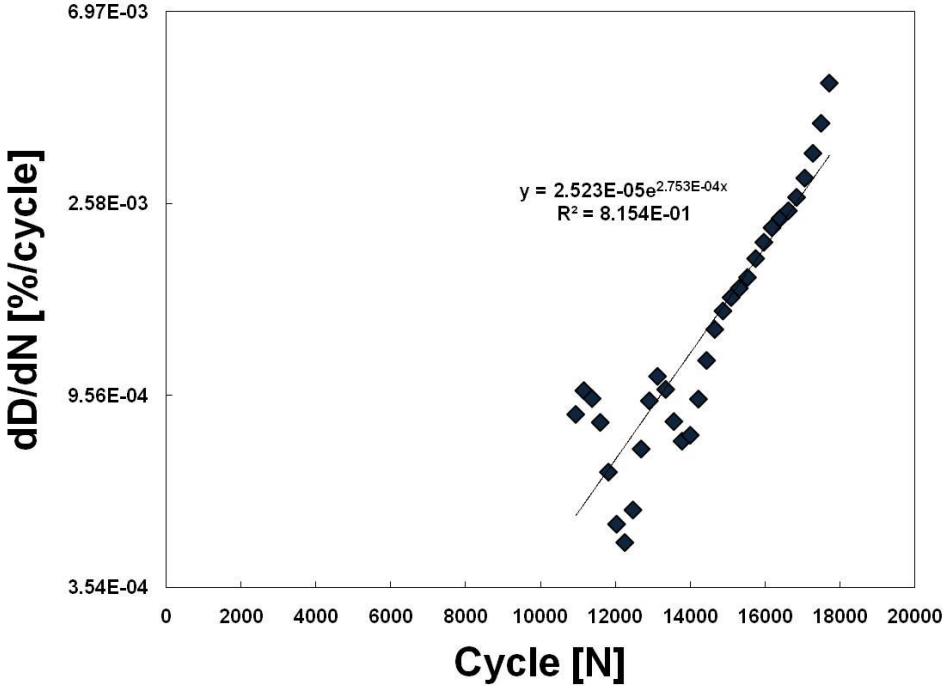

Figure E 89 - Rate of Damage accumulation of 12 month aged σ_3 – specimen 9.

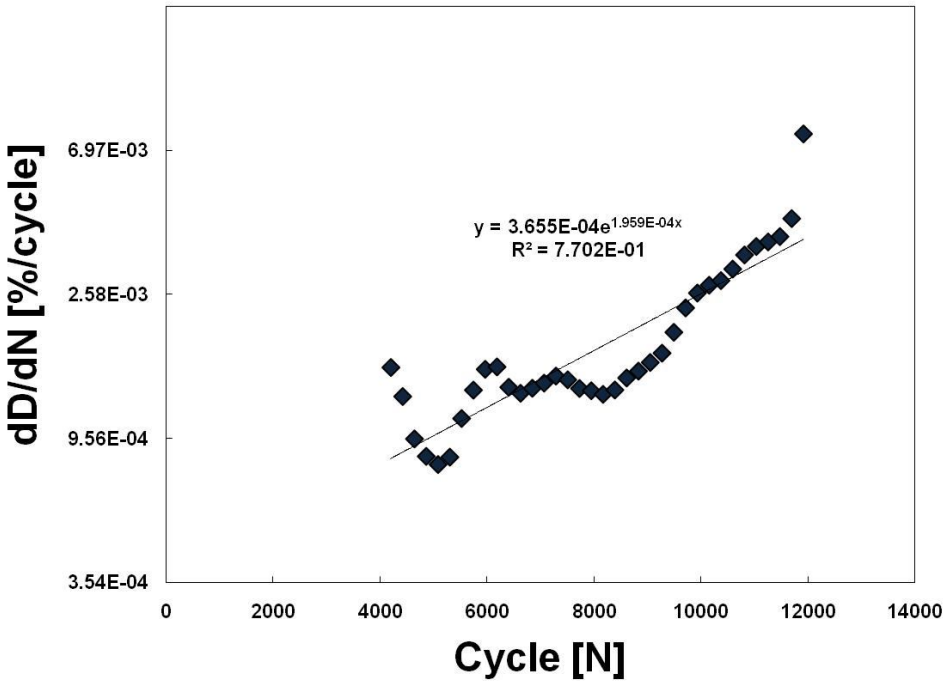

Figure E 90 - Rate of Damage accumulation of 12 month aged σ_3 – specimen 10.